Science and Engineering of Materials

Edited by
Mohd Rafie Johan and Noorsaiyyidah Darman Singho

TRANS TECH PUBLICATIONS

Science and Engineering of Materials

Edited by
Mohd Rafie Johan
Noorsaiyyidah Darman Singho

Science and Engineering of Materials

Selected, peer reviewed papers from the
1st International Conference on
Science & Engineering of Materials 2013
(ICoSEM 2013),
November 13-14, 2013, Kuala Lumpur, Malaysia

Edited by

Mohd Rafie Johan and Noorsaiyyidah Darman Singho

Trans Tech Publications Ltd
Kreuzstrasse 10
CH-8635 Durnten-Zurich
Switzerland
http://www.ttp.net

Volume 970 of
Advanced Materials Research
ISSN print 1022-6680
ISSN cd 1022-6680
ISSN web 1662-8985

Full text available online at *http://www.scientific.net*

***Distributed** worldwide by*

Trans Tech Publications Ltd
Kreuzstrasse 10
CH-8635 Durnten-Zurich
Switzerland

Fax: +41 (44) 922 10 33
e-mail: sales@ttp.net

and in the Americas by

Trans Tech Publications Inc.
PO Box 699, May Street
Enfield, NH 03748
USA

Phone: +1 (603) 632-7377
Fax: +1 (603) 632-5611
e-mail: sales-usa@ttp.net

PREFACE

The 1st International Conference on Science and Engineering of Materials 2013 (ICoSEM2013) was held 13 - 14 November 2013 in Kuala Lumpur, Malaysia. It was organised by Centre of Advanced Materials, Department of Mechanical Engineering, University of Malaya where the main objective of ICoSEM 2013 is to provide a platform for scientists, engineers and user worldwide who are working in different aspects of materials to share their knowledge and innovative thinking. During the conference, capital city of Malaysia was overwhelmed by the presence of more than 200 scientist, engineers, students and vendors from various countries.

4 plenary lectures, 15 talks and 150 oral contributions were delivered in 30 different sessions. The sessions were impressive and have demonstrated a high level of scientific knowledge and originality. In many cases, research ideas and activities have been accomplished or proposed. The same degree of achievement was also accomplished in many of the 50 posters that were displayed during 3 poster sessions. A special thanks goes to all speakers and presenters as well as the session chairpersons, who has chaired the sessions to be right on track, keeping them in time while permitting enriching discussions. In all, the different topics have been well presented and it is fair to be remarked that most all of the session have full participation. Regardless of the topic, the discussion have shown that the field of Materials Science and Engineering is very much active and the community of scientist, engineers and users are continuously pushing their limits and boundary to invent new materials, to improve the existing technique and equipments and thus to further enhance our understanding of these complex materials.

ICoSEM 2013 would not be a success if not for all the support, commitment and dedication that we received. First and foremost, i would like to express my gratitude to the International Advisory Committee and the Scientific Program Committee, whose members have gave us precious inputs and have stand side by side with the organizers throughout the journey. A thousand thanks to our Organizing Committee and the members of the staff, each of which have gave an outstanding contribution and played fundamental role in the conference preparation. The reviewers of the manuscript, those by tradition would remain anonymous, have been very helpful in efficiently reviewing the manuscripts, providing valuable comments well within the time allotted to them. For that, the Editors would like to express our sincere and grateful thanks to all reviewers. We are also very grateful for the cooperation and assistance that we received from the venue's personnel to ensure a smooth and pleasant events.

Finally, our sincere thanks to University of Malaya for providing a seed grant that enabled the initial conference work to take off.

Associate Professor Dr Mohd Rafie Bin Johan
Editor in Chief
ICoSEM2013

COMMITTEES

Chairman	: Prof. A. S. Md Abdul Haseeb
Co-chairman	: Assoc. Prof. Dr. Ibrahim Hendrik Matselaar : Dr. Amalina Muhammad Afifi
Secretary	: Dr. Ang Bee Chin
Treasurer	: Dr. Andri Andriyana : Dr. Wong Yew Hoong
Public Relations	: Dr. Nor Ishida Zainal Abidin : Dr. Mohammad Abul Fazal Md Ismail
Editor	: Assoc. Prof. Dr. Mohd Rafie Johan (Editor-in-chief) : Dr. Ching Yern Chee : Dr. Bui Duc Long : Ahmad Khairulikram Zahari : Nadiah Ghazali : Noorsaiyyidah Darman Singho : Sayang Ernina Erwin Suderman : Siti Nur Hasyimah Razali
Industrial Liaison Consultant	: Dr. Ali Jahanshahi

Table of Contents

Chapter 6: Electronic and Electronic Packaging

Chapter 7: Concrete and Structural Materials

Chapter 8: Material Modeling and Simulations

Chapter 9: Environmentally Sustainable Materials and Processing

Chapter 10: Materials Conversion and Renewable Energy

Chapter 11: Metal and Alloys

Chapter 12: Nanotechnology

Chapter 13: Polymers

CHAPTER 1:

Biomaterials

Advanced Materials Research Vol. 970 (2014) pp 3-6

doi:10.4028/www.scientific.net/AMR.970.3

Biomimetic Porosity of Gelatin-Hydroxyapatite Scaffold for Bone Tissue

M.Normahira[1*], R.K. Raimi[1], M.N.N.Fazli[1], A.R. Norazian[1], H.Adilah[1]

[1]Biomedical Electronics Engineering, School of Mechatronic Engineering,
Universiti Malaysia Perlis , UNIMAP, 02600 Arau, Perlis, Malaysia
[*]corresponding author: normahira@unimap.edu.my

Keywords: Biomimetic, Gelatin/hydroxyapatite, Porosity

Abstract. Biomimetic Porosity of Gelatin/hydroxyapatite (HA) scaffold was fabricated by using solvent casting method and particulate leaching technique. The composite solution were prepared by adding fixed weight percentages of HA (30wt%) with different concentration a gelatin solution (0.25wt%, 0.30wt%, 0.35wt%, 0.40wt% and 0.50wt%) . Five different composites polymers were poured into a mold with size of 15mm x 15mm x 10mm cube and dried in the oven dryer under 60°C to 90°C. After that, the dry composite scaffolds were immersed in the 8% of glutaraldehyde (GA) solution in a few minute for crosslinking process. Porosity of the scaffold is obtained by doing liquid displacement method. Meanwhile, the mechanical properties (Young's Modulus) of the scaffolds are obtained by doing compressive test on the scaffold. Lastly, the microstructure and morphology of the composite scaffolds were observed under Scanning Electron Microscope (SEM). It was found that, when gelatin concentration were increased in the composite scaffold, percentages of liquid adsorption will increase, thus indicate that, the scaffold which has high percentage of liquid adsorption has poor mechanical properties and excellent permeability. Besides, SEM result shows that, the scaffolds have pore size in the range of 3 μm - 22μm. and do not exhibit uniform pores distribution. Pore size of the scaffold depends upon the sizes of the NaCl particles.

Introduction

There are 2 main structure of human bone. Cortical bone is dense, has low surface area and forms a template around the marrow cavity. Cortical bone is harder, stiffer and provides more structural support for organs and joints and the whole body. The porosity of cortical bone is less than 30% [1]. Some research found that cortical bone has porosity about 5 % - 10 %. Trabecular or known as cancellous bone (spongy bone) has lower density and high surface area with porosity about 70% - 95% [2]. In order to produce scaffolds which are compatible with the implanted site in the body, the scaffold should be biocompatible, biodegradable and have same mechanical properties with the implanted site, but, practically, the scaffold only need to be strong enough to allow surgical handling during implantation [3].

Gelatin is biocompatible and has great affinity with hydroxyapatite (HA) [4, 5] and has similarity to collagen. Meanwhile, hydroxyapatite has quite similar component with natural bone and has great biocompatibility. However, due to its brittleness, hydroxyapatite (HA) is not suitable for hard tissue engineering. Hence, porous scaffold composites of hydroxyapatite (HA) and gelatin is expected to improve the criteria for hard tissue application and mimic the natural bones. Gelatin-hydroxyapatite (HA) composite scaffold were prepared by using solvent casting and particulate leaching. It is simple, easy, inexpensive technique and time consuming [6]. By using this method, a porous scaffold with porosity up to 93% and pore diameters up to 500μm will be obtained. The aims of this project is to determine the effect of varying the composition of the gelatin-hydroxyapatite (HA) scaffold on porosity characterization, the morphology and microstructure and mechanical strength of the composites scaffold.

Materials and Experimental Methods

Preparation of GEL/HA composites Scaffold. The dry gelatin powder (purchased from local market) is transformed into a solution state by dissolve it into the distilled water depend on the concentration that acquired in the experiment. In this experiment, 0.25 wt%-0.50 wt% concentration

of sol-GEL were prepared. After that, gelatin solution was stirred for a few minutes under temperature 45°C until 60°C. After gelatin turn to solution state, hydroxyapatite (HA) powder (purchased from Hasrat Bestari Sdn.Bhd) with respective amount was added in the gelatin-distilled water with continued stirring and heating under temperature 60°C until 90°C. After mix gelatin and HA powder together, sodium chloride (NaCI) particulates were introduced into the mixture. The ratio of sodium chloride (NaCl) to gelatin was 5 (NaCl: GEL = 5). Then, the mix poured into the Teflon mold with length of 15 mm, width of 15mm, height of 5mm and thickness of 5mm. The composites were oven dried at temperature of 60°C to 90°C until it fully evaporated. After that, the dry sample immersed into 8% of crosslinking agent, glutareldehyde (GA) for a certain period. Then, the cross linked composites were leaving in distilled water to remove the GA residues and to dissolve the salt. Lastly, the samples were dried at room temperature for 24 hours.

Scanning Electron Microscopy analysis (SEM). In this experiment, SEM is used to observe the microstructure of the scaffold. The morphology and microstructure of each sample were observed by using SEM tabletop microscope (Hitachi TM3000) at maximum excitation voltage, 15 kV at different value of magnifications which are varies from 1000 to 5000.

Measurements of porosity. A liquid displacement method was used to measure the porosity of each sample [7]. In this method, ethanol is used instead of water because ethanol can easily penetrated into the pores of the scaffold and will not lead to shrinkage or swelling of non-solvent of the polymers [8]. By doing porosity measurement, the information about permeability of the sample can be obtained. Porosity of the scaffold can be determined by calculating the percentage of water adsorption of the scaffold [9]. A scaffold of weight Wd was immersed in the petri dish containing fixed volume of ethanol solution for a few minutes until no bubble emerged from the scaffold indicating that the ethanol is fully forced into the scaffold [10]. Then, the total weight and ethanol was then recorded as Ws, was weighed. Finally, the scaffold was removed from the ethanol and wet scaffold was weighed as Ww. The percentage of water adsorption was calculated using the following equation (Eq.1):

$$Wads = [(Ww-Wd)/ (Ww - W_s)] \times 100\% \quad (1)$$

Mechanical properties. The Young's modulus of the scaffold was determined by using Instron materials testing machine with cross-head of 1 mm/min with 1kN load cell. The average size of each sample is about 15 mm x15 mm x 10 mm cubes.

Results and Discussion

Porosity. The porosity characterization is based on the liquid adsorption which is related to permeability of porous structure. Percentages of liquid adsorption can indicate the porosity of the scaffold. Liquid adsorption increased from 91% to 98% depending on the amount of NaCl in the composite scaffold. Each sample with different amount of NaCl had liquid adsorption of 91%, 95%, 94%, 97% and 98% respectively. Moreover, the addition of NaCl amount results in higher liquid adsorption, therefore the addition of NaCl amount can increase the porosity as well as permeability of the scaffold.

Scanning Electron Microscope (SEM). The open pores existed in the scaffold is controlled by the amount of porogen agent used. By using SEM, pores can be observed at the surface of the scaffold and their sizes ranged from 3µm - 22µm Besides, the images of HA/GEL scaffold of each sample as shown in Fig. 1, observed that, the pores of all composites scaffolds fabricated in this experiment are irregular and interconnected. This information prove that, by using particulate leaching method in scaffold fabrication the pores size and structure is controlled by the amount, shape and size of the porogen agent [11].

Mechanical Properties. Compressive test has been chosen since it has been accepted widely for the characterization of porous scaffold [5]. The load is applied on the sample until the sample cracked. The Young's modulus of the scaffold is determined by the slope of the initial linear portion of stress-strain graph. Young's Modulus of composites scaffold is decrease gradually i.e. 0.25wt%, 0.30wt%, 0.35wt%, 0.40wt% and 0.50wt% of gelatin contents composites had Young's Modulus of 28.45 MPa, 33.24 MPa, 27.70 MPa, 24.54 MPa and 21.33 MPa, respectively. The strength of scaffold is depends on the porosity. As the porosity increase, the strength of scaffold is lower. Hence, the composites scaffold with higher porosity will become weaker.

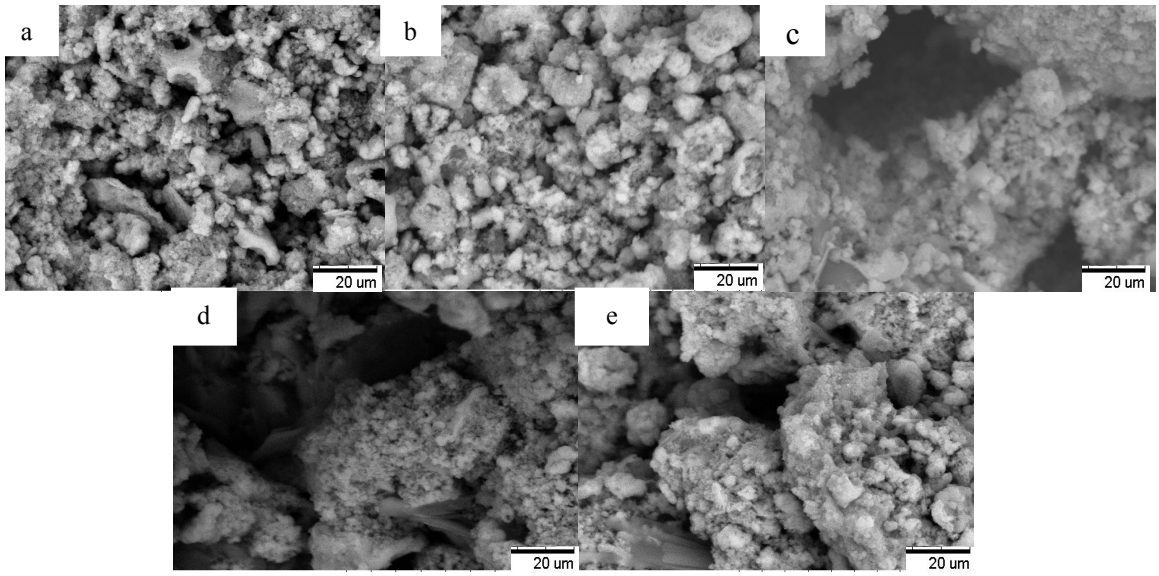

Fig.1 Morphology and microstructure of scaffold with different concentration a gelatin solution, a) 0.25wt%, b) 0.30wt%, c) 0.35wt%, d) 0.40wt% and e) 0.50wt% (under 3000 magnification)

Conclusions

In this project, GEL/HA scaffolds were fabricated through solvent casting and particulate leaching technique. This method is simple and can save the cost of experiment. This method also widely used to fabricate scaffold and used to create the pores on the scaffold. However, by using this technique, the pore shapes and sizes cannot be controlled. The scaffolds produced in this project, generally have high percentages of liquid adsorption as well as porosity and exhibit great permeability which is suitable for exchange of nutrition and interconnection. Osteoblast of human's bone cells only can pass through into pores greater than 20μm and porosity greater than 30% [10].

The porosity was found to increase from 91% to 98% depending on the amount of NaCl. The porosity of the composites scaffolds prepared in this experiment was sufficient for exchange of nutrition as well as interconnection of nutrition. However, the pores sizes generate in this experiment is beyond expectation. The pores are too small, about 3μm - 22μm, thus not suitable for development of bone cells. Hence, we should develop a composites scaffold with suitable pores for osteoblast penetration. In addition, the mechanical strength of scaffold is decrease gradually as porosity increase. The Young's Modulus of 21.33 MPa to 33.24 MPa were achieved which are comparable to human trabecular bone in specific anatomic location such as proximal tibia with Young's Modulus of 10 – 500 MPa, distal femur with Young's Modulus of 7.6 – 800 MPa, vertebral bodies with Young's Modulus of 10 – 428 MPa, calcaneus with Young's Modulus of 0.34 - 10.34 MPa, humerus and distal radius with Young's Modulus of 1.1 – 448 MPa [11]. Generall, eventhough the scaffold is not preferable for cells growth and osteoblast penetration, these 5 samples show the correllation between porosity and mechanical strength which is the strength of scaffold is depends on the porosity.

References

[1] McCalden, R. W., McGeough, J. A., Barker, M. B., and Court-Brown, C. M., Age-related changes in the tensile properties of cortical bone: The relative importance of changes in porosity, mineralization, and microstructure, J. Bone Joint Surg. 75A(8) (1993) 1193–1205.

[2] U.Vidyarthi, P. Zhdan, C. Gravanis,C.Lekakau. Gelatin-Hydroxyapatite Nanocomposites for Orthopedic Applications, 2007.

[3] O'Brien F., Biomaterials and scaffold for tissue engineering. Materials Today, 14(3) (2011).

[4] Jaya Sundaram, Timothy D. Durance, & Rhizi wang, Porous scaffold of gelatin-starch with nanohydroxyapatite composite processed via novel microwave vacuum drying. Acta BIOMATERIALIA (2008).

[5] Mehdi Kazemzadeh Narbat, Fariba Orang, Mehran Solati hashtjin, & Azadeh Goudarzi, Fabrication of Porous Hydroxyapatite-Gelatin Composite Scaffold for Bone Tissue Engineering. Iranian Biomedical Journal 10 (4) (2006) 215-233.

[6] Information on .<http://www.tankonyvtar.hu/hu/tartalom/tamop425/0011_1A_3D_en_book/ch01s05.html>

[7] Yang, Y., Degradation behaviours of nerve guidance conduits made up of silk fibroin in vitro and in vivo. Polymer Degradation and Stability (2009).

[8] Jianjun Guan,Kazuro L. Fujimoto,Michael S. Sacks and William R. Wagner, Preparation and characterization of highly porous, biodegradable polyurethane scaffolds for soft tissue applications. US National Library of Medicine (2005) 3961–3971.

[9] Y.S.Morsi, Virtual Prototyping of Biomanufacturing in Medical Applications. Virtual Prototyping & Bio Manufacturing in Medical Applications (2008).

[10] Plikk, P. Målberg, S. & Albertsson A. C., Design of resorbable porous tubular copolyester scaffolds for use in nerve regeneration. Biomacromolecules , 10(5) (2009) 1259-64.

[11] S.A. Goldstein, The Mechanical Properties of Trabecular Bone Dependence on Anatomic Location and Function. Journal of Biomechanics (1987).

Advanced Materials Research Vol. 970 (2014) pp 7-11

doi:10.4028/www.scientific.net/AMR.970.7

REMOVAL OF Pb(II) BY CS_2 MODIFIED KENAF POWDER

S.R. Zakaria[1,a*], M.A.K.M. Hanafiah[1,b], S.N.M. Khazaai[1,c] , Z.M. Hussin[1,d], W.K.A.W.M. Khalir[1,e], M.Ismail[1,f]

[1]Faculty of Applied Sciences, Universiti Teknologi MARA Pahang, 26400, Jengka, Malaysia.

[a*]sitiraihan@pahang.uitm.edu.my, [b]makmh@ pahang.uitm.edu.my,
[c]ctnorhafiza@ pahang.uitm.edu.my, [d]zurhana_mhussin@pahang.uitm.edu.my,
[e]khaima@pahang.uitm.edu.my, [f]marismael@pahang.uitm.edu.my

Keywords: characterization, isotherm, kenaf, kinetic, xanthation.

Abstract. Kenaf (*Hibiscus cannabinus*) is a hardy crop that has wide industrial applications such as insulator, paper, carpet padding, bedding and a good adsorbent for oil. This study investigated the ability of carbon disulfide (CS_2) modified kenaf (CMK) to remove toxic Pb(II) from waste water. Adsorbent characterization was carried out by Field Emission Scanning Electron Microscope and Energy Dispersive X-ray Spectroscope (FESEM-EDX) analysis. The adsorption kinetic data was well described by pseudo-second-order model and the adsorption isotherm study indicated that Langmuir model fitted well with the experimental data than the Freundlich model. Based on the Langmuir model, the maximum adsorption capacities of Pb(II) (q_{max}) was 63.3 mg g^{-1}. This study suggested that CMK has a good potential to be used as an adsorbent material for Pb(II) removal from aqueous solutions.

Introduction

Mercury, nickel, lead, arsenic, cadmium, aluminum and copper are examples of heavy metals which are very stable element and cannot undergo disintegration by body. These metals can be introduced into water supply by anthropogenic sources such as industrial and consumer waster, landfill leachate and wastes dumping [1]. Heavy metals can enter our bodies by various ways such as respiration, eating food and drinking water and they tend to bio accumulate. Therefore, dismissal of heavy metal is important and gain more advantages with the uses of low cost agricultural wastes. The alternative method which fulfills the demand is biosorbents (naturally abundant or dead biomass) [2]. It becomes the potential method of removal because of the cheap materials, availability, ease of operation with high affinity and capacity [3]. Plant materials consist numerous functional groups like carboxyl, hydroxyl, sulfate, phosphate, ether, amino group, lignin and cellulose which capable of binding heavy metal ions [4].

There are many chemicals used in treatment or modifications methods in order to maximize the metal adsorption capacity which include basic solution , mineral and organic acid solutions , oxidizing agents and organic compounds. Modification of adsorbents by using xanthates appeared as another alternatives treatment in enhancing the performance of heavy metal adsorption. The work conducted using cross linked xanthated chitosan (CMC) as an adsorbent for decontamination of lead ions has been reported that the adsorption capacity of modified chitosan flakes with xanthate was higher three times compared to the unmodified chitosan flakes[5].

In this study, the usefulness of CS_2 modified kenaf (CMK) to remove Pb(II) has been investigated. The main objectives of this study were to characterize CMK by spectroscopic analysis, to determine the adsorption capacity and to determine the rate of adsorption.

Materials and Methods

Chemically Modified of Adsorbent. Kenaf fiber powder (40 mesh) was obtained from a kenaf plantation in Kelantan, Malaysia. For modification, 15 g of kenaf powder was mixed with 200 mL (4.0 M) NaOH in a conical flask. The mixture was stirred for 2 h at room temperature (25.0 ± 0.5^{o}C). After 2 h, 10 mL CS_2 was added into the mixture and stirred again for another 2 h. The mixture then was allowed to settle for 30 min before extensively washed with 200 mL deionized

water for 20 times to remove excess base. Finally, the xanthated rubber leaf powder was dried in an oven at 50°C for 24 h and CS_2 modified kenaf fiber powder was designated as CMK.

Batch Pb(II) Adsorption Experiments. The adsorption of Pb(II) could be affected by initial Pb(II) concentration and contact time. Three different initial Pb(II) concentrations (10, 20 and 40 mg/L) were used to study the effect of initial Pb(II) concentration. The mixture of Pb(II) solution and adsorbent was stirred at 400 rpm and at various contact times from 0 to 120 min. The pH of solution was fixed at 4. Isotherm study was investigated by varying Pb(II) concentrations (10 to 150 mg/L) and mixed with 0.02 g CMK. The mixture was stirred for 120 min to ensure the equilibrium time was achieved. After adsorption, the mixture was filtered and the filtrate containing Pb(II) was analyzed by using Atomic Absorption Spectrometer (Perkin Elmer, AAS Pinacle 100, USA). Surface morphology and elemental characteristics of CMK was observed with Field Emission Scanning Electron Microscope (FESEM) and Energy Dispersive X-ray Spectrometer (EDX) (Joel, JSM7800F model, Japan). The CMK was coated with platinum to increase electric conduction and to improve the quality of FESEM image.

Results and Discussion

FESEM-EDX analysis. The surface morphology of CMK before and after Pb(II) adsorption is shown by FESEM images in Figure 1. FESEM images showed rough and uneven surface of CMK. The EDX spectrum of CMK before Pb(II) adsorption showed the presence of Na and S peak at 1.1 and 2.35keV, respectively. These peaks were observed in EDX spectrum due to xanthation process which involved the treatment with NaOH followed by CS_2. The FESEM-EDX analysis confirmed the attachment of sulfur groups on the CMK surface. The EDX spectrum of CMK after Pb(II) adsorption showed that the presence of Pb peaks at 1.9, 2.7 and 9.2keV. The appearance of Pb peaks confirmed the attachment of Pb on CMK surface. The disappearance of Na peaks in EDX spectrum of CMK after Pb(II) adsorption suggested that adsorption process involved ion exchange mechanism.

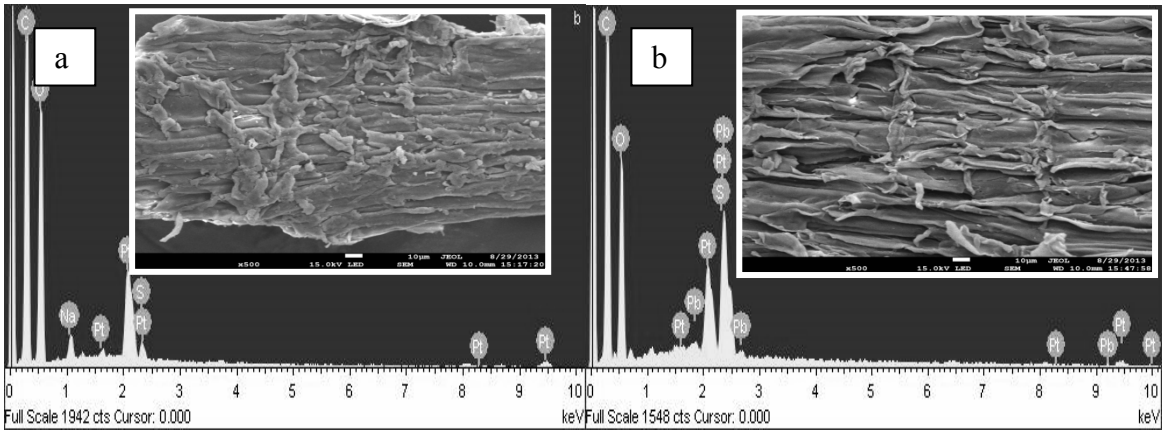

Figure 1: FESEM images (500x magnification) (inset) and EDX spectra of CMK (a) before Pb(II) adsorption and (b) after Pb(II) adsorption.

Effect of Initial Concentration and Contact Time. The amount of Pb(II) adsorbed increased when the initial concentration and adsorption time increased (Fig. 2). The plots showed that the equilibrium time was dependent on the initial concentration. Equilibrium time for 10 mg/L was achieved in less than 10 min and for 20 and 40 mg/L the equilibrium time took a slight longer time. The stage of rapid adsorption in the first 3 min showed that the adsorption occur very fast because there was a lot of available adsorption sites on CMK. Beyond 3 min, the adsorption rate slowly decreased as most of the adsorption sites were occupied by Pb(II). Increasing Pb(II) initial concentration increased the amount of Pb(II) adsorbed because higher concentration provides

higher driving force that accelerates the diffusion of Pb(II) onto the adsorbent surface. This force was able to overcome the mass transfer resistance between Pb(II) and CMK surface.

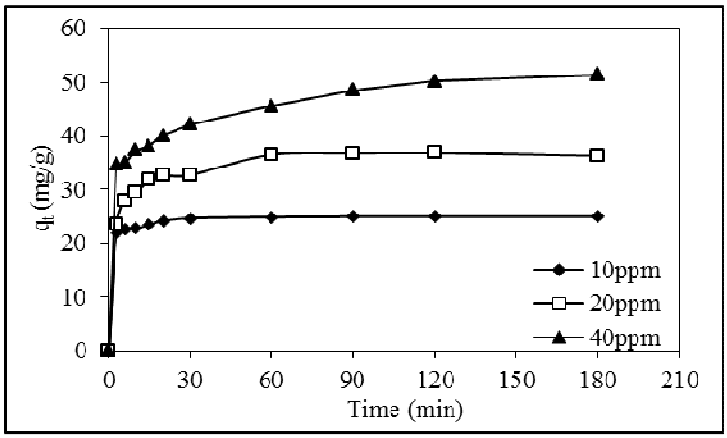

Figure 2 : Effect of initial concentration and contact time on the adsorption of Pb(II) by CMK.

Adsorption Kinetic. Kinetic study for adsorption of Pb(II) onto CMK surface was done by using pseudo-first-order and pseudo-second-order model as given by equations (1) and (2) below:

$$\log(q_e - q_t) = \log q_e - \frac{K_1}{2.303} t \quad (1)$$

$$\frac{t}{q_t} = \frac{1}{h} + \frac{1}{q_e} t \quad (2)$$

where q_t (mg g^{-1}) is the the amount of Pb(II) adsorbed at time t and q_e (mg g^{-1}) at equilibrium. K_1 (min^{-1}) h mg $(g.min)^{-1}$ are the pseudo-first-order rate constant and the initial adsorption rate in pseudo-second-order equation and can be calculated as $h=K_2qe^2$. K_2 (g(mg.min)) is the pseudo-second-order rate constant. Plots for both models (plots not shown) are linear with R^2 close to unity. Calculated adsorption capacity ($q_{e,cal}$) of pseudo-second-order model showed values close to the experimental value ($q_{e,exp}$) as tabulated in Table 1. From the kinetic model, it showed that the adsorption process followed pseudo-second-order model, which suggested that chemical adsorption as a rate determining step for Pb(II) adsorption [6].

Table 1: Kinetic model parameter for adsorption of Pb(II) onto CMK.

[Pb] mg L^{-1}		Pseudo- first-order			Pseudo-second-order			
	$q_{e,\,exp}$ mg g^{-1}	$q_{e,\,cal}$ (mg g^{-1})	K_1 (min^{-1})	R^2	h (mg (g.min) $^{-1}$)	K_2 (min^{-1})	$q_{e,\,cal}$ (mg g^{-1})	R^2
10	25.00	4.65	0.095	0.965	42.735	0.068	25.13	1.000
20	36.23	11.40	0.048	0.827	20.619	0.015	36.90	1.000
40	51.38	18.23	0.023	0.985	12.346	0.005	51.81	0.998

Adsorption Isotherm. The Langmuir isotherm model was used to describe the maximum adsorption capacity between CMK and Pb(II) concentration in the solution at equilibrium conditions. The linear form of Langmuir equation is given as:

$$\frac{C_e}{q_e} = \frac{1}{q_{max} b} + \frac{C_e}{q_{max}} \quad (3)$$

where C_e is the equilibrium Pb(II) concentration (mg L^{-1}), q_e is the amount of Pb(II) adsorbed at equilibrium (mg g^{-1}), q_{max} is the adsorption capacity (mg g^{-1}) and b is a constant (L mg^{-1}). The value of b reflects the binding strength between Pb(II) and CMK.

The values of q_{max}, b and correlation coefficient (R^2) for CMK are shown in Table 2. The high correlation coefficient ($R^2 \approx 0.99$) indicated the adsorption process occurred at specific homogeneous sites.

Table 2 : Langmuir parameters for adsorption of Pb (II) onto CMK at 302 K.

Langmuir			
q_{max} (mg g^{-1})	b (L mg^{-1})	R^2	$q_{e, exp}$ (mg g^{-1})
63.30	0.33	0.998	62.50

Values of q_{max} for a few plant wastes as adsorbents are represented in the Table 3. The adsorption capacity of CMK is higher than other plant species. Therefore, CMK has a potential as new adsorbent for the removal of Pb(II) in the solution.

Table 3 : Comparison of maximum adsorption capacity of Pb(II) by plant wastes as adsorbents.

Adsorbent	Modification	q_{max} (mg g^{-1})	Reference
CMK	CS_2	63.3	This study
Rubber leaf powder	Untreated	46.7	[7]
Wood sawdust	Thiol-Functionalized	43.1	[8]
Pine cone powder	Potassium hydroxide	32.3	[9]
Peanut hull hydrochar	Hydrogen peroxide	22.8	[10]
Corncorbs	Methanol and Hydrochloric acid	7.9	[11]

Conclusion

Chemical treatment was successfully done on CMK as sulphur peaks appeared on CMK surface as shown by the FESEM-EDX analysis. The study showed the adsorption kinetic data was more accurately represented by the pseudo-second-order model. The maximum adsorption capacity (q_{max}) calculated was 63.3 mg g^{-1}. The high amount of Pb(II) adsorbed suggests the good potential of CMK powder to be used as an adsorbent for Pb(II) removal in wastewater treatment process.

Acknowledgement

This investigation was supported by the Excellence Fund of Universiti Teknologi MARA (Project No. 011000110024).

References

[1] Z. Hamzah, A. Saat, A. K. Wood, Z. A. Bakar, A. S. Area, Sedimentation , Heavy Metals Profiles and Cluster Analysis of a Former Tin Mining Lake, Int. J. Environ. Technol. Manage. 2 (2011) 448-453.

[2] B. Pejic, M. Vukcevic, M. Kostic, P. Skundric, Biosorption of heavy metal ions from aqueous solutions by short hemp fibers: Effect of chemical composition, J. Hazard. Mater. 164 (2009) 146–153.

[3] A. Demirbas, Heavy metal adsorption onto agro-based waste materials : A review, J. Hazard. Mater. 157 (2008) 220–229.

[4] W. S. W. Ngah, M. A. K. M. Hanafiah, Adsorption of copper on rubber (*Hevea brasiliensis*) leaf powder : Kinetic, equilibrium and thermodynamic studies, J. Environ. Sci. 1 (2008a) 521–530.

[5] D.Chauhan and N. Sankararamakrishnan (2008). "Highly enhanced adsorption for decontamination of lead ions from battery wastewaters using chitosan functionalized with xanthate." Bioresource Technology 99(18): 9021-9024.

[6] W. S. W. Ngah and M. A. K. M. Hanafiah, Biosorption of copper ions from dilute aqueous solutions on base treated rubber (*Hevea brasiliensis*) leaves powder : kinetics, isotherm and biosorption mechanisms, J. Environ. Sci. 20 (2008b) 1168–1176.

[7] M.A.K.M. Hanafiah, W.S. Ngah, S.C. Ibrahim, H. Zakaria, W.A.H.W Alias, Kinetics and thermodynamic study of lead adsorption from aqueous solution onto rubber (*Hevea brasiliensis*) leaf powder, J. Appl Sci. 6 (2006) 2762-2767.

[8] Z. Wu, Z. Cheng, W. Ma, Adsorption of Pb(II) from glucose solution on thiol-functionalized cellulosic biomass, Bioresour. Technol. 104 (2012) 807-809.

[9] A.E. Ofomaja, E.B. Naidoo, S.J. Modise, Biosorption of copper(II) and lead(II) onto potassium hydroxide treated pine cone powder, J. Environ. Manage. 91 (2010) 1674-1685.

[10] Y. Xue, B. Gao, Y. Yao, M. Inyang, M. Zhang, A.R. Zimmermann, Hydrogen peroxide modification enhances the ability of biochar (hydrochar) produced from hydrothermal carbonization of peanut hull to remove aqueous heavy metals: Batch and column tests, Chem. Eng. J. 200-202 (2012) 673-680.

[11] G. Tan, H. Yuan, Y. Liu, D. Xiou, Removal of lead from aqueous solution with native and chemically modified corncorbs, J. Hazard. Mater. 174 (2010) 740-745.

Advanced Materials Research Vol. 970 (2014) pp 12-15

doi:10.4028/www.scientific.net/AMR.970.12

THE EFFECTS OF YSZ-Al_2O_3 ADDITION ON HYDROXYAPATITE FABRICTED BY POWDER METALLURGY

M.R.N. Liyana[1, a*], Nur Maizatul Shima Adzali[2, b], M.Z.M. Zamzuri[1, c], K.A Ismail[1, d] Mat Akhir Khalid Azadi[1, e]

[1]Schools of Manufacturing Engineering, University Malaysia Perlis (UNIMAP),

[2] Schools of Materials Engineering, University Malaysia Perlis (UNIMAP),

[a*]nurliyana.rosli13@gmail.com, [b]shima@unimap.edu.my, [c]mzamzuri@unimap.edu.my, [d]k.azwan@unimap.edu.my, [e]carlid_er@yahoo.com

Keyword: Yttria- stabilized zirconia, Alumina, Hydroxyapatite, Powder Metallurgy

Abstract. Yttria- stabilized zirconia (YSZ) becomes popular alternative to alumina (Al_2O_3) especially for hard tissue applications. Both zirconia and alumina own their good biocompatibility due to chemical inertness in body environment. Considering the bioactive of hydroxyapatite (HAP) will allow interfacial bond formation, it is desirable to combine the advantages of both materials, YSZ and Al_2O_3 with HAP. Various amounts (30, 40, 50, 60 wt. % of YSZ-Al_2O_3)/10HAP of composites have been prepared by powder metallurgy method. Several tests have been conducted to determine the effect YSZ addition on physical, mechanical properties and the microstructure of composites. The results showed that density and compressive strength increased with increasing wt. % of YSZ. Microstructural characterization has been observed by scanning electron microscope (SEM) showed the presence of pores reduced slightly in increasing of wt. % of YSZ. The prepared YSZ-Al_2O_3/10HAP composite is expected as a potential candidate for biomedical application.

Introduction

The demands of bioceramics have been revolutionizing the biomedical field in deployment as implant for humans. The medical community has accepted bioceramics materials after a number of clinical tests through a several in-vitro and in-vivo evaluations [1][2]. There are ongoing search of appropriate implant materials for replacement of musculoskeletal system as result of accident, disease or defect, attention has been focused to the potential bioceramics composites [3].

In order to fabricate the composites, powder metallurgy manufacturing method has been utilized. The ability to disperse among mixed powders leading to better control of microstructure make the powder metallurgy the most promising method for fabrication bioceramics composites [4]. It has been claimed that the microstructure of ceramics is highly dependent on the applied manufacturing process (sintering temperature, purity of the powder, size and distribution of the grains, density and porosity) and subsequently effect on both the mechanical and biological properties [5].

Hydroxyapatite (HAP, $Ca_{10}(PO_4)_6(OH)_2$), based bioceramics are successfully used as implants as they are chemically similar with human bones and teeth, that satisfying the strong biological fixation (bioactive) to body tissue [6]. However, HAP encountered with poor mechanical properties, particularly fatigue properties which means HAP cannot be used in bulk for orthopedics application [7]. There are several approaches to enhance mechanical properties of HAP by adding a hybrid or other reinforcement materials. Nowadays, yttria stabilized zirconia (YSZ) is a favorable among bioceramics material which offers chemically inertness properties and its ability to endure stress-induced phase transformation similar as Al_2O_3. The addition of Al_2O_3 to zirconia (ZrO_2) has been gaining much attention as it's provides a high elastic modulus and fine microstructure, often with greater toughness [8]. The reasons of excellent both YSZ and Al_2O_3 might be a good additive that may overcome the problem of HAP brittleness while maintaining its bioactivity.

In this present work, YSZ- Al_2O_3/10HAP was fabricated by powder metallurgy. The physical, mechanical properties and microstructure will be investigated according to the addition of YSZ content.

Materials and Methodology

Three kinds of powders were used as starting materials for preparation of powder metallurgy method. There were 3mol% yttria stabilized zirconia (YSZ) and α-Alumina (Al_2O_3). Both powders were added to hydroxyapatite (HAP) to overcome the brittleness of HAP. The powder blends with designed composition of 30, 40, 50, 60 wt. % of YSZ denoted as YSZ-Al_2O_3/10HAP composites were mixed in 3D shaker for 20 minutes at 96 rpm with addition of 10% stearic acid as a binder. The composites were fabricated using 13mm diameter steel die by uniaxial pressing at 150MPa. Sintering has been done using a sintering furnace (Carbolite STF 16/450) in an argon atmosphere at 1200˚C sintering temperature. The heating rate was set at 10˚C/min with 2 hours soaking time and subsequently left to furnace cool down. The density and porosity of sintered composites were determined according to Archimedes' principle. Compression tests were carried out for all sintered composites using Universal Testing Machine (Shimadzu UTM AG-250kN/300kNX plus). The characterizations for microstructure of composites were using scanning electron microscope (Hitachi SEM TM300).

Results and Discussion

Density and Porosity. Density of the samples was measured by the Archimedes Principle method, as described in ASTM B 962-13. From the analysis, the presence of YSZ in continuous increase in bulk density and subsequently resulted a decreased of porosity. Figure 1, shows the combination plot of bulk density and porosity. The density of the composite with 60 wt. % of YSZ was remarked higher than the other samples, which were 1.95 g/cm^3. In contrast, the porosity value obtained for the composite moderately decreased until 50% of porosity. When the composites being accompanied with YSZ, as transformation toughening agent acted to Al_2O_3 grains, which was possibly enhanced the physical and mechanical properties. The results obtained in this work were well agreement with the relationship on addition of zirconia to harder-to-sinter matrix enhanced densification [9].

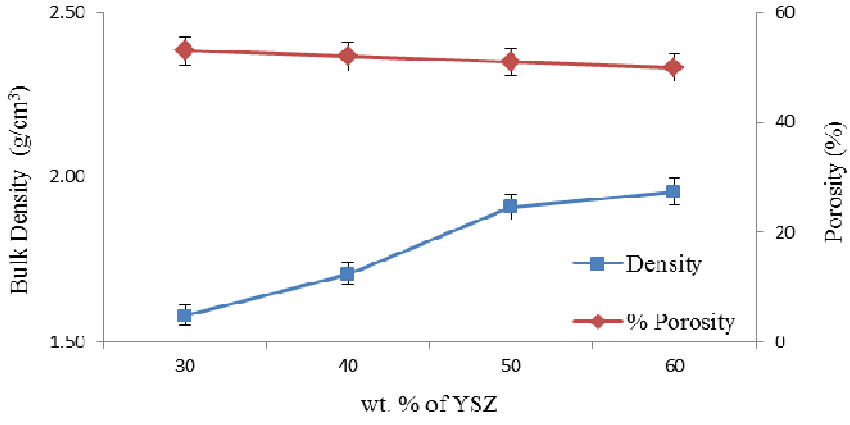

Figure 1 : Bulk density and porosity of sintered sample YSZ-Al_2O_3/10HAP at different wt. % of YSZ content.

SEM Microstructure. Figure 2 shows the SEM micrographs of the YSZ-Al_2O_3/10HAP composites with different amounts of YSZ and Al_2O_3 respectively. The pores observed in Figures 2 (a) – (d) were decreased slightly with the increasing of YSZ content as discussed earlier in Figure 1. The dark phases of Al_2O_3 turns to be coarse as appeared in the microstructure as shown in Figure2 (b). Prior to instable mixing process, there was considerable evidence of agglomerations of HAP powders seen in Figures 2 (c) – (d). In addition, lack of homogeneity in mixing and composition fluctuation during sintering due to agglomerations of particle will lead to coarsening [8]

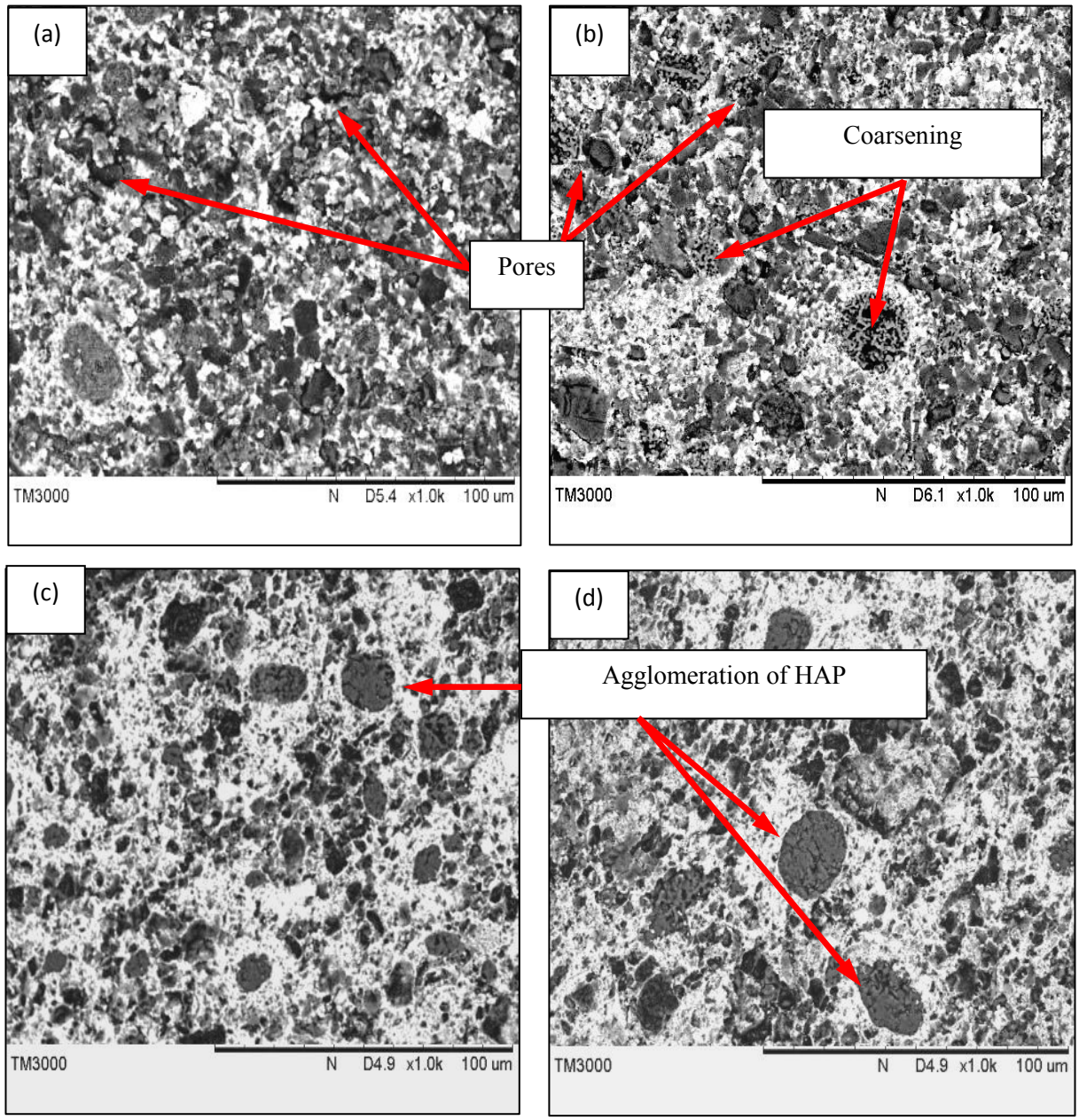

Figure 2 : SEM micrographs of sintered composites with difference YSZ content; (a) 30 wt.% of YSZ, (b) 40 wt.% of YSZ, (c) 50 wt.% of YSZ, (d) 60 wt.% of YSZ.

Compressive Strength. The compression strength of composites are shown in Figure 3, as the YSZ content was increased up to 60 wt. % of YSZ, the strength increased to 50 MPa. The porosity of composites (as discussed in Figure 1) created a significant affect towards the compression strength value. The composite obtained from sintered YSZ-Al_2O_3/10HAP showed similar trend in terms of their strength with respect to the addition of YSZ to Al_2O_3 and HAP amount, comparable with the findings of Y.Kong et.al and M. Yousefpour et.al [10][11]

Conclusions

Bioactive HAP composites were successfully fabricated with the addition of YSZ and Al_2O_3. The effect of YSZ addition and Al_2O_3 respectively on physical, mechanical properties and microstructural analysis of the composites was determined by powder metallurgy manufacturing method. As the amount of YSZ content was increased, the bulk density of composites increased up to 1.95 g/cm^3. The porosity created significant affect towards mechanical strength, denoted by the improvement of compressive strength from 10MPa to 50MPa. The microstructure observation of

composites showed the presence of pores reduced slightly with the increasing of wt. % of YSZ. The recommended composites sintered at 1200˚C were obtained by 60YSZ-Al_2O_3/10HAP as resulted in better mechanical properties while maintaining the biocompatibility benefit from the presence of YSZ and Al_2O_3 element. The bioceramics composites of YSZ-Al_2O_3/10HAP expected to be useful for orthopedic and dental applications.

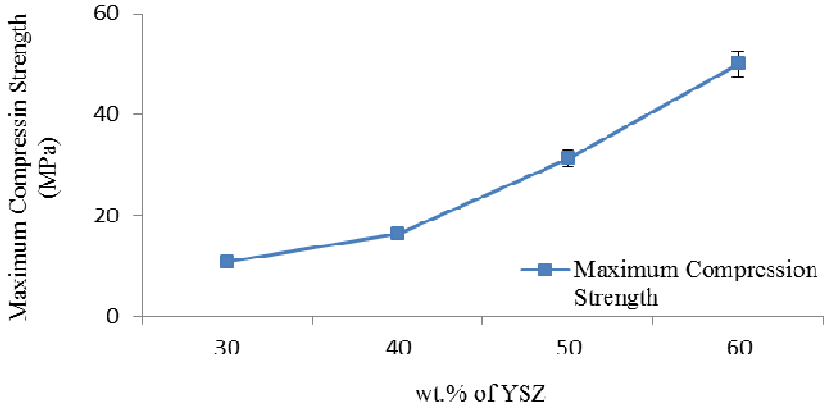

Figure 3 : Compressive strength with different addition of wt. % of YSZ content

References

[1] K. Y. Msahiro Inuzuka, Satoshi Nakamura, Shigeki Kishi, Katsumi Yoshida, Kazuaki Hashimoto, Yoshitomo Toda, "Effect of Hydroxyapatite dopant to Yttria Stabilized Zirconia Ceramics for biomedical application," *Phosphorus Research Bulletin*, vol. 16, pp. 75–82, 2003.

[2] Y. Nayak, "Hydroxyapatite - TZP Composites : Processing, Mechanical Properties, Microstructure and In-Vitro," 2010.

[3] C. Reidy, "Comparative Sintering of Zirconia and Hydroxyapatite-Zirconia Composites," University of Limerick, Ireland, 2010.

[4] Y. Mahani and H. Zuhailawati, "Effect of Compaction Pressure on Microstructure and Properties of Copper-based Composite Prepared by Mechanical Alloying and Powder Metallurgy," no. March, pp. 345–348, 2013.

[5] O. C. and J. . P. M Navarro*, A Michiardi, "Biomaterials in orthopaedics," *J. R. Soc. Interface*, vol. 5, no. October, pp. 1137–1158, 2008.

[6] A. Singh, "Hydroxyapatite, a biomaterial: Its chemical synthesis, characterization and study of biocompatibility prepared from shell of garden snail, Helix aspersa," *Bull. Mater. Sci.*, vol. 35, no. 6, pp. 1031–1038, Dec. 2012.

[7] M. Lakdawala, G. M. Malik, A. Appl, and S. Res, "Hydroxyapatite / Titania coating on titanium strip by brush coating," *Arch. Appl. Sci. Res.*, vol. 5, no. 3, pp. 137–141, 2013.

[8] C. Ângela, M. Volpato, L. Gustavo, D. A. Garbelotto, M. C. Fredel, F. Bondioli, and R. Emilia, "Application of Zirconia in Dentistry : Biological , Mechanical and Optical Considerations," in in *Advances in Ceramics*, 2011, p. 550.

[9] D. K. A. Yi Fang, Jiping Cheng, R.Roy, D.M.Roy, "Enhancing densification of zro2 containing ceramic matrix composites by microwave proocessing," *J. Mater. Sci.*, vol. 32, pp. 4925–4930, 1997.

[10] Y.-M. Kong, C.-J. Bae, S.-H. Lee, H.-W. Kim, and H.-E. Kim, "Improvement in biocompatibility of ZrO2-Al2O3 nano-composite by addition of HA.," *Biomaterials*, vol. 26, no. 5, pp. 509–17, Feb. 2005.

[11] A. A. and N. R. M. Yousefpour, N. Askari, H. Abdollah-Pour, "Investigation on Biological Properties of Dental Implant by Ce-TZP/Al2O3/ HA Bio-nano-composites," *J. Biotechnol. Biomater.*, vol. 01, no. 02, pp. 2–5, 2011.

Advanced Materials Research Vol. 970 (2014) pp 16-19

doi:10.4028/www.scientific.net/AMR.970.16

The Potential of Quercetin in *Psidium Guajava L.* leaves extract as Bioinhibitor for Controlled Released Fertilizer.

Nur Kamila Ramli[1,a*], Zahid Majeed[1,b], Anis Suhaila Shuib[1,c], Nurlidia Mansor[1,d], Zakaria Man[1,e]

[1]Department of Chemical Engineering, Universiti Teknologi PETRONAS, 31750, Tronoh, Perak, Malaysia
[a*]nurkamila_r@yahoo.com, [b]zahidfdb@gmail.com, [c]anisuha@petronas.com.my, [d]nurlidia_mansor@petronas.com.my, [e]zakaman@petronas.com.my

Keywords: *Psidium Guajava L.*, guava leaves extract, bioinhibitor, agriculture.

Abstract. This study was done to investigates the usage of natural products as one of the materials in fertilizer application. Urease inhibitors that are commonly used in agriculture are usually chemical based which affects the environment. Introducing natural products will ensure biodegradability of the material. *Psidium Guajava L.* (guava) has been reported to have properties such as antibacterial, anti-oxidant, anti-cancer, and anti ulcer for medical purposes. Guava leaves extract contains an active compound named quercetin that was successfully reported to exhibit significant urease inhibitory activities. Spectrophotometric method was used in this study with the theory of Beer's Law in order to measure the changes in ammonia concentration. Small reduction of ammonia (NH_3) concentration with different about 0.1 mol/L was calculated and the releasing was almost equal till the end of incubation time. The guava leaves extract prepared showed the potential to reduce the release of NH_3 concentration during urea application.

Introduction

Plant extracts have been discovered to become one of important source as bioinhibitor due to their environmentally acceptable, readily available and renewable source for wide range of inhibitors. They contained many sources of ingredients that highly efficient in inhibitory process [1]. Enzyme inhibitor for agricultural as well as medical purposes is well developed and been commercialized in terms of chemical based products [2]. In agriculture, high urease activity releases abnormally large amounts of ammonia into the atmosphere after urea application and causes significant environmental problems and economical loss [3]. In order to overcome this problem, the usage of inhibitors to inhibit urease enzyme has been applied which it prevents the hydrolysis of urea over a certain period of time by slowing down the rate at which urea hydrolyzes in the soil, thus avoiding or reducing volatilization losses of ammonia to the atmosphere [4]. N-N-(n-butyl) thiophosphoric triamide (NBPT) is one of the compound that has been found commonly in commercial urease inhibitor for agriculture. It has showed some visible effects which is on the first week of treatment, the leaf tips transforms from green color to yellow. Besides, plants treated with urea and NBPT were found to have higher urea content in their tissues and retard the plant growth [5]. Based on Department of Health and Ageing (2010) draft report, exposure of NBPT for 15 days on rats cause decrease in total cholesterol, triglyceride, brain red blood cells and the target organ is the liver. Urine sample from tested animal was taken and been reported to contain NBPT. This compound also affect fertility in animals and NBPT proved to cause weight changes in reproductive organs in both males and females, as well as abnormalities in sperm assessments [6]. Obviously, chemical based inhibitors have negative side effects, not safe and have low efficiency [7]. The research on bioinhibitor is due to world demanding on environmentally products from the natural sources. Due to this phenomenon as well as deeply concern about the environment, researchers try to discover on bioinhibitors. The search for green inhibitor is continuously and been confirmed by recent publications [8].

Guava (*Psidium guajava L.*) has been demonstrated to have several biological activities such as antidiabetic [9], anticough, antibacterial [10] and antispasmodic actions [11]. Guava tree is

member of myrtaceae family, all the parts of this tree widely use in curing many health problems. Extraction from guajava leaves mostly essential oil, tannins, flavonoids, phenol compounds, carotenoids and vitamin C. Flavonoids particularly rich in quercetin, saponins, alkeloids, cardiac glycosides, phlobatannis and anthraquinones. Guava leaves extract that contains an active compound named quercetin was successfully reported to exhibit significant urease inhibitory activities with IC_{50} value of 47.5 ± 2.3 [12]. The aim of this study is to investigate the capability of guava leaves extract that contain quecertin to inhibit urease enzyme in order to prevent the ammonia released.

Methodology

Materials. Guava (*Psidium guajava L.*) leaves extract, urease enzyme (Jack bean urease), urea (50 mM), phosphate buffer solution (50 mM, pH 7.80) was prepared by adjusting the pH of phosphoric acid with sodium hydroxide (NaOH), 2 mM of ethylenediaminetetraacetic acid (EDTA). Equipment used was UV-VIS Spectrophotometer.

Preparation of guava leaves extract. To prepare the extracts, 2 g powder of dry leaves were mixed with 200 ml of 0.9% NaCl (100°C, 5 min). The crude extract was filtered, centrifuged (1500 r/min, 5 min) to obtain the final extract. The supernatant was considered as the concentration at 1 g/ml of guava leaves [13].

Inhibition studies. Two main mixtures and one blank were prepared to undergo the inhibition process which is standard assay mixture and the enzyme-containing solution. Two standard assay mixture that consisted of 50 mM urea, 50 mM phosphate buffer solution (pH 7.8) and 2 mM EDTA. Meanwhile, the enzyme-containing solution is consisted of 50 mM phosphate buffer solution (pH 7.8), 2 mM EDTA urease enzyme and the guava leaves extract. Then, the mixtures was incubated at room temperature (25°C). During the incubations, 1 ml aliquots of the enzyme-containing solution at different time intervals were immediately transferred into the one of the standard assay mixtures to determine the urease activity. The other standard asssay was prepared as blank. The urease activity was determined by measuring ammonia concentration after 10 minutes of reaction time. Ammonia concentration was determined by the spectrophotometric, phenol–hypochlorite method where the absorbance was registered at 640 nm [14]. The procedure is repeated and the trend of analysis was observed.

Result and Discussion

Beer's Law equation was applied in this experiment to analyse the absorbance data obtained from UV-VIS spectrophotometer. The decreasing in value of ammonia concentration in this inhibition studies was calculated using the Beer's Law, Eq. 1 and was illustrated in Figure 2.

$$A_\lambda = \varepsilon\, c\, L\,. \qquad (1)$$

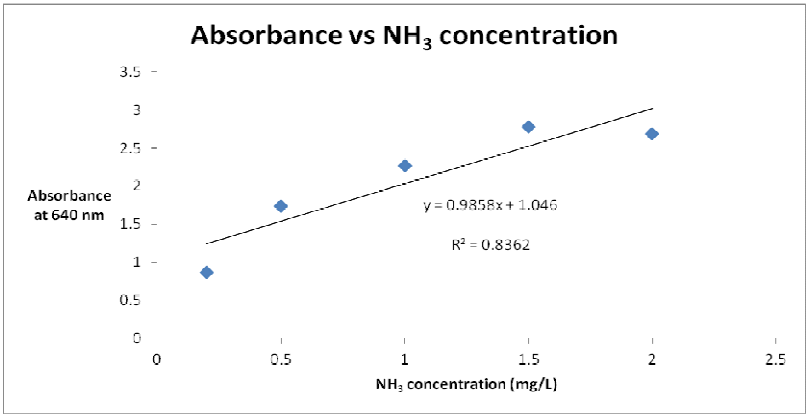

Figure 1: Standard calibration curve

The standard calibration curve using ammonium stock solution was prepared before undergoing the inhibition and data was recorded at 640 nm. The slope value obtained was used as the value for molar absorptivity, ε.

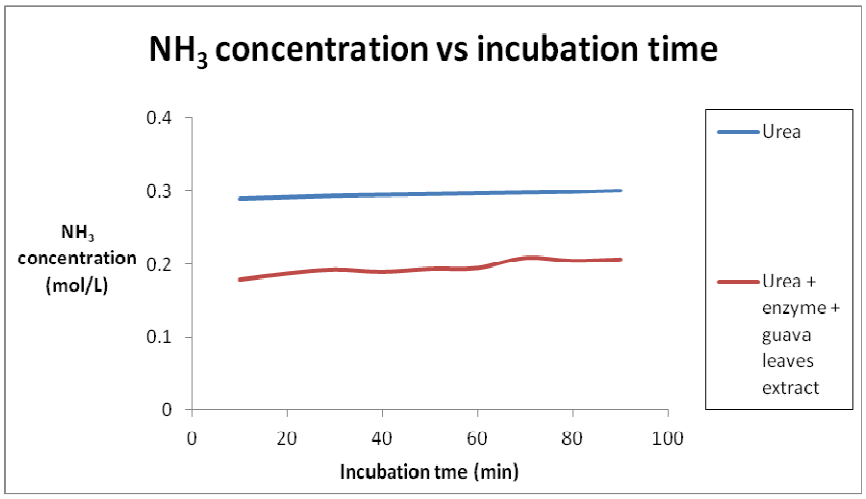

Figure 2: Ammonia concentration against incubation time

Eq. 1 is used to determine the concentration of ammonia for each amount of enzyme-containing solution that has been added in the standard assay solution. The result is shown in Figure 2 which illustrates the effect of guava leaves extract in urea-urease-guava leaves reaction on ammonia (NH_3) release. Urea solution that was prepared as a blank showed almost equal release of NH_3 concentration starting from 10 minutes of incubation time until 90 minutes. Meanwhile, urea solution with mixture of urease-guava leaves extract showed reduction in NH_3 concentration release. The reduction happened in small value with different around 0.1 mol/L and the releasing also was almost equal till the end of incubation time. This small reduction might be because of the concentration of guava leaves extract that been used is slightly low. However, the obtained result showed that guava leaves extract have the potential to reduce NH_3 concentration which is urease enzyme was conceptually inhibited by the active compound, quecertin that posses the inhibitory properties as reported before. The ten minutes as time interval for each reaction was showed the importance of time-dependant in the whole inhibition process.

Conclusion

The guava leaves extract prepared in this experiment was able to show some reduction in NH_3 concentration release during urea application. Process was happened caused by the reaction of the quecertin compound that contained in guava leaves extract.

Acknowledgement

This work is supported in a part by a Grant of Ministry of Higher Education of Malaysia under ONE-Baja project. Authors thank Department of Chemical Engineering, Universiti Teknologi PETRONAS for the facilities.

References

[1] Pandian Bothi Raja and Mathur Gopalakrishnan Sethuraman. 2008. Natural products as corrosion inhibitor for metals in corrosive media — A review.Materials Letters 62, 113–116. doi:10.1016/j.matlet.2007.04.079.

[2] Watson, C. J. 2005. Urease inhibitors. Department of Agriculture and Rural Development, Queen's University of Belfast, United Kingdom. IFA International Workshop on Enhanced-Effeciency Fertelizers.

[3] Khan, K., M., Wadood, A., Ali, M., Zia-Ullah, Ul-Haq, Z., Khan, M., Perveen, S., and Choudhary, M., I. 2010. Identification of potent urease inhibitors via ligand- and structure-based virtual screening and in vitro assays. Journal of Molecular Graphics and Modelling, 28, 792–798. doi:10.1016/j.jmgm.2010.02.004.

[4] Martin E. Trenkel. 1997. Controlled-Release and Stabilized Fertilizers in Agriculture. Published by the International Fertilizer Industry Association Paris, December. ISBN 2-9506299-0-3.

[5] P. M. Tejo et al. 2011. The effect of N-(n-butyl) thiophosphoric triamide on urea metabolism and the assimilation of ammonium into Triticum aestivum L. Plant Growth Regulation. 63:pp73-79.

[6] N-(n-butyl) thiophosphoric triamide (NBPT). 2010. In Australian Government, Department of Health and Ageing, Existing Chemical Secondary Notification Assessment. Australia.

[7] Zaborska, W. et al. 2009. Modification of jack bean urease thiols by thiolsulfinates contained in garlic extract: DTNB titration studies. Doi: 10.1016/j.foodchem.2008.05.029.

[8] Tarun, E., I., Rubinov, D., B., and Metelitza, D., I. 2004. Inhibition of Soybean Urease by Triketone Oximes. Biochemistry (Moscow), Vol. 69, No. 12, 2004, pp. 1344_1352. Translated from Biokhimiya, Vol. 69, No. 12, 2004, pp. 1649_1658.

[9] Oh, W. K., Lee, C. H., Lee, M. S., Bae, E. Y., Sohn, C. B., Oh, H., et al. (2005). Antidiabetic effects of extracts from Psidium guajava. Journal of Ethnopharmacology, 96, 411 – 415.

[10] Jaiarj, P., Khoohaswan, P., Wongkrajang, Y., Peungvicha, P., Suriyawong, P., Sumal Saraya, M. L., et al. (1999). Anticough and antimicrobial activities of Psidium guajava Linn. leaf extract. Journal of Ethnopharmacology, 67, 203-212.

[11] Lozoya, X., Reyes-Morales, H., Chavez-Soto, M. A., Martinez-Garcia, M. D. C., SotoGonzalez, Y., & Doubova, S. V. (2002). Intestinal anti-spasmodic effect of a phytodrug of Psidium guajava folia in the treatment of acute diarrheic disease. Journal of Ethnopharmacology, 83,19-24.

[12] Irshad Ahmad, Bashir Ahmad Chaudhary, Muhammad Uzair And Khalid Hussain Janbaz, Muhammad Ashraf. 2011. Urease Inhibitors and Antioxidants from *Vernonia cinerascens.* J.Chem.Soc.Pak., Vol. 33, No. 1, 114-117.

[13] Abreu P.R.C., Almeida M.C., Bernardo R.M., Bernardo L.C., Brito L.C., Garcia E.A.C., Fonseca A.S., Bernardo-Filho M. 2006. Guava extract (*Psidium guajava*) alters the labeling of blood constituents with technetium-99m. Journal of Zhejiang University SCIENCE B. ISSN 1673-1581 (Print); ISSN 1862-1783 (Online). *Univ SCIENCE B 2006 7(6):429-435*

[14] Parsons, T. R. et al. (1984). A Manual of Chemical and Biological Methods for Seawater Analysis. Pergamon Press, Elmsford, N.

Advanced Materials Research Vol. 970 (2014) pp 20-25

doi:10.4028/www.scientific.net/AMR.970.20

Synthesis and Properties of Biphasic Calcium Phosphate Prepared by Different Methods

NATASHA Ahmad Nawawi[1,a*], Ramesh Singh[1,b], Mohd Hamdi[1,c], Tan Chou Young[1,d], Judha Purbolaksono[1,e], Iis Sopyan[2,f] and Ranna Toulouei[3,g]

[1]Centre of Advanced Manufacturing & Material Processing (AMMP), Department of Mechanical Engineering, Faculty of Engineering, University of Malaya, 50603 Kuala Lumpur, Malaysia

[2]Department of Manufacturing and Materials Engineering, Kulliyyah of Engineering, International Islamic University Malaysia, 53100 Kuala Lumpur, Malaysia

[3]Faculty of Science and Engineering, Laval University, Quebec, G1V 0A6 Canada

[a*]natasha_nawawi@yahoo.com.my

Keywords: Calcium phosphate, synthesis, sol gel, wet precipitation, calcination, biphasic mixtures

Abstract. Hydroxapatite (HA) is a stable phase with low dissolution rate in body fluid. Meanwhile, β-tricalcium phosphate (β-TCP) is rather soluble but the dissolution rate is too fast for bone bonding. Therefore a mixture of both is desirable to control the bioresorbability. In this work, calcium phosphate powder has been synthesized via sol gel and wet precipitation method to compare phase behaviour of these powders upon calcination. XRD result clearly revealed that both as-synthesized powders were pure HA with good purity. The decomposition of HA to TCP took place in the range of 700-800 °C and 800-900 °C for sol gel and wet chemical precipitation powder, respectively. The weight loss detected at 700-850°C in TGA analysis confirmed the presence of this biphasic mixtures. From FTIR analysis, profound change in OH^- band intensity was attributed to the increased in HA crystallinity with calcination temperature.

Introduction

Calcium phosphate ceramics have started to marked its potential in biomedical applications, particularly orthopedics and dentistry field since the 1980s. Among various phases of calcium phosphate, hydroxyapatite [$Ca_{10}(PO_4)_6(OH)_2$, HA] with similar composition and crystal structure to natural bone, is the most commonly calcium phosphate ceramics used for medical purposes owing to its stable phase and biocompatibility [1]. Moreover, calcium phosphate ceramics does not exhibit any cytoxic effect and it can directly bond to the bone [2]. This material was used in a variety of physical forms such as porous, granular and dense [3,4]. Basically HA is produced via two method that are synthetic method and the other one is from natural bone [5]. The synthetic methods are by sol gel, hydrothermal, chemical precipitation and solid state reaction. However, the stability of crystal structure of calcium phosphate is higher than that of natural apatite [6]. Together with this, biphasic calcium phosphate (BCP) ceramics, a mixture of hydroxyapatite [HA, $Ca_{10}(PO_4)_6(OH)_2$] and β-tricalcium phosphate [β-TCP, β-$Ca_3(PO_4)_2$], has been introduced as sitable substitution materials for artificial bone grafts. This has been reported for nearly three decades [7]. This mixture is considered better when compared to either the single phase HA or β-TCP component, because of its unique dissolution characteristics of promoting new bone formation at the implant site [2, 8]. Although HA is a more stable phase, HA alone is not favoured as it is a non-biodegradable bone replacement materials. In comparison, application of β-TCP alone as a biomaterial for alveolar ridge augmentation resulted in too high rate of β-TCP degradation [9] which is likely not favoured too. In addition, BCP often exhibit a combination of enhanced bioactivity and mechanical stability that is difficult to achieve in a single phase material [6]. Hence, to balance the nonbiodegradablity of HA which is more stable phase and to slow the rate of biodegradation of β-TCP, the BCP characteristics have been well studied recently.

In this work, calcium phosphate powder was synthesized via sol gel method and wet chemical precipitation in order to compare the phase behaviour between the powders upon sintering. These two methods has been chosen because of their unique advantages above each other. Wet chemical precipitation method was proven to be one of the easiest ways of preparing HA powders [5,10]. For example, wet precipitation technique produces only water as by-product, low working temperatures, high percentages of pure products and inexpensive equipment requirement [10,11].

Meanwhile, sol gel method results in good homogeneity of powder due to good mixing of the starting materials which subsequently produced nanosize powder with high reactivity [2, 12,13]. Although known for its prolonged synthesis time, the sol gel method employed in this work is economically attractive, using nitrates compounds as raw materials which are cheaper and easily obtained [14,15], compared to conventional sol gel method which usually uses expensive alkoxide compounds [16].

Experimental Work

Powder Preparation via Sol gel Method. 250 ml of ammonium solution (11% solution) was heated at 60 °C and ethylenedinitrilotetraacetic acid (Titriplex III) (chelating agent) was added while stirring until dissolved clear solution is obtained. Then, 100 mL aqueous solution of calcium precursor, Ca $(NO_3)_2.4H_2O$ was poured into the mixture. Then, phosphorus precursor of *di*-ammonium hydrogen phosphate $(NH_4)_2HPO_4$) and urea, which act as gelling agent were subsequently added. The mixture is then refluxed at 100 ºC for 3-5 hours while stirring until a white gel was obtained. The 340 °C dried white gel was subsequently calcined under flowing air with a heating rate of 10 ºC/min and 2 hours holding time.

Powder Preparation via Wet Chemical Precipitation Method. The starting precursors used are calcium hydroxide $Ca(OH)_2$ (98% purity, R&M Chemicals) and orthophosphoric acid H_3PO_4 (85% purity, Merck). The prepared ammonium (NH_3) solution (25 % concentration) is added drop wise into the stirring suspension of $Ca(OH)_2$ in distilled water and pH was kept above 10.5 until it ended [17]. The stirring will be continued for another 6 hours after the titration process ended so that the precipitate will be allowed to settle down overnight before filtration. The precipitate will be rinsed off by using distilled water and subsequently dried overnight at 60°C. The dried filtered cake is then crushed and sieved to obtain HA powder.

Characterisation of Calcium Phosphate. Both as-synthesized powders were subjected to calcination at different temperatures ranging from 500 °C to 1200 °C with a ramp rate of 10 °C/min and holding time of 2 hours. The phase behaviour was identified via X-ray diffraction (XRD) analysis (Shimadzu, XRD6000) and Fourier transform infrared spectrometer (FTIR) spectroscopy (Perkin Elmer FTIR, Spectrum 100 Series). Thermogravimetric analysis (TGA) was performed in ambient air on the powder that exhibited optimum temperature for formation of biphasic mixtures using the Perkin Elmer apparatus (Pyris Diamond TG/DTA) with 2 °C/min heating rate.

Results and Discussion

Investigation on the effect of calcination temperature (in the range of 600–1200 °C) on phase behaviour conducted on both sol gel and wet precipitation as-synthesized powder is presented in Fig. 1. For both powders, XRD pattern at 600°C showed a poorly crystalline HA. Both powder showed the good purity of crystalline HA at 700 °C. Hence transformation to crystalline phase detected to have taken place at the temperature ranging from 600–700°C. Subsequently the appearance of β-TCP started to be detected at the temperature of 800°C and 900°C for sol gel and wet precipitation powders, respectively. The appearance of β-TCP peak is crucial, as it is the evident of the transformation of deficient apatite to biphasic mixtures of HA and β-TCP. At 900°C, calcined sol gel powder has showed the existence of β-TCP phase at highest resolution of peak that

confirmed the formation of biphasic mixtures at the optimum temperature. However, when the calcination temperature was increased up to 1200°C, the XRD pattern of the sol gel powder showed an increase in peak intensity of HA phases, accompanied by a reduction in β-TCP phase intensity. This result suggests that for sol gel powder, at higher calcination temperatures, reversible transformation of β-TCP phase into HA phase has occurred. Meanwhile, for wet precipitation powder, the existence of minor β-TCP phases with very low intensity is maintained up to the temperature of 1200°C.

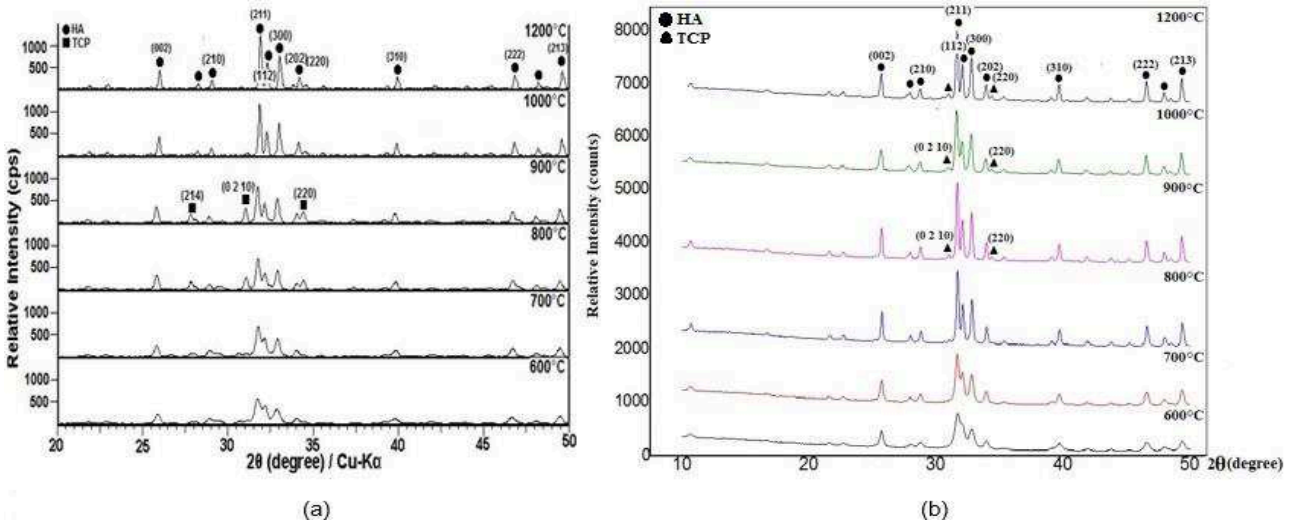

Figure 1. Patterns (XRD) of calcium phosphate powders at various calcination temperatures: (a) sol gel method and (b) wet precipitation method.

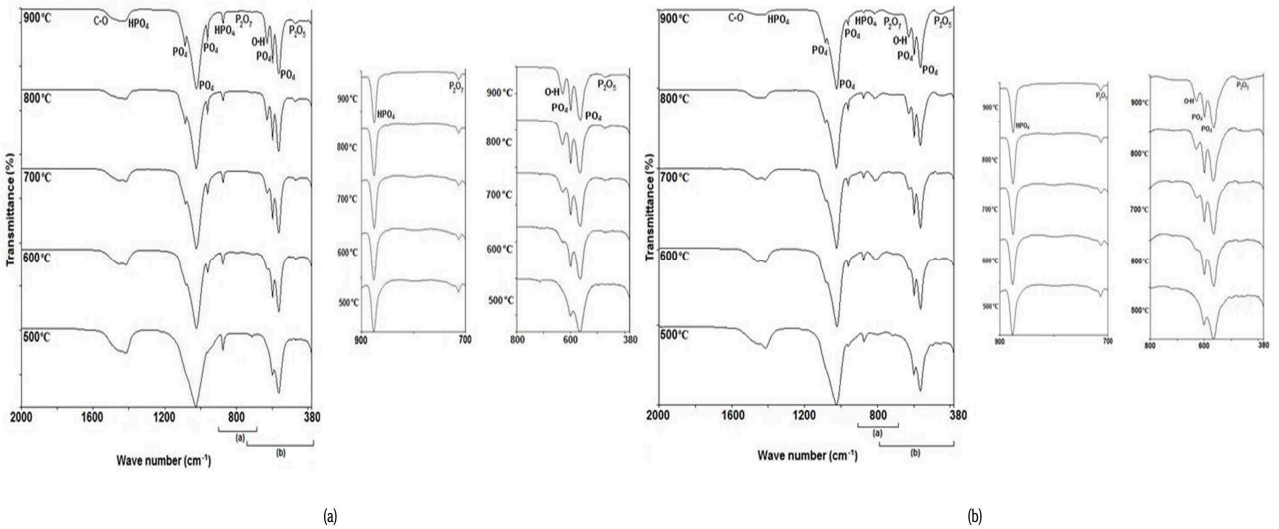

Figure 2. FTIR spectra of calcium phosphate at various calcination temperatures: (a) sol gel method and (b) wet precipitation method

Fig. 2 shows FTIR spectra of sol gel and wet precipitation derived calcium phosphate powders calcined at different temperatures ranging from 500-900 ºC. Characteristic peak of β-TCP, PO_4^{3-} band can be clearly observed from the band shoulder around ~1086 cm^{-1} [18] in temperature range of 700 ºC for sol gel and 900 ºC for wet precipitation powder. The result is in good agreement with the finding obtained in XRD analysis as in Fig. 1. Besides that, both spectrum also revealed that presence of hydrogen phosphate groups (HPO_4^{-2}) and pyrophosphate ($P_2O_7^{-4}$) bands are evident at 500°C, for peak at 875 cm^{-1} and 715 cm^{-1}, respectively. However, as the temperature increases, the bands of HPO_4^{2-} at 875 cm^{-1} and $P_2O_7^{4-}$ at 715 cm^{-1} in both spectrum are viewed with a decreasing intensity. This lead to the conclusion that this anion, HPO_4^{2-} exist in less crystalline phase. This

confirms the formation of biphasic mixtures of HA and β-TCP. Nevertheless, profound change in OH^- band intensity at 630 cm^{-1} was observed as the temperature increase from 700-900 ºC in both spectrum. This can be attributed to the increase in HA crystallinity with increase in calcination temperatures as also supported by their XRD patterns (Fig. 1).

Referring to the obtained XRD and FTIR result, it is proven that sol gel technique has lower biphasic mixtures formation temperature, 700-800 ºC with greater intensity compared to that of wet precipitation technique (800-900 ºC). Hence thermogravimetric analysis study has been conducted on sol gel derived powder for further investigation.

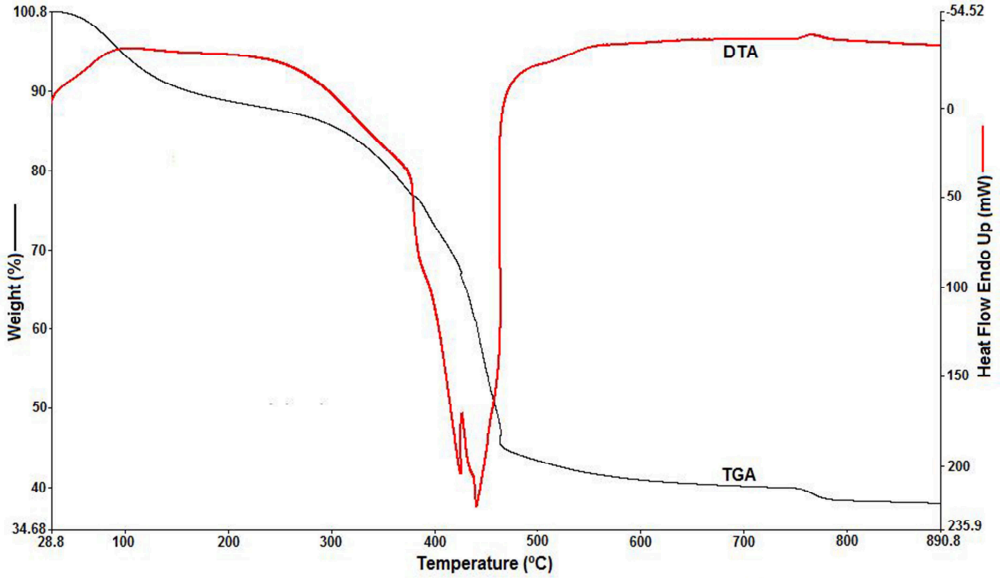

Figure 3. TG/DTA plot of sol gel derived black gel

The TGA plot of the black gel derived from sol gel technique is shown in Fig. 3. From room temperature to about 250 ºC, incorporated water is lost. A continuous weight loss was observed between 250 ºC and 550 ºC (exothermic peak as in DTA graph), which can be associated with the burning of organic substances and by-products such as NO_3^- and ammonia which become volatile upon heating. The weight loss also was described as the oxidation of the residual solvents and vigorous decomposition of the organic and inorganic precursors at 440 °C [20]. In other study it is stated that at approximately 400 °C, the condensation reaction of hydrogen phosphate ions has taken place [21]. Furthermore, in that temperature range (up to 440 °C), the sample has experienced weight loss of about 50 wt-%. At temperature higher than 440 °C up to 560 °C, the black gel started to experience endothermic process (as in DTA plot) as the calcination takes place and this has transformed the amorphous phase of the gel to crystalline phase of calcium phosphate.

The steps of weight loss between 700 and 800 ºC show the characteristic of calcium deficient apatite. To be exact, at the lowest of 710 ºC up to 800 ºC, the decomposition of HPO_4^{2-} and $P_2O_7^{4-}$ to biphasic mixtures has been detected [19, 22]. This is verified by the weight loss of about 2% of the sample. This result is derived from the condensation of the HPO_4^{2-} groups to yield $P_2O_7^{4-}$ (Eq. 1), which at higher temperatures, react further with HA to yield $Ca_3(PO_4)_2$ plus the volatile H_2O as in Eq. 2 [23,24].

$$2HPO_4^{2-} \quad P_2O_7^{4-} + H_2O. \tag{1}$$

$$P_2O_7^{4} + 2OH^- \quad 2PO_4^{3-} + H_2O. \tag{2}$$

The weight loss detected at ~750 °C (endothermic peak as in DTA plot) resulting from the decomposition of HA to biphasic mixtures was conformed to the XRD analysis whereby the presence of biphasic mixtures can be detected at 800 °C in calcined sol gel powder as in Fig. 1(a).

Conclusions

Pure and nanosized particles of calcium phosphate powders have been successfully prepared via sol gel and wet chemical precipitation method. The synthesized powders exhibited crystalline BCP characteristic after calcination at 700-800 and 800-900 ºC for sol gel and wet precipitation technique, respectively. sol gel technique has showed to have lower temperature for biphasic mixtures formation. The presence of its BCP characteristic at 700-800 °C is consistent with the result obtained in its thermal analysis. Reversible transformation of β-TCP phase into HA phase has occurred in sol gel powder as the temperature increased to 1200 °C.

Acknowledgements

The authors would like to acknowledge University of Malaya for providing the necessary facilities and resources for this research. This research was supported by the PPP grant no. PG079-2013A and UMRG grant no. RP011D-13AET.

References

[1] C.K. Hsu, The preparation of biphasic porous calcium phosphate by the mixture of $Ca(H_2PO_4)_2.H_2O$ and $CaCO_3$, Mater. Chem. and Phys. 80 (2003) 409-420.
[2] A.N. Natasha, I. Sopyan, S. Ramesh, Afzeri, Phase behaviour of manganese-doped biphasic calcium phosphate ceramics synthesized via sol-gel method, Asia-Pacific J. Chem. Eng. 6 (2011) 823-831.
[3] B. Liu, P. Lin, Y. Shen, Y. Dong, A novel sol–gel technique for hydroxyapatite preparation, J. Mater. Sci. Mater. Med. 19 (2008) 1203-1207.
[4] D. Tadic, F. Beckmann, K. Schwarz, M. Epple, A novel method to produce hydroxyapatite objects with interconnecting porosity that avoids sintering, Biomaterial., (25) 2004 3335-3340.
[5] A. Harabi, D. Belamri, N. Karboua, F.Z. Mezahi, Sintering of bioceramics using a modified domestic microwave oven: Natural hydroxyapatite sintering, J. Therm. Anal. Calorimet. (104) 2011, 383-388.
[6] M.O. Li, X. Xiao, R. Liu, C. Chen, L. Huang, Structural characterization and zinc-substituted hydroxyapatite prepared by hydrothermal method, J. Mater. Sci.: Mater. Med. (19) 2008, 797-803.
[7] I. Sopyan, M. Mel, R. Singh, K.A. Khalid, Porous hydroxyapatite for artificial bone applications, Sci. Technol. Adv. Mater. 8 (2007) 116-123.
[8] A.C. Tas, F. Korkusuz, M. Timucin, N. Akkas, An investigation of the chemical synthesis and high temperature sintering behavior of calcium hydroxyapatite (HA) and tricalcium phosphate (TCP) bioceramics, J. Mater. Sci.: Mater. Med. 8 (1997) 91-96.
[9] N. Kivrak, A.C. Tas, Synthesis of calcium hydroxyapatite-tricalcium phosphate (HA-TCP) composite bioceramic powders and their sintering behaviour, J. Am. Ceram. Soc. 81 (1998) 2245-2252.
[10] N. Monmaturapoj, Nano-size hydroxyapatite powders preparation by wet chemical precipitation route, J. Met. Mater. Miner. 18 (2008) 15-20.
[11] A. Paz, D. Guadarrama, M. Lopez, J.E. Gonzalez, N. Brizuela, J. Aragon, A comparative study of hydroxyapatite nanoparticles synthesized by different routes, Quim Nova. 35 (2012) 1724-1727.
[12] H.W. Kim, J.C. Knowles, H.E. Kim, Effect of biphasic calcium phosphate on drug release and biological and mechanical properties of poly (ε-caprolactone) composite membranes, J. Biomed. Mater. Res. A. 70A (2004) 467-479.
[13] F. Wang, M. Li, Y. Lu, Y. Qi, A simple sol-gel technique for preparing hydroxyapatite nanopowders, Mater. Lett. (59) 2005 916-919.
[14] K.P. Sanosh, M.C. Chu, A. Balakrishnan, T.N. Kim, S.J. Cho, Pressureless sintering of nanocrytalline hydroxyapatite at different temperatures, Met. Mater. Int. 16(4) (2010) 605-611

[15] K. Seema, B. Uma, K. Suhcita, Transformations in sol-gel synthesized nanoscale hydroxyapatite calcined under different temperatures and time conditions', *J. Mater. Eng and Perform.,* 2012, **21**, 1737-1743.
[16] Z. Xiu, M. Lu, S. Liu, G. Zhou, B. Su, H. Zhang, Barium hydroxyapatite nanoparticles synthesized by citric acid sol-gel combustion method, Mater. Res. Bull. 40 (2005) 1617-1622.
[17] S. Ramesh, Malaysia Patent PI 20043325. (2004).
[18] S.J. Kalita, S. Verma, Nanocrystalline hydroxyapatite bioceramic using microwave radiation: Synthesis and characterization, J. Mater. Sci. Eng. C. 30 (2010) 295-303
[19] R. Morrissey, L.M. Rodriguez-Lorenzo, K.A. Gross, Influence of ferrous iron incorporation on the structure of hydroxyapatite, J. Mater. Sci. Mater. Med. 16 (2005) 387– 392.
[20] A. Milev, G.S.K. Kannangara, B. Ben-Nissan, Morphological stability of hydroxyapatite precursor, Mater. Lett. 57 (2003) 1960-1965.
[21] E. Landi, G. Logroscino, L. Proietti, A. Tampieri, M. Sandri, S. Sprio, Biomimetic Mg substituted hydroxyapatite: from synthesis to in vivo behavior, J. Mater. Sci. Mater. Med. 19 (2008) 239-247.
[22] E.C. Victoria, F.D. Gnanam, Synthesis and characterization of biphasic calcium phosphate, Trends Biomater. Artif. Organs, 16 (2002) 12-14.
[23] A. Rapacz-Kmita, C. Paluszkiewicz, A. Slosarczyk, Z. Paszkiewicz, FTIR and XRD investigations on the thermal stability of hydroxyapatite during hot pressing and pressureless sintering processes, J. Mol. Struct. 744-747 (2005) 653–656.
[24] S. Lazic, S. Zec, N. Miljevic and S. Milonjic, The effect of temperature on the properties of hydroxyapatite precipitated from calcium hydroxide and phosphoric acid, Thermochim. Acta. 374 (2001) 13-22.

CHAPTER 2:

Catalytic Materials

Advanced Materials Research Vol. 970 (2014) pp 29-32

doi:10.4028/www.scientific.net/AMR.970.29

Decolorization of methylene blue by photocatalyst in the Ag_3PO_4-AgI system

Pongsaton Amornpitoksuk[1,2,a*] and Sumetha Suwanboon[3,b]

[1]Department of Chemistry, Faculty of Science, Prince of Songkla University, Hat-Yai, Songkhla, 90112, Thailand

[2]Center of Excellence in Nanotechnology for Energy (CENE), Prince of Songkla University,Hat-Yai, Songkhla, 90112, Thailand

[3]Department of Materials Science and Technology, Faculty of Science, Prince of Songkla University, Hat-Yai, Songkhla, 90112, Thailand

[a*]ampongsa@yahoo.com, [b]ssuwanboon@yahoo.com

Keywords: Photocatalyst, visible light, adsorption, Ag_3PO_4-AgI.

Abstract. The co-effect of PO_4^{3-} and I^- on the formation of a heterosturucture photocatalyst in the Ag_3PO_4-AgI system was studied by the co-precipitation method between $AgNO_3$ and the precipitating agent. The precipitating agent was prepared by varying the mole ratios between Na_2HPO_4 and KI. At 10 mol.% KI, the product showed the mixed phase between Ag_3PO_4 and un-identified phase. For 30 - 90 mol.% KI, the un-identified phase and AgI were detected in the x-ray diffraction patterns. The un-identified phase strongly adsorbed the methylene blue dye. The product prepared from 30 mol.% KI had the highest content of un-identified phase and also showed the highest degree of decolorization in the dark. The photocatalytic properties of products in this system were confirmed by the decolorization of methylene blue under visible illumination.

Introduction

In recent years, research on photocatalysts has received much attention because of world wide concern about energy consumption and environmental problem [1]. However, most photocatalysts usually absorb UV-light and generate reactive species that can degrade organic molecules including dye molecules [1]. This process is not so efficient when using sunlight, because most electromagnetic waves from sunlight fall in the visible region. Thus the development of the visible light based photocatalysts recently becomes of major interest. Silver orthophosphate (Ag_3PO_4) is one of the semiconductor based photocatalysts that show a moderately high efficiency for degrading dyes using visible light [2]. Its activity can be improved by coupling with other metals such as Ag or metal halides such as silver halides (AgX) [3]. AgI is one of these silver halide compounds that can enhance the photocatalytic activity of Ag_3PO_4. In general, the AgI/Ag_3PO_4 heterostructures can be synthesized by deposition of AgI on the surface of Ag_3PO_4 powders as a two-step method.

In this work, the co-effect of PO_4^{3-} and I^- on the formation of photocatlyst in Ag_3PO_4–AgI system was prepared by a single step method. The photocatalytic activities of these newly prepared compounds were also investigated through the decolorization of methylene blue (MB) solution under illumination by visible light.

Experimental

The heterosturucture compounds in Ag_3PO_4-AgI system were synthesized by the co-precipitation method. The precipitating agents were prepared by mixing Na_2HPO_3 with KI in various mole ratios. These solutions were added dropwise to an $AgNO_3$ solution. The precipitants were then moderately stirred at room temperature for 1 h and the precipitants were collected by

filtration, rinsed with distilled water several times, then collected and dried at 100 ^{o}C for 1 h. The structural characterization of these prepared compounds was carried out using the X-ray diffractometer (XRD, X'Pert MPD, Philips) and Cu K_{α} radiation.

The photocatalytic activity of the prepared powders was investigated by decolorization of an aqueous solution of methylene blue (MB). A mixture of 150 mL of 1 x 10^{-5} M MB solution and 150 mg of the prepared powders was stirred for 30 min in the dark to ensure that the adsorption/desorption of the MB on the catalyst surface was in equilibrium. Then, this mixture was illuminated using 3 fluorescent tubes (3 x 15 W, Philips). After illumination for the required time, 3 mL of MB was pipetted and the remaining MB concentration was determined using a UV-vis spectrophotometer (Lambda 25, Perkin-Elmer). The decolorization (%) was calculated by the following equation:

$$\text{Decolorization (\%)} = [(A_o - A_t)/A_o] \times 100$$

where A_o and A_t are the absorbances at 655 nm for the initial MB solution and the MB solution after irradiation for the required time, respectively.

Results and discussion

Fig. 1 shows the x-ray diffraction (XRD) patterns of the products prepared by different mole ratios between KI and Na_2HPO_4. In the absence of KI, Ag^+ reacted with PO_4^{3-} to from Ag_3PO_4 as shown in Fig. 1(a) and all diffraction peaks were matched well with JCPDS card number 06-0505. When KI was added to the Na_2HPO_4 solution, there was an un-identified phase labeled as "#" in the XRD pattern (Fig.1 (b)). This un-identified phase in this binary system has also been reported for the preparation of compound in Ag_3PO_4-AgI system by mechanical milling [4].

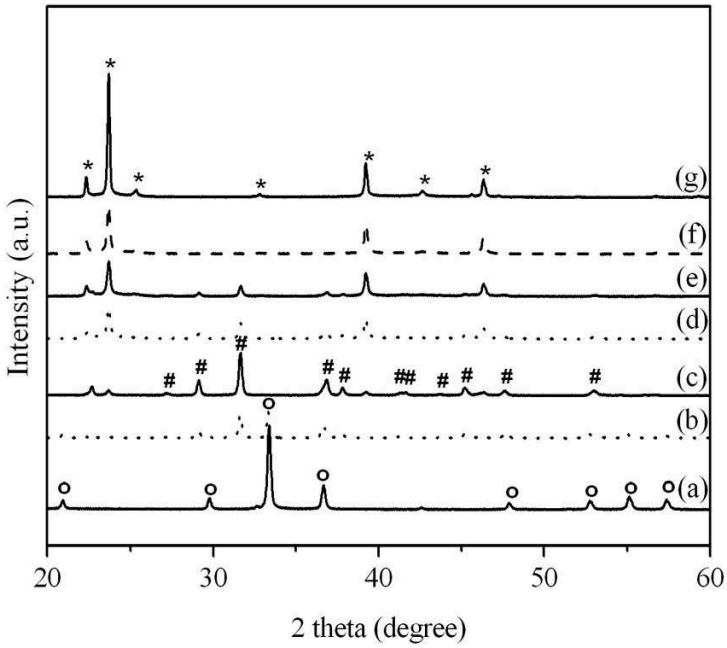

Fig. 1. XRD patterns of products in the Ag_3PO_4-AgI system prepared at (a) 0, (b) 10, (c) 30, (d) 50, (e) 70, (f) 90 and (g) 100 mol.% KI, respectively. The marked "o", "∗" and "#" represent Ag_3PO_4, AgI and un-identified phases, respectively.

When the KI concentration was increased, the amount of un-identified phase was also increased while the amount of Ag_3PO_4 phase was decreased as seen in Fig. 1(b-c). When the KI was greater than or equal to 30 mol.%, Ag_3PO_4 was not detected but there is another phase which was assigned as AgI (JCPSD card number 09-0374) in XRD pattern (Fig. 1(c)). If the KI was

continuously increased, the product tended to form the AgI phase rather than form the un-identified phase as shown in Fig. 1(d-f). In the absence of Na_2HPO_4, only pure AgI was presented in the XRD pattern as seen in Fig. 1(g).

The photocatalytic decolorization of MB dye by these compounds was studied under illumination from three fluorescent tubes as the visible light source. The prepared powders were stirred into the MB solution in the dark for 30 min and were then illuminated for 10 and 20 min, respectively. These results are shown in Fig. 2. From Fig 1 and 2, the decolorization efficiency in the dark corresponded with the amount of the un-identified phase. From Fig. 1, the product prepared from 30 mol.% KI had the highest content of un-identified phase and also showed the highest degree of decolorization in the dark as shown in Fig. 2. After this point, the un-identified phase decreased as seen in Fig. 1 then the degree of adsorption or decolorization in the dark also decreased with an increased KI concentration.

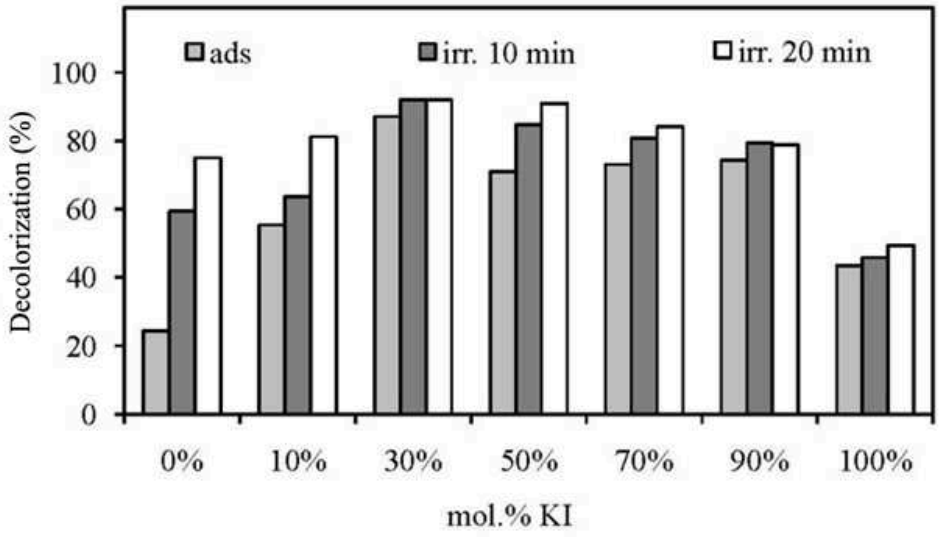

Fig. 2. Efficiency of MB decolourization by the powders prepared from the solution containing various mol.% KI in the Na_2HPO_4 solution ("ads" = dark and "irr" = irradiation).

After adsorption for 30 min in the dark, the decolorization efficiency did not significant increased but its efficiency was further increased when the visible light was irradiated as presented in Fig 2. This could confirm the photocatalytic reaction of prepared products. The photocatalytic decolorization of Ag_3PO_4 has been reported by the interaction between photogenerated holes in valence band of photocatalyst and dye molecules [5]. The photocatalytic efficiency of pure Ag_3PO_4 (0 mol.% KI) is more than pure AgI (100 mol.% KI) as presented in Fig. 2. Therefore, the photocatalytic ability of compounds in this system was also decreased with an increased KI content. The MB decolorization by these products in this system could be come from a combination between adsorption and photocatalytic phenomena.

Summary

The heterostructure of AgI/Ag_3PO_4 was not produced by the co-precipitation method between $AgNO_3$ and Na_2HPO_4 + KI solutions. At low concentration of KI, an un-identified phase and Ag_3PO_4 were detected in the XRD patterns while the mixed phase between the un-identified phase and the AgI was presented when the KI concentrations were between 30 and 90 mol.%. This un-identified phase showed a good adsorption phenomenon in the dark condition. Under visible light, the products in this system can reduce the MB concentration and this could confirm the presence of

photocatalytic reaction. Therefore, the MB decolorization by the products in this system could combine between the adsorption and photocatalytic phenomena.

Acknowledgments

The authors would like to thank Dr.Brian Hodgson for assistance with the English.

References

[1] J.M. Herrmann, Heterogeneous photocatalysis: state of the art and present applications, Top. Catal. 34 (2005) 49-65.

[2] Y.P. Bi, S.X. Ouyang, N. Umezawan, J.Y. Cao, J.H. Ye, Facet Effect of Single-Crystalline Ag_3PO_4 Sub-microcrystals on Photocatalytic Properties, J. Am. Chem. Soc. 133 (2011) 6490-6492.

[3] J. Cao, B. Luo, H. Lin, B. Xu, S. Chen, Visible light photocatalytic activity enhancement and mechanism of $AgBr/Ag_3PO_4$ hybrids for degradation of methyl orange, J. Hazard. Mater. 217-218 (2012) 107-115.

[4] N. Machida, S. Nishida, T. Shigematsu, H. Sakai, M. Tatsumisago, T. Minami: Mechano chemical synthesis of a silver ion conductor in the system $AgI–Ag_3PO_4$, Solid State Ionics 136-137 (2000) 381-386.

[5] Z. Yi, J. Ye, N. Kikugawa, T. Kako, S. Ouyang, H. Stuart-Williams, H. Yang, J. Cao, W. Luo, Z. Li, Y. Liu, R.L. Withers, An orthophosphate semiconductor with photooxidation properties under visible-light irradiation, Nature Mater. 9 (2010) 559-564.

CHAPTER 3:

Ceramics

Advanced Materials Research Vol. 970 (2014) pp 35-38

doi:10.4028/www.scientific.net/AMR.970.35

Investigation of Ultrasonic Pretreatment on the Synthesis of Zeolite-T and Its CO_2 Adsorption Characteristics

Y. F. Yeong[1]*, St. A. Novichaka[1], L.S. Lai[1], K. K. Lau[1], M. S. Azmi[1]

[1]School of Chemical Engineering, Universiti Teknologi PETRONAS, Bandar Seri Iskandar, 31750 Tronoh, Perak Malaysia

*yinfong.yeong@petronas.com.my

Keywords: Synthesis, Zeolite-T, Ultrasonic pre-treatment, CO_2 adsorption.

Abstract. In the present work, ultrasonic pretreatment method was firstly introduced in synthesizing of zeolite-T. The effect of ultrasonic pre-treatment on the synthesis duration was investigated. The structure and morphology of the resulting zeolite-T were characterized using several analytical tools such as X-ray diffraction (XRD), Scanning Electron Microscopy (SEM) and Fourier transfer infrared spectroscopy (FTIR). The CO_2 adsorption characteristic of the resulting zeolite-T was determined using CO_2 physisorption analyzer. Results showed that by introducing ultrasonic pre-treatment, the crystallization time was reduced from 7 days to 3 days, without affecting the structure, morphology and CO_2 adsorption capacity of the resulting zeolite-T.

Introduction

The increase used of fossil fuels during the past 200 years contributes to the steady rise of carbon dioxide (CO_2) level in the atmosphere, the most prominent major greenhouse gas that contributes significantly to global warming [1]. Carbon dioxide which is produced largely in petrochemical processes corrodes pipelines and storage systems within the transportation, due to its acidic property in the presence of water [2]. Furthermore, the reduction of the heat and energy content of natural gas has made the separation of CO_2 from methane in natural gas purification as an important and critical process [3]. Although the techniques used to decrease the emission of carbon dioxide have been extensively reported [3], adsorption has the potential for removal of CO_2 as compared to the other techniques by considering the high adsorption capacity and selectivity of the existed adsorbents such as activated carbon and crystalline aluminosilicate zeolites etc [4].

In the recent year, zeolite-T has been reported as a potential adsorbent for CO_2 removal due to its pore characteristics [3]. Zeolite T is an aluminosilicate molecular sieve which demonstrated crystalline structure of offretite (OFF) and erionite (ERI) zeolite structure with the pore size of 0.36 nm x 0.51 nm [5]. The pore size of zeolite-T is comparable to the kinetic diameter of CO_2 (0.33 nm) molecules which lead to high adsorption coverage of CO_2 in its zeolitic pores. Furthermore, T-type zeolite is a potential adsorbent in CO_2 adsorption process because it can adsorb relatively large quantities of adsorbate at either very low pressure or concentrations [6].

In spite of these advantages, there are remaining issues that need to be overcome so that high quality materials of zeolite-T can be easily synthesized. As reported from the literature [3,5], the crystallization time of zeolite-T was relatively time consuming as compared to the other types of zeolites, which was up to 7 days. In addition, there are limited information reported on the synthesis and characterization of zeolite-T. Therefore, the main objective of the present work is to investigate the effect of ultrasonic pre-treatment on the synthesis duration of zeolite-T. The crystallization times are varied in order to study the properties changes of the resulting zeolite-T. The structure and morphology of the samples were characterized using numbers of analytical tools. The CO_2 adsorption characteristic of zeolite-T was determined using CO_2 physisorption analyzer.

Experimental

Synthesis of Zeolite-T. Sodium hydroxide (NaOH, 99% wt., Merck), potassium hydroxide (KOH, 85% wt., Merck), sodium aluminate (NaAlO2, BDH [Na_2O, 41% wt. + Al_2O_3, 54% wt.]), precipitated silica (SiO_2, 99.8% wt., Aldrich), and deionized water were used as received.

The experiments were performed by following the method reported by Mirfendereski and coworkers [5]. The aluminosilicate gel with mole composition ratio of $1SiO_2$: $0.04Al_2O_3$: $0.26Na_2O$: $0.09K_2O$: $14H_2O$ was prepared. In order to study the effect of ultrasonic pre-treatment on the synthesis duration of zeolite-T, the synthesis solution was pre-treated under ultrasonicator for 30 minutes prior to hydrothermal growth at 120 ^oC in the oven. The synthesis durations were varied from 7 days (reference sample, without ultrasonic pre-treatment), 5 days, 4 days and 3 days. After washing and drying, the synthesized samples were stored in dessicator prior to characterization study and adsorption test.

Characterization. The crystalline structure of the samples were characterized using X-ray diffraction (STOE Stadi-P diffractometer) with CuKα radiation (λ = 1.54059 Å) in 2 theta range of 5-50°. The infrared (IR) spectra were recorded using Fourier Transform Infrared spectrometer (Perkin Elmer) in wavenumber range of 400- 4000 cm^{-1} using KBr method. The morphology of the samples were examined by scanning electron microscope (Hitachi SU 8000).

CO_2 Adsorption Test. Adsorption of CO_2 on the samples was analyzed using physisorption analyzer, BELSORP Mini II. Samples were outgassed in vacuum for at least 24 hours prior to sorption measurement.

Results and Discussion

X-ray Diffraction (XRD). As the main phase of zeolite-T is offretite, the peaks of zeolite-T are assigned according to the standard XRD pattern of offretite. Table 1 summarizes the experimental conditions and the XRD results for the zeolite-T samples synthesized in the present work.

Table 1: Experimental conditions and XRD results for the samples synthesized in this study

Samples	Crystallization Temperature (^oC)	Ultrasonic Treatment Duration (minutes)	Crystallization Duration (days)	Product Phase (XRD)
S1	120	0	7	Zeolite T
S2	120	30	5	Zeolite T
S3	120	30	4	Zeolite T
S4	120	30	3	Zeolite T

Fig. 1 shows the XRD patterns of zeolite-T synthesized with and without ultrasonic pre-treatment at different crystallization time. It was observed that all the samples shows zeolite-T morphology with the peaks at 2θ = 7.7°,13.5°, 20.5°, 23.5°, 24.8° and 31.5° [3]. These results show that by introducing ultrasonic pre-treatment, the crystallization time was shortened from 7 days to 3 days while the structure of zeolite-T was maintained with slightly decrease in crystallinity.

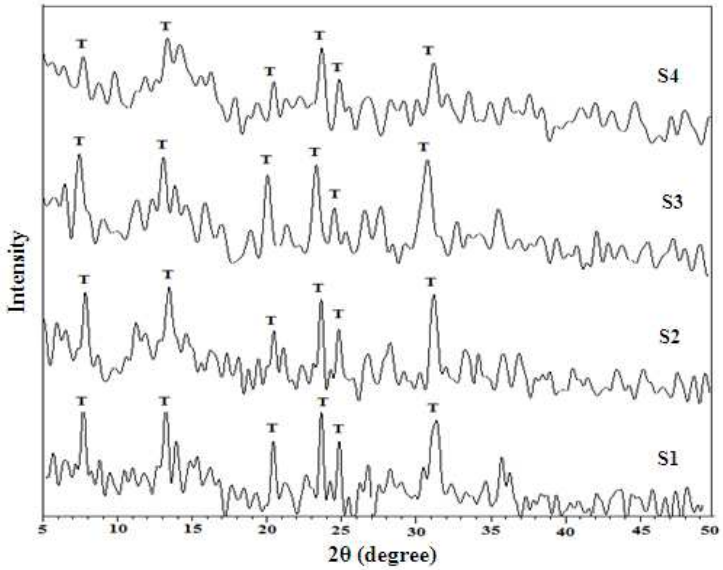

Fig. 1. XRD patterns of the samples

Fourier Transfer Infrared (FTIR). The infrared (IR) spectra of the resultant zeolite-T are illustrated in Fig. 2. IR spectra for all samples show similar peaks at 430, 470, 575, 615, 720, 775, 1040, and 1050 cm^{-1}, which consistent with the major absorbance peaks for zeolite-T reported in the literature [7]. Referring to Fig. 2, the peaks at 430 cm^{-1} and 470 cm^{-1} correspond to the T-O bonding in the zeolite-T topology. The peaks at 575 cm^{-1} and 615 cm^{-1} are attributed to the secondary building units of single 6-ring of zeolite-T structure. Meanwhile, peaks at 720 cm^{-1} and 780 cm^{-1} are due to the symmetric stretching vibration of double ring and peaks at 1040 cm^{-1} and 1150 cm^{-1} are attributed to asymmetric stretching vibration. From these results, it can be concluded that all the samples synthesized in the present work showed zeolite-T structure.

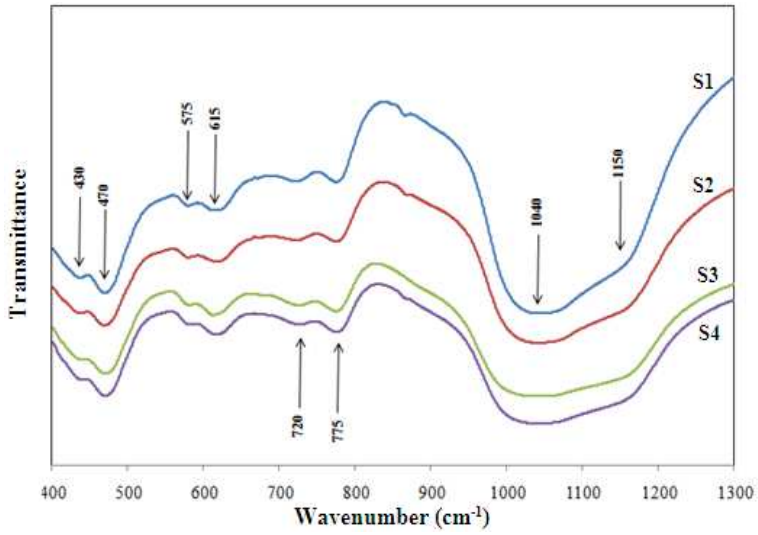

Fig. 2.FTIR spectra of the samples

Scanning Electron Microscopy (SEM). Fig. 3 shows the surface morphology of the synthesized zeolite-T. All the zeolite-T samples synthesized in the present work shows typical crystal rod-like morphology of zeolite-T reported in the literature [5]. The SEM images confirm the formation of zeolite-T for all the samples. The structure of zeolite-T is still maintained regardless of the reduction of crystallization time.

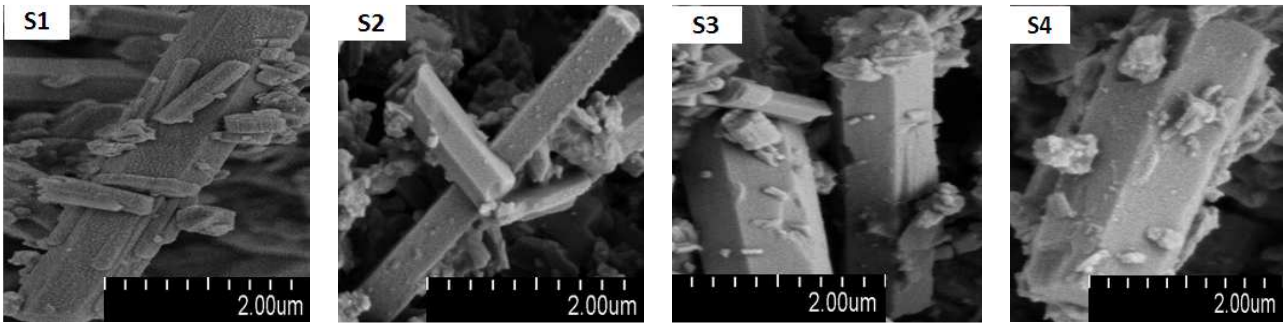

Fig. 3. SEM images of the samples

CO_2 Adsorption Study. The single gas adsorption isotherms of CO_2 were obtained at constant temperatures of 298 K for pressures variable in range of 0.1 – 1 kPa. The isotherms of all the zeolite-T samples are displayed in Fig. 4. It was observed that the CO_2 adsorption capacity of the sample increases slightly when crystallization time was shortened. The CO_2 adsorption capacity for S1, S2, S3, and S4 are 1.1039, 1.0894, 1.2634, and 1.5628 mmol/g, respectively, which was consistent with the CO_2 adsorption value reported in the literature (1.387 mmol/g) [3]. These results show that the ultrasonic pre-treatment not only successfully reduced the synthesis duration of the zeolite-T, but also leads to the slight increment of CO_2 adsorption capacity.

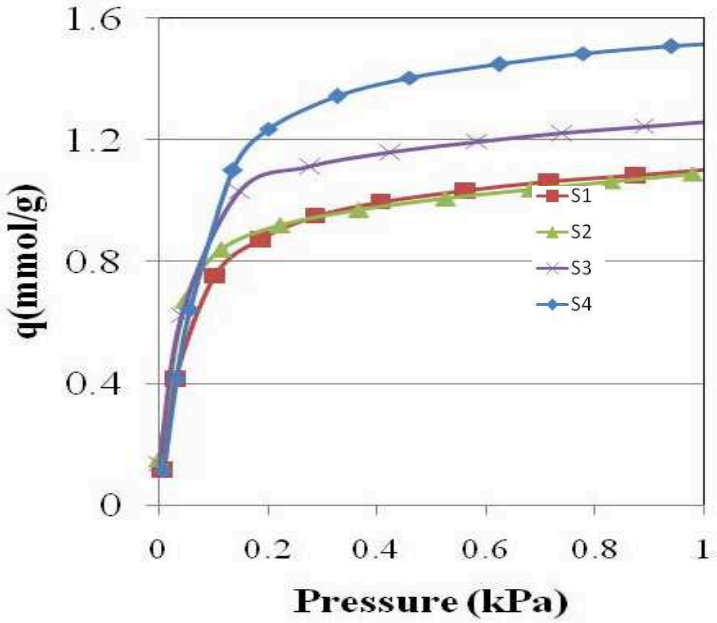

Fig. 4. Adsorption of CO_2 of the samples

Summary

We have successfully synthesized zeolite-T within shorter duration by introducing ultrasonic pre-treatment method. XRD results showed that all the samples synthesized in the present work exhibited zeolite-T topology. FTIR results further confirmed the structure of the zeolite-T. The SEM images displayed the typical rod-like crystals of zeolite-T for all the samples. Based on the physisorption test, the ultrasonic pre-treatment has slightly increased the CO_2 adsorption capacity from 1.10 mmol/g to 1.56 mmol/g. As conclusion, ultrasonic pre-treatment was proven as an effective method to reduce the crystallization time of zeolite-T from 7 days to 3 days and at the same time, maintaining the structure, morphology and CO_2 adsorption capacity of the samples.

Acknowledgements

The financial and technical supports provided by CO_2 Management (MOR) research group, Universiti Teknologi PETRONAS are duly acknowledged.

References

[1] D. Bonenfan , M. Kharoune, P.Niquette, M. Mimeault, R. Hausler, Advances in principal factors influencing carbon dioxide adsorption on zeolites, Sci. Technol. Adv. Mater. 9 (2008) 013007 (1-7).

[2] S. M. Mirfendereski, T. Mazaheri, M. Sadrzadeh, T. Mohammadi, CO_2 and CH_4 permeation through T-type zeolite membranes: Effect of synthesis parameters and feed pressure, Sep. Puri. Technol 61(2008) 317-323.

[3] M. D. Rad, S. Fatemi, S. M. Mirfendereski, Development of T type zeolite for separation of CO_2 from CH_4 in adsorption processes, Chem. Eng. Res. Des. 90 (2012) 1687–1695.

[4] Information on http://www.intechopen.com/books/advances-in-natural-gastechnology/

[5] M. Mirfendereski, M. Toraj, Investigation of hydrothermal synthesis parameters on characteristics of T type zeolite crystal structure, Powder Technol. 206 (2011)345-352.

[6] D. W. Breck and A, N. A. Tonawanda, U.S. Patent 2,950,952. (1958)

[7] Y. Sanyuan, N. P. Evmiridis, Synthesis and characterization of an offretite/erionite type zeolite, Micropr. Mater. 6 (1996)19-26.

Advanced Materials Research Vol. 970 (2014) pp 39-43

doi:10.4028/www.scientific.net/AMR.970.39

Sintering Effects on Microstructure and Electrical Properties of $(Na_{0.5}K_{0.5})_{0.94}Li_{0.06}NbO_3$ Lead- Free Ceramics

Pornsuda Bomlai[1,2,a*]

[1]Department of Materials Science and Technology, Faculty of Science, Prince of Songkla University, Songkhla, 90112, Thailand

[2]Center of Excellence in Nanotechnology for Energy (CENE), Prince of Songkla University, Songkhla, 90112, Thailand

[a*]ppornsuda@yahoo.com

Keywords: Lead-free materials, Two-step sintering, Electrical properties

Abstract. $(Na_{0.5}K_{0.5})_{0.94}Li_{0.06}NbO_3$ lead-free ceramics were prepared using two different sintering methods: a conventional sintering (CS) and a two-step sintering (TSS) techniques. Different sintering temperatures were considered to optimize the density, microstructure and electrical properties. For CS, the grain size of samples sintered in this method increased continuously with the density decreased. By TSS the sample initially heated to 1160 °C, highest density (97%) was achieved after holding at 980 °C for 6 h. SEM micrographs revealed that two-step sintering decreased the grain size from 7.0 μm to 2.5 μm compared with conventional sintering, as the result of a lower holding temperature. Moreover, the volatilization loss of Na and K elements could be inhibited by two-step sintering. XRD results indicated that the secondary phase formed in all samples but it decreased after increasing of CS-sintering temperature. It was also obtained that the two-step sintering improved electrical properties of samples. The Curie temperature (T_C) increased with increasing of the holding temperature. Sample with the optimal sintering process: T_1=1160 °C, t_1=10 min, T_2 = 940 °C, t_2 = 6 h, excellent properties of dielectric constant (ε_r) = 530, dissipation factor (tan δ) = 0.02, Curie temperature = 388 °C, and piezoelectric charge constant (d_{33}) =168 pC/N were achieved.

Introduction

In recent years, sodium potassium niobate ($Na_{0.5}K_{0.5}NbO_3$, NKN)-based lead-free piezoelectric ceramics have been widely studied to replace Pb-based ceramics as being more environmental friendly [1]. However, pure NKN ceramics are difficult to densify by normal sintering due to the high volatility of alkaline elements at high sintering temperatures, and so the NKN ceramics exhibit poor piezoelectric properties (d_{33} ~80 pC/N and k_p ~36%) [2].

The two-step sintering has been reported for preparing another ceramics to obtain fully dense nanograin ceramics because it suppresses grain growth in the final stage of sintering [3]. This special sintering process could be seen as the heating rate-controlled sintering and the low-temperature sintering process. It can eliminate the pores and reduce the volatilization of the low-melting-point substances [4]. Microstructures as well as electrical properties of NKN ceramics are extremely sensitive to sintering temperature and also the sintering time. Zhao et al. reported the piezoelectric coefficient of ~268 pC/N can be achieved by optimizing the sintering temperature of $LiTaO_3$-doped NKN ceramics [5]. In the present work, a study concerning the sintering of $(Na_{0.5}K_{0.5})_{0.94}Li_{0.06}NbO_3$ ceramics was carried out using the conventional and two-step sintering methods, and the effects of sintering condition on the phase structure, microstructure and electrical properties of $(Na_{0.5}K_{0.5})_{0.94}Li_{0.06}NbO_3$ ceramics was systematically investigated.

Experimental

$(Na_{0.5}K_{0.5})_{0.94}Li_{0.06}NbO_3$ (NKLN) lead-free ceramics were prepared by a conventional solid-state reaction process using two different sintering methods: a conventional sintering (CS) and a two-step sintering (TSS) techniques. The starting materials were Na_2CO_3 (99.9%), K_2CO_3 (99.0%), Li_2CO_3 (>99.0%) and Nb_2O_5. The powders in stoichiometric proportions were thoroughly mixed and ball-

milled in ethanol for 24 h using zirconia grinding media. After mixing, the slurry was dried and calcined at 800 °C for 2 h in air, then re-milled and dried again. The obtained powders with 3 wt% PVA binder were pressed into disc-shaped pellets of 15 mm in diameter at 100MPa. Sintering of the green bodies was carried out by CS and TSS methods. The CS was carried out at 1100 – 1160 °C (T_1) for 2 h (t_2) in air with a heating rate of 5°C/min. For the TSS, the sintering procedure was programmed from the first-step sintering temperature (T_1) with a rapid heating rate 10 °C/min, then held for 10 min (t_1), and then rapidly cooled to a lower second-step temperature T_2 at 20 °C/min. The temperature was held at T_2 for 6 h (t_2). The symbols ‘‘$T_1/t_1/0/0$’’ and ‘‘$T_1/t_1/T_2/t_2$’’ were used to indicate for conventional sintering and two-step sintering, respectively.

The phase structure of the samples was examined by the X-ray diffraction (XRD, X’Pert MPD, Philips) using CuKα radiation. Surface morphologies of sintered specimens were observed by a scanning electron microscope (SEM, Quanta400, FEI). The bulk density of sintered samples was determined by the Archimedes method. Silver paste was coated on both sides of the specimens after firing at 600 °C for 10 min to form electrodes for the dielectric and piezoelectric measurements. The dielectric constant as a function of temperature of the sample was obtained by using a high precision LCR meter (LCR 821, GW INSTEK). Piezoelectric properties were measured using a piezo- d_{33} meter (YE2730A d_{33} Meter, APC International, Ltd.).

Results and discussion

Figure 1 shows the XRD patterns of the NKLN samples sintered under CS and TSS conditions. Both the samples displayed a similar pattern to that reported previously for orthorhombic NKN-based ceramics [6]. It was also found the secondary phase of a tungsten bronze phase (e.g., $K_6Li_4Nb_{10}O_{30}$) formed in all samples but it decreased after increasing of CS-sintering temperature. In addition, the positions of the diffraction peaks of the ceramics slightly shifted to higher angles with increase of temperature T_1 and T_2. Therefore, the geometrical distortion of the ceramics was induced by sintering at high temperature.

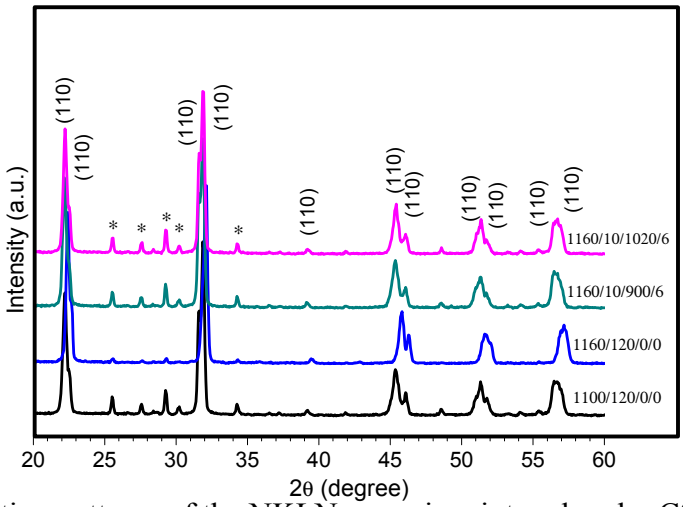

Figure 1. X-ray diffraction patterns of the NKLN ceramics sintered under CS (1100/120/0/0 and 1160/120/0/0) and TSS (1160/10/900/6, 1160/10/120/6) conditions (* = $K_6Li_4Nb_{10}O_{30}$).

The SEM micrographs of the samples sintered under CS and TSS conditions are shown in Figure 2. All compositions showed secondary recrystallization and the grains were generally rectangular in shape. For CS-samples, the microstructure became denser and the grains size was much larger (up to 7.0 μm) when T_1 increased from 1100 to 1160 °C. The reduction in grain size can be observed in the microstructure of TSS- samples. It is revealed that the two-step sintering had an evident effect on grain size reduction, as a grain growth inhibitor. A fine-grain microstructure can thus be obtained using two-step sintering with average grain sizes ~2.5 μm for sample with 1160/10/1020/6 condition. Thus, two-step sintering method avoids undesirable grain growth and provides a finer and uniform microstructure, which is an attractive feature for the processing of electroceramics.

The densities of the NKLN samples sintered under different condition are shown in Table 1. For CS, the highest density (4.256 ± 0.01 g/cm^3) was obtained for the samples with 1100/120/0/0 condition, equivalent to the relative densities of 94%. Further increasing sintering temperature to 1160°C led to the decrease of density, which was due to the volatility of K_2O and Na_2O in the ceramics for high sintering temperature. The sintering of NKLN ceramics was much improved for two-step sintering, and the sample with 1160/10/980/6 condition demonstrated the highest density of 4.375 g/cm^3, which corresponds to 97% of the theoretical density. This result indicates that the two-step sintering process is effective for the densification of lead-free NKLN ceramics, despite no sintering additive and cold isostatic pressing are used.

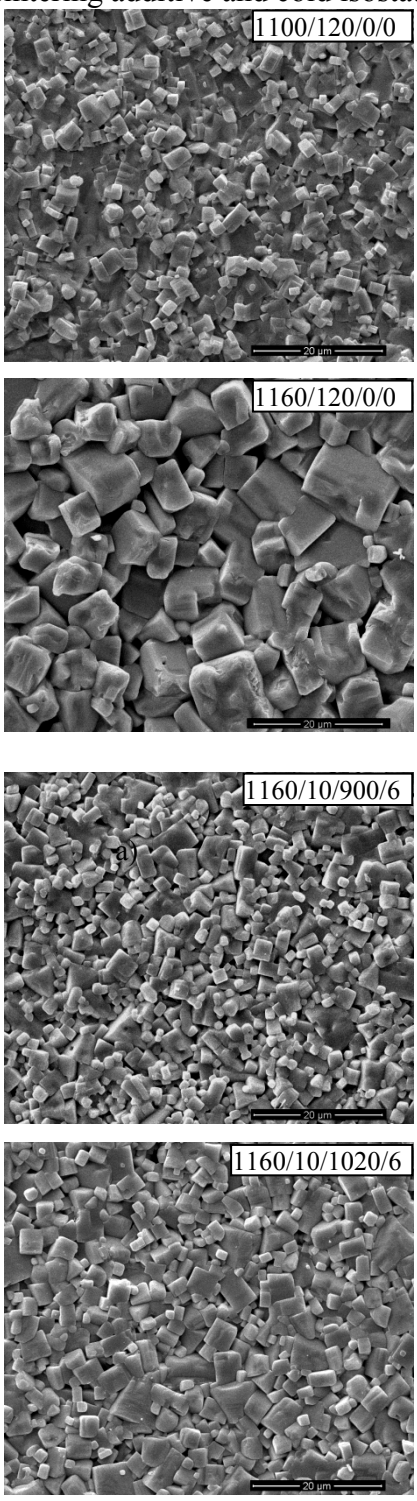

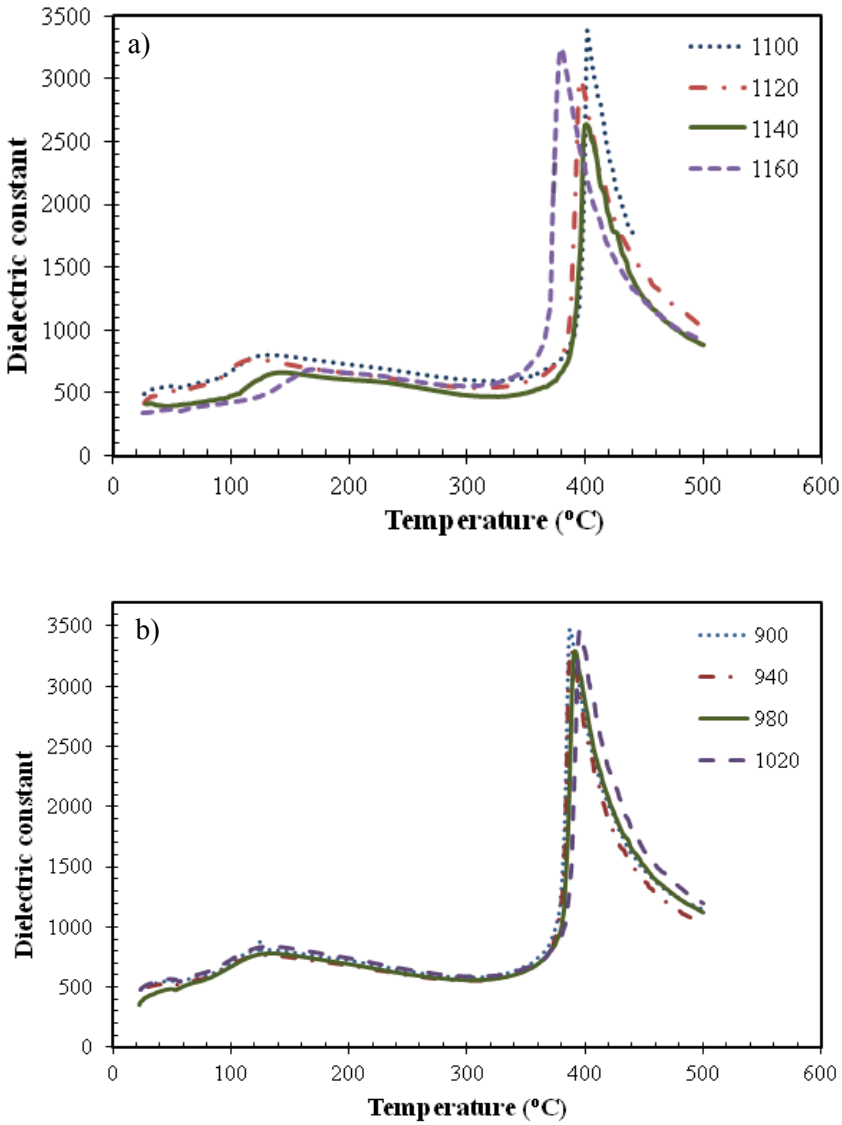

Figure 3. Temperature dependence of dielectric constant for the NKLN ceramics sintered under CS (a) and TSS (b) conditions.

Figure 2. SEM micrographs of the NKLN ceramics sintered under CS and TSS conditions.

The temperature dependence of the dielectric properties for the samples sintered under CS and TSS conditions measured at 10 kHz is shown in Figure 3, and Table 1. The two phase transitions, corresponding to the orthorhombic to tetragonal (T_{O-T}) and ferroelectric tetragonal to paraelectric cubic (T_C) phase transition, are clearly observed. It was found that the T_{O-T} and T_C of the CS-samples showed composition inhomogeneity with increasing sintering temperature T_1. After sintering by two-step sintering, the T_{O-T} shifted to higher temperature. The T_C value of the TSS-samples also increased slightly from 387 to 395 °C. It is obvious that the ε_r of the NKLN ceramics decreased after the sintering temperature T_1 and holding temperature T_2 increased. This is due to the increase in grain size.

The piezoelectric property of poled NKLN ceramics is shown in Table 1. The two-step sintering method greatly enhanced the piezoelectric properties of the NKLN ceramics. The best property with a d_{33} value of 168 pC/N was obtained in the composition with 1160/10/940/6 condition. It is believed that the observed high piezoelectric property should be ascribed to the high density, and good electrical resistivity of the ceramic. The CS-samples showed the lower value of the d_{33} value. It may be partly caused by the volatilization of alkali elements during the high temperature sintering.

Table 1. The density, ε_r and $\tan\delta$ at room temperature (RT) at 10 kHz, orthorhombic-tetragonal polymorphic phase transition temperature (T_{O-T}), Curie temperature (T_C) and piezoelectric constant (d_{33}) of the NKLN samples sintered under CS and TSS conditions.

Samples	Sintering condition	Density (g/cm^3)	$\varepsilon_{r,\ RT}$	$\tan\delta_{,\ RT}$	T_{O-T} (°C)	T_C (°C)	d_{33} (pC/N)
CS-sample	1100/120/0/0	4.256	486	0.031	132	402	129
	1120/120/0/0	4.162	431	0.033	121	396	116
	1140/120/0/0	4.014	416	0.232	142	401	114
	1160/120/0/0	4.018	340	0.217	167	380	95
TSS-sample	1160/10/900/6	4.260	519	0.029	125	387	163
	1160/10/940/6	4.280	530	0.021	126	388	168
	1160/10/980/6	4.375	433	0.017	130	391	150
	1160/10/1020/6	4.258	520	0.031	132	395	145

Summary

Two-step sintering method was successfully applied to improve density and piezoelectric property of the NKLN ceramics. Results show that an orthorhombic phase appeared in all samples. The density, microstructure and electrical properties of the ceramics sintered by conventional and two-step sintering techniques were obviously dependent on sintering temperature (T_1, T_2). The final grain size of the samples sintered by two-step method was ~ 2.5 μm, while it was ~ 7.0 μm for the conventional sintering. The two-step sintering also enhanced electrical properties of samples. The T_C increased with increasing of the holding temperature T_2. The sample with the optimal sintering condition: T_1=1160 °C, t_1=10 min, T_2 = 940 °C, t_2 = 6 h displayed excellent overall properties: ε_r = 530, $\tan\delta$ = 0.02, T_C = 388 °C and d_{33} =168 pC/N.

Acknowledgements

This research is financially supported by Prince of Songkla University under contract number SCI560371S.

References

[1] Y. Saito, H. Takao, T. Tani, T. Nonoyama, K. Takatori, T. Homma, T. Nagaya, M. Nakamura, Lead-free piezoceramics, Nature. 432 (2004) 84-87.

[2] H. Birol, D. Damjanovic, N. Setter, Preparation and characterization of $(K_{0.5}Na_{0.5})NbO_3$ ceramics, J. Eur. Ceram. Soc. 26 (2006) 861-866.

[3] I.W. Chen, X.H. Wang, Sintering dense nanocrystalline ceramics without final-stage grain growth, Nature. 404 (2000) 168-171.

[4] D.L. Wang, K.J. Zhu, H.L. Ji, J.H. Qiu, Two-step sintering of the pure $K_{0.5}Na_{0.5}NbO_3$ Lead-Free piezoceramics and its piezoelectric properties, Ferroelectric. 392 (2009) 120-126.

[5] P. Zhao, B. Zhang, J. Li, Enhanced dielectric and piezoelectric properties in $LiTaO_3$-doped lead-free (K, Na)NbO_3 ceramics by optimizing sintering temperature, Scripta. 58 (2008) 429-432.

[6] P. Bomlai, P. Wichianrat, S. Muensit, S.J. Milne, Effect of calcinations and excess alkali carbonate on the phase formation and particle morphology of $Na_{0.5}K_{0.5}NbO_3$ powders, J. Am. Ceram. Soc. 90[5] (2007) 1650-1655.

Advanced Materials Research Vol. 970 (2014) pp 44-47

doi:10.4028/www.scientific.net/AMR.970.44

Vapochromic Copper(I) Pyrazolate Complex Materials For Phosphorescent Chemosensors of Ethanol

N.F. Ghazalli[1,2,a], L. Yuliati[3,b], S. Endud[1,c], M. Shamsuddin[1,d] and H. O. Lintang[2,e*]

[1]Department of Chemistry, Faculty of Science, Universiti of Teknologi Malaysia, 81310 UTM Johor Bahru, Johor, Malaysia
[2]Department of Chemical Sciences, Faculty of Science and Technology, Universiti Malaysia Terengganu, 31020 Kuala Terengganu, Terengganu, Malaysia
[3]Ibnu Sina Institute for Fundamental Science Studies, Universiti Teknologi Malaysia, 81310 UTM Johor Bahru, Johor, Malaysia
[a]nur_fatiha85@yahoo.com, [b]leny@ibnusina.utm.my, [c]salasiah@kimia.fs.utm.my, [d]mustaffa@kimia.fs.utm.my, [e*]hendrik@ibnusina.utm.my

Keywords: Chemosensors, Vapochromic Complex, Copper(I) Pyrazolate Complexes, Volatiles Organic Compound, Metallophilic Interaction

Abstract. Here chemosensor materials of trinuclear copper(I) pyrazolate complexes have been successfully synthesized and isolated using two types of 3,5-dimethyl and 4-(3,5-dimethoxybenzyl)-3,5-dimethyl pyrazole ligands. Upon excitation at 280 nm, the resulting trinuclear 3,5-dimethyl copper(I) pyrazolate complex (complex **A**) and trinuclear 4-(3,5-dimethoxybenzyl) copper(I) pyrazolate complex (complex **B**) showed emission bands centered at 590 and 604 nm, respectively. These results were in good agreement with their greenish-white powders and it is characteristic of phosphorescent metal complexes from the weak Cu(I)-Cu(I) metallophilic interaction. Upon direct or stepwise exposure to ethanol vapor with series of concentrations (12.5, 25, 50, 100, 150 and 200 μL in 22 mg of chemosensor), the emission of chemosensor complex **A** was not shifted even after 1 d. Interestingly, chemosensor complex **B** showed gradually changes in both emission band with shifting from 602 to 552 nm and color with changing from orange to green under Ultra-violet (UV) hand lamp (254 nm) at the dark room due to the attachment of benzyl ring to the pyrazole ligand. This positive response for chemosensor complex **B** was reversible; hence, this optical phosphorescent material can be used for developing vapochromic sensors of ethanol.

Introduction

Recently, luminescent materials with their fluorescent and phosphorescent properties have gains great attention for development of chemical sensors (chemosensors) [1,2] especially in molecular recognition using supramolecular assembly of organic chromophores [3]. Since organic vapors have been found as one of pollutants with give health and environment problems [4], changes in color and emission properties of luminescent chemosensor materials have been optically utilized for detecting volatile organic compounds (VOCs) [3]. In this case, high performance chemosensors with capability to detect the changes of chromophores upon exposure to vapor (vapochromic) at low concentration, high sensitivity, selectivity and reusability as well as simple and low-cost technology are really required [5,6].

Since the discovery of vapochromic chemosensors using palladium (Pd) and platinum (Pt) double-complexes [4,7,8], phosphorescent copper complexes have been developed as a new optical sensor [2] because these complexes can be synthesized using less expensive precursors. Considering ethanol is one of the VOCs from alcohol family, copper(I) and copper(II) complexes have been used for chemosensor of ethanol using the changes in their weak intermolecular metal-metal interactions. However, all of reports have shown that the complete sensing can be achieved with either longer response time or On-Off changes such as irreversible changes in 2 h [9] and reversible change from luminescent to non-luminescent [10] using copper(I) complexes or irreversible changes in 2 d using copper(II) complex [11]. Therefore, it is interesting to develop new phosphorescent chemosensor materials with capability to detect ethanol in short response time and

reversible change as well as less amount of sensor. Here, we report phosphorescent trinuclear copper(I) pyrazolate complexes from two types of pyrazole ligands as optical chemosensors of ethanol. In particular, we highlight the importance of ligands in design of chemosensors to achieve high performance based on their sensitivity, re-usability and quick response time.

Experimentals

Synthesis of trinuclear pyrazolate copper(II) complexes. Trinuclear copper(I) pyrazolate complexes have been successfully synthesized by a Schlenk technique using two types of 3,5-dimethyl and 4-(3,5-dimethoxybenzyl)-3,5-dimethyl pyrazole ligands in the presence of tetrakis(acetonitrile)copper(I) hexafluorophosphate ($[Cu(MeCN)_4]PF_6$) according to previous report [12]. The resulting copper(I) pyrazolate complexes were successfully isolated in 80% for trinuclear 3,5-dimethyl copper(I) pyrazolate complex (complex **A**) and in 99% for trinuclear 4-(3,5-dimethoxybenzyl) copper(I) pyrazolate complex (complex **B**).

Characterizations. Emission spectra were recorded on a JASCO model FP-8500 spectrophotometer with measurement parameters for excitation and emission bandwidth of 5 nm, response time of 0.1 s, sensitivity of photomultiplier tube voltage at "very low mode (250 V)", measurement range of emission from 450 to 850 nm with scan speed of 1000 nm/min. UV hand lamp with a Vilber Lourmat model VL-4.LC with power of 8 W, intensity equivalent to 7 mW/cm^3 and filter lifetime for 2000 h was used to check of the color changes upon exposure to VOCs. Photographs were captured using a Panasonic model DMC-FZ38 digital camera with macro zoom tool under UV hand lamp at 254 nm at the dark room.

Result and Discussion

Photoluminescent spectrophotometer can be used for studying the optical properties of trinuclear copper(I) pyrazolate complex materials [13]. Two types of trinuclear copper(I) pyrazolate complexes as shown in Fig. 1a were successfully synthesized from different pyrazole ligands, where complex **A** in Fig. 1a(A) was prepared from 3,5-dimethyl pyrazole while complex **B** in Fig. 1a(B) was prepared from 4-(3,5-dimethoxybenzyl)-3,5-dimethyl pyrazole. Fig. 1b showed emission spectrum of complexes **A** and **B** upon excitation at 280 nm. These compounds displayed emission bands with a peak centered at 590 nm for complex **A** and 602 nm for complex **B**, indicating large Stokes shift for both of the complexes ($\Delta\lambda$ = 310 nm for complex **A** and 322 nm for complex **B**). These emissions were good agreement with their greenish-white powders as shown in inset images of Fig. 2a for complex **A** and Fig. 2b for complex **B**. Moreover, these results are characteristics of phosphorescent metal complexes modified by a *chair-like* coordination geometry of the weak intermolecular Cu(I)-Cu(I) metallophilic interactions from the triplet excited state [12].

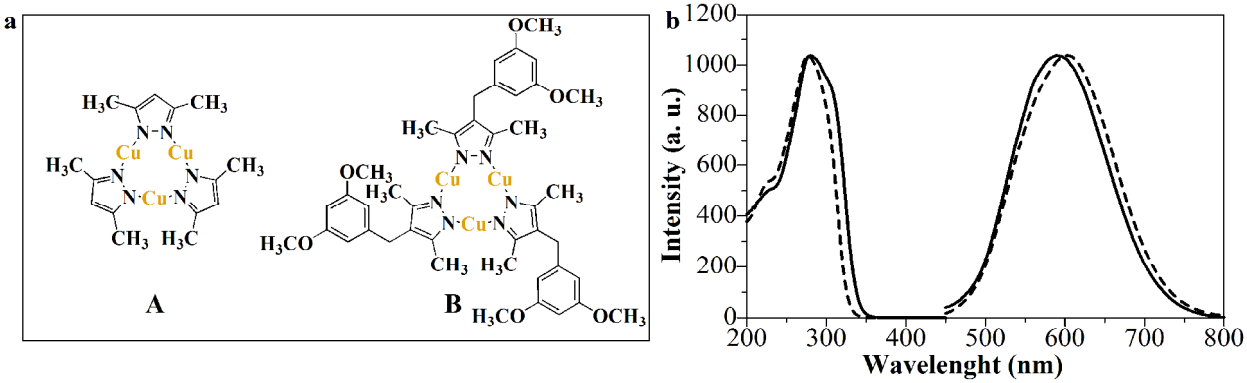

Figure 1: a) Molecular structures and b) luminescent profile (excitation and emission) of trinuclear 3,5-dimethyl copper(I) pyrazolate complex (complex A, ___) and trinuclear 4-(3,5-dimethoxybenzyl)-3,5-dimethyl copper(I) pyrazolate complex (complex B, _ _ _).

Fig. 2 showed the changes in emission of the chemosensors **A** and **B** upon stepwise exposure to ethanol with the concentration of 200 μL in 22 mg of chemosensor. When it monitored at 280 nm, the emission spectrum of complex **A** showed only a little bit changes with a blue shifting from 590 to 585 nm ($\Delta\lambda$ = 5-7 nm) even after 35 mins as shown in Fig. 2a including the inset figure. There were not anymore changes even the complex was continually kept in ethanol vapor for 1 d. Surprisingly, complex **B** showed quickly blue shifting of the emission even only exposure in 5 mins with $\Delta\lambda$ of 15 nm as shown in Fig. 2b. In the inset figure of Fig. 2b, these shifting were finally saturated starting from 25 to 35 mins to give $\Delta\lambda$ as high as 50 nm with an emission band centered at 554 nm. Interestingly, complex **B** showed automatically change of the emission band to the original of the luminescent by just standing the powder of the complex in room temperature without use external stimuli such heating at the boiling point of the vapor. Such reversible change can be repeated several times for detection of ethanol, indicating high sensing sensitivity and reusability of chemosensor complex **B** for detection of ethanol. These observation suggests that more short distance of the weak Cu(I)-Cu(I) metallophilic interaction in complex **B** effected by the presence of the benzyl ring at the pyrazole ring for light emission can be easily interrupted by the ethanol vapor.

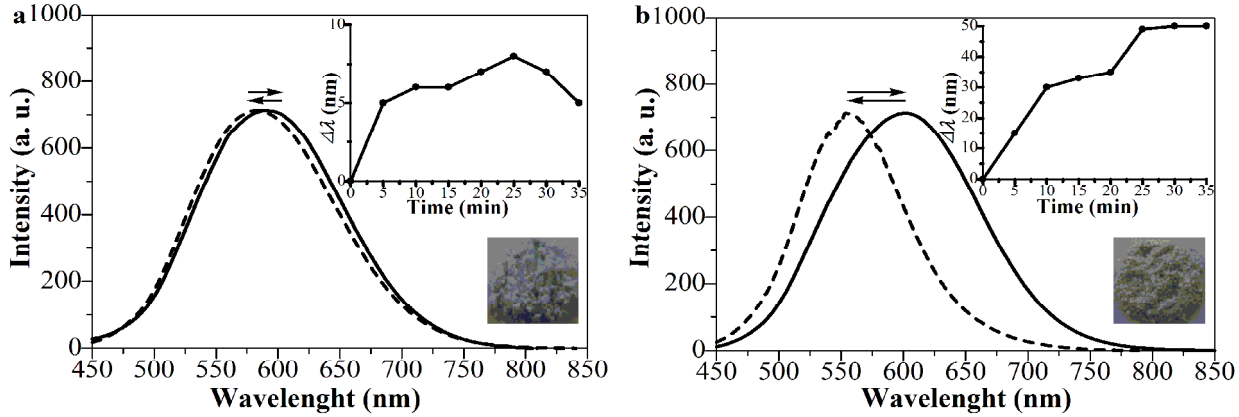

Figure 2: Emission spectral changes of (a) chemosensors complex A, and (b) complex B including their inset figures as a function of exposure times to the shifting with the excitation at 280nm upon exposure to the ethanol with concentration of 200µL in 22mg of chemosensor.

One of the advantages to use optical chemosensors is to monitor the sensing capability by capturing the color changes of the materials upon exposure to VOCs. In this research, in contrast to chemosensor complex **A**, chemosensor complex **B** (22 mg) showed emission color changes from orange to green upon exposure to ethanol (200 μL) in 35 mins as shown in Fig. 3 at the row-bottom. The color changes were also visualized even the concentration of the vapor as low as 50 μL per 22 mg of chemosensor. These observations were good agreement with their emission spectral changes as discussed above in Fig. 2 and for the each concentration.

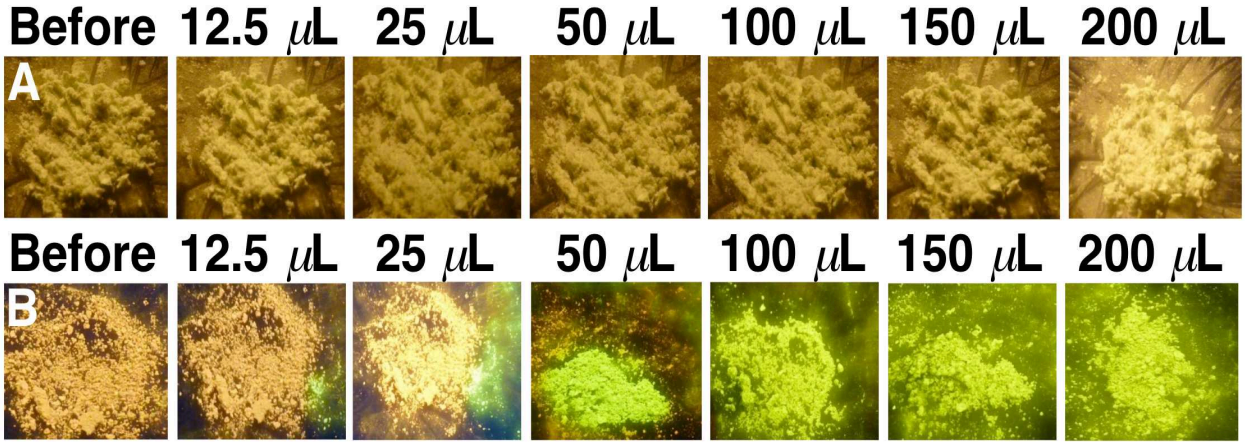

Figures 3. Photographs of chemosensor complexes **A** (row-top) and **B** (row-bottom) before and after direct exposure to ethanol (concentrations of 12.5, 25, 50, 100, 150 and 200 μL in 22 mg of chemosensor) in 35 mins at dark room under a UV hand lamp with excitation at 254 nm.

Summary

It is firstly demonstrated that trinuclear 4-(3,5-dimethoxybenzyl)-3,5-dimethyl pyrazolate complex material (complex **B**) showed phosphorescent chemosensor of ethanol even in the low concentration (50 to 200 μL in 22 mg of chemosensor) by shifting the emission band from 602 to 552 nm and by changing the color from orange to green. This chemosensor complex **B** can provide high sensing capability with quick response time and easy to re-use. In contrast to complex **A**, such sensing capability for chemosensor complex **B** can be only achieved by designing benzyl ring to the pyrazole ligand so that the short distance of the weak intermolecular Cu(I)-Cu(I) metallophilic interaction can be easily tuned by the presence of ethanol vapor. Further study on the effect of benzene ring from 3,5-diphenyl pyrazole ligand (without using benzyl ring) of the copper(I) pyrazolate complex for chemosensor of ethanol will be one of the approaches to study the above phenomena.

Acknowledgements

The authors thank Ministry of Higher Education (MOHE) through Fundamental Research Grant Scheme (FRGS 2013, Vot No. J.130000.7809.4F194), Universiti Teknologi Malaysia, UTM Malaysia for the financial support. The authors also acknowledge Ministry of Science, Technology and Innovation (MOSTI) through National Nanotechnology Directorate (NND), Malaysia for NanoFund Grant (Vote No. J.130000.7926.4H007) and Flagship Research Grant for NanoMalaysia CoE (Vote No. J.130000.7926.4S017) for providing fluorescent spectrophotometer. N. F. Ghazalli thanks Ministry of Higher Education (MOHE) and Universiti Malaysia Terengganu, Malaysia for the financial support in the doctoral course.

References

[1] A. P. de Silva, H. Q. N. Gunaratne, T. Gunnlaugsson, A. J. M. Huxley, C. P. McCoy, J. T. Rademacher, T. E. Rice, Signalling recognition events with fluorescent sensors and switches, Chem. Rev. 97 (1997) 1515-1566.

[2] O. S. Wenger, Vapochromism in organometallic and coordination complexes: chemical sensors for volatile organic compounds, Chem. Rev. 113 (2013) 3686-3733.

[3] F. Mancin, E. Rampazzo, P. Tecilla, U. Tonellato, Self-assembled fluorescent chemosensors, Chem. Eur. J. 12 (2006) 1844-1854.

[4] G. D. Lancaster, G. A. Moore and M. L. Stone, U.S. Patent 544,795. (1995)

[5] Q. Zhao, F. Li, C. Huang, Phosphorescent chemosensors based on heavy-metal complexes, Chem. Soc. Rev. 39 (2010) 3007-3030.

[6] T. W. Bell, N. M. Hext, Supramolecular optical chemosensors for organic analytes, Chem. Soc. Rev. 33 (2004) 589-598.

[7] C. C. Nagel, E. Patent 277,003. (1988)

[8] K. R. Mann, U.S. Patent 57,666,952. (1998)

[9] S. M. Mobin, A. K. Srivastava, P. Mathur, G. K. Lahiri, Single-crystal to single-crystal transformations in discrete hydrated dimeric copper complexes, Dalton Trans. 39 (2010) 1447.

[10] L. Malini, D. Braga, P. P. Mazzeo, B. Ventura, Polymorph and isomer conversion of complexes based on CuI and PPh_3 easily observed via luminescence, Dalton Trans. 41 (2012) 531.

[11] A. Cingolani, S. Galli, N. Masciocchi, L. Pandolfo, C. Pettinari, A. Sirono, Sorption-desorption behavior of bispyrazolato-copper(II) 1D coordination polymers, J. Am. Chem. Soc. 127 (2005) 6144-6145.

[12] M. Enomoto, A. Kishimura, T. Aida, Coordination metallacycles of an achiral dendron self-assemble via metal-metal interaction to form luminescent superhelical fibers, J. Am. Chem. Soc. 123 (2005) 179-183.

[13] H. V. R. Dias, H. V. K. Diyabalanage, M. G. Eldabaja, O. Elbjeirami, M. A. Rawashdeh-Omary, M. A. Omary, Brightly phosphorescent trinuclear copper(I) complexes of pyrazolates: substituent effects on the supramolecular structure and photophysics, J. Am. Chem. Soc. 127 (2005) 7489-7501.

CHAPTER 4:

Coating and Surface Engineering

Advanced Materials Research Vol. 970 (2014) pp 51-54

doi:10.4028/www.scientific.net/AMR.970.51

A Study On Biocompatibility Of Gadolinium Based Anodizing Coating AZ91D Magnesium Alloy in Simulated Body Fluid (SBF) Solution

A. A. F. Alina[1,a*], S. Norbahiyah[2,b], M. Z. M. Zamzuri[3,c]

[1,2,3]School of Manufacturing Engineering, Universiti Malaysia Perlis, Kampus Tetap Pauh Putra, Jalan Arau-Changlun, 02600, Arau, Perlis, Malaysia

[a*]farahalina89@yahoo.com, [b]norbahiyah@unimap.edu.my, [c]mzamzuri@unimap.edu.my

Keywords: Magnesium alloy, Gadolinium, Anodizing Coating, Corrosion Rate, SBF

Abstract. Pure Mg and AZ91D alloy was anodized with and without the gadolinium nitrate $Gd(NO_3)_3$ in different concentrations (0.001g/l, 0.025g/l, 0.05g/l, 0.075g/l and 0.09g/l) at a constant current density and treatment time of 10mA/cm^2 and 5 minutes. The results showed that the optimum gadolinium concentration is 0.075g/l due to obtaining the anodic film with high corrosion resistance. The surface morphology and microstructure of anodic coating were investigated by scanning electron microscopy (SEM) , optical microscope (OM), and potentiodynamic polarization, respectively.

Introduction

Magnesium and its alloy currently are interestingly considered as the potential lightweight and biodegradable implant materials because of their excellent biocompatibility, biodegradability, non-toxicity and non-necessity of a secondary surgery for implant removal [1]. The biodegradable implants can gradually be dissolved, absorbed, consumed or excreted after the bone tissue healing. A substantial amount of magnesium is taken into the human body daily and is beneficial for bone strength and growth. These properties make it valuable in a number of applications including biomedical industries. However, a major drawback of magnesium as a potential bone implant material is their poor corrosion resistance which may result in the sudden failure of the implants where they tend to corrode quickly before the natural healing process is complete [2]. So, it is important to control the corrosion rates of AZ91D magnesium to match the bone healing rate. Several coating techniques have been applied to decrease the degradation rate for biomedical application. Among these techniques [3-8], anodizing treatment is one of the most promising methods for magnesium alloys which enable to produce a relatively thick, hard, adherent and abrasion-resistance film to slow the corrosion [8]. So, gadolinium inhibitor in anodic oxidation technique for AZ91D magnesium alloy will be analyzed to improve the corrosion resistance performance. Although many authors state that gadolinium is highly toxic, the acute toxicity is only moderate. Some investigations have shown that gadolinium can be used to adjust the mechanical properties with a wide range of alloy compositions due to its large solubility og 23.49wt.% at the eutectic temperature.

Experimental Procedure

The commercial magnesium-based AZ91D alloy (Al 8.77, Zn 0.73, Mn 0.205 and Mg balance) was employed and mounted with epoxy resin before polished with emery paper #1000. The samples were anodized in solution containing various concentration of $Gd(NO_3)_3$ (0.001 g/l, 0.025 g/l, 0.05 g/l, 0.075 g/l and 0.09 g/l) at ambient temperature. After treatment, the samples were thoroughly rinsed with distilled water and dried for 24 hours at 343K. The surface morphology of the anodized specimen before and after the immersion in 3.5% SBF (containing NaCl, $NaHCO_3$, KCL, $K_2HPO_4.3H_2O$, $MgCl_2.6H_2O$, $CaCl_2$, Na_2SO_4, $(CH_2OH)_3CNH_2$ and Tris $(HOCH_2)_3CNH2$, following the preparation procedure of Ref. [13]) were observed by scanning electron microscopy (SEM). Potentiodynamic polarization tests were used to evaluate the corrosion behavior.

Result and Discussion

Evaluation of the film

The surface morphology of the gadolinium coating on the magnesium substrate were examined by SEM images after immersion in 3.5% SBF solution for 504 hours. The healing performance was evaluated as a function of $Gd(NO_3)_3$ solution concentration. In the Figure 1(a), as-polished untreated magnesium substrates showed many surface defects such as pitting and crevice corrosion on AZ91D magnesium alloy with zero healing performance. While the coated specimen of gadolinium revealed different ratios of self-healing abilities as a function of SBF solution concentration. When the ion concentration is increased to 0.075g/l, Figure 1(b), the tendency for self-healing action increases correspondingly, which can be explained by increasing the coating thickness. A flower-like morphology can be seen clearly in gadolinium concentration 0.075g/l which can be explained by the perfect self healing action to block the pitted areas due to corrosion attack.

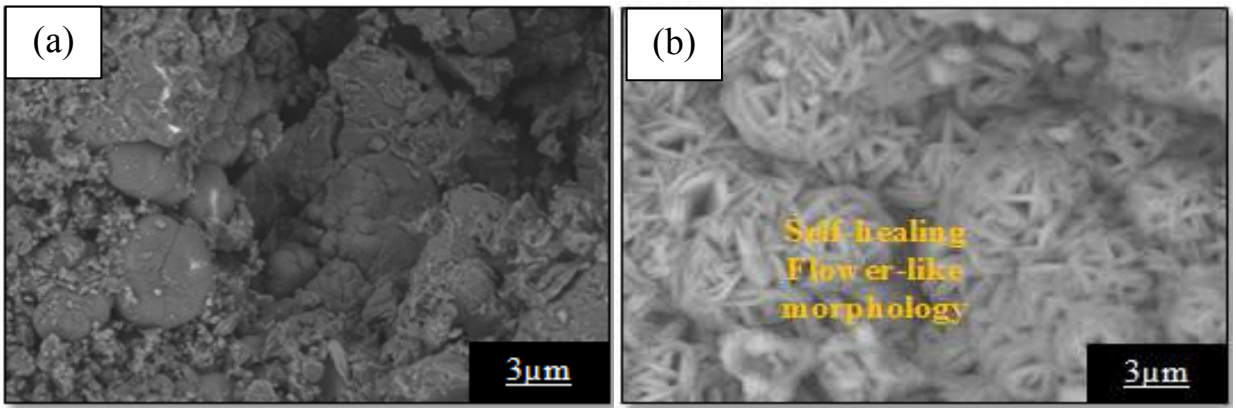

Figure 1: SEM images of the sample: a) untreated, and b) with Gadolinium treated at concentration 0.075g/l after 504 hrs of corrosion in 3.5% SBF solution

Fig. 2 shows the film formed due to $Gd(NO_3)_3$ coatings in solution concentration of 0.075 g/l is compact and uniformly distributed over magnesium substrate. It causes difficulty for corrosive ion to transfer from aggressive solution into the coating because the coating is act as a barrier [11].

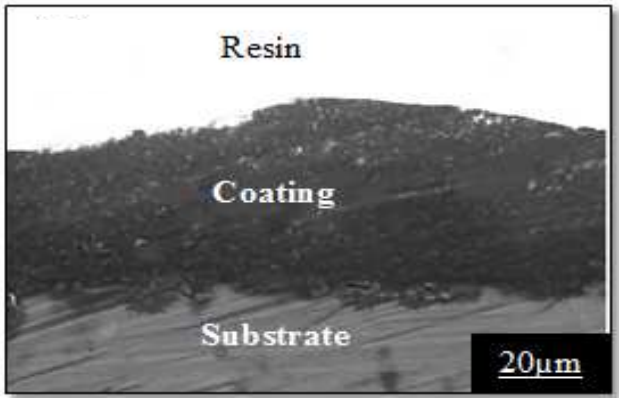

Figure 2: Cross-sectional morphologies with gadolinium treated at different concentration 0.075 g/l

Electrochemical measurement

The potentiodynamic polarization curves of the selected samples with different concentration of $Gd(NO_{3)3}$were investigated in 3.5 wt.% SBF solutions as shown in Figure 3. Based on the Figure 3, it can be seen that the specimen treated with 0.075g/l, having lowest corrosion current density and highest corrosion potential. Revealing that there is no severe dissolution reaction.

The Icorr values an be acquires from potentiodynamic polarization curves in Figure 3 and the data list in Table 1. As it was scientific to evaluate the corrosion rate by corrosion current density [12], it can be seen that the lower corrosion current density (Icorr), the higher corrosion resistance of the coatings. Table 1 shows the optimum concentration of the anodized film for an AZ91D magnesium alloy with best corrosion resistance is 0.075g/l. When the concentration exceeds 0.075g/l, the corrosion resistance of the anodized films begins to decrease with concentration/current density. However, the untreated sample represents the lower corrosion resistance compared to the treated samples because of the higher corrosion current density (Icorr). Thus,the sample treated with 0.075g/l $Gd(NO_{3)3}$was the most effective in 3.5% wt. SBF solutions.

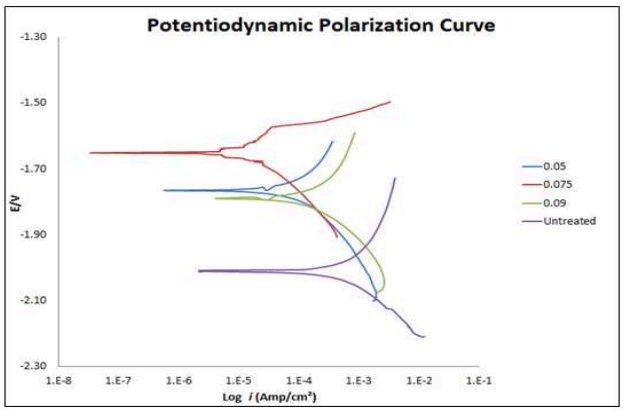

Figure 3: Potentiodynamic polarization curves of untreated specimen and anodized film with concentration 0.05g/l, 0.075g/l and 0.09g/l in 3.5 wt.% SBF solution

Table 1: Parameter values of potentiodynamic polarization curve of AZ91D Mg alloy in electrolytes containing different concentrations of $Gd(NO_3)_3$

Sample	b_a (V)	b_c (V)	E_{corr} (V)	I_{corr} (10^{-5}A/cm^2)	Rp (Ωcm^2)
0 (Untreated)	612.1E-3	313.0E-3	-2.010	70.1	128.30
0.050	644.3E-3	348.2E-3	-1.770	28.4	345.558
0.075	384.7E-3	216.9E-3	-1.750	14.0	429.62
0.090	766.8E-3	313.7E-3	-1.790	55.6	173.921

Corrosion rate

Figure 4 shows the corrosion rate of all specimens treated with and without immerse in the gadolinium based solution. It can be seen that all anodic coating specimens having lower corrosion rate than that of untreated specimen which is 18.5mm/year. When the concentration of $Gd(NO_3)_3$ is increased to 0.075 g/l, the anti-corrosion capacity of the specimen increases correspondingly. The corrosion rate is rising dramatically when the concentration increases to 0.09 g/l. Based on the figure below, the best corrosion resistance coating is formed in the electrolyte containing 0.075g/l $Gd(NO_3)_3$ with lowest corrosion rate which is 1.21mm/year. This reflect to the compaction of gadolinium over magnesium substrate that can be seen in cross-sectional morphologies.

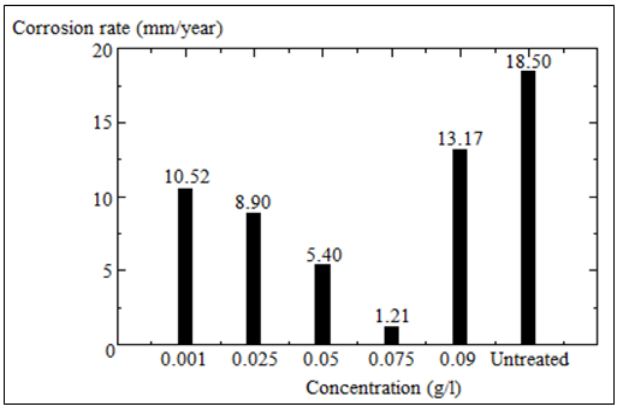

Figure 3.8: Corrosion rate of untreated specimen and anodized film with different concentration of $Gd(N0_3)_3$ solution, after immersing in 3.5 with% $Gd(NO_3)_3$ solution for 504 hours

Conclusion

Oxide film was succesfully produced on AZ91D magnesium alloy using anodized coating in $Gd(NO_3)_3$. The oxide film formed in 0.075 g/l $Gd(NO_3)_3$ provided significant corrosion resistance for magnesium alloy.

References

[1] Yanhong Gua, Cheng-fu Chen, Sukumar Bandopadhyay, Chengyun Ning, Yongjun Zhang, Yuanjun Guo, Corrosion mechanism and model of pulsed DC microarc oxidation treated AZ31 alloy in simulated body fluid, Applied Surface Science. 258 (2012) 6116-6126.

[2] Y.W. Song, D.Y. Shan, E.H. Han, Electrodeposition of hydroxyapatite coating on AZ91D magnesium alloy for biomaterial application, Materials Letters. 62 (2008), 3276–3279.

[3] Hsiao H Y, Tsai W T, Characterization of anodic films formed on AZ91 magnesium alloy. J. Surface & Coatings Technology. 190 (2005,) 299−308.

[4] Hsiao H Y, Tsung H C, Tsai W T, Anodization of AZ91D magnesium alloy in silicate-containing electrolytes, J. Surface & Coatings Technology. 199 (2005) 127−134.

[5] Mizutani Y, Kim S J, Ichino R, Okido M, Anodizing of Mg alloys in alkaline solutions, J. Surface & Coatings Technology. 169/170 (2003) 143−146.

[6] Zhang L J, Fan J J, Zhang Z, Cao F H, Zhang J Q, Cao C N, Study on the anodic film formation process of AZ91D magnesium alloy, J. Electrochimica Acta. 52 (2007) 5325−5333.

[7] Wu C S, Zhang Z, Cao F H, Zhang L J, Zhang J Q, Cao C N, Study on the anodizing of AZ31 magnesium alloys in alkaline borate solutions, J. Applied Surface Science. 253 (2007) 3893−3898.

[8] Zhang Y J, Yan C W, Wang F H, Lou H Y, Cao C N, Study on the environmentally friendly anodizing of AZ91D magnesium alloy, J. Surface and Coating Technology. 161 (2002) 36−43.

[9] G.Song, A. Atrens, X. Wu, Corrosion Science, 40(10) 1998. pp. 1769-1791.

[10] Y. Mizutani, Surface and Coatings Technology, 169-170 (2003), pp 143-146.

[11] Salih Durdu, Aylin Aytac, Metin Usta, Characterization and corrosion behavior of ceramic coating on magnesium by micro-arc oxidation, Journal of Alloys and Compounds. 509 (2011) 8601-8606.

[12] Y. W. Song, D. Y. Shan, R.S. Chen, Surf. Coat. Technology, 203, 2009, pp. 1107-1111.

[13] Kokubo T, Takadama H, How useful is SBF in predicting in vivo bone bioactivity?, Biomaterials. 27 (2006) 2907-2915.

Advanced Materials Research Vol. 970 (2014) pp 55-59

doi:10.4028/www.scientific.net/AMR.970.55

Characterization of oxide film by vanadium based anodic oxidation coating

T.N.Fadzilah [1, a*], S.Norbahiyah [2, b], M. Z. M. Zamzuri [3, c]

[1-3] School of Manufacturing Engineering, Universiti Malaysia Perlis, Kampus Tetap Pauh Putra, Jalan Arau-Changlun, 02600, Arau, Perlis, Malaysia

[a*]norfadzilah.toha@gmail.com, [b]norbahiyah@unimap.edu.my, [c]mzamzuri@unimap.edu.my

Keywords: Characterization, Corrosion resistance, Magnesium alloy, Oxide film, Vanadium.

Abstract. An oxide film was prepared on AZ91D magnesium alloy by anodizing in solution containing sodium metavanadate ($NaVO_3$). The corrosion resistance of the AZ91D magnesium alloy was investigated at fixed current density 10 mA/cm^2 for 5 min with different concentration of solution in the range of 0 – 1.0 g/l. The surface morphology, cross section morphology, phase structure, and surface roughness of oxide film were studied by optical microscope, scanning electron microscope (SEM) and energy dispersive spectrometry (EDS), atomic force microscope (AFM) and potentiodynamic polarization technique and corrosion test, respectively.

Introduction

Magnesium alloys are widely used for their superior properties such as low density and excellent mechanical strength [1]. However, the poor corrosion resistance of magnesium alloys hinders their further applications [2]. Protective coatings have been used to improve corrosion resistance of magnesium alloys. Numbers of surface treatments have been developed to generate protective coatings or surface coating for magnesium alloys [3]. Anodizing treatment has been proved to be one of the promising methods. Although anodizing treatment is more expensive than chemical surface treatment [4], it is usually chosen for special applications where high wear resistance or heavy duty corrosion resistance is required.

However, environmental harmful inorganic (such as fluoride [5], phosphate [6], or toxic organics (such as hexamethylenetetramine [7]) are still employed in the most of the existing anodizing process. Therefore, the new environmental friendly solution is needed to enhance the corrosion resistance of magnesium and its alloy. In this study, oxide film in solution contains of $NaVO_3$ are investigated aiming to increase the corrosion resistance of magnesium alloys by anodizing process.

Experimental Procedures

The commercial magnesium-based AZ91D alloy (Al 9.03, Zn 0.73, Mn 0.205 and Mg balance) was cut into dimension 10 mm × 10 mm × 10 mm. The samples were employed and mounted in epoxy resin with one surface exposed. The exposed surface was then ground with SiC paper #1000 and rinsed with distilled water.

The samples were anodized in a solution containing various concentrations of $NaVO_3$ (0.0 g/l-1.0 g/l) at ambient temperature. The current density was 10 mA/cm^2 and the duration of anodizing process was 5 min. After treatment, the samples were thoroughly rinsed and air dried for 24 hours at 343K. The surface and cross section morphology of the oxide film was observed by optical microscope and scanning electron microscopy (SEM). The chemical element of the film was investigated with EDX affiliated with SEM. The roughness of the oxide film were investigated with atomic force microscope (AFM). The corrosion resistance of oxide film on AZ91D alloy was performed in 3.5 wt% NaCl solution to determine the polarization resistance at ambient temperature. Then, the corrosion rate of oxide film was measured in accordance with JIS H 0524, which was reported earlier [8].

Results and Discussion

Morphology and Microstructure Analysis. Fig. 1 shows surface morphologies of samples treated in 0.05 of g/l $NaVO_3$ (a) and 0.1 g/l of $NaVO_3$ solution (b). The oxide film with 0.1 g/l of $NaVO_3$ has a relatively smooth surface appearance with fine grains and uniform in structure compared to that of sample with 0.05 g/l of $NaVO_3$. The oxide film is compact and uniformly distributed on magnesium alloy which acts as a barrier that causes difficulty for the corrosive ion to transfer from aggressive solution into the coating [9].

Fig. 2 shows the SEM images of the oxide film with different concentration of $NaVO_3$. It is obvious that more micro cracks were observed of oxide film treated in 0.05 g/l of $NaVO_3$. The EDX results of the oxide film at different concentrations of $NaVO_3$ are listed in Table 1. The oxide film was mainly consists of oxide particles as proved by EDX analysis that detects elements such as oxygen (O), magnesium (Mg), aluminum (Al), zinc (Zn), and vanadium (V). Sample that anodized in 0.1 g/l $NaVO_3$ has 53.9 wt % of oxygen element and the content of vanadium element increase as the concentration of $NaVO_3$ increase. The increasing oxygen and vanadium elements that incorporated in the oxide film are suggested to have a better corrosion resistance performance [8].

Fig. 3 shows the cross-sectional morphologies of the substrate at the different of $NaVO_3$ concentration. As demonstrated in Fig. 3(a), the film morphology with 0.1 g/l of $NaVO_3$ concentration has thicker and compact film compared to that of 0.05 g/l of $NaVO_3$ concentration (Fig. 3(b)) and the film thickness for 0.1 g/l of $NaVO_3$ was about 40µm. This suggested that thicker and compact film plays an important role in enhancing the corrosion resistance of the coatings [10].

Fig. 4 presents the roughness of the oxide film at 0.05 g/l and 0.1 g/ of $NaVO_3$. With the increasing of $NaVO_3$ from 0.05 g/l to 0.1 g/l, the roughness of oxide film decrease gradually. The results are consistent with the one of optical micrograph images. Sample at 0.1 g/l has a uniform surface with a little porous structure. Sample 0.05 g/l of $NaVO_3$ results in large size of pore on the oxide film. These large sizes of pores are responsible for the increased surface roughness [11].

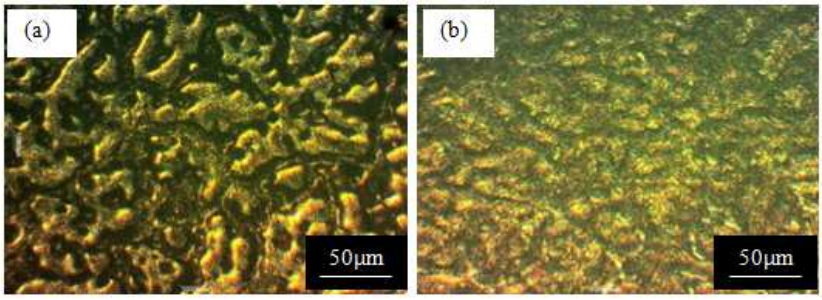

Fig. 1: Optical micrographs of samples treated with a) 0.05 g/l and b) 0.1 g/l of $NaVO_3$.

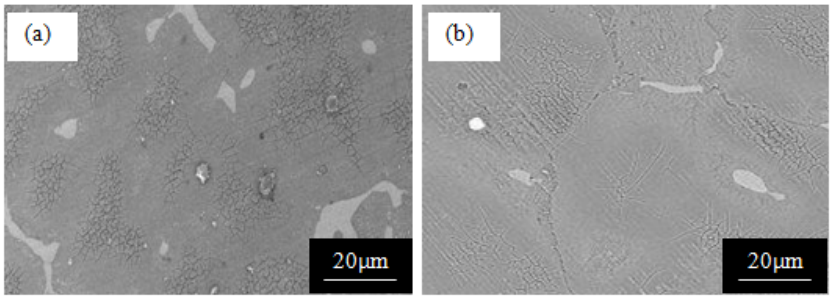

Fig. 2: SEM images of samples treated with a) 0.05 g/l and b) 0.1 g/l of $NaVO_3$.

Table 1: EDX analysis of samples treated with $NaVO_3$ at different concentration.

Concentration of $NaVO_3$	Element content (wt %)				
	Mg	**O**	**Al**	**V**	**Zn**
0.0 g/l	80.3	10.6	3.5	-	5.6
0.05 g/l	31.6	52.7	10.5	5.1	0.1
0.1 g/l	24.7	53.9	14.0	7.2	0.2

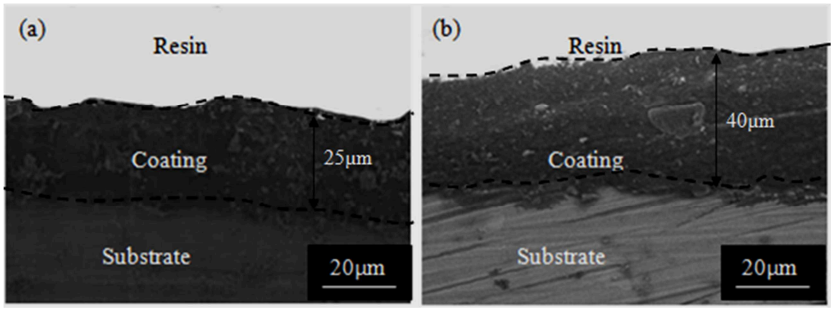

Fig. 3: Cross-sectional morphologies of samples treated with a) 0.05 g/l and b) 0.1 g/l of $NaVO_3$.

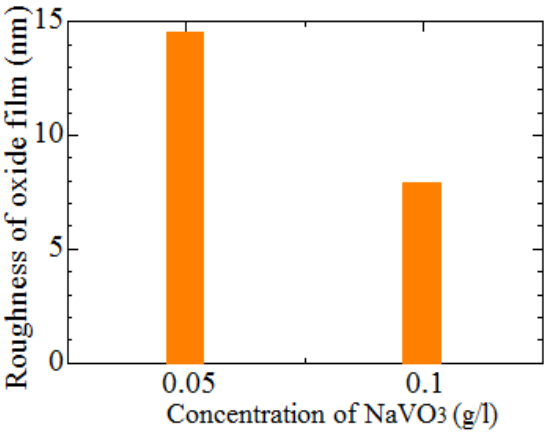

Fig. 4: Roughness of the oxide film formed in 0.05 g/l and 0.1 g/l of $NaVO_3$.

Corrosion resistance. Fig. 5 shows potentiodynamic polarization curve untreated and treated samples with different concentration of $NaVO_3$ in 3.5 wt. % NaCl solutions. All the values are listed in Table 2. The oxide film in 0.1 g/l of $NaVO_3$ has less corrosion current density (I_{corr}) as compared to others. Thus, the corrosion resistance of 0.1 g/l samples is higher as compared to 0.05 g/l and untreated samples. As reported, the less I_{corr}, the higher the corrosion resistance of the coatings [12].

Fig. 6 shows the corrosion rate of untreated and treated samples. It indicates that the corrosion rate decrease when the $NaVO_3$ is utilized in anodizing process as an electrolyte to form oxide film on magnesium alloy. It also can be seen that 0.1 g/l samples have the lowest corrosion rate as compared to 0.05 g/l and untreated samples.

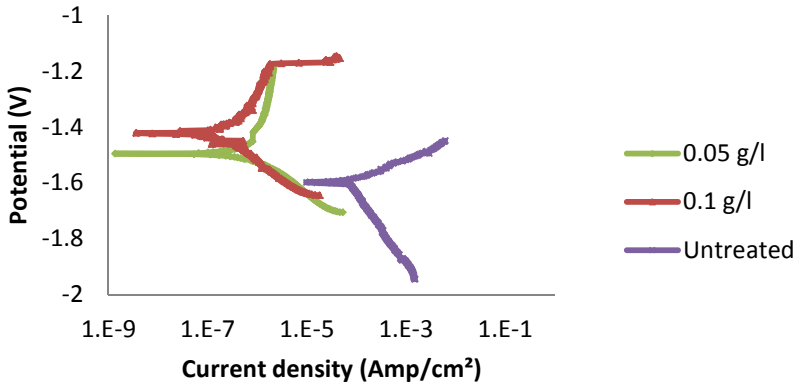

Fig. 5: Potentiodynamic polarization curves of treated sample with and without $NaVO_3$.

Table 2: Potentiodynamic polarization results of treated sample with and without $NaVO_3$

Concentration (g/l)	ba (V)	bc (V)	E_{corr} (V)	I_{corr} (10^{-5} A/cm²)	R_p (10^4 Ωcm²)
0.05	0.0739	0.0550	1.5196	0.0526	2.6030
0.1	0.0107	0.0112	1.3894	0.0041	5.8559
Untreated	0.0749	0.0812	1.6064	13.159	0.0129

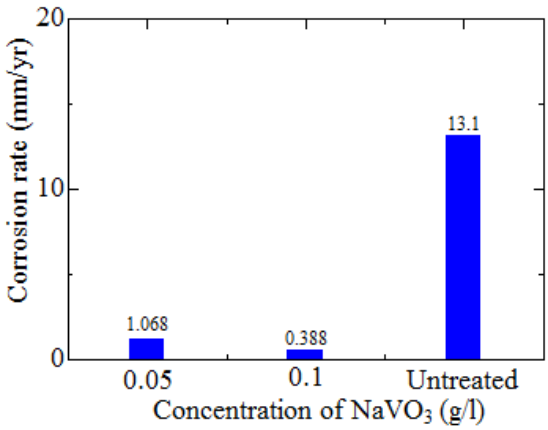

Fig. 6: Corrosion rate of treated sample with and without $NaVO_3$.

Conclusion

Oxide films on AZ91D magnesium alloy are successfully produced with a better corrosion resistance improvement. An oxide film with compact and uniform microstructure was produced in 0.1 g/l of $NaVO_3$. This study found that the concentration of $NaVO_3$ is an important factor in improving the corrosion resistance of AZ91D magnesium alloy.

References

[1] J.Q.Wang, Z.L.Ding, F.J.Qi, H.Zhu, Y.C.Fan. Journal Alloys and Compound. 24 (2010) 322–325.

[2] L.Wang, T.Shinohar, B.P.Zhang. Journal Alloys and Compound. 496 (2010) 500–507.

[3] M.Z.M.Zain, S.Illias, M.Mat Salleh, K.Azwan Ismail, Z.Nooraizedfiza. Applied Mechanics and Materials. 187 (2012) 210-214.

[4] M.Avedesin, in: H.Baker (Ed.), Magnesium and Magnesium Alloys, ASM Specialty Handbook, ASM International, Materials Park, OH, 1999.

[5] G.Lv, H.Chen, X.Wang, H.Pang, G.Zhang, B.Zou, H.Lee, S.Yang. Surface and Coatings Technology. 205 (2010) 36-40.

[6] L.Wang, L.Chen, Z.C.Yan, H.L.Wang, J.Z.Peng. Journal Alloys and Compound. 493 (2010)445–452

[7] A. Bai, Z.J.Chen. Surface Coating Technology. 203 (2009) 1956–1963.

[8] N.F.W.M.Sidik, M.Z.M.Zamzuri, M.Mat Salleh, K.A.Ismail. Advanced Materials Research. 576 (2012) 438-441.

[9] S. Durdu, A. Aytac, M.Usta. Journal Alloy and Compound. 509 (2011) 8601-8606.

[10] Y.Ma, H.Hu, D.Northwood, X.Nie. Journal of Materials Processing Technology. 182 (2007) 58-64.

[11] Y.K.Lee, K.S.Lee, T.Jung. Electrochemistry Communications. 10 (2008) 1716-1719.

[12] Y.W. Song, D.Y. Shan, R.S. Chen. Surface Coating Technology. 203 (2009) 1107–111.

Advanced Materials Research Vol. 970 (2014) pp 60-63

doi:10.4028/www.scientific.net/AMR.970.60

Investigation of surface characteristics of hydroxyapatite/titanium composite layer obtained by HF magnetron sputtering

A.A.Mamayeva[1,a*], A.V.Panichkin[1,b], R. K. Aubakirova[1,c]

[1] Center of Earth Sciences, Metallurgy and Ore Beneficiation, JSC,

29/133 Shevchenko Street, Almaty, 050010, Republic of Kazakhstan

[a*] ak78@mail.ru, [b]abpanichkin@mail.ru, [c]rashidakarim@rambler.ru

Keywords: High-frequency magnetron sputtering, Biocompatibility, Hydroxyapatite, Calcium phosphate coatings, Infrared spectroscopy, Titanium.

Abstract. Calcium phosphate coatings on the VT1-0 titanium substrate were obtained by high-frequency magnetron sputtering technique. Surface morphology, phase and elemental composition of the coatings were investigated by scanning electron microscopy, energy dispersive X-ray analysis and infrared spectroscopy. It was found formation of molecular bonds, those depending on the discharge power and isothermal annealing temperature, are typical for hydroxyapatite and accompanied by changes in the phase and elemental composition. Increase of discharge power up to 250 watt provides denser and thick coatings and promotes the formation of amorphous phase in the higher concentration – more than 20%. The ratio of the amorphous and crystalline phases determines the long-term strength of the coatings.

Introduction

Calcium phosphate-based ceramic-coated titanium and titanium alloys have become one of the most promising implant materials for orthopedics and stomatology due to their favorable biocompatibility and mechanical properties. Among the entire calcium phosphate family, the most interesting material is perhaps hydroxyapatite (HA), due to its stability in contact with body liquids. The HA has been widely used in biomedicine as synthetic bone graft and scaffold for tissue engineering.

The main techniques currently used to form coatings on medical biocompatible materials are: plasma spraying [1] micro arc oxidation [2], as well as methods based on crystallization from different coating solutions [3]. Each of these methods has its limitations: for example, poor adhesion of the coating to the substrate, the impossibility to regulate their elemental composition, limitation in the choice of substrate material to form a coating.

Selection of the method of high-frequency – HF magnetron sputtering [4-7] to produce coatings on implants is specified by the fact that HA is an insulator that can be effectively sprayed at high frequency only. Exploration objective is to obtain thicker and denser HA coatings, variation RF magnetron discharge power.

Materials and research methods

Titanium VT1-0 with the chemical composition Ti-99.45, Fe-0.25, Si-0.1, O-0.2 was selected as substrate. The target was powdery hydroxyapatite with dispersion of particulate <63 microns, which was prepared by pressing and subsequent sintering in air at 1100 ° C during 1h.

The commercially available installation 08PKHO-100T-005 for plasma etching with a custom-made flat HF-magnetron source 5.28 MHz was used to spatter the calcium phosphate coatings. Coatings formation occurred at high-frequency discharge power of 100W, 150W, 200W, 250 W, coatings were deposited at a pressure of 0.1 Pa, in argon atmosphere during 3 hours.

X-ray diffractometer and scanning electron microscopy were applied to identify the phases and the morphology of the coatings.

The study of surface morphology was conducted by scanning electron microscopy on JXA-8230 (JEOL) microscope at an accelerating voltage of 20 kV and a current of the electron beam up

to 7 nA. The mode of back scattered electrons COMPO was applied for all sections of samples selected for raster electron microscopy SEM study.

IR-Fourier spectroscopic studies were carried out on the spectrometer Nikolet Avatar 370 CsI within the range of 4000-400 cm^{-1}. The add-in device Smart Specul ATR was used in the experiments.

Roentgen phase analyzes were performed on X-ray diffractometer D8 Advance (BRUKER), radiation α-Cu.

Results and discussion

It was found that the surface of HA coatings formed by this HF-method is homogeneous, dense, and does not contain visible defects, honeycombs, bulges, cracks (Fig. 1 a, b, c).

Figure 1 shows the surface morphology of the coating and its elemental composition after sputtering at 100W, 200W, 250 W. The typical relief structure of the original Ti substrate was changed by the coating procedure, i.e. the thin coating the surface of underlying Ti substrate is followed by change of surface morphology. EDX analysis clearly shows the increasing elements of calcium phosphate composition (Fig. 1 d, e, and f).

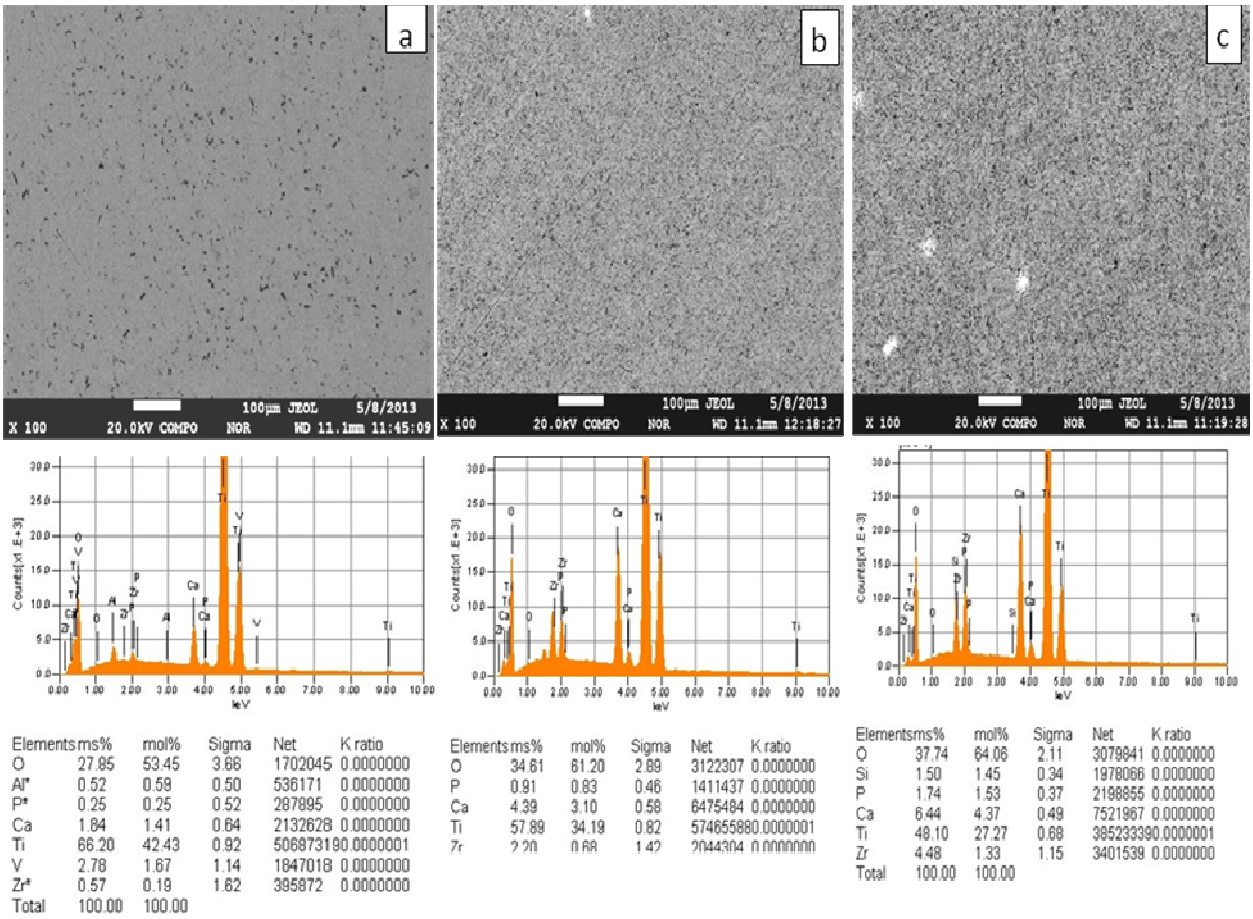

Fig. 1. (a – 100W, b – 200W, c – 250W) SEM image of the surface and (d – 100W, e – 200W, f– 250W) EDX spectra of coatings grown by RF magnetron sputtering

The results of X-ray diffraction analysis of obtained coatings are shown in (Fig. 2). An analysis of X-ray patterns showed the absence of crystalline phases corresponding to calcium phosphates. Only diffraction peaks of Ti substrate material were detected. Thus, the coatings obtained by HF magnetron sputtering method used in this study are characterized by an amorphous structure.

The IR spectra (Fig. 3) of the coatings obtained by HF magnetron sputtering method have absorption bands relating to vibrations of P–O bonds of the phosphate tetrahedron in the apatite structure.

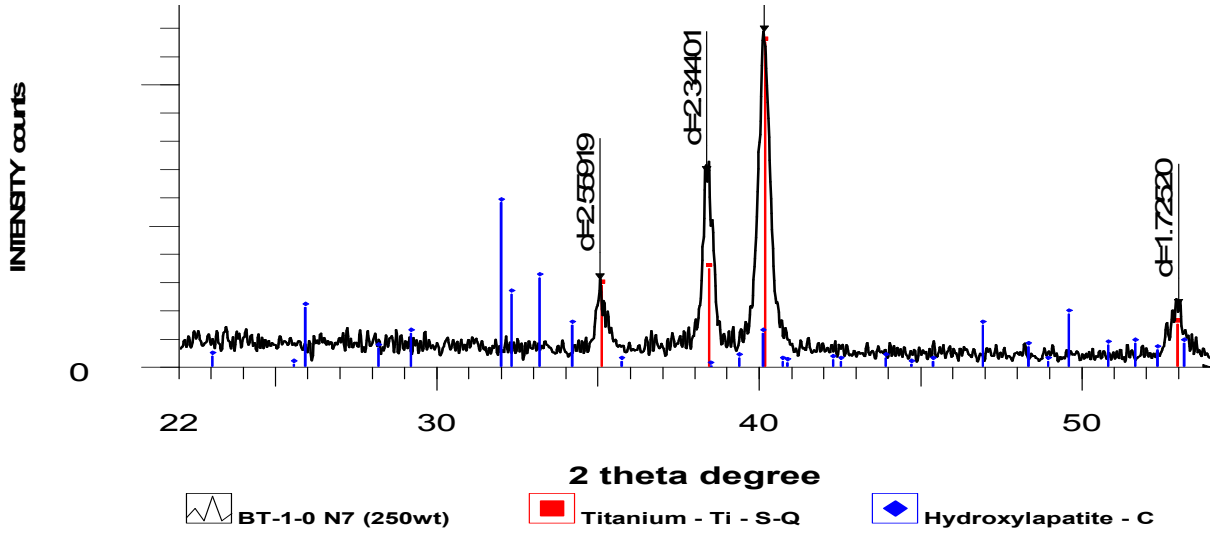

Fig. 2. X – ray patterns of surface layer

However, research of the coatings, IR-spectra shows the presence of molecular bonds typical for HA at HF sputtering with discharge power of 150, 200 and 250 W (Figure 3).

According to the IR-spectra of reflection (Fig. 3) it was established the presence of hydroxyl groups, polyhedrons $[PO_4]^3$, and methylene aliphatic hydrocarbon groups CH_2 in the coating's surface layer. The wave number values variation for the maximum of νOH valence vibrations' absorption band, namely 3564, 3565, 3543 cm^{-1} is registered. They characterize hydroxyl groups of hydroxyapatite - Ca5 $(PO_4)^3OH$ type mineral and increase of this band intensity, expressed in units of Kubelka – Munk in the row of samples with different irradiation power 0,4178, 0,852, 0,453.

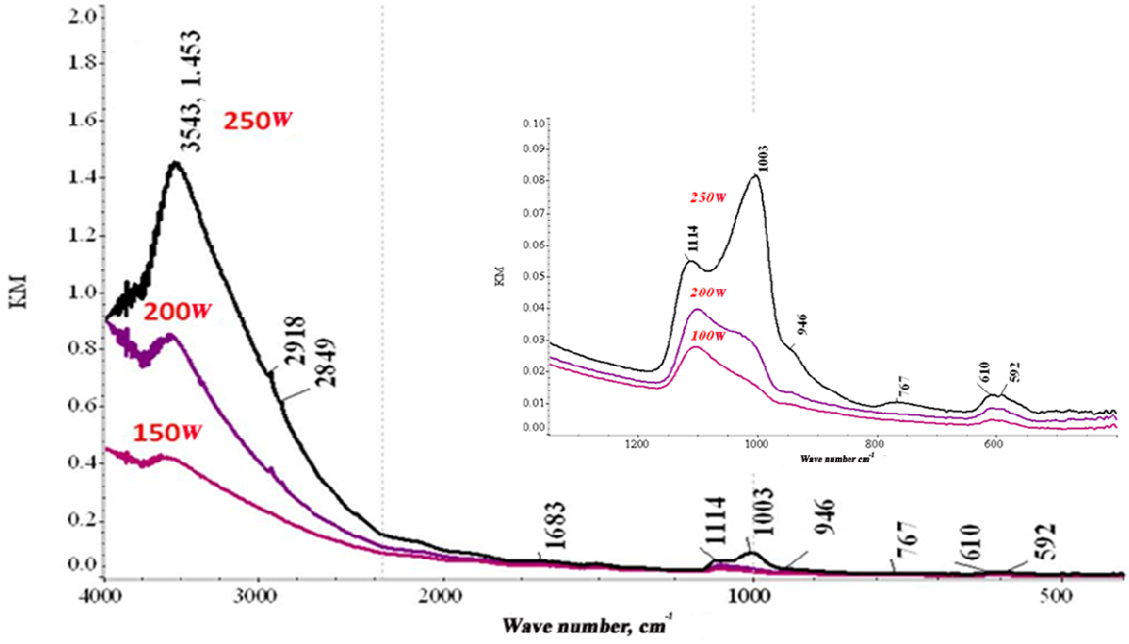

Fig.3 IR reflection spectra of coatings formed by HF magnetron sputtering with different power discharge

The figure 3 shows IR reflection spectrum of plate surface within spectrum range 1350-400 cm^{-1}. Coating structure in this case corresponds to partially dehydrated HA with a chemical formula

Ca_{10} $(PO_4)^6(OH)_2$. In the spectra of samples with different power discharge there is an increase of the absorption intensity in the range of the characteristic oscillations of polyhedral $[PO_4]^3$ visualization - which is probably caused by the higher value of the coating layer thickness. Contour of spectral curve changes symbately: with increase of the absorption band of νOH valent oscillations, absorption intensity near the wave number 1003 cm^{-1} also increases. The phase of type of brushite - $CaHPO_4 \cdot 2H_2O$ - 3543, 1114, 1003, 610, 592 cm^{-1} - dominates obviously on the surface.

The appearance in the spectrum of absorption bands of libration νL H_2O vibrations of water molecules with maximum at a wave number of 767 cm^{-1} probably reflects the hydration of coating by water molecules (possibly interlayer) which are outside of the phosphates structure.

Infrared spectrometry analysis of the metal plates surface identified the possible presence of hydroxyapatite - $Ca_5(PO_4)^3OH$ and brushite - $CaHPO_42H_2O$ in the coating's composition. The correlation between the intensity of the absorption bands of valent vibrations νOH and characteristic oscillations of polyhedral $[PO_4]^{3-}$ can be used to rank of the samples according to the thickness of the coating layer.

The fact that the value of the maximum absorption band of the valent vibrations νOH is determined by quantitative composition of the coating can be used to monitor of the coating quality during sputtering process.

It was found that at high-frequency magnetron sputtering on the surface of the titanium substrate compounds are formed, the molecular bonds of which are typical for hydroxyapatite. Spectral line parameters (amplitude, width at half maximum) of the coating are different from those of HA, which is caused by change of bonds surrounded PO_4^{3-} ions in the cell and the orientation of the crystallites in the coating composition.

Conclusions

It is found that at RF magnetron sputtering some compounds on the surface of titanium substrate are formed. Their molecular bonds are typical for hydroxyapatite (HA) [5]. Parameters of spectral lines (amplitude, with at half maximum) in the coating differ from corresponding parameters of HA. It was caused by change of bonds in the midst of PO43- ions in the unit cell composition, and also by crystallites' orientation change in the coating composition [7].

It was shown, that the most effective RF magnetron sputtering mode for denser, thicker and uniform HA coatings obtainment is: 250W discharge power and sputtering duration of 3 hours.

References

[1] Sun L., Berndt C.C., Gross K.A., Material Fundamentals and Clinical Performance of plasma sprayed hydroxyapatite coatings J. Biom. Mater. Res.2001.V. 58. P. 570–592.

[2] M Inagaki, Y Yokogawa, Apatite/titanium composite coatings on titanium or titanium alloy by RF plasma-spraying process Thin Solid Films. V 386, Issue 2, 2001, P. 222–226.

[3] Zamoume O, Thibault S, Regnie G, Fiallo M, Sharrock P. Macroporous calcium phosphate ceramic implants for sustained drug delivery Mater Sci Eng.V 289.2011. P.1352.

[4] Euler, M. Santosa, V.Simona, M. Mateescuc, J. Faerberb, M.Acostab. Physical–chemical and biological behavior of an amorphous calcium phosphate thin film produced by RF-magnetron sputtering Materials Science and Engineering: C. V. 32, Issue 7. 2012, P. 2086–2095.

[5] Shtanskij D.V., Glushakova N.A., Bashkova I.A., Haritonova M.A., Mojzhess T.G., Levashov E.A. Izvestija vuzov.Ser.Cvetnaja metallurgija. – 2004, № 6, 66–74. (in Russ.).

[6] G. Zhaoa, L. Xiaa, G. Wena, L. Songa, X. Wanga, Microstructure and properties of plasma-sprayed bio-coatings on a low-modulus titanium alloy from milled HA/Ti powders Surface and Coatings Technology. V 206, Issue 23, 2012, P. 4711–4719.

[7] Yonggang Y., Wolke J.G. Preparation and characterization of RF magnetron sputtered calcium pyrophosphate coatings//J. Biomed. Mater. Research. 2006. V.76A. P.744–752.

CHAPTER 5:

Composites

Advanced Materials Research Vol. 970 (2014) pp 67-73

doi:10.4028/www.scientific.net/AMR.970.67

Basalt Carbon Hybrid Composite for Wind Turbine Rotor Blades: A Short Review

A.N. Mengal[1, a], S. Karuppanan[2, b] and A.A. Wahab[3, c]

[1, 2, 3]Department of Mechanical Engineering, Universiti Teknologi PETRONAS, Bandar Seri Iskandar, 31750 Tronoh, Perak, Malaysia.

[a]aliract@gmail.com (Corresponding author), [b]saravanan_karuppanan@petronas.com.my, [c]azmi_awahab@petronas.com.my

Keywords: Hybrid Composite, Rotor blade, Basalt fiber, S-2 glass fiber, Fiber reinforced composite

Abstract. Wind turbine blades are the major structural element and highest cost component in the wind power system. Modern wind turbine blade sizes are increasing, and the driving motivation behind this is to increase the efficiency and energy output per unit rotor area, and to reduce the cost per kilowatt hour. However due to the increase in size the material selection for wind turbine has become critical and complex. To achieve the desired materials to improve the design of wind turbine blades several factors such as high fatigue strength, less weight, less cost and potential of recycling must be focused. Basalt fiber is a relative newcomer to fiber reinforced polymers and structural composites. Basalt fiber with their excellent mechanical properties represents an interesting alternative composite material for modern wind turbine blades. Some manufacturers claim that basalt fiber has similar or better properties than S-2 glass fiber and it's cheaper than carbon fiber. Basalt fiber together with carbon fiber are the most advanced and interesting area of hybrid technologies. This paper reviews extra ordinary properties of basalt fiber over other fiber reinforced composites and highlight how the basalt special properties together with carbon fiber will reduce the weight and cost of wind turbine blades while improving their performance. This paper also demonstrates why the basalt carbon hybrid composite material will be an ideal alternative for the wind turbine rotor blades.

Introduction

In wind turbine system, rotor blades are the major structural component used to achieve higher power generation [1]. Wind power system is increasingly receiving the attention of mankind due to increasing global demand of energy, green house effects and the environmental threats associated with fossil fuel consumption.

Modern wind turbine system has tremendous potential to fulfill the growing energy demand worldwide. For a greater efficiency and increased power generation, in recent years the size of wind turbine has increased with an increased rotor diameter [2]. The largest present day wind turbines have rotor diameter in excess of 120 meter and it is expected to increase more in future. With the increase in the size of wind turbine blades the material selection becomes critical. Several factors such as high fatigue strength, stiffness, low cost, less weight and potential of recycling must be focused while selecting the desired materials for wind turbine blades.

In the last decade, due to increasing economical and environmental demands intensive research has begun to develop new and advance composite materials for wind turbine blades. Several types of composite materials have been investigated and introduced for wind turbine rotor blades. Long fiber glass and carbon reinforced composites along with other kind of reinforces such as ceramic, aramid and natural fibers such as wood and hemp have been introduced [3]. But basalt fiber has gained increasing attention due to its extra ordinary mechanical properties.

This paper is focused on basalt fiber, and its combination with carbon fiber for wind turbine rotor blades. Basalt fiber is relatively a new comer to fiber reinforced polymers. There are not much works on basalt fiber available and published in the literature.

Basalt is a very hot fluid or semifluid mineral under the earth's crust, which originates from volcanic magma and flood volcanoes and solidified in the open air. The most abundant rock found

in earth's crust is basalt, and it's dark or black in color [4-6]. Basalt fiber is made from extremely fine fibers of basalt, which is composed of the minerals plagioclase, pyroxene, and olivine. Plagioclase is an important series of tectosilicate minerals within the feldspar family. The pyroxenes are a group of important rock-forming inosilicate minerals found in many igneous and metamorphic rocks. The mineral olivine is a magnesium iron silicate with the formula. It is a common mineral in the Earth's subsurface but weathers quickly on the surface.

The first attempt to produce basalt fiber filament was made in the USA in 1923. After the World War II, several countries advanced the research of basalt fiber. Most of the research and commercialization of basalt fiber products occurred in the past decade. Basalt fiber is an extremely fine fiber of basalt, obtained at higher temperature from chosen melted basalt rocks (e.g. spun basalt fiber). The current technology for production of continuous basalt fiber is much simpler than E-glass fiber manufacturing, as basalt fiber has a less complex composition [7]. The main difference is that basalt fiber is made from melting basalt rocks with no other additives, whereas glass fiber is made of complex batch of materials.

Mingchao et al. [8] studied the mechanical properties of basalt fiber reinforced plastic. He presented that the interface formed between basalt fiber reinforced plastic and epoxy resin is better than glass fiber reinforced plastic. Dorigat et al. [9] investigated the fatigue resistance of basalt fiber reinforced plastic laminates. The investigation of the fatigue behavior confirmed the better performance of basalt fiber reinforced plastic laminates with respect to glass fiber reinforced composites. Czigany et al. [10] examined the basalt fiber as a reinforcement of polymer composites. He presented that basalt fiber due to its outstanding mechanical properties can be an alternative for fiber glass. Khalili et al. [11] presented an experimental investigation on mechanical behavior of basalt fiber reinforced under tensile and bending loads. The results reveal that basalt fibers can be successfully used instead of glass fibers in fiber composite manufacturing. Zuoguang et al. [12] investigated the surface free energies and their dispersion/polar components of basalt and glass fibers using dynamic contact angle analysis. They found that the surface free energy of sized basalt fibers was higher than that of the sized glass fibers.

Much of the studies on basalt fiber have been done recently and much more work is needed in the future to study the basalt fiber performance, applications and its properties. Nevertheless, due to its excellent mechanical properties and low cost more and more sectors are becoming interested in basalt fiber. Different commercial products which are made by basalt fiber proved that this material can be an interesting alternative composite fiber for wind turbine rotor blades [13]. Basalt fiber has better fatigue strength characteristics than glass fiber. Compared to carbon fiber it has the features of higher compressive strength, higher shear strength, higher oxidation resistance and higher radiation resistance [14].

Table1. Comparison of chemical components between basalt fiber and glass fiber

Chemical composition %	Basalt	E Glass	S Glass
SiO_2	52.8	56	66
Al_2O_3	17.5	16	26
Fe_2O_3	10.3	0.4	0.3
CaO	8.59	25	0.3
MgO	4.63	5	11
Na_2O	3.34	2	0.3
K_2O	1.46	0.8	
TiO_2	1.38		
P_2O_5	0.28		
MnO	0.16		

The chemical composition of basalt differs to some degree, as shown in Table 1, only certain compositions can be used for making continuous filaments with a diameter range of 9 to 24 microns. Silicon oxide content about 46 percent in basalt rock is suitable for fiber production. Apart from chemical compositions, the mechanical properties of basalt fibers from different sources are also different [15], probably due to different chemical components and processing conditions. Young's modulus of Basalt fiber Varies between 78 and 93.1 GPa [7]. Compared to glass, most references claimed that basalt fiber has higher modulus and strength [16].

Properties of basalt fiber

Basalt fiber has attracted many researchers due to its excellent mechanical and thermal properties. Here we have restricted ourselves to the comparison of basalt fiber with carbon and glass fiber, which is useful for understanding basalt fiber reinforced composites potential applications. Table 2, describes the mechanical properties of basalt fiber compared with glass and carbon fiber [17]. On the basis of mechanical properties the basalt fiber shows superiority in terms of cost-performance ratio in comparison with glass and carbon fibers. Basalt fiber is able to sustain higher operating temperature, and it is more durable in boiling distilled water.

Table2. Mechanical properties of basalt fiber glass fiber and carbon fiber

Properties	Basalt fiber	E-glass	S-glass	Carbon fiber
Tensile strength (MPa)	4840	3800	4650	6000
Modulus of elasticity (GPa)	93.1	75.5	86	600
Breaking extension (%)	3.1	4.7	5.6	2.0
Filament diameter (μm)	21	21	21	15
Linear density (g/cm^3)	2.8	2.6	2.5	1.95
Min and Max temperature Range (˚C)	-260 -- +700	-50 -- +380	-50 -- +300	-50 -- +700

In Table 3, thermal properties of basalt fiber are reported [18]. Compared to glass fiber basalt fiber has excellent thermal properties. Unstressed basalt fibers can easily withstand the temperature up to 1250˚C, which makes them superior compared to glass and carbon fibers.

Due to the condition during its formation basalt fiber has several positive features. The excellent properties of basalt fiber include high modulus of elasticity, excellent heat resistance (better than glass), high strength, high temperature and corrosion resistance. Basalt fiber has outstanding vibration resistance compared to other fiber products [19]. Due to these extraordinary attributes of basalt fiber it has special importance in mechanical and civil construction. The good insulation property of basalt fiber makes them safer than carbon fibers. Through this characteristic they are excellent choice for wind turbine blades [20]. Chemically basalt fibers are more resistant to acids and alkaline.

Basalt is a major replacement to the cancerous asbestos in almost all its possible applications and has three times its insulating properties [21]. When in contact with other chemicals basalt fibers produce no chemical reactions, which may damage health and environment. Basalt fiber products are non-combustible and explosion proof. Basalt fiber has no toxic reaction with air and water. Basalt based products are easily recyclable, environmental friendly and non-hazardous [22].

Table3. Thermal properties of basalt fiber and glass fiber

Thermal properties	Basalt fiber	Glass fiber
Thermal conductivity (W/m K)	0.031-0.038	0.034-0.04
Thermal expansion coefficient (ppm/˚C)	8.0	5.4
Melting temperature (˚C)	1280	1120
Maximum operating temperature (˚C)	980	650
Sustained operating temperature (˚C)	700	480
Minimum operating temperature (˚C)	-260	-60

Basalt fiber applications

The field of application of basalt fiber products is extremely broad, depending on the specific properties of the fiber. This includes automotive, sporting goods, boat building, civil engineering and wind turbine blades [23].

Automotive industry. Basalt fibers are used in a wide range of products for automotive industry. High quality basalt fibers are used for the production of brake pads, mufflers, panels, screens, plastics, head liners and other parts for interior applications. Basalt chopped strands are used for manufacturing of fuel tanks, liquid petroleum gas (LPG) and compressed natural gas (CNG) cylinders [23].

Sporting goods. Basalt fibers have excellent mechanical properties and are highly suitable for the production of snow boards, skis, bicycles and other sporting goods [23].

Boat building. Basalt fiber unidirectional and multiaxial fabrics are used in boat building applications. Here the high corrosion resistance of basalt fiber plays the main role [23].

Building construction and reinforcements. Due to their durability and flexural strength, basalt fibers are used as warmed panels for construction of prefabricated houses, dropped ceilings, fire proof walls, floors, fire resistant doors and building plastics. Basalt filament unidirectional rods are the best reinforcements for roads, bridges, railway sleepers, runway of airports and construction of tunnels in seismic hazardous regions [24].

Agriculture applications. Basalt fibers can also be used in various agriculture applications. Basalt fiber tanks are used for storage and transportation of liquid chemical fertilizers and pesticides, pipes for irrigation and hosing and materials for agriculture machines construction [25].

Nuclear power engineering. Basalt fibers are immune to nuclear radiations, and are used as the potential material in production and transformation of radioactive materials. They are also the best protection for environment and human health against the radioactive wastes [26].

Electronic applications. Because of its good heat insulating properties basalt fiber are used in fire resistant cable construction components [27].

Basalt carbon hybrid composite

In hybrid composites two or more high performance reinforcements with different mechanical, thermal and chemical properties are combined. The purpose of hybridization is to achieve the best results from good properties of the materials and to lower the cost. Number of researchers have been studying and investigating the mechanical properties of hybrid composites for wind turbine rotor blades. Compared with single fiber reinforced composites hybrid composites improved failure strain, increased stiffness, strength and ductility by careful design of hybrid configuration [28].

Present day wind turbine blades are built from glass fiber reinforced plastic (GFRP) and carbon fiber reinforced plastic (CFRP). Glass Fiber is one of the most common fibers in the composites industry due to its low cost. Compared to carbon and basalt fibers the glass fibers have low stiffness and low fatigue strength. Carbon fibers provide the highest stiffness among all the fibers, however they have relatively low compressive strength, low damage tolerance and ultimate strain and are much more expensive than glass and basalt fiber. Due to their high cost carbon fibers have no prospects of mass application [29, 30].

The size of wind turbine is becoming increasingly larger, and this trend is expected to continue in the future. For very large blades carbon and glass are combined together in hybrid form by several manufactures to increase the fatigue resistance, strength and stiffness, and to reduce the

cost and weight. Although much improvement had been observed by the use of carbon and glass hybrid composite, but their weight, cost and low compressive fatigue strength are still problematic issues.

To increase the energy output, wind industry is constantly seeking for stiffer, lighter, less expensive and easily available materials with higher fatigue resistance and mechanical properties. Basalt fiber together with carbon are the most advanced and exciting area of hybrid technologies. Basalt special properties reduce the cost of product while improving the performance [31]. Due to its extraordinary properties over other fiber reinforced composites its use in wind turbine blades is ideal.

Grande [32] asserted that high quality basalt fibers are 30% stronger, 15-20% stiffer and 8-10% lighter than E-glass and cheaper than carbon fibers. The superior characteristics of basalt fiber make it possible for the production of longer blades with the same amount of fiber, to increase the energy output. Special basalt UD tapes and multiaxial fibers for wind turbine blade are currently under development.

Subagia et al.[33] studied the flexural properties of basalt carbon hybrid composites. He observed extra ordinary performance of basalt carbon hybrid composite under flexural loading. Chun Hua Zhang et al.[34] investigated the toughness properties of basalt carbon fiber hybrid composites. The experimental results confirmed that hybridization of brittle carbon fibers with ductile basalt fibers improved the fracture toughness properties of composites. Yonjig Kim et al.[35] observed the effect of the incorporation of basalt fibers on the tensile properties of carbon fiber-reinforced epoxy laminates manufactured by vacuum-assisted resin transfer molding. Basalt carbon hybrid composite has good stiffness and strength as compared to glass carbon hybrid composite.

Continuous basalt fiber is very compatible with carbon fiber and can be used as a hybrid composite for modern wind turbine blades with very high stiffness, low cost and light weight. Hybridization of carbon fiber with basalt fiber increases the strength of the product and expands the areas of application. Basalt carbon hybrid composite have better characteristics, and they significantly lower the wind turbine blade cost made only from carbon fiber. The combination of carbon fiber with basalt fiber increases the strength, stiffness and water resistance of wind turbine blades and reduces the weight and cost sharply, by several times [36].

Combining basalt fiber with carbon fiber with optimal mix ratios for wind turbine blades are expected to deliver better strength and strain to failures. However prior to the implementation of basalt fiber as the new composite material for wind turbine blades, more investigation is needed, especially dealing with their fatigue behavior in order to utilize the benefits associated with the material.

Conclusion

Basalt fiber with its extraordinary mechanical properties and low cost is now being a popular and most advance choice for wind turbine blades. This paper presents a short review of basalt carbon hybrid composite for future wind turbine blade developments. Characteristics of basalt fiber compared with glass and carbon fiber are explained, which can give good insight for material selection for advanced wind turbine blades. However very few data are available in the literature dealing with basalt fiber, so the need of further investigations on this relatively young material is evident.

References

[1] L. Mishnaevsky, Composite materials in wind energy technology, Encyclopedia of Life Support System (EOLSS); 2010, pp. 11-42.

[2] O.T. Thomson, Sandwich materials for wind turbine blades: Present and Future, Journal of Sandwich Structures and Materials:(2009)

[3] T. Czigany Discontinuous basalt fiber-reinforced hybrid composites, Polymer composites, Part IV, Springer, New York, 2005.

[4] Information on http://basaltfm.com/eng/index/html
[5] G. Deshmukh; Basalt - The Technical Fiber; Man-made Textiles in India; 2007, pp. 258-261.
[6] Information on http://www.seminarprojects.com/Thread-basalt-rock-fibre-brf
[7] R.V.Subramanian, H. F.Austin, Reinforcement of Polymers By Basalt Fibers: SAMPE Quarterly (1977)
[8] W .Mingchao, Z .Zuoguang, L .Yubin, L .Min , S. Zhijie, Chemical durability and mechanical properties of alkalipro of basalt fiber and its reinforced epoxy composites: Journal of Reinforced Plastic and Composite (2008)
[9] A. Dorigato , A. Pegoretti, Fatigue resistance of basalt fibers-reinforced laminates: Journal of Composite Materials (2012)
[10] T. Cziga´ny, Basalt fiber reinforced hybrid polymer composites:Mater Sci Forum (2005
[11] S.M.R. Khalili, V. Daghigh, R. Eslami Farsani ,Mechanical behavior of basalt fiber-reinforced and basalt fiber metal laminate composites under tensile and bending loads: Journal of Reinforced Plastics and Composites (2011)
[12] Zuoguang, L .Min, Z .Zuoguang, J .Jingjing,Surface free energy of basalt and glass fibers by contact angle method:
[13] B. Mislavsk, Advanced basalt fiber in high-tech applications, JEC Magazine. 44(2008) 22-24.
[14] M.Tierens, A. Palmieri, Basalt fibers mechanical properties and applications for concrete structures: proceedings of the international conference on Concrete Solutions (2009)
[15] S.E.Artemenko, Polymer Composite Materials Made From Carbon, Basalt, And Glass Fibers: Fiber Chemistry (2003)
[16] R.V. Subramanian, Basalt Fiber - A New Cost Mineral Fiber For Composites: Advanced Composites Technology (1978)
[17] C.J. Burgoyne, N. Taranu, K. Pilakoutas, A.Serbescu, V. Tamuzs, A. Weber, FRP reinforcement in RC structures, FIB technical report. Stuttgart: Sprint Digital Druck Editor (2007)
[18] V. D. Velde , P. Kiekens , V.L. Langenhove, Basalt fibers as reinforcement for composites: Proceedings of 10th international conference on composites/nano engineering, USA (2003)
[19] T. Czighny, Polymer composites, Part IV., Springer, US, 2005.
[20] Information on http://windgateenergy.com/?page_id=16
[21] F.M Kogan, O.V Nikitina, Solubility of chrysotile asbestos and basalt fibers in relation to their fibrogenic and carcinogenic action, PubMed. 102(1994) 205-206.
[22] Sim J, Park C, Moon DY. Characteristic of basalt fiber as a strengthening material for concrete structures: Procedia Engineering (2005)
[23] Information on http://www.basfiber.com/application.
[24] A G Novitskii, V Sudakov; An unwoven basalt-fiber material for the encasing of fibrous insulation: an alternative to glass cloth; Refractories and Industrial Ceramics; vol 45, no 4; 2004, pp. 234 - 241.
[25] Information on http://www.npo-vulkan.com/index_en.php.
[26] S. E. Artemenko, Y. A. Kadykova; Polymer composite materials based on carbon, basalt, and glass fibers; Fiber Chemistry (2008).
[27] J.M. Nolf, Basalt Fibers - Fire Blocking Textiles: Technical Usage Textile (2003)
[28] K. Singha, A short review on basalt fiber: International Journal of Textile Science (2012)
[29] J. F. Mendel, D. D. Samborsky, and D. S. Cairns, Fatigue of Composite Materials and Substructures for Wind Turbine Blades, Contractor Report SAND2002-0771, Sandia National Laboratories, Albuquerque, NM (2002).
[30] R. P. L. Nijssen, Fatigue Life Prediction and Strength Degradation of Wind Turbine Rotor Blade Composites, Contractor Report SAND2006-7810P, Sandia National Laboratories, Albuquerque, NM, (2006).
[31] Windgate energy, center for sustainable energy, basalt fiber properties http://windgateenergy.com.

[32] Grande, J.A, Wind Power Blades Energizes Composites Manufacturing, Plastic Technology, 54(10); 2008, pp. 68-75.
[33] A. Subagia, Y. Kim, A study on flexural properties of carbon-basalt/epoxy hybrid composites: Journal of Mechanical Science and Technology (2013)
[34] C.H. Zhang, J. B. Zhang, M.Chao, Toughness Properties of Basalt/Carbon Fiber Hybrid Composites: Advanced Materials Research (2011)
[35] A. Subagia, Y. Kim, Tensile behavior of hybrid epoxy composite laminate containing carbon and basalt fibers: Science and Engineering of Composite Materials (2013)
[36] S. E. Artemenko, Yu. A. Kadykova; Hybrid composite materials; Fiber Chemistry; 2008, pp. 490-492.

Advanced Materials Research Vol. 970 (2014) pp 74-78

doi:10.4028/www.scientific.net/AMR.970.74

Effect of Maleic Anhydride Grafted Poly(lactic acid) on Properties of Sawdust/Poly(lactic acid) Composites Toughened with Poly(butylene adipate-co-terephthalate)

Jiraporn Nomai[1, a] and Kasama Jarukumjorn[1, b*]

[1]School of Polymer Engineering, Institute of Engineering, Suranaree University of Technology, Nakhon Ratchasima 30000, Thailand

[a]jira_sut@hotmail.com, [b*]kasama@sut.ac.th

Keywords: Poly(lactic acid), Sawdust, Poly(butylene adipate-co-terephthalate), Maleic anhydride grafted poly(lactic acid), Mechanical properties, Thermal stability.

Abstract. Sawdust/poly(lactic acid) (PLA) composites toughened with poly(butylene adipate-co-terephthalate) (PBAT) were prepared using a melt blending process. Mechanical, thermal and morphological properties of the composites were investigated. With the addition of PBAT into the sawdust/PLA composite, elongation at break and impact strength increased whereas tensile strength and tensile modulus decreased. In addition, thermal stability of the PLA composite improved with the presence of PBAT. Maleic anhydride grafted poly(lactic acid) (PLA-g-MA) was used as a compatibilizer to improve the compatibility of sawdust/PLA/PBAT composites. The compatibilized composites showed higher mechanical properties and thermal decomposition temperatures than that of the uncompatibilized composite due to improved interfacial adhesion between constituents of the composites. The optimum content of PLA-g-MA for sawdust/PLA/PBAT composites was 5 wt%. SEM micrographs revealed some features of ductile fracture in the composites toughened with PBAT and confirmed that PLA-g-MA improved the compatibility of the composites.

Introduction

Poly(lactic acid) (PLA) has attracted increasing attention in various industrial applications. PLA has a number of interesting properties including biodegradability, high strength and high modulus. However, its high brittleness and high cost limit its applications. One of the possible methods to effectively minimize end product costs is to incorporate lignocellulosic fillers into PLA [1]. The major advantages of these composite materials are low cost, light weight, high specific strength and recyclability. In wood industries, large amounts of sawdust are always found as waste. This sawdust is commonly little used and often disposed as landfill or incinerated. Therefore, using sawdust as reinforcing filler for polymer composites is an alternative way to add value to sawdust and also benefit the environment. The main problem of using sawdust to reinforce PLA is the incompatibility between sawdust and PLA matrix, leading to poor mechanical properties of the composites. Alkali treatment is one of the most used chemical treatments to improve interfacial adhesion between lignocellulosic fillers and PLA matrix [2]. However, one obstacle that restricts the application of PLA based lignocellulosic filler composites is owing to a remarkable decrease of toughness of the composites. Therefore, the toughness of the PLA composites has to be improved to achieve balance overall properties. Recently, many considerable interests have focused on toughening lignocellulosic filler/PLA composite with biodegradable polymers due to their obvious environment friendly properties [3,4]. In the view of high flexibility and biodegradability, poly(butylene adipate-co-terephthalate) (PBAT) is considered as a good choice for toughening PLA based lignocellulosic filler composites. In fact, all of the investigated PLA/PBAT blends are immiscible or only partially miscible [5]. Therefore, interfacial adhesion between PBAT and PLA should be improved. Generally, maleic anhydride grafted poly(lactic acid) (PLA-g-MA) is considered to be an effective compatibilizer for improving the compatibility between PLA and PBAT [5]. Lignocellulosic filler/PLA composites gain more interest in the areas of interior automotive part such as indoor panel, seatback panels, armrest liner, console bins and trays. The

objective of this work is to investigate the effect of PLA-g-MA on mechanical, thermal and morphological properties of sawdust/PLA composites toughening with PBAT.

Experimental

Materials. Poly(lactic acid), (PLA, 3052D) was supplied from Natural Works LLC. Poly(butylene adipate-co-terephthalate) (PBAT, Ecoflex FBX 7011) was purchased from BASF Co., Ltd. Iron wood sawdust (*Hopea odorata* Roxb) with particle size between 300 and 425 μm was supplied by Piyarat sawmill, Nakhon Ratchasima, Thailand. Sodium hydroxide (NaOH, Carlo Erba) was purchased from Italmar (Thailand) Co., Ltd. Maleic anhydride (MA) and 2,5-bis(tert-butylproxy)-2,5 dimethylhaxane (L101) were purchased from Sigma-Aldrich. PLA-g-MA prepared in-house was used as a compatibilizer [5].

Preparation of Composites. Sawdust was treated with 2% w/v NaOH for 30 min at room temperature. The designation and composition of the composites are shown in Table 1. PLA/sawdust ratio was 70/30 w/w and PBAT content was fixed at 20 wt%. The composites were prepared using a twin screw extruder (Brabender, DSE 35/17D) at a barrel temperature of 175/170/165/160/155 °C. The screw speed was 15 rpm. Then, test specimens were molded using an injection molding machine (Chuan Lih Fa, CLF 80T).

Characterization of Composites.

Mechanical Properties. Tensile properties were obtained according to ASTM D638 using a universal testing machine (Instron, 5565) with a load cell of 5 kN and crosshead speed of 5 mm/min.

Unnotched izod impact test was performed according to ASTM D256 using an impact testing machine (Atlas, BPI).

Thermal Properties. Thermal stability of the composites was analyzed using a thermo-gravimetric analyzer (Perkin Elmer, SDT 2960). The specimens were heat from 30 °C to 600 °C with a heating rate of 10 °C/min under a nitrogen atmosphere.

Morphological Properties. Morphology of the tensile fractured surface of the composites was performed by a scanning electron microscope (JEOL, JSM6010). The fractured surface of specimens was coated with gold before analysis.

Table 1. Designation and composition of the composites

Designation	Sawdust/PLA [wt%]	PBAT [wt%]	PLA-g-MA [wt%]
Sawdust/PLA	100	-	-
nc-20PBAT	80	20	-
3c-20PBAT	77	20	3
5c-20PBAT	75	20	5
10c-20PBAT	70	20	10

Results and Discussion

Mechanical Properties. Tensile strength and tensile modulus of sawdust/PLA composite and sawdust/PLA/PBAT composites with different PLA-g-MA contents are shown in Fig. 1 (a). Tensile strength and tensile modulus of sawdust/PLA composite decreased with the addition of PBAT. This behavior was probably due to low stiffness of PBAT and incompatibility between constituents of the composite [4]. Elongation at break and impact strength of sawdust/PLA composite toughened with PBAT were higher than that of sawdust/PLA composite as shown in Fig. 1 (b). The addition of

PBAT exhibited 46% and 114% enhancement in elongation at break and impact strength of the PLA composite, respectively. The improvement of elongation at break and impact strength was attributed to the presence of soft elastomeric phase that exhibited high flexibility and toughness [3]. Moreover, adding PLA-g-MA enhanced mechanical properties of sawdust/PLA/PBAT composites. This may be due to improved interfacial adhesion between constituents of the composites [5]. As PLA-g-MA content increased from 3 to 5 wt%, tensile strength, elongation at break and impact strength significantly improved while tensile modulus relatively unchanged. When compared with the uncompatibilized sawdust/PLA/PBAT composite, the addition of 5 wt% PLA-g-MA improved tensile strength, elongation at break and impact strength of the composite up to 38%, 20% and 41%, respectively. However, tensile strength, tensile modulus, elongation at break and impact strength of the composites slightly decreased with further increasing PLA-g-MA content to 10 wt%. This may be due to the saturation of PLA-g-MA at the interface resulting in a decrease in mechanical properties of the compatibilized sawdust/PLA/PBAT composite [6].

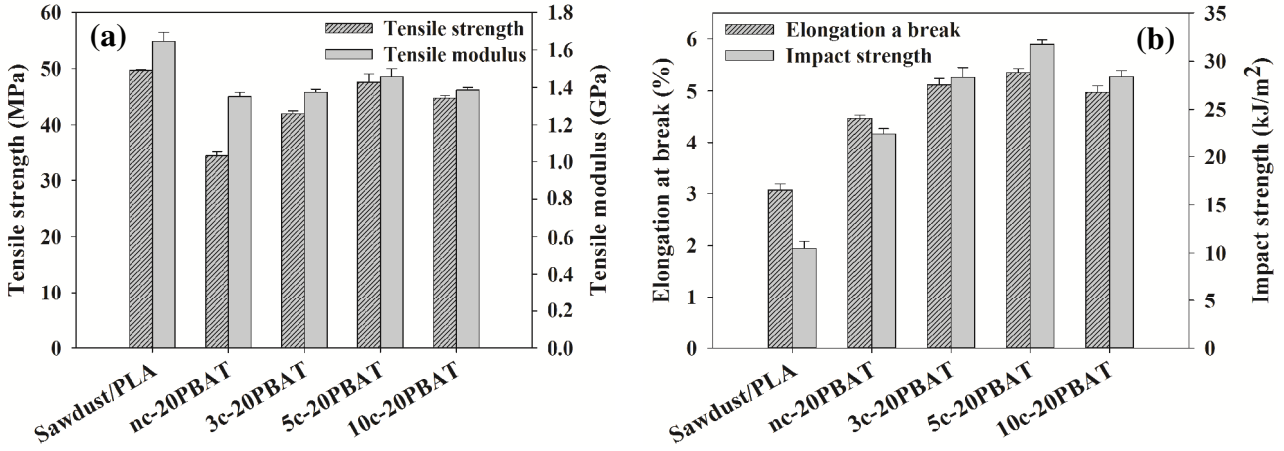

Figure 1. Mechanical properties of sawdust/PLA composite and sawdust/PLA/PBAT composites with different PLA-g-MA contents.

Thermal Properties. TGA curves of sawdust/PLA composite and sawdust/PLA/PBAT composites with different PLA-g-MA contents are shown in Fig. 2. Thermal decomposition temperature at 5% weight loss (T_5), thermal decomposition temperature at 50% weight loss (T_{50}) and thermal decomposition temperature (T_d) of the composites are summarized in Table 2. It could be seen that the decomposition of sawdust/PLA composite was in a single stage, as the decomposition stage of sawdust was overlapped with the decomposition stage of PLA [7]. T_5, T_{50} and $T_{d,1}$ of the sawdust/PLA composite were 293.34, 352.70 and 354.20 °C, respectively. With the addition of PBAT into the sawdust/PLA composite, the composite exhibited two stages of the decomposition with the first decomposition temperature ($T_{d,1}$) of sawdust and PLA at 357.14 °C and the second decomposition temperature of PBAT ($T_{d,2}$) at 399.03 °C. Moreover, T_5, T_{50} and $T_{d,1}$ of the sawdust/PLA/PBAT composite increased when compared to the sawdust/PLA composite, indicating the improvement of thermal stability of the composite [5]. The compatibilized sawdust/PLA/PBAT composites showed higher T_5, T_{50} and $T_{d,1}$ than that of the sawdust/PLA/PBAT composite without PLA-g-MA. This was because PLA-g-MA enhanced the compatibility between constituents of the composites [5]. However, T_5, T_{50}, $T_{d,1}$ and $T_{d,2}$ did not change significantly with PLA-g-MA content. Yao [8] also reported that compatibilizer content had no significant effect on thermal stability of rice straw fiber/high density polyethylene composite toughened with ethylene/propylene copolymer.

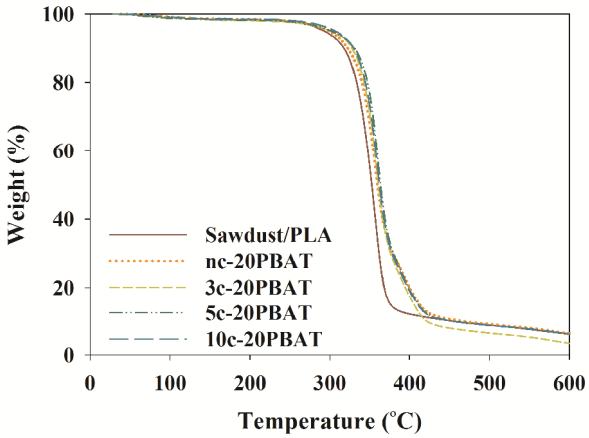

Figure 2. TGA curves of sawdust/PLA composite and sawdust/PLA/PBAT composites with different PLA-g-MA contents.

Table 2. Thermal decomposition temperatures of sawdust/PLA composite and sawdust/PLA/PBAT composites with different PLA-g-MA contents.

Designation	T_5 [°C]	T_{50} [°C]	$T_{d,1}$ [°C]	$T_{d,2}$ [°C]
Sawdust/PLA	293.34	352.70	354.20	-
nc-20PBAT	297.35	357.92	357.14	399.03
3c-20PBAT	304.87	362.86	361.74	399.14
5c-20PBAT	306.36	364.02	362.15	399.18
10c-20PBAT	307.88	364.71	362.49	399.43

Morphological Properties. Tensile fractured surface morphologies of sawdust/PLA composite and sawdust/PLA/PBAT composites are shown in Fig. 3. Sawdust/PLA composite exhibited smooth fractured surfaces as shown in Fig. 3 (a) and (b). This was attributed to brittle failure of the matrix system. The fractured surface morphologies of the composites toughened with PBAT showed some features of ductile fracture. This was evidence from rougher fractured surface (at 300x) and longer fibrils pulled out during tensile testing at high magnification (1500x) as shown in Fig. 3 (c) and (d), respectively. This indicated that matrix of the sawdust/PLA/PBAT composite was tougher than that of the composite without PBAT, resulting in the enhancement in elongation at break and impact strength of the composites [4]. However, gaps between the sawdust and the matrix were observed as shown in Fig. 3 (c). These characteristics indicated poor interfacial adhesion between constituents of the composites. PLA-g-MA compatibilized sawdust/PLA/PBAT composites showed good interfacial adhesion between the sawdust and the matrix as shown in Fig. 3 (e). These results suggested that PLA-g-MA provided good compatibility between the constituents of the composites, resulting in the improvement of mechanical properties of the composites.

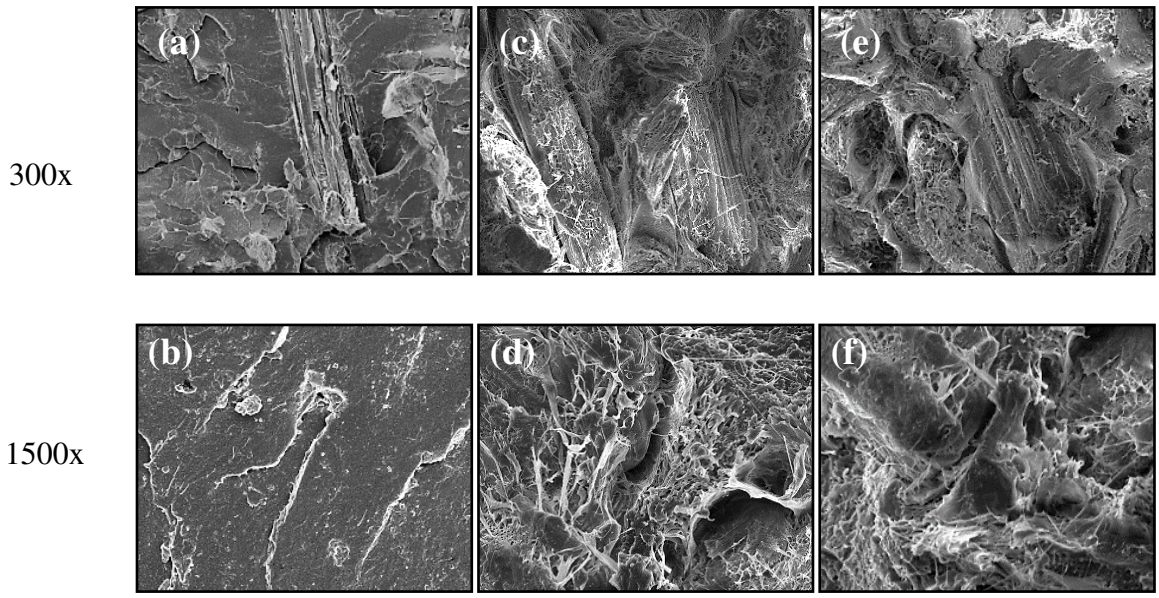

Figure 3. SEM micrographs of (a) sawdust/PLA (300x), (b) sawdust/PLA (1500x), (c) nc-20PBAT (300x), (d) nc-20PBAT (1500x), (e) 5c-20PBAT (300x), (f) 5c-20PBAT (1500x) composites.

Summary

Elongation at break and impact strength of the sawdust/PLA composites increased with the addition of PBAT while tensile strength and modulus decreased. Moreover, thermal stability of the composites was improved with the presence of PBAT. PLA-g-MA enhanced mechanical and thermal properties of the composites due to improved interfacial adhesion between the constituents of the composites. The optimum content of PLA-g-MA for sawdust/PLA/PBAT composites was 5 wt%. SEM micrographs revealed some features of ductile fracture in the composites toughened with PBAT and confirmed that PLA-g-MA enhanced the compatibility of the composites.

References

[1] M. Dimonie, M. Rapa, U.P.B. Sci. Bull. 72 (2010) 3-10.
[2] L. Liu, J. Yu, L. Cheng, X. Yang, Polym. Degrad. Stab. 94 (2009) 90-94.
[3] T. Qiang, D. Yu, H. Gao, J. Appl. Polym. Sci. 124 (2012) 1831-1839.
[4] B.K. Goriparthi, K.N.S. Suman, M.R. Nalluri, Polym. Compos. 33 (2012) 237-244.
[5] A. Teamsinsungvon, Physical properties of poly(lactic acid)/poly(butylene adipate-*co*-terephthalate) blends and their composites, Master's Thesis. Suranaree University of Technology (2011).
[6] P. Lomellini, M. Matos, B.D. Favis, Polymer. 37 (1996) 5689-5694.
[7] K.S. Chun, S. Husseinsyah, H. Osman, Polym. Eng. Sci. 53 (2013) 1109-1116.
[8] F. Yao, Rice straw fiber polymer composites: thermal and mechanical performance, Master's Thesis. Louisiana State University (2008).

Advanced Materials Research Vol. 970 (2014) pp 79-83

doi:10.4028/www.scientific.net/AMR.970.79

Effects of Sawdust Content and Alkali Treatment on Mechanical and Flame Retarding Properties of Sawdust/Recycled High Density Polyethylene Composites

Rapisa Jarapanyacheep[1,a] and Kasama Jarukumjorn[1,b*]

[1]School of Polymer Engineering, Institute of Engineering, Suranaree University of Technology, Nakhon Ratchasima 30000, Thailand

[a]Rapisa.j@gmail.com, [b*]kasama@sut.ac.th

Keywords: Recycled high density polyethylene, Sawdust, Alkali treatment, Mechanical properties, Flammability.

Abstract. Sawdust/recycled high density polyethylene (rHDPE) composites were prepared and their mechanical properties, flammability and morphology were investigated. Sawdust was used at contents of 30, 40 and 50 wt%. With increasing sawdust content, tensile strength and elongation at break of the composites decreased whereas tensile modulus increased. Flexural properties showed the same trend as tensile properties. Flammability of the composites enhanced with increasing sawdust content. Mechanical properties of alkali treated sawdust/rHDPE composites were higher than those of untreated sawdust/rHDPE composites at all sawdust contents. Moreover, alkali treatment improved flame retardancy of the composites. SEM micrographs showed that alkali treatment enhanced the interfacial adhesion between sawdust and rHDPE matrix.

Introduction

Wood/polymer composites (WPCs), made of virgin or recycled polymer and wood filler, have gained much attention both in the research area and the industry. The addition of wood filler into polymers improves stiffness and strength of the composites. The advantages of the wood filler include high modulus, high strength, low cost, low density, renewable nature, biodegradability and nonabrasiveness. Sawdust, by-product obtaining from the wood industry, is one the most used wood filler for the manufacture of WPCs. The use of sawdust in producing WPCs benefits to the enviroment and also adds value to sawdust. Many researchers have prepared WPCs from recycled thermoplastics and sawdust [1,2,3]. They reported that the composites, made of recycled high density polyethylene (rHDPE) and sawdust, showed similar mechanical properties but were much cheaper than the composites made from virgin HDPE [2,3]. However, the main drawbak of the WPCs is the incompatibility between hydrophilic sawdust and hydrophobic rHDPE matrix, leading to poor mechanical properties of the composites [4,5,6]. Many strategies, i.e. fiber surface treatment, matrix modification, adding compatibilizer, have been developed to improve the compatibility of the composites [7,8,9]. Alkali treatment, one of the most use chemical surface treatments, increases the fiber surface roughness by removal of waxes, pectin, lignin and hemicellulose on fiber surface, resulting in better mechanical interlocking between sawdust and rHDPE matrix [10,11,12]. This results in the improvement of the mechanical properties of the composites. Tensile and flexural properties of alkali treated piassava fiber/rHDPE composites were increased when compared to untreated piassava fiber/rHDPE composites due to improved adhesion between piassava fiber and rHDPE matrix [12]. In addition, alkali treatment increased char residue of rice husk fiber reinforced recycled low density polyethylene composites [13]. This led to the enhancement of flame retardancy of the composites because the char residue formed the protective layer and separated the underlying material from heat and oxygen [14]. The aim of this study is to investigate the effects of sawdust content and alkali treatment on mechanical and flammability of sawdust/rHDPE composites.

Materials and Methods

Materials. Recycled high density polyethylene (rHDPE) was obtained from a local plastic recycling plant. Indian Walnut sawdust *(Albizia lebbeck Benth)* with particle sizes of 425-600 μm was supplied from Huathalae sawmill, Nakhon Ratchasima. Sodium hydroxide (RPE-ACS, Carlo Erba) was purchased from Italmar (Thailand) Co., Ltd.

Sawdust Preparation. Sawdust was dried at 60°C for 24 h in a vacuum oven. This sawdust was called "untreated sawdust (UT)". Some of UT was treated with sodium hydroxide solution (NaOH). Sawdust was immersed and stirred in the 2% w/v NaOH solution for 30 min at room temperature, followed by wash with water several times until pH7 was attained. Then the sawdust was dried by an oven at 60°C for 24 h. This sawdust was called "alkali treated sawdust (AT)".

Composite Preparation. Composition of rHDPE composites and their designation used in this study are shown in Table 1. rHDPE composites were prepared using a twin screw extruder (Brabender, DSE 35/17D). The temperatures of the four processing zones were 175, 180, 185 and 190°C. The screw speed was 20 rpm. The test specimens were processed by a compression molding machine (Labtech, LP20-B) at 190°C under a constant pressure of 120 psi for 10 min.

Table 1. Composition and their designation of rHDPE, untreated sawdust/rHDPE composites and alkali treated sawdust/rHDPE composites

Designation	rHDPE [wt%]	Sawdust [wt%]	
		UT	AT
rHDPE	100	-	-
rHDPE/30UT	70	30	-
rHDPE/40UT	60	40	-
rHDPE/50UT	50	50	-
rHDPE/30AT	70	-	30
rHDPE/40AT	60	-	40
rHDPE/50AT	50	-	50

Composite Characterization.

Tensile Properties. Tensile tests were examined according to ASTM D638 using a universal testing machine (Instron, 5565) with a load cell of 5 kN and a crosshead speed of 50 mm/min.

Flexural Properties. Flexural properties of rHDPE and rHDPE composites were tested by following ASTM D790 using universal testing machine (Instron, 5565) with span length of 56 mm and crosshead speed of 15 mm/min.

Flammability. Flammability of rHDPE and rHDPE composites was investigated by a horizontal burning test according to ASTM D635. The specimen was held horizontally and a flame was applied to one end of the specimen. A burning time from the first reference mark, i.e. 25 mm from the end, to the second reference mark, i.e. 100 mm from the end, was recorded. Then, burning rates of the composites were calculated by using the equation:

$$V = L/t \quad (1)$$

where V is the burning rate (mm/min). L is the burned length (mm). t is the time (s) of burning.

Morphological Properties. Tensile fracture surfaces of untreated and alkali treated sawdust/rHDPE composites were examined using a scanning electron microscope (SEM, NeoScope JCM-6010). The fracture surface of the specimens was coated with gold before analysis.

Results and Discussion

Mechanical Properties. Tensile strength, tensile modulus and elongation at break of rHDPE and rHDPE composites are shown in Fig. 1 (a)-(c). With the addition of sawdust, tensile strength and tensile modulus of rHDPE were improved but elongation at break was reduced. This result suggested that sawdust acted as reinforcing filler in the system [15]. With increasing sawdust content, tensile strength of the composites decreased as illustrated in Fig. 1 (a). This may be due to the poor dispersion of sawdust in rHDPE matrix and the incompatibility between sawdust and rHDPE matrix [6,7]. From Fig. 1 (b), tensile modulus of the composites enhanced with increasing sawdust content indicating the ability of sawdust to impart greater stiffness to the composites [6]. The reduction of elongation at break of the composites was found with increasing sawdust content as shown in Fig. 1 (c). This was because the presence of sawdust caused matrix to lose its ability against elastic deformation [7]. Hence, the composites broke at a lower elastic deformation. Tensile strength, tensile modulus and elongation at break of alkali treated sawdust/rHDPE composites were slightly higher than that of untreated sawdust/rHDPE composites at all sawdust contents. This was because alkali treatment improved the fiber surface roughness by removal of waxes, pectin, lignin and hemicellulose on fiber surface resulting in better mechanical interlocking between sawdust and rHDPE matrix [10,11,12]. Flexural strength and flexural modulus of rHDPE, untreated and alkali treated sawdust/rHDPE composites are shown in Fig. 2 (a) and (b), respectively. Flexural properties of rHDPE composites showed the same trend as tensile properties. Flexural strength and flexural modulus enhanced with incorporating sawdust. Flexural strength of the composites decreased whereas flexural modulus increased with increasing sawdust content as illustrated in Fig. 2 (b). After alkali treatement, flexural strength and flexural modulus of alkali treated sawdust/rHDPE composites were slightly higher than those of untreated composites at all sawdust contents due to enhanced adhesion between sawdust and rHDPE matrix. Elzubair et al. [12] also reported that alkali treatment improved flexural properties of piassava fiber/rHDPE composites.

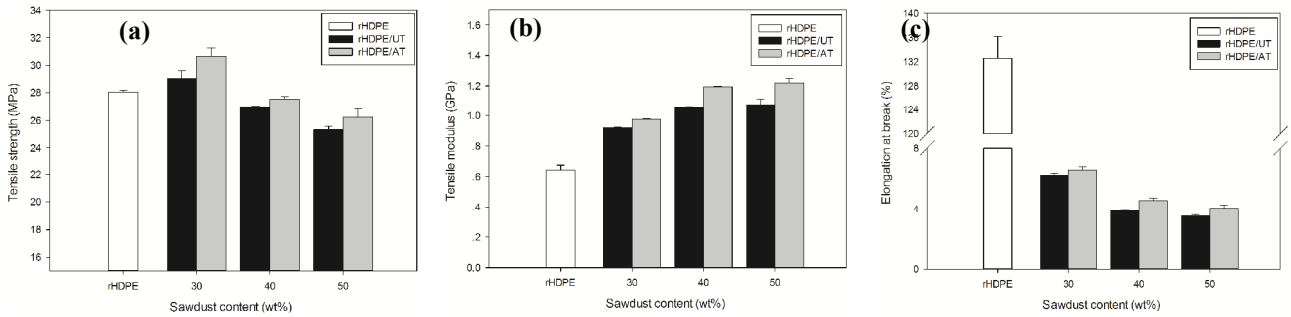

Figure 1. Tensile properties of rHDPE, untreated sawdust/rHDPE composites and alkali treated sawdust/rHDPE composites with different sawdust contents: (a) tensile strength, (b) tensile modulus and (c) elongation at break.

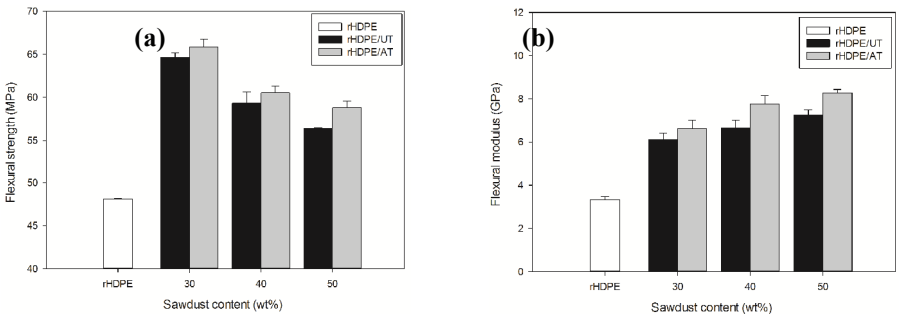

Figure 2. Flexural properties of rHDPE, untreated sawdust/rHDPE composites and alkali treated sawdust/rHDPE composites with different sawdust contents: (a) flexural strength and (b) flexural modulus.

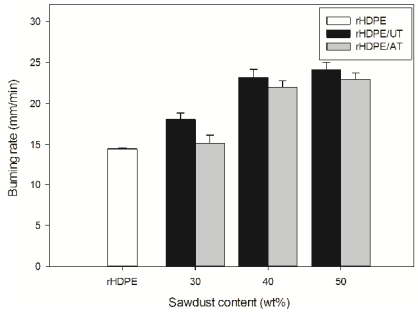

Figure 3. Burning rates of rHDPE, untreated sawdust/rHDPE composites and alkali treated sawdust/rHDPE composites with different sawdust contents.

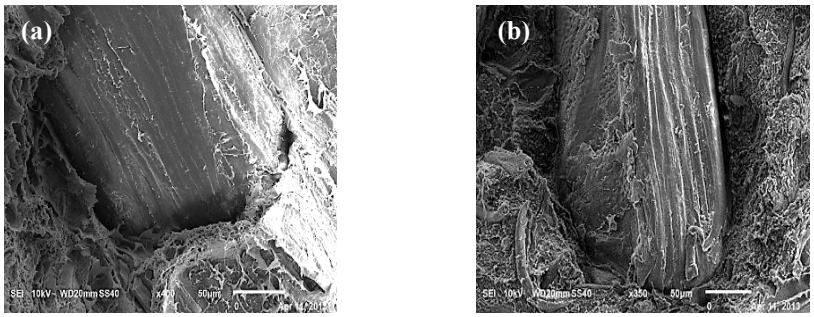

Figure 4. SEM micrographs of tensile fracture surface of the composites at 350x (a) rHDPE/30UT and (b) rHDPE/30AT.

Flammability. Horizontal burning rates of rHDPE, untreated and alkali treated sawdust/rHDPE composites are shown in Fig. 3. rHDPE composites had higher burning rate than rHDPE and the burning rate increased with increasing sawdust content. This indicated that sawdust/rHDPE composite had high sensitivity to flame [16]. Stark et al. [17] also found that flammability of wood flour/HDPE increased with increasing wood flour content. Alkali treated sawdust/rHDPE composites showed slightly lower burning rate than untreated sawdust/rHDPE composites. This may be due to an increase in char residue of the composites by alkali treatment [13]. As the char layer built up, it may separate the composites from heat and oxygen [14].

Morphological Properties. SEM micrographs of tensile fracture surfaces of untreated and alkali treated sawdust/rHDPE composites are shown in Fig. 4 (a) and (b). As shown in Fig. 4 (a), gap between rHDPE and sawdust was observed indicating the poor compatibility between sawdust and rHDPE matrix. This led to the reduction of mechanical properties of rHDPE composites. From Fig. 4 (b), alkali treatment enhanced the interfacial adhesion between sawdust and rHDPE matrix resulting in the improvement of the mechanical properties of the composites [11]. Elzubair et al. [12] also observed that alkali treatment improved the compatibility of piassava fiber/rHDPE composites.

Summary

Tensile strength and elongation at break of rHDPE reduced whereas tensile modulus improved with the incorporation of sawdust. With increasing sawdust content, tensile strength and elongation at break decreased but tensile modulus increased. Burning rate of rHDPE composites was higher than rHDPE and further enhanced with increasing sawdust content. Alkali treatment improved the interfacial adhesion between sawdust and rHDPE resulting in the improvement of mechanical properties at all sawdust contents. Furthermore, flame retardancy of alkali treated sawdust/rHDPE composites was higher than untreated sawdust/rHDPE composites. SEM micrographs revealed that alkali treatment improved the interfacial adhesion between sawdust and rHDPE matrix.

References

[1] H. P. S. A. Khalil, S. B. S. Shahnaz, M. M. Ratnam, F. Ahmad, N. A. N. Fuaad, Recycle polypropylene - wood sawdust composites - part 1: the effect of different filler size and filler loading on mechanical and water absorption properties, J. Reinforc. Plast. Comp. 25 (2006) 1291-1303.

[2] S. K. Najafi, E. Hamidinia, M. Tajvidi, Mechanical properties of composites from sawdust and recycled plastics, J. Appl. Polym. Sci. 100 (2006) 3641-3645.

[3] K. B. Adhikary, S. Pang, M. P. Staiger, Dimensional stability and mechanical behavior of wood-plastic composites based on recycled and virgin high-density polyethylene (HDPE), Comp. Part B. 39 (2008) 807-815.

[4] K. S. Aina, E. O. Osuntuyi, A. S. Aruwajoye, Comparative studies on physico-mechanical properties of wood plastic composites produced from three indigenous wood species, Int. J. Sci. Res. 2 (2013) 226-230.

[5] C. U. Atuanya, N. Solomon, Evaluation of the mechanical properties of recycled polyethylene/iroko wood saw dust particulate composite, J. Basic Appl. Sci. Res. 1 (2011) 2806-2810.

[6] N. Sombatsompop, C. Yotinwattanakumtorn, C. Thongpin, Influence of type and concentration of maleic anhydride grafted polypropylene and impact modifiers on mechanical properties of PP/wood sawdust composites, J. Appl. Polym. Sci. 97 (2005) 475-484.

[7] P. J. H. Franco, A. V. Gonzalez, A study of the mechanical properties of short natural-fiber reinforced composites, Comp. Part B 36 (2005) 597-608.

[8] P. W. Balasuriya, L. Ye, Y. W. Mai, J. Wu, Mechanical properties of wood flake-polyethylene composites. II. interface modification, J. Appl. Polym. Sci. 83(2002) 2505-2521.

[9] Y. Habibi, W. K. El-Zawawy, M. M. Ibrahim, A. Dufresne, Processing and characterization of reinforced polyethylene composites made with lignocellulosic fibers from Egyptian agro-industrial residues, Comp. Sci. Tech. 68 (2008) 1877-1885.

[10] H. Gu, Tensile behaviours of the coir fiber and related composites after NaOH treatment, Mater. Des. 30 (2009) 3931-3934.

[11] N. P. G. Suardana, Y. Piao, J. K. Lim, Mechanical properties of hemp fibers and hemp/PP composites: effects of chemical surface treatment, Mat. Phy. Mech. 11 (2011) 1-8.

[12] A. Elzubair, J. C. M. Suarez, Mechanical behaviour of recycled polyethylene/piassava fiber composites, Mater. Sci. Eng. A 557 (2012) 29-35.

[13] K. A. Tue, M. M. Thwe, Recycle of plastic waste and agricultural waste, Energ. Res. J. 4 (2013) 24-29.

[14] L. A. Lowden, T. R. Hull, Flammability behaviour of wood and a review of the methods for its reduction, Fire Sci. Rev. 2 (2013) 1-19.

[15] L. Danyadi, T. Janecska, Z. Szabo, G. Nagy, J. Moczo, B. Pukanszky, Wood flour filled PP composites: compatibilization and adhesion, Comp. Sci. Tech. 67 (2007) 2838-2846.

[16] M. Sain, S. H. Park, F. Suhara, S. Law, Flame retardant and mechanical properties of natural fiber PP composites containing magnesium hydroxide, Polym. Degrad. Stab. 83 (2004) 363-367.

[17] N. M. Stark, R. H. White, S. A. Mueller, T. A. Osswald, Evaluation of various fire retardants for use in wood flour polyethylene composites, Polym. Degrad. Stab. 95 (2010) 1903-1910.

Advanced Materials Research Vol. 970 (2014) pp 84-87

doi:10.4028/www.scientific.net/AMR.970.84

ELECTRON BEAM CROSSLINKING OF EVA/ENR-50/HNTS NANOCOMPOSITES IN THE PRESENCE OF TRIMETHYLOL PROPANE TRIACRYLATE, TMPTA

Amirah Kamal Rudin[1,a], Zurina Mohamad[1,b*], C. T. Ratnam[2,c], and Aznizam Abu Bakar[1,d]

[1]Department of Polymer Engineering, Faculty of Chemical Engineering, Universiti Teknologi Malaysia, 81310 UTM Skudai, Johor Bahru, Malaysia
[2]Radiation Processing Technology Division, Malaysian Nuclear Agency (Nuclear Malaysia), Bangi, 43000 Kajang, Malaysia.
[a]amirahkamalrudin@gmail.com, [b*]zurina@cheme.utm.my , [c]chantara@nuclearmalaysia.gov.my, [d]aznizam@cheme.utm.my

Keywords : Halloysite nanotubes; Trimethylol Propane Triacrylate (TMPTA); Co-agent; Irradiation crosslinking.

Abstract: Ethylene vinyl acetate/ Epoxidised natural rubber/ Halloysite nanotube (EVA/ENR-50/HNT) nanocomposite was prepared through melt blending process using twin screw extruder at 120 ºC and 50 rpm of screw speed. The ratio of EVA/ENR-50/HNT was fixed at 80:20:4. The nanocomposites were irradiated with a 3.0 MeV electron beam machine at doses ranging from 50 to 200 kGy in air at room temperature. The effect of irradiation dose and co-agent Trimethylol Propane Triacrylate (TMPTA) on tensile strength and gel content of EVA/ENR-50/HNT nanocomposite were studied. It was found that the tensile strength and gel fraction of the EVA/ENR-50/HNT nanocomposites increased with the increased of irradiation dose. In the presence of TMPTA, a better performance in tensile strength was achieved due to the increased efficiency of irradiation induce crosslinking of EVA/ENR-50/HNT nanocomposite.

Introduction

Enhancing polymer properties can be made in various way. As succesfully developed, many kind of polymer enhanced with filler or nanofiller, irradiation treatment, compatibilizer,additives, blending and etc. EVA/ENR-50 blend was found as a novel blend which can replace the uses of PVC in most of cable and insulator since PVC is not environmental friendly. An alternatives method such as addition of nanofillers and irradiation modification was introduced to develop a new polymer or composites with better quality of properties [1,2]. The presence of nanofillers in polymer can be found easily in the literature such as MMT, CNTs, HNTs, nanofillers. Halloysite nanotubes (HNTs) recently been used in polymers such as epoxy, polypropylene and polyvinyl alcohol in order to improve the mechanical and thermal properties of the nanocomposites.It is proved that mechanical properties such as stiffness and toughness, dimensional stability, electrical, barrier and thermal properties as well as fire retardant enhancements was enhanced[3,4]. In irradiation modification, a crosslinking agent is a good package in improving the properties of polymers [5,6]. The function of co-agents is to capture the free radical during irradiation as much as possible. Hence, degree of crosslinking of polymers increased significantly [7,8]. In this study, the attempts were made to investigate the effect of TMPTA on tensile properties of irradiated EVA/ENR-50/HNTs nanocomposites.

Materials and Methods

Epoxidised Natural Rubber with 50% epoxidation (ENR-50) was supplied by Malaysian Rubber Board, Malaysia (grade EPOXYRENE 50) with specific gravity value of 1.03 and Mooney viscousity (ML (1+4) at 100˚C) of 140 MU (Mooney unit). Ethylene Vinyl acetate (EVA) used in this study was bought from Polyolefin Company, Singapore (grade COSMOTHENE EVA H2181) containing 18 wt % vinyl acetate, with a melt flow index of 2.4 g/ 10 min (at 190˚ C and 2.16-kg load) and with density of 0.938 g/cc. Halloysite Nanotube (HNTs) and TMPTA was purchased from

Sigma Aldrich company, Malaysia. The EVA/ENR50/HNT/TMPTA nanocomposite was prepared by using the ratio of 80/20/4/4.ENR-50 were rolled and.dried blend with EVA,ENR50, and TMPTA. Then, the material mixed using Brabender twin screw extruder at 130˚ C with the screw speed of 60 rpm. Then, the compound was palletized and injection molded. The sample was irradiated in the presence of air at room temperature using 3.0 MeV Cockroft Walton type electron beam accelerator (model NHV EPS-3000 at dose range of 0-50 kGy.The gel content of the samples was determined using the solvent-extraction method according to the ASTM D-2765 method. The samples were refluxed with hot xylene for 18 h then the remaining insoluble sample was dried in oven to a constant weight. The tensile properties were measured with in general accordance to ASTM 638 using an Instron model 4411 testing machine (UK). The dumbbell-shaped specimens were extended at a crosshead speed of 50mm/min.

Results and Discussion

Gel Content. The effect of crosslinking agent, TMPTA on gel content (%) of EVA/ENR50/HNT nanocomposite at different irradiation doses was shown in Fig 1. In general, the gel content values increased with the increased of irradiation dose and the values further increased with the addition of TMPTA. A sharp increased of gel content was increased from 0 kGy to 50 kGy with both crosslinking agent inclusion and followed by slight increment of gel content with further increased of irradiaition dose. The nanocompsoites contain TMPTA crosslinking agent shown a better performance in gel content since the TMPTA having more reactive site for crosslinking reaction with EVA and ENR-50 compare with nanocomposite withour TMPTA. The consumption of TMPTA had reduced the optimum radiation dose and increased the tensile strength of the nanocomposites. The same observations was also reported in irradiated NR/PS blend in the presence of crosslinking agent. A minimal irradiation dose was found with the inclusion of crosslinking agent at 50 kGy and the compatibility of NR/PS was also imporved [9]. In the cases of EVA/ENR-50 blend, Zurina et al., [7] reported that, the existence of HVA-2 and TMPTA in the blend had improved the gel content of the blend. Crosslinking agent has accelerated the irradiation induced croslinking in the nanocomposite. It is worthwhile to note that TMPTA is effective crosslink agent to enhance crosslinking and reduce irradiation dose in irradiated EVA/ENR-50/HNTs nanocomposites. It can be seen from the results that the composite with and without HNTs recorded almost the same value of gel content. It can be conclude that HNTs has no effect in irradiation induced crosslinking.

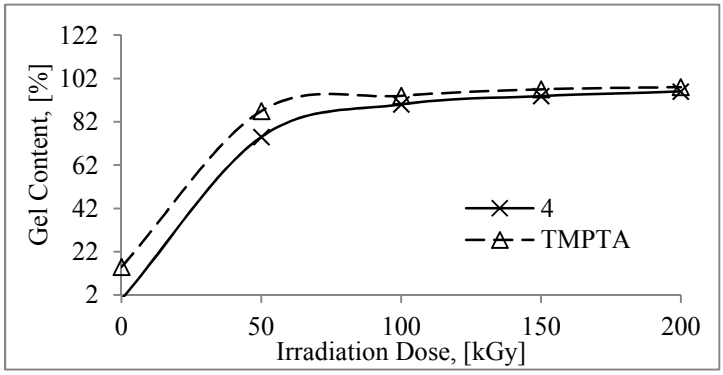

Fig 1: Effect of crosslinking agent on gel content at different irradiation dose

Tensile Properties. Fig 2 showing that the effect of crosslinking agent (TMPTA) at different irradiation dose on tensile strength of EVA/ENR50/4HNT nanocomposite. As mention earlier, TMPTA and irradiation dose successfully improved the gel content of nanocomposite. In general, the existence of TMPTA empower the tensile strength of the EVA/ENR50/4HNT nanocomposite. Moreover, combination of TMPTA and irradiation had further increased the tensile strength of nanocomposite. In Fig 2, TMPTA shows a potential as a good candidate to enhance the tensile strength of the nanocomposite. The increased of tensile strength is attributed to the increased irradiation induced crosslinking of the nanocomposite compared with the one without TMPTA.

Similar observation was also reported by other researchers in irradiated EVA/ENR50 system [6] and irradiated EVA/ENR50/CNT system [10] The irradiation induced crosslinking has led to the strengthening of chemical bonding structure , thus increased in tensile strength of nanocomposite. At higher irradiation dose (above 150 KGy), the tensile strength had reduced to the lower value. The drop of tensile strength is believed to be due to the embrittlement cause by excessive crosslinking in the sample [7,11]. For the nanocomposite without croslinking agent, the increament of tensile strength increased until 100kGy then after that is less remarkable due to the irradiation degradation at higher dosage. Oxidative crosslinking and chain scission are believed to take place [12,13].

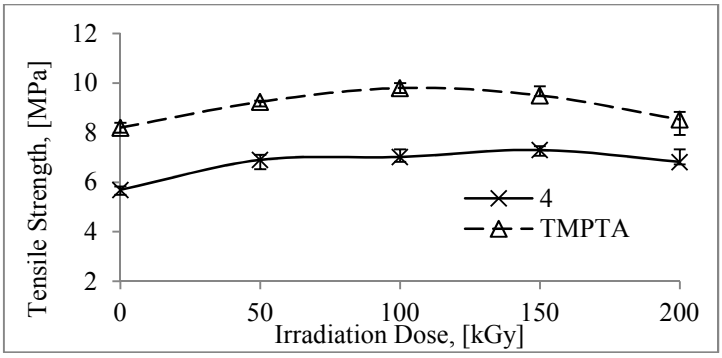

Fig 2: The effect of crosslinking agent TMPTA on EVA/ENR50/4HNT at different irradiation dose

The effect of croslinking agent TMPTA at different irradiation on the M100 of the EVA/ENR50/HNT nanocomposite is illustrated in Fig 3. A significant improvement was observed of M100 for the sample containing TMPTA. In general, the increment of M100 of the nanocomposites is affected by the extensive croslinking upon irradiation that explained earlier. The irradiation induced crosslinking and the reinforcement effect of HNTs had increased the energy needed to elongate the composition at 100%. The modulus depends directly on crosslink density or a perfect network. Thus, the increase in crosslink density is reflected from the enhancement in the M100 with the irradiation dose. The increase in M100 with the addition of the TMPTA indicate the acceleration of crosslinking by the additives.

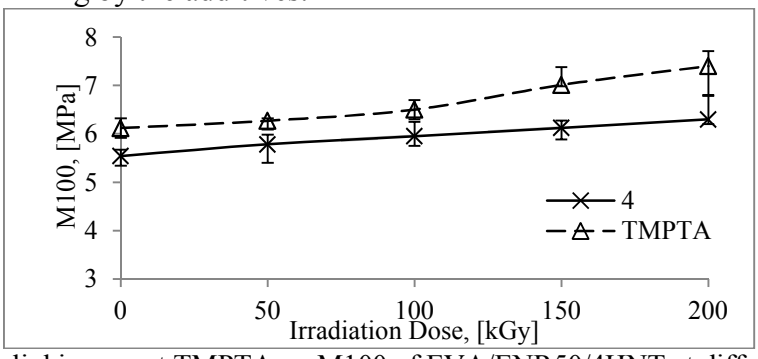

Fig 3: Effect of crosslinking agent TMPTA on M100 of EVA/ENR50/4HNT at different irradiation dose

The effect of TMPTA on elongation at break of EVA/ENR50/HNTs nanocomposites is illustrated in Fig 4. As expected, the reduction of elongation at break occurred reflected to the tensile strength result. The reduction of elongation at break of the nanocomposite is due to the reduction of the ductility of the nanocomposites. The movement of polymer chains of the nanocomposites becomes restricted as crosslinking increased upon irradiation. However the elonggation at break increased with the addition of TMPTA. The TMPTA is efficiently crosslink the EVA and ENR-50 phase upon irradiation compared with the one without TMPTA. The perfect crosslink of both phases lead to produce a compatible marix in nanocomposite thus increased its elonggation at break. Hence the elongation at break of the TMPTA recorded at the higher value. However the elongation at break of all samples shows some improvement at lower irradiation dose (50 kGy). This is believed due to the effect of nanosized HNTs particles are capable of interrupting the intermolecular attraction of matrix segments, thus allowing the ENR-50 backbone chains gained additionally segmental mobility. Besides that, the nature behaviour of rubbery type polymer also accounted.

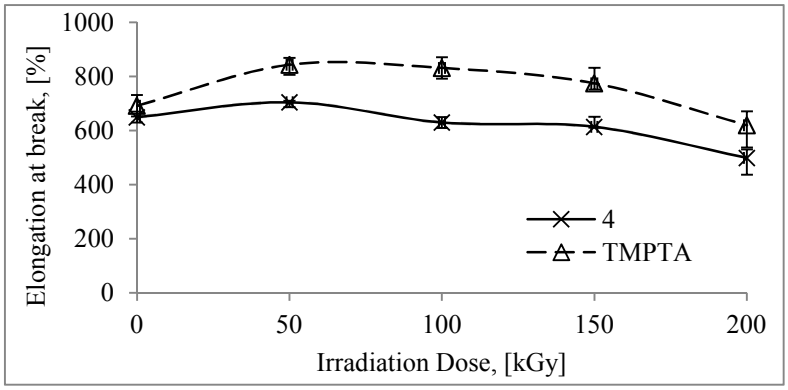

Fig 4: Effect of crosslinking agent TMPTA on elongation at break of EVA/ENR50/4HNT at different irradiation dose

Conclusion

A sharp increased in gel content of EVA/ENR-50/HNTs nanocomposites with irradiation indicate that the nanocomposites are crosslinked upon electron beam irradiationThe study showed that the electron beam irradiation incorporation of co-agent (TMPTA) and nanofiller (HNTs) is efficient method to enhance the properties of EVA/ENR-50/HNTs.

Acknowledgement

The authors gratefully acknowledge for the researcht grant from Ministry of High Education, UTM, researcht grant Vot no #08J54 and the staff of Universiti Teknologi Malaysia and Nuclear Malaysia for their cooperation and support to carry out this research.

References

[1] M. Alexandre, and P. Dubois, Polymer-layered silicate nanocomposites: preparation, properties and uses of a new class of materials Mater. Sci. and Eng.: R: Reports, Vol 28 (2000), p. 1-63
[2] Strong, A. B. Plastics: materials and processing: Pearson Prentice Hall (2006)
[3] K. Hedicke-Hoschstotter, G. T. Lim and V. Altstadt Novel polyamide nanocomposites based on silicate nanotubes of the mineral halloysite, Composites Science and Technology, Vol. 69, p. 330-334 (2009)
[4] P. Pasbakhsh, H. Ismail, M. N. Ahmad Fauzi and A. Abu bakar EPDM/modified halloysite nanotube, Apllied Clay Science, Vol 48, p. 405-413(2010)
[5] I. R. Gelling, Epoxidised natural Rubber in concise polymeric materials encyclopedia (Salamone, J. C. ed.). CRC Press, New York (1999)
[6] C.S. L. Baker, and I. R. Gelling, Epoxidized natural rubber in Developments in Rubber Technology-4, (Whelan, A. and Lee, K. S. Eds). Elsvier Applied Science, London (1987).
[7] M. Zurina, H. Ismail, and C.T. Ratnam, (2008) The effect of HVA-2 on properties of irradiated epoxidized natural rubber (ENR-50), ethylene vinyl acetate (EVA), and ENR-50/EVA blend. Polymer testing, 27, 480-490
[8] S. K. Datta, A. K. Bhowmick, T. K. Majali, A.B. Majali, R. S. Despande, Electron Beam initiated modification of ethylene vinyl acetate using trymethylolpropane trimethylacrylate Polymer Vol 37, p. 45-55
[9] M. Nor Hayati, A. Ibrahim, H.M. Dahlan Effects of EB-irradiation on 60/40 NR/PS blends in the presence of m-phenylenebismaleimide. Jurnal. Sains Nuklear. Malaysia., 20 (2002) 85-101
[10] M. Y. Norazlina, Y. Faridah, C. T. Ratnam, I. Sopyan, Irradiation modification of epoxidized natural rubber/ethylene vinyl acetate/carbon nanotubes nanocomposites. *Advanced Materials Research,* 364,(2012) 196-201
[11] M. Zurina, H. Ismail, C. T. Ratnam characterization of irradiation-induced crosslink of epoxidised natural rubber/ethylene vinyl acetate (ENR-50/EVA) blend, Polymer Degradation and Stability, 91 (2006), 2723-2730
[12] I. Banik, A.K. Bhowmick, Influeneces of electron beam radiation on the mechanical properties and crosslinking of fluorocarbon elastomer Radiation Physic Chemistry Vol 54, p. 135-142
[13] M. Khalid, A.F. Ismail, C.T. Ratnam, Y. Faridah, W. Rashmi, M.F. Al Khatib Effect of radiation dose on the properties of natural rubber nanocomposites.

Advanced Materials Research Vol. 970 (2014) pp 88-90

doi:10.4028/www.scientific.net/AMR.970.88

Quasi-Static Flexural and Indentation Behaviour of Polymer-Metal Laminate

S.M.S. Azwan[a*], YAZID Yahya[b], AMRAN Ayob[c], B. Abdi[d]
Centre for Composites (C*f*C), Faculty of Mechanical Engineering,
Universiti Teknologi Malaysia, 81310 UTM Johor Bahru, Johor, Malaysia
[a*]mr.syedmohd@yahoo.com, [b]yazid@fkm.utm.my, [c]amran@fkm.utm.my, [d]behzad.abdi@gmail.com

Keywords: Quasi-static, Polymer-Aluminium laminate, Flexural, Indentation

Abstract. Metal-polymer laminates were subjected to quasi-static flexural and indentation loading. The laminates were made of two aluminium skins heat-bonded (laminated) to a core made of polyethylene plastic material. The samples were trimmed into standard-sized beams and panels which were then tested in flexural and indentation using the Instron universal testing machine at loading rates of 1 mm/min, 10 mm/min and 100 mm/min. The load-displacement and energy absorption curves of the composite beams were recorded. It was found that the loading rate has a large effect on flexural and indentation behaviour of aluminium composite laminate.

Introduction

Sandwich structures consist of two thin and stiff skins bonded to a thick core made of honeycomb or foam. These high-performance structures are frequently used in a wide range of application such as marine, civil and aerospace industries as load-bearing structures [1]. In case of accidents where the structure is impacted visual inspection cannot reveal the damage between the impacted facesheet and the core. Reduction of structural stiffness and strength can occur and consequently propagate under further loading [2]. Therefore, research on these structures is important to predict the behaviour of the structure subject to impact loading.

Several studies were conducted in the field of composite sandwich panels subject to different types of loading [3-7]. For example, composite sandwich beams with foam core subject to indentation loading was studied by Navarro [8]. In this study, Navarro assumed that the behaviour of foam core in compression loading can be adjusted to an elastic-perfectly plastic behaviour. The load-displacement response of sandwich beams under static indentation was calculated and the results were compared with experimental tests and finite element analysis. Impact and indentation loading of composite sandwich panels made of jute-epoxy cork-core was studied [9]. It was found that the density of the core and impact energy have a large effect on the damage behaviour of sandwich panel including force and damage area.

The analysis of composite sandwich panel with aluminium facesheets and Nomex/aluminium honeycomb core subject to four point bending tests was done by Abbadi et al [10]. Using finite element modelling, the honeycomb core was modelled as a single solid layer with equivalent mechanical properties and then analysed using homogenization approaches.

Experimental Procedure

The structure is made of aluminium skins with thickness of 0.5 mm and a polyethylene core with thickness of 3 mm. Several plates with dimension of 100 mm × 30 mm and 100 mm × 100 mm were prepared for flexural and indentation tests, respectively. The tests were carried out using the Instron universal testing machine at loading rates of 1 mm/min, 10 mm/min and 100 mm/min. For indentation test, a hemispherical tip indenter with a diameter of 12.7 mm was used and the specimens were clamped in a steel square jig with dimension 100 mm × 100 mm. The support span for flexural tests was set at 64 mm in accordance with standard testing procedure. Each test was repeated three times and the average results were used for further analysis.

Results and Discussions

From Fig. 1, the flexural properties of aluminium composite panel increase with the loading rate. Increasing the loading rate from 1 mm/min to 10mm/min increases the maximum load and deflection by 8.13% and 20.7%, respectively.

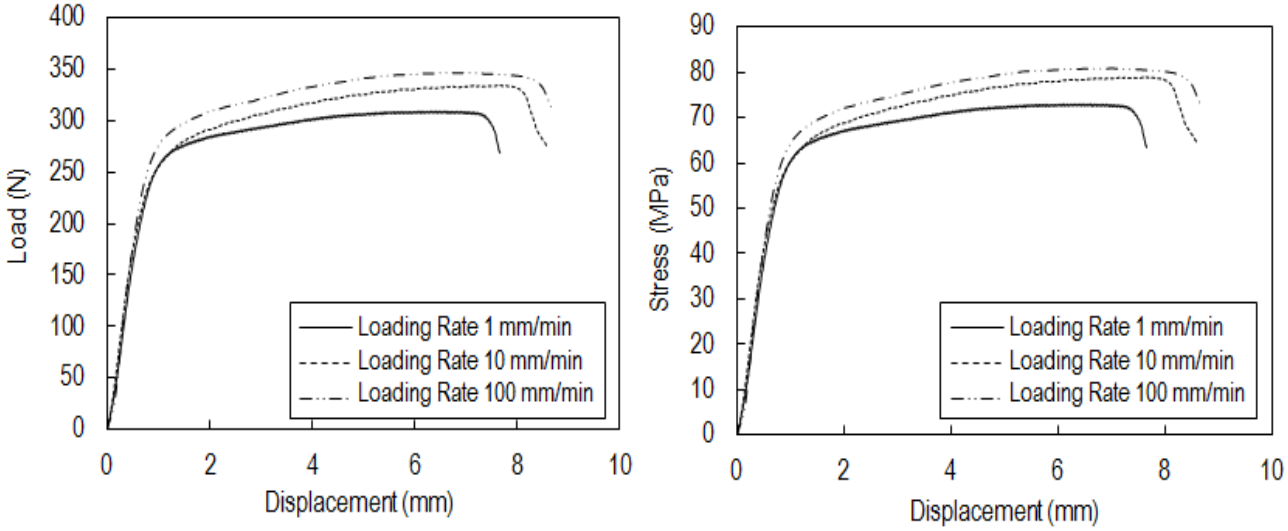

Figure 1. The transverse force and flexural stress behaviour of the composite laminate subject to different loading rates - flexural test.

Increasing the loading rate from 1 mm/min to 100 mm/min increases the maximum load and the deflection by 11.95% and 32.73%, respectively. Finally, by increasing the loading rate from 10 mm/min to 100 mm/min, the maximum load and deflection is increased by 3.5% and 9.97%, respectively. Thus, it reveals that the loading rate has an effect on flexural properties of aluminium composite laminate and should be considered in designing and analysis of the structures.

Fig. 2 shows the effect of loading rate on the applied force and energy absorbed of aluminium composite laminate during indentation loading. Increasing the loading rate from 1 mm/min to 10 mm/min increases the maximum force and energy absorption by 9% and 6.9%, respectively, and by 14.6% and 25.79% when the loading rate is increased from 1 mm/min to 100 mm/min. By increasing the loading rate from 10 mm/min to 100 mm/min, the maximum force and energy absorption are increased by 4.82% and 17.66%, respectively.

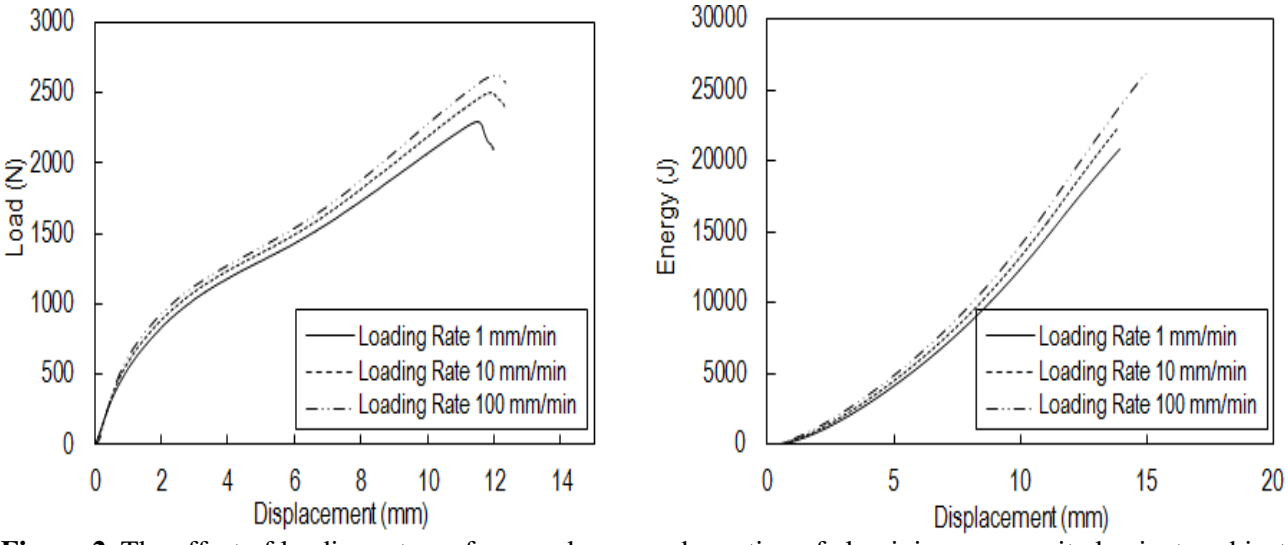

Figure 2. The effect of loading rate on force and energy absorption of aluminium composite laminate subject to indentation loading.

Conclusions

Aluminium-polymer composite laminates subject to quasi-static flexural and indentation loading was studied experimentally. It is found that the loading rate has a large effect on flexural and indentation behaviour.

Acknowledgements

The authors are grateful for the financial support of the Research University Grant from Universiti Teknologi Malaysia (Grant No. Q.J130000.2624.07J19), the Centre for Composites (C*f*C) for their support, and the award of UTM Zamalah Scholarship for Syed Mohd Saiful Azwan Syed Hamzah.

References

[1] S.M. Lee, T.K. Tsotsis, Indentation failure behavior of honeycomb sandwich panels, Compos. Sci. Technol. 60 (2000) 1147–1159.

[2] C.C. Foo, L.K. Seah, G.B. Chai, Low-velocity impact failure of aluminium honeycomb sandwich panels, Compos. Struct. 85 (2008) 20–28.

[3] V. Crupi, G. Epasto, E. Guglielmino, Collapse modes in aluminium honeycomb sandwich panels under bending and impact loading, Int. J. Impact Eng. 43 (2012) 6–15.

[4] F. Zhu, G. Lu, D. Ruan, Z. Wang, Plastic deformation, failure and energy absorption of sandwich structures with metallic cellular cores, Int. J. Protect. Struct. 1 (2010) 507–541.

[5] M. Nguyen, D. Elder, J. Bayandor, A review of explicit finite element software for composite impact analysis, J. Compos. Mater. 39 (2005) 375–86.

[6] I.M. Daniel, E.E. Gdoutos, K.A. Wang, Failure of composite sandwich beams, Adv. Compos. Lett. 11 (2002) 101–109.

[7] S. Zhu, G.B. Chai, Effect of adhesive in sandwich panels subjected to low-velocity impact, Proc. Inst. Mech. Eng. L: J. Mater. Des. Appl. 225 (2011) 171–181.

[8] P. Navarro, S. Abrate, J. Aubry, S. Marguet, J.F. Ferrero, Analytical modeling of indentation of composite sandwich beam, Compos. Struct. 100 (2013) 79–88.

[9] B. Hachemane, R. Zitoune, B. Bezzazi, C. Bouvet, Sandwich composites impact and indentation behaviour study, Compos. B: Eng. 51 (2013) 1–10.

[10] A. Abbadi, Y. Koutsawa, A. Carmasol, S. Belouettar, Z. Azari, Experimental and numerical characterization of honeycomb sandwich composite panels, Simul. Model. Pract. Th. 17 (2009) 1533–1547.

CHAPTER 6:

Electronic and Electronic Packaging

Advanced Materials Research Vol. 970 (2014) pp 93-96

doi:10.4028/www.scientific.net/AMR.970.93

Corrosion behavior of soldered and laser-welded Ni-free Co-Cr alloy joints in sodium chloride solution

P. Eutrirak[1,a], V. Srimaneepong[1,b], K. Saengkiettiyut[2,c*]

[1]Department of Prosthodontics, Chulalongkorn University, Bangkok 10330, Thailand
[2]Metallurgy and Materials Science Research Institute, Chulalongkorn University, Bangkok 10330, Thailand
[a]piyarach_e@hotmail.com, [b]viritpon.s@chula.ac.th, [c*]kanokwan.s@chula.ac.th

Keywords : Corrosion, Solder, Laser welding, Ni-free Co-Cr alloy, Polarization

Abstract. This paper investigates the quality and corrosion property of Ni-free Co-Cr alloy joints soldered and laser welded using filler. The soldered and laser-welded test specimens were sectioned at the center and rejoined by either soldering or laser welding using appropriate fillers. The joint area was analyzed using microfocus X-ray and the percentage of porosity, as a measure of joint quality, was calculated. The corrosion behavior of soldered and laser-welded test specimens was evaluated using a potentiodynamic polarization technique in a 0.9 wt.% NaCl solution, pH 2.3, at 37°C. The results indicated that the amount of porosity and cracks in soldered joints were less than those of the laser-welded joints, leading to a lower corrosion rate.

Introduction

In fixed prosthodontics, joining metal components is frequently necessary in the fabrication of multiunit prosthodontic structures, such as implant superstructures, or in repairing broken dental prostheses. While there are various joining techniques available in dentistry, soldering and laser welding are most commonly used [1]. The soldering process involves the parent metal, a filler metal, flux, and a heat source. The disadvantages of this technique are that it is time consuming, and has compromised precision. A soldered joint can have inferior joint strength compared to a one-piece casting due to air entrapment during melting of the solder with the torch and impurities from the flux material. The laser welding was used as a joining technique in which the parent metals were fused and the joint formed with or without a filler metal. Although filler is not necessary with the laser welding technique, it is commonly used to fill the gap or to add to the contact areas of dental prostheses. Among the metal alloys used in prosthodontics, Ni-free Co-Cr alloys have gained in popularity compared to conventional Ni-Cr alloys because of their higher biocompatibility [2].

For items to be used clinically, the optimal mechanical, physical, and biological properties of a suitable metal joining technique must be determined. Corrosion can induce biological responses, such as an allergic reaction, toxicity, or soft tissue inflammation [1]. External surface defects may contribute to plaque accumulation, which can accelerate joint corrosion. Therefore, joint quality should be carefully examined for evidence of defects.

While several studies have investigated joint strength and their microstructure [1,3], few studies have assessed corrosion resistance and joint quality when prepared using filler, which is typical in clinical practice. In our study, joining Ni-free Co-Cr alloy by soldering, or laser welding, using filler was evaluated in terms of joint quality and corrosion resistance using potentiodynamic polarization method in 0.9% NaCl solution. The metallography and corrosion behavior of these alloy joints were discussed.

Materials and Methods

Specimen preparation. Ni-free Co-Cr alloy (Argeloy NP special, Argen, USA) was selected for the study. The compositions of the alloys used in the study are shown in Table 1. Forty-five rectangular specimens sized 10×10×1 mm were prepared according to ISO standard 9333. The specimens were finished using green stone burs followed by grinding using an automatic grinding machine with silicon carbide paper from No.400–No.1200 and being cleaned in acetone for 5 min in an ultrasonic bath. The specimens were randomly divided into three groups (fifteen specimens for each group) as follows:

As-cast group. Uncut polished specimens were used as a control group.

Soldered group. The specimens were invested in soldering investment. After one hour, the soldering block was preheated at 600ºC for 40 minutes in an oven. Gas oxygen torch soldering was performed in a conventional manner at 1,180ºC using flux and soldering material (Wirobond, BEGO, Germany) following the procedures recommended by the solder manufacturer (BEGO, Germany). The specimens were bench cooled, divested, and sandblasted with 50µm aluminum oxide.

Laser-welded group. Specimens were welded under an argon gas atmosphere with an Nd:YAG laser welding machine set at 270-290 Volts, with a 7 ms pulse duration, and 0.7-1.0 mm weld spot diameter. The initial spot welding was done at three points as a pre-welding procedure. The gap was then continuously filled with Co-Cr filler wire (Wiroweld, BEGO, Germany) using a double sided laser welding technique with approximately 80% overlap.

Table 1. Chemical composition (wt.%) of the alloys used in the present study.

Alloys	Composition [wt.%]								Melting Range [°C]	Working Temp [°C]	Density [g/cm^3]
	Co	Cr	Si	Mo	Mn	Fe	C	B			
As-cast	59.5	31.5	2	5	1	-	-	-	1,240-1,350	1,480	8.8
Solder filler	60.5	28.5	4.5	3	-	<1	<1	<1	1,100-1,150	1,180	8.5
Laser-weld filler	63.5	29	1	5.5	1	-	-	-	N/A	N/A	8.3

Assessment of joint quality. All specimens were evaluated for joint quality by microfocus x-ray using an 8 µm focal spot. The parameters of the X-ray machine were set at a voltage of 75 kV, a current of 30 µA, an exposure time of 30 s, and the distance from the X-ray tube to the specimen was 4 cm. The images were analyzed using the Image Reader FLA-5000 Series v1.0 program. Joint quality was defined as the percentage of porosity in two-dimensions. The joint area was selected for calculating the percentage of porosity using the Image J program. A joint area of 0.4×10 mm (1024×40 pixel) was used in the analysis of all specimens.

Corrosion evaluation. The corrosion behavior was assessed by potentiodynamic polarization testing using µAutolab potentiostat. The electrolyte used in this study was a 0.9 wt.% NaCl solution, pH 2.3 at 37°C. The electrolyte was de-aerated by bubbling nitrogen gas for 30 min at 100 cm^3/min. The specimen (WE) was held with a teflon holder and a vitron o-ring. The exposed area of the specimen was 0.5 cm^2, which included the joint area and the heat-affected zone. A saturated calomel electrode and a platinum electrode served as reference electrode (REF) and counter electrode (CE), respectively (Fig. 1). The open circuit potential was measured for 60 minutes. The potentiodynamic scan was performed in the potential range of -0.5 to 2 V_{SCE} at a scanning rate of 1 mV/s. The data were statistically analyzed using a one-way analysis of variance (ANOVA) and Scheffe post hoc test at a significance level of 95%.

Fig. 1 Corrosion cell set up.

Results and discussion

X-ray examination of the samples revealed that the mean percentage of porosity of the laser-welded group was 3.58%, which was higher than that of the soldered (0.52%) and as-cast (0.06%) groups (Fig. 2). These values were significantly distinct among different groups ($p< 0.05$). The

present results revealed that the percentage of porosity of laser-welded joints was the highest, indicating the poorest joint quality. This laser-welded joint deficiency could be due to inadequate alloy penetration depth or types of alloys used. It should be noted that cracks and porosity are common types of defects found in laser-welded Co-Cr alloy joints [1]. In addition, some studies have reported that soldered joints of this alloy were of better quality [4]. The present study conforms to these studies. Regarding mechanical properties, soldered Co-Cr alloy joints have shown higher tensile strength than laser-welded joints [1]. This could be due to the soldering technique in which the molten solder is manipulated to flow into the joint space and completely fills the space before it solidifies leading to a low possibility of voids or porosities. The cracks in welded joints and heat-affected zones have been attributed to the residual stress induced by the rapid cooling of molten Co-Cr alloy, which may cause stress corrosion cracking. This can affect the longevity of laser-welded prostheses [5,6].

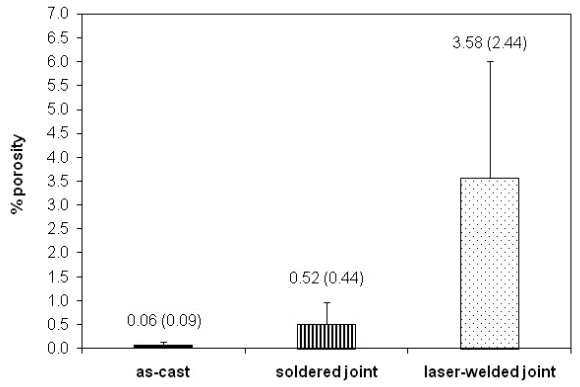

Fig. 2 Mean (SD) percentage of porosity from the total area of joint (100%) of the as-cast, soldered and laser-welded joints.

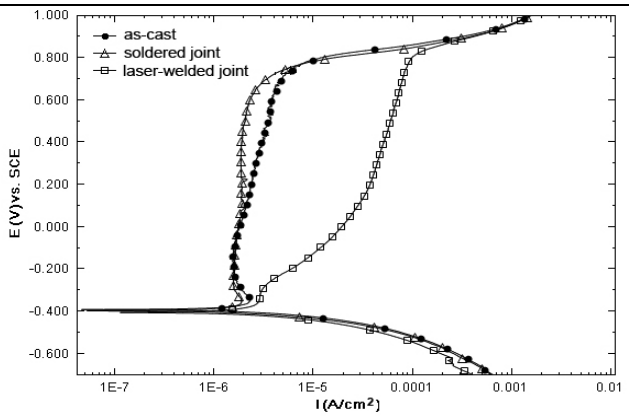

Fig. 3 Representative potentiodynamic polarization curves of as-cast, soldered and laser-welded joints, determined in 0.9 wt.% NaCl solution, pH 2.3 at 37°C.

The potentiodynamic curves obtained from the as-cast samples, soldered, and laser-welded joints are seen in Figure 3. The curves of the soldered and as-cast specimens were similar, showing stability of the passive film. The soldered and as-cast specimens had a lower passive current density than that of the laser-welded specimens. This indicates that the passive film of the laser-welded specimens had a lower resistance than that of the soldered and as-cast specimens. The results of corrosion parameters are seen in Table 2. The mean corrosion potential of the as-cast specimens was similar to that of the soldered joints, and while both groups displayed a higher corrosion potential than that of the laser-welded joints, there were no statistically significant differences between these groups. Both the corrosion current density and the mean corrosion rate values of the laser-welded joints were significantly higher than those of the other groups ($p< 0.05$), but there was no significant difference between the soldered joints and as-cast specimens. A previously published study by Zupancic et al [1] on corrosion resistance showed that the corrosion resistance of laser-welded joints was better than that of brazed joints. In contrast, our study found soldered joints had better corrosion resistance compared to laser-welded joints. This may be because the percentage of porosity and cracks in the welded-joints was greater than that of the soldered joints. Moreover, in our study, the entire specimen was tested, including both welded joint and as-cast area in order to simulate laser-welded dental prostheses in the mouth. This also included the heat-affected zone of laser-welded joints. These factors could be lower corrosion resistance of laser-welded Co-Cr alloy joint. In partially of the polarization curves of the as-cast group, it is similar to the laser-welded group. This may be due to internal flaws that could not be detected by visual examination.

Table 2. Mean values (SDs) of corrosion parameters

Specimens	E_{corr} [mV]	I_{corr} [µA/cm^2]	Corrosion rate [mm/y]
As-cast	-398.19 (5.98)	20.70 (3.49)	0.14 (0.02)
Soldered joint	-399.00 (14.00)	21.45 (3.22) *	0.14 (0.02) *
Laser-welded joint	-402.59 (13.09)	24.95 (3.31) *	0.19 (0.02) *

* statistically significant difference ($p< 0.05$)

Metallographic images obtained from the as-cast, soldered, and laser-welded joints are shown in Figure 4. The as-cast surfaces showed the dendritic microstructure. The dendrite region, which is enriched in Cr and Mo, tends to stabilize the ε phase [2]. Thus, the polarization curves of the as-cast specimens showed passive regions. The soldered joints demonstrated a few small porosities at the transition zone between the solder and the as-cast area, while the laser-welded joints had a fine precipitate in the joint area and had numerous cracks and porosities in both the joint area and the heat-affected zone. In laser-welded specimens, a precipitate of σ phase could be found in the interdendrite region of the heat-affected zone, which might cause corrosion [7]. This is in accordance with our finding that the passive current density of the laser-welded specimens was higher than the as-cast specimens. Moreover, our analysis showed more defects in the joint area such as pits, porosities, and cracks present in laser-welded joints. These may result in localized corrosion [1].

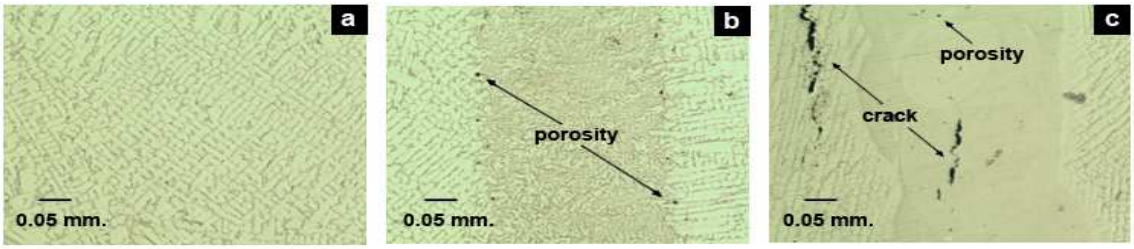

Fig. 4 Metallographic pictures showing a cross-section of (a) as-cast, (b) soldered and (c) laser-welded joints.

Conclusions

Joining Ni-free Co-Cr alloy using a laser welding technique tended to result in higher porosity and cracks, leading to a higher corrosion rate, compared to the soldered and as-cast groups. While more porosities were found in the soldered group than the as-cast group, the corrosion rate was comparable. The soldering technique therefore appears more attractive for joining Ni-free Co-Cr alloy because it provides better joint quality and corrosion resistance than the laser-welding technique.

Acknowledgements

The authors would like to acknowledge Department of Nuclear Technology, Chulalongkorn University, for their generous support in using microfocus x-ray. We are also grateful for a support from Chulalongkorn University granted to the Metallic Surface Coating Technology for Corrosion Protection (MCTC) Research Group under the Special Task Force for Activating Research Project (STAR) (G100STAR 55-006-62-001)

6. References

[1] R. Zupancic, A. Legat, N. Funduk, Tensile strength and corrosion resistance of brazed and laser-welded cobalt-chromium alloy joints, J Prosthet Dent. 96(2006) 273-282.

[2] V. Saji, H.C. Choe, Electrochemical behavior of Co-Cr and Ni-Cr dental cast alloys, Trans. Nonferrous Met. Soc. China. 19(2009) 785-790.

[3] J. Tambasco, T. Anthony, O. Sandven, Laser welding in the dental laboratory: An alternative to soldering, J Dent Technol (1996) 23-31.

[4] B. Cristina, G. Brandusa, B. Romeo, G. Otilia, Microscopic analyses of welding defects in RPD technology, TMJ. 60(2010) 23-28.

[5] D. NaBadalung, JI. Nicholls, Laser welding of a cobalt-chromium removable partial denture alloy, J Prosthet Dent. 79(1998) 285-290.

[6] N. Baba, I. Watanabe, J. Liu, M. Atsuta, Mechanical strength of laser-welded cobalt-chromium alloy. J Biomed Mater Res B Appl Biomater 69(2004) 121-124.

[7] S. Kurosu, N. Nomura, A. Chiba, Effect of sigma phase in Co-29Cr-6Mo alloy on corrosion behavior in saline solution, Materials Transactions. 47(2006) 1961-1964.

Advanced Materials Research Vol. 970 (2014) pp 97-101

doi:10.4028/www.scientific.net/AMR.970.97

Deposition of amorphous boron carbide films with pulsed magnetron sputtering and evaluation of their mechanical properties

K. Saito[1, a*], R. Fujii[1, b], N. Ohtake[1, c]

[1]Department of Mechanical Sciences and Engineering,

Tokyo Institute of Technology, 2-12-1 Ookayama, Meguro-ku, Tokyo 152-8552, Japan

[a*]saito.k.aq@m.titech.ac.jp, [b]fujii.r.ab@m.titech.ac.jp,

[c]ohtaken@mech.titech.ac.jp

Keywords: amorphous boron carbide, magnetron sputtering, pulsed power supply

Abstract. Amorphous boron carbide films were deposited with pulsed magnetron sputtering using a sintered B_4C target with Ar as the processing gas, and the chemical components, structure, and mechanical properties of the films were investigated. To deposit amorphous boron carbide films using a B_4C target, a pulsed power supply (14.4 kHz) was employed. Raman spectroscopy, Fourier transform infrared spectroscopy (FT-IR), and X-ray photoelectron spectroscopy (XPS) were used to characterize the chemical compositions and structure of the films. According to the results of XPS, the B/C ratio in the films synthesized with pulsed magnetron sputtering was 2.21. Nanoindentation tests and ball-on-disk (BoD) tests were performed to evaluate the mechanical properties. It was found that the films deposited by pulsed magnetron sputtering had an average hardness of 32.1 GPa and an average Young's modulus of 235.1 GPa.

Introduction

Boron carbide (B_4C) is the third hardest crystalline material at room temperature after diamond and cubic boron carbide (c-BN). Boron carbide has superior properties such as a low specific weight, high Young's modulus, high chemical and temperature stability, and high wear resistance [1]. Because of these properties, amorphous boron carbide (*a*-BC) films are considered to be a promising coating material for cutting tools, screws and other tools requiring high wear resistance.

a-BC films are synthesized with various methods such as plasma-enhanced chemical vapor deposition (CVD) [2], hot filament CVD [3], laser CVD [4], RF sputtering [5], and DC sputtering [6]. The temperature of CVD is usually high, which limits the selection of substrate materials, and films deposited by CVD contains hydrogen because gas such as CH_4 or B_2H_6 is used as source gas. Content of hydrogen in films leads to the decrease of hardness of films [7]. However sputtering does not have limitation of the selection of substrate materials [8] and films deposited with sputtering does not contain hydrogen. Furthermore, pulsed supply can enhance the plasma density when pulsed waves generates, which is contributed to deposition of high-density films.

In this study, *a*-BC films were deposited with pulsed magnetron sputtering using a sintered B_4C target. Moreover, after deposition of the films, the chemical composition, structure, and mechanical properties of the films were investigated.

Experimental details

Deposition of amorphous boron carbide films. *a*-BC films were deposited with pulsed magnetron sputtering using a sintered B_4C target. A pulsed power supply with a frequency of 14.4 kHz and a pulse width of approximately 75 μs was employed. Ar was used as the processing gas and the base pressure of the vacuum was 0.4 Pa. The total pressure and bias voltage were 0.8 Pa and -600 V, respectively. The thickness of the films was 1.2 μm. The films were synthesized on silicon (Si) substrates at room temperature. The substrates were cleaned by applying ultrasonic waves in pure water including a synthetic detergent (10 min, once), followed by in pure water (10 min, four times), in ethanol (10 min, twice), and in acetone (10 min, twice).

Evaluation of amorphous boron carbide films. To characterize the chemical structure of the *a*-BC films, Raman spectroscopy was performed. The chemical bonding and composition of the films were determined by Fourier transform infrared (FT-IR) spectroscopy and X-ray Photoelectron Spectroscopy (XPS).

The hardness of the deposited films was measured using a nanoindenter. A Vickers indenter tip (a pyramidal diamond) was used and the Young's modulus and hardness were measured as a function of the indentation depth.

The friction and wear properties of the *a*-BC films were evaluated by performing sliding tests using a rotational ball-on-disk (BoD) apparatus. Mirror-polished ASTM 52100 balls of 6.0 mm diameter were chosen as the counterpart material for the experiments. The specimen was mounted on a rotational table, and an ASTM 52100 was made to slide against the film deposited on a Si substrate with no additional lubrication. The friction coefficient was calculated from the normal load and the frictional force measured by a load cell. Friction tests were performed at room temperature in laboratory air of about 40-70% relative humidity. A sliding speed of 0.209 m/s and a normal load of 0.5-1.0 N were used.

Results and discussion

XPS. The chemical bonding and compositions of the films were analyzed by XPS with an Al Kα X-ray source. The XPS spectrum over a wide energy range is shown in Fig. 1. Figure 2 shows the result of peak fitting of the C1s spectrum. Before performing XPS analysis, the *a*-BC films were irradiated with an Ar laser to remove the effect of oxide films on their surface. The peaks at 282.3 eV and 283.1 eV were associated with C-B bonding and C=C bonding, respectively. According to the result of XPS analysis, the B/C ratio in the films was 2.21, which was smaller than that in the sputtering target (B_4C).

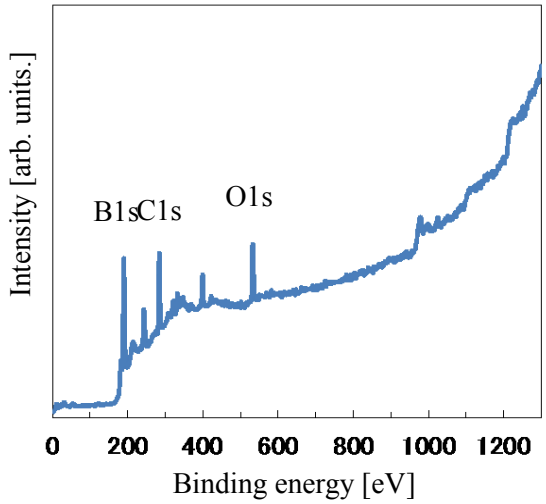

Figure 1. XPS spectrum (wide energy range)

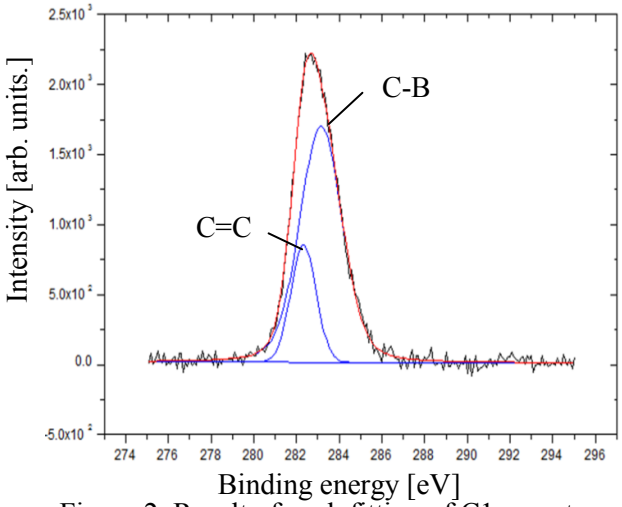

Figure 2. Result of peak fitting of C1s spectrum

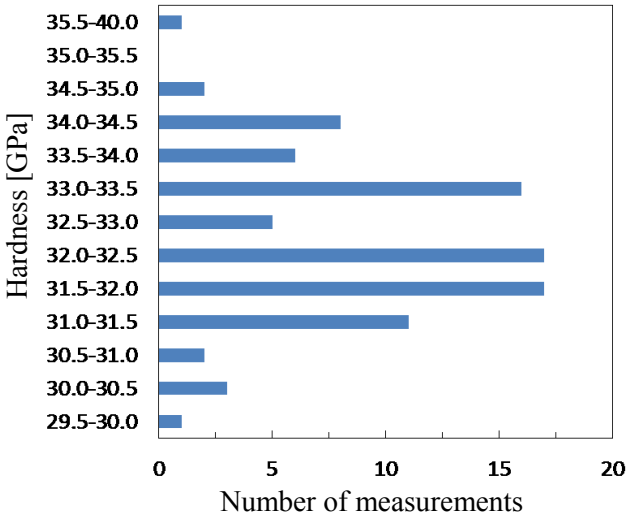

Figure 3. Hardness distribution of *a*-BC films

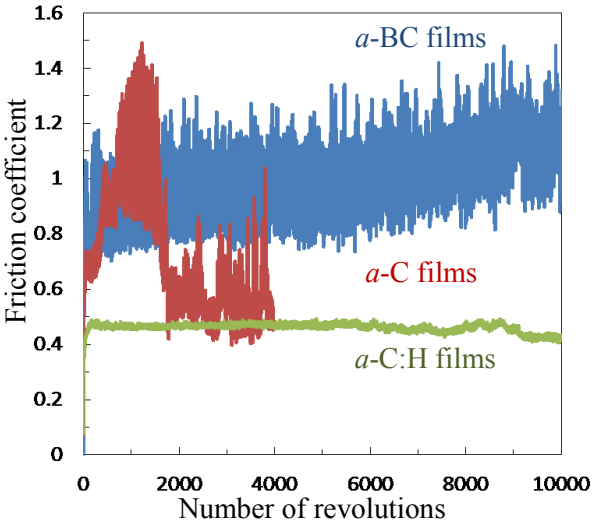

Figure 4. Friction coefficients of *a*-BC, *a*-C, and *a*-C:H films

Hardness. The hardness of the *a*-BC films was measured using a nanoindenter. Figure 3 shows the hardness distribution of the films. The number of measurements was 100 and the indentation load was set so that the indentation depth was no more than 10% of the thickness of the films to remove the effect of the substrate. The indentation load and indentation depth were 2.0 mN and approximately 100 nm, respectively. It was found that the deposited films had an average hardness of 32.1 GPa and an average Young's modulus of 235.1 GPa.

Ball-on-disk tests. The tribological properties of the *a*-BC films were evaluated by BoD tests. The wear resistance of the films was determined through the measurement of the wear track profile obtained by an optical microscope. The cross-sectional area of wear track was determined using the profile obtained by the optical microscope and the volume of wear was calculated by multiplying the length of the wear track by its cross-sectional area. The specific wear rate was also calculated by dividing the volume of wear by the normal load and sliding distance.

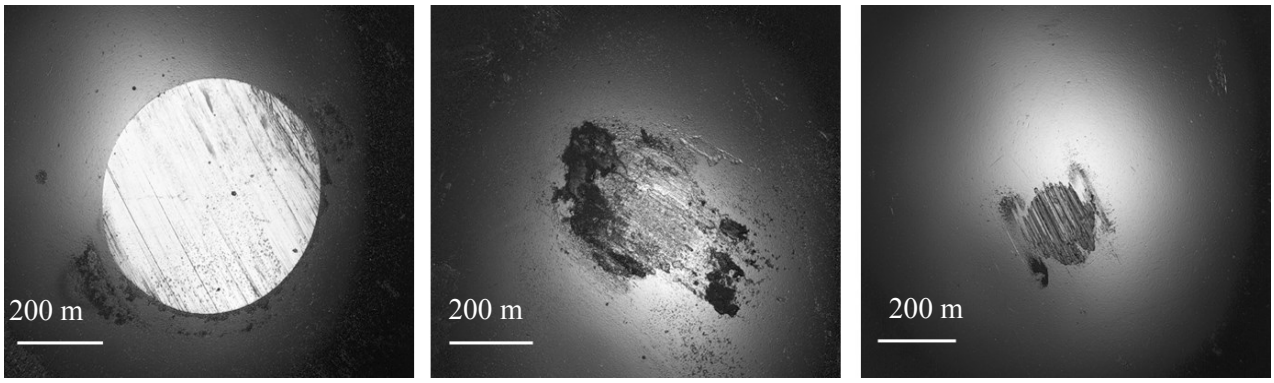

(a) *a*-BC films (b) *a*-C films (c) a-C:H films

Figure 5. Wear track of SUJ2 balls against *a*-BC, *a*-C and *a*-C:H films

For comparison, nonhydrogenated amorphous carbon (*a*-C) films deposited with pulsed magnetron sputtering using a sintered graphite target and hydrogenated amorphous carbon (*a*-C:H) films synthesized with pulsed CVD using acetylene gas were prepared. Figure 4 shows the friction coefficients of the *a*-BC films, the *a*-C films, and the *a*-C:H films as a function of the number of revolutions. From the result of the BoD tests, the friction coefficient of the *a*-BC films was 0.8-1.2, which was very high compared with that of the *a*-C:H films (approximately 0.4). Whereas, the *a*-C films deposited with the same method as the *a*-BC films were delaminated or worn out in a short time. The *a*-BC films exhibited lower wear resistance than the *a*-C:H films, and the specific wear rates of the *a*-BC and *a*-C:H films were approximately 3.4×10^{-5} mm^3/Nm and 2.5×10^{-7} mm^3/Nm, respectively.

Optical micrographs of the wear tracks of ASTM 52100 balls after the BoD tests are shown in Figure 5. It was observed that there was a transferred layer on the wear track of the ball against the *a*-C films and the *a*-C:H films, whereas almost no transferred layer was observed on the wear track of the ball used with the *a*-BC films. Furthermore, the area of the wear track of the ball against the *a*-BC films was larger than that for the other films. This result indicates the *a*-BC films deposited with a pulsed power supply are highly abrasive in the case of sliding against other materials.

Conclusion

a-BC films were fabricated on Si substrates with pulsed magnetron sputtering using a sintered B_4C target and were investigated to characterize the chemical bonding and composition and to evaluate their mechanical properties. XPS spectra of the films showed that B-C bonds were formed in the films and that the B/C ratio of the films was 2.21. According to the results of hardness measurements, the films deposited by pulsed magnetron sputtering had an average hardness of 32.1 GPa and an average Young's modulus of 235.1 GPa. Tribological properties were evaluated by BoD tests, and the *a*-BC films were found to have a high friction coefficient and to be highly abrasive in the case of sliding against other materials.

Acknowledgement

This work was supported by JSPS KAKENHI Grant Number 25289259.

References

[1] T. Hu, L. Steihl, W. Rafaniello, T. Fawcett, D.D. Hawn, J.G. Mashall, S.J. Rozeveld, C.L. Putzig, J. Blackson, W. Cernigiani, M.G. Robinson. Thin Solid Films 332 (1998) 80

[2] S. Lee, J. Mazurowski, W.L. O'Brien, Q.Y. Dong, J.J. Jia, T.A. Callcott, Y. Tan, K.E. Miyano, D.L. Ederer, D.R. Mueller, P.A. Dowben. J. Appl. Phys. 6919 (1993) 74

[3] P. Chaudhari, A. Singh, A. Topka, R. Dusane. Solid-State Electronics 78 (2012) 156-158

[4] J.C. Oliveira, O. Conde. Thin Solid Films 307 (1997) 2

[5] E. Vassallo, R. Caniello, A. Cremona, G. Croci, D. Dellasega, G. Gorini, G. Grosso, E. Miorin, M. Passoni, M. Tardocchi. Surface & Coatings Technology 214 (2013)59-62

[6] V. Kulikovsky, V. Vorlicek, R. Ctvrtlik, P. Bohac, L. Jastrabik, H. Lapsanska. Surface & Coatings Technology 205 (2011) 4052-4057

[7] K. Holmberg, A. Matthews, Coatings Tribology, 2nd Edition Properties, Mechanisms, Techniques and Applications in Surface Engineering (2009) pp. 267-269

[8] Z. Han, G. Li, J. Tian, M. Gu. Material Leteers 57 (2002) 899

Advanced Materials Research Vol. 970 (2014) pp 102-105

doi:10.4028/www.scientific.net/AMR.970.102

Fabrication and Characterization of RF Magnetron Sputtered Silicon Oxide Films

Jian-Wei Hoon[1], Kah-Yoong Chan[1*] and Cheng-Yang Low[1]

[1]Centre for Advance Devices and Systems, Multimedia University, Persiaran Multimedia, 63100 Cyberjaya, Selangor, Malaysia

[1*]kychan@mmu.edu.my

Keywords: Silicon oxide; Magnetron sputtering.

Abstract. In this work, silicon dioxide (SiO_2) films were fabricated on indium tin oxide (ITO) coated glass substrates by radio frequency (RF) magnetron sputtering deposition technique. The deposition rate of the magnetron sputtered SiO_2 films was investigated. The SiO_2 films were characterized with the atomic force microscopy (AFM) for their surface topology. In addition, the electrical insulating strength of the magnetron sputtered SiO_2 was examined.

Introduction

Thin-film transistors (TFTs) are the key element in large area electronic display applications. In TFTs, silicon dioxide (SiO_2) is often used as gate dielectric material [1]. Wide range of deposition techniques have been carried out to prepare the SiO_2 dielectric films in TFTs. These include plasma enhanced chemical vapor deposition (PECVD) technique and magnetron sputtering technique. The PECVD technique is deemed suitable for depositing SiO_2 films for thin film silicon based TFTs [2], while the magnetron sputtering technique is considered appropriate for depositing SiO_2 films for transparent TFTs [3].

In this work, magnetron sputtering deposition technique was employed to deposit the SiO_2 films on indium tin oxide (ITO) coated glass substrates. The advantages of the magnetron sputtering deposition technique are low temperature processing as well as good films uniformity [4]. Due to the insulating nature of the SiO_2, radio frequency (RF) magnetron sputtering technique was chosen instead of direct current (DC) sputtering technique [5]. The deposition rate, surface topology, and the electrical insulating properties of the SiO_2 films were investigated using Mahr surface profilometer, atomic force microscopy (AFM), and current-voltage (I-V) measurement techniques.

Experimental

A 100 ohm/sq ITO coated glass substrate was cut into the pieces with size of 12 mm x 6 mm x 1 mm. Initially, SiO_2 films were sputtered on the ITO-glass using RF magnetron sputtering techniques. The SiO_2 target (99.995-%, 0.125-in.) was installed at the cathode side in the vacuum chamber. For RF magnetron sputtering process, input power of 100 W was applied. Prior to the sputtering process, the base pressure was maintained 10^{-6} Torr. Argon (Ar) gas was maintained at 22 sccm. In addition, deposition pressure of 7 mTorr was used throughout the whole deposition process of the SiO_2 films. The deposition temperature was maintained at room temperature. The deposition duration was varied from 1 hour to 2 hours 30 min. The silver (Ag) electrode with electrode area of 1 mm^2 and 300 nm thick was deposited using DC magnetron sputtering technique on the SiO_2 films. The cross-sectional top view of the structure for dielectric layer investigation is shown in Figure. 1.

The thickness of the dielectric layer was measured by a Mahr stylus profilometer. A tapping mode AFM was employed to scan the surface topology of the SiO_2 films. The I-V measurements were performed using Keithley 236 Source Measure Unit (SMU) by sweeping voltage from -30 V to +30 V and measuring the current.

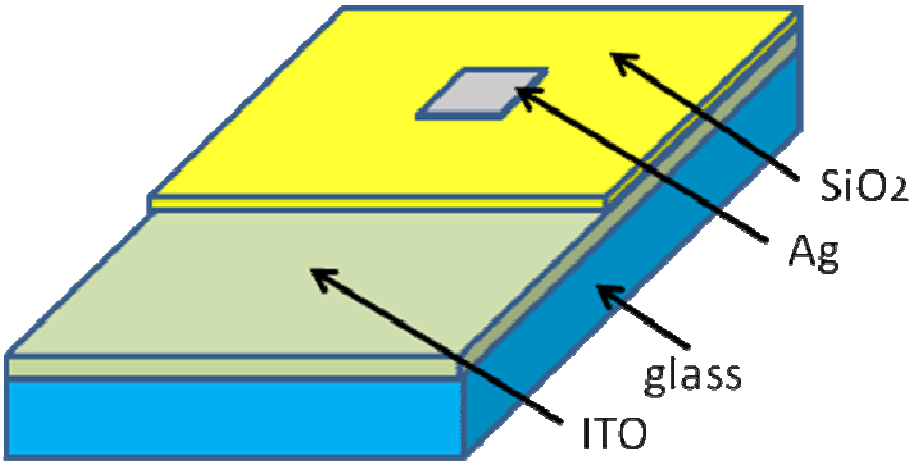

Figure 1. Cross-sectional top view of the structure for SiO_2 electrical measurements.

Results and discussion

Figure. 2 shows the film thickness of the SiO_2 as a function of the RF magnetron sputtering deposition duration. The thickness of the SiO_2 films increases from 160 to 475 nm with increasing deposition duration from 1 hour to 2 hours 30 min. The extracted deposition rate is more than 3.4 nm/min for the RF magnetron sputtered SiO_2 films.

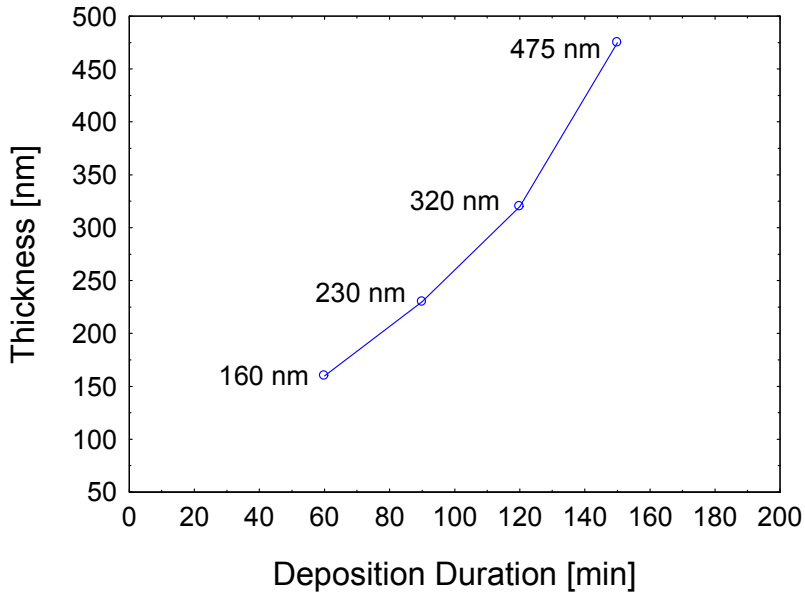

Figure 2. The SiO_2 film thickness as a function of magnetron sputtering deposition duration.

Apart from deposition rate, the study of surface topology is important because it will affect the characteristics of the SiO_2 films. The 1 µm x 1 µm AFM images of the SiO_2 films deposited with 160 and 475 nm are shown in Figure. 3. For SiO_2 films deposited with thickness of 160 nm, the lateral feature size and the root mean square (RMS) area roughness extracted from the AFM image are 98 nm and 3.65 nm, respectively. It is noticeable that grains appear in granular form in the SiO_2. When film thickness increases from 160 to 475 nm, the lateral feature size and the RMS area roughness are 250 nm and 4.66 nm, respectively. For the thicker film, the grains appear larger as shown in Figure. 3(b). The grains increase with increasing thickness is due to aggregation of atoms at the crystallite sides [6].

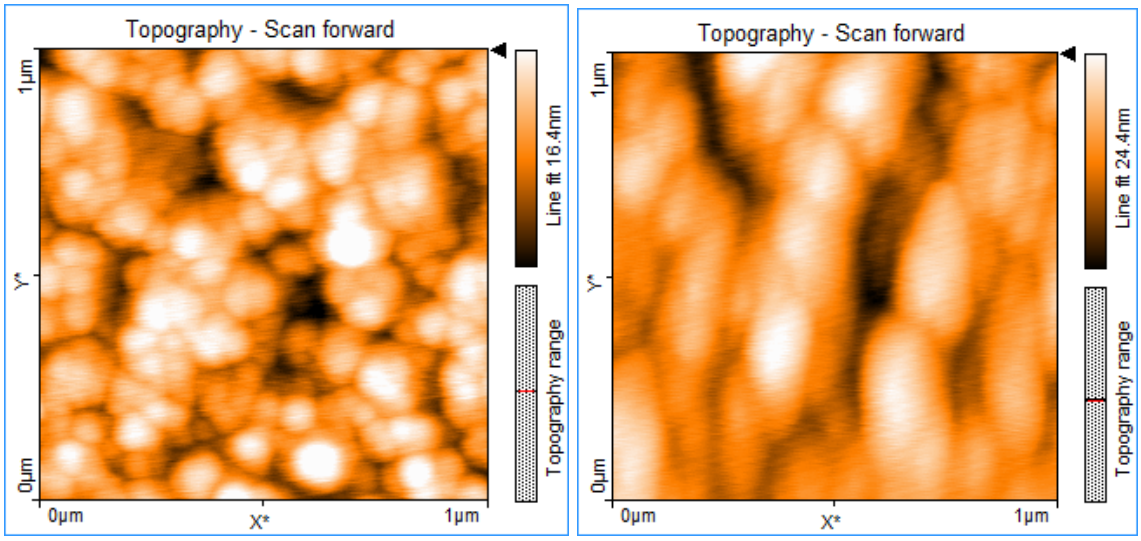

(a) (b)

Figure 3. AFM images of the SiO_2 films with thicknesses of (a) 160 nm and (b) 475 nm.

The I-V plots of the SiO_2 films are shown in Figure. 4 with measurement voltages ranging from -30 V to 30 V. The current measured between the underlying ITO and the top Ag electrode for the SiO_2 layer is plotted. The SiO_2 films can sustain up to 10 V before an increase in the leakage current.

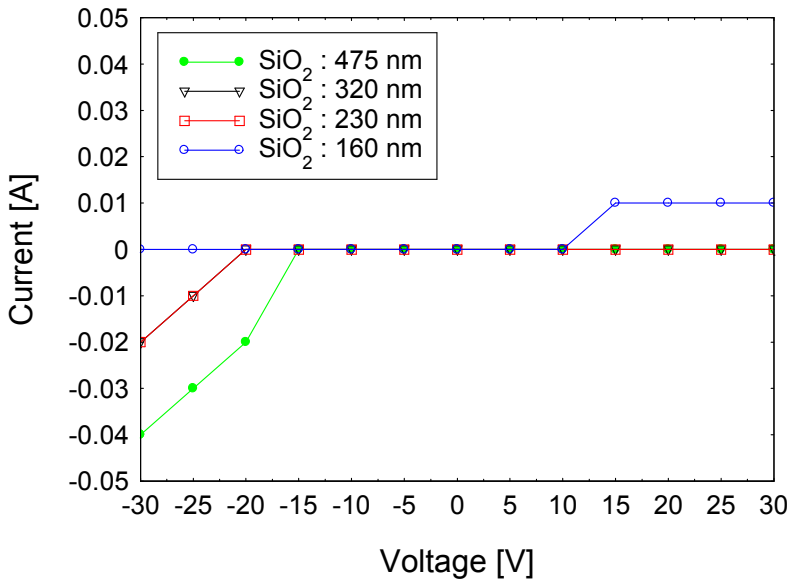

Figure 4. I-V measurements of the SiO_2 with different thicknesses.

Conclusion

In this paper, SiO_2 films ranging from 160 nm to 475 nm have been fabricated using RF magnetron sputtering deposition technique. The deposition rate achieved was more than 3 nm/min and the films exhibit RMS roughness of lower than 5 nm. The I-V measurements reveal that the SiO_2 films can sustain up to 15 V before an increase in the leakage current.

Acknowledgements

The authors would like to acknowledge the financial supports from the TM R&D (Project No.: RDTC/100763). The authors are also very thankful to the Faculty of Engineering of Multimedia University for facilitating this research project.

References

[1] S.-K. Rha, T.P. Chou, G.Z. Cao, Y.-S. Lee, W.-J. Lee, Characteristics of silicon oxide thin films prepared by sol electrophoretic deposition method using tetraethylorthosilicate as the precursor, Current Applied Physics, 9 (2009) 551–555.

[2] Z. Ye and M. Wong, Characteristics of plasma-fluorinated zinc oxide thin-film transistors, IEEE Electron Device Letters, 33 (8) (2012) 1147-1149.

[3] S.-H. Jeong, J.-K. Kim, B.-S. Kim, S.-H. Shim, and B.-T. Lee, Characterization of SiO_2 and TiO_2 films prepared using rf magnetron sputtering and their application to anti-reflection coating, Vacuum, 76 (2004) 507–515.

[4] K.S. Kim, H.W. Kim, and N.H. Kim, Structural characterization of ZnO films grown on SiO_2 by the RF magnetron sputtering, Physica B 334 (2003) 343–346.

[5] International Marketing and Emerging Technologies, Advances in RF sputtering, information on http://www.aultimut.com/technologies-2/plasma-processes/advances-in-rf-sputtering/ accessed on 22 September 2013.

[6] F. Elsholz, E. Schöll, C. Scharfenorth, G. Seewald, H.J. Eichler, and A. Rosenfeld, Roughness evolution in thin film growth of SiO_2 and Nb_2O_5, Journal of Applied Physics, 98 (2005)103516.

Advanced Materials Research Vol. 970 (2014) pp 106-110

doi:10.4028/www.scientific.net/AMR.970.106

FABRICATION METHOD OF MEMS BASED CLAMPED-CLAMPED RESONANT MAGNETOMETER

Omid Tayefeh Ghalehbeygi[1,a], Levent Trabzon[2,b*], Laurent Francis[3,c], Huseyin Kizil[4,d]

[1]Istanbul Technical University, Department of Electronics & Telecommunications Maslak, Istanbul, 34469, Turkey

[2]Istanbul Technical University, Department of Mechanical Engineering, Gumussuyu, Istanbul 34437, Turkey

[3]Universite Catholique de louvain, B-1348 Louvain-la-Neuve, Belgium

[4]Istanbul Technical University, Department of Metallurgical and Materials Engineering, Maslak, Istanbul, 34469, Turkey

[a] omid.tayefeh@gmail.com, [b*] levent.trabzon@itu.edu.tr,
[c] laurent.francis@uclouvain.be, [d] kizilh@itu.edu.tr

Keywords: Resonant Magnetometer, Lorentz force, MEMS.

Abstract. In this paper we present fabrication steps for manufacturing MEMS based magnetometer which is actuated by Lorentz force in the middle point of beam which has been fixed from both two edges (Clamped - Clamped). We utilized two different process sequences in order to fabricate microsystems properly. The structures were first fabricated on bulk Si-wafer and the fabrication of these sensors was characterized by built in stress in the beam and etching methods in the processes. The second approach was performed on SOI Si-wafer. Two fabrication routes are compared in terms of working MEMS structures. The microstructures are manufactured successfully by a process sequence based on SOI-Si wafer.

Introduction

In recent decades, MEMS devices have evolved several branches of science and industry, pressure sensors, magnetometers, switches [1, 2]. Magnetometers are sensors that are used in various environments and products of Industries and those of many are fabricated in microscale by Micro Electro Mechanical Systems (MEMS) technology and then they are packed into small dimensions, as well as integrate the mechanical and electronic components on a single chip [3-5]. Therefore, this technology allows to be embedded in portable devices such as cell phone and digital watches. These sensors offer a variety of contactless sensing for measuring magnetic fields have the unique ability to reveal realities that cannot be perceived by the human senses [6]. For using these sensors, it is important to fabricate resonators with very high mechanical quality factors (Q), where this parameter is proportional to the ratio of the stored energy to the total dissipated energy per cycle of vibration [7]. A low value of quality factor implies greater dissipation of energy and results in reduced sensitivity and increased power consumption. For improvement of quality factor the reasons, which interfere with that, should be verified. Due to geological effects on Earth's magnetic field, the performance limit of the future magnetic field sensors will be the variations. In this paper, fabrication processes of resonant magnetic field sensors based on MEMS technology by exploiting Lorentz force, has been proposed.

In this paper, we studied manufacturing steps for micro-resonator magnetometer structures. Structure layers of microsystems were Poly-Si (Si-Wafer) and epitaxial-Si (SOI-wafer) and there different masks were utilized to complete the fabrication. Due to built-in stress formation in the doping process, Poly-Si as a structural layer was not used, instead SOI-Si wafer was used to obtain working microstructures.

Fabrication Details

Authors studied two alternatives in fabrication of magnetometer. In the first approach, fine grain Poly-Si was utilized as active layer of microstructure. The Poly-Si was deposited on a sacrificial oxide with (100) Si wafer since this is less expensive fabrication scheme with respect to the second approach, i.e. use of SOI-wafer. Each step of microstructure fabrication was evaluated in details in order to obtain working MEMS structures. We utilized three different masks for SOI-based technology as follow; POLY, METALPAD, and CAVITY. The same masks were used in the case of Poly-Si on Si-wafer case except for CAVITY one. Finally, SOI wafer was exploited for producing these sensors due to the reasons which will be mentioned next chapter. Schematically, all of the processes in manufacturing SOI wafer are shown in figure 1.

Bulk Si-Wafer. Silicon dioxide, SiO2, was used in the fabrication of microsystems for being sacrificial layer. The Si-wafer is oxidized by wet oxidation for three and half hours at 1000˚C. The oxide thickness is nominally 400nm. Poly-Si was chemical-vapor deposited by the silane (SiH4) decomposition reaction at 630˚C and 400mTorr. The deposition temperature is about 10nm/min. and size of grains nominally is 80nm. The Poly-Si film was also doped by using solid P2O5 source at 900˚ C with placement of phosphorous oxide wafers and silicon wafers in alternating positions in a wafer boat. Dopants arrive on the wafer from the gas phase, and dopant supply is practically infinite. We run the doping process for 30min. and high doping levels of $10^{21}cm^{-3}$ results in polysilicon resistivity of 500µohm-cm. Electron mobility in polysilicon is an order of magnitude less than in single crystalline materials, 10 to 50 cm^2/Vs.

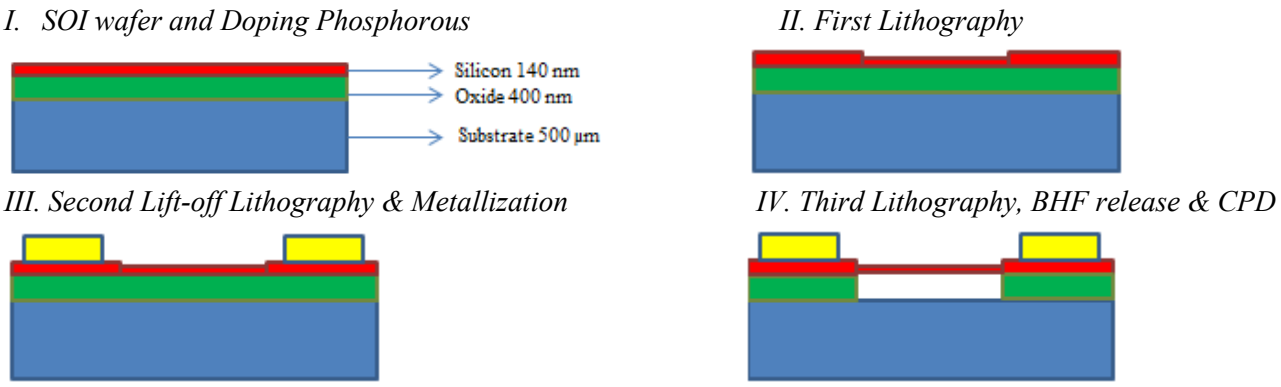

Figure 1: *The process flow of microstructures for SOI-Wafer (Process-B)*

This is doping dependent, and strongly dependent on deposition and annealing cycles. We used two different approaches in optical lithography, the first one is for the case without lift-off process and the other one is with lift-off one. The wafer was exposed to UV light for 2 sec. and then it was baked at 120˚ C for one and half minutes so that the lift-off process was run on the wafer. During this step, metal layer was completely deposited Si-wafer with identical thickness everywhere and followed by resist dissolution in solvent. Metal layers, not in contact with the former layer, were removed in the lift-off process. In our case, we used Al, Aluminum, for conducting layer with a thickness of 600nm, and contact layer for low resistivity layer, which is doped Poly-Si. HNO3 Fuming acid was used for dissolving photoresist with sonic vibrator. However, since metal deposition is conformal on surface in some structures those of them did not have any metal contact left after lift-off process. The thermal oxide etching was achieved by pure HF for 1 min with an etching rate of 1.5–2µm/min. In the drying process of microstructures, critical point dryer was used so that structures were not exposed to permanent deformation. Since, surface tension is much more lowered in the case of CO_2 use than use of Isopropyl Alcohol (IPA). The critical point of CO_2 was set to 35˚C with 1200 psi, and then drying processes in releasing of microstructures were obtained without any damage.

SOI Wafer. The SOI-wafer consists of three layers of single crystalline Si with thickness of 140nm at the top, Silicon-Oxide with thickness of 400nm, and Si-wafer s with thickness of 500µm. As it is seen from SOI wafer we do not need any more thermal oxidation and deposition part where was discussed in previous section. On the other hand, other steps of processing were implemented with minor differences. SOI wafer process was started from doping phosphorous to increase conductivity of silicon layer and it was held in the furnace for 60 min, instead. The major difference between process flow of the bulk silicon and SOI wafer is using the third mask in the releasing step. Due to the high etch rate of HF, etching control is a little bit difficult, so that BHF (Buffered HF) is other etch-solution of oxide with lower etching rate. Nevertheless, BHF is also etching Al, thus. It is avoided by using a third mask, CAVITY, in the case of SOI-process. The CAVITY mask is a dark mask and whole of structures are covered by photoresist except for beam or membrane areas.

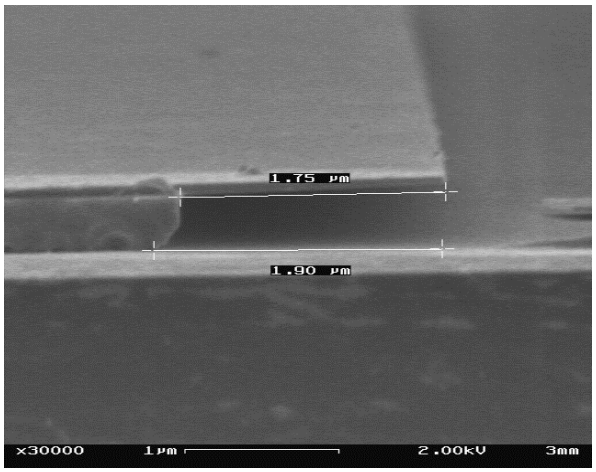

Figure 2: *Etching silicon oxide with BHF solvent for 23 min in SOI Process case.*

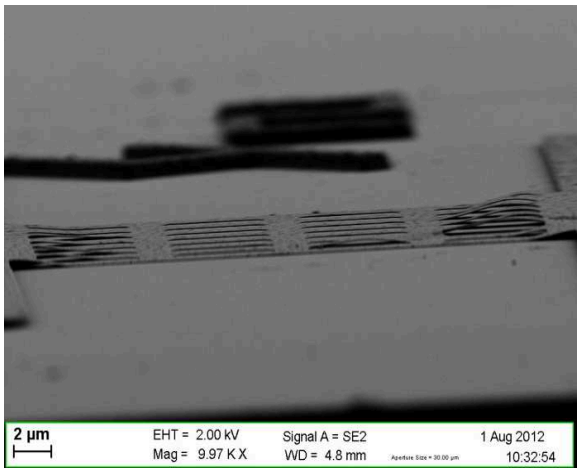

Figure 3: *Buckling of suspended polysilicon layer after etching (Process-A).*

We used mixture of NH4 40% : HF 49% (7 : 1) BHF for our experiments and we empirically calculated etching rate around 60nm - 65nm per minute for thermal oxidation of SOI wafer. After immersing sample in BHF for 23 min. the profile under etch was revealed as shown in the figure 2. As it is observed, there is a taper shape at anchor region. The upper side has been etched 1.75µm and lower 1.90µm that is acceptable. Because we design each perforation in membrane with maximum 2µm distance from each other and etching each one of them from both sides with this rate. Thus, it is assured there is no any silicon oxide left under any membrane.

Results and Discussion

As mentioned in the previous part, P-doping is a necessary step in the sequence of fabrication of microsystem. There is stress formation during P-doping and such a built-in stress must be measured and eliminated. The built-in stress, σ_f, in doping is calculated by measuring the curvature radius of polysilicon or silicon layer with use of following formula (equation 1),

$$\sigma_f = -\frac{1}{6}\frac{E_s}{1-v_s}\frac{h_s^2}{h_f}\left(\frac{1}{R}-\frac{1}{R_0}\right) \qquad (1)$$

Where R_0 and R are the curvature radius of the substrate before and after deposition of the film, respectively; *Es*, *vs* and *hs* are the Young's modulus, Poisson ratio, and thickness of the substrate, respectively, and *hf* is the thickness of the film.

For Poly-Si wafer (Process-A), R_0 = 34.41m and R = 29.07m and for SOI-wafer (Process-B) R_0 = 91.31m and R = 93.12m were measured, which mean -3.77 × 10^8 Pa and 3.42 × 10^7 Pa respectively. As it is calculated, the sign of the σ_f became negative and positive in Poly-Si and SOI-Si respectively. It means that built-in stress due to P-doping in Poly-Si is compressive and tensile in the case of SOI-Si. The vibration frequency of the beam is decreased with the compressive stresses as well as there would be complete collapse of the beam after release step as seen in figure 3.

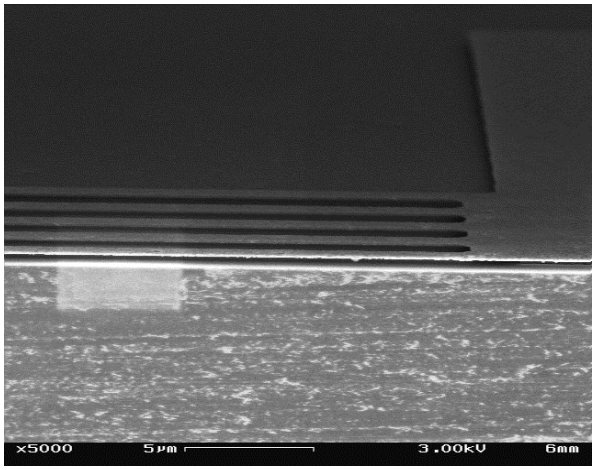

Figure 4: *Cross section of beam from SOI wafer (Process-B) after drying process.*

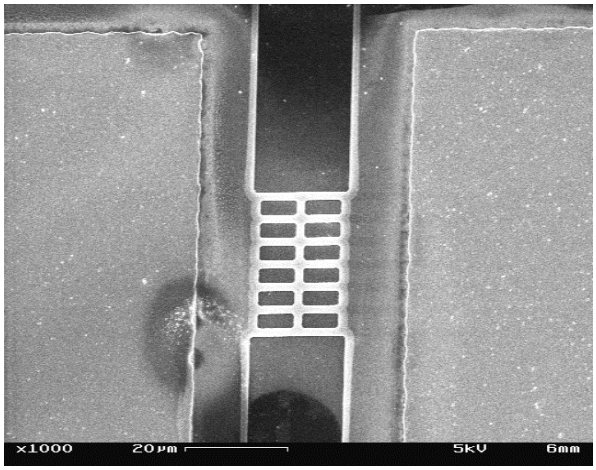

Figure 5: *White shadow indicates existence of photoresist on the microstructures.*

On the other hand, there is tensile stress in the beams of process-B and natural frequency will be shifted to upper frequency with possible buckling again in the opposite direction. But, built-in stress in the beams of process-B is not high enough to cause any permanent changes of beam geometry, as shown in figure 4.

Another challenge in process-B is to remove remaining photoresist form the surface after even after CPD step. If not properly removed, figure 5 presents remnants of resist material on the microstructures. As known, it is not possible to use liquid medium to remove any remaining resist on the surface due to possible sticking problem in the beams. Thus, O_2-plasma was utilized to clean the surface from resist material, however many of long microsystems were damaged due to plasma environment in the chamber. Therefore we tried to remove it during BHF process. After BHF and rinsing sample with DI water, wafers were put it in acetone to remove photoresist and then put them in methanol and thus to make ready to dry it with CPD. Nevertheless, after CPD, there were black or circular areas around microstructures during the CPD as seen figure 6. The use of methanol in cleaning step is to be cause for the observation due to its remaining on surface after rinsing with IPA. Hereby, the use methanol is removed after acetone in the cleaning step of BHF process, the microstructures were fabricated successfully, as seen in figure 7.

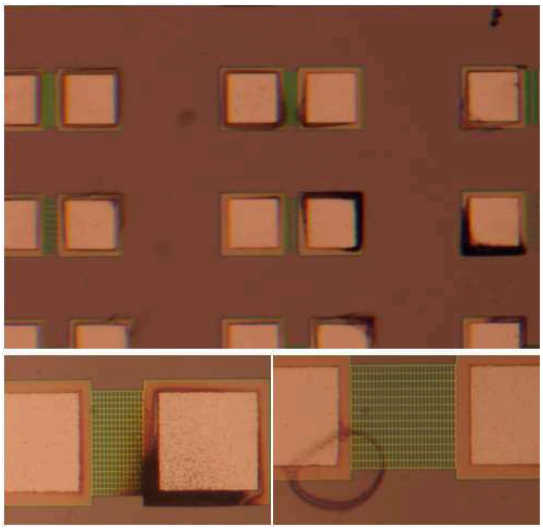

Figure 6: *Burned microstructures after CPD with methanol use (Process-B).*

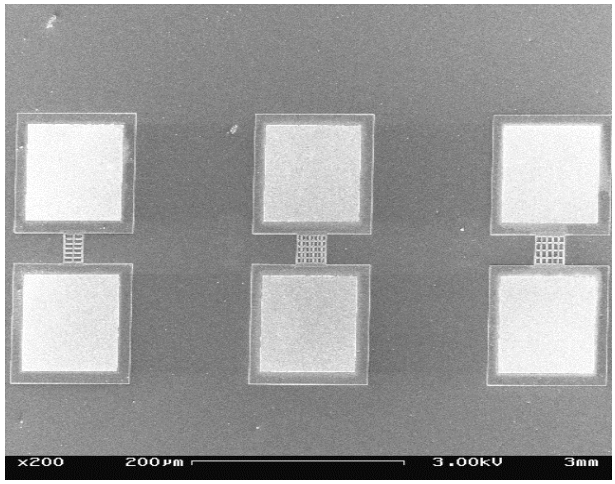

Figure 7: *Working microstructures after CPD without methanol use (Process-B).*

Conclusion

In this work, we tried to fabricate micro-beams for resonant magnetometer sensor; two different fabrication schemes were compared to each other. Due to high level of compressive built-in stress formation, Poly-Si case is not utilized to fabricate working microstructures. On the other hand, SOI-Si gives us a successful alternative way of fabricating suspended microstructures. Micro-bridges and cantilevers were obtained in SOI-Si case by modifying cleaning process and etching regime of different layers of materials.

References

[1] B. Bahreyni and C. Shafai, "A resonant micromachined magnetic field sensor," *Sensors Journal, IEEE,* vol. 7, pp. 1326-1334, 2007.

[2] A. Boé, A. Safi, M. Coulombier, T. Pardoen, and J.-P. Raskin, "Internal stress relaxation based method for elastic stiffness characterization of very thin films," *Thin Solid Films,* vol. 518, pp. 260-264, 2009.

[3] M. J. Thompson and D. A. Horsley, "Parametrically amplified MEMS magnetometer," in *Solid-State Sensors, Actuators and Microsystems Conference, 2009. TRANSDUCERS 2009. International*, 2009, pp. 1194-1197.

[4] M. J. Thompson and D. A. Horsley, "Parametrically Amplified Z-Axis Lorentz Force Magnetometer," *Microelectromechanical Systems, Journal of,* vol. 20, pp. 702-710, 2011.

[5] H. Xie, H. Sun, K. Jia, D. Fang, and H. Qu, "Multi-axis integrated CMOS-MEMS inertial sensors," in *Solid-State and Integrated Circuit Technology (ICSICT), 2010 10th IEEE International Conference on*, 2010, pp. 1394-1395.

[6] D. Ren, L. Wu, M. Yan, M. Cui, Z. You, and M. Hu, "Design and analyses of a MEMS based resonant magnetometer," *Sensors,* vol. 9, pp. 6951-6966, 2009.

[7] D. Antonio and D. Lopez, "Micromechanical magnetometers based on clamped-clamped high-Q nonlinear resonators," in *Solid-State Sensors, Actuators and Microsystems Conference (TRANSDUCERS), 2011 16th International*, 2011, pp. 2851-2854.

Advanced Materials Research Vol. 970 (2014) pp 111-114

doi:10.4028/www.scientific.net/AMR.970.111

Humidity Sensors on Thermally Oxidized Silicon Substrates

Cheng-Yang Low, Kah-Yoong Chan[a*], Zi-Neng Ng,
Jian-Wei Hoon and Wai-Leong Pang

Centre for Advanced Devices and Systems, Faculty of Engineering,

Multimedia University, Persiaran Multimedia, 63100 Cyberjaya, Selangor, Malaysia.

[a]kychan@mmu.edu.my

Keywords: ZnO, humidity sensors, thermally oxidized silicon substrates

Abstract
In recent years, as a ceramic semiconducting material, zinc oxide (ZnO) has received great attention in sensing applications, including ultra-violet (UV), gas, and humidity sensors. In this work, ZnO based humidity sensors were fabricated on thermally oxidized silicon substrates. The contact electrodes for the sensors were realized using patterned aluminium (Al) films. ZnO films were deposited on the substrates as the active layer for the sensors using radio frequency (RF) magnetron sputtering technique. The electrical properties of the sensors were tested in various relative humidity (RH) levels. The ZnO humidity sensors have showed a decrease in resistance with increasing humidity level. The fabrication process and the characteristics of the ZnO humidity sensors will be revealed in this work.

Introduction

The implementation of humidity sensors is crucial in medicine, food processing, storage, and manufacturing sectors in providing suitable environment moisture levels. Humidity sensors can be fabricated using various materials such as ceramics [1], semiconductors [2], and polymers [3]. Zinc oxide (ZnO) is a promising material owing to its n-type semiconducting behaviour, low cost, and being abundant. Oxygen vacancies which are available on the surface of ZnO may exhibit high degree in sensitivity towards the humidity in environment [4]. Various fabrication techniques have been developed in synthesizing ZnO humidity sensors, such as sol-gel method [5], magnetron sputtering [6], and chemical vapour deposition [7]. Among these techniques, magnetron sputtering is dominantly used in the industry due to its significant competitiveness in producing films with uniform thickness and conformal coverage [8].

In this study, radio frequency (RF) magnetron sputtering technique was employed to deposit aluminium (Al) electrodes and ZnO films as the active material for the humidity sensors on thermally oxidized silicon substrates. Using a customized enclosed chamber, the variation of the electrical resistance under different relative humidity levels was investigated.

Experimental

Sensor Preparation

The oxidized silicon samples were initially pre-cleaned using isopropanol and acetone. Next, aluminium (Al) films with 300nm in thickness were patterned on the silicon substrates to form interdigitated electrodes for the sensors, as shown in Figure 1a. ZnO target with 2 inches in diameter and 99.99% in purity were then sputtered into a 200nm thick film on the substrates as active sensing material for the sensors. The deposition pressure, sputtering power and substrate temperature were 7mTorr, 100 watt and 250˚C, respectively. Prior to measurement, the sensors were annealed in a vacuum furnace at 200˚C for 30 minutes. The snapshot of the resultant humidity sensor is shown in Figure 1b.

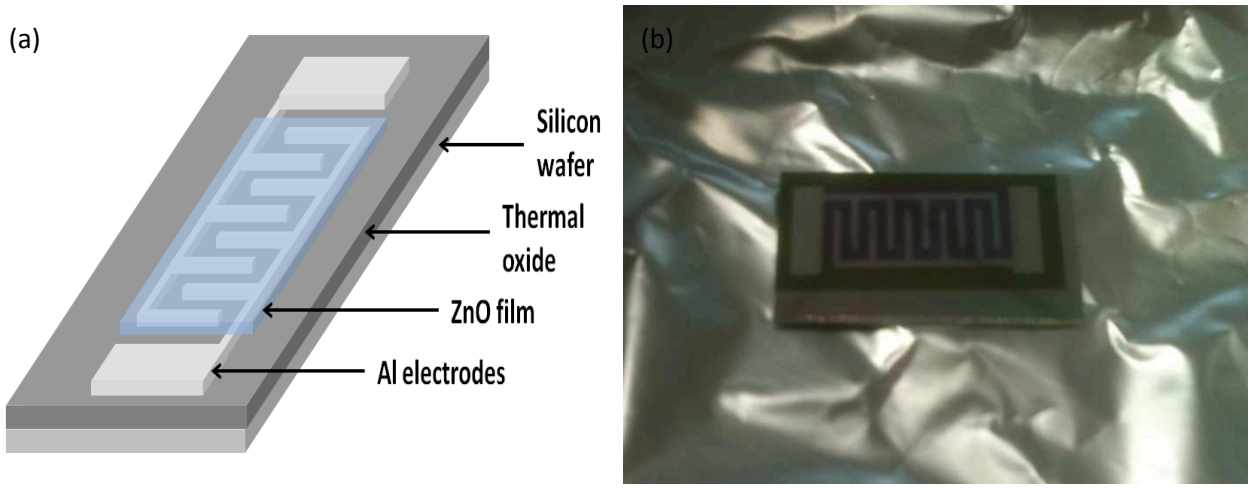

Figure 1: a) Schematic cross-sectional top view of the sensor. b) Snapshot of the sensor.

Humidity Measurement Setup

Figure 2 shows the customized chamber for humidity sensing measurement. The enclosed chamber contains a stage with measurement probes, a hygrometer, a dehumidifier, and a fan. A multimeter and an ultrasonic humidifier were connected from the outside the chamber. The hygrometer was employed to detect the changes in relative humidity, while the fan was used to promote the air ventilation and uniformity of humidity level within the chamber. The ultrasonic humidifier was used to deliver moisture vapour into the enclosure to increase the humidity without changing the temperature, whereas the dehumidifier which contained silica gels was used to absorb moisture vapour within the chamber, decreasing the humidity. Al electrodes of the sensors were connected to probes of the multimeter. Electrical resistance was recorded when the moisture level was varied from 30% to 90% relative humidity (RH) under room temperature. RH is a measure of the moisture density in the air with relative to the maximum quantity of moisture the air can hold at prescribed temperature.

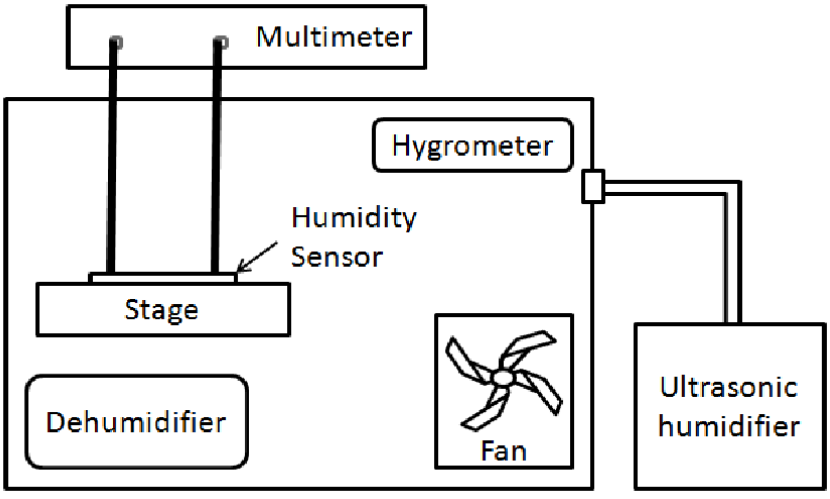

Figure 2: Customized chamber for humidity sensing measurement.

Discussion

The humidity sensor was measured for its sensing capability in a customized chamber by varying the RH level by controlling the ultrasonic humidifier and dehumidifier, as illustrated in Figure 2. Figure 3 shows the response in electrical resistance of the humidity sensor. At 10% RH, the measured resistance was 11.78 MΩ. When the RH level was increased to 90%, the measured electrical resistance decreased to 5.48 MΩ. Temperature in the enclosure was maintained at room temperature (27˚C) throughout the measurement process. The significant drop in the electrical resistance when the humidity level was increased is due to Grotthuss mechanism occurred on ZnO

film [9]. Water vapour molecules condense on the surface of the ZnO film and form chemically absorbed layers [10]. These layers would collect and scatter the electrons dominantly on the surface and therefore cause a decrease in film's resistance [6]. The measurement response here demonstrates the functionality of the ZnO as active material in humidity sensing devices.

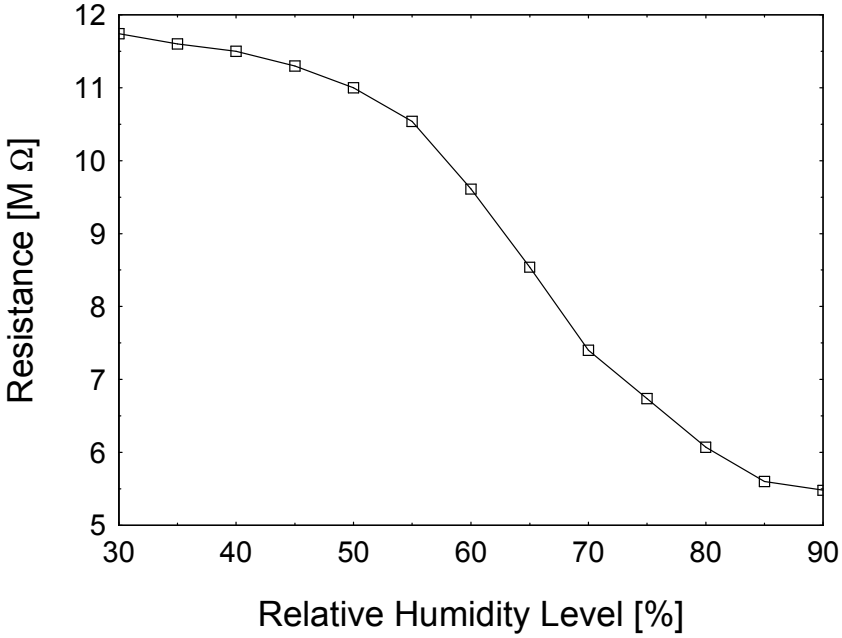

Figure 3: Variation in electrical resistance against changes in relative humidity percentage level (%).

Conclusion

RF magnetron sputtered ZnO films were utilized as active sensing layers on thermally oxide silicon substrates. The electrical resistance decreased from 11.78 MΩ to 5.48 MΩ as the RH increased from 30% to 90%. The significant decrease of the resistance was attributed to the Grotthuss mechanism that occurred on the ZnO film when the environment was humid. The work here would shed the light for the future realization of commercial humidity sensors based on low cost ZnO films.

Acknowledgement

The authors would like to express their utmost gratitude to Faculty of Engineering, Multimedia University at Cyberjaya, Malaysia, for facilitating and supporting this project, and the funding agency, Telekom Malaysia Research and Development (TM R&D) for the financial support.

References

[1] K. Arshaka, K. Twomey, and D. Egan, A Ceramic Thick Film Humidity Sensor Based on MnZn Ferrite, *Sensors*, vol. 2, no. 2, (2002), pp. 50–61.

[2] K. Arshak and K. Twomey, Thin films of In2O3/SiO for humidity sensing applications, *Sensors*, (2002), pp. 205–218.

[3] J. S. Atchison and C. L. Schauer, Fabrication and characterization of electrospun semiconductor nanoparticle-polyelectrolyte ultra-fine fiber composites for sensing applications., *Sensors (Basel, Switzerland)*, vol. 11, no. 11, (2011), pp. 10372–87.

[4] L. Schmidt-Mende and J. MacManus-Driscoll, ZnO–nanostructures, defects, and devices, *Materials Today*, vol. 10, no. 5, (2007), pp. 40–48.

[5] M. Awalludin, M. H. Mamat, M. Z. Sahdan, Z. Mohamad, and M. Mohammad Rusop, Nanostructured Zinc Oxide Thin Film Based Humidity Sensor Prepared by Sol-Gel Immersion Technique, *Advanced Materials Research*, vol. 667, (2013), pp. 553–557.

[6] P. K. Kannan, R. Saraswathi, and J. B. B. Rayappan, A highly sensitive humidity sensor based on DC reactive magnetron sputtered zinc oxide thin film, *Sensors and Actuators A: Physical*, vol. 164, no. 1–2, (2010), pp. 8–14.

[7] P. Biswas, S. Kundu, P. Banerji, and S. Bhunia, Super rapid response of humidity sensor based on MOCVD grown ZnO nanotips array, *Sensors & Actuators B: Chemical,* vol. 178, (2013), pp. 331-338.

[8] J.-W. Hoon, K.-Y. Chan, J. Krishnasamy, T.-Y. Tou, and D. Knipp, Direct current magnetron sputter-deposited ZnO thin films, *Applied Surface Science*, vol. 257, no. 7, (2011), pp. 2508–2515.

[9] B. C. Yadav, R. Srivastava, and C. D. Dwivedi, Synthesis and characterization of ZnO–TiO2 nanocomposite and its application as a humidity sensor, *Philosophical Magazine*, vol. 88, no. 7, (2008), pp. 1113–1124.

[10] K. Chou, T. Lee, and F. Liu, Sensing mechanism of a porous ceramic as humidity sensor, *Sensors and Actuators B: Chemical*, vol. 56, no. 1–2, (1999), pp. 106–111.

Advanced Materials Research Vol. 970 (2014) pp 115-119
© (2014) Trans Tech Publications, Switzerland
doi:10.4028/www.scientific.net/AMR.970.115

Influence of Spinning Speed on the Properties of Sol-Gel Spin Coated ZnO Films

Zi-Neng Ng[1], Kah-Yoong Chan[1, a*], Sharul Ashikin Kamaruddin[2], and Mohd Zainizan Sahdan[2]

[1] Centre for Advance Devices and Systems,
Multimedia University, Persiaran Multimedia, 63100 Cyberjaya, Selangor, Malaysia

[2] Faculty of Electrical and Electronic Engineering, Universiti Tun Hussein Onn Malaysia, 86400 Batu Pahat, Johor, Malaysia

[a*]kychan@mmu.edu.my

Keywords: ZnO films, sol-gel spin coating, spinning speed

Abstract. In this work, ZnO films were fabricated by sol-gel spin coating technique. Different spinning speeds of 1000 to 6000 revolutions per minute (RPM) were used in order to study the changes on the properties of the ZnO films. The characterizations were conducted using surface profilometer for thickness measurement, atomic force microscopy (AFM) for surface scanning, X-ray diffractometer (XRD) for structural analysis, and ultraviolet-visible (UV-VIS) spectrophotometer for optical transmittance. The influence of spinning speed and the mechanisms which affect the growth of the ZnO films will be revealed.

Introduction

Zinc oxide (ZnO) film is well-known with its useful characteristics in the area of transparent electronics, such as the wide energy band gap (3.3 eV), large free exciton binding energy (60 mV), low resistivity (10^{-4} Ωcm), high carrier mobility, and high visible light transmittance [1]. As a result, ZnO film was studied intensively in recent years in order to utilize it in potential applications such as sensors, transparent electrodes, thin film transistors, and photovoltaic cells. Numerous ZnO films deposition methods have been attempted namely pulsed laser deposition (PLD) [2], molecular beam epitaxy (MBE) [3], metal-organic chemical vapor deposition (MOCVD) [4], and sputtering technique [5]. These sophisticated methods are able to produce high quality films, but the downsides are the complicated process and the use of high end equipments which often result in higher production costs. The sol-gel spin coating method offers simple and low cost process to coat ZnO film on glass substrate. Despite that, various processing parameters of this method are controllable, such as the precursor concentration [6], pre-heating temperature [7], and annealing temperature [8]. In the work of Smirnov et al. [9], the changes on the optical band gap and structural properties of the ZnO film with the spinning speed of 700 revolution per minute (RPM) to 1600 RPM had been reported. The influence of the spinning speed on the thickness of the films was also observed. However, the report lacked of higher spinning speed results. Many works on ZnO films coated by sol-gel spin coating process was conducted using the spinning speed varied from 3000 RPM to 4000 RPM [7], [10]–[12]. Higher spinning speed may lead to thinner film thickness, but it may have the advantage in terms of uniformity of the coatings. In this research, the influence of higher spinning speed on the structural and optical properties of the sol-gel spin coated ZnO films was investigated.

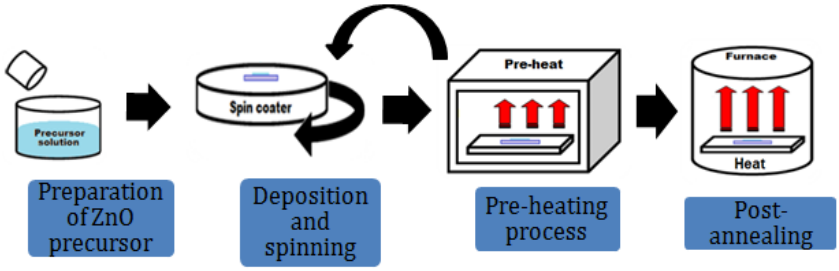

Figure 1: Experimental setup and procedure

Experimental

The ZnO solution was prepared with zinc acetate dihydrate [Zn(CH3COO) 2.2H2O, ZnAc] as precursor at 0.5 M, Isopropanol (IPA) as solvent and monoethanolamine (MEA) as stabilizer, respectively. The molar ratios of MEA/ZnO were

kept at 1:1. The solution was stirred at 60 °C for 2 hours, and then left for ageing process at room temperature for another 22 hours to yield a transparent and clear solution. The coating process was performed at room temperature by spinning the solution on glass substrate for 25 seconds. Different spinning speeds of 1000 RPM, 2000 RPM, 3000 RPM, 4000 RPM, 5000 RPM, and 6000 RPM were explored. The illustration of the experimental process and setup is shown in Fig. 1. The thickness, surface morphology, structural, and optical properties of the ZnO films were determined by performing measurements using the surface profilometer (Mahr Perthometer S2), atomic force microscope (AFM) (Nanosurf), X-ray diffractometer (XRD) (Bruker), and ultraviolet-visible (UV-VIS) spectroscopy (Ocean Optic), respectively.

Results and Discussions

The thickness of ZnO films spin coated at 1000 RPM to 6000 RPM is 445 nm, 375 nm, 295 nm, 280 nm, 246 nm, and 214 nm, respectively. The graph as shown in Fig. 2 shows a decreasing trend on the film thickness with increasing spinning speed. The increased spinning speed has raised the level of centrifugal force applied to the ZnO solution on the substrate during spinning process, resulting in thinner coatings. The graph also shows the improvement on the uniformity of the films spin coated at higher speed. At spinning speed less than 3000 RPM, the thickness variation from the center to the edge of the films is 12.3%, whereas at spinning speed more than 3000 RPM, the thickness variation has reduced to 5.7%. This is again due to the increase of centrifugal force during higher spinning speed, in which the solution was able to spread across the substrate more evenly, and results in more consistent coatings. However, the drawback is that higher spinning speed will producer thinner films. This can be solved by coating more layers [13].

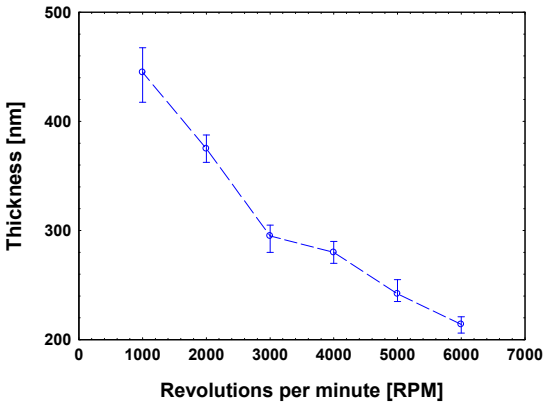

Figure 2: Thickness vs. RPM

A slight decrement in lateral feature size as the spinning speed increases can be observed in AFM micrographs in Fig. 3. The change in thickness has contributed to the formation of grains. As reported by Mridha et al. [14], larger grain size was also seen on thicker films. The atoms on thicker films are more sufficient and chances are higher for the grains to agglomerate into larger grains.

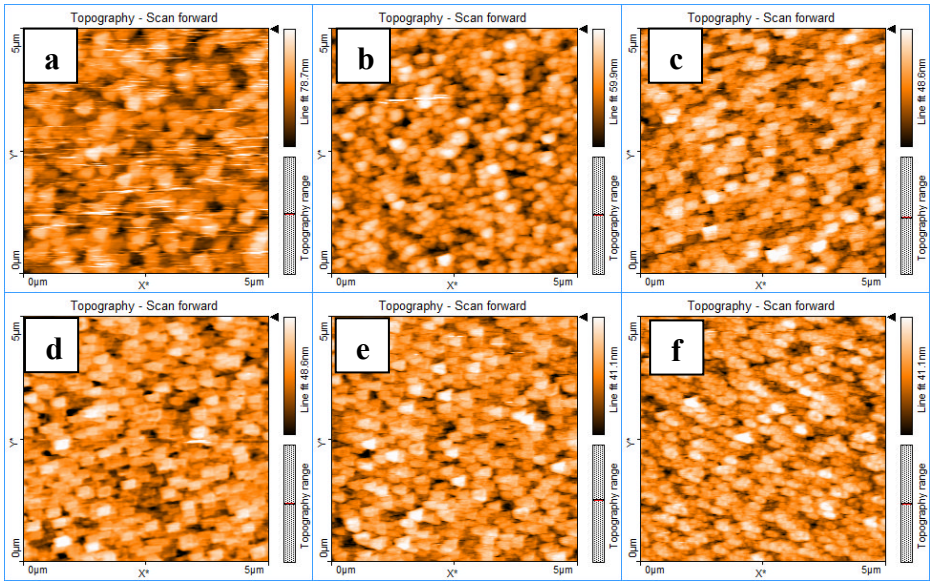

Fig. 3: AFM micrograph for ZnO films spin coated at a: 1000 RPM; b: 2000 RPM; c: 3000 RPM; d: 4000 RPM; e: 5000 RPM; f: 6000 RPM

As a result, the roughness of the films is affected as well. The RMS area roughness extracted from the AFM micrographs shown in Fig. 4 are 13.3 nm, 10.9 nm, 9.0 nm, 8.9 nm, 7.5 nm, and 7.4 nm for ZnO films spin coated at 1000 RPM to 6000 RPM, respectively. Consistant with the lateral feature size, the RMS roughness has decreased with higher spinning speed due to reduced lateral feature size.

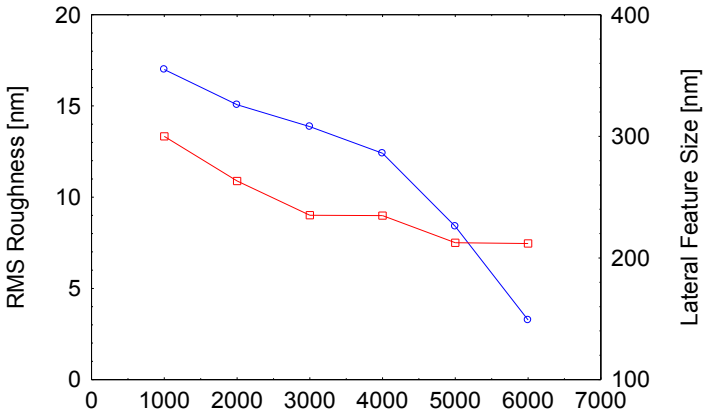

Figure 4: RMS roughness and Lateral feature size vs. RPM

The inset of Fig. 5 shows the XRD patterns of the ZnO films spin coated at different speeds. All diffraction peaks are in match with the reflection of wurtzite structured ZnO planes while having a strong peak at (0 0 2), indicating the growth of preferred orientation along c-axis. The crystallinity of the films was further investigated by determining the crystallite size based on the XRD data obtained, estimated by Scherrer's formula:

$$D = \frac{0.9\lambda}{\beta \cos\theta} \qquad (1)$$

where D is the crystallite size of the films, λ is the wavelength of incident X-ray from XRD, β is the FWHM measured in radians and θ is the Bragg angle of diffraction peak. The estimated crystallite sizes of the films are plotted in Fig. 5. The results are consistent with AFM micrograph which shows a decreasing trend of lateral feature size. The decrease in crystallite size with increasing spinning speed indicates that the crystallinity degraded due to the decrease in film thickness.

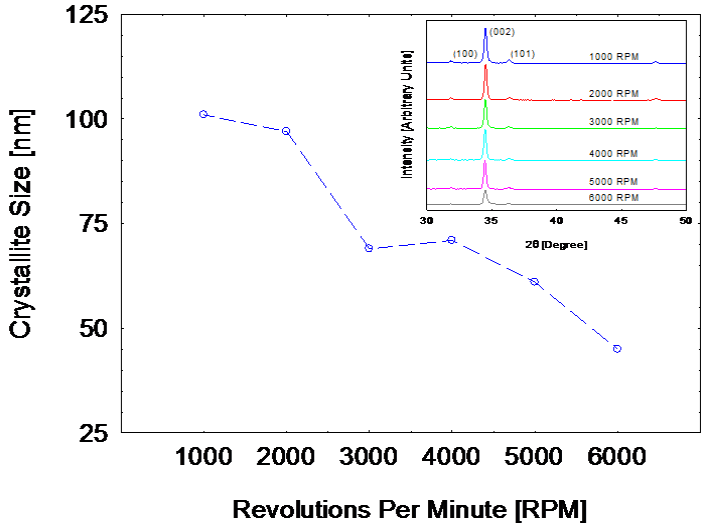

Figure 5: Crystallite size and XRD pattern (inlet)

The optical transmittance spectra of the ZnO films are plotted in Fig. 6. All ZnO films are visibly transparent in the wavelength region of 380 nm to 800 nm, ranging from 80 % to 95 % transmittance. The thinner films produced by higher spinning speed is the reason for the improvement in transmittance. However, this will affect the level of absorption in the UV region. The up-shift of the absorption level as spinning speed is increased indicates that the band gap absorption has reduced slightly. Thicker ZnO films are able to absorb higher level of energy, allowing less light source to pass through the films. As a result, the absorption level of

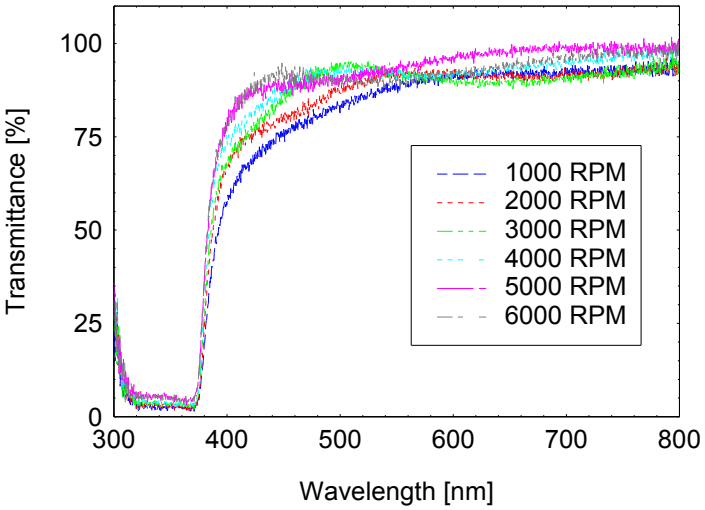

Figure 6: Optical transmittance of ZnO films spin coated at different speed

ZnO film spin coated at 1000 RPM is closer to zero due to thicker coatings, as compared to thinner films spin coated at higher speed.

Conclusion

In this work, ZnO films were successfully fabricated using low cost sol–gel spin coating technique. The effects of spinning speed have been elucidated. The thickness and the uniformity of the films were significantly affected by the spinning speed, making the spinning speed a very important parameter to control film thickness and assure good quality films. The AFM results show a decrement in lateral feature size and RMS surface roughness with increasing spinning speed. Higher (0 0 2) peaks were observed in thicker films, which indicates better crystallinity. The optical transmittance of the ZnO films spin coated at higher speed was generally improved, as higher transmittance and sharper absorption edge can be seen. All the films fabricated in this work have the average optical transmittance of 90%, which are suitable to be used as transparent conductive oxide (TCO).

Acknowledgement

This project is funded by Ministry of Science, Technology and Innovation (MOSTI)'s Escience Fund. The authors would like to thank MOSTI for the financial support, as well as Multimedia University for providing the necessary facilities.

References

[1] L. Znaidi, "Sol – gel-deposited ZnO thin films : A review," vol. 174, pp. 18–30, 2010.

[2] K. Matsubara, P. Fons, K. Iwata, A. Yamada, and S. Niki, "Room-temperature deposition of Al-doped ZnO films by oxygen radical- assisted pulsed laser deposition," vol. 422, pp. 176–179, 2002.

[3] X.-A. Zhang, J.-W. Zhang, W.-F. Zhang, D. Wang, Z. Bi, X.-M. Bian, and X. Hou, "Enhancement-mode thin film transistor with nitrogen-doped ZnO channel layer deposited by laser molecular beam epitaxy," *Thin Solid Films*, vol. 516, no. 10, pp. 3305–3308, Mar. 2008.

[4] G. Du, J. Wang, X. Wang, X. Jiang, S. Yang, Y. Ma, W. Yan, D. Gao, X. Liu, H. Cao, J. Xu, and R. P. H. Chang, "Influence of annealing on ZnO thin film grown by plasma-assisted MOCVD," *Vacuum*, vol. 69, no. 4, pp. 473–476, Jan. 2003.

[5] J.-W. Hoon, K.-Y. Chan, J. Krishnasamy, T.-Y. Tou, and D. Knipp, "Direct current magnetron sputter-deposited ZnO thin films," *Appl. Surf. Sci.*, vol. 257, no. 7, pp. 2508–2515, Jan. 2011.

[6] S. A. Kamaruddin, K.-Y. Chan, H.-K. Yow, M. Zainizan Sahdan, H. Saim, and D. Knipp, "Zinc oxide films prepared by sol–gel spin coating technique," *Appl. Phys. A*, vol. 104, no. 1, pp. 263–268, Nov. 2010.

[7] Y.-S. Kim, W.-P. Tai, and S.-J. Shu, "Effect of preheating temperature on structural and optical properties of ZnO thin films by sol–gel process," *Thin Solid Films*, vol. 491, no. 1–2, pp. 153–160, Nov. 2005.

[8] Z.-N. Ng, K.-Y. Chan, and T. Tohsophon, "Effects of annealing temperature on ZnO and AZO films prepared by sol–gel technique," *Appl. Surf. Sci.*, vol. 258, no. 24, pp. 9604–9609, Oct. 2012.

[9] M. Smirnov, C. Baban, and G. I. Rusu, "Structural and optical characteristics of spin-coated ZnO thin films," *Appl. Surf. Sci.*, vol. 256, no. 8, pp. 2405–2408, Feb. 2010.

[10] S.-Y. Kuo, W.-C. Chen, and C.-P. Cheng, "Investigation of annealing-treatment on the optical and electrical properties of sol–gel-derived zinc oxide thin films," *Superlattices Microstruct.*, vol. 39, no. 1–4, pp. 162–170, Jan. 2006.

[11] M. Sharma and R. M. Mehra, “Effect of thickness on structural, electrical, optical and magnetic properties of Co and Al doped ZnO films deposited by sol–gel route,” *Appl. Surf. Sci.*, vol. 255, no. 5, pp. 2527–2532, Dec. 2008.

[12] S. W. Xue, X. T. Zu, W. G. Zheng, M. Y. Chen, and X. Xiang, “Effects of annealing and dopant concentration on the optical characteristics of ZnO:Al thin films by sol–gel technique,” *Phys. B Condens. Matter*, vol. 382, no. 1–2, pp. 201–204, Jun. 2006.

[13] H. Wang, M. Xu, J. Xu, L. Yang, and S. Zhou, “Effects of annealing temperature and thickness on microstructure and properties of sol–gel derived multilayer Al-doped ZnO films,” *J. Mater. Sci. Mater. Electron.*, vol. 21, no. 2, pp. 145–148, Apr. 2009.

[14] S. Mridha and D. Basak, “Thickness dependent photoconducting properties of ZnO films,” *Chem. Phys. Lett.*, vol. 427, no. 1–3, pp. 62–66, Aug. 2006.

Advanced Materials Research Vol. 970 (2014) pp 120-123

doi:10.4028/www.scientific.net/AMR.970.120

MICROSTRUCTURAL AND ELECTRICAL CONDUCTIVITY OF ANNEALED ZnO THIN FILMS

Peh Ly Tat[1, a*], Karim Deraman[1, b], Wan Nurulhuda Wan Shamsuri[1, c], Rosli Hussin[1, d], and Zuhairi Ibrahim[1, e]

[1]Phosphor Materials Research Group, Department of Physics, Faculty of Science, Universiti Teknologi Malaysia, 81310 UTM Skudai, Johor, Malaysia.

[a*]lyyan89@hotmail.com (*corresponding author), [b]karimderaman@utm.my, [c]wnurulhuda@utm.my, [d]rbh@dfiz2.fs.utm.my, [e]zu@dfiz2.fs.utm.my

Keywords: ZnO thin films; sol-gel dip coating; annealing temperature; electrical conductivity.

Abstract. Undoped nanocrystalline ZnO thin films were deposited onto the glass substrates via the low cost sol-gel dip coating method. The as-grown ZnO films were annealed at the temperatures ranging from 400 °C to 550 °C. The X-ray diffraction (XRD) pattern revealed that the annealed ZnO films were polycrystalline with hexagonal wurtzite structure and majority preferentially grow along (002) c-axis orientation. Atomic force microscopy (AFM) micrographs showed the improvement of RMS roughness and grain size as annealing temperature increased. The ZnO films that annealed at 500 ºC exhibited the lowest resistivity value.

Introduction

Zinc oxide (ZnO) is an II-VI n-type semiconductor with a wide direct band gap of E_g = 3.37 eV and large exciton binding energy of 60 meV compared to GaN (24meV) and ZnSe (19meV) at room temperature [1, 2]. Furthermore, ZnO also have some unique and fascinating properties such as high optical transparency conductive in visible region, good piezoelectricity, photoelectric property, and chemical stability. Thus, ZnO nanostructure thin films have attracted a lot of interest among researchers recently due to these excellent properties and potentially in wide range of application such as photocatalyst devices [1], transparent electrodes for solar cells panel [2], and gas sensor [3].

Various thin films growth techniques have been used to fabricate the ZnO films including pulse laser deposition (PLD) [4], rf magnetron sputtering [5], and sol-gel method [6]. Among them, sol-gel deposition method become preferential due to its simplicity, ability to deposition large scale area of thin film, low costing and homogeneity.

This work aims to study the effect of annealing temperature on the microstructural and electrical conductivity of ZnO films prepared via the low cost sol-gel dip coating method.

Experimental Procedure

A 0.30 M precursor solution was prepared by dissolving the zinc acetate dehydrate [$Zn(CH_3COO)_2 \cdot 2H_2O$] into isopropanol and hence adding an appropriate volume of diethanolamine (DEA) which act as the stabilizer in order to obtain the 1:1 molar ratio of DEA to [$Zn(CH_3COO)_2 \cdot 2H_2O$]. This solution was stirred at 70 ºC for 1 hour to catalyst the hydrolysis process, hence yield a clear and homogeneous solution. After aging for 24 hours, the resultant solution is used as coating solution.

The cleaned glass substrate was dipped into the ZnO coating solution with the constant withdrawal speed of 10mm/min. After the coating, the film was pre-heated at 200 ºC for 20 minutes to completely evaporate the solvent and to remove organic residuals. The dip coating and pre-heating process were repeated nine times to obtain the films with a thickness of approximately 325 nm. The ZnO films were then annealed at the temperatures of 400 ºC, 450 ºC, 500 ºC, and 550 ºC respectively.

The crystalline structure of annealed ZnO films were investigated by Bruker AXS D8 Advance X-ray diffraction (XRD) with Cu K_α radiation (λ= 0.15406nm) and surface morphology

were observed via ND-MDT Ntegra Prima atomic force microscopy (AFM). The electrical resistivity of annealed ZnO films was measured by a two-point probe resistivity measurements method.

Results and Discussion

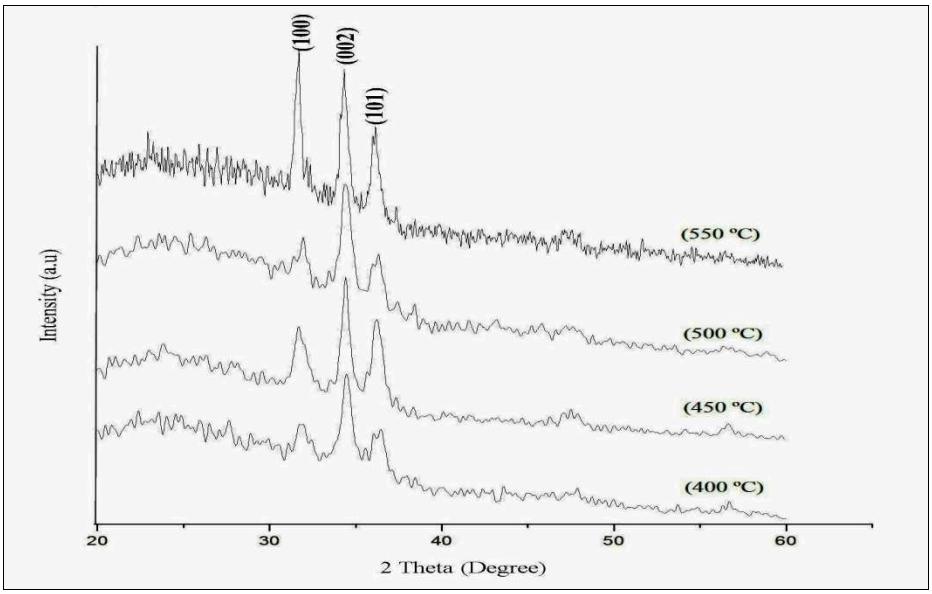

Figure 1 XRD patterns of annealed ZnO thin films.

Figure 1 shows the XRD patterns of annealed ZnO films at temperatures ranging from 400 °C to 550 °C. The XRD spectrum shows the diffraction peaks corresponding to (100), (002), and (101) respectively. These peaks revealed that all the annealed ZnO films are polycrystalline with a hexagonal wurtize structure [7]. The preferred (002) c-axis orientation is observed for annealed ZnO films with temperature above 400 °C. As the annealing temperature increases up to 550 °C, the films preferred a-axis orientation due to the intensity of (100) reflection plane which become dominant. Meanwhile, the 450 °C annealed ZnO films shows the highest intensity for the (002) diffraction peak and it was an indication of the large volume of grains growth preferentially oriented perpendicular to the substrate surface [7]. Previously, some researchers reported that the crystallinity of ZnO films can be improved by increasing the thermal annealing temperature [7,8]. However, in our work, we observed decrement of crystallinity of ZnO films annealed above 450 °C. This is probably due to the higher calcinations temperature (>450 °C) affect the unidirectional grains growth and cause the demolishment of ZnO films crystallization [9]. The estimated crystalline size were calculated by using the Debye Scherrer's formula as shown in Eq. 1 and the value are as shown in Table 1 [8]

$$D = 0.9 \lambda / \beta \cos \theta \quad (1)$$

where D, λ, β, and θ are the crystallite size, wavelength of the X-ray radiation (1.5406 Å), full width at half maximum of the diffraction peak and Bragg diffraction angle of the peak respectively. The crystal lattice constants for ZnO films annealed at 450 °C are a = 3.25 Å and c = 5.20 Å which are close to a = 3.25 Å and c = 5.21 Å of bulk ZnO (JCPDS No. 0036-1451).

Table 1. Properties of annealed ZnO films

Annealing Temperature, [°C]	Crystallite Size (XRD), [nm]	Lattice Constant a, [Å]	Lattice Constant c, [Å]	RMS Roughness, [nm]	Grain Size (AFM), [nm]
400	19.95	3.25	5.21	0.20	11.90
450	35.23	3.25	5.20	2.14	45.60
500	23.09	3.23	5.79	2.69	28.00
550	25.84	3.25	5.21	2.08	43.20

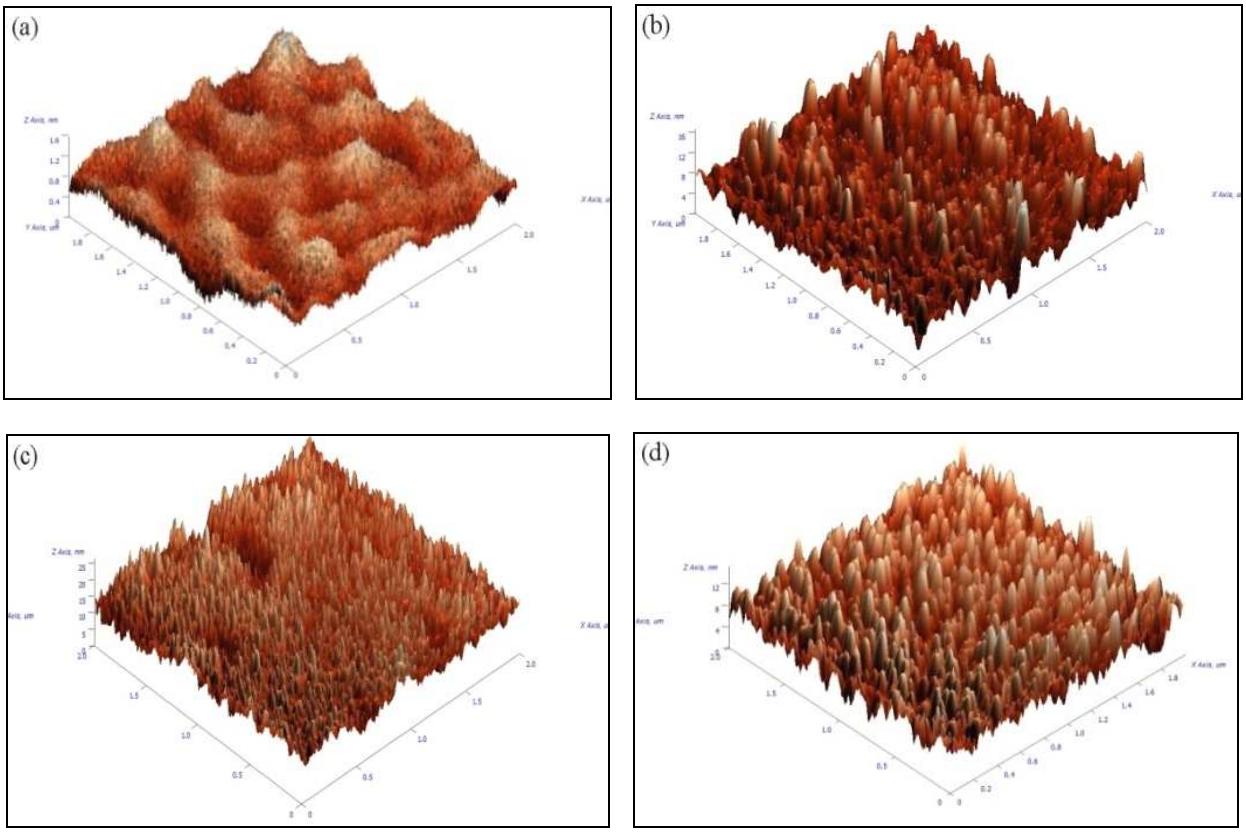

Figure 2 AFM surface morphology micrographs of the ZnO films annealed at the temperature of (a) 400 °C (b) 450 °C, (c) 500 °C, (d) 550 °C

The AFM surface morphology micrographs of the annealed ZnO films are shown in Figure 2. From the AFM images, we observed that ZnO films annealed above 450 °C consists of many columnar and uniform grains. The root mean square (RMS) roughness increased with the increasing of annealing temperature up to 500 °C as shown in Table 1. Most of the researchers claimed that the roughness of the films increased as annealing temperature increased [6,8]. However, we found that as the annealing temperature increases to 550 °C, the RMS roughness decreases to 2.08 nm in our work. The ZnO films annealed at 500 °C has a relatively rough surface which may be due to the vaporization of ZnO and caused the effect of depreciation ZnO mass transport in grain growth [10]. This explanation is also in good agreement with the XRD results which shows that 550 °C annealed ZnO films preferred with (100) a-axis orientation rather than c-axis orientation. From Table 1, we can summarize that the average grain size that is determined by AFM is consistent with the estimated crystallites size by XRD.

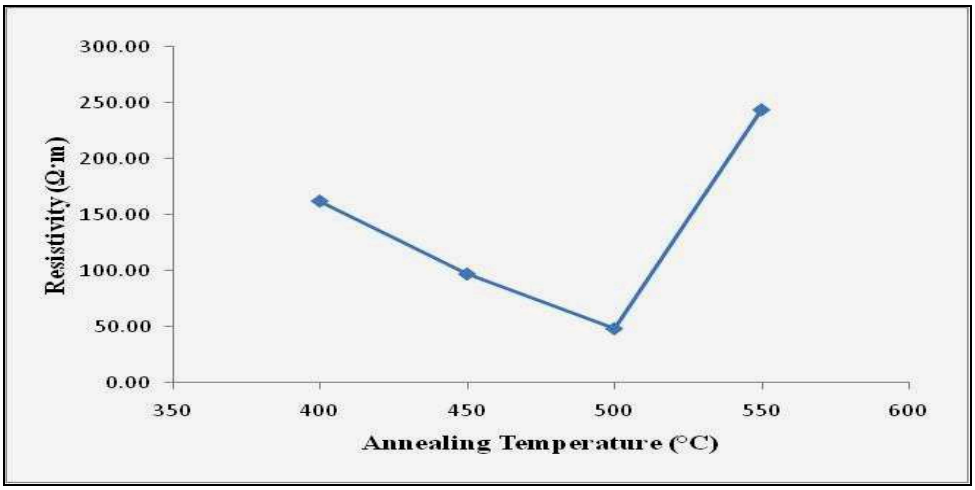

Figure 3 Electrical resistivity of annealed ZnO films

The resistivity of annealed ZnO films is plotted in Figure 3. The resistivity value decreased as annealing temperature increased up to 500 °C with the lowest resistivity of 48.75 Ω·m. However, the films resistivity increased during 550 °C. As the annealing temperature increases above 500 °C, this may have catalyst the oxygenation of the interstitial zinc atoms. With the decreasing number of zinc atoms and large numbers of oxygen molecules being absorbed at the grains boundaries, it will create potential barriers which resist the transportation of electron [3]. Thus, the films resistivity sharply increased.

Conclusions

ZnO thin films were deposited onto the glass substrates by low cost sol-gel dip coating technique and annealed at the temperatures range from 400 °C to 550 °C. All the annealed films are polycrystalline with hexagonal wurtize structure. The annealed ZnO thin films have a preferred (002) c-axis orientation and reached the highest peak intensity at 450 °C. The RMS roughness of the films increased as the annealing temperature increased. The ZnO films annealed at 500 °C exhibited the lowest resistivity value of 48.75 Ω·m among all ZnO annealed films.

Acknowledgments

The authors gratefully acknowledgments the technical support of Faculty of Science, UTM, the financial support from Ministry of Higher Education (MOHE) Malaysia, Universiti Teknologi Malaysia (UTM) under RUG 07J63 for managing the grants.

References

[1] Patcharee Jongnavakit, Pongsaton Amornpitoksuk, Sumetha Suwanboon, Tanakorn Ratana, Surface and photocatalytic properties of ZnO thin film prepared by sol-gel method, Thin Solid Films 520 (2010) 5561-5567.

[2] Seung Hwangbo, Yun-Ji Lee, Kyu-Seog Hwang, Photoluminescence of ZnO layer on commercial glass substrate prepared by sol-gel process, Ceramic International 34 (2008) 1237-1239.

[3] Fawzy A.Mahmoud, G. Kiriakidis, Nanocrystalline ZnO thin film for gas sensor application, Journal of Ovonic Research 5 (2009) 15-20.

[4] B.J. Jin, H.S. Woo, S. Im, S.H. Bae, S.Y. Lee, Relationship between photoluminescence and electrical properties of ZnO thin films grown by pulsed laser deposition, Applied Surface Science 169-170 (2001) 521-524.

[5] Rajesh Kumar, Neeraj Khare, Vijay Kumar, G.L Bhalla, Effect of intrinsic stress on the optical properties of nanostructured ZnO films grown by rf magnetron sputtering, Applied Surface Science 254 (2008) 6509-6513.

[6] J.R. Casnova, E.A. Heredia, C.D. Bojorge, H.R. Canepa, G. Kellermann, A.F. Craievich, Structural characterization of supported nanocrystalline ZnO thin films prepared by dip-coating, Applied Surface Science 257 (2011) 10045-10051.

[7] Mujdat Caglar, Saliha Ilican, Yasemin Caglar, Fahrettin Yakuphanoglu, Electrical conductivity and optical properties of ZnO nanostructured thin film, Applied Surface Science 255 (2009) 4491-4496

[8] Kyu-Seong Hwang, Yun-Ji Lee, Seung Hwangbo, Growth, structure and optical properties of amorphous or nano-crystalline ZnO thin films prepared by prefiring-final annealing, Journal of Ceramic Research Vol.8 No.5 (2007) 305-311.

[9] Kyu-Seo Hwang, Bo-An Kang, Ju-Hyun Jeong, Young-Sun Jeon, Byung-Hoon Kim, Spin coating-pyrolysis derived highly c-axis oriented ZnO layers pre-fired at various temperature, Current Applied Physics 7 (2007) 421-425.

[10] Jin-Hong Lee, Kyung-Hee Ko, Byung-Ok Park, Electrical and optical properties of ZnO transparent conducting films by the sol-gel method, Journal of Crystal Growth 247 (2003) 119-125.

Advanced Materials Research Vol. 970 (2014) pp 124-127

doi:10.4028/www.scientific.net/AMR.970.124

Preparation and Mechanical Characterization of Amorphous B-C Films

Shahira Liza[1,a*], Hiroki Akasaka[1,b], Masayuki Nakano[2,c], Naoto Ohtake[1,d]

[1]Department of Mechanical Sciences and Engineering, Tokyo Institute of Technology, 2-12-1 O-okayama, Meguro-ku, Tokyo, 152-8552, Japan

[2]Department of Chemical Science and Engineering, Tokyo National College of Technology, 1220-2 Kunugida, Hachiouji, Tokyo 193-0997, Japan

[a*]shahiraliza@gmail.com, [b]akasaka@mech.titech.ac.jp, [c]nakano@tokyo-ct.ac.jp, [d]ohtaken@mech.titech.ac.jp

Keywords: Amorphous carbon; amorphous B-C film; Plasma CVD; Wear

Abstract. This study has demonstrated that trimethylboron, $B(CH_3)_3$ is a suitable boron source material for the fabrication amorphous boron carbide (*a*-BC:H) films. *a*-BC:H films were deposited by pluse plasma chemical vapor deposition on a silicon substrate (100) with different gas pressures and gas flow rates at constant voltage, -5 kV . The grown *a*-BC:H films were found to be porous surface and their thickness were in the range of 0.95 to 1.56 μm for 3 h of deposition time. Results indicated that the boron contents, morphologies and mechanical properties of the *a*-BC:H films were dependent on the gas pressures and gas flow rate. The increased of boron content will introduce more porous film surface. The effect of boron content on the mechanical properties such as hardness, Young's modulus, and wear resistance were discussed. The good quality film is obtained from $B(CH_3)_3$ at 5 Pa and gas flow rate of 15 cm^3/min which boron to carbon atomic ratio is 0.43. This film has lower friction coefficient (0.3) sliding against stainless steel ball, high hardness (8.1 GPa) and Young's modulus (62.2 GPa).

Introduction

The deposition of amorphous boron-carbide (*a*-BC) film has been widely studied in various applications such as biomedical, photovoltaic and electronic applications [1-3]. Incorporation of boron in carbon films are applied as high performance films for sliding parts to achieve higher adhesion strength and excellent tribological properties [4]. Numerous superior qualities of this material have been reported from the previous study such as have high hardness and modulus of elasticity, low compressive stress and good adhesion film [3,5,6]. Recently, it has been interest on the preparation and adhesion strength improvement of incorporation of B into carbon film in the biomedical application used for bone fixation [3].

However, less investigation on the influence of B content on the mechanical properties such as hardness and tribological properties of film, to the best of our knowledge, has been presented. The previous study only limited which devoted to study bonding configuration in B contained carbon film and the chemical states of B [7,8]. In practice, B can be introduced during the deposition by various fabrication methods. Plasma chemical vapor deposition (CVD) is highly expected to be applied in industry because it enables the fabrication of carbon films at low temperature without the need to consider base material softening, dimensional changes and other problems caused by the increased temperature during film fabrication. In this study, the trimethylboron, $B(CH_3)_3$ is used as a suitable boron source material for the fabrication hydrogenated amorphous boron-carbide (*a*-BC:H) films due the much less hazardous substances [9].The effect of boron content through different deposition parameters on the mechanical properties such as hardness, Young's modulus, and wear resistance of film were discussed.

Experimental Details

a-BC:H films were prepared by pulse plasma CVD on a silicon (100) substrate from trimethylboron, $B(CH_3)_3$. Figure 1 shows the schematic diagram of the experimental equipment. The silicon substrate was cleaned ultrasonically with distilled water, methanol and acetone each for 40, 20 and 20 min, respectively. Afterward, the substrate was placed on the sample holder and loaded into the deposition chamber. The vacuum chamber was evacuated to a background pressure below 4.0 x 10^{-7} Pa using turbo molecular pump. Monopolar pulse power supply 2 kHz was used for plasma generation. Prior deposition, the surface of substrate was sputter-cleaned by argon plasma for 20 min at a voltage of -5 kV with gas flow rate of 10 cm^3/min. The films were deposited at various working gas pressure and gas flow rate and the deposition conditions were as follows; working gas pressure of 5 Pa (with gas flow rate of 10, 15 and 20 cm^3/min) and 10 Pa (with gas flow rate of 15 and 20 cm^3/min) constant bias voltage of -5 kV. The deposition time was 3 hours.

The film thickness was measured by surface profilometer (Surftest SV-600, Mitutoyo Co., Ltd). The surface of the films was examined by optical microscope. The chemical composition of the film was measured with X-ray photoelectron spectroscopy (XPS) system (ESCA-1700R, Physical Electronics Co., Ltd). AlK_α X-ray source was used for XPS measurement. The hardness and Young's modulus of the deposited film was measured by indentation (PICODENTOR HM-500, Fischer Instruments K.K.). The measurements were conducted under load of 1 μN for 100 indentations. The ball on disk tribometer was employed to measure the friction coefficient of the deposited film at room temperature with a relative humidity of about 24%. A ball of 5 mm diameter made of stainless steel was pressed against the films with a normal load of 1 N. The tests were conducted under the sliding velocity of 0.209 m/s and sliding wear duration lasted for 50000 cycles.

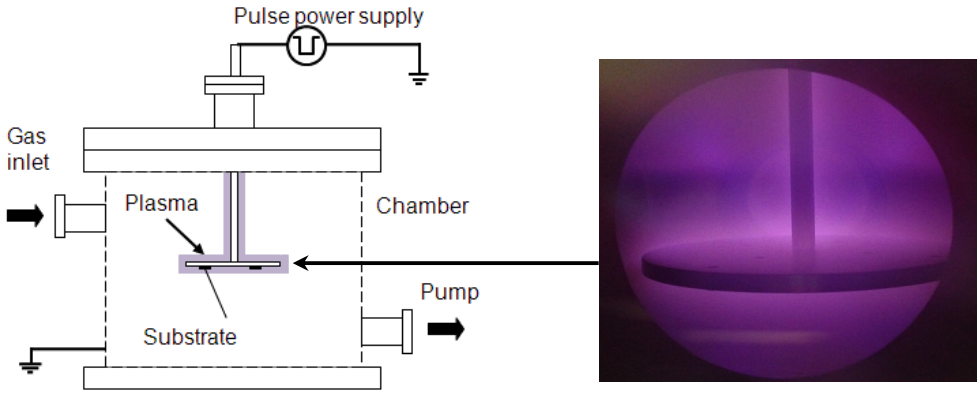

Fig. 1. Schematic diagram of pulse plasma CVD system for the deposition of *a*-BC:H film.

Results and Discussion

Table 1 shows the summary of *a*-BC:H films growth conditions and chemical composition according to the different deposition parameters such as gas pressure and gas flow rate. The thickness of the deposited films is significantly increased by increasing both gas pressure and gas flow rate. B content in the *a*-BC:H films is found to decrease about 4 at.% when the gas pressure is increasing from 5 to 10 Pa. When gas pressure is maintained at 5 Pa, the B content could be seen increasing with the increasing gas flow rate. However, at 10 Pa, the B content decreases as the gas flow rate are increased. The difference of the increment between those two gas pressures may be due to the difference condition during the deposition. The reason for the B content in the *a*-BC:H films deposited at 10 Pa are much lower compared with the 5 Pa, which could be related due to the presence of the oxygen. The atomic percentage of oxygen is found to be at 15 at.% for gas pressure of 10 Pa which is higher 4 at.% from 5 Pa. The oxygen absorption maybe occurred during post-deposition exposure to atmospheric air which might arise as a result of hydrocarbons, water, oxygen and other adsorbents picked up when the film was transported through air.

The optical micrograph of the surface of *a*-BC:H films as shown in Figure 2 revealed the presence of voids or porosity at all deposited surface films. By comparing the surface, it was found that film deposited at pressure of 5 Pa and gas flow rate of 20 cm^3/min contained more voids on the surface. From the XPS measurement, the film which deposited at this condition has more B content. This implied that films which have higher B content would have more voids. Therefore, it can be deduced that the formation of void are induced by the deposition of Boron atom. Other studies reported that the void formation on the surface of film maybe attributed from the oxidation process [10]. Those voids are expected to play roles of oil pits and accumulation of debris, like segment-structured DLC films [11,12].

Table 1. Growth conditions and chemical composition of *a*-BC:H films grown by pulse plasma CVD.

Sample	A	B	C	D	E
$B(CH_3)_3$ flowrate (cm^3/min)	10	15	20	15	20
Pressure (Pa)	5	5	5	10	10
Thickness (μm)	0.95	1.13	1.24	1.06	1.56
Boron (at.%)	25.8	25.8	27.0	21.0	19.0
Carbon (at.%)	63.1	60.2	60.3	63.8	65.6
Oxigen(at.%)	11.1	14.0	12.7	15.2	15.4
B/C ratio	0.41	0.43	0.45	0.33	0.29

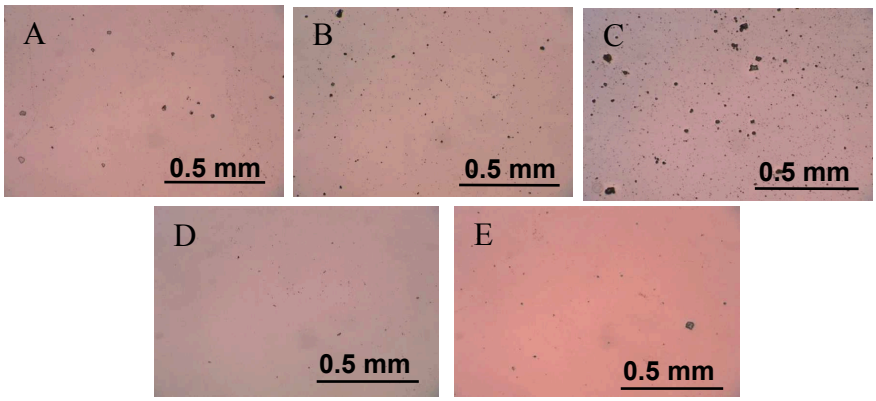

Fig. 2. Optical micrographs of the surface of the *a*-BC:H film deposited at 5 Pa (A) 10 cm^3/min, (B) 15 cm^3/min, (C) 20 cm^3/min, and 10 Pa, (D) 10 cm^3/min, (E) 15 cm^3/min at constant voltage, -5 kV.

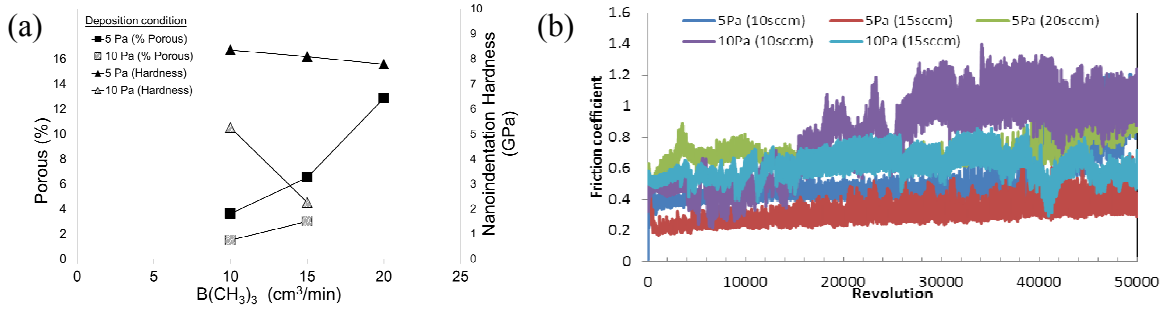

Fig. 3. (a) Nanoindentation hardness and Young's modulus and (b) friction coefficient of the *a*-BC:H film at constant voltage, -5 kV.

As can be seen in Figure 3a, both hardness and Young's modulus of the coatings are reduced with increasing of gas pressures from 5 Pa (sample A, B, C) to 10 Pa (Sample D, E). A hardness value of 7.7-8.3 GPa and Young's modulus of 59.5-63.8 GPa could be achieved at 5 Pa of gas pressure. In contrast, at 10 Pa of gas pressure the both hardness and Young's modulus value dropped to 2.2-5.2 GPa and 28.2-38.7 GPa respectively. It is noticeable that the increased of gas

flow rates also will reduce the value of hardness and Young's modulus at the fixed gas pressure. From above discussion, at 5 Pa of gas pressure the deposited film contained more concentration of B. This result suggested that the film which content higher B exhibit a higher hardness and Young's modulus. Figure 3b shows friction coefficient of the *a*-BC:H film. The friction coefficient was varied between 0.3 and 0.7. Sample B which deposited at 5 Pa and 15 cm^3/min was found to have the lowest friction coefficient of about 0.3.

Conclusions

In this study, the B concentration in the carbon film was found increase as the gas flow rate increased at gas pressure of 5 Pa and voltage, -5 kV. An increase in the B content leads to an increase in hardness in the range from 7.7-8.3 GPa and Young's modulus of 59.5-63.8 GPa. On the other hand, an increase of voids was found on the surface film because the effect of high concentration of B content. According to the results in the discussion, the *a*-BC:H film fabricated at 5 Pa and gas flow rate of 15 cm^3/min with B/C ratio is 0.43 has lower friction coefficient (0.3) sliding against stainless steel ball, high hardness (8.1 GPa) and Young's modulus (62.2 GPa).

References

[1] J. Podder, M. Rusop, T. Soga and T. Jimbo, Boron doped amorphous carbon thin films grown by R.F. PECVD under different partial pressure, Diamond Relat. Mater. 14, (2005) 1799-1804.

[2] T. S. Chen, S.E. Chiou and S. T. Shiue, The effect of different radio-frequency powers on characteristics of amorphous boron carbon thin film alloys prepared by reactive radio-frequency plasma enhanced chemical vapor deposition, Thin Solid Films 528, (2013) 86-92.

[3] A. A. Ahmad and A. M. Alsaad, Adhesive B-doped DLC films on biomedical alloys used for bone fixation, Bull. Mater. Sci. 4, (2007) 301-308.

[4] H. Nakazawa, A. Sudoh, M. Suemitsu, K. Yasui, T. Itoh, T. Endoh, Y. Narita and M. Mashita, Mechanical and tribological properties of boron, nitrogen- coincorporated diamond-like carbon films prepared by reactive radio-frequency magnetron sputtering, Diamond Relat. Mater.19 (2010) 503-506.

[5] X. M. He, K.C. Walter and M. Nastasi, Plasma-immersion ion-processed boron-doped diamond-like carbon films, J. Phys.:Condens. Matter. 12, (2000) 183-189.

[6] M. Tan, J. Zhu, J. Han, X. Han, L. Niu and W. Chen, Stress evolution of tetrahedral amorphous carbon upon boron incorporation, Scripta Mater. 57, (2007) 141-144.

[7] M. Chhowalla, Y. Yin, G. A. J. Amaratunga, D. R. McKenzie and T. Frauenheim, Boronated tetrahedral amorphous carbon, Diamond Relat. Mater. 6 (1997) 207-211.

[8] M. Tan, J. Zhu, J. Han, W. Gao, A. Liu and Xiao Han, Raman characterization of boron doped tetrahedral amorphous carbon films, Mat. Res. Bull. 43 (2008) 453-462.

[9] T. Tsubota, T. Fukui, T. Saito, K. Kusakabe, S. Morooka and H. Maeda, Effect of total reaction pressure on electrical properties of boron doped homoepitaxial (100) diamond films formed by microwave plasma-assisted chemical vapor deposition using trimethylboron, Diamond Relat. Mater., Vol. 9, (2000) 1079–1082.

[10] M. Rusop, S. Abdullah, J. Podder, T. Soga and T. Jimbo, Effect of gas pressure on the boron doped hydrogenated amorphous carbon thin films grown by radio frequency plasma-enhanced chemical vapor deposition, Surf. Rev. Lett. 13 (2006) 7-12.

[11] Y. Aoki and N. Ohtake, Tribological properties of segment-structured diamond-like carbon films, Tribo. Int. 37 (2004), 941-947.

[12] M. Takashima, T. Kuroda, M. Saito, N. Ohtake, M. Matsuo and Y. Iwamoto, Development of antiwear shim inserts utilizing segment-structured DLC coatings, JSME Int J., Ser. A. 3(6) (2009), 841-852.

Advanced Materials Research Vol. 970 (2014) pp 128-131

doi:10.4028/www.scientific.net/AMR.970.128

RELATIONSHIP BETWEEN PRECURSOR GAS FLOW RATE WITH THE STRUCTURAL AND MORPHOLOGY PROPERTIES OF DIAMOND LIKE CARBON FILMS

Ong Wai Kit[1, a], Karim Deraman[1, b], Wan Nurulhuda Wan Shamsuri[1, c] and Jackie Chen Keng Yik[1, d]

[1]Phosphor Materials Research Group, Department of Physics, Faculty of Science, Universiti Teknologi Malaysia, 81310 UTM Skudai, Johor, Malaysia.

[a]derek_1220@hotmail.com, [b]karimderaman@utm.my, [c]wnurulhuda@utm.my and [d]chenjack6526@gmail.com

Keywords: Diamond like carbon (DLC) films; DC-PECVD; precursor gas flow rate; structural properties; morphology properties.

Abstract. Diamond like carbon (DLC) thin films were grown onto glass substrates by using direct current plasma enhance chemical vapour deposition (DC-PECVD) system. Films were deposited under fixed deposition pressure (4 x 10^{-1} Torr), substrate temperature (500 ^{o}C) and deposition time (3 hours) but with different flow rate of precursor gas (methane, hydrogen and argon). The fabricated films were characterized by using x-ray diffraction (XRD) and atomic force microscopy (AFM). XRD has revealed that the DLC films were having amorphous phase as the XRD spectrum did not show any obvious sharp peak. From AFM, it was discovered that the precursor gas flow rate has inversely relationship with the grain size and surface roughness of films.

Introduction

DLC films have captured attention from many fields due to its economical fabrication and environmental friendly application [1]. DLC films are greatly contributing in semiconductor, mechanical, optical, electronic and medical technology [2] with its unique physical and chemical properties such as chemical inertness, high hardness, and high optical transparency in visible and infrared regions, high electrical resistivity and good chemical stability [2]. Moreover, DLC films can exhibit the quality and properties which close to the diamond thin films yet easier and cheaper to be fabricated as compared to diamond thin films [2]. Low pressure plasma decomposition of hydrocarbon gases is preferred being used to deposit DLC films for industrial application [2]. In addition, DLC films deposition with mixed gas containing H_2, and hydrocarbon such as CH_4 is favourable chosen for plasma enhance chemical vapour deposition (PECVD) [3]. The objective of the present work is to study the relationship between precursor gas flow rate with the structural and morphology properties of DLC films.

Experimental Procedure

In this present work, DLC films were deposited with 1% methane (CH_4), 39% hydrogen (H_2) and 60% argon (Ar) by different flow rate. To start the deposition, a vacuum environment has to be created in the reactor chamber and nitrogen gas was introduced into reactor chamber for flushing. Then, the precursor gases will be controlled with the flow rate in the range between 0.2 l/min to 0.8 l/min with the deposition pressure of 4.0 x 10^{-1} Torr at 500 ^{o}C substrate temperature in 3 hours deposition time.

The structural properties of DLC films were characterized by using Bruker AXS D8 Advance x-ray diffractometer (XRD) and ND-MDT Ntegra Prima atomic force microscopy (AFM) was used to observe the surface morphology of the films.

Result and Discussion

XRD Analysis. Figure 1 shows the XRD pattern of DLC films deposited on glass substrate. It was clearly seen that the DLC films which deposited with 4.0 x 10^{-1} Torr deposition pressure at 500 ^{o}C by varying precursor gases from 0.2 l/min, 0.4 l/min, and 0.6 l/min to 0.8 l/min were in amorphous structure. DLC films are amorphous materials with carbon atoms bonded in maily sp^2 and sp^3 hybridizations [4]. It is made from random alternations between cubic and hexagonal lattices. The atoms have no long range order. Hence, DLC films have no fracture planes along which to break and very hard.

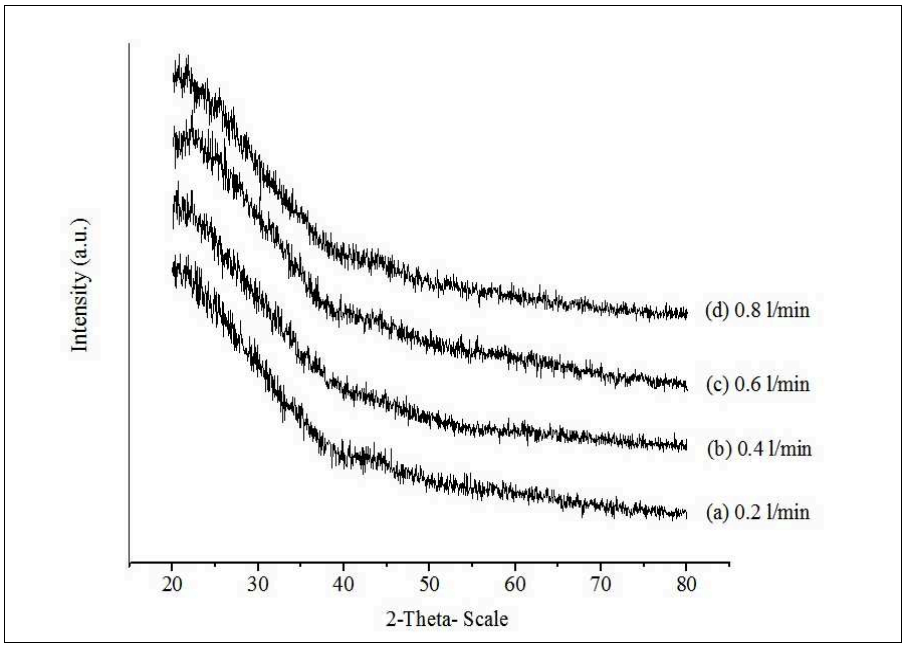

Figure 1 XRD pattern of DLC films grown at precursor gas flow rates (l/min) of:
(a) 0.2 (b) 0.4 (c) 0.6 and (d) 0.8

Surface Morphology Analysis. DLC films were deposited under various precursor gas flow rate and the surface morphology micrographs were shown in figure 2. Yang et al. and Won Seok Choi et al. have claimed that the RMS roughness will decrease with the increasing of methane flow rate [5, 6]. However, our work shows that the RMS roughness of DLC films was increasing from 0.961 nm to 3.059 nm respectively to the precursor gas flow rate from 0.2 l/min to 0.4 l/min. While the precursor gas flow rate was increased from 0.4 l/min to 0.8 l/min, the RMS roughness shown to be decreased from 3.059 nm to 1.749 nm.

This can be explained as the chemical effects allow the hydrogen atoms to form C-H bonds and etching of sp^2 carbon [7]. At precursor gas flow rate above 0.4 l/min, low reactivities between hydrogen molecules and carbon atom [7] cause the hydrogen molecules to evolve easily from the films surfaces due to the formation of voids in DLC films and result as degradation of surface morphology.

Moreover, our results obtained from AFM has shown that the grain size of films increased from 39.8 nm to 83.9 nm with the increment of precursor gas flow rate from 0.2 l/min to 0.4 l/min. X. Lu et al stated that low hydrogen flow rate will cause DLC grain size to be decreased because of the small DLC grains increase the electron conduction channels which facilitate the electron transport inside DLC films [8]. Conversely, while the precursor gas flow rate was increasing from 0.4 l/min to 0.8 l/min, the films grain size was decreasing from 83.9 nm to 25.6 nm as observed from AFM. This has been reported by T. Mikami who claimed that the higher the hydrogen gas ratio, the amount of hydrogen atoms in the plasma will be higher. Hence, the hydrogen atoms have the effect to improve the surface morphology of DLC films by decreasing its grain size and the surface of

films will become smoother [7]. As shown in figure 2, with the increment of precursor gas flow rate, the surface morphology of DLC films changed from faceted surface to be more ball type surface. This result is consistence with the research of Chen et al. [9].

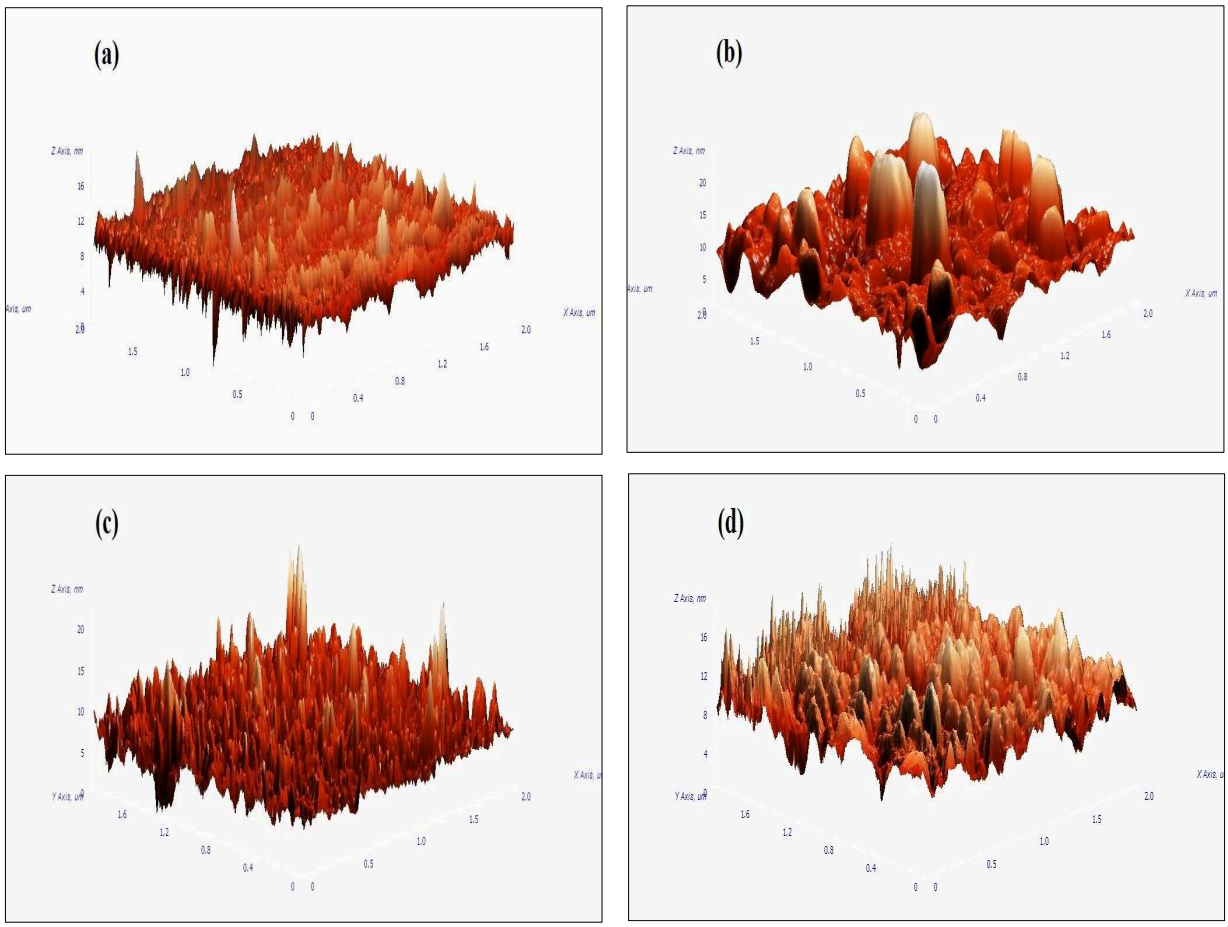

Figure 2 AFM surface morphology of the DLC films deposited at precursor gas flow rates (l/min) of: (a) 0.2 (b) 0.4 (c) 0.6 and (d) 0.8

Conclusions

In this paper we have reported the effect of precursor gas flow rate with the structural and morphology properties of DLC films deposited by DC-PECVD system. The results show that the variation of precursor gas flow rate has a significant influence on the structural, RMS roughness, grain size and surface morphology of the DLC films. XRD patterns of the DLC films exhibit that no obvious sharp peak of spectra and hence the amorphous structure of films can be identified. The RMS roughness and grain size of DLC films are decreasing as the precursor gas flow rate is increasing from 0.4 l/min to 0.8 l/min. AFM has revealed that the surface morphology of DLC films will become more ball type surface as the increment of precursor gas flow rate.

Acknowledgement

The authors gracefully acknowledge the technically support of Faculty of Science, UTM, the financial support from Ministry of Higher Education (MOHE) Malaysia, Universiti Teknologi Malaysia (UTM) under Vote RUG 09J53 for managing the grants.

References

[1] Dilip Chandra Ghimire, Sudip Adhikari, Hare Ram Aryal, Golap Kalit, Hideo Uchida, Masayoshi Umeno, Effect Of Process Parameter On The Properties Of Diamond Like Carbon Films Deposition By Microwave Surface-Wave Plasma CVD, Journal of IEEE, 2008.

[2] S. B. Singh, M. Pandey, R. Kishore, R. Ramaseshan, N. Chand, S. Dash, A. K. Tyagi, D. S. Patil, Mechanical Properties Of Diamond Like Carbon Coatings Prepared By Mircowave Electron Cyclotron Resonance Plasma Chemical Vapour Deposition Process, Journal of Physics, 114 (2008) 012044.

[3] J. Huran, N. I. Balalykin, A. A. Feshchenko, P. Bohacek, A. P. Kobzev, V. Sasinkova, A. Kleinova, B. Zat'ko, Plasma Enhanced Chemical Vapor Deposition Of Deuterated Diamond Like Carbon Films For Photocathode Application, International Symposium on Plasma Chemistry, 2013.

[4] Alfred Grill, Diamond-Like Carbon: State of the Art, Journal of Diamond and Related Materials, 8 (1999) 428-434.

[5] Q. Yang, S. Yang, Y. S. Li, X. Lu, A. Hirose, NEXAFS Characterization Of Nanocrystalline Diamond Thin Films Systhesized With High Methane Concentrations, Journal of Diamond and Related Materials, 16 (2007) 730-734.

[6] Won Seok Choi, Byungyou Hong, Synthesis And Characterization Of Diamond Like Carbon Protective AR Coating, Journal of the Korean Physical Society, 45 (2004) 864-867.

[7] T. Mikami, H. Nakazawa, M. Kudo, M. Mashita, Effectd Of Hydrogen On Film Properties Of Diamond Like Carbon Films Prepared By Reactive Radio Frequency Magnetron Sputtering Using Hydrogen Gas, Journal of Thin Solid Films, 488 (2005) 87-92.

[8] X. Lu, Q. Yang, C. Xiao, A. Hirose, Effects Of Hydrogen Flow Rate On The Growth And Field Electron Emission Characteristics OF Diamond Thin Films Synthesized Through Graphite Etching, Journal of Diamond and Related Materials, 16 (2007) 1623-1627.

[9] W. Chen, X. Lu, Q. Yang, C.Xiao, R. Sammynaiken, J. Maley, A. Hirose, Effects Of Gas Flow Rate On Diamond Deposition In A Microwave Plasma Reactor, Journal of Thin Solid Films, 515 (2006) 1970-1975.

Advanced Materials Research Vol. 970 (2014) pp 132-135

doi:10.4028/www.scientific.net/AMR.970.132

SURFACE PLASMA CHARACTERIZATION OF POLYIMIDE FILMS FOR FLEXIBLE ELECTRONICS

Huseyin Kizil[1,a*], M.O. Pehlivaner[1,b], Levent Trabzon[2,c]

[1]Istanbul Technical University, Department of Metallurgical and Materials Engineering, 34469 Maslak - Istanbul, Turkey

[2]Istanbul Technical University, Department of Mechanical Engineering, 34437 Gumussuyu - Istanbul, Turkey

[a]kizilh@itu.edu.tr, [b]pehivanerm@itu.edu.tr, [c]trabzonl@itu.edu.tr

Keywords: Flexible electronics, polyimide, plasma surface treatment

Abstract: Flexible electronics have drawn much attention due to vast application possibilities. Polyimide was the substrate of choice as a flexible substrate owing to its properties such as good mechanical strength, high temperature resistance, good dimensional stability, and low dielectric constant. The adhesion between metal and polymer substrate plays a crucial role for reliability of these applications and low adhesion was the cause for most failures. In this study, plasma surface treatments were applied on polyimide surface by inductively coupled plasma (ICP) treatment system. The results of contact angle measurements and atomic force microscopy (AFM) show a large increase in surface roughness with increasing treatment time. Complete wetting was found for both argon and oxygen plasma treatment. Analysis of chemical composition by FTIR reveals an increase in carbon-oxygen functional groups and the concentration of oxygen on the surfaces.

Introduction

Polyimide (PI) is the material of choice as a substrate for flexible electronics and Micro-Electro-Mechanical-Systems (MEMS). Silicon based MEMS are not appropriate for non-rigid or non-planar surfaces while flexible substrates can bend and twist so as to absorb the stress besides they provide low-cost and ease of fabrication. In literature, many studies can be found using PI substrates including flexible thin films transistor, flexible printed circuit boards, organic light emitting devices, photovoltaic devices, flexible MEMS systems, liquid crystal displays, flexible flat panels [1-11]. Flexible tactile sensors used as the fingertips or hands of robots in the area of medicine and industrial automation are among the most studied areas in flexible MEMS [2]. To improve the strength of the boundary layer between polyimide and metal, different types of treatments such as plasma [1,3,4], ion beam [5,6], or chemical treatment [7] were used. Different types of gases were used for surface treatment on PI materials; such as Kapton E and Upilex S [3,8,9]. Plasma surface modification has an enormous effect on surface energy on PI films. Nano scale surface roughness may decreases the contact angle by generating hydrophilic functional groups or increases the contact angle by generating hydrophobic functional groups on the surface [10].

Experimental

The surface of the PI substrates, Kapton TABE and Kapton HN, was cleaned with methanol in an ultrasonic water bath for 30 min and then dried in a vacuum oven at room temperature. The plasma modification was carried out in inductively coupled plasma system (ICP-DRIE). The reactor chamber was pumped down to a chamber pressure less than 50 mTorr by mechanical vacuum pump, then molecular pump was started to obtain desired low vacuum. Plasma gases of argon or oxygen were fed in to chamber at a flow rate of 30 sccm. As the chamber pressure stabilizes at 30 mTorr after gas flowing, the power of 40 W and 125 W was applied to top and bottom electrode. Surface treatment of PI films was carried out for 1, 3, and 5 min. The surface morphologies of the PI substrates were studied by AFM, an area of 4x4 μm was scanned using tapping mode. FTIR spectra was taken to obtain chemical bonding change.

Results and Discussion

The wettability of the PI films was evaluated by measuring the contact angle between the film surface and a DI water droplet, using KSV CAM200. An average of ten measurements with a standard deviation below 1 degree was obtained.

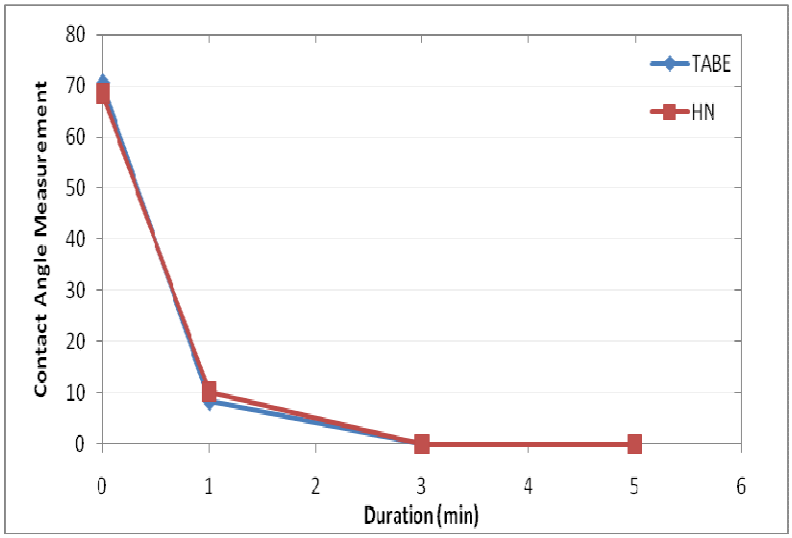

Fig. 1: Contact angle values of Ar plasma treated Kapton HN and Kapton TABE films as a function of time

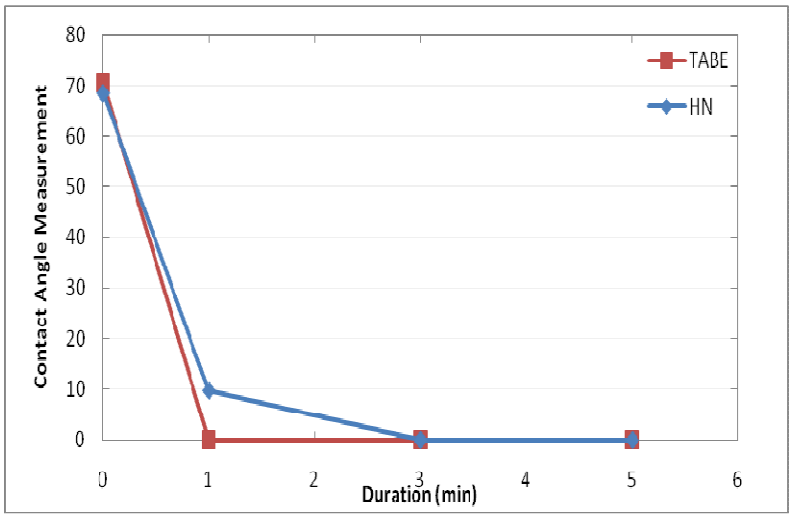

Fig. 2: Contact angle values of O_2 plasma treated Kapton HN and Kapton TABE films as a function of time

Figure 1 shows the measured contact angle values of Ar plasma treated Kapton TABE and Kapton HN films at top power of 40W, substrate bias power of 125W and gas flow rate of 30 sccm. While the contact angle of the untreated Kapton TABE was 70.55°, contact angle of Kapton TABE films was reduced to 8.37° after 1 min. of treatment. While the contact angle of the untreated Kapton HN was 68.55°, contact angle of Kapton HN films was reduced to 10.16° after 1 min. After 3 minutes of treatment, the contact angles for both films were reduced to 0°. Figure 2 shows the measured contact angle values of the O_2 plasma treated Kapton TABE and Kapton HN films. The contact angle value of Kapton TABE films was reduced to 0° after 1 min. of treatment. On the other hand,

the contact angle value of Kapton HN films was reduced 0° after 3 minutes. Figure 3 shows AFM image of the O2 treated Kapton TABE surface as a function of time. The RMS roughness values after 1, 3, and 5 min. of treatment were increased to 7.05, 18.96, and 28.55 nm, respectively. As the treatment time increases, the surface roughness increases, which attributed to more cross linking in the polyimide structure. Excessive treatment of the polyimide substrates under intense ion bombardment can induces the intensive chain scission and affects the adhesion strength negatively [11].

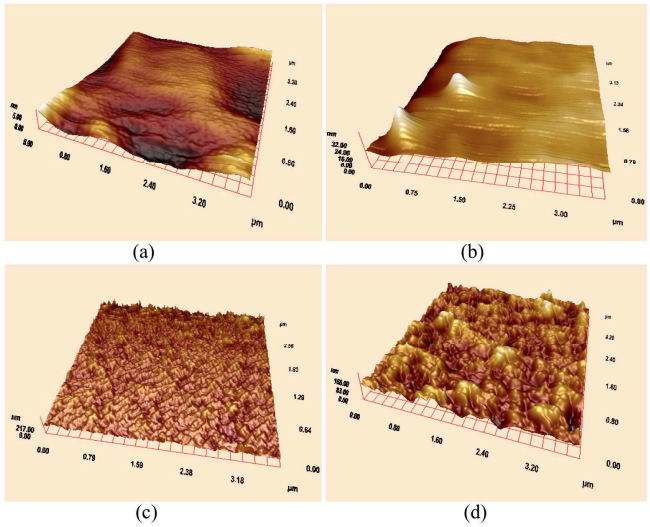

Fig. 3: AFM image of oxygen plasma treated Kapton TABE surfaces as a function of time: (a) untreated, (b) 1 min, (c) 3 min, (d) 5 min.

FTIR spectra of Ar plasma treated Kapton TABE films as a function of duration is shown in Figure 4. The bands observed around 717, 1083, 1238, 1350, 1500, 1707, 1774, were assigned respectively to the C=O bending, C-O-C stretching, C-O-C asymmetrical stretching, C-N stretching, aromatic C=C ring stretch, C=O symmetrical stretching and C=O asymmetrical stretching. The C=O bending and symmetrical stretching peaks at 717 and 1770 cm^{-1} and C-O-C stretching and asymmetrical stretching peaks at 1083 and 1238 cm^{-1} become stronger after 1 min. of treatment but become weaker with increasing time. C-N chemical bonds gives strong peaks (corresponding to 1350 cm^{-1}) after 1 min. and decreases with increasing time. New peaks were observed at 3485 cm^{-1} (O-H stretching) and 3746 cm^{-1} (N-H stretching) after 1 min. of treatment.

Summary

The results of contact angle measurements and atomic force microscopy (AFM) show a large increase in surface roughness with increasing treatment time. Complete wetting was found for both Ar and O_2 plasma treatment. Analysis of chemical composition by FTIR reveals an increase in carbon-oxygen functional groups and the concentration of oxygen on the surfaces.

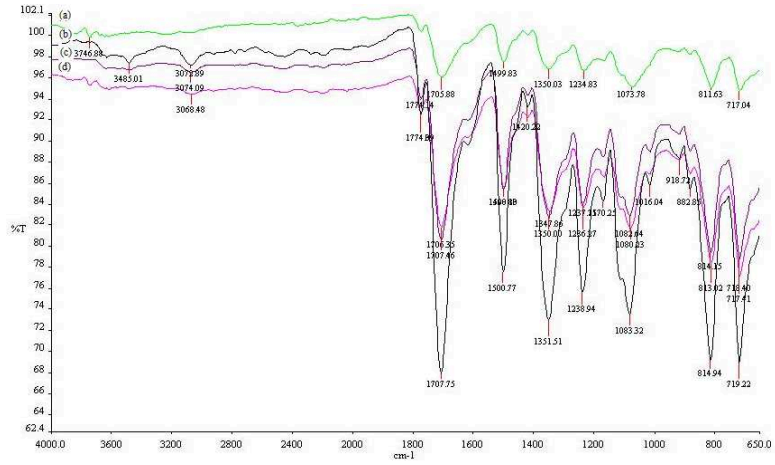

Fig. 4: FTIR spectra of Ar plasma treated Kapton TABE films as a function of time : (a) 5 min, (b) 1 min, (c) 0 min, (d) 3 min.

References

[1] S. H. Cho, S. H. Kim, N.-E. Lee, H. M. Kim and Y. W. Nam, Micro-scale metallization on flexible polyimide substrate by Cu electroplating using SU-8 photoresist mask, Thin Solid Films 475, (2005) 68-71.

[2] K. Kim, K. R. Lee, W. H. Kim, K.-B. Park, T.-H. Kim, J.-S. Kim, and J. J. Pak, Polymer-based flexible tactile sensor up to 32x32 micron arrays integrated with interconnection terminals, Sensors and Actuators A: Physical 156, (2009) 284-291.

[3] Y.-S. Lin and H.-M. Liu, Enhanced adhesion of plasma-sputtered copper films on polyimide substrates by oxygen glow discharge for microelectronics, Thin Solid Films 516, 1773-1780 (2008).

[4] D. L. Pappas, J. J. Cuomo, and K. G. Sachdev, Studies of adhesion of metal films to polyimide, J. of Vac. Sci. Technol. A 9 (5), (1991) 2704-2708.

[5] A. M. Ektessabi and S. Hakamata, XPS study of ion beam modified polyimide films, Thin Solid Films 377-378, 621-625 (2000).

[6] S. C. Park, S. S. Yoon, and J. D. Nam, Surface characteristics and adhesive strengths of metal on O2 ion beam treated polyimide substrate, Thin Solid Films 516, 3028-3035 (2008).

[7] N. Inagaki, S. Tasaka, and M. Masumoto, Improved Adhesion between Kapton Film and Copper Metal by Plasma Graft Polymerization of Vinylimidazole, Macromolecules 29, 1642-1648 (1996).

[8] Y.-S. Lin, H.-M. Liu, and H.-T. Chen, Surface modification of polyimide films by argon plasma for copper metallization on microelectronic flex substrates, J. Appl. Polym. Sci. 99, 744-755 (2006).

[9] Y.-S. Lin, H.-M. Liu, and C.-W. Tsai, Nitrogen plasma modification on polyimide films for copper metallization on microelectronic flex substrates, J. Polym. Sci. B Polym. Phys. 43, 2023-2038 (2005).

[10] S.-J. Park and H.-Y. Lee, Effect of atmospheric-pressure plasma on adhesion characteristics of polyimide film, Journal of Colloid and Interface Science 285, 267-272 (2005).

[11] S. H. Kim, S. W. Na, N.-E. Lee, Y. W. Nam, and Y.-H. Kim, Effect of surface roughness on the adhesion properties of Cu/Cr films on polyimide substrate treated by inductively coupled oxygen plasma, Surface and Coatings Technology 200, 2072-2079 (2005).

Advanced Materials Research Vol. 970 (2014) pp 136-139

doi:10.4028/www.scientific.net/AMR.970.136

UNDOPED DIAMOND-LIKE CARBON THIN FILMS GROWN BY DIRECT CURRENT-PLASMA ENHANCED CHEMICAL VAPOUR DEPOSITION: STRUCTURAL AND ELECTRICAL PROPERTIES

Jackie Chen Keng Yik[1,a*], Karim Deraman[1,b], Ong Wai Kit[1,c],

Wan Nurulhuda Wan Shamsuri[1,d], and Rosli Hussin[1,e]

[1]Phosphor Materials Research Group, Department of Physics, Faculty of Science, Universiti Teknologi Malaysia, 81310 UTM Skudai, Johor, Malaysia.

[a*]Chenjack6526@gmail.com, [b]karimderaman@utm.my, [c]derek_1220@hotmail.com, [d]wanhuda@dfiz2.fs.utm.my, [e]rbh@dfiz2.fs.utm.my

Keywords: Diamond-like carbon, Direct current-plasma enhanced chemical vapour deposition, amorphous carbon, Surface roughness, I-V characteristic measurement.

Abstract. Undoped diamond – like carbon thin films have been grown by DC - PECVD system. The synthesis of the DLC films was carried out in the presence of gas of (CH_4 + H_2 + Ar) in a custom – made reactor. The substrate temperature was initiated from the range of 300 ^{0}C to 600 ^{0}C under an optimum pressurized medium. The AFM image reveals that the optimization of DLC films growth at the substrate temperature 400 ^{0}C has a significant surface roughness and average grain size which is compatible to the result of film thickness measurement. The sample J400 shows an excellent nonlinear rectifying diode-like characteristic across the small potential difference.

Introduction

Diamond-like carbon (DLC) thin films have drawn a much attracted attention in the past two decades due to its remarkable unique and extraordinary properties. These films exhibit some of the important mechanical, electrical and optical characteristic which similar to the natural diamond and graphite. Those relatively characteristic involved such as their extreme hardness, high wear resistance, high electric resistivity, good thermal conductivity, optical transparency and chemical inertness [1-3] respectively. These characteristic is more or less correlated to the surface morphological studies of the DLC films which subjected to the film thickness, grain size, grain boundaries and r.m.s roughness. The typical amorphous nature of DLC thin films consisted of the high accessibility sp^3 matrix are divided variously into few categories: amorphous carbon (i-C), hydrogenated amorphous carbon (a-C:H) [4,5], tetrahedral amorphous carbon (ta-C) and amorphous conducting carbon (a-CC) [6] respectively. In this studies, a distinguished uniformity of sample was obtained by the customized DC-PECVD system which unlike to the other deposition method in previous research [7]. These rectified deposition reactor keen to produce a low cost of fabrication and high quality thin films in higher substrate temperature which varied from 300 ^{0}C to 600 ^{0}C. Several structural examination and electrical measurement were further presented in detailed.

Experimental

Diamond-like carbon (DLC) thin films were synthesized using a home-made Direct Current-Plasma Enhanced Chemical Vapour Deposition (DC-PECVD) system. The admission of the chemical gas mixture which according to the ratio of CH_4 (1%) + H_2 (39%) + Ar (60%) were introduced and the gas flow rate was controlled at 0.2 l/m respectively under the vacuum pressure of 8.0 x 10^{-2} Torr inside the reactor. The corning glass substrates with a dimension of 1.5 cm^2 were placed on the substrate holder or heater which connected to the power supply as well as thermocouple. The DLC films were grown in a different substrate temperature according from 300 ^{0}C to 600 ^{0}C at the deposition pressure of 4.0 x 10^{-1} Torr after been maintained for few minutes. Once the desired parameter was fixed, the DC voltage supply of ~800 V was altered to initiated the plasma reaction to cause the chemical reaction occur in the deposition compartment.

Scanning probe microscopy (SPM) with the model of NTEGRA Prima was employed in the examination of surface morphology in order to determine the atoms or structure surface profile. Film thickness measurement was carried out by using the surface profiler (Alpha-Step IQ) works as part to further study the structural properties.

The electrical properties of diamond – like carbon films were determined using a two-point probe station from (EVERBEING INT'L CORP) for the I-V characteristic measurement. The data such as the voltage range and the width of electrode were inserted into the system via its software.

Results and Discussion

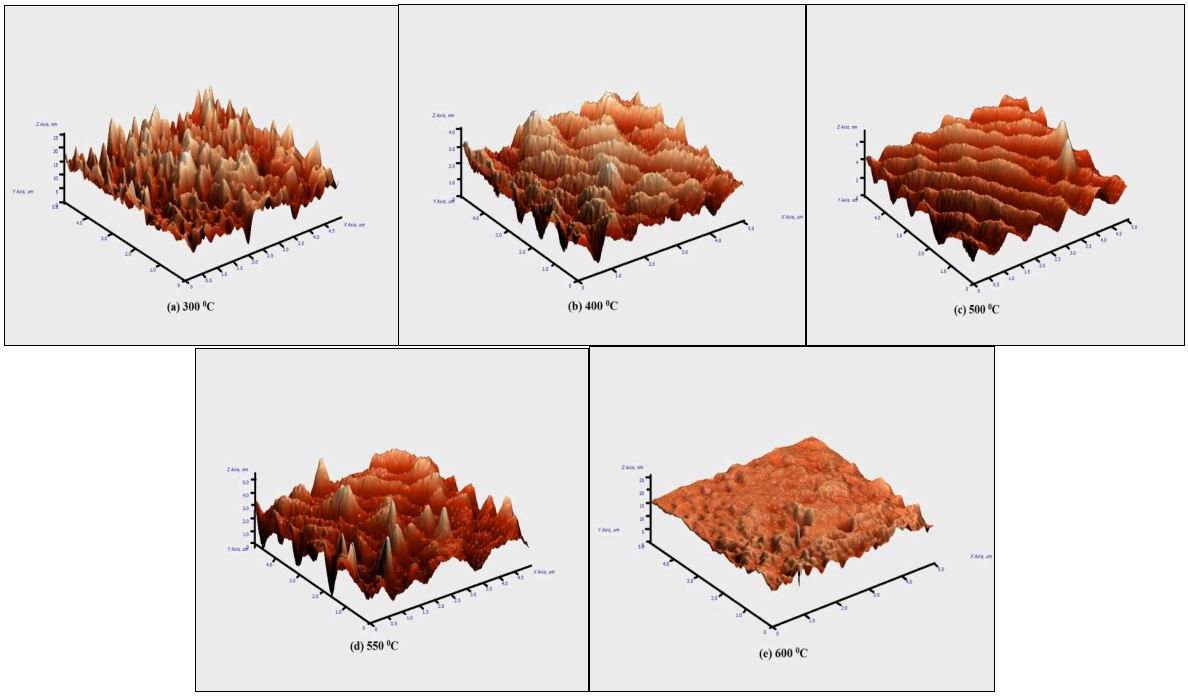

Fig. 1 The AFM image of DLC films deposited on corning glass at different substrate temperature.

Fig. 1 shows that the 3D surface roughness profile of DLC thin films growth in an ascending substrate temperature as 300 ^{0}C, 400 ^{0}C, 500 ^{0}C, 550 ^{0}C and 600 ^{0}C respectively. From the results, we can clearly observe that the obviously high surface roughness were presented at lowest substrate temperature 300 ^{0}C whereas the low surface roughness was observed at substrate temperature 400 ^{0}C. The appearance of the sharp mountain-like feature formed at the early stage of substrate temperature 300 ^{0}C deemed as the DLC structure (Rusop *et al.,* 2004) [9]. There are the plenty carbon clusters nucleated on the surface of DLC films that deposited at 300 ^{0}C and 400 ^{0}C. These can be explained by the sub-plantation model [10] which the carbon atom has low interstitial tendency and immobile for most substrate deposited at low substrate temperature. From fig. 1(c) and 1(d), it can be observed that the island begin to coalesce across the substrate temperature 500 ^{0}C to 550 ^{0}C on the films surface. These are due to high energy carbon atom sufficiently incorporated onto the films surface and hence induce the stress. The surface morphology of the film deposited at 600 ^{0}C, fig. 1(e) sculpts as a smoother surface. As a results, the thin films are encountered the stress among the structure without any medium to release. Therefore, the stress reduction mechanism was employed by refining the sp^3 bonding to sp^2 bonding during the deposition in nature (P.N Vishwakarma *et al*, 2005) [6,8]. Meanwhile, it also used to retain the disorder configuration of amorphous carbon and hence cause the film thickness to decreases.

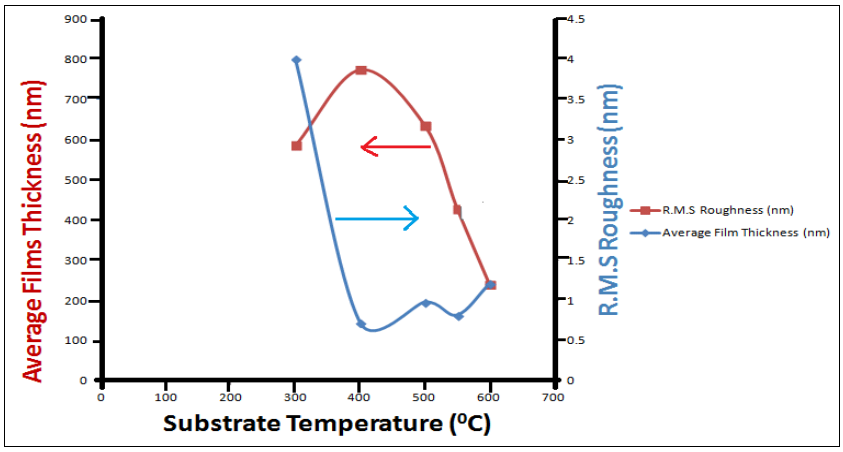

Fig. 2 The Average films thickness and R.M.S roughness VS substrate temperature.

Fig. 3 shows that I – V relationship of the DLC thin films across the area of cross-section at different substrate temperature. First of all, there are two different range of current density of DLC thin films were presented in the log data plot.

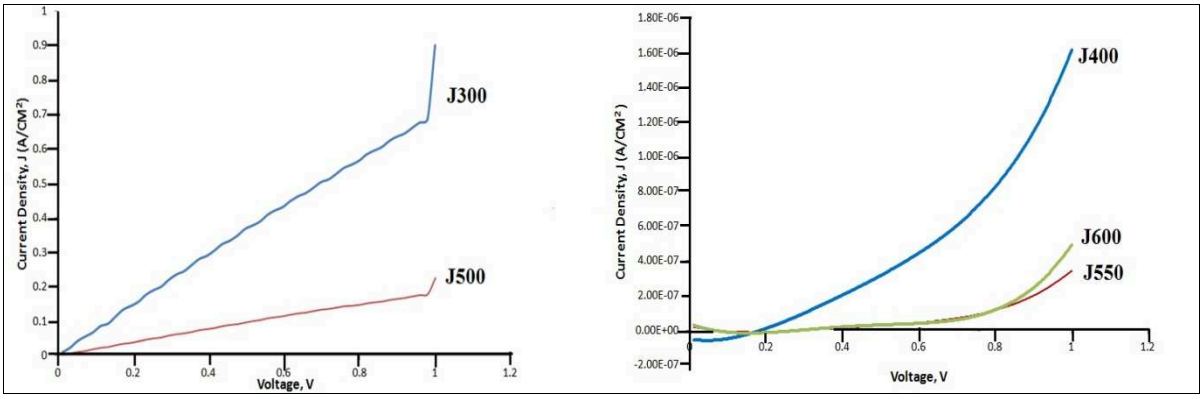

Fig. 3 The I – V characteristic of the DLC thin films deposited at different substrate temperature.

From the fig. 3, it ca be clearly seen that the ohmic behaviour is dominated in both of the sample J300 and J500 with small resistance and high resistance repectively. This could be explained and related to the surface morphology and film thickness obtained as we discussed. The sample J400 is illustrated as the metal-semiconductor junction with a nonlinear diode-like characteristic. Thus, the greater field emission properties is presented but the insight anomalies have to further study. The sample J550 and J600 show an adjacent current-voltage characteristic which exhibit the same fashion curve in the graph. Meanwhile, the existing saturated current of both sample are caused by the thermal effect which results the bulk diffusion to release the stress inside and hence cause the stigma to prevent the electrical current flow across the small potential drop.

Conclusion

The undoped diamond – like carbon (DLC) thin film were successively been fabricated in the optimum substrate temperature of 400 ^{0}C which is unraveled by the significant surface roughness and grain size in AFM image. Film thickness measurement provide a qualitative data which compatible to result, growth of DLC thin films in this optimum substrate temperature was presented while the issues of previous thickness analysis was affirmative. The current-voltage characteristic of DLC thin film was determined.

Acknowledgements

The authors gratefully acknowledgments the technically support of Faculty of Science, UTM, the financial support from Ministry of Higher Education (MOHE) Malaysia, Universiti Teknologi Malaysia (UTM) under vote RUG 09J53 for managing the grants.

References

[1] Da-Yung Wang, Chi-Lung Chang, Wei-Yu Ho, Oxidation behavior of diamond-like carbon films, Surface and Coatings Technology. 120-121 (1999) 138-144.

[2] Sam Zhang, Hong Xie, Xianting Zeng, Peter Hing, Residual stress characterization of diamond-like carbon coatings by an X-ray diffraction method, Surface and Coatings Technology.122 (1999) 219-224.

[3] A. Erdemir and C. Donnet, Wear: Materials, Mechanisms and Practice, G. W Stachowiak (Ed), New York: Wiley, 2006, pp. 191-209.

[4] Q. Wei, R.J.N., A. K. Sharma, J. Sankar, and J. Narayan, Preparation and mechanical properties of composite diamond-like carbon thin films. Vacuum, Surfaces, and Films, 6, 1999.

[5] Md. Kamrul Hassan, B.K.P.a.A.H., Electrical Resitivities of the Diamod-Like carbon Films Fabricated from Methane and Acetylene Using RF Plasma. New diamond and Frontier Carbon Technology, 16 (2006) 211-219.

[6] P N Vishwakarm et al, Structural morphology of amorphous conducting carbon film. Bull. Mat. Sci. 28 (2005) 609-615.

[7] P. Gupta, Synthesis, Structure and Properties of Nanolayered DLC/DLC Films, Engineering Science, 2003.

[8] A. Endemir and G. R Fenske, Tribological performance of diamond and diamondlike carbon films at elevated temperature, Tribol.Trans. 39(1996)787-794.

[9] M. Rusop, S. M. Mominuzzaman, T. Soga and T. Jimbo, Preparation and microstructure properties of tetrahedral amorphous carbon films by pulsed laser deposition using camphoric carbon target, Diamond and Related Materials 13:11-12(2004) 2174-2179.

[10] Lifshitz, Y. Lempert, G. D. Grossman, E. Avigal, I. Uzan-Saguy, C. kalish, R. Kulik, J. Marton, D.and Rabalais, J. W, Growth Mechanisms of Dlc Films From C+ Ions: Experimental Studies, Diamond and Related Materials. 4(1995) 318-323.

CHAPTER 7:

Concrete and Structural Materials

Advanced Materials Research Vol. 970 (2014) pp 143-146

doi:10.4028/www.scientific.net/AMR.970.143

Effects of Aggregate Size on Concrete Shear Strength

Lau Teck Leong[1a*], Chen Zhe[1b], Abdullahi Ali Mohamed[1c], and Choong Wee Kang[1d]

[1] Department of Civil Engineering, The University of Nottingham
Jalan Broga, Semenyih, 43500, Selangor, Malaysia.

[a*]TeckLeong.Lau@nottingham.edu.my, [b]keex2cze@nottingham.edu.my,
[c]Abdullahi.Ali@nottingham.edu.my, [d]Choong.WeeKang@nottingham.edu.my.

Keywords: Micro Concrete, Aggregate Size, Concrete Shear Strength.

Abstract. In view of the importance of the applicability of small-scale beam specimens in replicating the shear behaviour of prototype reinforced concrete structures, this study was conducted on beam specimens cast with micro-concrete having scaled aggregates (maximum sizes: 10mm, 5mm, and 2mm) to investigate whether the use of micro-concrete impose any reduction in their shear strength. The results indicate the maximum aggregate size(s) has negligible effects on concrete shear strength, and the micro-concrete beam specimens replicate the shear behaviour of normal concrete.

Introduction

Shear failure in reinforced concrete beam structures is a rupture failure mechanism that occurs at the vicinities of the supports. Since the introduction of reinforced concrete structures considerable amounts of works [1- 4] have been carried out on full /or large scale specimens to study their shear behaviour. In recent years, the use of small scale specimens, cast with micro-concrete, has become increasing popular due to their environmental and economical benefits.

However, despite the popularity of small scale specimens, the universal consensus on the scaling effects of micro-concrete cast with scaled aggregates has not been established. Different researchers [4-5] have adopted different scaling approaches in the use of micro-aggregates for casting of their micro-concrete specimens. As a result, it is unclear whether the results are applicable in replicating the shear behaviour of prototype beam structures.

In view of the importance of the applicability of scaled specimens in replicating the shear behaviour of prototype structures, attempt [6] have been carried out, via Mattock push off tests, to investigate the aggregate scaling effects on the shear behaviour of scaled concrete, $1/2^{nd}$ (max. 10mm), and $1/10^{th}$ (max. 2.36mm), with respect to the prototype conventional concrete (max. 20mm). It can be noted from the results that when concrete scaled to $1/10^{th}$ micro-concrete, the residual shear strength dropped to a level of about 70% of its peak as the shear displacement increases, while the peak shear strength of $1/10^{th}$ scaled micro-concrete remains at par with those of $1/2^{nd}$ and full scale concrete. The $1/2^{nd}$ scaled micro-concrete exhibited nearly identical stress-strain relationship with that of prototype concrete.

Although results of the recent works [6] indicate notable reduction in shear strength resulting from the use of $1/10^{th}$ scale micro-concrete through mattock push off tests, the reduced residual value only becomes applicable if the widths of the shear cracks exceed the displacement that coincided with the peak shear strength. Therefore, this study was conducted on beam specimens cast with micro-concrete having scaled aggregates (maximum sizes; 10mm, 5mm, and 2mm) to investigate whether the use of micro-concrete impose any reduction in their shear strength.

Methodology

A series shear tests were carried out on reinforced concrete beam specimens cast with scaled aggregates (maximum sizes: 10mm, 5mm, and 2mm) to determine if there are any variation or

reduction in their shear strength. Further discussions on the results are presented in the "Analysis of Test Results and Discussions" section below.

Tests setup: All tests were setup and carried out in accordance to standard testing procedures for compressive test and four points shear test. All beams spanned 900mm (centre to centre) between supporting rollers, and loaded via loading rollers spaced at 50mm apart. All loads applied via means of hand operated hydraulic jack, and increased at intervals of 4.21 kN until failures. Deflections (mid-span) and shear cracks (near supports) were recorded and marked after every load interval.

Specimen details: Eighteen cubes & nine beams were cast and tested in this research, of which, six cubes were casted along with every three beams that constituted of aggregates having maximum sizes of 10mm, 5mm, and 2mm, respectively. All cube specimens cast were of standard dimensions, 100mm x 100mm x 100mm, while, beam specimens were, 100mm x 200mm x 1500mm, reinforced with 2T16, as shown in Fig 1. All specimens were water cured after casting until the day of testing.

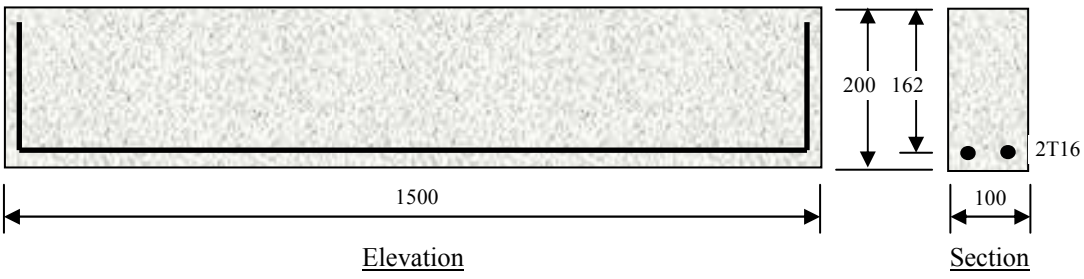

Fig 1. Details of beam specimen.

Aggregates: All aggregates were sieved and scaled in accordance to their intended scale(s) /or maximum size(s) of: 10mm, 5mm, and 2mm. In all cases, the aggregates were then remixed in accordance to their scaled sieve distributions, as shown in Fig 2.

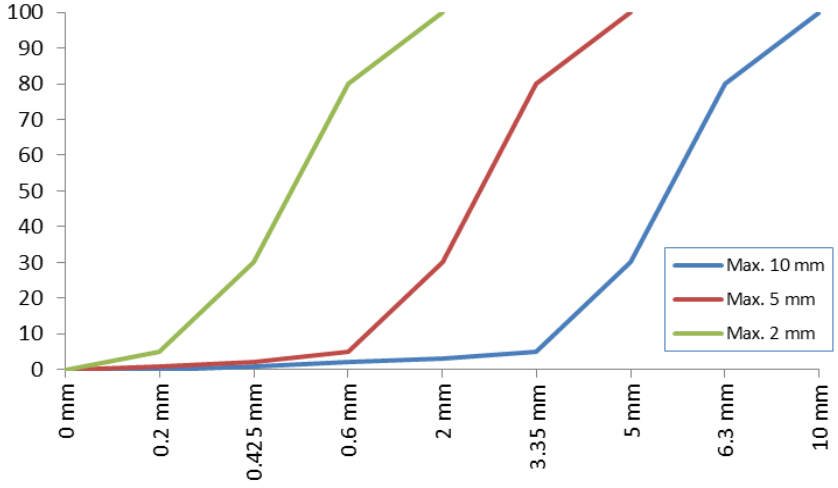

Fig 2. Aggregate sieve gradings.

Concrete Mixes: A standard concrete mix, with the aim to achieve a compressive strength (25 N/mm^2) was adopted. Details of the mix design are summarised and presented in Table 1.

Table 1 Concrete mix

Cement content (kg/m^3)	Scaled aggregates (kg/m^3)	Water-cement ratio (w/c)
600	1360	0.50

Analysis of Test Results and Discussions

The test results have been summarised and presented in Table 2. Each of the concrete cube strengths shown is the average value of six cube specimens.

Ultimate shear failure loads: In general, it can be noted that beams cast with micro-concrete having maximum aggregates, 10mm and 5mm, exhibited similar ultimate shear resistance, while those cast with 2mm maximum aggregates exhibited a 12.5% drop. However further investigation into these results revealed the observed drop in shear strength coincided with the drop (19.6%) in concrete strength. Hence, if taken account of the drop in concrete strength, which would incur a reduction in shear strength by the magnitude of power of a third thus resulting in a 9% drop in shear strength, the drop observed can therefore be expected.

Table 2: Failure loads of beam specimens

Beam no.	Ultimate shear failure loads, V_{ult} (kN), for beam specimen cast with;		
	Max. aggregate 10mm, f_{cu} = 25.30 N/mm^2	Max. aggregate 5mm, f_{cu} = 26.15 N/mm^2	Max. aggregate 2mm, f_{cu} = 20.32 N/mm^2
1	29.47 kN	33.68 kN	25.36 kN
2	33.68 kN	33.68 kN	31.58 kN
3	37.89 kN	29.47 kN	31.58 kN
Mean	33.68 kN	32.28 kN	29.47 kN

Although such results contradict to Wong's findings [6] where a 30% drop can be noted in the residual shear strength, the works were carried out on Mattock type tests that allowed for the post peak shear strength displacement (beyond 0.5mm) to be developed. Whilst, the shear displacement of a simply supported reinforced concrete beam, described in the current paper, are believed to take place within the displacement range (0 to 0.5mm) of the peak shear strength.

Initial shear cracking loads: The observed initial shear cracking loads are summarised and presented in Table 3. It can be noted that all beams exhibited similar initial cracking loads with respect to their ultimate failure loads, as shown in percentages within the brackets in Table 3.

Table 3: Observed cracking loads of beams

Beam no.	Observed cracking loads, V_{crack} (kN), for beam specimen cast with;		
	Max. aggregate 10mm, (% failure loads)	Max. aggregate 5mm, (% failure loads)	Max. aggregate 2mm, (% failure loads)
1	25.26 kN (86%)	25.26 kN (75%)	18.95 kN (75%)
2	25.26 kN (75%)	25.26 kN (75%)	23.16 kN (73%)
3	23.16 kN (61%)	25.26 kN (86%)	23.16 kN (73%)
Mean	24.56 kN (74%)	25.26 kN (79%)	21.75 kN (74%)

Mid-span deflections: Series of typical mid-span deflections under loads are presented in Fig 4. It can be inferred that beams cast with micro-concrete having maximum aggregates, 10mm and 5mm, exhibited similar initial cracking loads, while those cast with 2mm maximum aggregates exhibited a 11.5% drop. Such phenomenon is believed to be attributed to the lower concrete strength found in micro-concrete cast with 2mm maximum aggregates.

Further investigation into these load deflection curves revealed that, despite the drop in the initial cracking loads, a similar elastic-plastic load deflection relationship can be found between specimens cast with different maximum aggregate sizes (10mm, 5mm, and 2mm). With only a sharper change in angle (from elastic to plastic) noted in beams cast with 5mm micro-aggregates. Such similarity noted is believed to be attributed to the common elastic moduli found in the aggregates used for casting, which in turn, resulted in identical concrete elastic moduli in the beams.

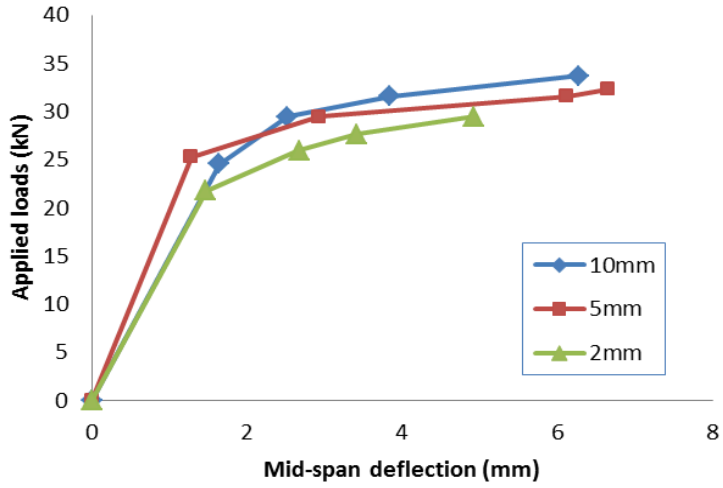

Fig 4. Load vs deflections.

Conclusions

The results of this study indicate similar shear behaviour between beams cast with concrete having different maximum aggregate sizes: 10mm, 5mm, and 2mm. In all cases, similar initial cracking loads with respect to the ultimate failure loads have been noted. In addition, similar mid-span load deflection relationships have also been noted, and are believed to be attributed to the similarities found in elastic moduli of the aggregates used.

The ultimate shear resistances are found to be comparable and exhibited only negligible reductions (up to 3.5%) as the maximum aggregate size reduces from 10mm to 2mm. It is believed that all beams failed in shear with their shear crack widths fall within the range associating to the peak of shear strength. As such, it can be concluded that the use of micro-concrete in simply supported beams replicates shear behaviour of prototype structures.

References

[1] Fenwick, R.C, and Paulay, T., *"Mechanism of Shear Resistance of Concrete Beams"*, Journal of the Structural Division, ASCE Vol.94, No. ST10, Proc. Paper 6167, Oct., 1968, pp2325-2350.

[2] Kennedy, R.P., *"A Statistical Analysis of the Shear Strength of Reinforced Concrete Beams"*, Technical Report No. 78, Department of Civil Engineering, Stanford University, April, 1967.

[3] Taylor, H.P.J., *"Shear Stresses in Reinforced Concrete Beams without Shear Reinforcement"*, Technical Report TRA 407, Cement and Concrete Association, London, England, Feb., 1968.

[4] Taylor, H.P.J., *"Shear Strength of Large Beams"*, Journal of the Structural Division, ASCE Vol.94, No. ST11, Proc. Paper 9329, Nov., 1972, pp2473-2490.

[5] Belgin,C.M., and Sener S., *"Size effect on failure of over reinforced concrete beams"*, Engineering Fracture Mechanics, 75 (2008), 2308-2319.

[6] Boswell L.F. and Wong S.S., *"The shear behaviour of micro-concrete and its inclusion in a proposed yield criterion"*, Proceedings of Cement and Concrete Association Research Seminar, 1981, pp 217-227.

Advanced Materials Research Vol. 970 (2014) pp 147-152

doi:10.4028/www.scientific.net/AMR.970.147

IMPROVING THE PROPERTIES OF OIL PALM SHELL (OPS) CONCRETE USING POLYVINYL ALCOHOL (PVA) COATED AGGREGATES

Chai W.W.S.[1,a], Teo D.C.L.[1,b*] and Ng C.K.[1,c]

[1]Faculty of Engineering, Universiti Malaysia Sarawak,
94300 Kota Samarahan, Sarawak, Malaysia.

[a]kyozchai@gmail.com, [b]tdelsye@feng.unimas.my (*corresponding author),
[c]ckng@feng.unimas.my

Keywords: compressive strength, water absorption, renewable resource, agricultural waste, structural lightweight concrete

Abstract. Recycling and reusing waste materials as aggregate replacement play an important role in solving issues associated with environmental problems and depletion of non-renewable resources. The use of these waste materials as aggregate is highly desirable as it can serve to sanitise the environment and create cheaper, renewable aggregates which will provide a double advantage as cost effective construction material and waste disposal at the same time. Hence, there is growing interest in this research area to promote safe and economical use of waste material as aggregate alternative in concrete. In Malaysia, where oil palm shell (OPS) is generated in abundance from the oil palm industry, reusing OPS as concrete aggregate replacement has been widely studied. Results from previous studies have shown that OPS concrete can be used in practical application as structural lightweight concrete. However, the properties of OPS can be further improved to achieve better performance of the resulting concrete. Polyvinyl alcohol (PVA) is a water-soluble synthetic polymer which is extensively used in all kinds of industries, such as papermaking, adhesive for plywood, printing and even in the construction industry as internal wall coating, plasterwork and joint sealing. It has been found that PVA has the potential to improve the quality of the OPS aggregates and hence enhance the resulting concrete properties. In this paper, an experimental program on concrete produced from PVA coated OPS aggregates is presented. The PVA treated OPS concrete was tested for slump, air-dry density, compressive strength, and water absorption. It was found that PVA treated OPS concrete had significant improvement in its compressive strength as compared to raw OPS concrete. It was determined that PVA treated OPS concrete can achieve 28-day compressive strength of up to 33.53 MPa. Moreover, it was also determined that there was a decrease of 0.67% in the water absorption of PVA treated OPS concrete as compared to the raw OPS concrete. In general, the investigation results showed that PVA can be used to improve the OPS concrete properties for the production of structural lightweight concrete.

Introduction

Due to environmental problems and depletion of non-renewable resources, there is a growing interest in the research area to promote safe and economical use of concrete produced from recycled wastes. The utilisation of these types of waste to produce "new" concrete is an alternative means for achieving a more environmentally friendly concrete as it provides a double advantage as cost effective construction material and waste disposal at the same time. Malaysia is the world's second largest palm oil producer producing more than 17 million tons of palm oil in year 2010 [1]. Subsequently, this has generated over 4.8 million tons of waste oil palm shell (OPS) in year 2010 which shows an increment of 0.8 million tons from 2006 [2]. This OPS waste is often disposed through incineration or left to rot in huge mounds. Consequently, this has caused a nuisance to the environment and become one of the main contributors to the nation's pollution problem. Moreover, due to rapid global development, the demand of raw materials for the production of concrete has increased intensely. Therefore, OPS as a renewable resource has high potential as an alternative to

the non-renewable stone aggregates in the concrete making industry. Exploitation of waste OPS as sustainable building material in the construction industry will not only fulfil the high demand of raw materials, but also helps to preserve natural resources and maintain ecological balance. To build environmentally sustainable structures, especially in developing countries such as in Malaysia, the possibility of using OPS waste as construction materials will be highly desirable and has several practical and economic advantages.

Many studies have demonstrated the feasibility of using OPS as concrete coarse aggregates [2-8]. Promising results from these studies have shown that OPS concrete can be used in practical applications as structural lightweight concrete. However, the properties of OPS can be further improved to achieve better performance of the resulting concrete. Polyvinyl alcohol (PVA) is a water-soluble synthetic polymer which is widely used in all kinds of industries, such as papermaking, adhesive for plywood, printing and even in the construction industry as internal wall coating, plasterwork and joint sealing. Research has shown that PVA has the capability to improve the properties of OPS aggregate and hence enhance the resulting concrete properties [7]. Therefore, PVA has a great research potential to be used in enhancing the quality of OPS aggregate and further investigations are required to confirm its improvement in the resulting concrete.

The objective of this paper is to investigate the engineering properties of PVA treated OPS concrete namely the slump, fresh and air-dry density, compressive strength and water absorption.

Materials

Locally available raw materials were used in this study which consists of OPS as coarse aggregate, river sand as fine aggregate, ordinary Portland cement, Type-F PolyCaboxylic Ether (PCE) based superplasticiser and portable water. The river sand used in this study has a maximum grain size of 1.18 mm and a specific gravity of 2.44. The OPS used in this study was divided into two categories namely raw OPS and treated OPS. The treated OPS was prepared in the laboratory using 20% PVA solution. They were both used to fully replace conventional stone aggregates in the concrete. During material preparation, the collected OPS from a local oil palm mill was first exposed to natural weathering for 1 – 2 weeks to remove any surface oil coating and only OPS with particle size distribution between 5 to 14 mm was used for mixing. The particle size distribution of the OPS aggregate is shown in Fig. 1 while the properties are presented in Table 1.

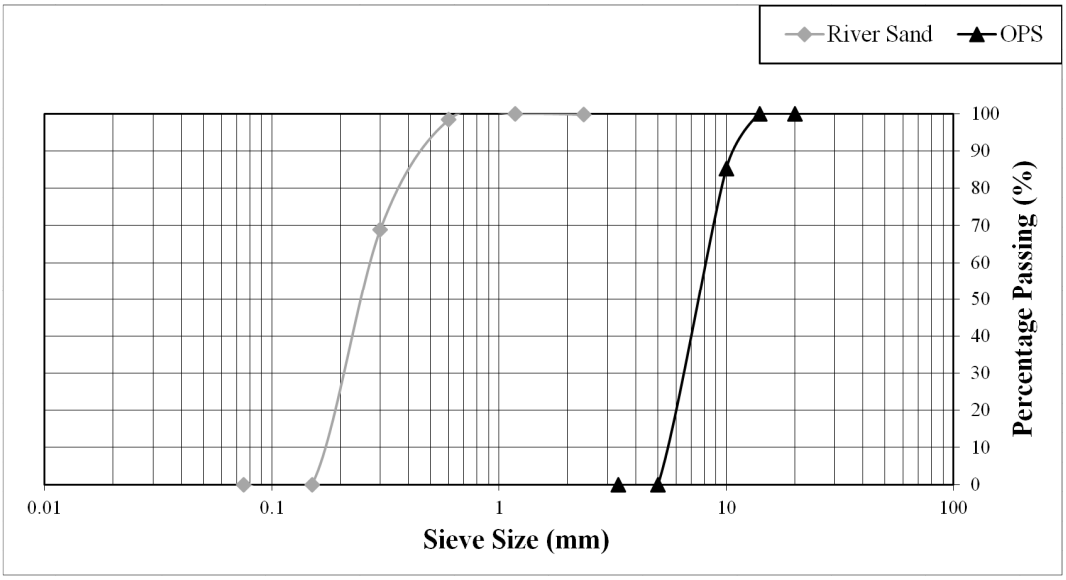

Fig 1: Gradation curve of river sand and OPS.

From the comparison in Table 1, it is observed that PVA treated OPS has noticeable improvement especially in its aggregate crushing value and water absorption. More specifically, PVA treated OPS has an improvement in aggregate crushing value of up to 6.1%, whereas the water absorption for PVA treated OPS shows 18.85% improvement as compared to the raw OPS. It has been mentioned that for good quality aggregates to be used in structural applications, the water absorption is usually not more than 15% [9]. Although PVA treated OPS has shown improvements in its water absorption, the water absorption is still more than 10%. Therefore, in order to control both raw and PVA treated OPS aggregate from absorbing additional water content during the concrete mixing, they are mixed in saturated surface dry (SSD) state [9].

Table 1: Properties of aggregates used.

Properties	Raw OPS	PVA Treated OPS
Maximum grain size [mm]	12.5	12.5
Shell thickness [mm]	0.4 – 3.0	0.5 – 3.2
Specific gravity	0.90	1.03
Bulk unit weight [kg/m^3]	393	403
Fineness modulus	6.15	6.15
Aggregate crushing value [%]	8.27	2.17
24 hour water absorption [%]	32.91	14.06
Natural moisture content [%]	13.72	7.51

Concrete Mix Proportion. There is no standard mix design procedure for OPS aggregate concrete. Hence, ACI Committee 211 [10] for natural aggregate was used as a guideline to determine the preliminary mix proportion for PVA treated OPS concrete. Subsequently, modifications of trial mixes were made to achieve a practical end result. The optimum mix proportion consisted of 550 kg/m^3 cement, 897 kg/m^3 river sand, 252 kg/m^3 PVA treated OPS and 201.4 kg/m^3 water with a free water/cement ratio of 0.37. The cement content used was within the range for lightweight concrete [11]. The superplasticiser used in this study was added according to the recommended concentration range [2] of 1.4 litres/ 100 kg cement. The mix proportion was in the order of 1:1.63:0.46 (C:S:OPS) by weight. The optimum mix proportion was used throughout the entire investigation. For comparison, a mix containing raw OPS was prepared with the same mix proportions.

Specimens Casting and Testing. Thirty six standard 100 mm raw and PVA treated OPS concrete cube were cast. The specimens were cured in water (temperature ranging of 26 – 28 ºC) until testing commenced. Only specimens for the 28-day air-dry density testing were left in air-dry condition. Several tests were conducted to determine the engineering properties of the raw and PVA treated OPS concrete. All tests were carried out according to the provisions of the relevant British Standards as shown in Table 2.

Table 2: British Standards followed in the experimental work.

Test Description	Specification
Concrete mixing and sampling	BS 1881 – 125 [12]
Slump	BS 1881 – 102 [13]
Density (fresh concrete)	BS 1881 – 107 [14]
Density (hardened concrete)	BS 1881 – 114 [15]
Compressive strength	BS 1881 – 116 [16]
Water absorption	BS 1881 – 122 [17]

Experimental Results and Discussion

Slump and Density. The fresh concrete properties of raw and PVA treated OPS concrete are presented in Table 3. The slump of PVA treated OPS concrete is observed to be slightly higher than that of raw OPS concrete. This could be due to the additional coating of PVA which caused the surface of treated OPS aggregate become smoother than the raw OPS aggregate. Similar trends were reported by [7] and [8]. Both slump had a medium degree of workability and was within the workable concrete range of 25 mm – 75 mm [10]. In general, both OPS concretes can be classified as lightweight concrete as their 28 days air-dry densities were less than 2000 kg/m^3 [18].

Table 3: Fresh concrete properties of raw and PVA treated OPS concrete.

	Slump	Fresh Concrete Density (kg/m^3)	28 Days Air-Dry Density (kg/m^3)
Raw OPS concrete	50	2052.3	1932.3
PVA treated OPS concrete	55	2046.8	1950.0

Compressive Strength. Fig. 2 shows the compressive strength test results at 3, 7 and 28 days for raw and PVA treated OPS concrete. It was observed that PVA treated OPS concrete had a higher compressive strength as compared to raw OPS concrete where its 28 days compressive strengths reached 33.53 MPa. There is an improvement of 15.22% in PVA treated OPS concrete compressive strength. At 7 days, the compressive strength of PVA treated OPS concrete almost achieved the 28 days compressive strength of raw OPS concrete which presents promising results. Overall, raw and PVA treated OPS concrete meet the minimum required strength of 17 MPa for structural lightweight concrete [18].

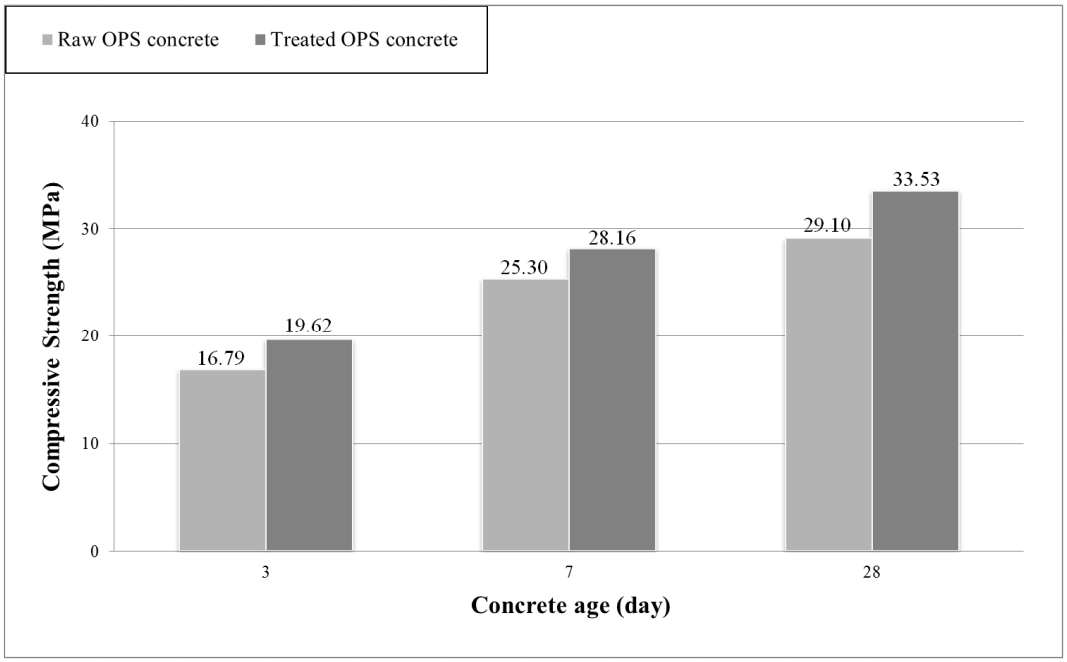

Fig. 2: Compressive strength of raw and PVA treated OPS concrete.

Water Absorption. Water absorption is an important key indicator to determine the durability of hardened concrete. Reduction in water absorption can significantly improve the long-term performance and service life of concrete under aggressive service environments. Although water absorption cannot be used to examine the quality of concrete, most good concretes have water

absorption of below 10% by mass [9]. Fig. 3 shows the results of raw and PVA treated OPS concrete at 7 and 28 days of age. A comparison was made between raw and PVA treated OPS concrete and it was observed that PVA treated OPS concrete has lower water absorption compared to raw OPS concrete. At 28 days, PVA treated OPS concrete registered an improvement of up to 32.06% as compared to the raw OPS concrete. Besides that, Fig. 3 also shows that as the concrete age increases, with the development of concrete ages, there is a higher reduction in water absorption for PVA treated OPS concrete as compared to raw OPS concrete. These experimental results indicated the significant effect of treated OPS with PVA towards reduction of water absorption in the resulting concrete and consequently enhancing the durability of the concrete.

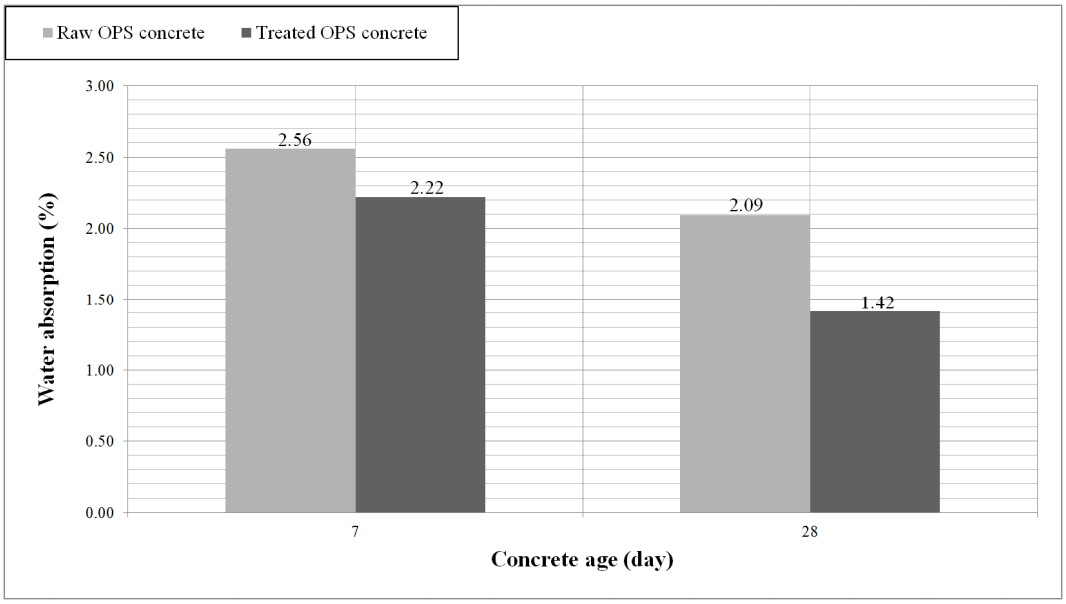

Fig. 3: Water absorption of raw and PVA treated OPS concrete.

Conclusions

From the current experimental investigation, it was observed that the 20% PVA treated OPS concrete showed significant improvement in its compressive strength and water absorption properties as compared to raw OPS concrete. More specifically, PVA treated OPS concrete exhibited a 15.22% improvement in compressive strength as compared to raw OPS concrete. On the other hand, the 28 days water absorption of raw and PVA treated OPS concrete were 2.09% and 1.42% respectively which shows a 32.06% improvement. This investigation gives encouraging results for PVA to be used to improve the OPS concrete properties.

Acknowledgements

This project is funded by Osaka Gas Foundation in Cultural Exchange (OGFICE) Research Grant Scheme. The authors would also like to thank Universiti Malaysia Sarawak (UNIMAS) for providing financial support to present these findings.

References

[1] Malaysian Palm Oil Board, Overview of Malaysian oil palm industry 2010 [online], 2011, Available from: http://econ.mpob.gov.my/economy/Overview%202010_final.pdf.

[2] D.C.L. Teo, M.A. Mannan and V.J. Kurian, Structural concrete using Oil Palm Shell (OPS) as lightweight aggregate, Turkish Journal of Engineering and Environmental Sciences, 30 (2006) 251-257.

[3] D.C.L. Teo, M.A. Mannan and V.J. Kurian, Flexural behaviour of reinforced lightweight concrete beams made with Oil Palm Shell (OPS), Journal of Advanced Concrete Technology, 4 (2006) 1-10.

[4] M.A. Mannan and C. Ganapathy, Concrete from an agricultural waste-Oil Palm Shell (OPS), Building and Environment, 39 (2003) 441-448.

[5] D.C.L. Teo, M.A. Mannan, V.J. Kurian and I. Zakaria, Flexural behaviour of lightweight OPS concrete beams, Proceedings of the 9th International Conference on Concrete Engineering & Technology, Malaysia, (2006) 244 - 252.

[6] D.C.L. Teo, M.A. Mannan, V.J. Kurian and C. Ganapathy, Lightweight concrete made from oil palm shell (OPS): Structural bond and durability properties, Building and Environment, 42 (2007) 2614-2621.

[7] M.A. Mannan, J. Alexander, C. Ganapathy and D.C.L. Teo, Quality improvement of Oil Palm Shell (OPS) as coarse aggregate in lightweight concrete, Building and Environment, 41 (2006) 1239-1242.

[8] C.W. Lim, Engineering properties of concrete with PolyVinyl Alcohol (PVA) treated Oil Palm Shell (OPS) aggregates, Bachelor Thesis, Faculty of Engineering, Universiti Malaysia Sarawak, 2010.

[9] A.M. Neville, Properties of concrete, Pearson Education Limited, England, 1995.

[10] ACI Committee 211, Standard practice for selecting proportions for normal, heavyweight, and mass concrete, American Concrete Institute, U.S.A, 2002.

[11] S. Mindess, J.F. Young, D. Darwin, Concrete, 2nd edition, Prentice Hall, USA, 2003.

[12] BS 1881-125, Methods for mixing and sampling fresh concrete in the laboratory, British Standards Institution, London, 1986.

[13] BS 1881-102, Method for determination of slump, British Standards Institution, London, 1983.

[14] BS 1881-107, Method for determination of density of compacted fresh concrete, British Standards Institution, London, 1983.

[15] BS 1881-114, Methods for determination of density of hardened concrete, British Standards Institution, London, 1983.

[16] BS 1881-116, Method for determination of the compressive strength of concrete cubes, British Standards Institution, London, 1983.

[17] BS 1881-122, Method for determination of water absorption, British Standards Institution, London, 1983.

[18] ACI Committee 213, Guide for structural lightweight-aggregate concrete, American Concrete Institute, U.S.A, 2003.

CHAPTER 8:

Material Modeling and Simulations

Advanced Materials Research Vol. 970 (2014) pp 155-165

doi:10.4028/www.scientific.net/AMR.970.155

Development of Rapid Tooling for Investment Casting using Fused Deposition Modeling Process

Addanki Sambasiva Rao[1,a*], Medha A Dharap[1,b], J V L Venkatesh[2,c]

[1]Department of Mechanical Engineering, Veermata Jijabai Technological Institute, Mumbai, India.
[2]Production Engineering Department, Shri Guru Gobind Singhji Institute of Engineering & Technology, Nanded, Maharashtra, India.
[a*]asrao@vjti.org.in, [b]madharap@vjti.org.in, [c]meghavenkatesh@gmail.com

Keywords: Chemical Treatment Process, Fused Deposition Modeling, Silicone Rubber Moulding, Rapid Tooling, Feasibility of FDM Tooling

Abstract. Fused Deposition Modeling (FDM) process can be used to produce the rapid tooling directly or indirectly. However, rapid tooling application demands good surface finish since the poor surface finish of FDM parts has become a limitation for its tool application. So there is need to improve the surface finish of FDM made tools. In this study, surface roughness of FDM tools are drastically reduced by a post processing technique called chemical treatment process. Surface finish was improved by filling the gap between layers by diffusion of parent material. Thus FDM made tools can be used as direct as well as indirect tools after the chemical treatment. Comparative study was made between Silicon Rubber Moulding and FDM Tooling towards the cost, time, life of mould, quality and feasibility aspects. It was found that FDM tooling is more economical, easy to use, reduced cycle time, improved quality, long life of mould and more feasibility towards complex parts etc.

Introduction

In today's modern manufacturing industry the cycle time taken to produce the product is important along with the part quality. 'Rapid Tooling (RT)' is one of the prominent applications of Rapid Prototyping. RT is an attempt to make the tools rapidly to produce the parts from these tools. The rapid tools like "moulds, patterns and inserts etc." are produced using additive processes which reduces the time and cost drastically. The application of this new technology reduces the number of design iterations as well testing trials required before introducing a new product in to the market. The rapid tooling can be mainly divided into two types i.e. Direct Tooling and Indirect Tooling. In direct tooling the pattern or mould is made directly from CAD data and used for actual production of the parts where as in indirect tooling patterns are made from CAD data and are used as master pattern to produce moulds through which actual production of the parts is obtained like in silicone rubber moulding and epoxy resin moulding etc. The silicone rubber moulding is widely used as indirect tool in Investment Casting(IC).The IC is one of the most economical ways to produce quality and complex parts. The quality of IC parts mainly depends on quality of master patterns produced by rapid prototyping process. So it has become necessary to study the quality behavior of tooling produced by various rapid prototyping processes.

Out of the available RP processes, FDM (Fused Deposition Modeling) RP process has become more popular because it has benefits such as its a clean, easy and economical process and its parts are stronger compared to other RP process like SLA, 3D printing etc. But surface roughness is high in FDM parts due to the stair case effect, the surface roughness is the main limitation of FDM process for its use as a tool.

In literature various researchers have carried out several studies to improve the surface finish, in one of such studies the authors[1] have applied metal paint on surface of the FDM tool but it was observed that the metal paint cannot cope with wax pattern temperature which is about 80ºC even though it has shown good thermal conductivity. Similar research[2] was carried out to improve surface of FDM tools by using thin coat of polymer solution followed by providing light sanding using abrasive paper. In this method light sanding using abrasive paper was carried out manually

and requires skill. One more study [3] the authors of this present study had applied post processing technique i.e. optimized chemical treatment process technique to improve surface finish of FDM parts. The authors [4] have applied different methods to improve surface finish of FDM parts. It is also necessary to evaluate performance of rapid tooling fabricated from various rapid prototyping processes. Most of such studies have proved that master patterns fabricated from rapid prototyping can be burnt out without any significant residual ash for investment casting. One of such methods is direct tooling method in which the authors have evaluated the quality characteristics of various RP patterns that were fabricated by various RP processes such as 3D Printer (3DP), Fused Deposition Modeling (FDM) and Multijet Modeling (MJM). Their results showed that FDM and MJM processes were superior in terms of mould cleanliness since no residual ash was observed during the burn out stage. Significant oxidation of ceramic powder was observed on the moulds of the 3DP patterns which need to be removed manually from the moulds. So they had recommended that FDM and MJM are only suitable RP process for master patterns to be burn out. Another study on investment casting using FDM made patterns, the authors[5] have used two types part building methods i.e. Hollow and Solid. They have compared both the methods with respect to dimensional accuracy, collapsibility and distortion characteristics of FDM built parts. Results of their study revealed that the hollow pattern built parts are much better than solid pattern built parts in terms of dimensional accuracy and collapsibility point of view. The solid pattern built parts are much better than hollow pattern built parts while considering less distortion aspects i.e. the hollow pattern built parts show 33.11% higher distortion than solid pattern built parts. This study also proved that ABS-P400 material was more feasible to be used as an investment casting pattern material.

In RT, all of the forming stages influence the dimensional accuracy of the die. The forming stages include slicing the CAD model to the STL file, making the prototype using an RP machine and obtaining the ceramic mould and transforming the ceramic mould to a metal die.

In an attempt to study the dimensional accuracy of the rapid tool, the authors[6] developed non linear coupled thermo-mechanical analysis for solidification process of transforming the ceramic mould to a metal die. In [7] the authors further automated the RT process by avoiding preparation of CAD model, instead of preparing CAD model they have used direct 3D digitizing which a reverse engineering(RE) method and obtained point cloud data. This point cloud data was used directly to prepare RP tool and also they analyzed RP tool for by finite element analysis (FEA), to assure the metrological accuracy of tooling geometry and optimization of foundry process parameters. The method of electro less plating for obtaining patterns with high level of electrical conductivity and finishing was suggested by authors[8] in this method different behavior of ABS FDM parts has been found in terms of metalizing procedure. To improve the surface finish the researchers [9] focused to develop appropriate deposition scheme and adaptive slicing. Authors [10] suggested the use of adaptive slicing to overcome the stair case effect problem in FDM process. In [11] authors suggested need of analysis of variety of factors to improve parts precision, those factors are extrusion temperature, envelope temperature, extrusion velocity, filling velocity, orientation, slicing thickness, filament-width compensation, and delay time etc.

In continuation of study done by authors [3], the present study is focused on improvement of surface finish of FDM tools using chemical treatment technique which is economical and safer process. By using present study the FDM process can produce tools (moulds & patterns) which can be used as a manufacturing tool after applying appropriate chemical treatment on FDM tools to produce wax patterns.

Methodology

FDM parts are used to produce direct tooling by using burnout process; however no significant efforts to use these FDM parts as a direct tool in form of mould for producing wax patterns have been made. The FDM moulds have a higher life as compared to the rubber moulds produced by existing process silicone rubber moulding. However the surface roughness associated with the FDM

parts make it less suitable for using it as a direct tool. Also the wax gets trapped in the layer to layer gap and hence the removal of the wax pattern without damaging the pattern is not possible. Here the authors have made an effort to produce FDM moulds and used the existing chemical treatment process[3] for reducing the surface roughness so that it can be used as direct tooling in place of metal moulds which are made by SLS, DMLS etc., rapid prototyping processes.

The benefits of the FDM direct tools are :

- No intermediate process required (like SLA patterns in case of silicone rubber moulding or RP patterns for producing metal tools) and tools can be made directly from CAD data.
- Time saving as intermediate step of pattern making is not required.
- Tools produced from FDM are stronger, economical, easy to manufacture and have longer life than current silicone rubber moulding.
- Complicated parts which are not possible to be made using silicone rubber moulding are possible using FDM.

For the validation of the process a number of criteria are selected and two different case studies are taken. These are then evaluated for the performance of the FDM direct tool and the IC patterns produced. The following are the selected criteria :

- Cost associated for fabrication of FDM tool and post processing.
- Time required for tooling design and manufacturing the tool.
- Life of the tool and reusability options.
- Surface finish and dimensional accuracy of the FDM tool.
- Quality (surface finish and dimensional accuracy) of the wax patterns produced.

Two case studies were taken for the validation and performance evaluation, Case study-1 is *Fork* which is a gear box component used in the tractor, as shown in Figure1. Case study-2 selected is a *Pump Impeller* as shown in Figure 2. Tooling for parts like 'impeller' which have such a complex internal features is not possible using silicone rubber moulding hence to verify the effectiveness of FDM direct tool it is a best suited component for case study.

Case Study-1: In case study-1 various attempts were made to use FDM moulds as direct tools. The problems were analyzed after every attempt and finally the relevant solution was adopted.

Attempt-1: In the first attempt mould for the fork part was designed with a shrinkage allowance of 1.4% and other allowances and features were modeled into the mould. The mould was then manufactured using Stratasys Dimension SST 1200(At Technical Excellence centre, Department of Mechanical Engineering, VJTI Mumbai, India). Figure 3 shows CAD model of the fork mould and the same mould was used to fabricate FDM mould and then to produce wax patterns for investment casting. Figure 4 (a) & (b) show the wax pattern produced.

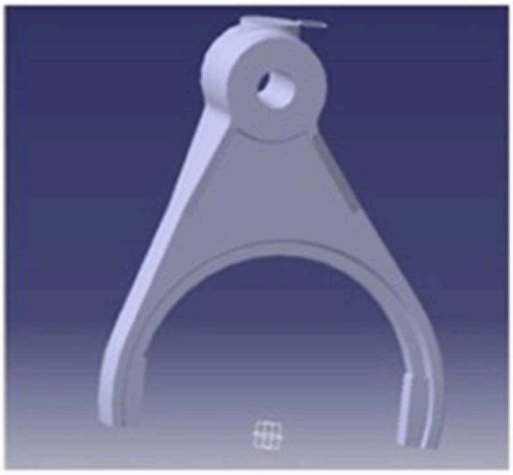

Fig.1-CAD model of Fork (Case study-1)

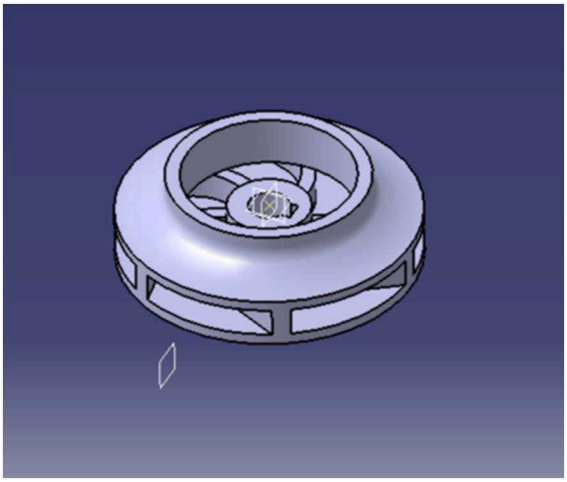

Fig.2-CAD model of Pump Impeller (Case study-2)

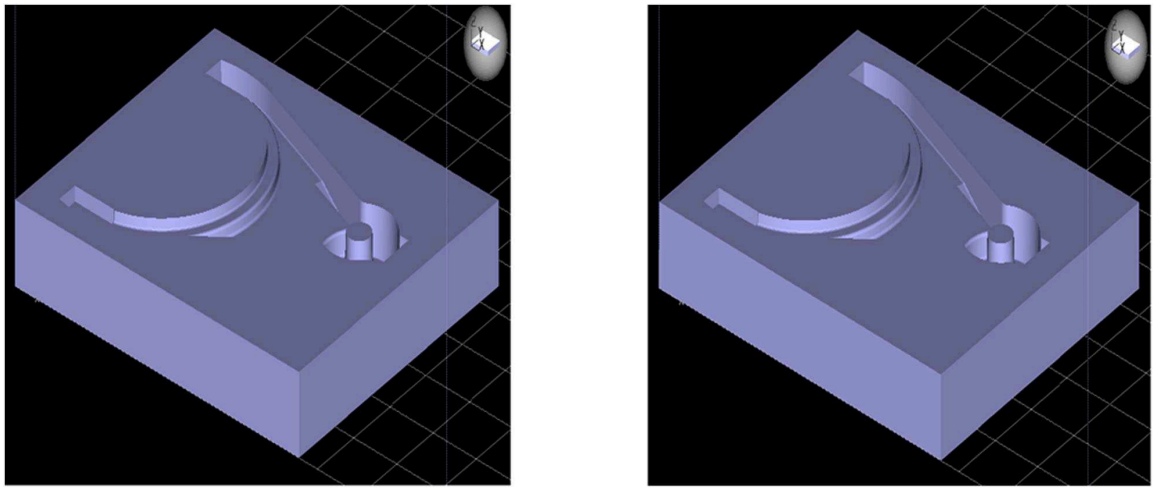

Fig.3 CAD model of fork mould (Two halves)

Fig.4(a)-Wax pattern side1

Fig.4(b)-Wax pattern side 2

Figure 5 shows the failed mould pieces after attempt-1. Mould after attempt-1 was analyzed and following problems were identified:-

1. Wax leaked out of the cavity between the two pieces due to which mould halves could not be separated easily.
2. Wax was trapped in the layer to layer gap due to which wax pattern bonded with the mould and wax pattern damaged while removing as seen in Figure 4(a)
3. A design flaw in the mould which didn't allow ejection of wax pattern.
4. Additional vent holes were required.

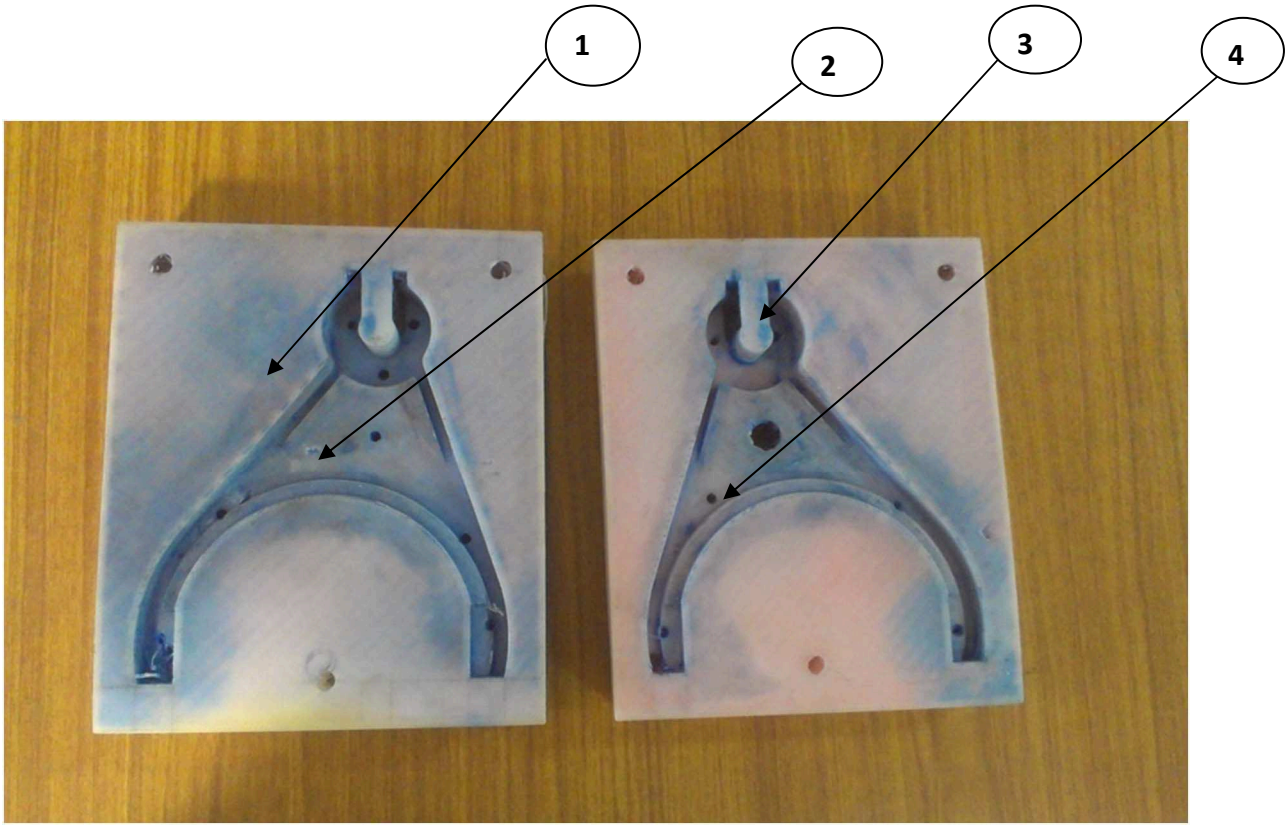

Fig.5-Failed fork mould of attempt-1(Two halves)

Attempt-2:

The failure of the first attempt led to in-depth analysis of the problems and the following solutions for the problems were adopted for the second attempt.

Solutions adopted for second attempt:

1. To prevent the wax leakage design of mould was modified and a guarding wall was provided.
2. To prevent the wax from getting trapped in the gaps between layers chemical treatment process was employed. The parts were treated in the optimized condition as prescribed by the authors[3]. After the chemical treatment the parts experienced significant reduction in the surface roughness.
3. The design of mould was changed to enable removal of wax pattern.
4. Proper vent holes and injection system was modeled in the parts.
5. Ejection slots were provided to facilitate the ejections.

After adopting the chemical treatment process as a step in the rapid tooling process following would be the process flow as shown in Figure 6.

Fig.6-Process flow diagram for FDM rapid tooling

The modified design and chemically treated mould is shown in Figure 7. The chemically treated mould was successfully used to produce wax patterns for investment casting. Figure 8 shows the wax pattern produced from the chemically treated mould.

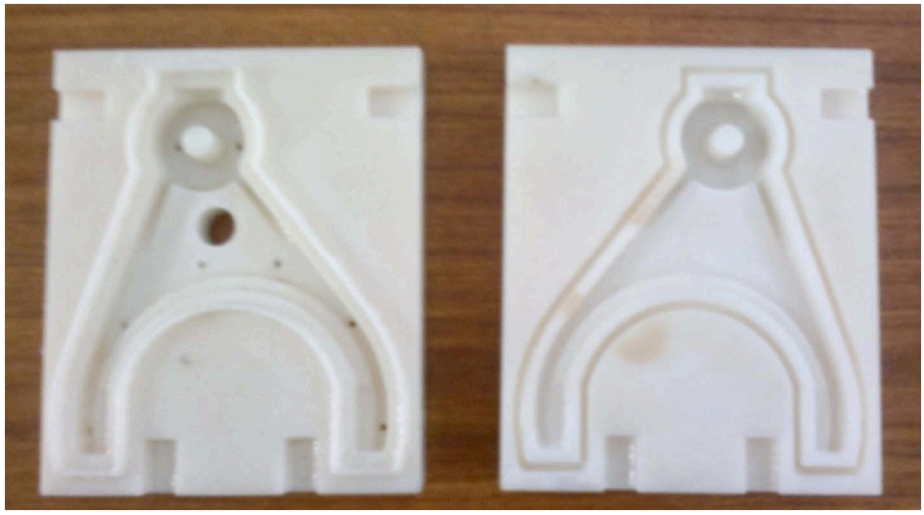

Fig.7 Chemically treated fork mould (Two halves)

Fig.8 Wax pattern produced through from the chemically treated fork mould

The successful production of the wax pattern from the FDM tool validates the process and moreover the surface finish of the produced wax pattern is at par with that achieved in SRM.

The life of the mould can be increased by repeating process of chemical treatment on the used mould without effecting dimensional accuracy. Figure 9 shows the retreated mould ready for reuse.

Case Study-2 : The pump impeller is one of the very complex parts and cannot be made through silicone rubber moulding. Figure 9 shows CAD model of pump impeller mould. For such part burnout process using FDM pattern has been suggested. Here the same piece was produced using FDM mould as direct tool.

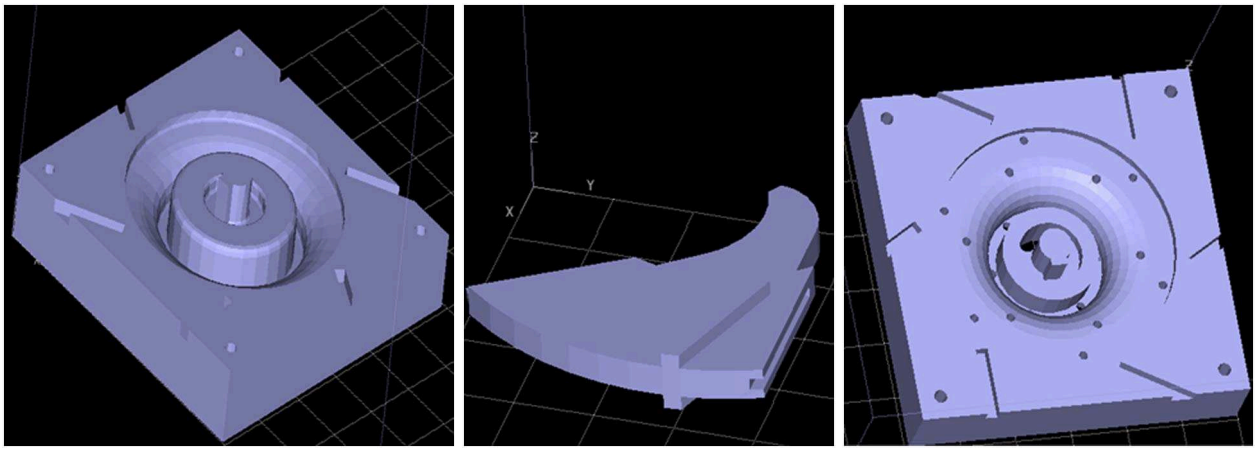

Fig.9 CAD model of pump impeller mould (Two halves with insert)

The tooling design for impeller was one of the major challenges. The mould was made in three pieces. The top piece, bottom piece and the middle piece comprising of six inserts. The FDM mould for impeller was fabricated; Figure 10 shows the fabricated mould.

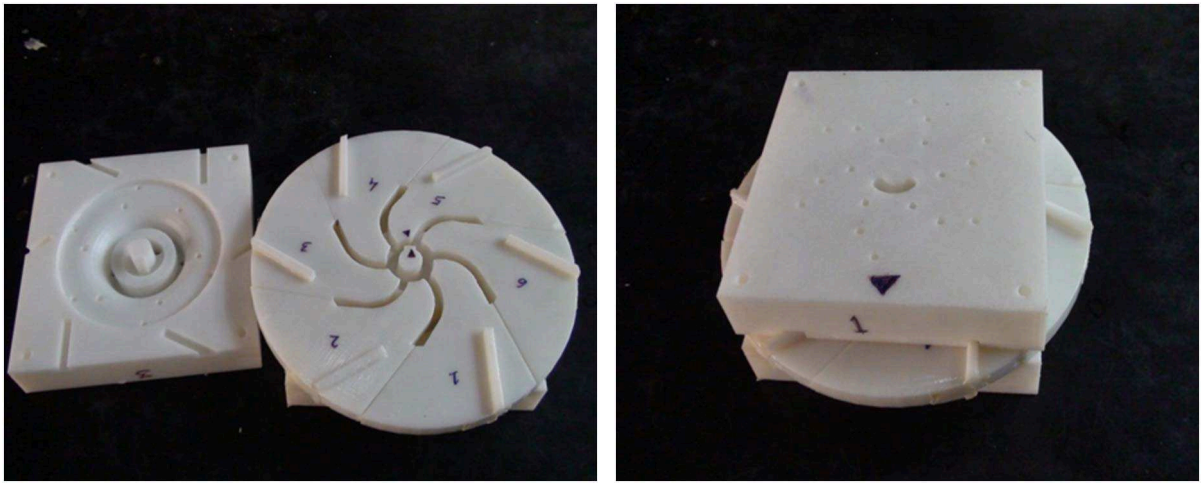

(i) Exploded view of Impeller mould (ii) Assembled view of Impeller mould

Fig.10 Fabricated FDM mould of impeller

This mould was used to produce wax pattern for investment casting. The wax pattern was successfully moulded out of the FDM tool. Figure 11 shows the FDM mould of impeller after treated with optimized chemical treatment process. Figure 11 also shows improved version of the mould in which the size of vent holes are increased to vent out vapors more easily and thereby to solidify the wax pattern more quickly.

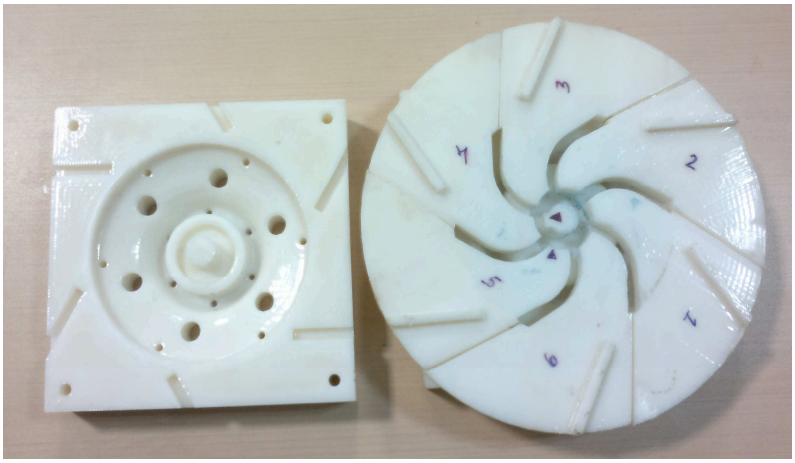

Fig.11 Fabricated FDM mould of impeller (improved version) after chemical treatment

Figure 12 shows the wax pattern produced using FDM made mould of impeller used as direct tool after treated with optimized chemical treatment process.

(i) Wax pattern of impeller in the mould

(ii) Top view of wax pattern of impeller

Fig.12-Wax pattern of impeller produced from chemically treated FDM mould

Results and Discussion

The produced FDM direct tool was used by M/s Protosys Technologies Limited, Mumbai, India for production of wax patterns required for investment casting, FDM moulds were successfully implemented for direct tooling and comparison data between FDM and SRM was provided by them. Based upon this data both the processes were compared. The FDM tools were analyzed for verification on five points cost, tool life, tool quality, time for fabrication and pattern quality. Table 1 shows the comparison of FDM tool with SRM. The patterns produced from FDM and SRM were also compared in terms of surface finish, dimensional accuracy and ease of removal. The comparison for the same is shown in Table 2

Table 1 Comparison between FDM and SRM produced moulds

	Cost (INR)	Time (in Hrs)	Life of mould (pieces/mould)	Surface finish(microns)	Dimensional accuracy(%)
FDM	12000	12	38	<8	97
SRM	18000	18	22	<5	99

Table 2 Comparison between FDM and SRM produced wax patterns

Wax patterns from	Surface finish (microns)	Dimensional accuracy (%)	Ease of removal
FDM	<8	94	Low
SRM	<5	98	High

It was seen that the time associated in fabrication was much less in FDM tool as compared to the SRM. In case of FDM tool cost, tool life and time for fabrication was much less as compared to SRM also surface finish and dimensional accuracy was at par with SRM. Figure 13 shows a comparison between FDM and SRM.

Further comparison between SRM and FDM tools were made based upon the mode of fabrication (Solid fill or Sparse in case of FDM) and the initial pattern used for tool fabrication (SLA pattern or metal prototype in case of SRM). It was observed that time and cost mentioned in Table 1 is valid if a pattern for fabrication of SRM is available. In case when pattern is not available an SLA pattern is required to be manufactured. Also the cost and time of tooling mentioned are considered when a sparse fill option of FDM tooling is used. Table 3 shows a comparison between SRM and FDM when a pattern is not available.

Table 3 Comparison between FDM and SRM produced moulds when pattern is unavailable

	Cost (in Rs.)	Time (in Hrs)	Life of mould (pieces/mould)	Surface finish(microns)	Cost per piece (INR)
FDM	7600	7	28	<8	271
SRM	27000*	25	22	<5	864**

*Total cost i.e. cost of SLA pattern (Rs12000) and SRM mould(Rs15000).

** Cost of SLA pattern is considered to be Rs 4000 (i.e. Rs12000/3) since each SLA pattern could be used to make 3 to 4 silicon rubber mould.

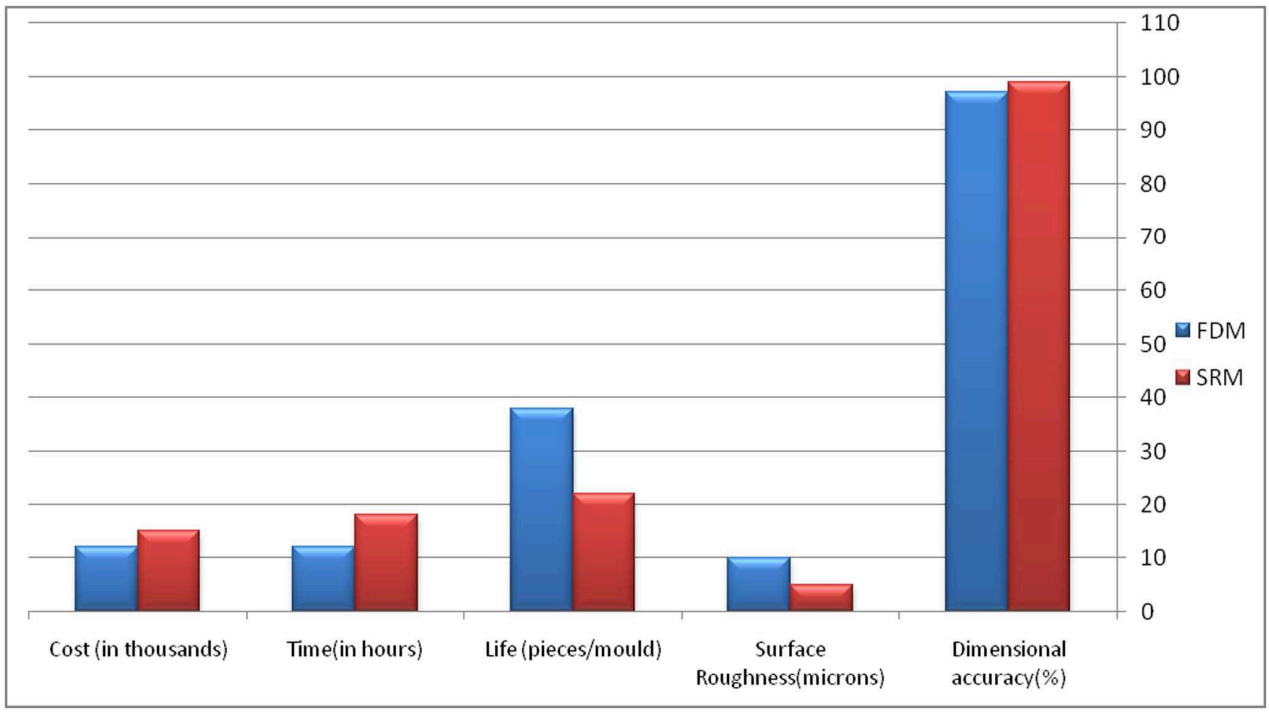

Fig.13 Comparison between FDM and SRM.

Conclusions

It was observed that FDM moulds can be successfully used as direct tooling after the chemical treatment process. The quality of the wax pattern produced by FDM tool is at par with that produced with SRM. Though SRM produced wax pattern have an edge over FDM produced patterns in surface finish and ease of removal but tooling life was observed to be more in case of FDM tools making it cheaper and direct process. In case where tooling is done for a new developed product SRM requires an SLA master pattern to be made whereas direct tool can be designed by FDM. As observed in Table 3 the cost per piece in case of SRM is three times the cost in case of FDM produced wax pattern. Further for complex parts like impeller taken as case study-2 SRM fails to produce tooling and FDM tools is the most easy and economical solution for such complicated tooling.

It is obvious that FDM moulds can be very effectively used as direct tooling with considerable cost reduction and time saving, it gives high tool life and the quality of parts produced is at par with those produced through SRM. FDM tools can also be used for complicated parts having internal features requiring inserts or a three piece moulds for which SRM fails to deliver. Another important aspect is the cost per piece in case of FDM is $1/3^{rd}$ the cost per piece obtained from SRM. This is a huge reduction of cost making FDM tooling a very strong contender to be used as direct tooling.

References

[1] Dilip Sahebrao Ingole, Abhay Madhusudan Kuthe, Shashank B. Thakare, Amol S. Talankar, Rapid prototyping – a technology transfer approach for development of rapid tooling, Rapid Prototyping Journal, 15/4 (2009) 280–290

[2] C. W. Lee, C. K. Chua, C. M. Cheah, L. H. Tan, C. Feng, Rapid investment casting: direct and indirect approaches via fused deposition modeling, International Journal of Advanced Manufacturing Technology (2004) 23: 93–101

[3] Addanki Sambasiva Rao, Medha A. Dharap, J V L Venkatesh, Deepesh Ojha, Investigation of post processing techniques to reduce the surface roughness of fused deposition modeled parts, International Journal of Mechanical Engineering and Technology, Volume 3, Issue 3, September - December (2012), pp. 531-544

[4] Omar M.F.M., S. Sharif, M. Ibrahim, H. Hehsan, M.N.M. Busari and Hafsa M.N., Evaluation of Direct Rapid Prototyping Pattern for Investment Casting, Advanced Materials Research Vols. 463-464 (2012) pp 226-233, Trans Tech Publications, Switzerland.

[5] W. S. W. Harun, S. Safian & M. H. Idris, Evaluation of ABS patterns produced from FDM for investment casting process, Computational Methods and Experiments in Materials Characterization IV 319, WIT Transactions on Engineering Sciences, Vol 64, © 2 009 WIT Press

[6] Yuhua Song, Yongnian Yan, Renji Zhang, Qingping Lu, Da Xu, Three dimensional non-linear coupled thermo-mechanical FEM analysis of the dimensional accuracy for casting dies in rapid tooling, Finite Elements in Analysis and Design 38 (2001) 79-91.

[7] J.C. Ferreira, N.F. Alves, Integration of reverse engineering and rapid tooling in foundry technology, Journal of Materials Processing Technology 142 (2003) 374–382

[8] M.D. Monzon, N. Diaz, A.N. Benitez, M.D. Marrero, P.M. Hernandez, Advantages of Fused Deposition Modeling for making electrically conductive plastic patterns, 2010 International Conference on Manufacturing Automation, 978-0-7695-4293-5/10, 2010 IEEE DOI 10.1109/ICMA.2010.36

[9] Sarat Singamneni, Roger Anak Joe, Bin Huang, Adaptive Slicing for Fused Deposition Modeling and Practical Implementation Schemes, Advanced Materials Research Vol. 428 (2012) pp 137-140

[10] P.M. Pandey, N.V. Reddy, S.G. Dhande, Real time adaptive slicing for fused deposition modeling, International Journal of Machine Tools & Manufacture 43 (2003) 61—71, Pergoman, Elsevier.

[11] Anhua Peng, Zhiming Wang, Researches into Influence of Process Parameters on FDM Parts Precision, Applied Mechanics and Materials Vols. 34-35 (2010) pp 338-343

Advanced Materials Research Vol. 970 (2014) pp 166-171

doi:10.4028/www.scientific.net/AMR.970.166

Modeling the Release of Urea from Coated Urea: The Constant Release Stage

Thanh H. Trinh[1,a*], KuZilati KuShaari[1,b], Anis Shuib[1,c], Lukman Ismail[1,d], Abdul Basit[1,e], Babar Azeem[1,f]

[1]Department of Chemical Engineering, Universiti Teknologi PETRONAS,

31750 Seri Iskandar, Perak, Malaysia

[a*]onalone2000@gmail.com, [b]kuzilati_kushaari@petronas.com.my, [c]anisuha@petronas.com.my, [d]lukmis@petronas.com.my, [e]abdulbasit135@gmail.com, [f]engrbabara@gmail.com

Keywords: urea release, urea diffusion, finite element method, multi-diffusion modeling

Abstract. Controlled release fertilizer (CRF) plays an important role in nutrient loss prevention by plants and its utilization enhancement. This study uses multi-diffusion model to simulate the release of urea for two coating materials: modified polyolefin (MPO) and latex film, based on COMSOL Multiphysics software. Effective diffusivity and lag time (t_0) are determined based on experimental data. Modeling results well simulate the experimental data of "constant release" stage. Standard error of estimate (SEE) ranges from 0.012 - 0.017 for MPO and 0.0316 for Latex film. The validated model is then utilized to study the effect of coating thickness (l), saturated urea concentration (C_{sat}) and effective diffusivity (D_e) on the urea release profile. Release time increase with increasing coating thickness or decreasing saturated urea concentration, effective diffusivity. In addition, a change in effective diffusivity does not make significant change in percentage of urea at the end of "constant release" stage.

Introduction

The idea of controlled release fertilizer (CRF) is to prevent nutrient loss and enhance nutrient utilization efficiency of plants [1]. The amount of fertilizers recovered by plant when applied in conventional forms is only 30-50%. CRFs possess manifold advantages including fertilizer use economy through least possible losses of the fertilizer, prevention of the seedling damage and better protection of the ecosystem in the case of biodegradable carriers [2].

The application of controlled release technology to fertilizers was first conducted in 1962 by Ortil et al. [3]. The nutrient release from coated CRFs is usually controlled by the diffusion through the coating layer. In 1987, Glaser *et al.* studied the release of polymer-coated granule and applied one-dimensional coordinate diffusion system [4]. Gambash *et al.* used semi-empirical model in their study [5]. Lu and Lee applied the Fick's law in spherical coordinate for the release of latex coated urea (LCU) [6]. Al-Zahrani modeled unsteady state of polymeric membrane particle and assumed a well-mixing condition inside sphere particle [2]. Most of modeling efforts were based on the assumption that nutrient release of nutrients from coated fertilizer is controlled by simple solute diffusion. In 2003, Raban's experiments showed that the release from a single granule of a polymer coated CRFs consists of three stages: an initial stage during which no release is observed (lag period), a stage of constant release, and finally a stage of gradual decay of the release rate [3]. In 2007, Lu proposed a mathematical model for the release of a scoop of polymer coated urea which took into account the effect of granule population. This model was based on mass balance equation of pseudo-steady state of Fick's law. However, the first stage of release process was neglected, and "trial and error" method was used to estimate diffusion coefficient [7].

Understanding the release of urea through the coating layer is very important to predict nutrient release behavior. Therefore, there are many efforts in understanding the controlling release mechanism and pattern to obtain a model which could be used for predicting the release of nutrients under laboratory and field conditions and also as a design tools for technologists [8]. This study

investigates the urea release through coating layer into the outer environment (water) using multi-diffusion model on two coating materials: Modified Polyolefin (MPO) and Latex film. Effects of coating thickness, urea saturated concentration and effective diffusivity on the urea release is also studied in this study.

Methodology

Model development and validation. Simulations are based on the multi-diffusion model developed in our previous studies [9, 10]. The dissolving model of a spherical urea is described in Fig. 1a. In this model, coated urea granule is surrounded by water environment. Urea granule consists of two parts: urea core and coating layer outside the urea core. Model is assumed that coating layer is saturated with water, and water at the surface of urea core quickly dissolves solid urea. Whenever solid urea presents in the core, urea concentration is kept at saturated level. Urea begins to release through the coating layer by mean of diffusion. There are two diffusion processes occuring in the release of urea. First, the diffusion of urea through the coating layer described by mass transport equation in porous medium as below [7, 11]:

$$D_e\left[\frac{\partial^2 C}{\partial r^2}+\frac{2}{r}\frac{\partial C}{\partial r}\right]=\varepsilon\frac{\partial C}{\partial t}. \tag{1}$$

where C is the concentration of urea in mol/m^3, D_e is effective diffusivity (diffusion coefficient) of urea in porous medium in m^2/s, ε is porosity of the coating in percentage (%).

Second, the diffusion of urea from the interface of coating to the liquid is calculated based on mass transport equation of urea in water. The equation for urea diffusion can be written as:

$$D_{urea}\frac{\partial^2 C}{\partial r^2}+\frac{2D_{urea}}{r}\frac{\partial C}{\partial r}=\frac{\partial C}{\partial t}. \tag{2}$$

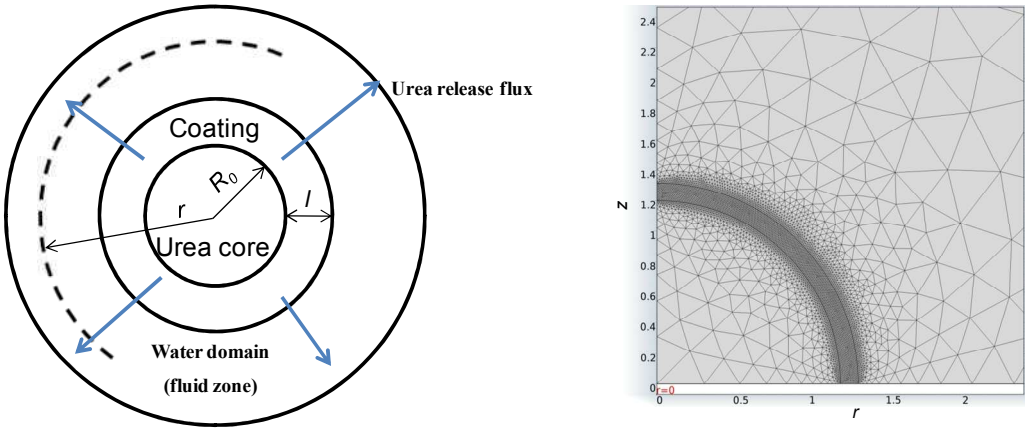

(a) (b)

Fig. 1. (a) Urea dissolution models for coated urea and (b) mesh generation.

Four simulations are run following the input data in Table I. These data are based on previous publications from Lu & Lee, and Shaviv *et al.* [3, 6]. Geometry and meshing steps are done for urea granules with radius and coating thickness following Table I and Fig. 1b. Fluid zone, which is defined as the distance from center of the urea granule to outer boundary of water domain, is set 22 times of the radius of urea core [9]. Initial values and boundary conditions are specified for the model. At the time t_0, urea concentration at the surface of urea core is saturated, and concentration is zero at the outer layer of fluid field. In these simulations, calculation time depends on the amount of urea (size and shape), coating material (thickness and properties) and saturated concentration.

"Constant release" stage is considered from the beginning of the release to the time solid urea is totally dissolved. When solid urea totally dissolved, the amount of urea in the core is

$$m_{core} = m_{sat} = M_{urea} C_{sat} V_{core} . \quad (3)$$

where m_{sat} is mass of urea core when solid urea is totally dissolved in g, C_{sat} is saturated urea concentration in mol/m^3.

Equation 3 specifies as the stop condition for "constant release" stage. This model focuses on the "constant release" stage, and validates with Modified Polyolefin (MPO) and Latex coating material experiments. Lag time (t_0) is determined based on each experiment. Data are extracted using Engauge Digitizer 4.1. Based on information from these papers and extracted data, simulation and experiment data are overlaid to validate the model.

Effect of coating thickness, saturated urea concentration and effective diffusivity on the release of urea. After validation process, the model is used to study the effect of coating thickness, saturated urea concentration, and diffusive flux to urea released profile.

Effect of coating thickness is studied with three thicknesses as 0.0375, 0.0917 and 0.1833 mm respectively. Effective diffusivity for these simulations is 1×10^{-5} cm^2/day, and urea core radius is 1.2mm.

For the effect of saturated urea concentration, the release of urea is conducted with concentrations as 10486, 11083, 12275, 13339 and 14403 mol/m^3. Core radius is 1.2mm, coating thickness is 0.0375mm, and effective diffusivity is 1×10^{-5} cm^2/day.

Five effective diffusivities (0.8, 1.0, 1.5, 2.0 $\times$ 10^{-5} cm^2/day) is used to study the relationship between diffusivity and release time. In this case, coating thickness is 0.0375 mm, and urea core radius is 1.2 mm.

Results and discussion

Model development and validation. At the beginning, urea core is solid so it keeps urea concentration in urea core at saturated level. As in Fig. 2, the urea core will decrease its mass by diffusion through coating layer (blue line). The constant release stage will end when solid urea is totally dissolved. At this moment, urea mass reaches the red dashed line, which is equivalent to saturated urea concentration.

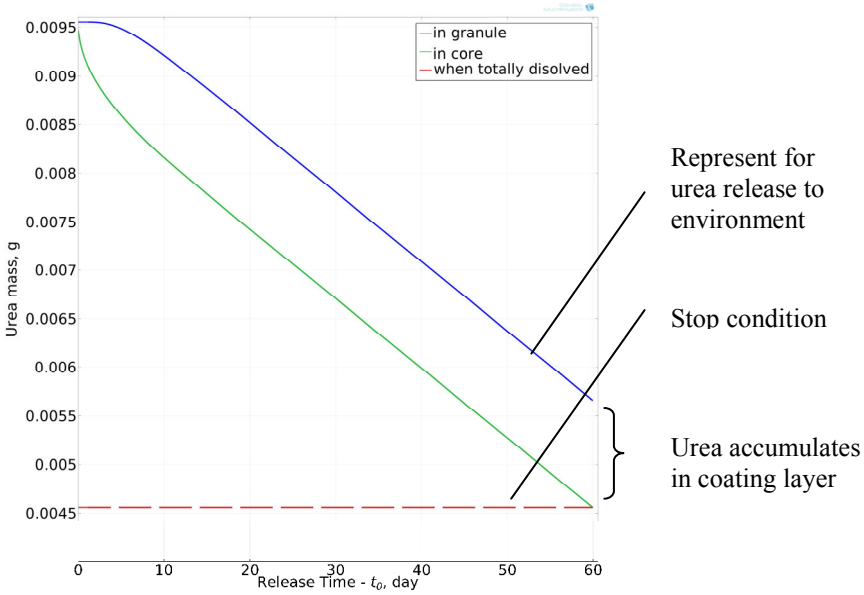

Fig. 2. Urea mass profiles in core and granule, and the stop condition for "constant release" stage

Simulations are conducted using information in Table I. For MPO coating material, effective diffusivity, in all three simulations, is 1×10^{-5} cm^2/day. In Fig. 3a, simulation data corresponds with experiments from Shaviv *et al.* literature [3]. It means that the model well simulates the release of urea during "constant release" stage. Another simulation is run and validated with experiment from Lu and Lee which Latex film was used as coating material [6]. In Fig. 3b, red square markers and green line are experiment and simulation results from Lu and Lee; and blue line is simulation results obtained from our study. This plot also shows that modeling results are in good agreement with the experimental data. Standard error of the estimate (SEE) ranges from 0.012 - 0.017 for MPO and 0.0316 for Latex film. The simulation results are also similar to the modeling results had been done by Lu and Lee [6] as seen in Fig. 3b. However, there is a small discrepancy at the end of the constant release stage between Lu and our simulation.

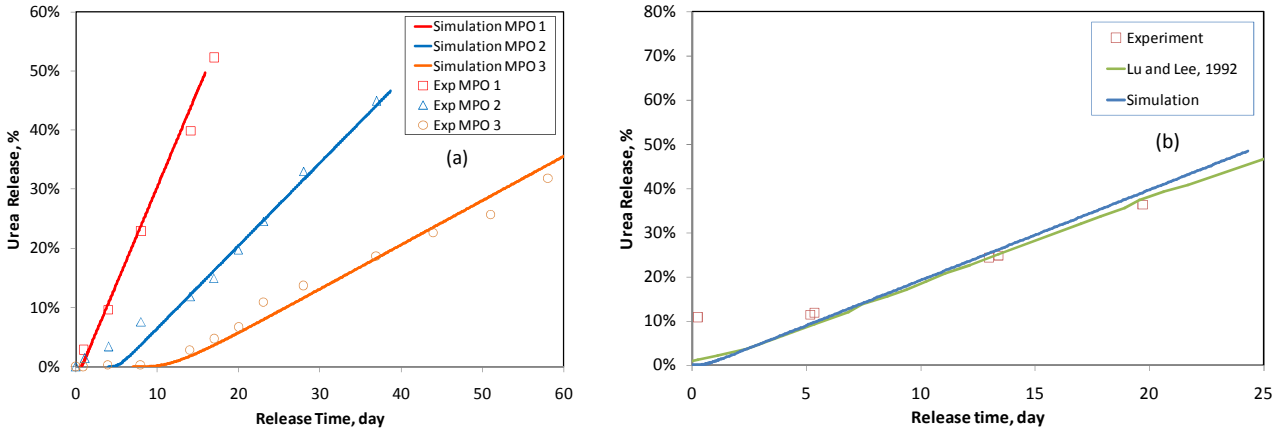

Fig. 3. Urea release profile during constant release stage for (a) MPO and (b) Latex film

Table I. Simulation input and output

No.	Coating Material	Urea Radius [mm]	Coating thickness [mm]	Lag time t_0 [days]	Release time [days]	Percentage release [%]	Source
1	MPO[a]	1.2	0.0375	0.5	15.89	49.71	Shaviv, 2003
2	MPO[a]	1.2	0.0917	4	38.72	46.66	
3	MPO[a]	1.2	0.1833	7	66.84	40.72	
4	Latex	15	0.3500	22	24.31[b]	48.48	Lu and Lee, 1992

[a] Modified Polyolefin

[b] Lag time t_0 is not included

Effect of coating thickness on urea release time. Simulation results are summarized as in Table I. As coating thickness increases, release time also increases. This result was also mentioned in Lu and Lee's study [6]. It causes by the increase in diffusion resistant. Beside, “constant release” stage ends at different percentage of urea released depending on coating thickness. Percentage of urea released decreases as coating thickness increases (Table I). This finding is very interesting because the percentage of the urea released is not the same in all cases although the stop condition does not change. Moreover, the coating thickness does not affect the stop condition.

This can be explained by the difference between amount of dissolved urea inside the core and amount of urea release to environment. In these simulations, stop condition is

$$m_{core} = m_{sat} = M_{urea} C_{sat} V_{core} . \quad (4)$$

Stop condition depends on mass of dissolved urea in core while the percentage release depends on mass of urea released to environment. The different amount is accumulated in the coating layer. This finding also shows that measured urea is not the actual urea dissolved in core, and release curve has late response to the urea dissolving curve. This phenomenon strongly affects the

prediction of the end point of the release, amount of urea dissolved and urea released. Thus, it will lead to false modeling which increases error between simulation and experimental results.

Effect of saturated urea concentration on the release. Based on the model of urea release, effect of saturated urea concentration on the release of urea has been investigated as in Fig. 4a. Table II shows that the higher the saturated urea concentration, the shorter the "constant release" stage is. Release time is 15.89 days when saturated concentration is 10486 mol/m^3. It becomes 7.68 days as saturated concentration is 14403 mol/m^3. Simulations also show a linear relationship between saturated urea concentration and percentage of urea release during "constant release" stage.

$$Percentage\ released\ (\%) = 4\times10^{-11}C_{sat}^2 - 5\times10^{-5}C_{sat} + 0.997\ ;\ R^2 = 1. \quad (5)$$

Effect of effective diffusivity on the release. Effect of diffusivity on the release has also been studied and results are shown in Fig. 4b. The smaller the diffusion coefficient, the longer the "constant release" stage is. Release time decreases from 19.83 to 8.14 days when effective diffusivity changes from 0.8 × 10^{-5} to 2.0 × 10^{-5} cm^2/day. However, there is no significant change in the percentage release at the end of "constant release" stage as effective diffusivity changes. Meanwhile, this change is significant in case of coating thickness or saturated urea concentration.

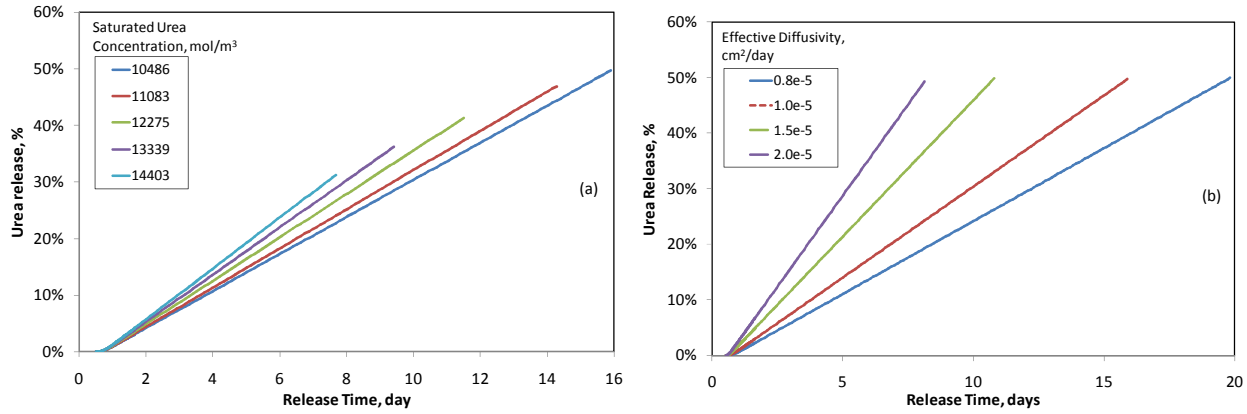

Fig. 4. Release profile of urea for (a) different saturated urea concentration (10486, 11083, 12275, 13339, 14403 mol/m^3); (b) different effective diffusivities (0.8, 1.0, 1.5, 2.0 *x* 10^{-5} cm^2/day)

Table II. Release time and percentage release vs. saturated urea concentration

Saturated Urea Concentration [mol/m^3]	Release time [days]	Percentage release [%]
10486	15.89	49.71
11083	14.27	46.92
12275	11.50	41.31
13339	9.41	36.20
14403	7.68	31.27

Conclusion

The "constant-release" stage of urea release has been modeled by applying finite element method to the urea diffusion model. This model is validated with experimental data and is shown to successfully simulate the release of urea. However, this model focuses mainly on the constant release stage. It needs to enhance to suit with three stages of the release.

Effect of parameters like coating thickness, saturated urea concentration and effective diffusivity has been studied on "constant release" stage. Increase in urea coating thickness results in longer release time, and 'constant release' stage ends at lesser percentage of urea release. This can be explained by the fact that the reduced amount of urea release is due to retention of urea in the coating layer. This factor should always be taken into account for the modeling urea release.

Saturated urea concentration has a linear relationship with the percentage of urea released. An increase in saturated urea concentration decreases the duration of 'constant release' stage. Decrease in effective diffusivity increases the duration of 'constant release' stage, however, it does not have any effect on the percentage of urea released at the end of 'constant release' stage.
Although this model simulates well the 'constant release' stage of urea fertilizer, it needs modification to simulate the overall urea release process including all the three-stage release.

Acknowledgment

The authors present their feelings of gratitude to Ministry of Higher Education (MOHE) for their financial support in this research.

References

[1] M. E. Trenkel, Controlled-release and stabilized fertilizers in agriculture, Paris: International Fertilizer Industry Association, 1997.

[2] S. M. Al-Zahrani, Controlled-release of fertilizers: modelling and simulation, International Journal of Engineering Science. 37 (1999) 1299–307.

[3] A. Shaviv, S. Raban, and E. Zaidel, Modeling Controlled Nutrient Release from Polymer Coated Fertilizers: Diffusion Release from Single Granules, Environ. Sci. Technol. 37 (2003) 2251–6.

[4] V. Glasser, P. Stajer, J. Vidensky, P. Svandova, and V. Knor, Urea-formaldehyde resins as packaging materials for industrial fertilisers with protracted action. Part 4, International polymer science and technology. 14 (1987) 127.

[5] S. Gambash, M. Kochba, and Y. Avnimelech, Studies on Slow-Release Fertilizers: II. A Method for Evaluation of Nutrient Release Rate From Slow-Releasing Fertilizers, Soil Science. 150 (1990) 446 – 450.

[6] S. M. Lu and S. F. Lee, Slow release of urea through latex film, J.Controlled Release. 18 (1992) 171–80.

[7] S. M. Lu, S.-L. Chang, W.-Y. Ku, H.-C. Chang, J.-Y. Wang, and D.-J. Lee, Urea release rate from a scoop of coated pure urea beads: Unified extreme analysis, Journal of the Chinese Institute of Chemical Engineers. 38 (2007) 295–302.

[8] A. Shaviv, Controlled release fertilizers. in *IFA International Workshop*, Frankfurt, Germany. 2005.

[9] H. T. Trinh, K. Z. K. Shaari, A. S. Shuib, and L. Ismail, Modeling of urea release from coated urea for prediction of coating material diffusivity. in *Proceeding of the 6th International Conference on Process Systems Engieering*, Kuala Lumpur, Malaysia. 2013. 20.

[10] Thanh H. Trinh, KuZilati KuShaari, Abdul Basit, Babar Azeem, and Anis Shuib, Use of multi-diffusion model to study the release of urea from urea fertilizer coated with Polyurethane-like coating (PULC), APCBEE Procedia. (2013) 149–53.

[11] Savithri S. and Manju M. S., Kinetics of the Carbothermal Reduction of Ilmenite: Grain Pellet Model, *Excerpt from the Proceedings of the COMSOL Conference 2009*, Bangalore, 2009.

Advanced Materials Research Vol. 970 (2014) pp 172-176

doi:10.4028/www.scientific.net/AMR.970.172

Statistical Analysis of Binder Behavior during Debinding Step in Powder Injection Molding (PIM)

Parinya Chakartnarodom [1] and Nutthita Chuankrerkkul [2,*]

[1]Department of Materials Engineering, Faculty of Engineering, Kasetsart University, Ngam Wong Wan Road, Chatuchak, Bangkok, 10900, Thailand

[2]Metallurgy and Materials Science Research Institute, Chulalongkorn University, Phyathai Road, Pathumwan, Bangkok, 10330, Thailand

*nutthita.c@chula.ac.th (corresponding author)

Keywords: statistical analysis, powder injection molding, Avrami equation, debinding

Abstract. The aim of this paper is to propose the approach for applying statistical methods (linear regression and statistical hypothesis testing) to study the behavior of binder during binder removing (debinding) step in powder injection molding (PIM) and also the parameters that affect the binder removing rate. In this work, the binder system under the investigation is the composite binder of 85wt% polyethylene glycol (PEG) and 15 wt% poly (methyl methacrylate) (PMMA) where PEG can be removed from the green product by using warm water while PMMA is removed later during sintering. At 0.05 level of significance, the linear regression method and the statistical hypothesis test prove that the dissolution behavior of PEG can be described using Avarami equation. Furthermore, the dissolution rates of PEG were independent of all parameters used in this study including binder contents in the green products, temperatures, and powder sizes.

Introduction

Powder injection molding is a method that can form the small and complex-shape parts with high precision from the powder materials, which are metal powder, ceramic powder, or the mixture of both. Before injection molding process, the mixed powders must be mixed with the binder. This binder assists the flow of the powders during injection process and help hold powders into shape during sintering [1,2]. It was found that the composite binder of polyethylene glycol (PEG) and polymethyl methacrylate (PMMA) was the good binders for powder injection molding because PEG can be removed from the product before sintering by warm water, which saves time and the energy cost of the process [3,4,5]. According to Oliveira et al [6], binder removing (debinding) is a crucial step for powder injection molding because structural change of the green product caused by improper debinding rate will create the defects in the final products such as surface cracking, large internal void, blistering, and expanding.

Statistical methods are commonly used in many industries for forecasting, production planning, work study, experimental design, quality control and assurance, etc. Linear regression and statistical hypothesis test are the examples. Linear regression is a method to determine the correlation between the independent variable X and the dependent variable Y, and statistical hypothesis test is the method to make the decision based on the available data. The aim of this paper is to propose the approach for applying these statistical methods (linear regression and statistical hypothesis testing) to study the behavior of PEG in the composite binder PEG/PMMA during binder removing step in powder injection molding and also the parameters that affect PEG removing rate. In this work, PEG/PMMA composite binder was used with the mixture of 90 wt% AISI 304 L stainless steel powder and 10 wt% tungsten carbide (WC) powder for forming WC-reinforced stainless steel using powder injection molding [7]. The experimental parameters under the investigation were water temperature for removing PEG, WC particle sizes in the powder mixtures, and the binder contents in the green products after injection molding process.

Experimental Procedure

Specimen Preparation. The rectangular specimens (5x5x55 mm) consisting of AISI 304L stainless steel powder, WC powder, and PEG/PMMA composite binder were prepared by powder injection molding. Table 1 summarizes the specimen formula used in this work. The powder of AISI 304L stainless steel was from Epson Atmix, Japan, and the WC powder was from ATI Alldyne.

Table 1 Formula for sample preparation

Formula	Average WC powder size [μm]	Amount of Mixed Powders [vol%]	Binder Content (85 wt% PEG/ 15 wt% PMMA) [vol%]
A	4.8	52.5	47.5
B	1.6	52.5	47.5
C	4.8	55.0	45.0
D	1.6	55.0	45.0

PEG Leaching. To remove PEG from the specimens, the specimens were soaked in the warm water at either 40 or 60 ^{o}C, which were below and above the melting temperature of PEG (~45^{o}C), for 0.5, 1, 2, 3, 4, 6, and 24 hours. The microstructures of the specimens before and after PEG leaching were observed by XL30CP scanning electron microscope (SEM). The fraction of mass loss of the specimen due to PEG dissolution was calculated by using Eq. 1 where X_{PEG} is the mass fraction of PEG that dissolve in the water, m_i is the initial mass of the specimen, m_t is the mass of the specimen after soaking time t, m_{PEG} is the mass of PEG in the specimen initially.

$$X_{PEG} = \left(m_i - m_t\right)/m_{PEG} \quad (1)$$

Mathematical Model.

Avrami Equation. Avrami equation is an equation describing the material transformation behavior at a constant temperature [8] (e.g. austenite to pearlite transformation and crystallization in polymer). In this work, the fraction of mass loss of the specimen due to PEG dissolution was fitted with Avrami equation in Eq. 2 where t was the soaking time, while k and n were the time-independent constant, which were determined using Eq. 3 and the linear regression method. Eq. 3 is the linear equation form of Eq. 2, in which n is the slope and ln k is the y-intercept of the equation. Obviously, Eq. 2 shows that when $t \to 0$ then $X_{PEG} \to 0$ (i.e. none of PEG dissolve), and when $t \to \infty$ then $X_{PEG} \to 1$ (i.e. all PEG dissolve in the water). Furthermore, the rate of PEG dissolution was defined by the time required for 50% dissolution of PEG (i.e. $X_{PEG} = 0.5$).

$$X_{PEG} = 1 - \exp\left(-kt^n\right) \text{ and } \ln\left(\ln\left(1/\left(1 - X_{PEG}\right)\right)\right) = n\ln t + \ln k \quad (2) \text{ and } (3)$$

Statistical Analysis [9]

Linear regression. For the linear correlation between $x = \ln t$ and $y = \ln\left(\ln\left(1/\left(1 - X_{PEG}\right)\right)\right)$ in Eq. 3, the slope (n) and y-intercept (ln k) were calculated by using least-square estimation and the uncertainties of the slope (n) and y-intercept (ln k) were calculated from their 95% confidence interval.

Testing of the Linear Correlation. Table 2 summarizes the required equations for the statistical hypothesis test of the linear correlation between $x = \ln t$ and $y = \ln\left(\ln\left(1/\left(1 - X_{PEG}\right)\right)\right)$ in Eq. 3. In Table 2, H_o is the null hypothesis, H_1 is the alternative hypothesis, ν is the degree of freedom, $T_{\alpha/2,\nu}$ is the value of t- distribution with degree of freedom ν for two-tailed test, N is the number of data point, α is the significance level, ρ is the population correlation coefficient, and R is the sample correlation coefficient. When the value of the test statistic (T_o) is greater than $T_{\alpha/2,\nu}$, there is

the linear correlation between $x = \ln t$ and $y = \ln\left(\ln\left(1/(1-X_{PEG})\right)\right)$ (i.e. PEG dissolution behavior obeys Avrami equation).

Table 2 Statistical hypothesis test for linear correlation between two variables (x and y)

H_o	H_1	Test statistic	Degree of freedom	Critical region
$\rho = 0$	$\rho \neq 0$	$T_o = \frac{R\sqrt{N-2}}{\sqrt{1-R^2}}$	$\nu = N-2$	$\lvert T_o \rvert > \lvert T_{\alpha/2,\nu} \rvert$

Results and Discussion

Specimen Microstructure after PEG Leaching. SEM micrograph of the specimens from formula B and D before and after 24-hours PEG leaching at 60 °C are shown on Fig. 1. Before leaching process (Fig. 1 (a) and (c)), the particles were covered with the binder. However, after 24 hours (Fig. 1 (b) and (d)), the particles inside the specimens were revealed on the micrograph, which indicate that PEG was removed from the specimens by dissolving in the water.

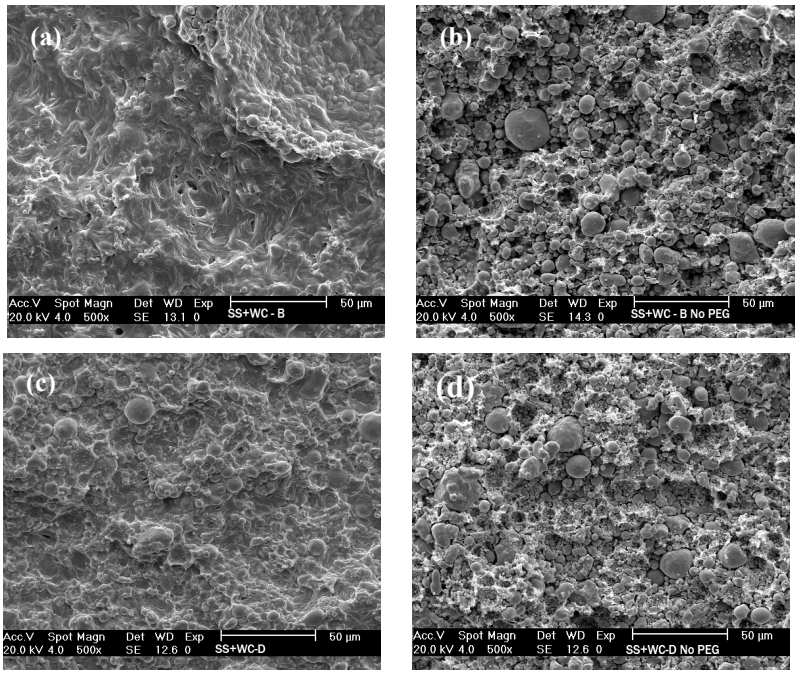

Figure 1. Formula B (a) before and (b) after 24-hours PEG leaching at 60 °C in the water, and formula D (c) before and (d) after 24-hours PEG leaching at 60 °C in the water

Mathematical modelling and Statistical Analysis. Fig. 2 (a) and (b) show that $\ln\left(\ln\left(1/(1-X_{PEG})\right)\right)$ increased with ln t. and the data could be fitted with the linear equation. Table 3 summarizes the slope, y-intercept, R^2, and the values of the test statistic (T_o) for each specimen formula and each water temperature. At 0.05 level of significance (α=0.05), the value of t-distribution for two-tailed test and degree of freedom ν=5 is 2.571. Thus, from Table 3, there was the linear correlation between ln t and $\ln\left(\ln\left(1/(1-X_{PEG})\right)\right)$ in all cases. Hence, PEG dissolution behavior in this work obeys Avrami equation (Eq. 3).

Furthermore, the time required for 50% dissolution of PEG and their uncertainties were calculated by using the data from Table 3 and shown on Fig. 3. Obviously, the ranges for possible values of the time required for 50% PEG dissolution for each case were overlapped and did not show significance difference. Therefore, PEG dissolution rate was independent from WC particles size, amount of composite binder in the specimen, and water temperatures used in the work.

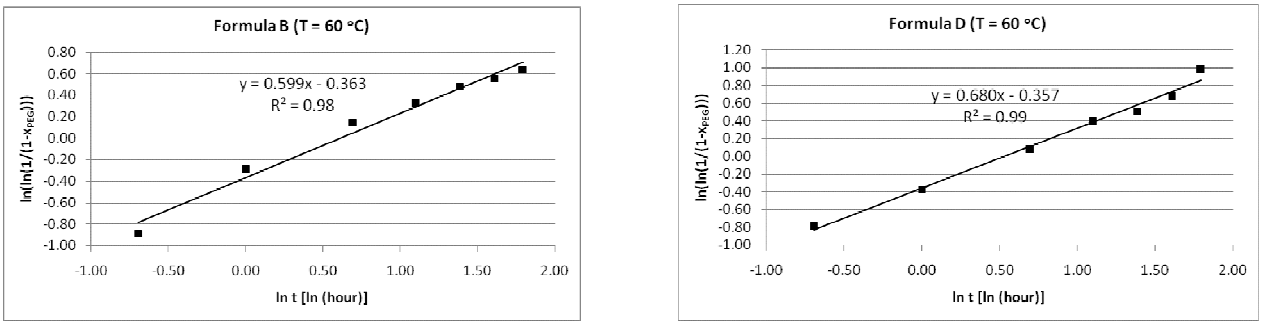

(a) (b)

Figure 2 $\ln(t)$ vs. $\ln(\ln(1/(1-X_{PEG})))$ of the specimens in the water at 60 °C from (a) formula B and (b) formula D

Table 3 The slope and y-intercept of the linear equations between ln t and $\ln(\ln(1/(1-X_{PEG})))$ for each sample formula and water temperature

Formula	Water temperature = 40 °C				Water temperature = 60 °C			
	Slope (n)	y-intercept (ln k)	R^2	T_o	Slope (n)	y-intercept (ln k)	R^2	T_o
A	0.475±0.161	0.201±0.191	0.92	7.60	0.517 ± 0.139	-0.188 ± 0.166	0.95	9.55
B	0.581±0.103	0.456±0.122	0.98	14.51	0.599 ± 0.094	-0.363 ± 0.112	0.98	16.21
C	0.570±0.054	0.387±0.064	0.99	27.11	0.630 ± 0.049	-0.272 ± 0.058	0.99	33.35
D	0.650±0.073	0.522±0.086	0.99	23.13	0.680 ± 0.088	-0.356 ± 0.104	0.99	19.92

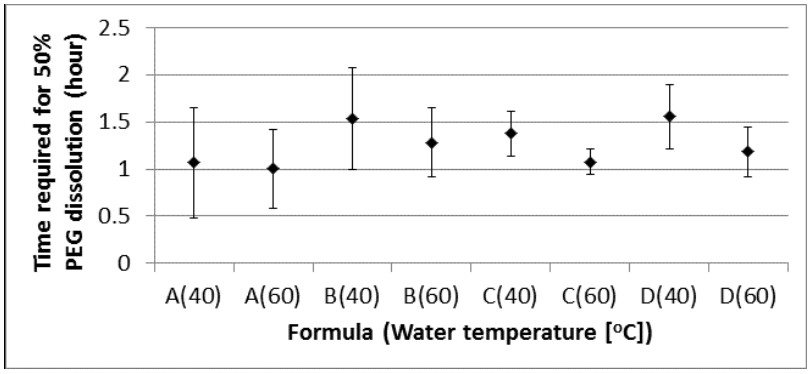

Figure 3 Time required for 50% PEG dissolution

Conclusions

In this work, the proposed statistical methods proved that, at 0.05 level of significance (α=0.05)), the dissolution behavior of PEG could be described using Avarami equation. Furthermore, the dissolution rate of PEG was surprisingly independent of all parameters used in this study including binder contents in the specimens, temperatures, and powder sizes.

Acknowledgements

This research was partially funded by Faculty of Engineering, Kasetsart University, Ratchadapiseksompoj Endowment Fund, Asia Research Center and Center of Innovative Nanotechnology, Chulalongkorn University. The authors would like to thank Epson Atmix, Japan for material supply, and Department of Materials Engineering, Kasetsart University and National Metal and Materials Technology Center for supporting of scientific equipment. Materials Innovation Center of Kasetsart University, Chulalongkorn University Centenary Academic Development Project, Ms. Prattana Supjan, and Ms. Kasamon Chusri are acknowledged also.

References

[1] M.P. Groover, Fundamentals of Modern Manufacturing: Materials, Processes, and Systems, Prentice-Hall Inc., New Jersey, 1996
[2] T. Udomphol, B. Inpanya, N. Chuankrerkkul, Adv. Mater. Res. 383-390 (2012) 3234-3240.
[3] N. Chuankrerkkul, P.F. Messer, H.A. Davies, Powder Metall. 51 (2008) 72-77.
[4] M.A. Omar, H.A. Davies, P.F. Messer, B. Ellis, J. Mater. Process Technol.113 (2001) 477-481.
[5] N. Chuankrerkkul, P. Sooksaen, , P. Pakunthod, T. Kosalwit, W. Pinthong, Key Eng. Mater. 545 (2013) 173-176.
[6] R.V.B. Oliveira, V. Soldi, M.C. Fredel and A.T.N. Pires, J. Mater. Process Technol. 160 (2005) 213-220.
[7] N. Chuankrerkkul, P. Chakartnarodom, Mater. Sci. Forum 706-709 (2012) 638-642.
[8] W.D. Callister, D.G. Rethwisch, Materials Science and Engineering, eight ed., Wiley, 2011
[9] R.E. Walpole, R.H. Myers, Probability and Statistics for Engineers and Scientists, fifth ed., Prentice-Hall Inc., New Jersey, 1993

Advanced Materials Research Vol. 970 (2014) pp 177-184

doi:10.4028/www.scientific.net/AMR.970.177

Rigid-plastic Finite Element Simulation of Cold Forging and Sheet Metal Forming by Eulerian Meshing Method

Wen Chiet Cheong[1,a*], Heng Keong Kam[2,b], Chan Chin Wang[3,c] and Ying Pio Lim[4,d]

[1-4]Department of Mechanical and Material Engineering
Universiti Tunku Abdul Rahman
Kuala Lumpur, Malaysia

[a*]cheongwc@utar.edu.my, [b]kamhk@utar.edu.my, [c]wangcc@utar.edu.my, [d]limyp@utar.edu.my

Keywords: Rigid-plastic FEM; eulerian meshing; cold forging; aluminium extrusion; sheet metal forming; clinching

Abstract. A computational technique of rigid-plastic finite element method by using the Eulerian meshing method was developed to deal with large deformation problem in metal forming by replacing the conventional way of applying complicated remeshing schemes when using the Lagrange's elements. During metal forming process, a workpiece normally undergoes large deformation and causes severe distortion of elements in finite element analysis. The distorted element may lead to instability in numerical calculation and divergence of non-linear solution in finite element analysis. With Eulerian elements, the initial elements are generated to fix into a specified analytical region with particles implanted as markers to form the body of a workpiece. The particles are allowed to flow between the elements after each deformation step to show the deforming pattern of material. Four types of cold forging and sheet metal clinching were conducted to investigate the effectiveness of the presented method. The proposed method is found to be effective by comparing the results on dimension of the final product, material flow behaviour and punch load versus stroke obtained from simulation and experiment.

Introduction

The finite element method (FEM) has been widely used especially at the design stage to analyse material flow behaviour in metal forming processes such as bulk forming and sheet metal forming because it can accurately simulate the deformation of material.

In bulk forming, C.C. Wang[1] introduced rigid-plastic finite element method using Euler's fixed element to replace Lagrange's element and it is found to be effective in forging process. S.A.S. Javanmard et al.[2] proposed natural element method to implement meshless analysis on backward extrusion simulation.

In sheet metal forming, S. Andrzej[3] used coupled Eulerian-Largragian approach to simulate riverting process where the rivet was modeled by Eulerian elements while tools was modeled by Lagrangian elements to solve large displacement problem. Besides, X. Zhuang et al.[4] employed the Arbitary Lagranian-Eulerian method where a Largrangian step is followed by an Euler step to deal with large localised deformation occurred in sheet metal extrusion. In mechanical clinching, Varis and Lepistö[5] and Lee et al.[6] used the finite element method for clinching tool design.

In metal forming, the material undergoes a severe working condition of extremely high contact pressure with tools and dies during the deformation process. This may shorten the die's life because of the escalation of wear and tear if the design is inappropriate. Therefore, FEM become a reliable tool used to design new formed products, analyse the deformation process and improve the existing processes. Despite several commercial FEM codes available for simulation metal forming processes, the input procedures are not flexible in term of defining material model and working

conditions to match the actual situation for forging operation. Thus, the development of forging simulator with customized pre- and post-processors are essential to suit the user's need.

In this study, the implementation of Eulerian meshing method based on rigid-plastic finite element was applied in cold forging and sheet metal forming. Four types of cold forging which including backward, forward-backward, double cup, axi-symmetric ring cup extrusion and sheet metal clinching were conducted to investigate the effectiveness of the presented method. The validity of the proposed method was examined by comparing the results from FEM simulation and experiment.

Rigid-plastic Finite Element Method

The FEM for the analysis of metal forming can be classified into two categories, i.e., rigid-plastic and elasto-plastic analysis. The rigid-plastic FEM is normally used for simulating bulk forming processes like forging and extrusion, because the deforming behavior of the material is assumed to be largely governed by the plastic strains rather than the elastic ones when large deformation is given. Thus, in the rigid-plastic finite element analysis, a relatively large incremental step of deformation can be taken to shorten the computing time without considering the yielding of elastic zone. On the other hand, the elasto-plastic FEM is mainly employed to sheet forming, where the springback caused by elastic strains is an important factor to deal with. The present rigid-plastic FEM is formulated on the basis of plasticity theory for a material with slight compressibility[7,8]. In the plastic theory, the Von Mises yield criterion is approximated to have small pressure sensitivity;

$$\frac{3}{2}\sigma_{ij}'\sigma_{ij}' + g\sigma_m^2 - \bar{\sigma}^2 = 0 \qquad (1)$$

Where σ_{ij}' is the deviatoric stress tensor, g is a small positive constant (0.01-0.0001) compared with unity, σ_m is the hydrostatic stress and $\bar{\sigma}$ is the flow stress flow stress. The flow stress $\bar{\sigma}$ can be expressed as a function of equivalent strain $\bar{\varepsilon}$ and strain rate $\dot{\bar{\varepsilon}}$, which can deal with the material work-hardening effect and visco-plastic behaviours. By using the associated flow rule, the stress and strain-rate relations for the slightly compressible rigid-plastic material can be derived from yield criterion of Eq. (1).

Meshing Method in Forging Simulation. The isoparametric quadrilateral elements with four nodal points are employed to two-dimensional simulation for forging process (See Fig. 1(a)) In this situation like forward-backward extrusion as shown in Fig. 1(b), the elements are heavily distorted due to the drastic flow of material which subjected to large shearing and compressive deformation around the tool corner. The distorted elements can cause the instability of numerical calculation when converging the nonlinear solution, and therefore remeshing procedure is accompanied to reinstall proper elements for replacing the distorted ones.

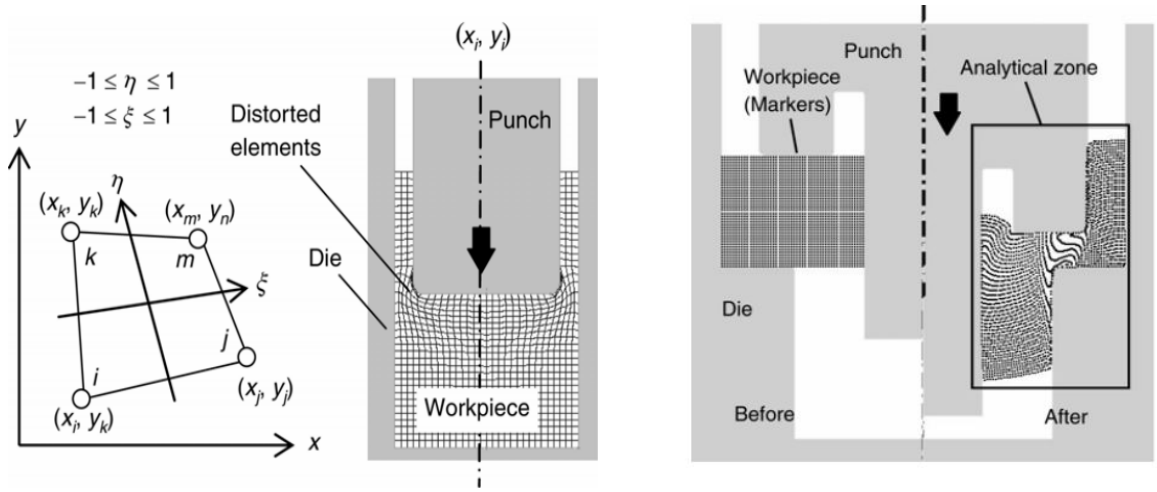

(a) (b)

Figure 1 (a) Type of element and simulation of backward extrusion. (b) Axi-symmetric simulation of forward-backward extrusion using the Eulerian meshing method.

In the case like extruding a product which has the complicated shape of many sharp edges, remeshing is required at almost every calculation step until the end of the process. As a result, this will not only affect on overall accuracy of the simulated result caused by the error in volume loss, but also give a longer computing time with smaller time step and more elements by the remeshing procedure.

Eulerian Element. For solving the remeshing problem in forging process, instead of using the conventional Lagrange's element, the Eulerian element based on infinitesimal deformation approach has been proposed by the authors. With the method, the meshes are initially generated to fix into a specified analytical region with particles implanted as markers to form the body of a workpiece. The particles are allowed to flow between the meshes and carry the information like equivalent strain, temperature and others.

Experiments

Compression Test and Tensile Test. Compression tests of the aluminium billets were carried out to measure the flow stress curves for extrusion and tensile test of steel metal sheets were carried out to measure the flow stress curve for clinching. The material properties and working conditions used for the simulation are listed in Table 1.

Table 1: Material properties and working conditions for the simulation.

Specimen material	Aluminium billet for extrusion	Steel metal sheet for clinching
Dimension of specimen (mm)	ϕ14 x 14	100 x 20 x 1.1
Lubricant	Mechanical oil	Without lubricant
Flow stress curve (MPa)	$\overline{\sigma} = F\overline{\varepsilon}^{n}$ $F = 415.16$ $n = 0.082$	$\overline{\sigma} = F\overline{\varepsilon}^{n}$ $F = 507$ $n = 0.32$

Cold Forging. Fig. 3(a) shows the experiment setup of extrusion. Four types of experiments, backward, forward-backward, double cup and another axi-symmetric extrusion were carried out. The ϕ14 x 14 mm cylindrical aluminium billets was placed inside the die and the upper punch moved downward accordingly until the desired stroke obtained to complete the process.

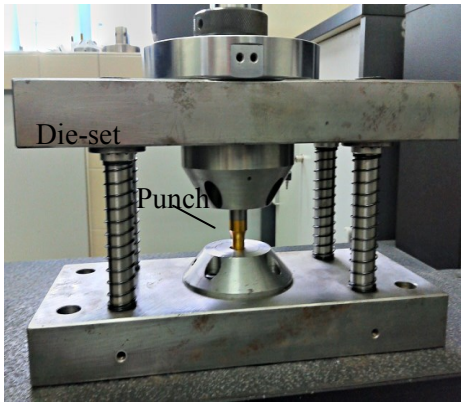

(a)

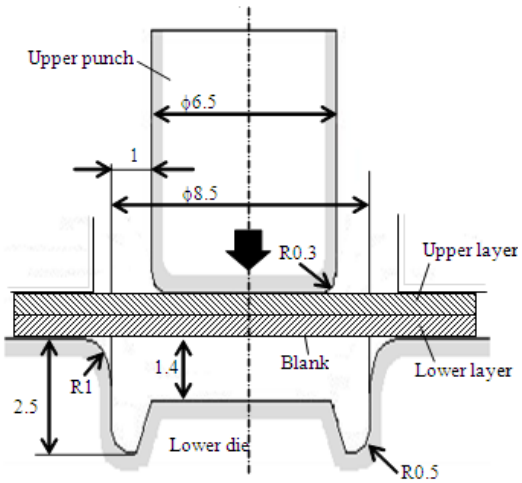

(b)

Figure 3 Tooling setup for backward, forward-backward, double cup, axi-symmetric extrusion and clinching.

Sheet Metal Clinching. Fig. 3(b) shows the experiment setup of clinching, sheet metals of 1.1mm thickness were prepared with dimension of 100mm x 20mm. The clinching process was carried out with two layers of metals sheets placed on the lower clinching tool and the upper punch moved downward accordingly until the desired stroke obtained.

Comparison of Simulation and Experimental Results

Part (a) in Fig. 4 to Fig. 8 shows the comparison between the extruded shape obtained by the calculation and experiment. The shapes for both simulation and experimental results are identical. The punch loads obtained by the calculation and experiment are compared in part (b) for all the mentioned figures. Generally, fluctuation of the calculated curves is mainly due to the iteration of numerical calculation in simulation. Besides, significant deviation between simulation and experimental results at the early stage of the punch load curve is due to the formulation of Rigid-plastic finite element method where this method tend to ignore the elastic region and the beginning portion of plastic region, thus only the plastic deformation after the mentioned regions is considered thoroughly. The results obtained reveal a close agreement between the calculations and experiments. This can be seen in Fig. 6 where both the simulation and experimental results show that the height of H_1 is higher than H_2. In Fig. 7, the inner extrusion is higher compare to outer ring for both experimental and calculated results because the distribution of stress value is higher at center axis.

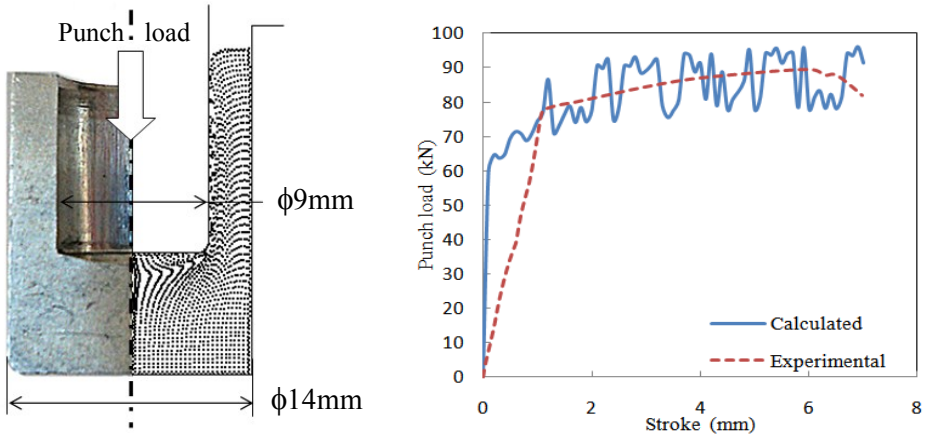

(a) Extruded shape (b) Punch load curve

Figure 4 Comparison between calculation and experiment for backward extrusion (Extrusion ratio = 0.41).

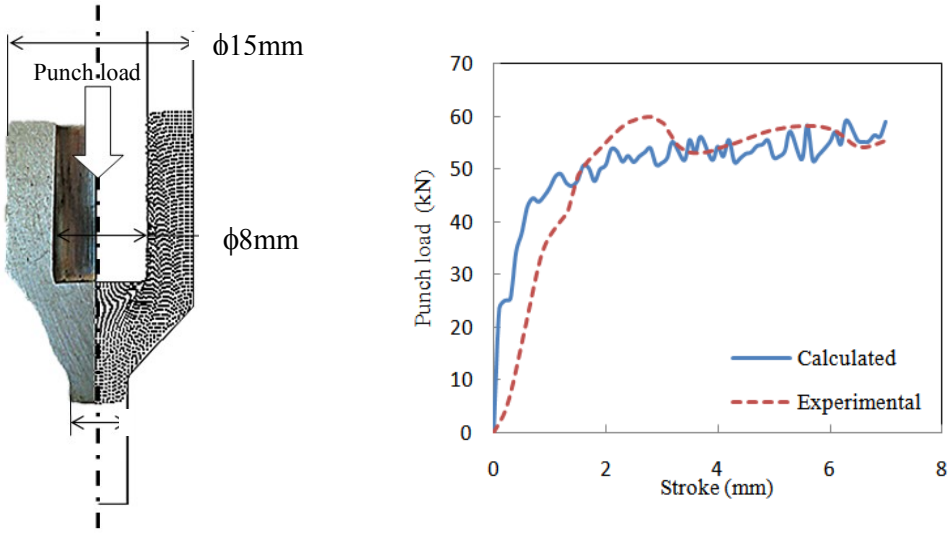

(a) Extruded shape (b) Punch load curve

Figure 5 Comparison between calculation and experiment for forward-backward extrusion (Extrusion ratio = 0.28).

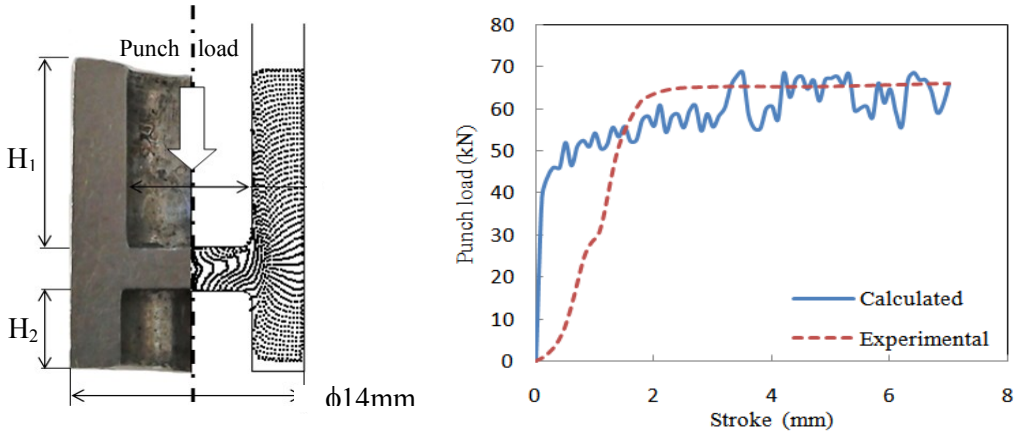

(a) Extruded shape (b) Punch load curve

Figure 6 Comparison between calculation and experiment for double cup extrusion (Extrusion ratio = 0.29).

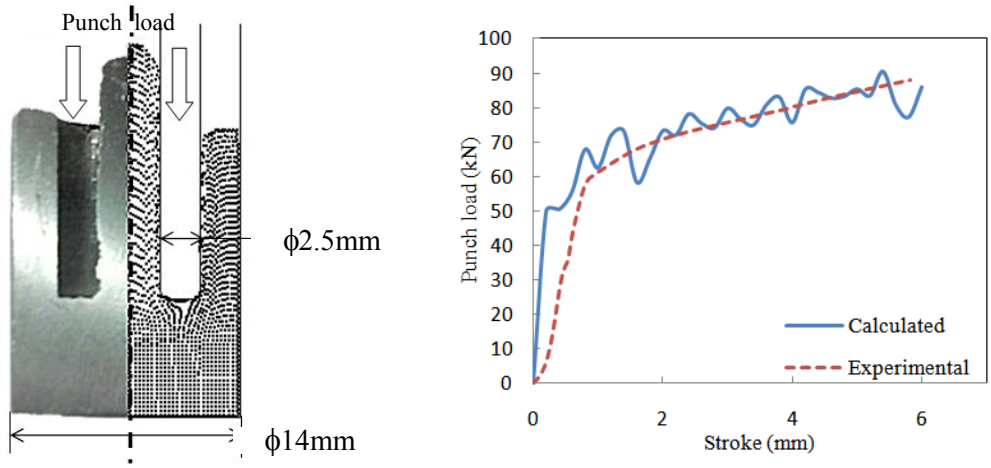

(a) Extruded shape (b) Punch load curve

Figure 7 Comparison between calculation and experiment for axi-symmetric ring cup extrusion (Extrusion ratio = 0.33).

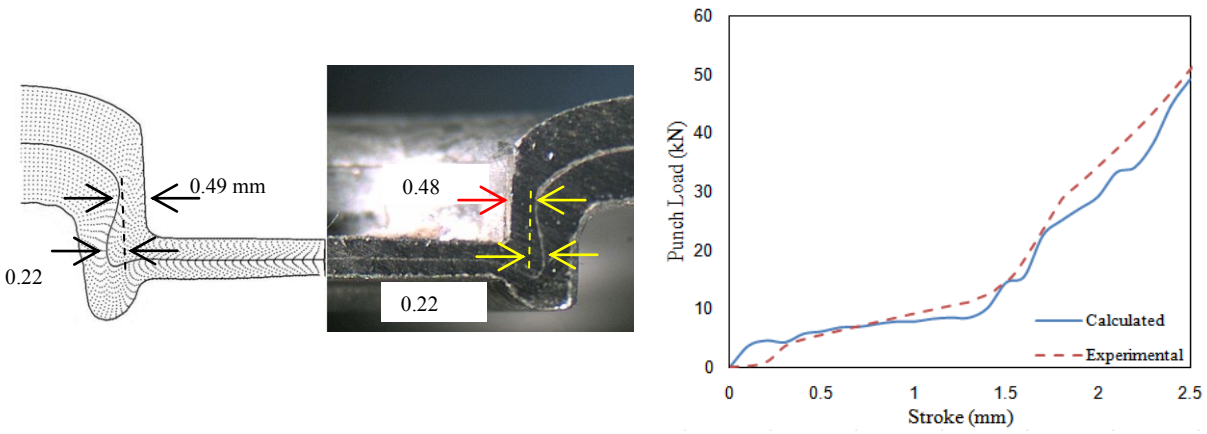

(a) Formed shape (b) Punch load curve

Figure 8 Comparison between calculation and experiment for sheet metal clinching.

Conclusion

The two dimensional rigid-plastic finite element simulator using the Eulerian meshing method was developed to clarify the dimension of the final product, deformation behavior and material flow for cold forging and sheet metal forming. Cold forging processes such as backward, forward-backward, double cup, axi-symmetric ring cup extrusion and sheet metal clinching were conducted to investigate the effectiveness of Eulerian meshing method. The following results were obtained:

1. The predicted punch load and stroke obtained by simulations agree well with those obtained from experiments.
2. Dimension and shape of the extruded parts are well predicted.
3. Eulerian meshing method is proved to be effective to deal with actual work for cold forging and sheet metal forming.

References

[1.] C.C. Wang: 'Development of Finite Element Method Simulator for Forging Process Design using Euler's Fixed Meshing Method', Int. J. Precision Technology, 2009, Vol. 1, No. 2.

[2.] S.A.S. Javanmard, F. Daneshmand, M.M. Moshksar and R. Ebrahimi: 'Meshless Analysis of Backward Extrusion by Natural Element Method', IJST, Transaction of Mechanical Engineering, 2011, Vol. 35, No. M2, pp 167-180.

[3.] S. Andrzej: 'Application of Coupled Eulerian-Lagrangian Approach in Metal Forming Simulation', Zeszyty Naukowe Politechinki Rzeszowskiej Mechanika z. 84 (4/12), 2012.

[4.] X. Zhuang, Z. Zhao, H. Xiang and L.I. Cong-xin: 'Simulation of Sheet Metal Extrusion Processes with Arbitary Lagrangian-Eulerian Method', Trans. Nonferrous Met. Soc. China 18, 2008, 1172-1176.

[5.] Varis, J.P. and Lepistö, J: 'A Simple Testing-based Procedure and Simulation of The Clinching Process Using Finite Element Analysis for Establishing Clinching Parameters', Thin-Walled Structures 41, 2003, 691–709.

[6.] Lee, C.J., Kim, J.Y., Lee, S.K., Ko, D.C. and Kim, B.M.: 'Design of Mechanical Clinching Tools for Joining of Aluminium Alloy Sheets', Materials and Design 31, 2010, 1854–1861.

[7.] K.Osakada., J. Nakano and K. Mori: 'Finite Element Method for Rigid-plastic Analysis of Metal Forming – Formulation for Finite Element', Int. J. Mech. Sci. 24, 1982, 459-478.

[8.] K. Mori, K. Osakada and T. Oda: 'Simulation of Plane-strain Rolling by The Rigid-plastic Finite Element Method', Int. J. Mech. Sci. 24, 1982, 519-527.

CHAPTER 9:

Environmentally Sustainable Materials and Processing

Advanced Materials Research Vol. 970 (2014) pp 187-191

doi:10.4028/www.scientific.net/AMR.970.187

Development of Water Adsorbents Synthesized From Spent Bleaching Earth To Dehydrate Ethanol Water Mixture

Azharin Shah Abd Aziz[1,a*], Abdurahman Hamid Nour[2] and Rosli Mohd Yunos[3]

[1]TATI UC, Telok Kalong, 24000 Kemaman, Terengganu, Malaysia

[2,3] FKKSA, University Malaysia Pahang, Gambang, 26300 Kuantan, Pahang, Malaysia

[a] azharinshah@yahoo.com

Keywords: Water adsorbents, spent bleaching earth, modified fusion method, ethanol water mixture.

Abstract. Water adsorbent to dehydrate water ethanol mixture was synthesized from spent bleaching earth (SBE) using modified fusion method. The SBE was regenerated using heat at 750^{o}C. Predetermined alumina, Al_2O_3 and a stochiometric amount of KOH was added to the regenerated SBE, mixed and fused at several temperatures for 12 hours in a furnace. The fused mixture was grounded and mixed with water to get 40-55% KOH solution in water. This mixture was aged for several pre determined temperature for several pre determined days in a closed container before crystallization took place in 5 part by weight 5% KOH for 48 hours. The product obtained was washed 3 times with distilled water using filtration set and dried in oven at 220^{o}C for 20 hours. Results from Karl Fischer Titration showed that the product was able to absorb water up above 0.0200 g/g adsorbent which was approximately 50% performance of commercial zeolite A. The best conditions for synthesizing the water adsorbent from SBE were : 80 g alumina added per 100 gram kaolin, fused temperature of 650^{o}C, aging temperature of 80^{o}C for 5 days. However, XRD results showed that the synthesized product was not the type of zeolite A.

Introduction

Energy crisis spurred the researches of renewable fuel such biodiesel and bio ethanol throughout the world. Bio ethanol is cited as one of the most promising fuel alternatives. In order for ethanol to be used as fuel in internal combustion engine, it must be anhydrous with purity of at least 99.5% by volume at 15.6 ^{o}C. Ethanol water mixture forms azeotrope at the composition of 95.6% ethanol and 4.4% water by weight with boiling point of 78.2^{o}C at atmospheric pressure. Due to this constraint, conventional distillation is not able to purify ethanol water mixture beyond 95.6% ethanol by weight. Various techniques were developed to break the azeotrope of the ethanol water mixture such as azeotropic distillation, extractive distillation, pervaporation, pressure swing method, adsorption and etc [1]. Each of the techniques has their own advantages and disadvantages.

One of the attractive methods was adsorption using water adsorbent. It was claimed that adsorption was one of the technique that used less energy [4,13]. There were varieties of methodologies to produce water adsorbent especially zeolite A from various silica and alumina sources. Hayden et al. [12], synthesized zeolite A from calcined kaolin using hydrothermal treatment with NaOH as the promoter. Klamrassame et al. [8], synthesized sodium alumino silicate from coal fly ash using fusion method followed by hydrothermal treatment. Rios et al. [7], produced zeolite A from kaolin and NaOH using fusion and hydrothermal treatment. Purnomo et al. [11], produce different type of zeolites from bagasse fly ash using silicate extraction method followed by hydrothermal treatment.

Spent bleaching earth (SBE), is a solid waste from palm oil refineries and the annual generated SBE in Malaysia alone is approximately 120,000 tons and about 600,000 tons of bleaching earth is utilized worldwide in palm oil refining plant [2]. Past practice showed that the spent bleaching earth is disposed off in land filled without treatment. This poses an acute problem to the environment. To overcome this environmental problem, the SBE should be recycled such as

producing fuel briquette made from the SBE [3], production of biodiesel from residual oil recovered from the SBE [4] and pyrolysis of the residual oil in SBE to produce alternative fuel and chemicals [5].

In this research work the SBE were transformed into water adsorbent material using modified fusion method and used to dehydrate ethanol water mixture. It is hoped that the value of SBE will increase and simultaneously contribute to the reduction of waste by the SBE.

Experimental

The method used to synthesize water adsorbent was modified fusion method. SBE was heated in furnace at 750 ^{o}C to remove organic matter, for 12 hours. Alumina, Al_2O_3 Sigma Aldrich) was added to the regenerated SBE (20 gram Al_2O_3 per 100 gm SBE, 40 gram Al_2O_3 per 100 gm SBE, 60 gram Al_2O_3 per 100 gm SBE and 80 gram Al_2O_3 per 100 gram SBE etc.). Then a stoichiometric amount of potassium hydroxide, KOH (Merck) was added to the mixture and thoroughly mixed. The mixture of SBE, alumina and KOH was fused at several predetermined temperature (550 ^{o}C, 650 ^{o}C and 750 ^{o}C) for 12 hours in a furnace (Carbolite, ELF 11/6B). After 12 hours, the fused mixture was grounded using mortar and mixed with distilled water to get 40-55% KOH solution in water. This mixture was aged for several pre determined temperature (40 ^{o}C, 60 ^{o}C and 80 ^{o}C) for several pre determined days (1, 3, 5, 7 days etc.) in a closed container. Later, the mixture was reflux in 5% KOH in water for 48 hours. The amount of aqueous KOH used was 5 times the weight of the mixture. After 2 days, the product obtained was washed 3 times with distilled water using filtration set and dried in oven at 220 ^{o}C for 20 hours and ready to be tested.

Water analysis for water adsorbance test from ethanol water mixture was carried out using Karl Fisher Titrator (Metrohm, 870 KF Titrino Plus). The determination of regeneration temperature of SBE was carried out using Thermogravimetry Analyzer, TGA (Mettler Toledo, TGA SDTA 851e). X-Ray diffractometry measurements (Rigaku, Miniflex II) were conducted to identify types of water adsorbent present in some selected synthesized samples at ambient temperature with CuKα at 30 kV and 15 mA in the range of 2θ from 3 – 80^{o} with sampling step of 0.02^{o}.

Results and Discussion

This experiment was carried out to determine the most suitable regeneration for SBE before being used as the raw material for water adsorbent synthesis. Figure 1 showed the results of thermogravimetric analysis of SBE samples at the temperature of 650 ^{o}C, 750 ^{o}C and 850 ^{o}C in air. The onset temperatures were 242.92 ^{o}C, 243.40 ^{o}C and 731.89 ^{o}C while the endset temperatures were 653.83 ^{o}C, 720.64 ^{o}C and 731.89 ^{o}C respectively. The onset temperature was the temperature in which organic matter such as triglyceride, phospholipid, free fatty acids and soaps, coloring matter and minor oil constituent of SBE started to decompose. The results showed that nearly all the organic matter decomposed or burnt at the temperature of at least 732 ^{o}C. In this experiment the suggested temperature to regenerate SBE was 750 ^{o}C. Abd Wafti et al. [6], regenerated spent bleaching earth at the temperature ranging from 400^{o}C to 1000 ^{o}C for 1 hour.

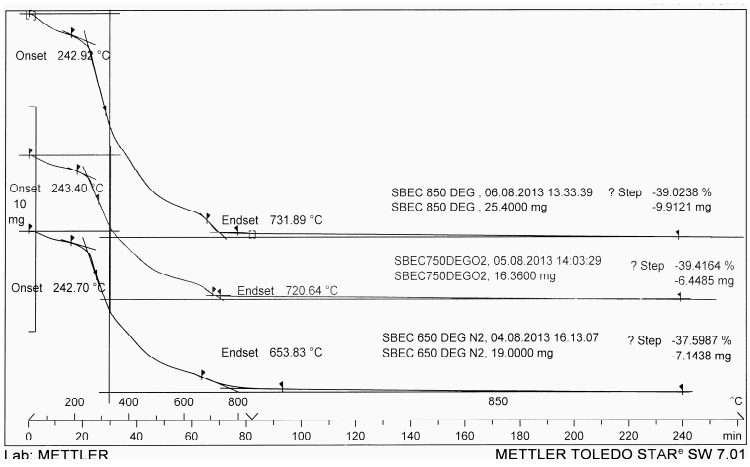

Fig 1. Thermogravimetric analysis of SBE.

Figure 1, figure 2, figure 3 and figure 4 shows the results of studied parameter to the performance of the water adsorbent. The performance of the synthesized water adsorbent was measured by the water adsorption capacity (g H_2O per g water adsorbent). Figure 2 showed the effect of the fused temperature to the average water adsorbed by the adsorbent. It was clearly seen that the fused temperature of 650 ^oC was the best temperature to yield adsorbent with average water adsorbance of 0.0218 ± 0.0034 g H_2O/g adsorbent. Lower fusion temperature, 550^oC and higher fusion temperature, 750^oC and 900^oC did not produce good water adsorbent. Rios et al. [7] suggested that alkaline fusion was very effective in extracting the silicon and aluminum species from kaolin.The Al_2O_3 and SiO_2 from the starting materials were converted into sodium/potassium salts (Na_2SiO_3 + Na_2AlO_2). Klamrassame et al. [8] found that the optimum fusion temperature was 450 ^oC for 1 hour for the synthesis of water adsorbent (sodium alumino silicate) from coal fly ash. Fusion method was used followed by hydrothermal treatment. Rios et al. [9] fused kaolin with NaOH at the temperature of 600 ^oC for 1 hour to produce zeolite A. The results showed that the best fusion temperatures were not similar for different starting raw material. This may be attributed to the different composition of the starting material.

Figure 3 showed the histogram of the effect of added alumina to the average water adsorbed by the adsorbent synthesized from SBE. From the histogram, the best weight of alumina to be added was 80 g alumina per 100 g material. The adsorbent using this value, fused at 650 ^oC, aged at 80 ^oC for 5 days was able to adsorb more than 0.0200 gram water per gram adsorbent. This result showed that excess or lack of alumina was not able to produce good water adsorbent. Alumina was added because the ratio of Si/Al affected the type of water adsorbent produced especially zeolite A. Tanaka and Fujii [10] reported pure zeolite A was obtained from coal fly ash when the ratio of SiO_2/Al_2O_3 was 1.0. At the ratio of SiO_2/Al_2O_3 = 0.5, zeolite A was still present with trace amount of hydroxysodalite and Na-X zeolite started to emerge at the $SiO_2/Al_2O_3 \geq 2$. Purnomo et al. [11] studied the synthesis of zeolite from bagasse fly ash using silicate extraction method followed by hydrothermal treatment. They found that at Si/Al ratio less than 1.8, zeolite Na-A plus Na-X was formed and pure Na-A can be produced using Si/Al ≤ 1.

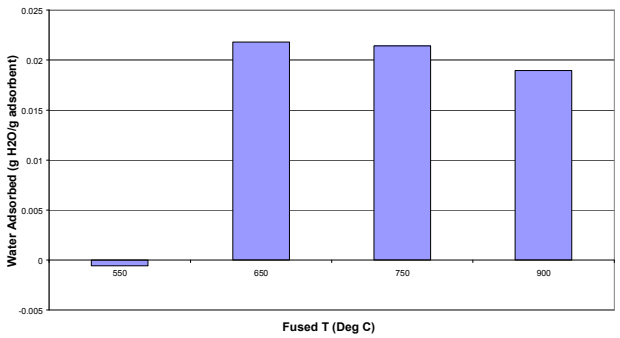

Fig 2: Effect of fused temperature to the water adsorbed by the adsorbent.

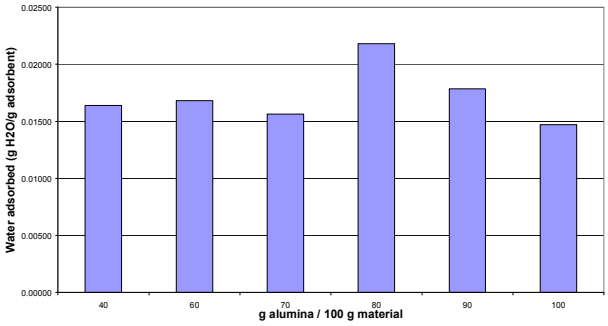

Fig 3: Effect of added alumina to the water adsorbed by the adsorbent.

Figure 4 showed the effect of aging time to the average water adsorbed by the adsorbent. The histogram showed that the best aging time to produce the best water adsorbent was 5 days. Aging was a process to create nucleate before crystallization took place. It was difficult to compare aging time of this experiment to other researchers due to insimilarity of synthesizing methods and starting raw materials. Hayden et al. [12] used the aging time of 96 hours when synthesizing zeolite A from kaolin. In their work, 60 parts by weight of kaolin was mixed and thoroughly blended with 43.2 parts by weight of 50% NaOH solution and shaped into pellets. The pellets were aged for 96 hours at 100^oF before crystallization took place. Rios et al. [9], aged their hydrogels under static conditions for 24 hours. In their experiment, kaolin was mixed with NaOH and fused for 1 hour at 600 ^oC. The fused product was ground and mixed with distilled water to form amorphous precursor

under stirring condition. This hydrogels were aged for 24 hours before hydrothermal reaction took place.

Figure 5 showed the diffractogram of the synthesized products from SBE and diffractogram of commercial zeolite 3A. Autosearch function of the XRD software revealed that the products were not the type of zeolite A. The diffractogram suggested that both products were similar in phases The product of SBE vial 175 has the ability to adsorb 0.0222 g H_2O/g whilst the product of SBE vial 164 has low ability to adsorb water from ethanol water mixture. For comparison, the commercial zeolite 3A has the ability to adsorb 0.0421 g H_2O/g.

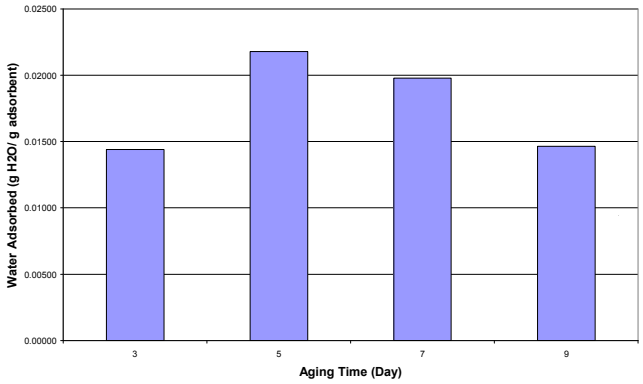

Fig 4: Effect of fused aging time to the average water adsorbed by the adsorbent.

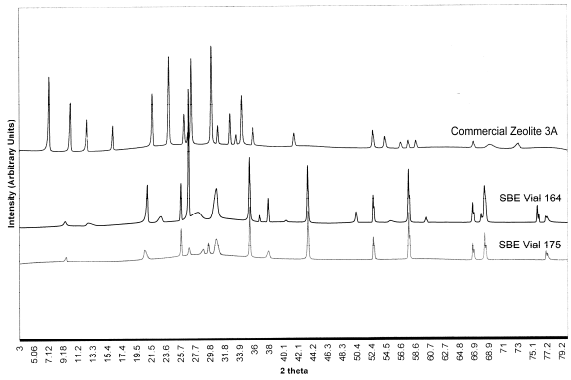

Fig 5: Diffractogram of the adsorbent synthesized from SBE.

Conclusion

Water adsorbent can be synthesized from SBE using modified fusion method. The SBE suggested regeneration temperature was 750^{o}C from TGA analysis. The best conditions to synthesize the water adsorbent were: 80 g alumina per 100 g SBE, fused temperature of 650^{o}C, aging temperature of 80^{o}C with aging time of 5 days. Autosearch results of XRD software revealed that the products were not the type of zeolite A as expectation. However, the product was able to adsorb water from ethanol water mixture.

References

[1] S.Kumar, N. Singh and R Prasad, Anhydrous Ethanol: A Renewable Source of Energy, Renewable and Sustainable Energy Reviews. 14 (2010) 1830-1834.

[2] R. Mat, O.S Ling, A. Johari and M. Mohamed, In Situ Biodiesel Production Residual Oil Recovered From Spent Bleaching Earth, Bulletin of Chemical Reaction Engineering & Catalysis, 6(1) (2011) 53-57.

[3] S. Suhartani, N. Hidayat and S. Wijaya, Physical Properties Characterization of Fuel Briquette Made From Spent Bleaching Earth, Biomass & Bioenergy, 35 (2011) 4209-4214.

[4] Y.P. Huang and J.I. Chang, Biodiesel Production From Residual Oils Recovered From Spent Bleaching Earth, Renewable Energy, 35 (2009) 269-274.

[5] P.L. Boey, M.I Saleh, N. Sapawe, S. Ganesan,G.P. Maniam and D.M. Hag Ali, Pyrolysis of Residual Palm Oil in Spent Bleaching Clay by Modified Tubular Furnace and Analysis of the Products by GC-MS, Journal of Analytical and Applied Pyrolisis, 91 (2011) 199-204

[6] N.S. Abd Wafti, C. Kien Yew, T.C. Shean Yaw and L.C. Abdullah, Regeneration and Characterization of Spent Bleaching Clay, J. of Palm Oil Research. 23 (2011) 999-1004.

[7] C.A. Rios, C.D.William and O.M. Castellanos, Crystallization of Low Silica Na-A and Na-X Zeolites From Transformation of Kaolin and Obsidian by Alkaline Fusion, Ingeniera y Competitividad, 14(2) (2012) 125-137.

[8] T. Klamrassame, P. Pavasant and N. Laosiripojana, Synthesis of Zeolite From Coal Fly Ash: Its Application as Water Adsorbent, Engineering Journal, 14(1) (2010) 37-44.
[9] C.A. Rios, C.D. Williams and M.A. Fullen, Nucleation And Growth History of Zeolite LTA Synthesized From Kaolinite By Two Different Methods, Applied Clay Science, 42 (2009) 446-454.
[10] H. Tanaka and A. Fujii, Effect of Stirring On The Dissolution of Coal Fly Ash And Synthesis of Pure-Form Na-A and –X Zeolites By Two Step Process, Advanced Powder Technology, 20 (2009) 473-479.
[11] W.P. Purnomo, C. Salim and H. Hinode, Synthesis of Pure Na-X and Na-A Zeolite From Bagasse Fly Ash, Microporous and Mesoporous Material, 162 (2012) 6-13.
[12] Haden W.L., Metuchen J. and Dzierzanowski.,US Patent 2992068. (1961).
[13] M. Simo, C.J. Brown and V Hlavacek, Simulation of Pressure Swing Adsorption In Fuel Ethanol Production Process, Computers and Chemical Engineering, 32 (2007) 1635-1649.

Advanced Materials Research Vol. 970 (2014) pp 192-197

doi:10.4028/www.scientific.net/AMR.970.192

Kinetic and Isotherm Adsorption Studies of Methylene Blue on Sulfuric Acid Treated Spent Grated Coconut (*Cocos nucifera)*

K. Khalid[1, a*] and M.A.K.M. Hanafiah[1, b]

[1]Faculty of Applied Sciences, Universiti Teknologi MARA, 26400, Jengka, Pahang, Malaysia

[a*]khadijah788@yahoo.com.my, [b]makmh@pahang.uitm.edu.my,

Keywords: Adsorption, Isotherm, Kinetic, Methylene blue, Spent grated coconut

Abstract. A new biosorbent, sulfuric acid (H_2SO_4) treated spent grated coconut (*Cocus nucifera*) (SSGC) showed a good ability to remove methylene blue (MB) from aqueous solutions. Equilibrium time was achieved within 300 min for all MB concentrations, and the kinetic data was best modeled by pseudo second-order. The adsorption data fitted the Langmuir isotherm model, suggesting monolayer coverage of MB over a homogeneous adsorbent surface. The experimental maximum adsorption capacity was 366.50 mg/g, obtained at 318 K, adsorbent dosage of 0.6 g/L and at pH 6. The attachment of MB on SSGC was confirmed by Fourier Transform Infrared (FTIR) spectroscopy.

Introduction

Methylene blue (MB), is one of the most commonly used dyes and has many applications, such as for dying cottons, wools and silks [1]. It also serves as a model compound for dyes and organic contaminants removal study from aqueous solutions due to its known strong adsorption ability onto solid [2]. The downside effects of MB are alarming. It can cause harmful effects to human and animals through inhalation and ingestion. Generally, removal of dyes by conventional techniques is inefficient and ineffective at low concentration, and activated carbon is normaly used but is expensive. Therefore, a research on the removal of MB from aqueous solution by adsorption technique has gained much interest as it utilizes a cheap, abundantly available and renewable biomaterial [3].

Coconut (*Cocos nucifera*), a member of the *Arecaceae* (palm family) and widely grown throughout the tropics is one of the most important crops in Malaysia [4]. Spent grated coconut (SGC) from a defatted coconut residue is a by-product of a coconut milk factory. After the extraction of coconut milk, inedible SGC by-product finds little applications apart from its use as fertilizers and animal feed. Coconut residues contains 63.24% dietary fiber [5], which refers to the plant substances including plant cell wall (cellulose, hemicellulose, pectin and lignin), as well as intracellular polysaccharides [6]. These compounds may provide a lot of binding sites responsible for many physical and chemical adsorptions. According to Asgher [7], the cell wall of plants and microbial cells are the essential places where numerous metabolism-independent processes take place such as physical and chemical adsorption, electrostatic interaction, ion exchange, complexation, chelation, and microprecipitation. Abundance of coconut waste materials had been investigated for MB removal from aqueous solution [3]. The study on SGC however, has not been reported in the literature. Thus, this study aimed to investigate the adsorption characteristics of SGC particularly after chemical modification (SSGC), to be utilized as a value-added by-product for industrial application specifically in water purification as well as helping industries in reducing the cost of waste disposal.

Materials and Methods

Adsorbent Treatment and Characterization. SGC was obtained from a food factory in Kuching, Malaysia. After the process of dehusking, grating and screw-pressing to remove the coconut milk, SGC was dried in an oven at 278 K overnight. Pretreatment of SGC was done by mixing the SGC

with hexane (R & M Chemicals, UK) in the ratio of 1.0 g of SGC to 10 mL of hexane (1:10, w/v) and stirred using a magnetic stirrer for 16 h to remove fat [5]. This process was done to eliminate the presence of organic interferents in the sample matrix. The pretreated sample was then filtered and again oven dried at 333 K for 3 h. The hexane-washed SGC was labeled as HSGC. Acid treatment was carried out as it enhances the adsorption capacity by increasing the porosity of the adsorbent. Chemical activation by H_2SO_4 in particular is widely used as it improves pores development [8]. The treatment method was adapted from Montes et al. [9] and Lin et al. [10] with some modification where HSGC was mixed in the ratio of 3.0 g of HSGC to 50 mL, 2.0 M H_2SO_4 (3:50, w/v). The concentration of 2.0 M H_2SO_4 was chosen after the optimization studies done for a series of H_2SO_4 concentration ranging from 0.5 to 5.0 M. The mixture was stirred continuously at 480 rpm and at temperature 373 K for 3 h, cooled to room temperature (298 K), and washed twice with 200 mL of distilled water. The slurry was filtered, and then soaked in 100 mL of 1% (w/v) $NaHCO_3$ solution for 24 h to neutralize the solution. The sample was washed thoroughly with distilled water until the pH of the effluent was close to 7. The H_2SO_4 treated HSGC was dried for overnight in an oven at 378 K, ground and sieved to obtain a particle size of 120-250 µm, and finally designated as SSGC. The Brunauer–Emmett–Teller (BET) surface area and pore diameter of HSGC and SSGC were determined from the N_2 adsorption at 77 K (Thermo Scientific, Surfer, Italy). The functional group characterization was carried out using Fourier Transform Infrared (FTIR) spectrophotometer (Spectrum 100, Perkin Elmer, USA) by making 1% sample pellet of spectrophotometric potassium bromide (KBr). The FTIR analyses were done on SSGC for MB loaded and unloaded samples.

Batch Experiment. Methylene blue (MB), a basic and cationic dye, has a chemical formula of $C_{16}H_{18}N_3S^+Cl^-$ and a molecular weight of 319.5 g/mol. MB powder of analytical reagent grade (QRec, Malaysia) was used to prepare a 1000 mg/L of MB solution. Dilute solutions of required MB concentrations were successively prepared for batch adsorption experiments. Batch experiments were carried out by mixing 0.03 g of SSGC powder with 50 mL MB solution of fix concentration in 100 mL conical flasks for a specific period of time. All experiments were done at pH 6 (optimum pH). After the experiment, the sample was centrifuged at 5000 rpm for 5 min to separate SSGC from the solution. The amount of MB in the residual solution was analyzed by using UV-Visible spectrophotometer (UV-1800, Shimadzu, Japan) at λ_{max} of 664 nm. All experiments were performed in duplicates and the results were reported as average with RSD<5%. The amount of MB adsorbed, q_e (mg/g) was calculated by using Eq. (1), while the percentage of removal of MB was calculated using Eq. (2):

$$q_e = \frac{C_o - C_e}{m} V . \quad (1)$$

$$\text{Removal } (\%) = \frac{C_o - C_e}{C_o} 100. \quad (2)$$

where, C_o and C_e are MB concentrations (mg/L) before and after adsorption respectively; V is the volume of MB solution (L) and m is the weight of the adsorbent (g). The kinetic study was conducted using different concentrations of MB solutions (10, 30 and 60 mg/L) and the mixtures were stirred at different time intervals from 0 to 360 min. The data were analyzed by using the pseudo first-order and pseudo second-order models. The isotherm study was carried out with varied concentrations of MB solution (10, 30, 60, 100, 150, 200, 300 and 400 mg/L) at 298, 308 and 318 K, respectively. The data obtained were analyzed by using the two main isotherm models namely Langmuir and Freundlich.

Results and Discussion

Characterization of SSGC. Results showed that the BET surface area of HSGC was 0.829 m^2/g, but increased to 23.673 m^2/g in SSGC. The average pores diameter decreased from 1.575 Å (SGC) to 1.250 Å (SSGC). These could explain the increase of adsorption capacity upon acid treatment, as a high surface area can increase higher adsorption capacity due to the existence of large number of binding sites and pores.

FTIR. The FTIR spectrum of SSGC MB unloaded (Figure 1a) showed a strong band observed at 3431 cm^{-1} which showed evidence of O-H stretching due to hydroxyl and N-H groups. The band at 1714 cm^{-1} suggested the existence of the carbonyl C=O group stretching due to ester. Two strong peaks at 2923 cm^{-1} and 2852 cm^{-1} appeared due to C-H stretching. Peak observed at 1622 cm^{-1} could be due to the aromatic skeletal vibrations and carboxylate whereas at 1385 cm^{-1} could be evidence of C-N stretching. Another peak was observed at 1185 cm^{-1} could be the evidence of C-O stretching, suggesting a relative increased in functional groups with single oxygen bonds (such as phenols, ethers and lactones), while peak observed at 1044 cm^{-1} could be due to the inorganic sulfate ions residual. The spectrum of SSGC loaded with MB (Fig. 1b) showed some of the peaks had shifted to lower frequencies or markedly changed in their degree of attenuation, indicating that the MB molecules had bound to the SSGC. A band at 1622 cm^{-1} shifted slightly to 1604 cm^{-1} with even stronger intensity. The appearance of significant and intense peaks within 1400-800 cm^{-1} region marked the aromatic ring system vibrations, which suggested MB adsorption onto the SSGC. The FTIR spectra suggested that MB adsorption on SSGC occurred through hydrogen bonding, ion-exchange and electrostatic interactions.

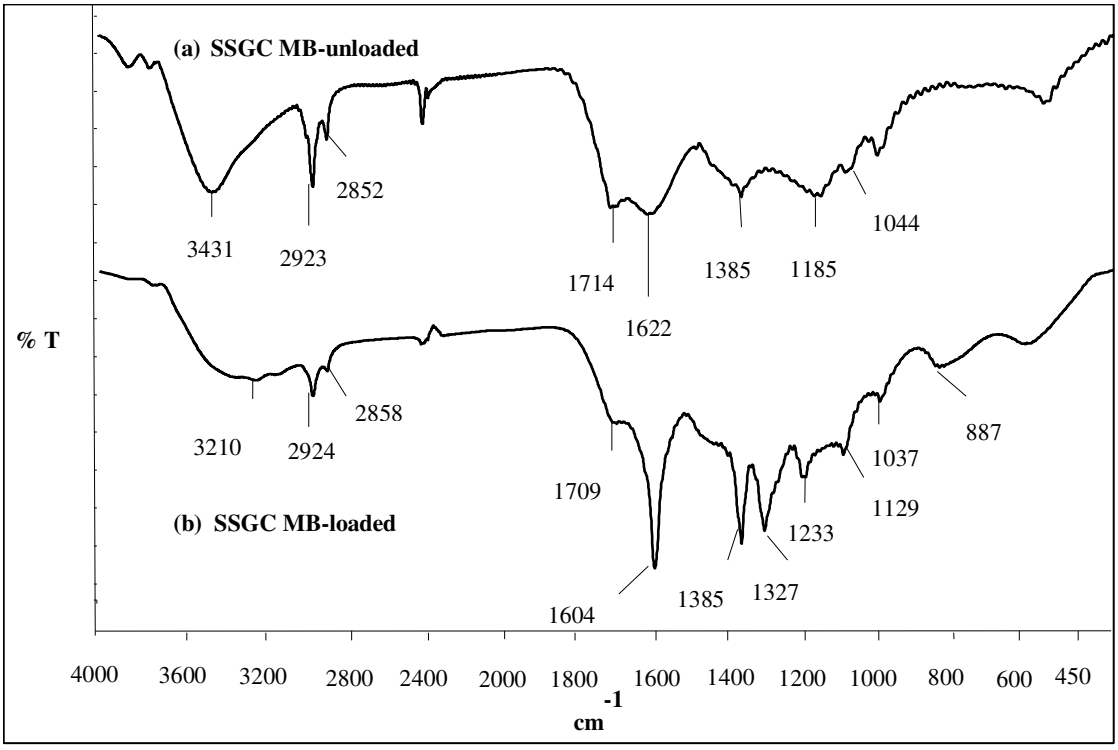

Figure 1- FTIR spectra of SSGC (a) MB-unloaded and (b) MB-loaded

Kinetic Study. Figure 2 showed a rapid adsorption process took place in the first 30 min. Increasing the solution concentration had increased the driving force impacted by the increased of concentration gradient [11].

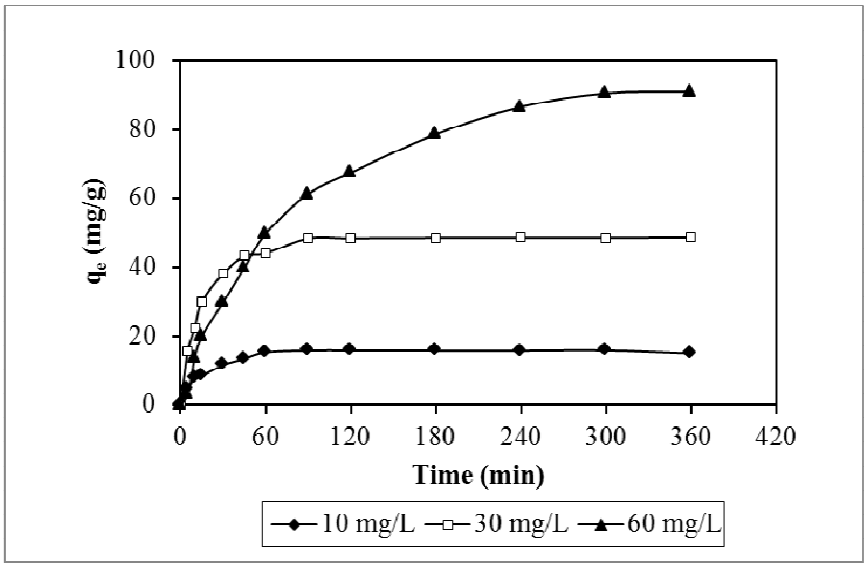

Figure 2- Effect of concentration and contact time on MB adsorption onto SSGC

Thus, as the concentration increased, more MB ion surrounded the active sites on the SSGC surface which led to higher equilibrium adsorption capacity. The delay in the equilibrium time reached by increased concentration however could be due to competition among ions for the available sites as a result of concentration gradient.

The data from the effect of contact time and initial concentration studies are crucial in the investigation of adsorption kinetic models which leads to the understanding of adsorption mechanisms and processes. In this study, two adsorption kinetic models namely pseudo first-order [12] and pseudo second-order [13] were employed. The linear form of pseudo first-order is expressed as Eq. (3) and followed by the pseudo second-order given by Eq. (4):

$$\log (q_e - q_t) = \log q_e - \frac{k_1}{2.303} t \,. \tag{3}$$

$$\frac{t}{q_t} = \frac{1}{h} + \frac{1}{q_e} t. \tag{4}$$

where q_e and q_t are amount adsorbed (mg/g) at equilibrium and at time t (min), respectively and k_1 is the pseudo-first order rate constant (min^{-1}). For the pseudo second-order model, $h = k_2 q_e^2$ can be regarded as the initial adsorption rate (mg/g.min), and k_2 is the rate constant (g/mg.min).

The results obtained from Table 1 showed that MB adsorption on SSGC was well fitted to the pseudo second-order for all concentrations with R^2 values close to unity. The experimental adsorption capacity and the calculated adsorption capacity were also found close with each other for pseudo second-order.

Table 1- Pseudo first-order and pseudo second-order constants at different concentrations of MB

MB [mg/L]	$q_{e,exp}$ [mg/g]	Pseudo first-order			Pseudo second-order			
		$q_{e,cal}$ [mg/g]	k_1 [min^{-1}]	R^2	$q_{e,cal}$ [mg/g]	k_2 [g/mg.min]	h [mg/g·min]	R^2
10	15.79	21.56	0.065	0.974	15.85	8.92 x 10^{-3}	2.24	0.997
30	48.62	28.02	0.036	0.958	50.25	2.36 x 10^{-3}	5.95	0.999
60	101.84	88.67	0.012	0.992	120.48	8.36 x 10^{-3}	1.21	0.945

Isotherm. Isotherm is important for estimating the maximum amount of adsorbate adsorbed by a given amount of adsorbent [14]. The Langmuir isotherm assumes monolayer coverage of the adsorbent, occurs on or over a homogeneous adsorbent surface with each molecule adsorbed having identical adsorption activation energy, while the Freundlich model assumes a multilayer adsorption with non-uniform distribution of energy over the heterogeneous surface. The linear Langmuir equation can be written as Eq. (5) whereas the linear Freundlich equation is given as Eq. (6):

$$\frac{C_e}{q_e} = \frac{1}{q_{max} b} + \frac{C_e}{q_{max}} . \quad (5)$$

$$\log q_e = \log K_F + \frac{1}{n} \log C_e . \quad (6)$$

where q_e is the amount adsorbed at equilibrium (mg/g), q_{max} is the maximum adsorption capacity (mg/g) and b is the Langmuir constant (L/mg) related to energy of adsorption. K_F represents Freundlich constant related to maximum adsorption capacity (mg/g) and *n* is related to adsorption intensity (unitless).

The isotherm plots for all temperatures studied (not shown) indicated steeper slope at lower initial concentration before they reached a plateau at higher concentration. These plots are of the "H" type of isotherm according to Giles classification system, suggesting high affinity or strong interaction between adsorbate and adsorbent.

Table 2 summarizes the Langmuir and Freundlich constants, maximum adsorption capacities (q_{max}) and correlation coefficients (R^2) for MB at different temperatures. Overall, it was found that MB adsorption favored higher temperature. The experimental maximum adsorption capacity of MB onto SSGC was 366.50 mg/g with Langmuir as the best fitted isotherm model (R^2>0.999). This was supported by the calculated maximum adsorption capacities (q_{max}) closed to the experimental maximum adsorption capacities in contrast to a much lesser extent by Freundlich models. Although the values of *n* calculated from Freundlich showed favourable adsorption (*n*>1), the K_F values were not comparable with the experimental adsorption capacities.

Table 2- Langmuir and Freundlich isotherm constants and correlation coefficients for MB adsorption at concentration 10-400 mg/L

Temp.	Experimental	Langmuir			Freundlich		
[K]	q_{max} [mg/g]	q_{max} [mg/g]	b [L/mg]	R^2	K_F [mg/g]	*n*	R^2
298	303.50	300.30	0.461	0.998	2.04	5.45	0.926
308	334.50	334.45	0.624	0.999	2.33	11.53	0.814
318	366.50	363.64	0.753	0.999	2.32	8.47	0.933

Conclusion

SSGC after undergoing chemical treatment by using H_2SO_4, has proven to be a good adsorbent for MB removal. The adsorption data fitted well with the pseudo second-order for the kinetic model and Langmuir for the isotherm model. MB adsorption was more favored at higher temperatures. Based on the characterization studies, kinetic and isotherm models, it is suggested that the possible adsorption mechanisms involved could be through the formation of hydrogen bonding, ion-exchange and electrostatic attraction.

Acknowledgement

This work was financially supported by the UiTM Research Grant Scheme (Dana: 600-RMI/ST/DANA 5/3/Dst(179/2011).

References

[1] V.M. Vučurović, R.N. Razmovski, M.N. Tekić, Methylene blue (cationic dye) adsorption onto sugar beet pulp: Equilibrium isotherm and kinetic studies, J. Taiwan Inst. Chem. E. 43 (2012) 108–111.

[2] B.H. Hameed, T.M. Din, L. Ahmad, Adsorption of methylene blue onto bamboo-based activated carbon: Kinetics and equilibrium studies. J. Hazard. Mater. 141 (2007) 819–825.

[3] A. Bhatnagar, V.J.P. Vilar, C.M.S. Botelho, R.R. Boaventura, Coconut-based biosorbents for water treatment- A review of the recent literature, Adv. Colloid Interface Sci. 160 (2010) 1–15.

[4] B.H. Hameed, D.K. Mahmoud, L. Ahmad, Equilibrium modeling and kinetic studies on the adsorption of basic dye by a low-cost adsorbent: Coconut (*Cocos nucifera*) bunch waste, J. Hazard. Mater. 158 (2008) 65–72.

[5] S. Raghavendra, S.R. Ramachandra Swamy, N.K. Rastogi, K.S.M.S. Raghavarao, S. Kumar, R.N. Tharanathan, Grinding characteristics and hydration properties of coconut residue: A source of dietary fiber, J. Food Eng. 72 (2006) 281-286.

[6] S. Raghavendra, N. Rastogi, K.S.M.S. Raghavarao, R.N. Tharanathan, Dietary fiber from coconut residue: Effects of different treatments and particle size on the hydration properties, Eur. Food Res. Technol. 218 (2004) 563-567.

[7] M. Asgher, Biosorption of Reactive Dyes: A Review, Water, Air, Soil Pollut. 223 (2011) 2417–2435.

[8] C.K. Singh, J.N. Sahu, K.K. Mahalik, C.R. Mohanty, B.R. Mohan, B.C. Meikap, Studies on the removal of Pb(II) from wastewater by activated carbon developed from Tamarind wood activated with sulphuric acid, J. Hazard. Mater. 153 (2008) 221–228.

[9] S. Montes, G. Montes-Atenas, F. Salomo, E. Valero, O. Diaz, On the adsorption mechanisms of copper ions over modified biomass, Bull. Environ. Contam. Toxicol. 76 (2006) 171–178.

[10] J.X. Lin, S.L. Zhan, M. H. Fang, X.Q. Qian, H. Yang, Adsorption of basic dye from aqueous solution onto fly ash, J. Environ. Manage. 87 (2008) 193–200.

[11] R. Han, W. Zou, W. Yu, S. Cheng, Y. Wang, J. Shi, Biosorption of methylene blue from aqueous solution by fallen phoenix tree's leaves, J. Hazard. Mater. 141 (2007) 156–162.

[12] Y.S. Ho, G. Mckay, A comparison of chemisorption kinetic models applied to pollutant removal on various sorbents, Process Saf. Environ. Protect. 76 (1998) 332–340.

[13] Y.S. Ho, J.C.Y. Ng, G. McKay, Kinetics of Pollutant Sorption By Biosorbents: Review, Sep. Purif. Rev. 29 (2000) 189–232.

[14] M.A.K.M. Hanafiah, W.S.W. Ngah, S.H. Zolkafly, L.C. Teong, Z.A.A. Majid, Acid Blue 25 adsorption on base treated Shorea dasyphylla sawdust: Kinetic, isotherm, thermodynamic and spectroscopic analysis, J. Environ. Sci. 24 (2012) 261–268.

Advanced Materials Research Vol. 970 (2014) pp 198-203

doi:10.4028/www.scientific.net/AMR.970.198

Monosodium Glutamate Functionalized Chitosan Beads for Adsorption of Precious Cerium Ion

M. A. K. M. Hanafiah[1,a], Z. M. Hussin[1,b*], N. F. M. Ariff[2,c], W. S. W. Ngah[3,d], S.C. Ibrahim[2,e]

[1]Faculty of Applied Sciences, UniversitiTeknologi MARA (Pahang), 26400,Jengka, Malaysia

[2]Faculty of Applied Sciences, UniversitiTeknologi MARA, 40450, Shah Alam, Malaysia

[3]School of Chemical Sciences, UniversitiSains Malaysia, 18100, Penang, Malaysia

[a]makmh@pahang.uitm.edu.my, [b*]zurhana_mhussin@pahang.uitm.edu.my, [c]noorulfarhanaariff@gmail.com, [d]wsaime@usm.my, [e]sha88@salam.uitm.edu.my

Keywords: Adsorption, chitosan, cerium, kinetic, isotherm

Abstract. Monosodium glutamate functionalized chitosan (MSGC) beads were synthesized and used as an adsorbent for recovering precious cerium ion from aqueous solutions. Several parameters which can affect adsorption efficiency such as effect of pH and adsorbent dosage have been investigated. The optimum pH for Ce(III) adsorption was 4. The rate of Ce(III) uptake was fast as the time to reach equilibrium was less than 10 min. Based on the applied kinetic model, Ce(III) adsorption onto MSGC fitted well with pseudo-second-order model. The maximum adsorption capacity recorded from the Langmuir isotherm model was 369.0 mg g^{-1} at 300 K.

Introduction

In recent years, rare earth elements (REEs) have been used in various fields. Cerium, the most abundant REE in the crust (0.0046%) is widely used in various industries as magnetism, catalyst, polishing powder and ceramic technology[1]. Due to the wide range of applicationsof REEs, degradation of environmental quality is expected to arise in the next few decades[2]. Thus, REEs need to be recovered from water stream in order to maintain the water quality. Researchers have come out with various methods of REEs removal which include precipitation, solvent extraction, ion exchange and adsorption. Based on previous research, adsorption was found to be the most effective, cheapest and easiest way to remove REEs from water stream [3].

Chitosan, is a biopolymer derived from chitin by using strong alkaline solution (normally sodium hydroxide) and it exhibits good adsorption properties such as non-toxic, biological tolerance, renewable, hydrophilic, biocompatible, biodegradable and anti-bacterial [4]. Besides, chitosan also showed goodadsorption performance in removing dyes, heavy metal ions and protein. Good adsorption performance of chitosan is associated with the presence of amino ($-NH_2$) and hydroxyl (-OH) groups, which can serve as the coordination or adsorption sites [5]. Unfortunately, chitosan is soluble in acid medium. This leads researchers to come out with various chemical modifications in order to enhance the adsorption ability as well as preventing chitosan from dissolving in acid [6, 7].

Oxidation, reduction, precipitation, membrane filtration, ion exchange and adsorption are the common methods for waste water treatment. Adsorption itself became the most superior technique for removal of contaminants for the past two decades [8, 9]. Very few studies regarding adsorption of Ce(III) have been done and the work on it is still ongoing.

The main objectives of this study were to synthesize and to evaluate the potential of monosodium glutamate functionalized chitosan (MSGC) beads as an adsorbent for Ce(III). Physicochemical parameters that can affect Ce(III) adsorption such as pH, adsorbent dosage and Ce(III) initial concentration were also investigated. Kinetic and isotherm studies were studied to understand the behavior of adsorption process.

Materials and Methods

Preparation of MSGC beads. The method of preparing MSGC beads was described by Gong et. al [10] with some modification. A weight of 2.0 g chitosan was mixed with 80 mL (5 %, v/v) acetic acid and was left overnight. The mixture was poured into 500 mL (0.50 M) NaOH solution under continuous stirring at 100 rpm. The resulting beads were mixed with 240 mL of 99% (v/v) dioxane, 40 mL of 99% (v/v) epichlorohydrin (ECH) and 24 mL of 20% (w/v) NaOH solution. The mixture was stirred at 65°C for 5 h and left overnight as the heating process completed. The beads were then rinsed with dioxane followed by a buffer solution at pH 10. A volume of 150 mL dioxane was mixed with 12 g monosodium glutamate (MSG) and a few drops of phenolphthalein. A solution of 20 % (w/v)NaOH was added drop wise until the solution turn into pink. Chitosan beads were added into this mixture and stirred for another 4 h at 50°C. The mixture was left overnight once the heating process completed before being rinsed thoroughly with deionized water. The MSGC beads formed were air-dried before finally ground and sieved to obtain adsorbent size of <100 μm. This adsorbent size was used throughout the adsorption experiments.

Batch adsorption study. A stock solution of 1000 mg L^{-1} Ce(III) was prepared from cerium (III) chloride salt (Acros, New Jersey USA). The stock solution was diluted to 20 mg L^{-1} (unless otherwise stated). In general, adsorption experiments were conducted by adding 0.02 g of MSGC beads (unless otherwise stated) into 50 mL Ce(III) solutions in 100 mL conical flask, stirred at 500 rpm at room temperature (300 K). After adsorption, the mixture was filtered and analyzed for remaining Ce(III) at a wavelength of 413.8 nm using inductively coupled plasma-optical emission spectrometer (ICP-OES).

The effect of initial pH of the solution on adsorption of Ce(III) onto MSGC was performed at pH 2 to 6. The pH of the solution was adjusted by adding drops of 0.10 M HCl or NaOH solutions. The pH dependence study was performed at 500 rpm stirring speed for 60 min. In the kinetic study, 50 mL of 50 mg L^{-1}Ce(III) solution was stirred with 0.02 g MSGC beads at pH 4. The mixture was stirred at different time intervals (0 – 60 min).The maximum adsorption capacity was determined from the isotherm study. This was done by adding 0.02 g MSGC beads into 50 mL Ce(III) solutions at various concentrations (20 – 600 mg L^{-1}) and stirred for 60 min at 300 K.The amount of Ce(III) adsorbed, q_e (mg g^{-1}) and percentage of removal were calculated by using the following equations:

$$q_e = \frac{C_o - C_e}{m} V \quad (1)$$

$$\text{Removal (\%)} = \frac{C_o - C_e}{C_o} \times 100 \quad (2)$$

where C_o and C_e are the concentrations(mg L^{-1}) of Ce(III) before and after adsorption,respectively; V is the volume of the Ce(III) used (L) and m is weight of MSGC beads (g).

Results and Discussion

Effect of pH of Ce(III) solution and MSGC dosage. pH of the solution is the most crucial part in an adsorption study. Fig. 1 shows the effect of pH on the adsorption of Ce(III) onto MSGC beads. At pH 2, no adsorption was recorded. This was due to the active siteswere occupied by H_3O^+[3]. As the pH increased to 3, the amount of Ce(III) adsorbed increased drastically to 38.6 mg g^{-1} (77% of removal). The amount of Ce(III) adsorbed further increased withthe increment of pH from 4 to 5, which were 44.7 and 48.2 mg g^{-1},respectively. With the increase in pH, the number of H^+ ions decreased and the adsorbent surface carried more negative charges resulting in greater attraction between an adsorbent and cationic form of adsorbate [11]. At pH 6, the amount of Ce(III) adsorbed decreased due to the formation of precipitate. To ensure the free Ce(III) species in the solution, the pH of all solutions in adsorption studies was kept to 4.

Meanwhile, weights of 0.005 to 0.03 g MSGC beads were added into 50 mL Ce(III) solutions.Based on Fig. 2, the percentage of removal did not change very much as the adsorbent weight increased. The removal of an adsorbate usually increases with the increase in adsorbent dosage, which is attributed to the increasing number of adsorption sites. Thus, more Ce(III) in the solution could interact with the binding sites which finally resulted in a higher percentage of Ce(III) removal. On the other hand, when the MSGC dosage increased, the adsorption sites on the surface remain unsaturated. Thus, the amount of Ce(III) adsorbed per unit weight of adsorbent was reduced as the dosage increased [12]. For ease of preparation however, the weight of 0.02 g MSGC was used for other adsorption studies.

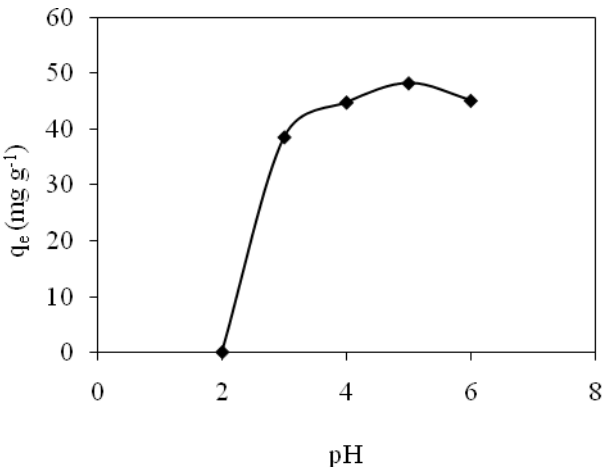

Fig. 1: Effect of initial pH on the adsorption of Ce(III)

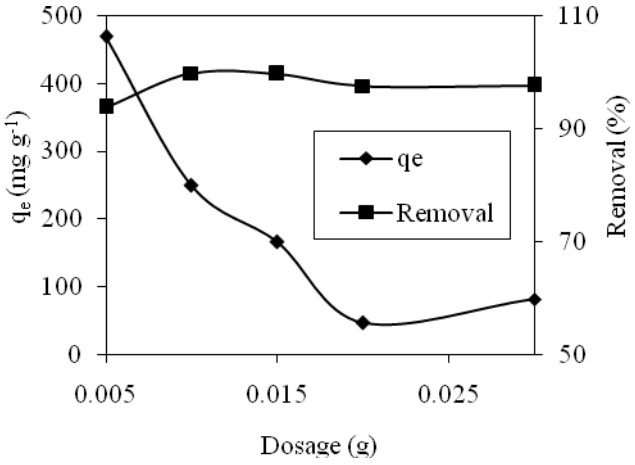

Fig. 2: Effect of adsorbent dosage on the adsorption of Ce(III)

Kinetic results. Based on the plot shown in Fig. 3, adsorption of 50 mg L^{-1} Ce(III) onto chitosan-MSG beads exhibited a fast adsorption process as the equilibrium time was reached in less than10 min. The experimental data was further analyzedusing pseudo-first-order and pseudo-second-order kinetic models in order to identify the rate limiting step. The pseudo-first-order equationis given below:

$$\log (q_e - q_t) = \log q_e - \frac{k_1}{2.303} t \quad (3)$$

where q_t and q_e areconcentrations of the adsorbate (mg g^{-1}) at time t (min) and at equilibrium, and k_1 is the rate constant of the pseudo-first-order adsorption process (min^{-1}). The pseudo-second-order is given as:

$$\frac{t}{q_t} = \frac{1}{h} + \frac{1}{q_e} t \quad (4)$$

where $h = k_2 q_e^2$ can be regarded as the initial sorption rate as $t \rightarrow 0$, and k_2 is the rate constant of pseudo-second-order adsorption (g mg^{-1} min^{-1}).

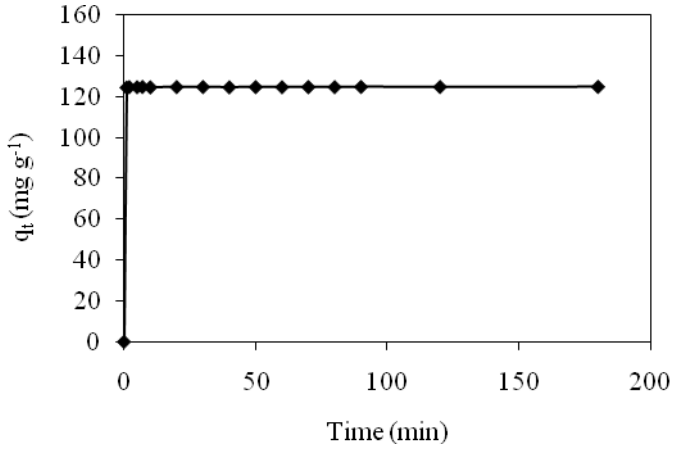

Fig. 3: Time profile of Ce(III) adsorption onto MSGC at 300 K.

Based on Table 1, pseudo-first-order model did not correlate well with the experimental data as a very low correlation coefficient was recorded. The pseudo-second-order model showed good linearity and the calculated adsorption capacity ($q_{e,cal}$) is closed to the experimental data ($q_{e,\ exp}$). Based on this observation, the rate limiting step is associated with chemical adsorption [13].

Table 1 : Comparison between pseudo-first-order and pseudo-second-order rate constants and calculated and experimental q_e values for 50 mg L^{-1}Ce(III) concentration.

$[Ce^{3+}]$	Pseudo-first-order			Pseudo-second-order				$q_{e,\ exp}$
(mg L^{-1})	$q_{e,\ cal}$ (mg g^{-1})	k_1 (min^{-1})	R^2	$q_{e,\ cal}$ (mg g^{-1})	k_2 (g mg^{-1} min^{-1})	h (mg g^{-1} min^{-1})	R^2	(mg g^{-1})
50	1.92	4.05×10^{-2}	0.259	125	0.43	6.67×10^{3}	1.000	124.8

Adsorption isotherm. Two most common isotherm models were further applied for describing the adsorption data, which were Langmuir and Freundlich isotherm models.The linearized Langmuir equation is given as:

$$\frac{C_e}{q_e} = \frac{1}{q_{max}\, b} + \frac{C_e}{q_{max}} \tag{5}$$

where C_e is the equilibrium Ce(III) concentration (mg L^{-1}), q_e is the amount of Ce(III) adsorbed at equilibrium (mg g^{-1}), q_{max} is the capacity (mg g^{-1}) and b is a constant (L mg^{-1}). The value of b reflects the binding strength between Ce(III) and adsorbent surface. The Freundlich model is expressed as:

$$\log q_e = \log\ K_F + \frac{1}{n}\ \log\ C_e \tag{6}$$

where K_F represents Freundlich constant (mg g^{-1})and n is considered as the heterogeneity of the adsorbent surface and its affinity for the adsorbate.

Table 2 shows Langmuir and Freundlich parameters obtained from the experimental data. Based on the correlation coefficient valuesfor both models, Langmuir model correlated with the experimental data better. This suggests a monolayer type of adsorption occurred on MSGC surface. As the value of n is > 1, it indicated that the adsorption process is favorable[14].

Table 2: Langmuir and Freundlich parameters for adsorption of Ce(III) onto MSGC beads at room temperature

Temperature (K)	Langmuir			Freundlich			$q_{e, exp}$
	q_{max} (mg g^{-1})	b (L mg^{-1})	R^2	K_F (mg g^{-1})	n	R^2	(mg g^{-1})
300	369.0	0.011	0.931	106.9	8.47	0.283	343.5

Adsorption of Ce(III) onto MSGC demonstrates fast adsorption of Ce(III) with high adsorption capacity. This is much better compares to studies done by other researcher (Table 3):

Table 3: Comparison of adsorption of Ce(III) done by other researchers.

Adsorbent	Equilibrium time	Qmax (mg g-1)	Reference
MSGC	10 min	343.5	This study
D151 resin	10 h	392.0	[3]
Grapefruit peel	60 min	159.3	[15]

Conclusion

This study demonstrates the good applicability of MSGC beads in the removal of Ce(III) from aqueous solutions. This is due to the rapid uptake of Ce(III) and a very high maximum adsorption capacity wasrecorded. However, the efficiency of adsorption process was dependenton physicochemical factors such as pH and adsorbent dosage. Based on kinetic study, adsorption of Ce(III) obeyed pseudo-second-order model better than pseudo-first-order. The maximum adsorption capacity in this experiment was 343.5 mg g^{-1}, while adsorption isotherm followed Langmuir isotherm model.

Acknowledgement

The authors are very grateful to the Malaysian Ministry of Education for the financial support under Fundamental Research Grant Scheme (FRGS, Project No. 600-RMI/FRGS 5/3 (1/2012).

References

[1] L. Zhu, J. Chen, Adsorption of Ce(IV) in nitric acid medium by imidazolium anion exchange resin, J. Rare Earths. 29 (2011) 969 - 973.

[2] A.A. Volokh, A.V. Gorbunov, S.F. Gundorina, B.A. Revich, M.V.Frontasyeva, S.P. Chen, Phosphorus fertilizer production as a source of rare earth elements polluiton of the environment. Sci. Total Environ. 95 (1990) 141- 148.

[3] C. Yao, Adsorption and desorption properties of D151 resin for Ce(III), J. Rare Earths. 28 (2013) 183 - 188.

[4] W.S. Wan Ngah, S. Fatinathan, Adsorption of Cu(II) ions in aqueous solution using chitosan beads, chitosan-GLA beads and chitosan-alginate beads, Chem. Eng. J. 143 (2008) 62 - 72.

[5] M.Y. Chang, R.S. Juang, Adsorption of tannic acid, humic acid, and dyes from wastewater using the composite of chitosan and activated clay, J. Colloid Interface Sci. 278 (2004) 18 - 25.

[6] E. Guibal, Interactions of metal ions with chitosan-based sorbent: a review, Sep. Purif. Technol. 38 (2004) 43 - 74.

[7] E. Guibal, T. Vincent, R.N. Mendoza, Synthesis and characterization of a thiourea derivative of chitosan for platinum recovery, J. Appl. Polym. Sci. 75 (2000) 119 - 134.

[8] N. Boujelben, J. Bouzid, Z. Elouear, Adsorption of nickel and copper onto natural iron oxide-coated sand from aqueous solutions: Study in single and binary systems. J. Hazard. Mater. 163 (2009) 376 - 382.

[9] M. Wawrzkiewicz, Z. Hubicki, Removal of tartrazine from aqueous solutions by strongly basic polystyrene anion exchange resins. J. Hazard. Mater. 164 (2009) 502 - 509.

[10] R. Gong, M. Feng, J. Zhao, W. Cai, L. Liu, Functionalization of sawdust with monosodium glutamate for enhancing its malachite green removal capacity, Bioresource Technology. 100 (2009) 975-978.

[11] M.J. Iqbal, M.N. Ashiq, Adsorption of dyes from aqueous solutions on activated charcoal. J. Hazard. Mater. 164 (2007) 57 - 66.

[12] Y. Jiang, H. Pang, and B. Liao, Removal of copper(II) ions from aqueous solution by modified bagasse, J. Hazard. Mater. 164 (2009) 1 - 9.

[13] Y.S. Ho, G. McKay, The kinetics of sorption of divalent metal ions onto sphagnum moss pea,. Water Research. 34 (2000). 735 - 742.

[14] Y.S. Al-Degs, M.I. El-Barghouthi, A.A. Issa, M.A. Khraisheh, G.M Walker, Sorption of Zn(II), Pb(II), and Co(II) using natural sorbents: Equilibrium and kinetic studies. Water Res. 40 (2006) 2645 - 2658

[15] M. Torab-Mostaedi, M. Asadollahzadeh, A. Hemmati, A. Khosravi, Biosorption of lanthanum and cerium from aqueous solutions by grapefruit peel: equilibrium, kinetic and thermodynamic studies. Research on Chemical Intermediates. DOI 10.1007/s11164-013-1210-4 1-15.

Advanced Materials Research Vol. 970 (2014) pp 204-208

doi:10.4028/www.scientific.net/AMR.970.204

Preliminary Study on Analysis of The Chemical Compositions and Characterization of Empty Fruit Bunch (EFB) In Malaysia

C.H. Nurul Hazirah[1,a*], M. Masturah[1,b], H. Osman[2],
M.J. Jamaliah[1], H. Shuhaida[1]

[1]Department of Chemical and Process Engineering, Faculty of Engineering and Built Environment, University Kebangsaan Malaysia, 43600 UKM Bangi, Selangor, Malaysia

[2]Department of Science Chemistry and Food Technology, Faculty of Science and Technology, University Kebangsaan Malaysia, 43600 UKM Bangi, Selangor, Malaysia

[a*]nhch_hazirah@yahoo.com, [b]masturah@eng.ukm.

Keywords: Empty fruit bunches; fiber; chemical composition; biohydrogen.

Abstract. Oil palm (*Elaeis guineensis*) is the most important crop of Malaysia. Malaysia can be considered as the world's largest producer and exporter of crude palm oil. The objectives of this work are to analyze and investigate the chemical compositions and the characterization of empty fruit bunches. The chemical compositions of EFB are analyzed using National Renewable Energy Laboratory method. Milled empty fruit bunches submitted to different treatments are characterized by FTIR spectroscopy, carbon-hydrogen-nitrogen analyzer (CHN), thermo gravimetric analysis (TGA), and surface morphology. Chemical compositions which are analyzed include glucan, xylan, arabinan, extractive, ash and lignin contents. The compositions of EFB are determined in two forms which are extractive free sample and native whole sample. The results obtained show that extractive free sample has higher glucan and xylan contents which are 37.8% and 20.5% as compared with whole native sample which are 34.3% and 19.7% respectively. However, the contents of arabinan and lignin of extractive free sample which are 1.5% and 21.8% are much lower than whole native sample which are 2% and 28.7% respectively. The ash content for both samples is 5.2%. The result for extractive analysis of extractive free sample is 15%. The basic functional groups and elements which present in EFB are obtained by FTIR and CHN analysis respectively. TGA analysis curve shows the decomposition of EFB peak value at 312.5ºC. The morphology study of EFB carried out using Scanning Electron Microscopy (SEM) shows a roughness surface.

Introduction

Malaysia produces approximately 47% of the world's palm oil supply [1]. Hot and wet weather throughout the year in this country provides the optimum conditions needed for palm oil growth [2]. Besides palm oil, Malaysia yields abundance quantity of biomass waste in the form of trunks, fronds, fibers, shells and empty fruit bunches (EFB) [1, 3]. Empty fruit bunches (EFB) is the major solid waste produced from the milling process in obtaining palm oil. It can be used as biomass feedstock for the production of renewable energy. Biomass can produce biofuel in liquid or gas state. Some example of liquid biofuel is ethanol, while gas biofuel is biohydrogen. Currently, more investigations are focusing on biohydrogen gas because it is clean and has a high calorific value of fuel. Bioydrogen is expected to be the main source of energy in the near future [4]

EFB is lignocellulosic biomass that comprises three main components which are cellulose (40-50%), hemicellulose (20-30%) and lignin (15-20%) [5]. The cellulose and hemicellulose in EFB will undergo hydrolysis process to recover sugars (C5 and C6) which can be further used as carbon source for biohydrogen production by fermentation. Lignin surrounds hemicellulose and cellulose to form a more complex structure where lignin acts as barrier layer around both components. This barrier prevents enzymes such as cellulase from penetrating the EFB. Therefore, the complex structural of EFB hinders enzymatic hydrolysis to access on cellulose and hemicellulose thus it requires a pretreatment steps. Pretreatment is the most important step in biohydrogen production where it alters the structure of cellulose and makes cellulose more accessible to the enzymes that

convert carbohydrate into fermentable sugars [3]. In order to get high sugar yield for biohydrogen production, the structure of EFB need to be examined. Therefore, in this study the chemical compositions and characterization of EFB are analyzed. EFB is characterized by FTIR spectroscopy, CHN analyzer, TGA analysis and surface morphology.

Experimental Procedure

The empty fruit bunches fiber (EFB) were obtained from Sime Darby Sdn. Bhd. palm oil milling, Pulau Carey, Selangor in the form of 3-2 m long fibres. The samples had less than 10 wt % moisture. They were grinded into 2 mm particle size using grinder. The particle size EFB was used throughout the study. The samples were prepared using NREL/TP-510-42620 standard method. Chemical composition in these samples such as glucan, xylan, arabinan, lignin, extractive and ash content were determined accordance with NREL/TP-510-42618, NREL/TP-510-42619 and NREL/TP-510-42622 standard method respectively. The Fourier transform infrared (FTIR) spectra of EFB were recorded on the Thermo Scientific Nicolet 6700FT-IR. The percentages of carbon, hydrogen and nitrogen in EFB sample were obtained using a CHNS/O analyzer (model Fison EA1108). The thermal degradation behavior of EFB was determined using a thermogravimetric analyzer (model NETZSCH STA 449F3). The morphology of the samples was observed under Scanning Electron Microscope, SEM model Philips XL30 to study the fiber structure.

Results and Discussion

The chemical compositions of EFB fibers are listed in Table 1. The results show that extractive free sample has higher value of glucan and xylan contents which are 37.8% and 20.5% as compared with whole native sample which are 34.3% and 19.7% respectively. However, the content of arabinan and lignin of extractive free sample which are 1.5% and 21.8% are much lower than whole native sample which are 2% and 28.7% respectively. The difference is because for extractive free sample, the sample undergoes two stages of soxhlet extraction process which are using water and ethanol (98%) as solvent. The soxhlet extraction led to thermal degradation of the EFB fibers. Physical and chemical bonds in the EFB such as those in large long-chain of cellulose, hemicellulose and lignin were broken down. The microfibrils of fibers were separated and make the cellulose more exposed to the acid during acid hydrolysis compared with native whole sample. High lignin content in whole native sample might be due to incomplete acid hydrolysis in EFB fibers because inaccessibility of acid to cellulose in complex structure. In comparison with study by Rahman [6] and Chong [7] the result for glucan, xylan are lower while lignin is higher. However in this study the value of arabinan is determined. The ash content in this EFB is 5.2% much higher than reported by Rahman [6] and Chong [7]. The differences in percentage of ash content are related to washing and drying process during sample preparation [3]. Washing sample gave lower ash content compared to unwash samples. The value of extractive for extractive free sample is 15%, almost same as reported by Chong [7].

The percentages of EFB elementals as recorded from the CHN analysis showed a carbon, hydrogen and nitrogen contents of 45.02%, 5.23% and 1.05%. These values are similar to those reported by Mohammed [1].

Table 1 The chemical composition of empty fruit bunch

Main Composition (%)	Extractive free sample	Native whole sample	Rahman et. al., 2006	Chong, P.S. et. al., 2013
Glucan	37.8 ± 1	34.3 ± 2.7	44.76	38.09
Xylan	20.5 ± 1.1	19.7 ± 1.5	22.1	29.93
Arabinan	1.5 ± 1.7	2 ± 0.1	-	-
Lignin	21.8 ± 1.8	28.7 ± 4.5	11.7	15.96
Ash	5.2 ± 0.3	5.2 ± 0.3	0.52	0.54

Extractive	15 ± 2.4	-	-	15.48
Other	-	10.1	20.92	-
Total	101.8	100	100	100

*Standard deviation for 3 replicates

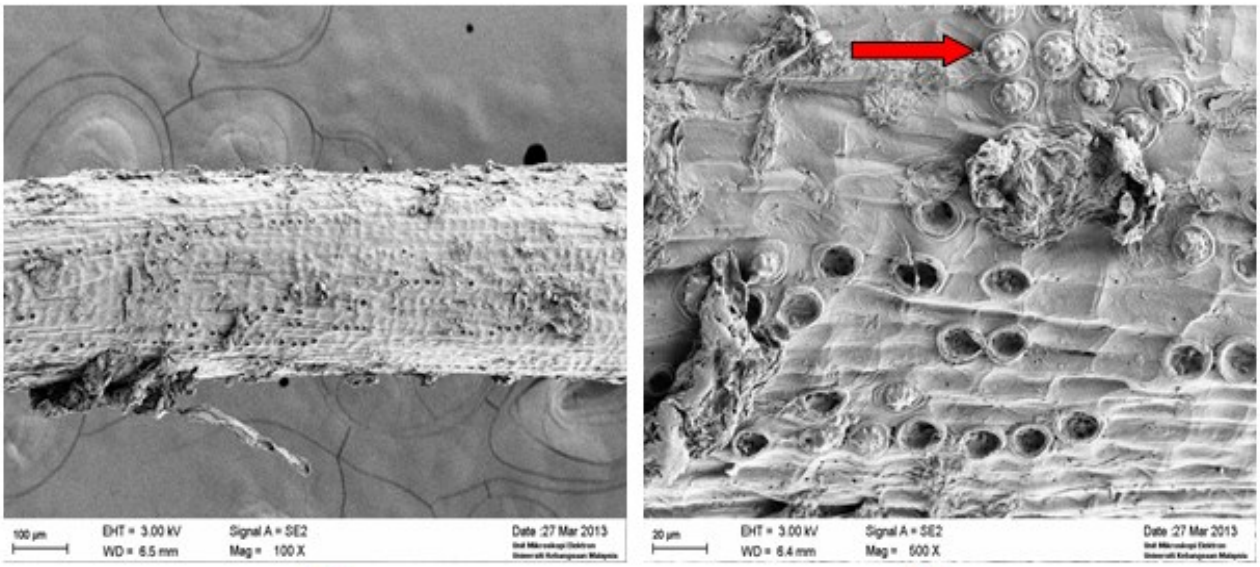

Figure 1 SEM micrograph of EFB fiber: (a) at magnificent 100x and (b) at magnificent 500x; Arrow indicates silica bodies on the EFB strand.

Scanning electron microscopy (SEM) analysis is shown in Fig. 1 (a) and (b). From this analysis it is observed that EFB has a rough surface with the silica bodies on the surface strand. The structure looks very rigid and solid because the surface of the fiber is covered by a layer of matrix material like lignin or waxes [3]. EFB fibers are lignocellulosic fibers while the cellulose and hemicelluloce are covered by lignin matrix. The changes in fibers morphology are very important to predict the interaction between cellulose, hemicellulose and lignin.

The thermal degradation characteristics of EFB are displayed in Fig. 2 by thermogravimetry (TG) and differential thermogravimetry (DTG). According to Spinace [8] the TGA curve can be divided into four degradation processes which are moisture evolution, hemicellulose, cellulose and lignin degradation. The initial weight loss occurred at 75ºC attribute to water loss in the form of absorbed moisture. The second process at temperature 220ºC to 290ºC is attributed to the decomposition of hemicellulose. The third process occurred from 285ºC to 360ºC with maximum decomposition rate at 312.5ºC is attributed to the decomposition of cellulose degradation. Lastly lignin degradation occurred at 360ºC and above because it is difficult to decompose.

Fig. 3 showed FTIR analysis of EFB. The FTIR analysis is done to obtain the basic functional group present in EFB. The absorption peaks are assigned based on literature data. The EFB spectrum shows absorption at 3325.6 cm^{-1} indicating the presence of hydroxyl groups in the phenolic and aliphatic compounds. The absorption peak at 2921.0 - 2851.6 cm^{-1} is also identified which attributed to the stretchiness of (C-H) band of methyl group. Peaks at 2096.4 and 1976.6 cm^{-1} are considered aromatic overtones. The absorption peak at 1742.6 cm^{-1} represents the C=O bonds and acetyl groups, characteristic of the hemicellulose. The peaks at 1619.2 and 1376.6 cm^{-1} represent stretching of (C=C) and (C-C) respectively in aromatic derived form. Peaks at 1242.4 and 1159.3 cm^{-1} could be assigned to (C-O) bonds of alcohol group in ethers. The peak at 1034.3 cm^{-1} attributes to glycosidic bonds, indicating the characteristic of cellulose [9].

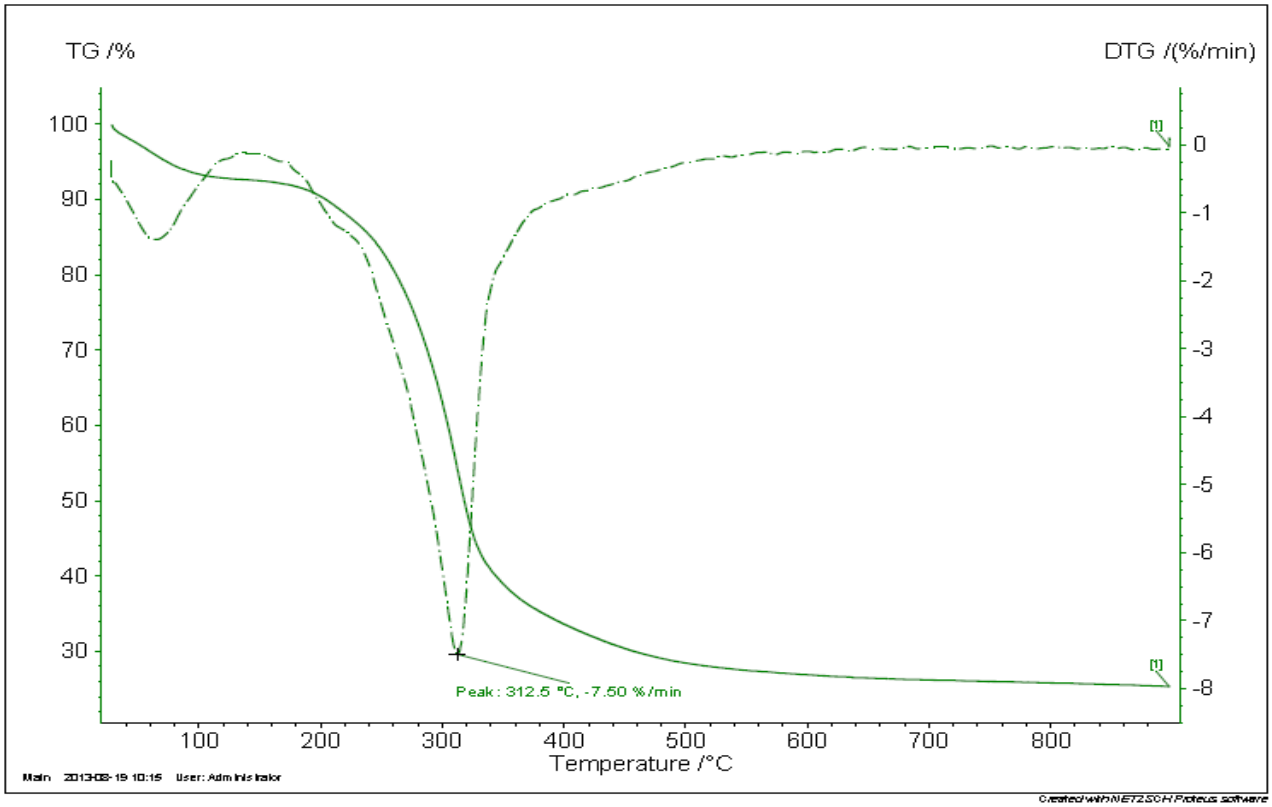

Figure 2 Thermogravimetric and differential thermogravimetric analysis of EFB

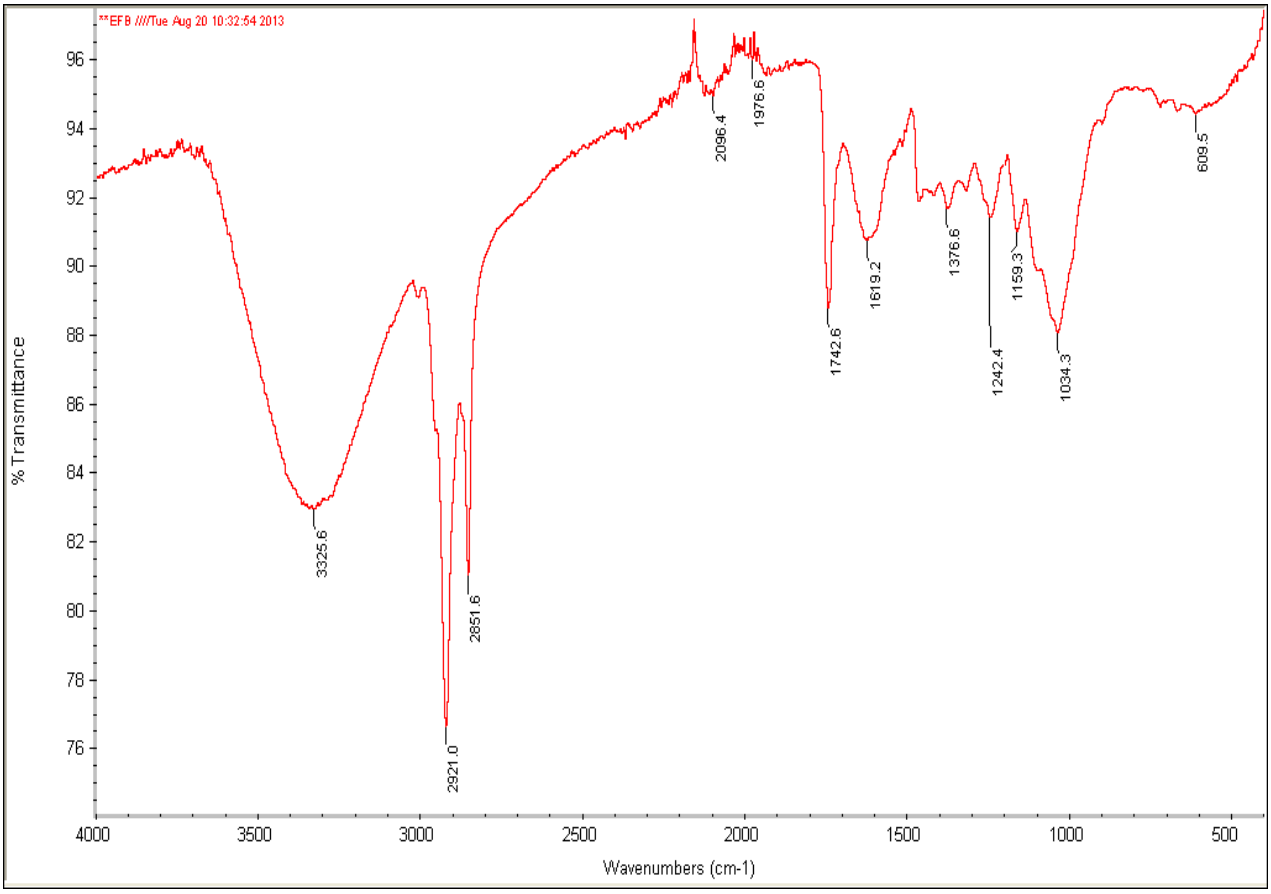

Figure 3 FTIR spectra of EFB

Conclusion

In this study, the composition of EFB for extractive free sample and native whole sample were determined. Extractive free sample gave higher value of glucan (3.5%) and xylan (0.8%) but much lower arabinan (0.5%) and lignin (7%) as compared to native whole sample. The analysis studied by CHN, FTIR and TGA showed the basic functional group, elements and decomposition of EFB. SEM images showed a rough surface with the silica bodies observed on the surface strands. Therefore, high content of glucan in EFB compared to other components as well as the characterization of EFB indicated that EFB fiber is suitable to be used as carbon source for biohydrogen production by fermentation.

Acknowledgement

The authors would like to thank Universiti Kebangsaan Malaysia and KURSI UKM-Yayasan Sime Darby (UKM-YSD) for sponsoring this work.

References

[1] Mohammed, M.A.A., Salmiaton, A.,Wan Azlina, W.A.K.G. & Mohamad Amran, M.S. 2012. Gasification of Oil Palm Empty Fruit Bunches: A Characteriztaion and Kinetic Study, Bioresorce Technology, 110: 628-636.

[2] Wendy, P.Q.N., Hon, L.L., Foo, Y.N., Mustafa, K. & Heng, J.E.L. 2012. Waste to-Waste: Green Potential from Palm Biomass in Malaysia, Journal of Cleaner Production, 34: 57-65.

[3] Saleha, S., Umi Kalsom, M.S., Huzairi, Z., Suraini, A.Z., Siti Mazlina, M.K., Yoshihito, S. & Mohd Ali, Hassan. 2012. Effect of Steam Pretreatment on Oil Palm Empty Fruit Bunch for The Production of Sugars, Biomass and Bioenergy, 36: 280-288.

[4] Mohammed, M.A.A., Salmiatona, A., Wan Azlinaa, W.A.K.G., Mohammad Amrana, M.S., Fakhru'l-Razia, A. & Taufiq-Yap, Y.H. 2011. Hydrogen Rich Gas From Oil Palm Biomass as A Potential Source of Renewable Energy in Malaysia, Renewable and Sustainable Energy Reviews, 15:1258–1270.

[5] Azman, H., Arshad, A.S., Farid, N.A. & Aznizam, A.B. 2010. A Review on Oil Palm Empty Fruit Bunch Fiber-Reinforced Polymer Composite Material, Polymer Composites, 31: 2079–2101.

[6] Rahman, S.H.A., Choudhury, J.P. & Ahmad, A.L. 2006. Pruduction of Xylose from Oil Palm Empty Fruit Bunch Fiber Using Sulfuric acid, Biochemical Engineering Journal, 30**:** 97-103.

[7] Chong, P.S., Jamaliah, M.J., Shuhaida, H., Lim, S.S., Sahilah, A.M., Osman, H. & Mohd Tusirin, M.N. 2013. Enhancement of Batch Biohydrogen Production From Prehydrolysate of Acid Treated Oil Plam Empty Fruit Bunch, International Journal of Hydrogen Energy, 38: 9592-9599.

[8] Spinace, M.A.S., Lambert, C.S., Fermoselli, K.K.G. & Paoli, M.A.D. 2009.Characterization of Lignocellulosic Curaua Fibres, Carbohydrate Polymers, 77: 47-53.

[9] Mohamad Nasir, M.I., Mohamed Rashid, A.H., Sipaut, C.S., Hassan, Y.A.E. & Abdullahi Ali, M. 2010. Preparation and Characterization of a Newly Water Soluble Lignin Graft Copolymerfrom Oil Palm Lignocellulosic Waste, Carbohydrate Polymers, 80: 1102-1110.

Advanced Materials Research Vol. 970 (2014) pp 209-213

doi:10.4028/www.scientific.net/AMR.970.209

Solvent Extraction of Light Rare Earth Ions Using D2EHPA from Nitric Acid and Sulphuric Acid Solutions

M.T. Khaironie[1,a*], M. Masturah[1,b], M.S. Meor Yusoff [2], S. Nazaratul Ashifa[2]

[1]Department of Chemical and Process Engineering, Faculty of Engineering and Built Environment, Universiti Kebangsaan Malaysia, 43600 UKM Bangi, Selangor, Malaysia.

[2]Malaysia Nuclear Agency, 43000 Bangi, Selangor, Malaysia

[a*]khaironie@gmail.com, [b]masturah@eng.ukm.my

Keywords: solvent extraction, light rare earth, D2EHPA, extraction percentage

Abstract. A study on solvent extraction of a mixture of light rare earths ions (La(III), Nd(III) and Ce(IV)) from nitric and sulphuric acid solutions with di-(2-ethylhexyl) phosphoric acid (D2EHPA) in kerosene as an extractant has been carried out. The influences of D2EHPA and acid concentrations on the extraction efficiency of rare earth metal ions were evaluated. It was found that the extraction percentage of La, Nd and Ce decreased as the acids concentrations increased. On the contrary, the extraction efficiency of these ions increased as D2EHPA concentration increased. The utmost extraction percentage of La, Nd and Ce (99.4%, 99.7% and 100% respectively) was extracted from 0.1 M HNO_3 using 1.0 M D2EHPA. The order of extraction ability of the studied rare earth elements by D2EHPA decreased in the series of Ce(IV)>Nd(III)>La(III).

Introduction

Rare earths (REs) are a group of fifteen lanthanides series of elements from lanthanum to lutetium, plus scandium and yttrium. Generally, rare earth elements are separated into two groups of: light rare earths or LREs (La, Ce, Pr, Nd, Pm, Sm) and heavy rare earths or HREs (Eu, Gd, Tb, Dy, Ho, Er, Tm, Yb, Lu, Sc, Y). These groups are often referred as rare earth metals but most of the time as lanthanides. RE elements all occur in nature relative to one another. As the chemical and physical properties of all elements are very similar, the purification to pure metal is rather challenging.

In recent years, the needs of REs for commercial purpose are arising as they are used in wide range products and processes such as catalysts, high refractive index glass, magnets, household batteries, ceramics and nuclear technologies [1, 2]. Therefore, separation and recovery of individual elements or groups of REs from major sources (mineral monazite, xenotime, and bastnasite) and other secondary sources (residues from processing activities, waste rock, sludges and scrap material) has to be both economically and environmentally significant, to accommodate the critical demand in a rapidly growing and developing world.

There are various types of separation method available for separation and recovery of RE elements namely solvent extraction, membrane separation, chemical absorption, and distillation [3]. Among these methods, solvent extraction or liquid–liquid extraction has been commonly applied for the separation of rare earth metals since 1940s [4-6]. It is a method used to separate compounds on the basis of two immiscible liquids, usually an organic solvent containing an extractant with an aqueous solution containing the metal of interest. Solvent extraction is the most applicable method for separating LREs than HREs [7]. Among the several solvent extraction approaches, the use of organophosphorus extractants like di-(2-ethylhexyl)-phosphoric acid (D2EHPA) and 2-ethylhexylphosphonic acid mono-2-ethylhexyl ester (PC 88A) from mineral acid media has been highlighted [8-13]. However, D2EHPA is the prominence investigated extractant in separation of rare earth elements since the pioneering work of Peppard et al. [14]. The extensively used of D2EHPA as the extractant in separating rare earth ions from aqueous solutions by solvent extraction was mainly due to its high sorption rate, chemical stability and low aqueous solubility properties [4, 10, 12, 13].

This study was focusing on extracting the mixture of three LRE elements (La(III), Nd(III) and Ce(IV)) from nitric acid and sulphuric acid solutions by using D2EHPA in kerosene as extractant. The key objectives of the present study were to separate these metal ions and determine the effects of D2EHPA concentration on the extraction efficiency of the elements. Additionally, the types of acid as feed solutions and the effects of their concentrations were equally investigated.

Experimental

Reagents. Three different rare earth elements in oxide form (La_2O_3, Nd_2O_3 and CeO_3) with purity >99% and the extractant, di-(2-ethylhexyl) phosphoric acid (95%), were obtained from Sigma-Aldrich Chemical Co. The extractant diluent, kerosene, as well as both medium solutions, sulphuric (95%) and nitric (65%) acid was obtained from R&M Chemical in Malaysia. All the chemicals used were of analytical grade.

Stock solution of rare earth ions (La(III), Nd(III) and Ce(IV)) mixture was prepared by dissolving the known amount of the corresponding rare earth oxides in minimum volume of concentrated hydrochloric acid. After evaporating to near dryness, it was then diluted to 1L with double distilled water. The aqueous solutions were prepared in the concentration of 0.1-0.5 M by mixing fixed volumes of stock solution with varying volumes of concentrated HNO_3 and H_2SO_4 prior to diluting with double distilled water. The organic solution was at concentration of 0.1, 0.5 and 1.0 M by dissolving varying volumes of D2EHPA in kerosene.

Apparatus. An inductively coupled plasma mass spectrometry (ICP-MS) was used for determination of rare earth elements concentrations in the aqueous phase.

Procedure. The experiments were performed at room temperature by contacting equal 20mL volumes of aqueous and organic solutions (A/O=1) in a covered Erlenmeyer flask. The content was agitated using a mechanical shaker for 15 min to reach equilibrium. After equilibrium, the contents were allowed for phase disengagement. The disengaged phases then separated using an appropriate separating funnel. Each experimental condition was performed twice and two samples were obtained. Rare earth elements concentrations in aqueous phase before and after extraction were determined by ICP-MS and the contents in the organic phase were obtained by mass balance.

The distribution ratio (D) which is expressed as the ratio of the concentration of metals present in the organic phase to that in the aqueous phase at equilibrium was calculated using the following equation:

$$D = \frac{C_o - C}{C}. \quad (1)$$

Where, C_o is the metal concentration in the aqueous phase before extraction and C is the metal concentration in the aqueous phase after extraction. The extraction percentage (%E) was determined from D value as the following equation:

$$\%E = \frac{D \times 100}{D + (\frac{V_{aq}}{V_{org}})}. \quad (2)$$

Where, V_{aq} and V_{org} denote the volume of aqueous and organic phases, respectively. In this paper, V_{aq}/V_{org} is equal to 1.

Results and Discussion

Effect of acids concentrations in aqueous phase. Extraction behaviour of a mixture of LREs using D2EHPA (0.1, 0.5 and 1.0M) with varies nitric and sulphuric acid concentrations ranging from 0.1 to 0.5 M was studied. The results of extraction efficiency of La, Nd and Ce were shown in Fig. 1. It was observed that in all cases, the extraction percentage of La and Nd decreased with the increased of acids concentrations in the aqueous feed solutions, whereas Ce was nearly 100%

separated in all experimental conditions. The results clearly suggested that the studied metals could be effectively extracted from lower concentration of feed solutions. The extraction behaviour of the metal ions from HNO_3 and H_2SO_4 was almost similar to each other except for minor differences in the extraction percentage of each metal. Between the two studied aqueous solutions, the extraction of La, Nd and Ce was considerably more effective from HNO_3 than H_2SO_4. With D2EHPA concentration range from 0.1 to 1.0 M, La and Nd from 0.1 M HNO_3 as shown in Fig. 1(a) were extracted in the range of 71.7 - 99.4% and 85.5 - 99.7%, respectively. For H_2SO_4, a range of extraction percentage of 66.1 - 94.7% for La and 72.7 - 98.3% for Nd was obtained as can be seen in Fig.1 (b).

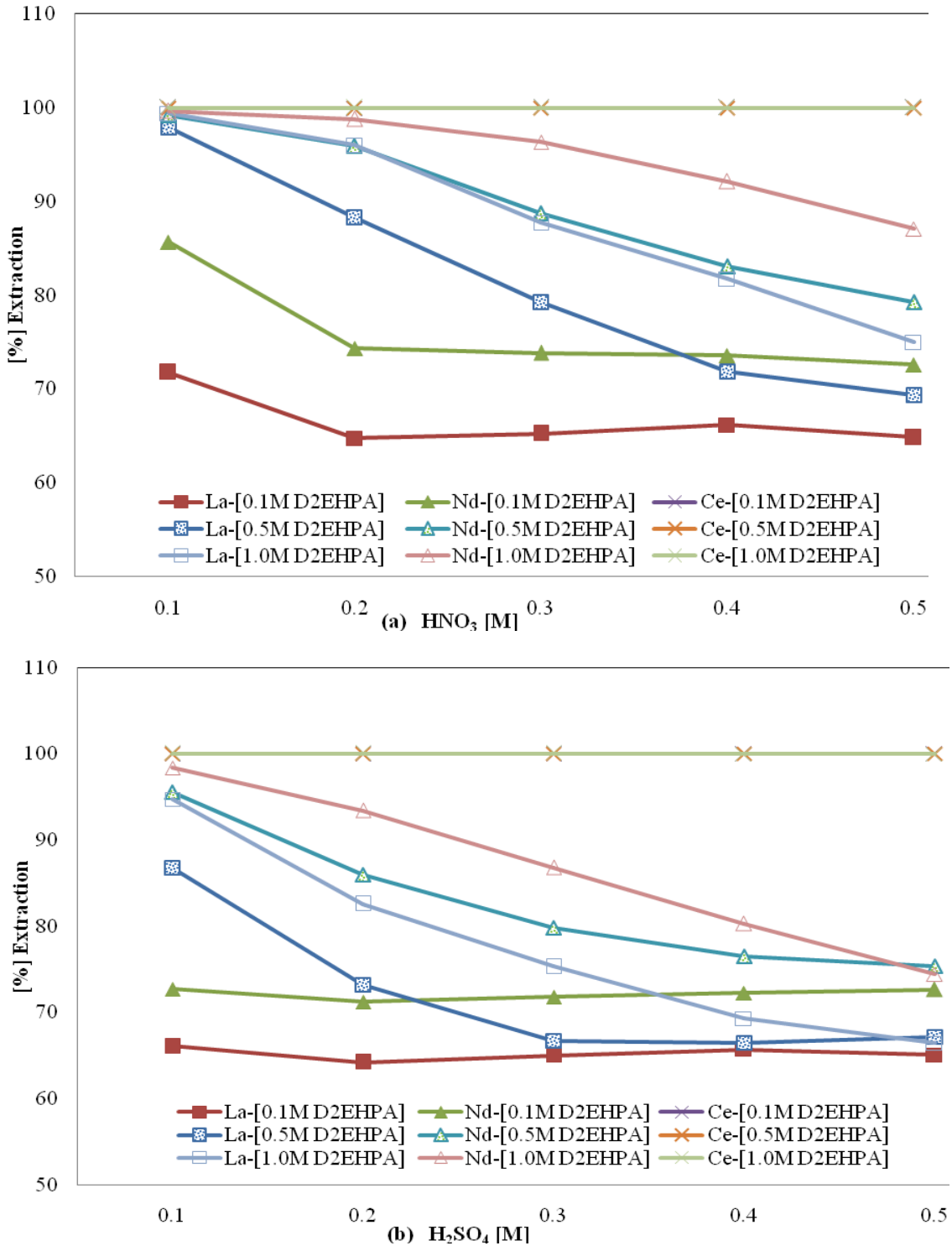

Figure 1. Effect of acids concentrations (a) HNO_3 and, (b) H_2SO_4 on extraction percentage of LREs

From the results, it is considered that the highest extraction percentage of the studied rare earth ions was obtained from 0.1 M HNO_3 aqueous feed solutions.

Effect of D2EHPA concentration in organic phase. To study the influence of D2EHPA concentration on the extraction efficiency of La(III), Nd(III) and Ce(IV), results from the lowest concentration of aqueous feed solutions were evaluated. Effect of variations of D2EHPA concentration (0.1 to 1.0 M) on the extraction percentage of LREs at 0.1 M HNO_3 and 0.1 M H_2SO_4 were presented separately in Fig. 2(a) and 2(b). With 0.1 M D2EHPA, the extraction percentage of La, Nd and Ce from HNO_3 were 71.7, 85.7 and 100%, respectively. From H_2SO_4, the observed percent of extractions were 66.1% for La, 72.7% for Nd and 99.9% for Ce. With 1.0 M D2EHPA, all LREs from HNO_3 solutions were extracted in the range 99.4-100% while a slightly lower extraction percentage of 94.7% for La and 98.3% for Nd were observed from H_2SO_4. Generally, with increased in D2EHPA concentration, the extraction percentage of LREs were also increased. These results denoted that La, Nd and Ce from both aqueous feed solutions were easily extracted into the organic phase using D2EHPA. Therefore, within D2EHPA concentration range 0.1-1.0 M, the highest %E of all LREs was obtained from 1.0 M D2EHPA. From these results, it can also be concluded that D2EHPA works more efficient with HNO_3 than H_2SO_4. The extraction ability of the RE elements from this study is in the order of Ce(IV)>Nd(III)>La(III).

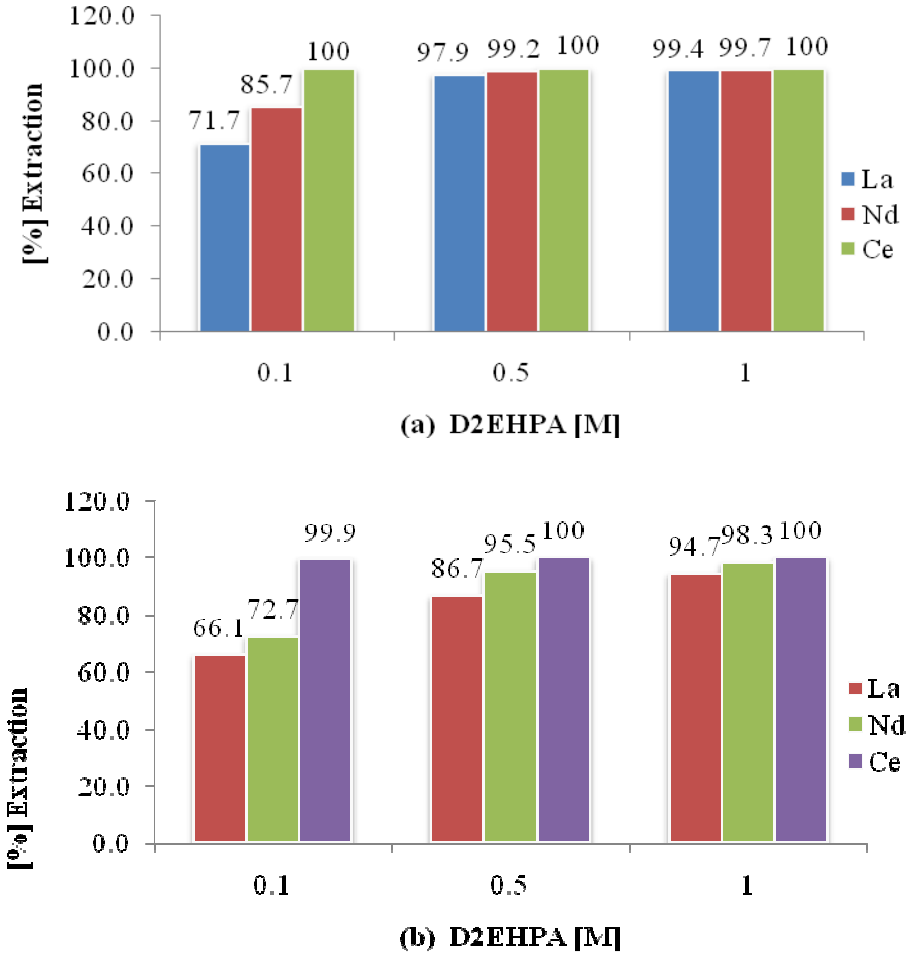

Figure 2. Effect of D2EHPA concentration on extraction percentage of LREs from (a) 0.1 M HNO_3 and (b) 0.1 M H_2SO_4

Conclusions

Solvent extraction of the mixture of LREs from HNO_3 and H_2SO_4 medium has been investigated using D2EHPA with different concentrations. The distribution of elements from an aqueous to an organic phase increased with concentration of D2EHPA and decreased as the concentration of

HNO_3 and H_2SO_4 increased. The work has confirmed that rare earth metal ions transfer to the organic phase follows ion exchange type mechanism [15]. The results pointed out that the extraction percentage of La(III) and Nd(III) from nitric solution were slightly higher than from sulphuric. Under all of the conditions in this study, Ce(IV) was nearly 100% distributed. In general, HNO_3 is a preferred medium for extracting LREs using D2EHPA. All metals were effectively separated from 0.1 M HNO_3 using 1.0 M D2EHPA with the extraction percentage was 99.4% for La, 99.7% for Nd and 100% for Ce. The extraction order resulted as Ce(IV)>Nd(III)>La(III). In conclusion, the separation path for lanthanum, cerium and neodymium ions contained in liquid waste solution could be determined by establishing an appropriate combination of organic solvent and aqueous solution concentrations at normal working conditions.

References

[1] C.K. Gupta, N. Krishnamurthy, Extractive Metallurgy of Rare-Earths, CRC press, 2004.

[2] S.B. Castor, J.B. Hedrick Rare earth elements. In: Kogel, JE, Tivedi, NC, Barker, JM, and Krukowski, ST (editors): Industrial Minerals and Rocks Commodities, Markets and Uses, 7th edition, Society for Mining, Metallurgy and Exploration, Littleton, Colorado 2006, pp. 1555-1568.

[3] P. Ramakul, T. Supajaroon, T. Prapasawat, U. Pancharoen, A.W. Lothongkum, J. Ind. Eng. Chem. 15 (2009) 224.

[4] S.F. Douglas, Solvent extraction in hydrometallurgy: the role of organophosphorus extractants, Journal of Organometallic Chemistry 690 (2005) 2426-2438.

[5] V. K. Jain, S. G. Pillap, H. C Mandal, "Liquid-Liquid Extraction, Pre concentration and Transport Studies of Lanthanum(III) with Calix [4] Resorcinarene-Hydroxamic Acid (C4RAHA)," J.Chil. Chem. Soc., 52 (2) (2007) 1177-1181

[6] B.N. Kokare, A.M. Mandhare, M.A. Anuse, "Liquid-liquid extraction of cerium (IV) from salicylate media using N-7V-octylaniline in xylene as an extractant" J.Chil. Chem. Soc., 55(4) (2010), 431-435

[7] B.W. Moore, U.S. Patent 6093376 (2000)

[8] T. Sato, Liquid-liquid extraction of rare-earth elements from aqueous acid solutions by acid organophosphorus compounds, Hydrometallurgy 22 (1989) 121-140.

[9] E. Antico, A. Masanaa, M. Hidalgo, V. Salvado, M. Iglesias, M. Valiente, Solvent extraction of yttrium from chloride media by di(2-ethylhexyl)phosphoric acid in kerosene, Anal. Chim. Acta 327 (1996) 267–276.

[10] N.V. Thakur, Separation of rare-earths by solvent extraction, Miner. Process. Extr. Metall. Rev. 21 (1–5) (2000) 277–306.

[11] Rabie, A group separation and purification of Sm, Eu and Gd from Egyptian beach monazite mineral using solvent extraction. Hydrometallurgy 85 (2–4) (2007) 81–86.

[12] X. Huang, J. Li, Z. Long, Y. Zang, X. Xue, Z. Zhu, Synergistic extraction of rare earth by mixtures of 2-ethylhexyl phosphoric acid mono-2-ethylhexyl ester and di-(2-ethylhexyl) phosphoric acid from sulfuric acid medium, J. Rare Earths. 26 (3) (2008) 410-413.

[13] C. Basualto, F. Valenzuela, L. Molina, J.P. Munoz, E. Fuentes, J. Sapag, Study of the solvent extraction of the lighter lanthanide metal ions by means of organophosphorus extractants, J. Chill. Chem. Soc., 58 (2) 2013 (1785-1789)

[14] P. Miranda, Jr. and L.B. Zinner. Separation of samarium and gadolinium solutions by solvent extraction[J].Journal of Alloys and Compounds, 249(1-2) (1997), 116-118

[15] B.R. Reddy, S. Radhika, B.N.P. Kumar, Liquid–liquid extraction studies of trivalent Yttrium from phosphoric acid solutions using TOPS 99 as an extractant, Sep. Sci. Technol. 45 (2010) 1426–1432.

CHAPTER 10:

Materials Conversion and Renewable Energy

Advanced Materials Research Vol. 970 (2014) pp 217-223

doi:10.4028/www.scientific.net/AMR.970.217

A NON-ISOTHERMAL THERMO GRAVIMETRIC KINETIC ANALYSIS OF MALAYSIAN POULTRY-PROCESSING-DEWATERED-SLUDGE

A. H. Abbas[1a*] , M. Fadhil[1,b], M. S. Aris[1,c], A. B. A. Ibrahim[1,d], N. Aniza[1,e]

[1]Mechanical Engineering Department, Universiti Teknologi PETRONAS, Seri Iskandar, 31750, Perak, Malaysia

[a*]engabbas78@gmail.com, [b]farfiez@yahoo.com, [c]mshiraz_aris@petronas.com.my, [d]saadalla_85@yahoo.com, [e]noor.aniza87@gmail.com

Keywords: poultry sludge, waste, thermogravimetric, kinetics parameters, activation energy

Abstract. Poultry processing dewatered sludge which consisting of trimmings, fat, feathers and liquid discharges from processing slaughtered chicken is typically land filled in specialized sites. It is a costly process to manage and if not handled according to stringent procedures can be harmful to the surrounding environment. The use of this waste material as an alternative fuel can be an effective solution, as it not only contributes as an energy source but also solves environmental issues related to poultry sludge disposal. Combustion, gasification and pyrolysis are efficient techniques of utilizing energy effectively from poultry sludge. The performances of mathematical models to predict the product gas quality is rely on characterization of feed materials as well as the reaction kinetics of their thermal degradation. The aim of this study is to determine selected physical and chemical properties of poultry sludge associated with thermochemical conversion. Thermogravimetric analyses were performed at heating rates of 10, 20, 30, and 40 K/min in an air (oxidizing) atmosphere. The parameters of the reaction kinetics such as activation energy and reaction order were obtained by the application of Ozawa–Flynn– Wall and Vyazovkin kinetic models.

Introduction

The dewatered poultry sludge (DPS) is one of the waste products generated daily from poultry industry. Today in Malaysia, this poultry industry is growing not only to support the local consumption but is also part of the Malaysian government's plans to become a major supplier of chicken meet for Asian market. The slaughtering of chicken and the subsequent processes in the poultry plant generate the substantial amount of wastes such as feather, bone meal, blood and offal[1] and cannot be used for human consumption. The recovery of useful energy from this waste material has been an ongoing effort to help meet energy demands and to mitigate waste disposal issues. Of late the management of waste through its disposal in landfills has become a much discussed topic due to the scarcity of land and the resulting environmental effects at dumpsites. Early disposal techniques which involve the use of direct combustion methods are worth revisiting in-light of improvements in the gas cleaning techniques available in the market. A combination of direct combustion and the recovery of energy as heat and electricity is now an option worth exploring. Before embarking on the energy recovery option, it is important to gauge the suitability of DPS as a fuel or energy source. One method of measurement can come from the characterization of DPS for combustion properties and chemical composition. Thermogravimetric analysis (TGA) is able to provide a rapid assessment of the fuel value and to determine at which temperatures the reaction starts and ends and can be used to measure the maximum reactivity temperature or total combustion times[2]. The TGA can also used to determine the thermal degradation characteristics and kinetic parameters to provide general information on overall reaction kinetics [3].

Analytical measurements using the TGA have been largely used to characterize the thermal decomposition of solid fuels such as coal [4] and different types of biomass. D.K. Shenet et al. [5] investigated the combustion kinetics of four different wood based solid fuels under an oxidative

atmosphere with TGA and found the respective mass loss and ignition characteristics. The thermal decomposition of palm kernel shell (PKS) and palm oil fronds (POF) using TGA under non-isothermal conditions have been widely studied and reported in numerous publications. Khan et al. [6] reported on the activation energy, pre-exponential factor and order of reaction from a temperature range between 50 and 900°C using a heating rate of 20 °C/min. Other related studies investigated the co – combustion of sewage sludge with coal using TGA[2], [4], [7]–[10]. However studies on thermochemical conversion of poultry sludge is extremely scarce; and there are deficiencies in kinetics information on combustion of DPS. This paper presents the properties of DPS related to thermochemical conversions. and and to determine and analyze the reaction kinetics of DPS in oxidizing atmospheres using non-isothermal thermogravimetric kinetic analysis by applying the Ozawa–Flynn– Wall (Ozawa, 1965; Flynn and Wall, 1966) and the Vyazovkin (Vyazovkin, 1997) kinetic models, which, will allow the calculation of the activation energy and reaction order of sewage sludge combustion. The experimental results would also allow for measurements of TG and DTG parameters to be made and analyzed.

Experimental

Material characterization. The DPS samples used in this study were collected from a few closer chicken broiler factories that have their own water treatment system. The samples were first dried in an oven at 105°C while constant checks were carried out on the sample's weight loss to record the moisture content. Experimental procedures were performed to measure the heating values and chemical compositions. The heating value procedure was carried out in accordance to ASTM D2015. The proximate analysis involved the use of a Thermogravimetric Analyzer (TGA-Perkin Elmer PYRIS1TGA) to determine moisture content (MC), volatile matter (VM), fixed carbon (FC) and ash.The ultimate analysis involved the use of a CHNS analyzer (Leco CHNS-932, VTF-900) to find the Carbon (C), Hydrogen (H), Nitrogen (N) and Sulfur (S) content in the sample. The average values of the chemical and physical properties of the DPS samples measured is summarized in Table 1

Table 1 Properties of DPS samples used in this study

Property	Average
Proximate analysis (wt %)	
Moisture content	4
Volatile matter	75
Fixed carbon	13
Ash	8
Ultimate analysis (wt %)	
Carbon	68.96
Hydrogen	9.78
Nitrogen	3.14
Sulfure	0.27
Oxygen	54.8
Higher heating value (MJ/Kg)	33.97±1.72

TGA setup. Samples of 10 mg each were analyzed in the TGA from room temperature to 850°C under an air flow of 20 mL/min at a gauge pressure of 101 kPa. Four different heating rates ($\beta = dT/dt$) were used to carry out separate dynamic runs; the β values of 10 Kmin-1, 20 Kmin-1, 30 Kmin-1, and 40 Kmin-1 which are suitable for homogeneous ignition and to minimize mass transfer effect[8].

Theory

The mathematical descriptions of heterogeneous solid-state reactions are commonly defined in terms of their kinetic parameters [9], activation energy, E, Arrhenius parameter, A. An algebraic expression of the kinetic model for the solid state reactions, as a function of the fractional conversion α, f (α) can be written as, related to experimental data as shown bellow[2], [7]–[9], [11]:

$$\frac{d\alpha}{dt} = Ae^{-E/RT} f(\alpha) \tag{1}$$

The two common techniques used to find the kinetic parameters are Model Fitting for the identification of kinetic reaction models and Iso-Conversional i.e. model-free for which the rate of decomposition must follow Eq.(1)[8], [9]. The iso-conversional method is more widely used compared to the fitting models as it provides the ability to compute kinetic parameters without prefixing the reaction order[2], [9], [12]. Also known as "Model Free", this method is sufficiently flexible to allow for a change of mechanism during the course of the reaction and mass transfer limitations are reduced by the use of multiple heating rates. In contrast, the model-fitting kinetic method generally involves the use of a single heating rate, which will result in a variation of activation energy values due to mass and heat transfer effects [8]. In the model free method the rate of heterogeneous solid-state reactions described in Eq. (1), as suggested by[2], [8]–[10], [12], can be transformed into a non-isothermal rate expression, as a function of temperature at constant heating rate β,

$$\beta = dT/dt = cons\tan t \tag{2}$$

Replacing the constant heating rate in Eq. (1) and integrating will result in the following equation:

$$\int_0^\alpha \frac{d\alpha}{f(\alpha)} = g(\alpha) = \frac{A}{\beta}\int_{To}^{T} e^{-E/RT} dT \tag{3}$$

The model free method requires input from a series of TG experiments which are carried out at different heating rates for at least three different β values as suggested in[7]–[9].

Based on equation (3), a considerable number of approaches to derive kinetic parameters have been developed. One approach suggested in[8]–[10], to obtain the activation energy from dynamic data is the Flynn, Wall and Ozawa approach which involves measuring the temperatures corresponding to fixed values of α from experiments at different heating rates. This is one of the integral approaches used to calculate the activation energy without prefixing the reaction order as described in the following equation.

.

$$\ln(\beta) = \ln\left[\frac{AE}{Rg(\alpha)}\right] - 5.331 - 1.052\frac{E}{RT} \tag{4}$$

From equation (4), the activation energy E can be estimated by plotting ln (β) vs. 1/T at different conversion values (α).

Another method to calculate the activation energy is developed by Vyazovkin and Lesnikovick (1988)[2], [9], [10].

In Eq. (3), since E/2R>> 1, the temperature integral can be approximated by

$$\int_{To}^{T} e^{-E/RT} dT \approx \frac{R}{E} T^2 e^{-E/RT} \tag{5}$$

Substituting the temperature integral and taking the logarithm, we obtain

$$\ln\frac{\beta}{T^2} = \ln\left[\frac{RA}{Eg(\alpha)}\right] - \frac{E}{R}\frac{1}{T} \tag{6}$$

For each conversion value (α), the ln (β/T2) vs. 1/T plot will give a straight line with an –E/R slope from which E is obtained as a function of the conversion.
In order to determine the reaction order, Avrami's theory is used to describe the variation of the degree of conversion with temperature and heating rate, and results in the following equation [8]:

$$\ln[-\ln(1-\alpha(T)] = \ln A - \frac{E}{RT} - n\ln\beta \tag{7}$$

A plot of ln [-ln (1 – α (T))] vs. ln β, obtained at the same temperature from a number of isotherms taken at different heating rates, would yield straight lines whose slope will have the value of the reaction order or the Flynn–Wall–Ozawa exponent, n [8].

In this work the Model Free method, in combination with the solutions suggested from the Flynn, Wall and Ozawa and Vyazovkin and Lesnikovick approaches, have been used to determine the activation energy of DPS combustion reactions. And Avrami's theory has been used to find out the combustion reaction order.

Results and discussion

The TG curves obtained for the DPS samples in this work for the different heating rates (β) of 10 K/ min, 20 K/min, 30 K/ min and 40 K/ min are shown in Fig. (1). The four different conversion percentages (α) (20, 30, 40, and 50%) are also indicated for the curve sets. All heating rates were observed to have the similar effect on the TG curves as shown from their start through to the end temperatures. However the heating rate (temperature scan rate) tended to slightly increase the start and end temperatures of each stage.The DPS combustion interval can be divided into four temperature stages, 200 – 280, 290–380 ◦C, 390–550 ◦C and 560–640 oC. These temperature stages represent the different processes which takes place when the samples are exposed an increase in temperature.

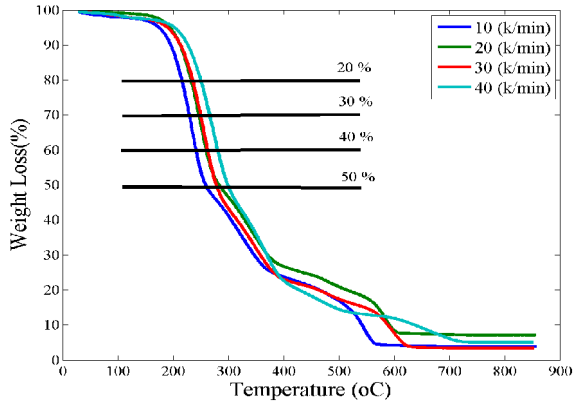

Fig. (1). Curves of fitting to kinetic model proposed by Ozawa‑Flynn‑Wall to various conversion Percentages corresponding to the combustion of dewatered poultry sludge at different heating rate.

The plots of log β vs. 1/T corresponding to the several conversion degrees of the process are shown in Fig. (2). The trends in the plots allowed for the ctivation energy E to be calculated. Fig. (3) Shows the plot of ln (β/T2) vs. 1/T corresponding to the several conversion degrees (α). The slopes corresponding to linear fittings together with the corresponding correlation coefficients (R2) and

calculated activation energy using the Ozawa–Flynn–Wall kinetic method and the Vyazovkin and Lesnikovick approaches are listed in Table (2). As it is listed in table (2) the correlation coefficients obtained by the Vyazovkin and Lesnikovick is lower than the values obtained by the Ozawa–Flynn–Wall approach in all cases. The Ozawa–Flynn–Wall approach was also found result in higher activation energy values compared to the Vyazovkin and Lesnikovick approach and this finding is consistent with earlier work by [2], [9]. The activation energies for both these approaches are estimated at 19 and 16 kJ/ mol, respectively. M. Otero et al in[2], [9] calculated the activation energy for the combustion of two types of sewage sludge in Spain using the above mentioned approaches and found the values to be 138.1, 126.2 and 99.3, 85.7 kJ/mol respectively. M.E. Sanchez et al. reported the activation energy of sewage sludge also in Spain using the Ozawa–Flynn–Wall approach to be143kJ/mol[8]. Comparing previous work to the results presented in this paper, the activation energies of different sewage sludge samples are higher than DPS. Comparing coal which is a common power plant solid fuel with the DPS used in this paper, the activation energy corresponding to the DPS is noticeable lower than those corresponding to coal[2], [9], [12]. and also is lower than animal manure (AM) and the organic fraction of municipal solid waste (OFMSW) [8]. To calculate the reaction order of the DPS, the ln [-ln (1 –α (T))] vs. ln β relationship was graphed as shown in Fig. (4). The reaction order varied from 0.085 almost zero (zero reaction order) to 0.7, M.E. Sanchez et al. mentioned the reaction order is not constant throughout the reaction which is evidence of the multiple step process, according to their finding the reaction order for sewage sludge vary from 0.08 to around 0.23 with an average value of 0.14. This is lower than the reaction order of DPS carried out in this study 0.3 [8]. The combustion characteristics and kinetic information of DPS obtained in this study can be used to evaluate its potential as energy source and to study the combustion performance of this material.

Conclusion

The combustion of DPS was analyzed by the model-free approaches under non-isothermal condition. The activation energies obtained by the Ozawa‑Flynn‑ Wall method was relatively higher than Vyazovkin method and this values are slightly lower than those has been reported in the literature review for sewage sludge and those found for coal. The reaction order was found to vary along the reaction pathway. The average reaction order corresponding to combustion of DPS was (0.3). TG curves showed that DPS exhibit three distinct reaction zones during the combustion corresponding to moisture content released and volatile matter and fixed carbon combustion. The high heating value and high reactivity (low activation energy) of DPS compare to other biomass is considered the major advantages for using this material as a biomass fuel.

Table 2. Slopes, correlation coefficients and activation energies corresponding to linear fittings according to the Ozawa‑Flynn‑Wall model and Vyazovkin - Lesnikovick

Conversion %	Ozawa‑Flynn‑Wall		Vyazovkin and Lesnikovick	
	R^2	Activation energy (KJ/mol)	R^2	Activation energy (KJ/mol)
20	0.94	17.6	0.9	15
30	0.94	18.6	0.9	15.5
40	0.93	19.2	0.89	15.9
50	0.84	20.5	0.8	17

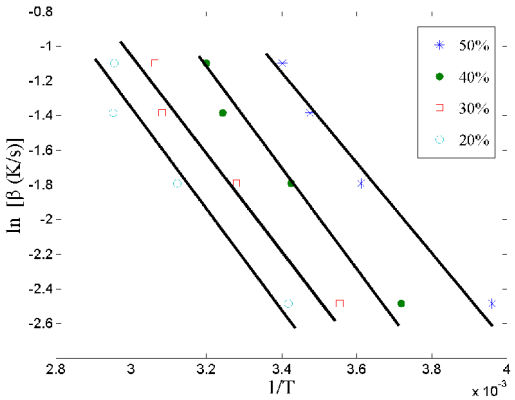

Fig. (2). Curves of fitting to kinetic model proposed by Ozawa‑Flynn‑Wall to various conversion Percentages corresponding to the combustion of dewatered poultry sludge at different heating rate.

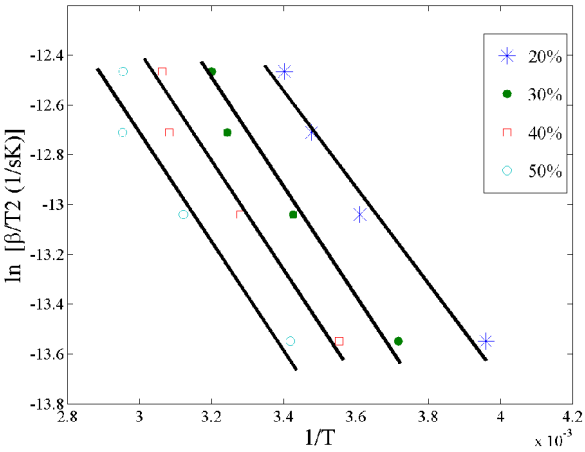

Fig. (3). Curves of fitting to kinetic model proposedby Vyazovkin and Lesnikovick to various conversion Percentages corresponding to the combustion of dewatered poultry sludge at different heating rate.

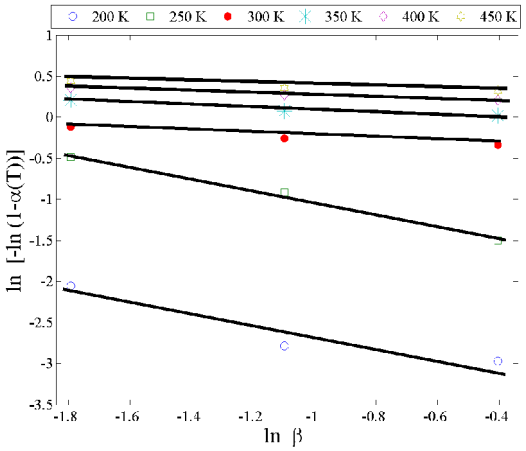

Fig. (4). Curves of fitting corresponding to the reaction order n for different temperatures Along the combustion of DPS

References

[1] C. Marculescu and C. Stan, "Poultry processing industry waste to energy conversion," *Energy Procedia*, vol. 6, pp. 550–557, 2011.

[2] A. M. Otero, M., L. F. Calvo, M. V. Gil, A. I. Garcia, "Co-combustion of different sewage sludge and coal : A non-isothermal thermogravimetric kinetic analysis," *Bioresource Technology*, vol. 99, pp. 6311–6319, 2008.

[3] Ajay Kumar, "BIOMASS THERMOCHEMICAL GASIFICATION : EXPERIMENTAL STUDIES AND MODELING," *PhD dissertation*, no. University of Nebraska, ProQuest, 2009.

[4] X. Hanmin, M. Xiaoqian, and L. Kai, "Co-combustion kinetics of sewage sludge with coal and coal gangue under different atmospheres," *Energy Conversion and Management*, vol. 51, no. 10, pp. 1976–1980, 2010.

[5] D. K. Shen, S. Gu, K. H. Luo, A. V Bridgwater, and M. X. Fang, "Kinetic study on thermal decomposition of woods in oxidative environment," *Fuel*, vol. 88, no. 6, pp. 1024–1030, 2009.

[6] M. M. A. Zakir Khan, Suzana Yusup, "Thermogravimetric Analysis of Palm Oil Wastes Decomposition," no. IEEE First Conference on Clean Energy and Technology CET, pp. 205–208, 2011.

[7] J. Jiang, X. Du, and S. Yang, "Analysis of the combustion of sewage sludge-derived fuel by a thermogravimetric method in China," *Waste Management*, vol. 30, no. 7, pp. 1407–1413, 2010.

[8] A. M. M. E. Sanchez, M. Otero, X. Gomez, "Thermogravimetric kinetic analysis of the combustion of biowastes," vol. 34, pp. 1622–1627, 2009.

[9] M. Otero, X. Gómez, a I. García, and a Morán, "Effects of sewage sludge blending on the coal combustion: a thermogravimetric assessment.," *Chemosphere*, vol. 69, no. 11, pp. 1740–50, Nov. 2007.

[10] H. Xiao, X. Ma, and Z. Lai, "Isoconversional kinetic analysis of co-combustion of sewage sludge with straw and coal," *Applied Energy*, vol. 86, no. 9, pp. 1741–1745, 2009.

[11] M. B. Folgueras, R. M. Díaz, J. Xiberta, and I. Prieto, "Thermogravimetric analysis of the co-combustion of coal and sewage sludge," *Fuel*, vol. 82, no. 15–17, pp. 2051–2055, Oct. 2003.

[12] L. Yanfen and M. Xiaoqian, "Thermogravimetric analysis of the co-combustion of coal and paper mill sludge," *Applied Energy*, vol. 87, no. 11, pp. 3526–3532, 2010.

Advanced Materials Research Vol. 970 (2014) pp 224-227

doi:10.4028/www.scientific.net/AMR.970.224

Enhancement of the Efficiency of Dye-sensitized Solar Cells (DSSC) by Utilizing Silver Plasmonic Nanoparticles on Hydrothermally-Treated Titania (TiO_2) Photoanode

Daniel Angelo C. Camacho[1a], Jenrry T. Daulo[1b*]

[1]Department of Mining, Metallurgical, and Materials Engineering, College of Engineering, University of the Philippines – Diliman, Philippines

[a] dccamacho1@upd.edu.ph, [b*] jtdaulo@up.edu.ph

Keywords: dye-sensitized solar cells, titania nanotubes, silver nanoparticles, plasmon enhanced absorption

Abstract. Titanium dioxide (TiO_2) has been long used as a photoanode for dye-sensitized solar cells (DSSC) for its high photoreductive capability. One approach towards increasing the performance of TiO_2 is to load silver nanoparticles (Ag NP) unto the substrate. In this study, hydrothermal treatment of as-received TiO_2 anatase was utilized to fabricate nanostructures that could increase the overall efficiency of DSSC. This hydrothermally-treated TiO_2 was loaded with Ag NP via the photodegration of silver nitrate ($AgNO_3$). Characterization of Ag-loaded TiO2 (Ag-TiO2), done using Raman Spectroscopy and Field Emission Scanning Electron Microscopy (FESEM), reveal the anatase characteristic of the samples after hydrothermal treatment, as well as the crystalline structure transformation from tetragonal to monoclinic. Furthermore, upon application of the produced TiO_2 samples in DSSC, photovoltaic characteristics were obtained. There was an increase in the current density of all of the Ag-TiO_2 samples as compared to the untreated TiO_2 sample. The DSSC produced using 0.20 Ag-TiO_2 ratio exhibited the highest conversion efficiency, resulting to more than 3000% increase in conversion efficiency from the untreated TiO_2 sample.

Introduction

To increase its marketability as an alternative to silicon solar cells, it is necessary for dye sensitized solar cells (DSSC) to further improve. DSSC mainly consists of a contact, a dye-sensitized titanium dioxide (TiO_2) photoanode, electrolyte, and a counter electrode. TiO_2 is known to promote directional flow of electrons as well as prevent rapid recombination of electrons to its hole. It is also liable to scatter more light to pass through the film and is photostable [1].

Loading silver nanoparticle is an effective way to attain a significant increase on the efficiency of the solar cells. Doping silver provides TiO_2 photoanode plasmonic effect, due to localized surface plasmons that enhances the light absorption of dye in spectral range. Because of strong coupling, nanoparticles tend to have intense absorption of light, even on near UV spectrum [2]. Furthermore, silver has been known to experience low absorption losses at optical frequencies as compared to other metals and due to its high scattering efficiency [3].

Experimental

Fabrication of Hydrothermally-treated TiO_2. To produce hydrothermally-treated TiO_2, 3.75 grams of as-received TiO_2 anatase **(SA)** powder was dissolved in 30 mL of 10 M NaOH in a Teflon beaker through recrystallization. After recrystallization, 0.1 M hydrochloric acid (HCl) was added to TiO_2 to neutralize the solution. The precipitates were then filtered, dried, and crushed to form the powder. The formed powder was annealed for three hours at 450°C. After annealing, a change in the crystallinity of the as-received TiO_2 is expected.

Nanosilver Deposition on Hydrothermally Treated Titania (Hy-TiO_2). Dissolved TiO_2 nanotubes powder was then mixed with varying concentrations of silver nitrate ($AgNO_3$). Using $5x10^{-3}$ M oxalic acid, pH was maintained to 3-3.5. The solution was then stirred at 120 rpm for one

hour. Neutralization of the solution was done using 0.1 M NaOH solution and was exposed to ultraviolet (UV) light for three hours. The precipitates were then recovered by filtering and drying the solution at 100°C.

Fabrication of Dye Sensitized Solar Cells. The Ag-loaded Hy-TiO_2 paste was applied to the FTO glass via doctor blade method, and was dried for five minutes. The impregnated FTO glass was then annealed at 450°C for 30 minutes to ensure good electrical contact. The FTO glass was immersed in 0.5 mM Ru-polypyridine dye-ethanol solution for 24 hours at room temperature. A few drops of the electrolyte solution (0.5M KI, 0.5M I_2, Acetonitrile, Ethylene glycol) were then applied on the film. It was immediately covered with the carbon counter electrode and secured with binder clips.

Results and Discussion

Fig. 1 presents the FESEM images of SA, S0, S1, and S4 samples. Titanate structures, with sizes ranging from 500 nm to 40 nm, are present in all of the hydrothermally-treated samples. The appearance of columnar structures was further noted with the hydrothermally-treated samples, such was not seen on the as-received anatase sample. The merged and compacted nanospheres seen in the untreated anatase sample (Fig. 1a) are also seen to have been dispersed or made discrete after the hydrothermal treatment, (Fig. 1b). The individual nanospheres could be the result of premature recrystallization of TiO_2 while being dissolved in the 10 M NaOH solution. The particles were able to detach themselves from the bulk but failed to recrystallize or undergo nanofolding.

As seen from Fig. 2, samples consisting hydrothermally treated and Ag-loaded TiO_2 exhibited the same peaks of 398 cm^{-1}, 514 cm^{-1}, and 640 cm^{-1} that coincides to that of untreated TiO_2 anatase. Raman peak is also observed at 798 cm^{-1} for the untreated TiO_2 and is absent on the hydrothermally-synthesized TiO_2. This is to confirm that the hydrothermal treatment conducted on the samples left anatase characteristics on the overall sample. Difference in the intensity of the peaks could correspond to the distortion of the crystal lattice upon the suspected change in crystalline structure from anatase to monoclinic. Due to this phase transformation, the anatase characteristic became less pronounced as compared to the untreated anatase sample. The presence of these anatase peaks can be associated with the undissolved anatase nanospheres present in the hydrothermally-treated samples. It is worth considering also that the anatase signals are intrinsic to the titanate structures. [5] Obtained peaks at 275 cm^{-1}, 440 cm^{-1}, and 820 cm^{-1} are typically identified with hydrothermally-synthesized TiO_2 nanotubes and/or nanoparticles [5, 6], and nanorods [4]. The Raman peaks can be associated with the Ti-O-Ti crystal phonons in the titanate structures. [5]

In addition, Hy-TiO_2 samples exhibited peaks around 700 cm^{-1}, a peak that is caused by the second order phonon of the inactive phonon of rutile activated by the distorted crystallinity. The peak at 900 cm^{-1} for the unloaded Hy-TiO_2 is the characteristic band for the Ti-O-Na bond. [6] This implies a presence of anatase precursor that was probably not neutralized upon addition of HCl to the highly-basic solution during recrystallization.

Energy Dispersive X-ray Spectroscopy (EDX) was also done to observe any change in the composition percentages upon subjecting the sample under UV light. From the EDX Spectra (Fig. 3), only three elements were observed: titanium, oxygen, and silver. Absence of other elements in the EDX Spectra suggests total degradation of $AgNO_3$ to Ag^0. Silver nanoparticles are deposited on the TiO_2 into a solution by exposing it under ultraviolet (UV) light. The calculated element percentage of Ag in the S3 is 13.23%. This is almost the same with the observed percentage under EDX Spectra. This implies that all of the Ag atoms from the weighed $AgNO_3$ was transformed into Ag^0.

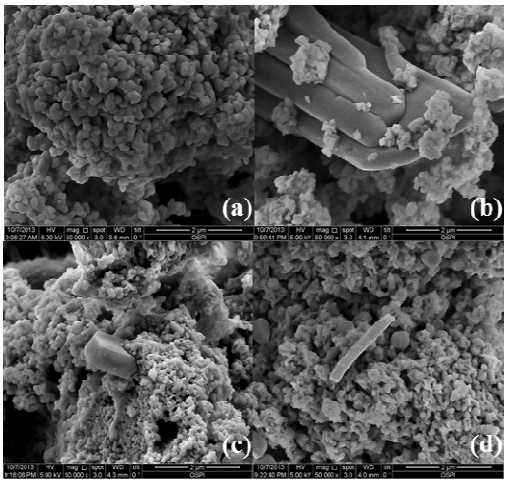

Figure 1. FESEM images of (a) SA, (b) S0, (c) S1, and (d) S4 samples. Magnification of the micrographs is 50kx at 5.00 k

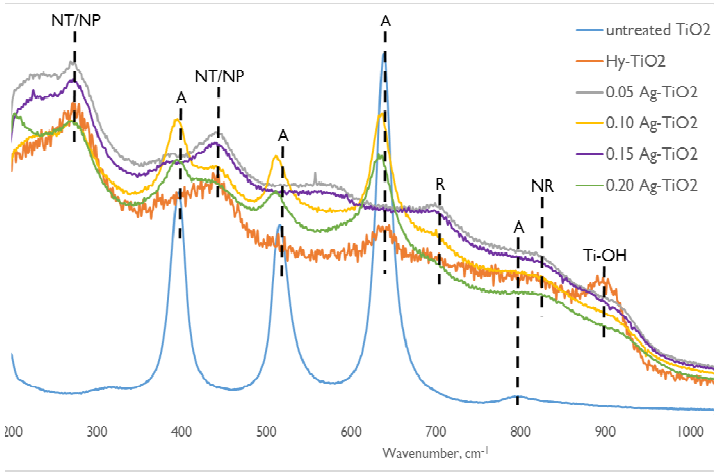

Figure 2. Raman spectra of hydrothermally untreated TiO_2 (SA), Hy-TiO_2 (S0), and Ag-TiO_2 samples (S1-4), Raman peaks identified.

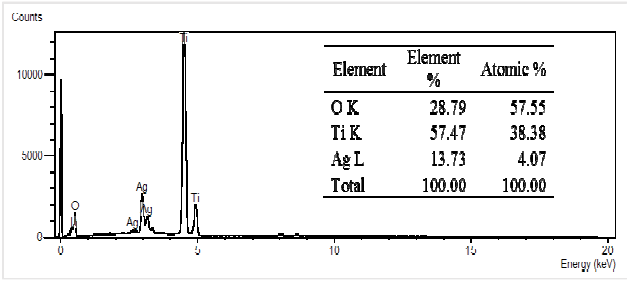

Figure 3. EDX Spectra for 0.15 Ag-TiO_2 sample.

Table 1. Summary of I-V Performances of untreated, Hy-TiO_2, and Ag-TiO_2 DSSCs.

Sample	Composition	Voc (mV)	Isc (mA)	Vmp (mV)	Imp (mA)	Jsc (mA/cm^2)	FF	η (%)
SA	untreated	84.75	0.015	78.104	0.013	0.007	0.8	0.0006
S0	Hy-TiO_2	124.36	0.008	118.697	0.003	0.004	0.348	0.0002
S1	0.05 Ag-TiO_2	123.03	0.073	94.476	0.073	0.033	0.769	0.0041
S2	0.10 Ag-TiO_2	129.9	0.175	102.289	0.09	0.078	0.575	0.0077
S3	0.15 Ag-TiO_2	95.32	0.22	86.712	0.188	0.098	0.785	0.0097
S4	0.20 Ag-TiO_2	138.17	0.411	99.692	0.252	0.183	0.667	0.0224

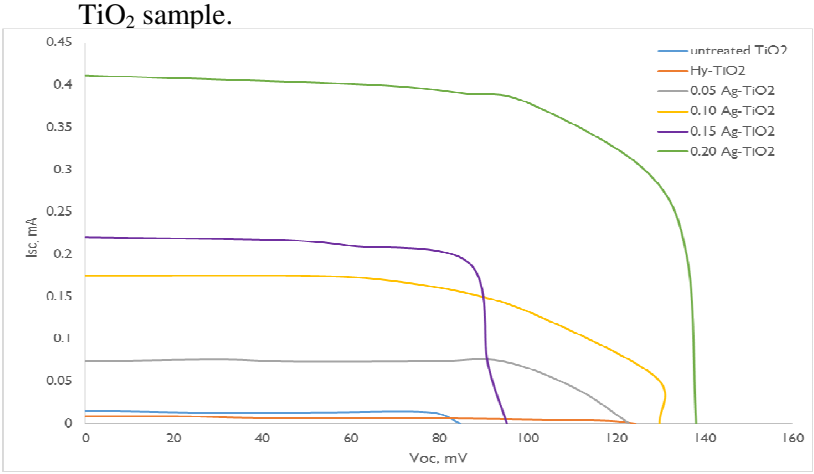

Figure 4. I-V curve of the untreated TiO_2anatase-, Hy-TiO_2-, and Ag-TiO_2-DSSCs.

Fig. 4 shows the summary of the measured I-V characteristics of the untreated TiO_2 anatase-, Hy-TiO_2-, and Ag-TiO_2-DSSCs under the solar simulator. The photoelectric energy conversion efficiency (η), open circuit voltage (Voc), short circuit current (Isc), voltage at maximum power (V_{MP}), current at maximum power (I_{MP}), and fill factor (FF) of the cells were determined from these measured I–V characteristics. Table 1 shows the corresponding values of the mentioned parameters of each DSSCs variant.

There is an increase in the I_{SC} of the Ag-TiO_2 samples as the Ag NP concentration is increased (Fig. 4); showing a drastic jump at S4. This may due to the improved carrier transport done by Ag NP by boosting the electrical conductivity. [7] Another likely reason for the increase of I_{SC} is that loading silver provides plasmonic effect to the TiO_2 matrix. This is due to the localized plasmons

that enhance light absorpitivity [2]. Plasmonic effect is due to the excitation of electrons from the effect of electromagnetic radiation of light.

Overall, the increase in I_{SC} of the Ag-TiO_2 resulted to the increase in photo conversion efficiency, η. This is considering the insignificant change in the V_{OC} of the Ag-TiO_2 DSSCs. The highest obtained efficiency is that of S4 DSSC, with corresponding value of η = 0.0224%. Upon addition of 20% Ag NP to the unloaded Hy-TiO_2, there was an observed increase of more than 3000%.

Conclusions

The hydrothermal treatment utilized in this experiment was able to produce monoclinic titanate nanostructures. These structures are present in the treated TiO_2, together with the nanospheres that resulted from premature recrystallization of TiO_2 anatase.

From the I-V curves obtained, it can be noted that increasing the amount of Ag loaded in the treated TiO2 corresponds to an increase the I_{SC} value. For the V_{OC}, loading Ag increased its value from 84.75 to 138.17 mV, while for I_{SC}, there was an increase of 0.396 mA. These trends causes the overall conversion efficiency also to increase from 0.0006 to 0.0224, more than 3000% increase from the untreated TiO_2 photoanode.

References

[1] J. Archana, M. Navaneethan, Y. Hayakawa. Journal of Power Sources 242 (2013) 803-810

[2] K. Guo, M. Li, X. Fang, X. Liu, B.Sebo, Y. Zhu, Z. Hu, X. Zhao. Journal of Power Sources 230 (2013) 155-160

[3] W. Liu, X. Wang, Y. Li, Z. Geng, F. Yang, J. Li.Solar Energy Materials and Solar Cells 95 (2011) 693-698

[4] Yury V. Kolen'ko, Kirill A. Kovnir, Anton I. Gavrilov, Alexei V. Garshev, Johannes Frantti, Oleg I. Lebedev, Bulat R. Churagulov,OGustaaf Van Tendeloo, and Masahiro Yoshimura.J. Phys. Chem. B 2006, 110, 4030-4038

[5] I. Tacchini, A. Ansón-Casaos, Youhai Yu, M.T. Martínez, M. Lira-Cantu. Materials Science and Engineering B 177 (2012) 19– 26

[6] Lei Qian, Zu-Ling Du, Sheng-Yi Yang, Zhen-Sheng Jin. Journal of Molecular Structure 749 (2005) 103–107

[7] Sang Hoon Nam, Hee-Sang Shim, Yong-Su Kim, Mushtaq Ahmad Dar, Jong Guk Kim, Won Bae Kim. Applied Materials & Interface 2 (2010) 2046

Advanced Materials Research Vol. 970 (2014) pp 228-232

doi:10.4028/www.scientific.net/AMR.970.228

THE PROSPECTS OF ELECTRICITY GENERATION FROM POULTRY PROCESSING DEWATERED SLUDGE (PPDS) IN MALAYSIA

M Fadhil[1,a*], A. Hassan[1,b], Shiraz Aris[1,c], A. Abdalla[1,d], N. Aniza[1,e]

[1]Mechanical Engineering Department, Universiti Teknologi PETRONAS,

Seri Iskandar, 31750, Perak, Malaysia

[a*]farfiez@yahoo.com, [b]engabbas78@gmail.com, [c]mshiraz_aris@petronas.com.my,
[d]saadalla_85@yahoo.com, [e]noor.aniza87@gmail.com

Keywords: biomass, poultry waste, re-energy, sludge

Abstract. Biomass today is considered a potential source of electricity generation in Malaysia under its National Renewable Energy Policy 2010. Among them, less attention has been paid to sludge waste even though its production is increasing. Therefore, the large amount of poultry processing dewatered sludge (PPDS) from a chicken-broiler-factory can be intensely analyzed and transformed to valuable fuel. From Malaysian PPDS, the preliminary findings reported in this paper are; **a) ultimate** *analysis (Carbon; 55.68-67.38%, Hydrogen; 7.61–9.81%, Nitrogen; 3.28-4.41%, and Sulphur; 0.42-0.49%)*, **b) bomb calorimeter** *(heating value; 27-34 MJ/kg),* **c) moisture content;** *69% - 74% and* **d) proximate analysis** *(Moisture content; 3%, volatile matter; 77%, fixed carbon; 8.31%, and ash; 11%).* The usage of PPDS as an alternative fuel is cost-effective and viable given by the high HHV relative to coal that is currently used in local power plants. The results from this study are expected to deliver a significant impact to both the poultry processing and the power generation industries based on the increasing poultry production trend in Malaysia.

Introduction

The demand for poultry products in Malaysia, as in other countries, follows an increasing demand trend. It is assumed that the Malaysian production and demand statistics for poultry products can be correlated to other global locations which have a similar demographical representation [1]. Isolated instances where disease outbreaks related to chicken raring may have affected certain countries but the general trend of increasing demand remains the same elsewhere.

Currently there are 131 factories [2] for poultry processing in Malaysia, and this number is expected to increase in-line with the Malaysian government's aspiration to become an Asian hub for halal chicken meat supply. The number of chickens processed daily in Malaysia is difficult to ascertain given the confidentiality of information coming-off of producers due to the fierce competition amongst them. Nonetheless correlations of data obtained from the individual plants visited are used as a main indicator of how much PPDS is produced from the entire broiler process on a daily basis.

The poultry-processing related industry generates a substantial amount of processed chicken by-products are not intended for human consumption. This waste is called offal and consists of trimmings, feathers, blood, internal organs and other byproducts that are rich in proteins and fats; they enter into a waste water treatment process within the processing plant and leave with a sludge like consistency known as poultry processing dewatered sludge (PPDS). PPDS consists of suspended solids and polymers with a limited amount of biological materials.

The most common disposal method of PPDS is through the agricultural fields whereby PPDS is used as a fertilizer supplement. Besides this, it is also disposed of in specialized landfills. PPDS with a high amount of organic content is suitable in agriculture as a fertilizer to enrich the quality of agricultural soil. However, the use of PPDS in agricultural fields carries the risk of transferring

pollutants to the human food chain. This method has caused environmental problems in the form of organic pollution and the increase in microbial loads [3].

Perhaps the safest method to dispose PPDS, in terms of reducing any chance of infection or microbial contact, is through incineration. The incineration process can also recover energy and reduce the volume of solid waste that needs to be disposed [4]. Power generation can be used to earn income or supplement the energy requirements of the plant. The closet example of a power generation application related to the chicken processing industry involve the very upstream of chicken farming whereby 800 000 t of chicken litter per year is collected to generate approximately 64MW of electricity [5]. To date there has not been any power generation plants operating on PPDS as fuel reported in literature.

To qualify as a fuel substitute, it is very important to identify and analyze the properties of PPDS fuel characterization have been previously carried out inferring the amount of carbon, hydrogen, nitrogen and sulphur through an ultimate analysis to the potential energy recovery from samples tested [6]. The use of proximate analysis to quantify the amount of fixed carbon, volatile matter, moisture content, and ash is also part of a common fuel characterization exercise. A much quicker procedure to ascertain energy available or heating value in a potential fuel sample is through the use of bomb calorimeter.

The main purpose of this study is to explore the potential of PPDS as a fuel source whilst mitigating the disposal issues of poultry processing plants. The gaps in current research work with regard to poultry processing waste material and its potential application in power generation will be duly addressed once the proposed characterization study has completed.

Experimental Setup

Waste sample collection. Establishing a sound database on the fuel characteristics of PPDS is of utmost importance in pursuing the current research objectives. Samples of PPDS from three different poultry processing plants in Malaysia were collected at different intervals throughout the year to explore the repeatability and the dependence of the key fuel parameters on variables such as time, location and the time of year.

To maintain consistency the samples were collected from plants which use similar chemical coagulation and sedimentation processes in their water treatment plant. In terms of location these three plants represent the North, Central and Southern Malaysian states respectively.

Moisture Content Analysis. The water content, w (%) of the samples was determined as the weight loss percentage after being heated in an oven at 105^{o}C. The set temperature was chosen to ensure that complete evaporation complete evaporation would have taken place from the sludge sample. A total of 30 samples from each plant, were dried for the subsequent tests to ensure repeatability. Illustrations of the sample appearance before and after drying and the moisture contents in the as-received samples are shown in Fig 2 and 3 respectively.

Fig. 2: Fresh “as-received” samples

Fig. 3: Dried samples

Analytical Analysis. Analytical analyses were the used to characterize PPDS for its fuel properties. The common list of bench-top tests consisting of Bomb calorimeter, Proximate and Ultimate Analysis which are used to characterize solid fuels were used for the PPDS samples. A LECO AC600 bomb calorimeter was used to determine the higher heating value of PPDS samples in accordance to ASTM D2015. The heating value of solid fuels is an early indication of the amount of energy available in the tested material if it were to be fully combusted under controlled conditions. To measure inherent moisture, volatile matter, fixed carbon and ash, a NETZSCH model STA 449 F3 JUPITER was used. Air was introduced at the 900 ^{o}C during each test run to initiate combustion and record all effects related to this mode of thermal treatment. An ultimate analysis was then carried out using a LECO CHNS-932.

Results and Discussion

Moisture Content. The moisture in the as-received sample was measured after the drying process, where the reduction of final sample mass indicated the amount of water which remained in the sample after the de-watering process at the plant.

The samples collected from three different plants recorded a moisture range of between 69% and 74% (Table 1). Although the plant adopted similar dewatering processes, the difference in results suggests that factors within the process have had an influence in the dewatering efficiencies of the respective plants.

Heating Value. The variation of the gross heating value, measured using a bomb calorimeter, of the PPDS samples collected from the different processing plants are shown in Table 1. From these results, the mean heating values of the PPDS were calculated to be in the range of 27-34 MJ/kg.

The relatively high HHV, in comparison to coal (27 MJ/kg) [7], indicate the potential of PPDS as an alternative fuel. Research and development work in Malaysia, with regard to the utilization of biomass waste as a fuel source, are typically focused on the by product of the oil palm industry [8] i.e. empty fruit bunch (EFB) - 14.6 MJ/kg, fiber (F) – 14.8 MJ/kg and shell (S) – 19 MJ/kg. In comparison to these waste material, the HHV of PPDS appears be to significantly higher. This is further proof that PPDS should be explored for its potential as a fuel source.

Table 1: Sample location, designation and results

No	Plant Location	Designation	Moisture Content (%)	Heating Value (MJ/kg)
1	Setiawan, Perak	Sample S	69	34
2	Klang, Selangor	Sample K	72	28
3	Melaka, Melaka	Sample M	74	27

Ultimate Analysis. The C, H, N and S content for the PPDS samples from the different locations are shown in Table 2. The values of these critical elements in fuel samples are indicators that will correlate to the energy content and are ultimately used in chemical equations to obtain further information on reaction rates and identification of exhaust emission components.

Based on the PPDS chemical properties found in Table 2, the following chemical formula can be used to predict the combustion behavior of PPDS.

$$C\,H_{1.75}\,N_{0.04}\,S_{0.002} \quad (1)$$

In complex combustion stoichiometry, considering low chemical composition of nitrogen and sulfur, the following chemical balance can be written:

$$CH_{1.75} + 1.44O_2 + 5.44N_2 \rightarrow CO_2 + 0.88H_2O + 5.44N_2 \quad (2)$$

Table 2: Ultimate analysis results

Sample	C (%)	H (%)	N (%)	S (%)
Sample S	66.32	9.54	3.45	0.48
Sample K	56.35	8.25	3.82	0.59
Sample M	55.17	7.67	4.41	0.49

Proximate Analysis. In analyzing the PPDS samples for volatiles, inherent moisture and combustion, the following heating programme was used in the Thermogravimetric Analyzer,
a) Heating up to 100°C and kept at 100°C for 5 minutes in N2 atmosphere in order to dry the sample.
b) Heating up to 900°C at 20 K/min in N2 atmosphere. At 900°C, the gas atmosphere was switched to air and the sample was heated up further to 1500°C at 20 K/min.

PPDS is found to contain 8.3% fixed carbon. It is also made up of 11% ash. A Further increase in the amount of ash content may reduce burning capacity in combustion and may affect combustion efficiency. However, with a high HHV the handling of ash in full scale PPDS combustion will need to be explored.

One of the key findings in a TGA procedure is the amount go volatiles present in a sample. Volatile matter is composed of methane, hydrocarbons, hydrogen, carbon monoxide and incombustible gases like carbon dioxide and nitrogen. The high amount of volatiles present in the tested samples, at approximately 77%, will be conducive for ignition in a combustion chamber.

Full Scale Implementation

The fuel characteristics embedded within PPDS is evident from the analytical tests carried out on the collected samples. In looking into a full scale application of PPDS in the power generation industry factors such as sustainability of supply, total energy content, storage and handling of this waste material will need to be looked into.

On an average, PPDS accounts for 28% of the live weight of one broiler chicken [9]. Thus, a typical processing plant slaughtering 100,000 broilers per day with a mean live weight of 5.0 lbs (2.3 kg) will produce 70 tons of PPDS per day. Malaysia has 9 major poultry processing companies in the country contributing a daily combined dewatered sludge supply of approximately 1065 tons from 131 active plants. The estimated availability will be feasible for a small scale biomass power plant of less than 100 MW [10] or a large scale coal power plant with a co-combustion strategy with the existing coal stock pile.

To supplement the positive early findings on the energy content in PPDS a complete energy conversion, assessment is required. The two aspects that need to be considered are the fuel combustion efficiencies and the overall thermal efficiency of the steam cycle. By using the combustion of coal as a reference , the typical estimate for combustion efficiency is 88% on an HHV basis 42% for the overall plant thermal efficiency based on an available Rankine cycle component assessment. Thus, the overall conversion efficiency for this process is estimated at (88% x 42%) 36.96%.

The conversion of a fuel into useful energy, using the above conversion efficiency assumptions, will then require a 9740 kJ/ kW hr heat rate input. Since PPDS has an average specific heat value of 34,000 kJ/kg, based on the analytical tests, an estimated 28600 kg/hr (28.6 T/hr) will be required for an electrical output of 100 MW. In correlating these calculations to the available PPDS supply of

1065 ton/day a 100MW plant is estimated to be in continuous operation for a 37 hour period for each day's supply of PPDS.

Conclusions

The basic fuel characterization of Malaysian Poultry Processing Dewatered Sludge (PPDS) was successfully carried out to evaluate its potential source of energy. The samples collected from three local waste-water treatment plants of chicken broiler factories were found to have the potential as a fuel for combustion in an energy recovery plant. The preliminary results show its capability to produce energy for electrical. The advantage of using PPDS, of course, the tariff charge for local electricity consumption can be reduced when the fuel source is free or cheaper in price.

Even though the use of energy from poultry waste has many benefits, however, it faces numerous challenges. The first challenge is the availability of commercially ready technology to store, handle and manage PPDS as a fuel source. Second is the lack of information on the combustion characteristics and how it may be used to correlate to a full scale energy conversion scheme to meet the needs. Third is the less of reliable information on the potential supply of renewable energy at the national level. Besides, the low demand for energy from renewable resources is also hindering the utilization of this energy.

The findings from the current work have managed to find early indicators to the potential use of PPDS in a full scale energy conversion application. With further research emphasis on sustainability issues and with appropriate attention to storage, handing and transportation research questions, PPDS has the potential to be positioned as an alternative biomass waste in power plant applications.

References

[1] Global Poultry Trends in Asia Leads the World in Chicken Demand (2010), information on http://www.thepoultrysite.com
[2] Information on http://www .superpages.com
[3] Wei-Sheng Chen, The characteristics of organic sludge/sawdust derived fuel, Bioresource Technology 102 (2011) 5406-5410.
[4] Abelha P., Gulyutlu I., Boavida D., Seabra Barros J., Cabrita I., Leahy J., Kelleher B. And Leahy M., Combustion of poultry litter in a fluidised bed combustor, Fuel. 82 (2003): 687 – 692
[5] Industrial "Fibrowatt Group, Information on http://www.fibrowatt.com.
[6] Roberto García, Consuelo Pizarro, Antonio G. Lavín, Julio L. Bueno , Characterization of Spanish biomass wastes for energy use, Bioresource Technology 103 (2012) 249–258.
[7] PTM (Malaysia Energy Centre), Biomass Power Generation & Cogeneration Project (BioGen). Information on: http://www.ptm.org.- my/New_BioGen_Web_II.
[8] Dr. Adlansyah Abd RAhman, Potential for Cofiring Biomass with Coal in Malaysia, Centre for Renewable Energy (2010), UNITEN.
[9] Husain S. Plumber and Brian H. Kiepper, Impact of poultry processing by-products on wastewater generation, treatment, and discharges, Proceedings of the 2011 Georgia Water Resources Conference
[10]Information on http://en.wikipedia.org/wiki/List_of_power_stations_in_Malaysia.

CHAPTER 11:

Metal and Alloys

Advanced Materials Research Vol. 970 (2014) pp 235-239

doi:10.4028/www.scientific.net/AMR.970.235

A Study of Surface Hardening on Local Bolts (C= 0.01%) at a Temperature of 400°C for 5 and 6 Hours With Nitrocarburizing Using RF-Plasma Apparatus

Usman Sudjadi

Center for Nuclear Fuel Technology – National Nuclear Energy Agency

Kawasan PUSPIPTEK – Tangerang Selatan 15314, Indonesia

Phone: +62-21-7560915, Fax: +62-21-7560909

usmannunung@yahoo.com

Keywords: Nitrocarburizing, RF- plasma, local bolt component, hardness, microstructure

Abstract. A study of surface hardening on local bolts (C=0.01%) at a temperature of 400°C for 5 and 6 hours with nitrocarburizing using RF-plasma apparatus. The objective of this experiment was to seek a surface material of local bolts that is more resistant to friction and having better surface uniformity, higher hardness and higher corrosion resistance. The experiment was conducted on the local bolts (C = 0.01%) with a radio-frequency (RF) plasma nitrocarburizing equipment. The nitrocarburization was done on the local bolts at a temperature of 400°C, with a variation of nitrocarburizing times of 5 and 6 hours. The results showed that the average hardness of local bolt samples before nitrocarburization was 136.08 kgf/mm^2. After nitrocarburization at a temperature of 400°C for 5 hours, the average hardness of local bolt samples was 199.1 kgf/mm^2. After nitrocarburization at a temperature of 400°C for 6 hours, the average hardness of local bolt samples was 201.12 kgf/mm^2. The matrixes on the base material were ferrite, austenite, and pearlite.

Introduction

Bolts are among the components that are widely used in so many fields such as in mechanical engineering, civil engineering, and nuclear reactor facilities. Bolts, gears, bearings, pistons, and disc brakes are components of motorized vehicles. These machine elements are components that rub against each other. In nuclear facilities, bolts are used as supporters in the construction of the building, in the conveyor of a hot cell in a post irradiation examination (PIE) facility, in the bearing of a turbine generator, in the axis of a blower exhaust, in the axis of an electrical motor, in the lifting devices, in the plunger of a pneumatic/hydraulic system, in the manipulators of a hot cell, and so on. They are also components that rub against each other. Therefore, the surface of the component's material should have a frictional resistance. There are many methods to make the surface of the components frictional resistant. Conventional methods to obtain surface hardening of the materials so that the surface of the material components will be frictional resistant are nitriding, carburizing, and nitrocarburizing. But the conventional methods do not utilize plasma in the process, so that homogeneity cannot be achieved. Currently there are advanced methods that utilize plasma in the process. Among them are DC plasma nitriding, DC plasma carburizing, DC plasma nitrocarburizing, radio-frequency (RF) plasma nitriding, RF plasma carburizing, RF plasma nitrocarburizing, plasma immersion implantation (PIII), and low pressure plasma assisted nitriding. [1-7]. The advanced methods utilizing plasma get results which have more homogeneity, higher surface hardness, and higher corrosion resistance. This paper reports the results of the study of surface hardening on local bolts at a temperature of 400°C for 5 and 6 hours with nitrocarburizing using radio-frequency plasma apparatus.

Methodology

The local bolts observed were made of low carbon steel (see Table 1). At the beginning the bolts were cleaned with distilled water. After that, they were cleaned with acetone. The natural oxide

layer on the surface of the bolts was etched with HF for 1 to 3 minutes. The bolts were cleaned again with distilled water. Then the bolts were sprayed with nitrogen gas. After that, RF plasma nitrocarburization was done on the bolts at a temperature of 400°C for 5 and 6 hours (see Fig. 1). Sample number 1 was the sample before nitrocarburization. Samples number 2 and 3 were samples after nitrocarburization at a temperature of 400°C for 5 and 6 hours consecutively. The gases used in the experiment were C_6H_6 and high-purity nitrogen. Then, the nitrocarburized bolts were cut as samples for microstructure observation. The samples were mounted, polished, and etched for microstructure observation with optical microscope. The surface hardness of the samples was tested with O.M.A.G Vickers microhardness MHX 10 apparatus. The expenses tracking was 300 grf, the time of tracking was 15 seconds, and the distance limitation is 0.15 mm. Optical emission spectrometer apparatus was used for chemical composition test of the local bolts.

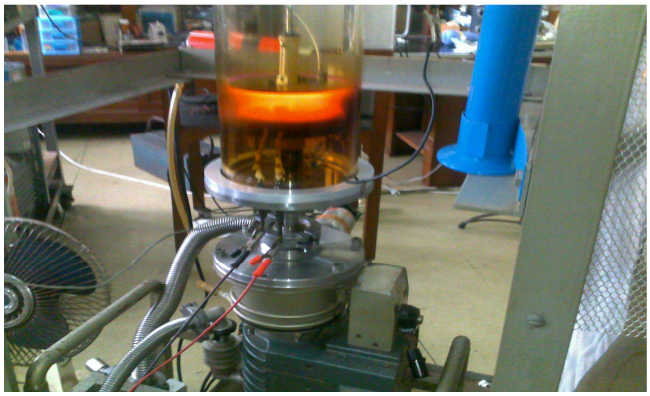

Figure 1: The radio-frequency plasma nitrocarburizing apparatus for this experiment

Table 1: The chemical composition of the local bolts (before nitrocarburization)

Elements	% wt
C	0.010
Si	0.101
S	< 0.003**
P	0.007
Mn	0.508
Ni	0.044
Cr	0.099
Mo	0.010
Ti	< 0.002**
Cu	0.291
Nb	< 0.002**
V	< 0.002**
Al	< 0.001**
Fe	Bal.

** (<) indicates that the value is below the quantification limit of the testing equipment

Results and Discussion

Table 2 shows the hardness of the bolt before nitrocarburization. The hardness was tested at 5 tracking points. The average hardness of all hardness measurements was 136.08 kgf/mm^2.

Table 2: Hardness of the local bolt sample before nitrocarburization (Sample 1).

No	Average Diagonal (mm)	Hardness (kgf/mm^2)
1	52	137.1
2	52	137.1
3	52	137.1
4	52	137.1
5	53	132
	Average	136.08

Table 3: Hardness of the local bolt sample after nitrocarburization at a temperature of 400°C for 5 hours.

No	Average Diagonal (mm)	Hardness (kgf/mm^2)
1	49	231.6
2	52	205.7
3	54	190.7
4	55	183.9
5	55	183.9
	Average	199.1

Table 4: Hardness of the local bolt sample after nitrocarburization at a temperature of 400°C for 6 hours.

No	Average Diagonal (mm)	Hardness (kgf/mm^2)
1	48	241.4
2	52	205.7
3	54	190.7
4	55	183.9
5	55	183.9
	Average	201.12

Table 5: Average hardness of the local bolt samples before and after nitrocarburization

No	Samples	Average Hardness (kgf/mm^2)
1	Before nitrocarburization	136.08
2	After nitrocarburization at a temperature of 400°C for 5 hours	199.1
3	After nitrocarburization at a temperature of 400°C for 6 hours	201.12

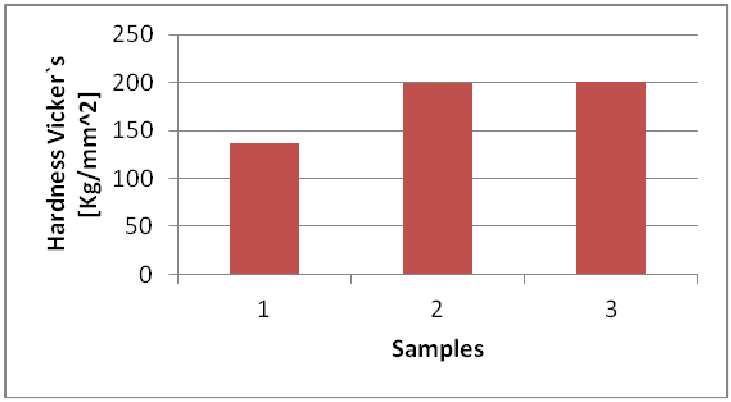

Figure 2: Average hardness of the bolt samples (1 = before nitrocarburization, 2 = after nitrocarburization at a temperature of 400°C for 5 hours, 3= after nitrocarburization at a temperature of 400°C for 6 hours.

From hardness testing it could be seen that the average hardness of the sample before nitrocarburization was 136.08 kgf/mm^2. The average hardness sample after nitrocarburization at a temperature of 400°C for 5 hours was 199.1 kgf/mm^2. The average hardness sample after nitrocarburization at a temperature of 400°C for 6 hours was 201.12 kgf/mm^2. So, it is concluded that if the time of nitrocarburization increases, then the surface hardness of the bolts will be slightly increasing. Moreover, their wear resistance and corrosion resistance will be also slightly increasing [2-6] (see Tables 2-5 and Fig. 2). This shows that diffusion process of nitrogen and carbon atoms to local bolt samples occurred [3-6]. This means that in a change of nitrocarburization time from 5 hours to 6 hours, the number of nitrogen and carbon atoms that have diffused into the local bolt material did not increase much. So, the hardness changed slightly (see Figs. 3, 4, and 6). The results of microstructure observation can be seen in Figures 3-8. Fig. 3 shows the microstructure of the local bolt sample before nitrocarburization at a magnification of 500x.

Figure 3. Microstructure of the local bolt sample before nitrocarburization (magnification 500x)

Figure 4. Microstructure of the local bolt sample after nitrocarburization at a temperature of 400^{o}C for 6 hours (magnification 500x)

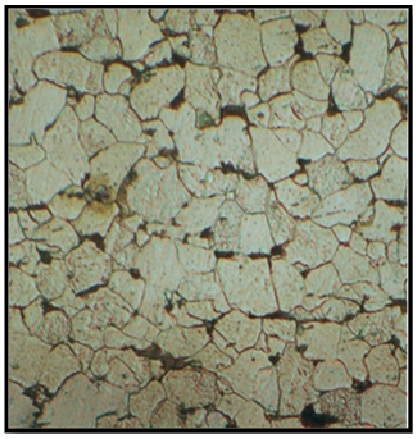

Figure 5. Microstructure of the local bolt sample after nitrocarburization at a temperature of 400^{o}C for 6 hours (magnification 500x, core part of the material)

Figure 6. Microstructure of the local bolt sample after nitrocarburization at a temperature of 400^{o}C for 5 hours (magnification 500x)

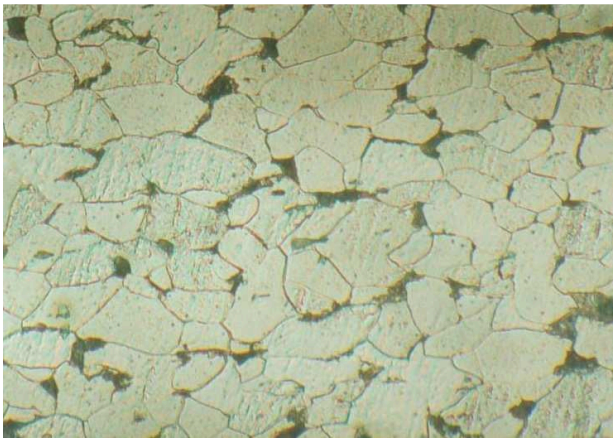

Figure 7. Microstructure of the local bolt sample after nitrocarburization at a temperature of 400^{o}C for 5 hours (magnification 500x, core part of the material)

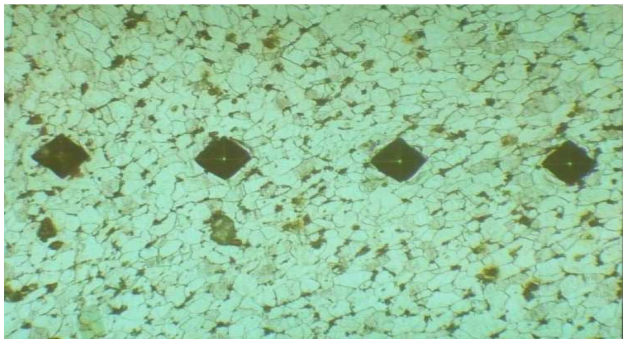

Figure 8. Microstructure of the local bolt sample after nitrocarburization at a temperature of 400^{o}C for 5 hours (hardness testing)

Figure 4 shows the microstructure of the local bolt sample after nitrocarburization at a temperature of 400^{o}C for 6 hours with a magnification of 500x. Figure 5 shows the microstructure

of the local bolt sample after nitrocarburization at a temperature of 400^{o}C for 6 hours with a magnification of 500x at the core part of the material. Figure 6 shows the microstructure of the local bolt sample after nitrocarburization at a temperature of 400^{o}C for 5 hours with a magnification of 500x. Figure 7 shows the microstructure of the local bolt sample after nitrocarburization at a temperature of 400^{o}C for 5 hours with a magnification of 500x at the core part of the material. Figure 8 shows the microstructure of the local bolt sample after nitrocarburization at a temperature of 400^{o}C for 5 hours at a magnification of 200x for the hardness testing. In Fig. 8 the traces of diamond pyramid were visible. Figures 3-7 shows the matrixes of ferrite, pearlite, austenite, and grain boundaries. The EDAX (Energy Dispersive Analysis X-Ray) or EDS (Energy Dispersive Spectroscopy) apparati can be used to more clearly demonstrate the observation results.

Conclusion

Nitrocarburizing on the local bolts using RF plasma apparatus had truly resulted in a higher hardness. Before nitrocarburization, the average hardness of the samples was 136.08 kgf/mm^2. The average hardness of the samples after nitrocarburization at a temperature of 400^{o}C for 5 hours was 199.1 kgf/mm^2. The average hardness of the samples after nitrocarburization at a temperature of 400^{o}C for 6 hours was 201.12 kgf/mm^2. The matrixes of the base material were austenite, ferrite, and pearlite. So it is concluded that nitrocarburization time is directly proportional to the resulting surface hardness. Consequently, the wear resistance of the bolts becomes slightly higher, and their corrosion resistance is also slightly increasing.

References

[1] G. Leonard Devila, et al., Physics Scripta, T131 014011(4pp), 2008.
[2] V.A. Dutka, Journal of Super-hard Materials, 1063-4576, Vol. 30, Number 5, 2008.
[3] S. Gredelj, et al., Thin Solid Films, Science Direct, online at www.sciencedirect.com , 2006.
[4] R. Valencia et al., Brazilian Journal of Physics, Vol.34, No.4B, 2004.
[5] U. Sudjadi, Research Report, Financed by Indonesian Ministry of Research and Technology, 2012.
[6] U. Sudjadi, 13th International Conference of Quality in Research, June 25-28, Indonesia, 2013.
[7] U. Sudjadi, Indonesian Patent No. P.00201300400, 2013.

Advanced Materials Research Vol. 970 (2014) pp 240-243

doi:10.4028/www.scientific.net/AMR.970.240

Effects of Complexing Agent Concentration and Bath pH on Electroless Nickel Deposition for Tungsten Carbide Powders

P. Rattanawaleedirojn[1,a*], K. Saengkiettiyut[1,b], Y. Boonyongmaneerat[1,c], N. Chuankrerkkul[1,d], S. Saenapitak[1,e]

[1]Metallurgy and Materials Science Research Institute, Chulalongkorn University, Phayathai Road, Bangkok 10330 Thailand

[a*]pranee.r@chula.ac.th, [b]kanokwan.s@chula.ac.th, [c]yuttanant.b@chula.ac.th
[d]nutthita.c@chula.ac.th, [e]sawalee.s@chula.ac.th

Keywords: Nickel, Electroless plating, Tungsten carbide powder

Abstract. An elemental nickel (Ni) or cobalt (Co) is typically introduced to tungsten carbide (WC) prior to powder injection moulding process (PIM) for hard metal fabrication to enhance toughness and tool life. Mixing of powders is normally practiced, although it requires a long processing time for homogeneous mixing. In this study, as an alternative method, an addition of Ni via the electroless deposition method is investigated. The key process parameters, including the concentration of the complexing agent, namely sodium citrate, and bath pH, are systematically examined in relation to deposition rate and deposits' size, microstructure, and chemical compositions. As the bath pH is increased to higher alkalinity of 10 and the Ni ion to complexing agent mole ratio is controlled under 1:1, a stable electroless nickel solution and a relatively high deposition rate with about 15% weight gain for 1 hour deposition duration are achieved. The phosphorus (P) content, obtained in the range of 5-9 wt%, is largely influenced by the bath pH. While a rapid deposition rate is associated with preferentially deposition of Ni on pre-deposited Ni sites, a low to moderately high deposition rate results in more uniform incorporation of Ni-P alloys in WC powder mixture.

Introduction

Tungsten carbide (WC) powders are commonly used in manufacturing of cutting tools and industrial machinery. Nickel and cobalt have been reported to be used as binder materials for tungsten carbide powders to improve the properties such as rupture strength and hardness of the materials [1]. With its decent corrosion protection characteristics at reasonable price, nickel has attracted extensive attention for applications of machining parts in both severe abrasive and corrosive conditions.

Electroless plating technique has been reported to provide uniform Ni coating onto ceramic powder [1,2]. Hence, it could serve as an alternative route for a mixing step of WC powders prior to PIM process to overcome the homogeneity problem in the conventional mechanical mixing method. In this work, Ni-deposited WC powders were prepared by electroless plating process. The effects of complexing agent and bath alkalinity on deposition rate, morphology and composition of the deposits were investigated.

Experimental

WC powders, supplied by ATI Alldyne, USA were used in this study. Prior to the coating process, the powders were treated with 14 wt% HCl for 15 min, water rinsed, and sensitized by immersing in a mixed solution of $SnCl_2$ (5.00 g), $PdCl_2$ (0.10 g), conc. HCl (9.2 ml) and deionized water (100 ml) for 10 min. After 3 times of water rinsing, the powders were then oven dried at 110 °C for 24 hrs. Ni was electrolessly deposited onto the pretreated WC powders from aqueous solution containing $NiSO_4.6H_2O$ (0.152 M), $Na_3C_6H_5O_7.2H_2O$ (0.12, 0.16, 0.20 M), $NaH_2PO_2.H_2O$ (0.189 M), $(NH_4)_2SO_4$ (0.227 M) and thiourea (0.8 ppm). The pH values of the solutions from 8 to 12 were adjusted with sodium hydroxide. The pretreated WC powders (10.00 g) were kept suspended in the electroless plating solution (300 mL; 80± 2°C) in an ultrasonic environment

throughout the coating process of 1 hr. The deposited WC powders were then removed from the solution, rinsed two times with deionized water, and oven dried at 110 °C for 24 hrs.

The weight gain of the deposits was measured using an analytical balance with a resolution of 0.0001 g. The particle size of WC powders was measured by a laser particle size analyzer (Malvern, Master sizer S). The surface morphologies and the chemical composition of the deposits were examined by a Philips, XL 30CP scanning electron microscope (SEM) equipped with energy dispersive X-ray (EDX) spectrometry.

Results and Discussion

The percent weight gains of the deposited materials obtained from the pH 9 and pH 10 electroless plating baths are shown in Fig. 1 as a function of the sodium citrate concentrations. The results show that the deposition rate of the pH 10 bath is slightly faster than that of the pH 9 bath. As the concentration of sodium citrate is increased from 0.12 M to 0.20 M, the weight gain percentage is decreased from 14.6% to 10.5%. The decreasing trend of the deposition rate corresponds well with the particle size analysis results, also shown in Fig. 1. It should be noted that the average particle sizes of the uncoated WC powders and the sensitized powders are 3.2 and 3.7 microns, respectively. By increasing the concentration of the complexing agent, the average size of the Ni-deposited WC powders from the pH 10 bath decreases from 8.9 to 6.6 microns, signifying decelerating effects in the Ni reduction reaction by the citrate complexing agent.

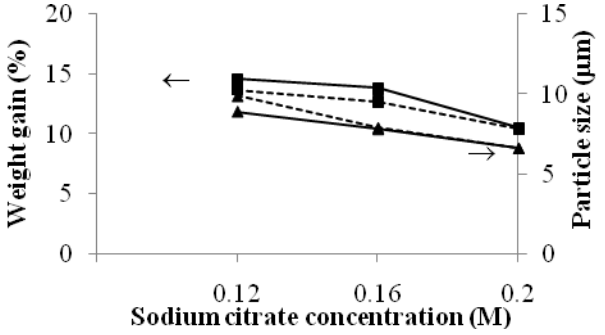

Fig. 1 Effect of citrate concentration on weight gain (■) and particle size (▲) of Ni coated WC powders after plating at pH 9(- - -) and 10(—).

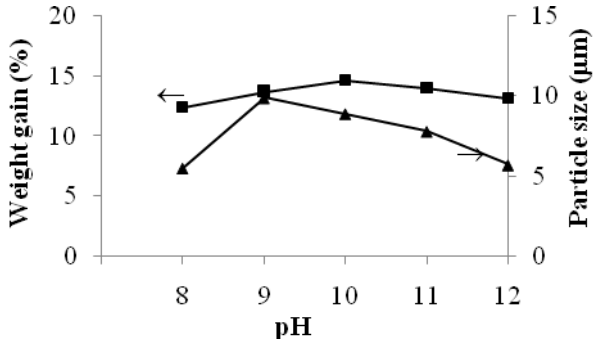

Fig. 2 Effect of bath pH on weight gain (■) and particle size (▲) of Ni coated WC powders, as investigated from baths with 0.12 M sodium citrate.

Particularly, when the concentration of sodium citrate is 0.12 M, some of the Ni ions are in the form of a simpler metal complex, $[Ni(Cit)]^-$, which enables relatively rapid deposition of metallic Ni. As the complexing agent is increased, a stable metal complex of $[Ni(Cit)_2]^{4-}$ is predominated [3]. At the other end, however, too low amount of sodium citrate could result in precipitation of low solubility nickel salt. From the experimental results, a reasonably high plating rate of Ni that is free of precipitates in the alkaline bath can be achieved when the complexing agent to nickel ion mole ratio is kept below 1:1.

The dependency of the deposition rate and particle size of Ni-deposited WC particles on the bath alkalinity is illustrated in Fig. 2. By controlling the amount of the complexing agent at 0.12 M, the deposition rate of Ni reaches a maximum at pH 10 with 14.6% weight gain. Then the plating rate decreases with further increase of the bath pH. A similar concave trend is observed in the pH-particle size curve, except that the peak occurs at pH 9. Agglomeration of the particles may be responsible for overestimation of particle size at such pH condition.

The primary step of Ni deposition mechanism in alkaline bath involves the reaction of hypophosphite with hydroxide ion according to Eq. 1 [4]. As the bath pH is raised, the reaction is spontaneous in the forward direction. The presence of H^- enhances not only the reduction reaction of Ni ions but also hypophosphite ions to form elemental P in the competing reactions. Excess amount of hydroxide ion at pH ≥ 11, however, may cause the precipitation of nickel salts that adversely influence the kinetics of Ni deposition.

$$2H_2PO_2^- + 4OH^- \rightarrow 2HPO_3^{2-} + 2H_2O + 2H^- \quad (1)$$

Generally, electroless Ni coatings are composed of phosphorus (P) owing to hypophosphite that is used as a reducing agent. An increase of the P content may alter the properties of the Ni deposits, and therefore, an investigation of the P content is important. In this work, the contents of the deposited Ni and P that are mixed with WC particles as measured by EDX analysis are represented in Fig. 3. By increasing the concentration of the complexing agent at pH 9, it can be seen that the relative content of P increases from 4.74% to 8.41%. The respective decrease of Ni content could be owed to the result of nickel complex stability, as observed in other works [5] However, for the pH 10 bath, the Ni and P contents appear to be somewhat stable regardless of the complexing agent concentrations. Fig. 4 shows that raising the bath pH from 8 to 12 results in an increase of the relative P content from 4.69 to 9.45%, all of which can be classified as medium phosphorus content for Ni-P alloys [6]. This result differs from the previous result of electroless Ni-P plating on the sheet-form steel substrate [7] that shows that the P content tends to decrease with the bath alkalinity. This suggests that the type of substrate may have some influence on the kinetic of the deposition process.

SEM micrographs (Figs. 5-6) show that the pure WC powders form aggregates consisting of small particles of less than 1 micron in size. In general, Ni-P deposits are found to form cluster of nodules on the surface of WC powders. For those with rapid deposition rates, such as the conditions with low concentration of the complexing agent with pH 9-11 solutions, the Ni-P atoms appear to preferentially deposit on the pre-deposited Ni-P sites. This results in wavy branches of Ni-P in the WC agglomerates. To achieve more evenly-distributed Ni-P incorporated in WC powder mixture, a low to moderately high deposition rate of electroless plating is favorable.

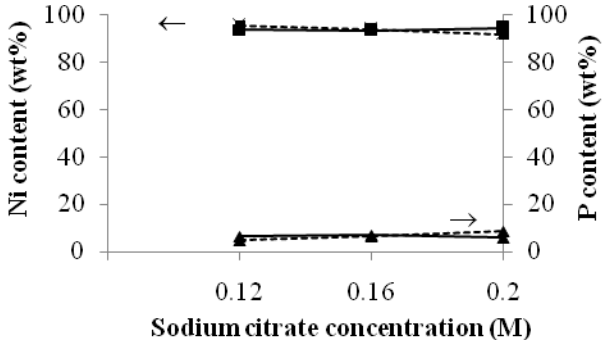

Fig. 3 Ni (■) and P (▲) content in the deposits after electroless plating at pH 9 (- - -) and 10 (—) with various concentration of citrate.

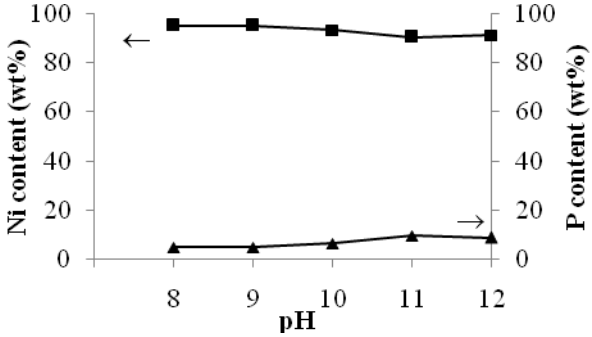

Fig. 4 Effect of bath pH on Ni (■) and P (▲) content in the deposits, as investigated from baths with 0.12 M sodium citrate.

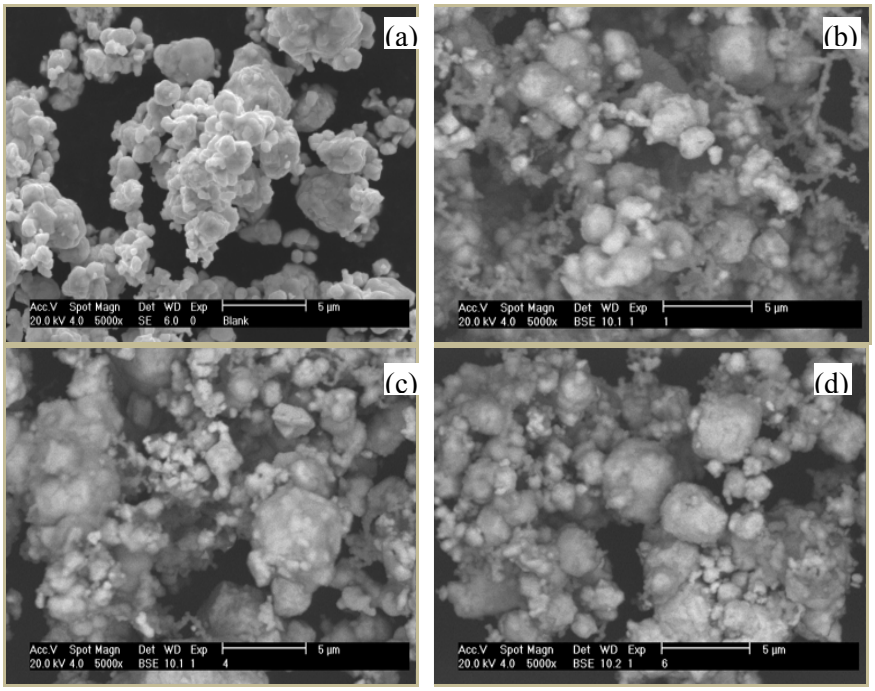

Fig. 5 SEM images of (a) the pure WC powders and Ni-deposited WC powders processed at pH 9 using various concentrations of sodium citrate: (b) 0.12 M (c) 0.16 M and (d) 0.20 M.

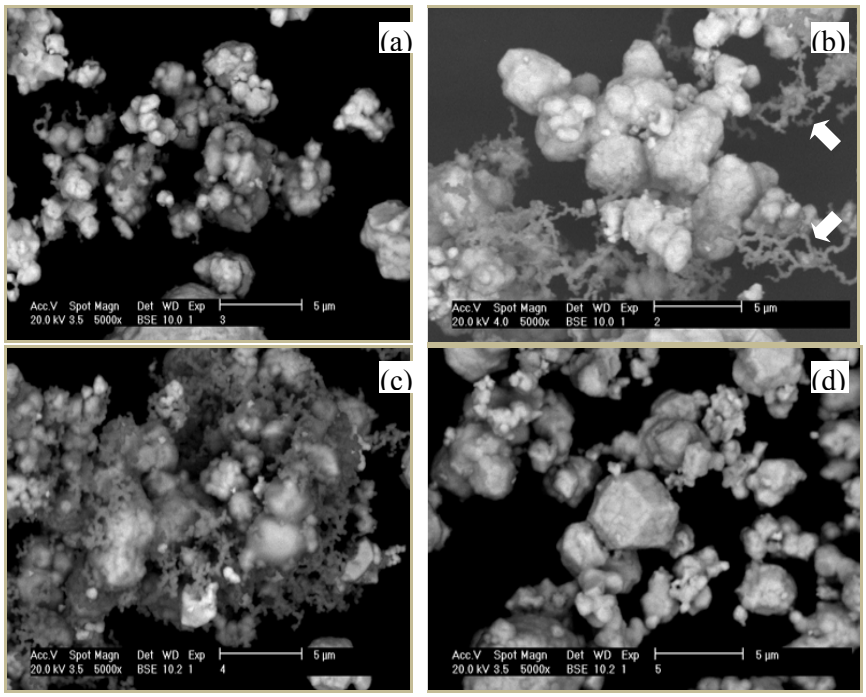

Fig. 6 SEM images of Ni–deposited WC powders at various bath pH: (a) 8 (b) 10 (c) 11 and (d) 12.

Conclusion

Ni-deposited WC particles were prepared by electroless deposition using alkaline citrate bath. The concentration of the complexing agent and the alkalinity of the electroless plating bath show influences on the deposition rate and the chemical composition of the deposits. By decreasing the concentration of the complexing agent or increasing the bath pH, the deposition rate is increased. An increase in particle size caused by Ni-P deposits as the cluster of nodules and agglomeration of the WC powders after deposition was observed. While a rapid deposition rate is associated with preferentially deposition of Ni on pre-deposited Ni sites, a low to moderately high deposition rate results in more uniform incorporation of Ni-P alloys in WC powder mixture.

Acknowledgements

This work is funded by the National Metal and Materials Technology Center (MT-B-53-MET-09-228G). The support from Chulalongkorn University granted to the Metallic Surface Coating Technology for Corrosion Protection (MCTC) research group under Special Task Force for Activating Research (STAR) (G100STAR 55-006-62-001) is also gratefully acknowledged.

References

[1] S.F. Moustafa, Z. Abdel-Hamid, O.G. Baheig, A. Hussien, Synthesis of WC hard materials using coated powders, Adv. Powder Technol. 22 (2011) 596-601.

[2] A. Kilicarslan, F. Toptan, I. Kerti, Electroless nickel-phosphorus coating on boron carbide particles, Mater. Lett. 76 (2012) 11-14.

[3] O. Younes-Metzler, L. Zhu, E. Gileadi, The anomalous codeposition of tungsten in the presence of nickel, Electrochim. Acta 48 (2003) 2551-2562.

[4] G.O. Mallory. The fundamental aspects of electroless nickel plating, In: G.O. Mallory and J.B. Hajdu (Eds.), Electroless plating: Fundamentals & applications, American Electroplaters and Surface Finishers Society, Orlando, FL. 1990.

[5] X.C. Wang, W.B. Cai, W.J. Wang, H.T. Liu, Z.Z. Yu, Effects of ligands on electroless Ni-P alloy plating from alkaline citrate-ammonium solution, Surf. Coat. Tech. 168 (2003) 300-306.

[6] J.R Henry, Electroless (autocatalytic) plating. Met. Finish. 98(1) (2000) 424-435.

[7] A.S. Hamdy, M.A. Shoeib, H. Hady, O.F. Abdel Salam, Electroless deposition of ternary Ni-P alloy coatings containing tungsten or nano-scattered alumina composite on steel, J. Appl. Electrochem. 38 (2008) 385-394.

Advanced Materials Research Vol. 970 (2014) pp 244-247

doi:10.4028/www.scientific.net/AMR.970.244

Formation of Expanded Austenite using Hybrid Low Temperature Thermochemical Heat Treatment on 2205 Duplex Stainless Steel

M.S. Adenan[1, a*], M.N. Berhan[1, b] and E. Haruman[2, c]

[1] Centre for Advanced Materials Research (CAMAR), Faculty of Mechanical Engineering, Universiti Teknologi MARA, Shah Alam, Malaysia

[2]Faculty of Industrial Engineering, Universitas Bakrie, Jakarta, Indonesia

[a*]mshahriman.adenan@gmail.com, [b]berhan@salam.uitm.edu.my, [c]esaharuman@gmail.com

Keywords: Duplex stainless steel; Hybrid heat treatment; Low temperature; Expanded austenite.

Abstract. Surface modification on 2205 duplex stainless steel (DSS) was performed by low temperature thermochemical hybrid (nitrocarburizing) heat treatment at temperature of 450° C and at holding time of 30 hours. During the process, carbon and nitrogen elements were simultaneously introduced onto the surface of DSS with composition of 5%CH_4 + 25% NH_3 + 70% N_2. Microstructural observations reveal the formation of thick diffusional hybrid layer on the surface of 2205 DSS with very high hardness at cross sectional area. Both carbon and nitrogen diffusions formed expanded austenite ($\gamma_{N/C}$) and expanded ferrite (α_C), however precipitation of nitride (Cr_2N) which also occurred at the layer may deteriorate the corrosion resistance of 2205 DSS. Further investigation is required based on the parameters used in the process to produced precipitation free hybrid layer.

Introduction

Duplex stainless steel (DSS) has a good combination of mechanical properties and corrosion resistance due to the mixture of equal amount of austenite and ferrite in it structure. Therefore DSS is widely used in various petrochemical, refinery, oil and gas industries. DSS however requires improvement in the area of wear resistance and surface hardness so that it can be used extensively in severe environments and improve its lifecycle [1, 3]. In this study SAF 2205 duplex stainless steel (2205 DSS) was chosen since it represents 70% of the application DSS worldwide [2].

Numbers of approached have been made to improve the wear resistance and surface hardness of DSS. Typically the method used is based on the surface engineering techniques by using various platform of plasma, liquid and gas. Surface improvement of DSS depends on the formation of expanded austenite phase and capability of the process to sustain the corrosion resistance by preventing precipitation of chromium to happen.

In this study a conventional thermochemical heat treatment was used to improve the surface of 2205 DSS. The process was performed by simultaneous introduction of nitrogen and carbon elements onto the surface of 2205 DSS which it is almost similar with nitrocarburizing technique. However, since the thermochemical process was performed at low temperature of 450° C, the process is considered as hybrid treatment process [4]. Investigation on low temperature hybrid heat treatment process was studied since very minimal information has been reported regarding this process for DSS.

This work investigates the effect of temperature and holding time using the hybrid process by assessing the microstructure, phases and hardness profile on surface modification of treated 2205 DSS. Consequently, the surface composition and structure should change to expanded structure and forming uniform layer with improvement on the surface hardness.

Experimental Method

The specimen used in this study was duplex stainless steel type 2205 (2205 DSS) that has been prepared into disc form of 25 mm diameter with 6 mm of thickness with chemical composition as in Table 1. The specimen was ground and polished up to 1 μm using sand papers and Al_2O_3 pastes producing mirror finish on the surface. The specimen also cleaned using ultrasonic bath with acetone and distilled water to removed dirt and grease on the surface. Prior to the hybrid treatment process, the specimen was soaked into concentrated HCl (2M) solution for 15 minutes to remove the native oxide layer on the surface of 2205 DSS. The hybrid treatment process was performed using horizontal tube furnace at temperature of 450° C with holding time of 30 hours. The gasses used in the process are methane (CH_4), ammonia (NH_3) and nitrogen (N_2) with composition of 5% CH_4 + 25% NH_3 + 70% N_2. After the hybrid process completed, the specimen were cooled down to room temperature.

Table 1. Chemical composition of 2205 DSS specimen (wt %).

Element	C	Si	Mn	Ni	Cr	Mo	Cu	N	S	Fe
Weight (%)	0.03	0.75	2.00	6.50	23.00	3.50	0.75	0.18	0.01	Balance

The phase structure of treated specimen was analyzed using Rigaku Ultima IV X-ray diffractometer. The radiation source used was CuKα (λ = 1.54 Å) at measurement angles between 30° to 100°. Cross sectional observation was done using optical microscope (OM) and scanning electron microscope (SEM). Prior to the observations, the sample was cut and mounted using bakelite. The cross section of the specimen was ground and polished as in the preparation before performing the hybrid treatment process. Kalling's no. 2 reagent was used as the etchant to reveal the microstructure at the cross section of treated 2205 DSS. Hardness profile at the cross section of specimen was performed by Mitutoyo Vickers microhardness tester with 10 g load for 10 seconds.

Results and Discussions

Phase Analysis. Fig. 1(a). Shows the comparison of x-ray diffraction patterns between untreated specimens of 2205 DSS with low temperature hybrid thermochemical treated of 2205 DSS. The untreated specimen indicates the austenite and ferrite peaks of the two phase microstructures. The layer produced during hybrid heat treatment process has shown the formation of expanded austenite and expanded ferrite. Diffraction pattern for hybrid treated specimen point out the peaks for austenite and ferrite have shifted at lower angle 2θ. Fig. 1(b). clearly indicates the sifted phases where the peaks become visible at 2θ = 44.5°, 2θ = 47.5° and 2θ = 71°, indicating the formation of expanded austenite [1,4] and 2θ = 42° and 2θ = 64.5° correspond to the formation of expanded ferrite [4,5]. The expanded austenite peaks at 2θ =44.5° and 2θ = 71° were indexed as γ_N (111) and $\gamma_{N/}$ (220) equivalent to lattice parameters of 1.0985 nm and 0.8143 nm while 2θ =47.5° as γ_C (200) with lattice parameter of 1.0443 nm, indicating the lattice expansion up to 3%. The expanded ferrite were indexed as α_C (110) and α_C (200) at 2θ = 42.5° and 2θ = 64.5°. The lattice expansion of both expanded ferrite peaks is about 2% with maximum lattice parameter of 1.1397 nm. The pattern however show the unavailability of nitrogen expanded ferrite showing no diffusion of nitrogen into ferrite phase during hybrid process treatment. Respectively, these results confirm the formation of expanded austenite and expanded ferrite in the hybrid layer from the hybrid heat treatment process. Diffraction pattern at fig. 1(b) also shows the formation of Cr_2N in the hybrid layer. The formation of nitride at the layer happens because of precipitation of chromium with nitrogen in the austenite and ferrite grains. This is due to limit solubility of nitrogen already reached at 2205 DSS [4]. The formation indicates that hybrid heat treatment at of 450° C, treated at prolong 30 hours creates precipitation of chromium that may deteriorate the corrosion resistance of 2205 DSS [1,3-5].

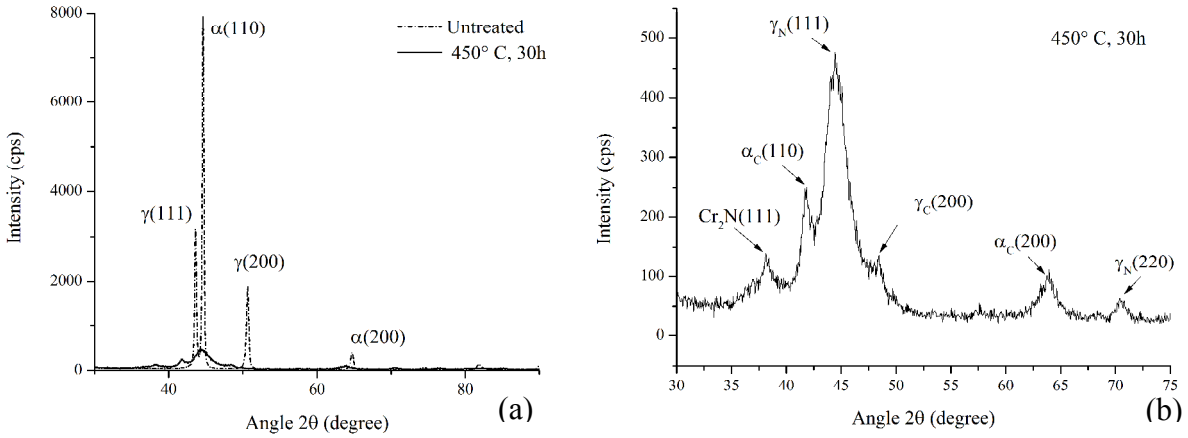

Figure 1(a). XRD patterns of untreated and treated specimens at 450° C for 30 hours ,1(b) pattern for treated at range from 30º to 75º.

Microstructure. Fig. 2(a) shows the microstructure of cross-sectional of hybrid treated 2205 DSS specimen. It can be seen clearly that a uniform hybrid layer formed at the austenite and ferrite grains of the specimen. The dissolution of elements of carbon and nitrogen which were simultaneously supplied during the heat treatment process expanded both phases forming expanded austenite and expanded ferrite phases and stabilized the grains [4]. Fig. 2(b) indicates that minor cracks occured at the diffused phase, especially at the expanded austenite phase. Occurrence of cracks at the layer happens due to high stress at the lattice as imposed by supersaturation of carbon and/or nitrogen [5]. Fig. 2(b) also shows formation of Cr_2N at some area in the ferrite grains validate the outcome from the phase analysis of diffraction pattern of hybrid treated 2205 DSS. Observation also shows the formation of nitride layer mostly occurred at ferrite grain may be due to higher chromium content at ferrite grain than austenite grain.

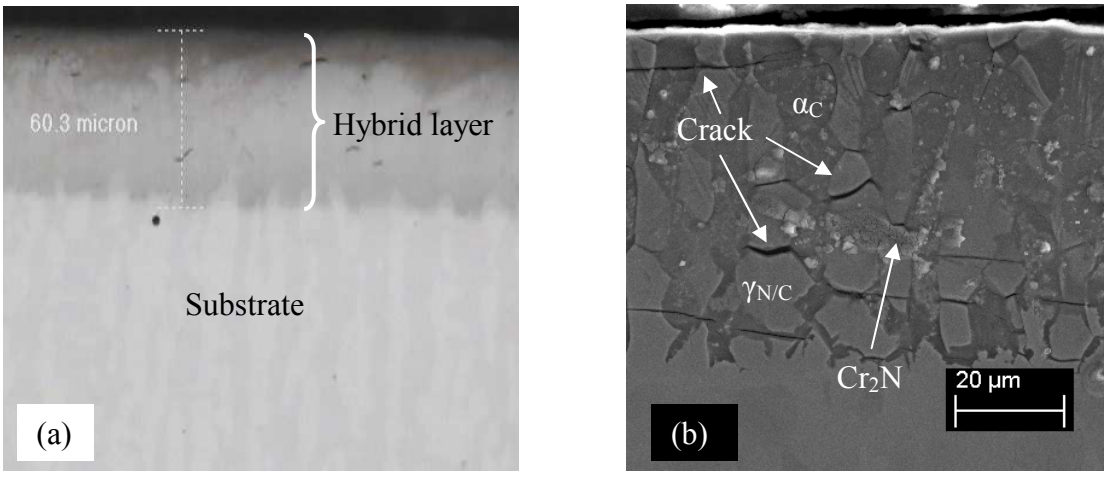

Figure 2(a). Formation of diffuional layer at the cross section of hybrid treated 2205 DSS at 450° C for 30 hours.OM, 2(b). Formation of γ_N, γ_C, α_C and Cr_2N at the layer. SEM.

Depth Hardness Profile. Fig. 3. shows microhardness profile at the cross section of hybrid treated 2205 DSS indicating high hardness value near the top surface around 1200 HV. The hardness however decreases down until about 300 HV starting after 60 µm from the top surface. This has demonstrates the transition between diffusion layer produced and DSS substrate [1,3-5]. The much improved hardness layer produced however being influenced by the formation of Cr_2N beside the

formation of expanded austenite and expanded ferrite structures which can lead the 2205 DSS to lose it capability on corrosion resistance [1,3-5]. Therefore high hardness on the layer is considered unacceptable although it has been achieved. Factors such as gas compositions, lower treatment temperature and shorter holding time need to be consider in producing precipitation-free hybrid heat treated layer.

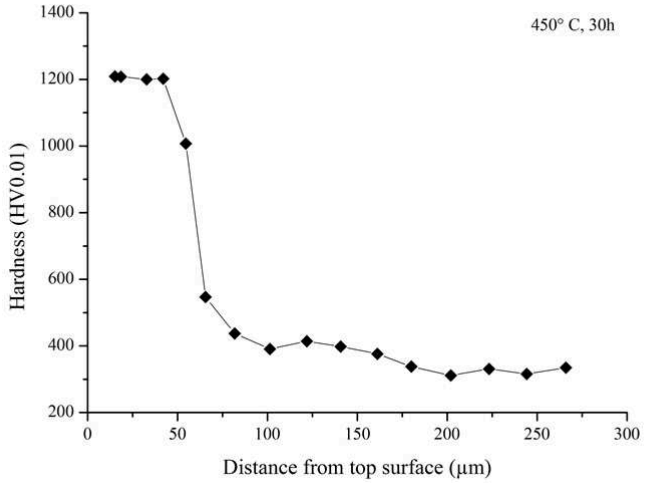

Figure 3. Microhardness depth profiles from top surface towards core of specimen

Conclusions

Low temperature thermochemical hybrid heat treatment process which simultaneous introduction of nitrogen and carbon elements onto the surface of 2205 DSS was performed at temperature 450° C and holding time of 30 hours. The process produces a very high hardness of uniform layer with formation of expanded austenite and expanded ferrite phase. However, drawback from the process indicates precipitation of chromium with nitrogen and carbon that occur respectively at ferrite grain which may effects on retaining the corrosion resistance of treated 2205 DSS. Therefore, further study is required by controlling the parameters used in the process to produce precipitation free hybrid treated layer in 2205 DSS.

References

[1] Thomas C, Marcel A.J.S, Characterisation of low temperature surface hardened stainless steel, Struers Journal of Materialography, 9/2006

[2] http:// www.outukompu.com/stainless/na accessed on July 10, 2013

[3] Kliauga, A. M. and M. Pohl (1998). "Effect of plasma nitriding on wear and pitting corrosion resistance of X2 CrNiMoN 22 5 3 duplex stainless steel." Surface and Coatings Technology 98(1-3): 1205-1210

[4] Y. Sun, Hybrid plasma surface alloying of austenitic stainless steels with nitrogen and carbon, Materials Science and Engineering A 404 (2005) 124–129

[5] C.M. Garzon, A.P. Tschiptschin, New high temperature gas nitriding cycle that enhances the wear resistance of duplex stainless steels, Journal of Materials Science 39 (2004) 7101-7105

Advanced Materials Research Vol. 970 (2014) pp 248-251

doi:10.4028/www.scientific.net/AMR.970.248

High temperature oxidation effect on the dissolution rate of hot-dip aluminized steel in aluminum melt

Ayeh Mohsenifar[1,a], M.Reza Aboutalebi[1,b*], and S.H. Seyedein[1,c]

[1]Centre of Excellence for High Strength Metals Processing and Technology
School of Metallurgy and Materials Engineering, Iran University of Science and Technology
Narmak, Tehran, Iran

[a]ayehmf@yahoo.co.uk, [b*]mrezab@iust.ac.ir, [c]seyedin@iusct.ac.ir

Key words: low carbon steel, hot-dip aluminizing, high temperature oxidation, corrosion protection, dissolution

Abstract. Hot dip aluminizing of low carbon steel followed by high temperature oxidation in air was carried out to evaluate the dissolution rate of coated sample in molten aluminum. The microstructure of oxide and aluminide layers was investigated using scanning electron microscopy and X-ray diffraction methods. The characterization of the coating showed that Fe_2Al_5 has been the major phase formed on the surface of specimen before high temperature oxidation. Isothermal oxidation of the coating as resulted in the formation of Al_2O_3 while Fe_2Al_5 phase transformed into FeAl and Fe_3Al phases. The coated samples were further subjected to corrosion in molten aluminum. It was proved that the oxide layer formed on the coating and developed FeAl and Fe_3Al intermetallic phases play the major role in protecting the specimen from corrosion in molten aluminum.

Introduction

Aluminizing is a viable method for improvement of high temperature corrosion resistance of steels [1-3]. During the aluminizing process Fe_2Al_5 is the major compound to be formed [4-7]. It is believed that Fe_2Al_5 phase contains 30% vacancies through which the rate of diffusion of atoms enhances significantly [4, 8]. Thus, Fe_2Al_5 phase grows fast by increasing the temperature due to high vacancies [6,9]. Aluminized steel is protected against corrosion by formation of dense Al_2O_3 layer during oxidation at high temperatures [4,10]. In addition Fe_2Al_5 is converted to the phases with lower aluminum content like FeAl and Fe_3Al which improve the corrosion resistance of the coating [4,11]. Numerous studies focused on the formation mechanism of intermetallic layer during the coating process [4-7, 11, 12]. Despite the numerous studies focused on the corrosion of aluminized steel in different NaCl environments [2,3], few work has been done on the hot corrosion of coating in molten aluminum. Thus the present work was undertaken to investigate the corrosion behavior of hot-dip aluminized mild steel followed by high temperature oxidation in aluminum melt.

Materials and Experimentals

Preparation of samples. Low carbon steel rods with 8mm diameter and 30 cm length were prepared and used as substrate for hot-dip aluminizing. The chemical composition of the mild steel is given in Table 1. High pure aluminum (>99.9%) was used for preparation of the molten bath.

Table1. Chemical compositions of the steel substrate

Elements	C	Si	Mn	P	S	Fe
Composition (wt. %)	0.12	0.17	0.68	0.112	0.033	Balance

Pre-treatment of samples. Prior to dipping the steel samples in molten aluminum, they were prepared by emery paper and they were degreased in a 3wt% Na_2CO_3 solution for 5 minutes and rinsed with distilled water. Then they were descaled by immersing in a 10wt% HCl solution for 5 minutes followed by rinsing in distilled water. Finally the samples were dipped in NaF- KCl- NaCl flux for 15 minutes.

Aluminizing and high temperature oxidation. The prepared samples were aluminized at 750°C for 4 minutes and then were taken out from the melt and cooled in air to room temperature. Finally the samples were placed in a furnace under air atmosphere at 1000°C for 20 minutes. Then samples were cooled in temperature of environment.

Corrosion test in aluminum melt. The corrosion behaviour of the heat treated samples was evaluated at 800 and 900°C temperatures for different times by immersing the samples in molten aluminum. 100 gram aluminum was used for every corrosion test.

Analysis of samples. The metallographically prepared samples were etched in 2% Nital solution. Microstructure analysis was carried out by scanning electron microscopy (SEM). X-ray diffractometery (XRD) analysis was used to determine phase structures. Corrosion of the samples in aluminum melt was evaluated by the amount of iron dissolved in the melt. The iron content of the melt was measured using atomic absorption spectroscopy.

Results and Discussion

Microstructure investigations. After aluminizing, microstructure of the coating was examined by SEM. The microstructure of the coating layer is given in Fig.1. The intermetallic layer is grown towards the substrate and therefore an un-evenly interface is formed between these [4-6,13,14]. X-ray diffraction and EDS analysis show that the dominant phase in intermetallic layer is Fe_2Al_5.

Heat treatment. Fig.2 illustrates SEM image of specimen which aluminized and then heat treated in air atmosphere at 1000°C for 20 minutes. It can be seen the new phase by the side of substrate has no cracks. EDS analyses of marked points in this figure is given in Table 2. The aluminum consumption mainly occurs in two ways. One is the outward diffusion of aluminum to form Al_2O_3 scale, and the other one is aluminum inward diffusion toward the steel substrate [5]. Oxygen diffuses into Fe_2Al_5 phase because of large lattice interstice. It is realized from EDS results that aluminum oxidation occurs and aluminum content becomes less appreciated by other researchers [4,11].

Fig.3 shows XRD analysis for specimen aluminized at 750°C for 4 minutes and heat treated in air atmosphere at 1000°C for 20 minutes. It can be found that Fe-Al intermetallic layer formed is transformed from layer with a higher iron composition into layers with a lower iron composition. In other words $FeAl_3$ and Fe_2Al_5 with a serrated interface with the substrate converted to FeAl and Fe_3Al with a continuous interface [15]. It can be distinguished by XRD analysis of the surface that Al_2O_3 is formed on the surface of coating.

Corrosion in molten aluminum. The aluminized and oxidized samples were stirred in molten aluminum at 800 and 900°C for different time. The dissolved iron content in molten bath at various times is shown in Fig. 4. Corrosion resistance was improved in coated sample as shown in this figure. Uncoated sample was fallen apart in molten aluminum after 1 hour at 900°C. It can be seen after oxidation for 20 minutes intermetallic layers miss their finger-like shape. So stress concentration could be removed. FeAl and Fe_3Al are phases with higher corrosion resistance comparing to Fe_2Al_5 [1, 15, 16].The aluminum oxide formed on the coated sample acts as a barrier for contact between steel and molten aluminum.

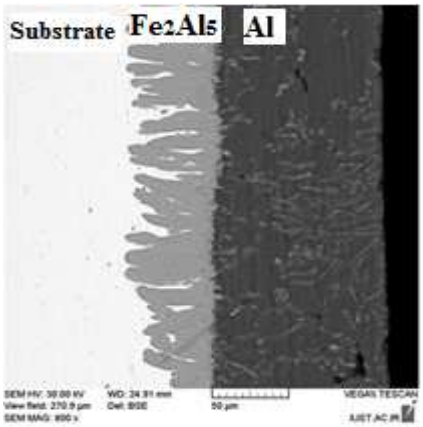

Figure 1. SEM micrograph of aluminized specimen at 750°C for 4 minutes.

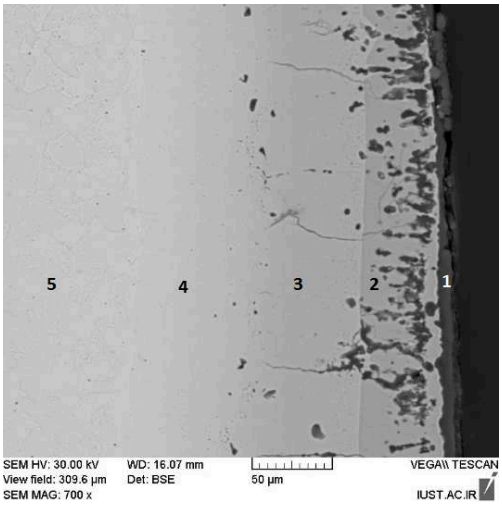

Table 2. EDS analysis of the marked points in Fig.2

Elements (wt. %) / Marked Points in Fig.2	O	Al	Fe	Au (coated for SEM)
1	60.4	33.3	5.1	Bal.
2	9.2	46.5	43.1	Bal.
3	0	33.6	65.2	Bal.
4	0	12.5	85.7	Bal.
5	0	0	97.83	Bal.

Figure 2. Back scatter electron image of aluminized mild steel for 4 minutes at 750°C and oxidized for 20 minutes at 1000°C.

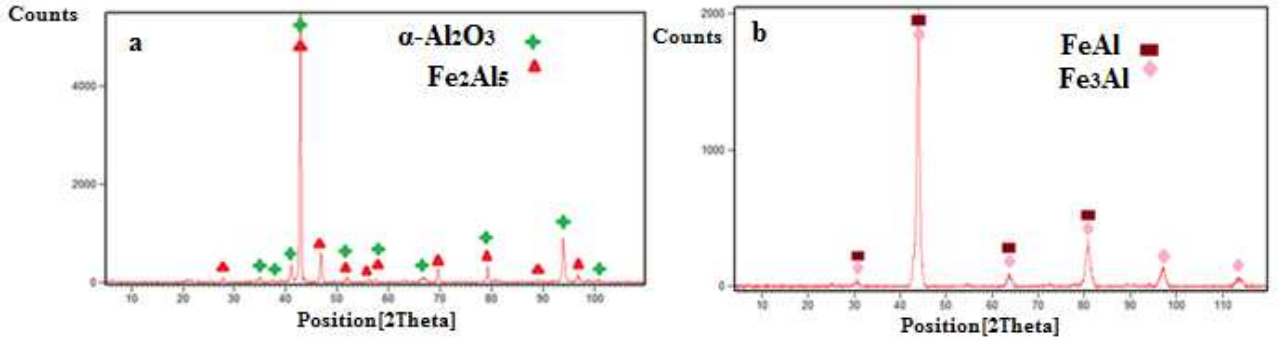

Figure 3. XRD pattern of specimen aluminized at 750°C for 4 minutes and heat treated at 1000°C for 20 minutes. Sample surface, b) surface of the sample after removal a 100µm layer from the surface by machining.

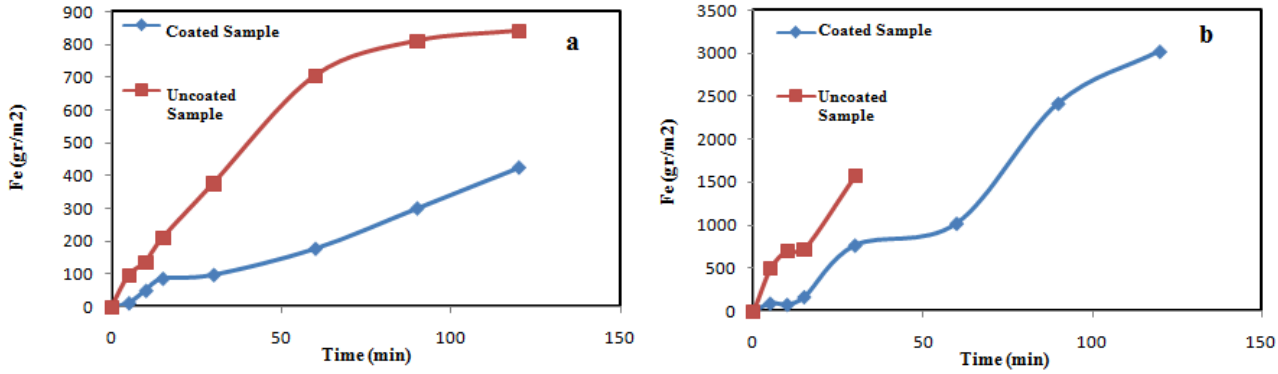

Figure 4. Corrosion rate curves of coated and uncoated samples in aluminum melt at different temperatures; a) 800°C and b) 900°C.

Conclusions

Based on the results obtained in this work, the following conclusions can be drawn:

1) After aluminizing an intermetallic layer with an un-evenly interface is formed at the interface of steel substrate and aluminum layer. XRD and EDS analysis proved that this phase was Fe_2Al_5.
2) The oxidation treatment of aluminized steel sample at high temperature in air resulted in the formation of α- Al_2O_3 thin layer on the surface of the sample.
3) The oxidation of aluminized sample at high temperature makes Fe_2Al_5 phase be converted into intermetallic phases with less aluminum content including FeAl and Fe_3Al.

4) Aluminizing and consequent oxidation treatment improves the corrosion resistance of mild steel in molten aluminum at 800°C very significantly.
5) Aluminizing and subsequent oxidation prevent the coating from falling apart in molten aluminum at 900°C.

Acknowledgments

The authors would like to express their gratitude to Mr.H.Mehrjou and Mrs.Rahimi for their assistances in carrying out the experiments.

References

[1] C.J. Wang, J.W. Lee, T.H. Twu, Corrosion Behavior of Low Carbon Steel, SUS310 and Fe-Mn-Al Alloy with Hot-Dipped Aluminum Coatings in NaCl-induced Hot Corrosion, J. Surface and Coatings Technology. 163 (2003) 37-43.
[2] C.C. Tsaur, J.C. Rock, Y.Y. Chang, The Effect of NaCl Deposit and Thermal Cycle on an Aluminide Layer Coated on 310 Stainless Steel, J. Materials Chemistry and Physics. 91 (2005) 330-337.
[3] H.H. Liu, W.J. Cheng, C.J. Wang, The Mechanism of Oxide Whisker Growth and Hot Corrosion of Hot-Dipped Al–Si Coated 430 Stainless Steels in Air–$NaCl_{(g)}$ Atmosphere, J. Applied Surface Science. 257 (2011) 10645– 10652.
[4] W. Deqing, Phase Evolution of Aluminized Steel by Oxidation Treatment, J. Applied Surface Science. 254 (2008) 3026-3032.
[5] C.J. Wang, S.M. Chen, The High Temperature Oxidation Behavior of Hot-Dipping Al-Si Coating on Low Carbon Steel, J. Surface and Coatings Technology. 200 (2006) 6601-6605.
[6] W.J. Cheng, C.J Wang, Growth of Intermetallic Layer in the Aluminide Mild Steel during Hot-Dipping, J. Surface and Coatings Technology. 204 (2009) 824-828.
[7] G. Palombarini, A. Casagrande, M. Carbucicchio, R. Ciprian, Protection Against Corrosion of Iron Alloys by Aluminized Coatings Produced Using Two Different Processes, J. Hyperfine Interact. 187 (2008) 125-130.
[8] W.J. Cheng, C.J. Wang, Effect of Silicon on the Formation of Intermetallic Phases in Aluminide Coating on Mild Steel, J. Intermetallics (2011) 1-6.
[9] W. Deqing, S. Ziyuan, Z. Longjiang, A Liquid Aluminum Corrosion Resistance Surface on Steel Substrate, J. Applied Surface Science. 214 (2003) 304-311.
[10] W.J. Cheng, C.J. Wang, EBSD Study of Crystallographic Identification of Fe-Al-Si Intermetallic Phases in Al-Si Coating on Cr-Mo Steel, J. Applied Surface Science. 257 (2011) 4637-4642.
[11] W.J. Cheng, C.J Wang, Microstructural evolution of intermetallic layer in hot-dipped aluminide mild steel with silicon addition, J. Surface and Coatings Technology. 205 (2011) 4726-4731.
[12] H.R. Shahverdi, M.R. Ghomashchi, S. Shabestari, J. Hejazi, Microstructural Analysis of Interfacial Reaction Between Molten Aluminum and Solid Iron, J. Materials Processing Technology. 124 (2002) 345-352.
[13] W.J. Cheng, C.J. Wang, Study of Microstructure and Phase Evolution of Hot-Dipped Aluminide Mild Steel during High-Temperature Diffusion Using Electron Backscatter Diffraction, J. Applied Surface Science. 257 (2011) 4663-4668.
[14] G.H. Awan, F.U. Hasan, The Morphology of Coating/Substrate Interface in Hot-Dip-Aluminized Steels, J. Materials Science and Engineering. A 472 (2008) 157-165.
[15] B. Abdolahi, H.R. Shahverdi, M.J. Torkamany, M. Emami, Improvement of the Corrosion Behavior of Low Carbon Steel by Laser Surface Alloying, J. Applied Surface Science. 257 (2011) 9921-9924.
[16] P.F. Tortorelli, J.H. DeVan, Behavior of iron aluminides in oxidizing and oxidizing/sulfidizing environments, J. Materials Science and Engineering. A 153 (1992) 573-577.

Advanced Materials Research Vol. 970 (2014) pp 252-255

doi:10.4028/www.scientific.net/AMR.970.252

Investigation the structural and magnetic properties of FINEMET type alloy produced by mechanical alloying

T. Gheiratmand[1*], S. Mohammadi Siyani[1], H. R. Madaah Hosseini[1] and P. Davami[1]

[1]Department of Materials Science and Engineering, Sharif University of Technology, Azadi Ave., Tehran, Iran, P.O. Box 11155-9466

*T.gheiratmand@yahoo.com

Key words: FINEMET, Mechanical alloying, TEM, XRD

Abstract. In this research, FINEMET alloy with composition of $Fe_{73.5}Si_{13.5}B_9Nb_3Cu_1$ was produced by mechanical alloying from elemental powders. The effect of milling time on the magnetic and structural properties of alloy has been investigated using X-ray diffraction, scanning electron microscopy, transmission electron microscopy and vibrating sample magnetometery. The results showed that milling for 53 hr leads to the formation of Fe supersaturated solid solution which includes Si, B and Nb atoms with mean crystallite size of ~30 nm. The shift of the main peak of Fe to the higher angles indicated that Si and B atoms dissolve in the Fe solid solution, at primary stage of mechanical alloying, up to the 42 hr while Nb atoms dissolve at final stages. The magnetization of milled powder for 53 hr was 173.7 emu/g, almost the same as that of the melt-spun ribbon. In addition; the coercivity reached to 15.5 Oe after 53 hr of milling. The higher value of coercivity in mechanically alloyed samples is attributed to strains induce to the structure during milling and the lack of amorphous phase and exchange interaction between nano grains.

Introduction

Finemet soft magnetic alloys with composition of $Fe_{73.5}Si_{13.5}B_9Nb_3Cu_1$ have unique combination of high saturation magnetization, high permeability and very low coercivity [1, 2]. Theses good soft magnetic properties originate from formation of the Fe(Si) nanocrystalline phase in an amorphous matrix. Actually, when the grain size is much smaller than the exchange interaction length, the effective anisotropy will be three orders of magnitude smaller than when the reverse condition is provided [1].

The main technique for producing Finemet alloys is melt spinning followed by vacuum annealing to produce nanocrystalline structure with an amorphous intergranular phase. High energy ball milling is another technique for producing nanostructured powders with grain size smaller than 10 nm. Obviously, during this solid state process repeated cold welding and fracturing of particles occur causing the particles to be mechanically alloyed. This method allows production of homogeneous materials from elemental powders and achievement of different microstructures in term of nanocrystalline grain size [3-5]. So far, there haven't been many reports in the literatures focusing on magnetic properties changes during mechanical alloying of Finemet alloy from elemental powders. Other studies have focused on mechanically milling of melt-spun ribbons to produce Finemet powder which is suitable for consolidation. The scope of the present paper was production of Finemet powder alloy by mechanical alloying and investigation the magnetic properties variations during milling.

Experimental procedure

The FINEMET alloy with nominal composition of $Fe_{73.5}Si_{13.5}B_9Nb_3Cu_1$ was produced from pure elemental powders. Mechanical alloying was performed using a Fritch 5 planetary mill for 51 h. The ball to powder weight ratio was fixed to be 10:1. The milling process was performed at speed of 750 rpm. To avoid excessive heating, each 60 minutes of milling was followed by 30 minutes pause. Milled powders were investigated by Philips X'PERT diffractometer using Cu-Kα radiation.

The mean size of crystallites was estimated from broadening of the X-ray diffraction lines using Williamson-Hall Method. The step size was selected as 0.03 degrees. The morphology and microstructure of powders were characterized using both scanning electron microscope SEM (VEGA- TESCAN) and Transmission electron microscope TEM ((Tecnai G2 20) operating at 200 kV. Magnetic properties of supersaturated solid solutions and annealed samples were measured using a Vibrating Sample Magnetometer (VSM) at external magnetic field of 10 kOe.

Results and discussion

The XRD patterns of milled powders for different times are shown in Fig. 1. As could be deduced from this figure, with increasing milling time the intensity of Fe solid solution peaks decreases. At primary stages of milling the Si and B atoms with smaller atomic radius and faster diffusing rate dissolve in Fe while the Nb atoms dissolve at final stages causing the shift of main peak of Fe solid solution to lower angles. At the beginning of mechanical alloying process, the peaks of Fe and Si atoms could be observed and those of the other elements could not be distinguished due to the low sensitivity of XRD method. Dissolving of B toms with negative and large enthalpy of mixing (-45 kJ/mol) in Fe unit cell causes the d (110) of Fe solid solution becomes smaller thus according to the Bragg theory, the shift of main peak of Fe to higher angles is predictable [6]. It seems that dissolving of Si atoms occurs mostly after 20 hr of milling up to 42 hr. The interesting point was that after 53 hr of milling the main peak of Fe solid solution shifted from 44.68 º to 44.64 º (Fig. 2). This phenomenon could be related to dissolution of large Nb atoms in Fe solid solution thus d (110) of Fe becomes greater. These results are in line with the other reports. Manivel et al. [4] exhibited that after 60 hr of milling the Fe(Si) phase develops in the structure while Aleg et al. [7] demonstrated the formation of both Fe(Si,B) and Fe_2B phases after 150 hr of milling. The average crystallite size of the Fe(Si,B) phase has been calculated using Williamson-hall method as 30 nm which is in agreement with TEM image (Fig. 3).

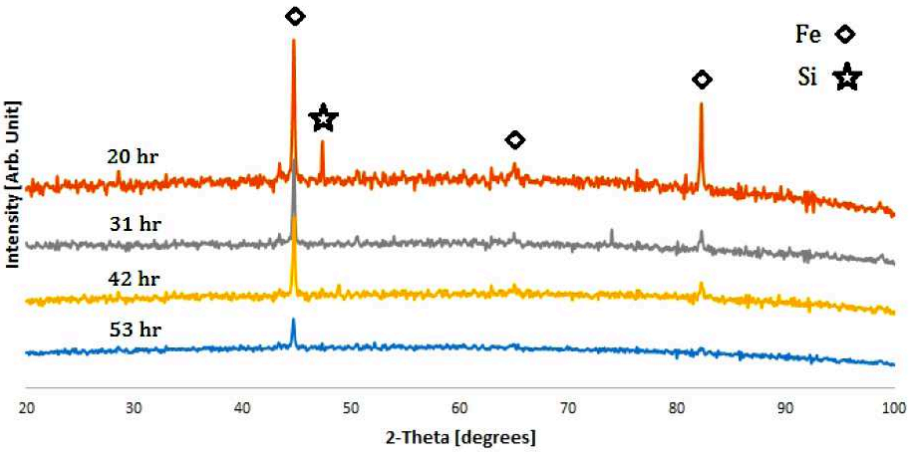

Figure. 1. XRD patterns of different milled samples.

The SEM micrograph of different milled samples is shown in Fig. 4. It could be observed that the morphology and particle size changes are not significant after 20 hr of milling verifying that the equilibrium condition between cold welding and fracturing of particles has been achieved before 20 hr of milling.

The average particle size in different samples is ~20 μm. Aleg et al. [6] have obtained the particle size in the range of 6-10 μm in powders with similar conditions.

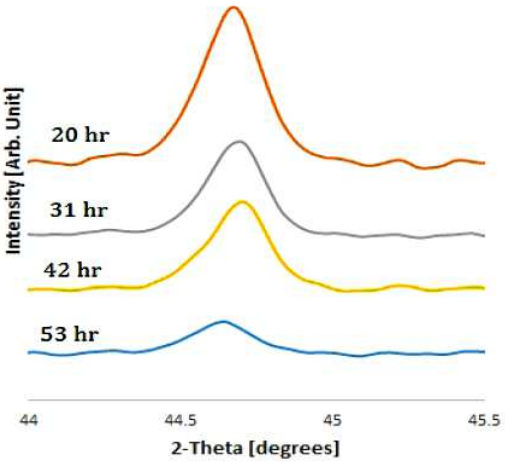

Figure. 2. The shift of main peak of Fe in different powders.

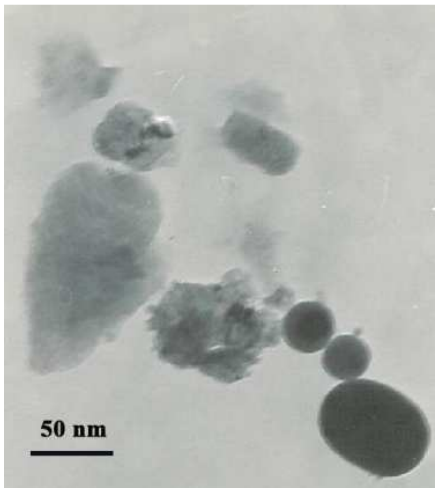

Figure. 3. TEM image of milled powder for 53 hr.

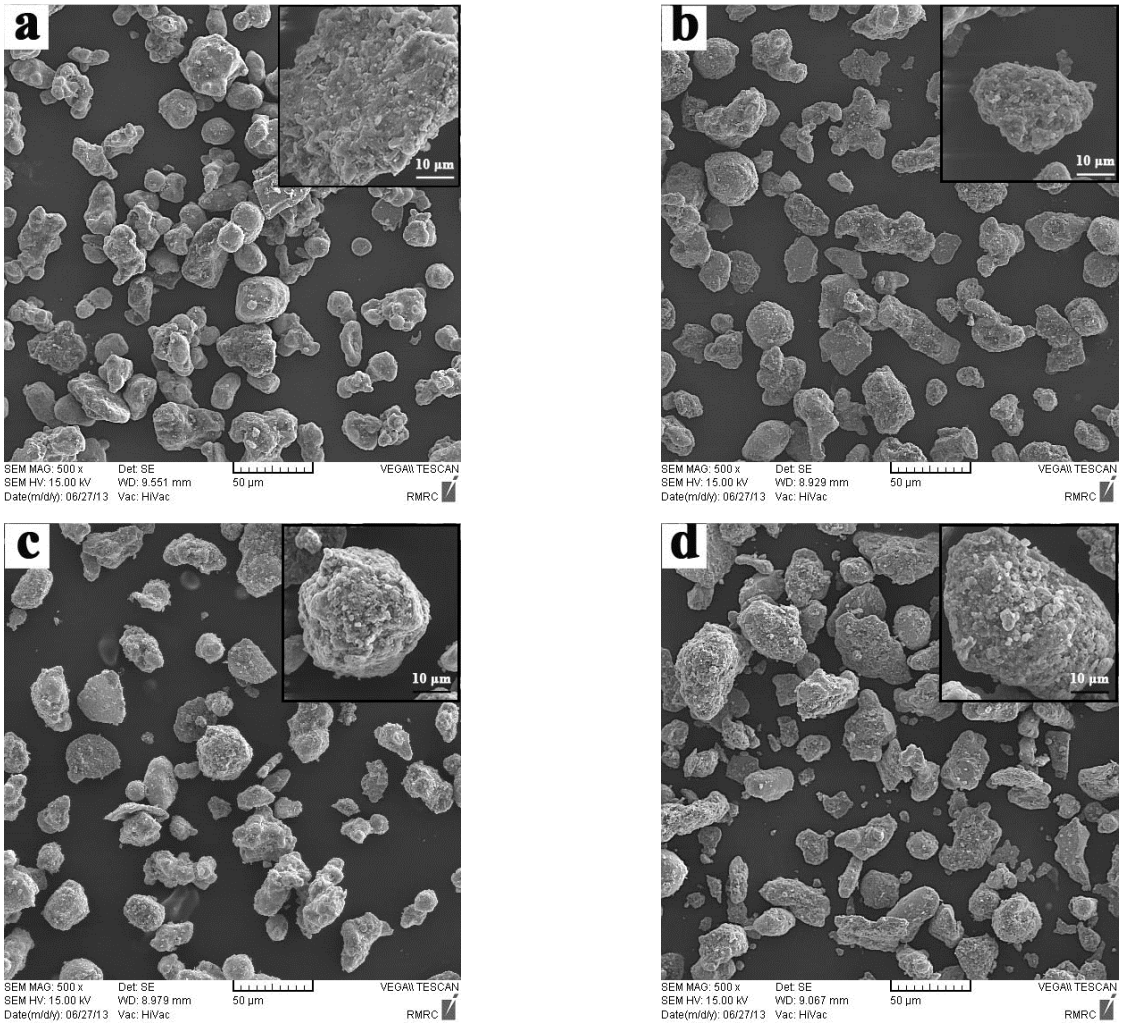

Figure. 4. SEM images of different milled sample, a) 20 hr, b) 31 hr, c) 42 hr and d) 53 hr.

The values of saturation magnetization and coercivity have been demonstrated in Table 1. Clearly, by increasing the milling time from 20 to 53 hr the coercivity increases from 12.4 to 15.5 Oe, respectively. The higher value of coercivity in powder samples than melt spun and annealed ribbons is due to higher internal strain and the lack of amorphous phase which cause the total magnetostriction becomes greater and exchange interaction between the Fe(Si) crystalline phase

weakens. The values of magnetization at different milling times are close to those of melt-spun ribbons. Actually, the type of the Fe nearest neighbor atoms determines the magnetization value. Dissolving of these atoms in Fe solid solution depend on the time of milling. In addition; the formation of low amount of boride phases until 31 hr of milling, which could not be distinguished by XRD analysis, may be responsible for magnetization decrease.

Table 1. Saturation magnetization and coercivity of different milled samples

Time of milling	Magnetization (emu/gr)	Coercivity (Oe)
20	172.6	12.4
31	169.4	13.7
53	173.7	15.5

Conclusion

This paper sought to demonstrate the effect of milling time on the microstructure and magnetic properties of FINEMET alloy produced by mechanical alloying of elemental powders. The emphasis was placed on the investigation of the type of dissolved atoms in Fe solid solution during different periods of milling which has not been discussed in previous studies. The results showed that B and Si atoms dissolve in Fe solid solution up to 42 hr of milling. Afterward; the Nb atoms dissolve causing the shift of main peak of Fe to the lower angle. The average crystallite size was measured as 30 nm. The higher value of coercivity in mechanical alloyed powders is due to the internal strains and the lack of amorphous intergranular phase which weakens the exchange interaction between the Fe(Si) nanocrystaline phases as well as the increase of total magnetostriction.

References

[1] Gheiratmand T, Hosseini HRM, Davami P, Ostadhossein F, Song M, Gjoka M. Nanoscale 2013;5:7520.

[2] Gheiratmand T, Madaah Hosseini HR, Davami P, Gjoka M, Loizos G, Aashuri H. Journal of Alloys and Compounds 2014;582:79.

[3] Suryanarayana C. Progress in Materials Science 2001;46:1.

[4] Manivel Raja M, Chattopadhyay K, Majumdar B, Narayanasamy A. Journal of Alloys and Compounds 2000;297:199.

[5] López M, Marín P, Agudo P, Carabias I, de la Venta J, Hernando A. Journal of Alloys and Compounds 2007;434–435:199.

[6] Alleg S, Kartout S, Ibrir M, Azzaza S, Fenineche NE, Suñol JJ. Journal of Physics and Chemistry of Solids 2013;74:550.

[7] Alleg S, Ibrir M, Fenineche NE, Azzaza S, Bensalem R, Suñol JJ. Journal of Alloys and Compounds 2010;494:109.

CHAPTER 12:

Nanotechnology

Advanced Materials Research Vol. 970 (2014) pp 259-262

doi:10.4028/www.scientific.net/AMR.970.259

EFFECT OF SEPIOLITE CONTENT ON MECHANICAL AND FLAMMABILITY PROPERTIES OF ETHYLENE VINYL ACETATE NANOCOMPOSITE

Hossein Cheraghi Bidsorkhi[1a], Zurina Mohamad[1b*]

[1]Department of Polymer Engineering, Faculty of Chemical Engineering, Universiti Teknologi Malaysia, 81310 UTM Johor Bahru, Johor

hossein.oranos@gmail.com[a], zurina@cheme.utm.my[b*]

Keywords: Sepiolite, Ethylene Vinyl Acetate, Mechanical properties, Flame retardant, nanocomposite

Abstract. Ethylene Vinyl Acetate (EVA)/Sepiolite nanocomposites were prepared by melt extrusion using a counter-rotating twin-screw extruder followed by injection molding. Sepiolite was loaded in EVA is varies at 1, 3, 5 and 7 wt%. The mechanical properties of EVA/Sepiolite nanocomposites were studied through tensile test. The flame retardancy of nanocomposites were studied for limiting oxygen index (LOI). LOI tests show that the flame retardancy of nanocomposites were increased with increase ratio of sepiolite in EVA/Sepiolite nanocomposite. The tensile properties of EVA/Sepiolite nanocomposites were also increased with increased Sepiolite content in nanocomposites.

Introduction

In recent years, polymer/clay nanocomposites have drawn considerable interest because of their enhanced properties, including flame resistance, gas barrier properties, mechanical properties, thermal stability, and biodegradability[1] . Polymer/clay nanocomposites have also been used in various consumer products and in construction and transportation industry [2].

The aim of this work is to investigate the mechanical and flame retardancy properties of EVA based nanocomposites as a function of the different amount of Sepiolite content. EVA is particularly flammable, which restrict their practical applications. Clay that is frequently used for improvement of EVA because the EVA contains polar group that can be easily incorporation with it such as organophilic clay (OMMT), ufunctionalized clay (Na-MMT) and sepiolite[3, 4].Sepiolite belongs to the structural family of 2:1 phyllosilicates, which is a hydrous magnesium silicate with$(Si_{12}Mg_8O_{30})(OH)_4(OH_2)_4 \cdot 8H_2O$ as the theoretical unit cell formula which has good flame retardancy and with high aspect ratio which can improve both flame retardancy and mechanical properties of nanocomposites. The mechanical properties and the flammability properties are studied by Tensile test and Limiting oxygen index (LOI) tests respectively[2].

Experimental

The Sepiolite was obtained from Lingshou Jiali Mineral Products Processing Factory China Company with melting point of 1200 °C, the average length of 44μm and also the average diameter in between 100 to 150 nm. EVA used in this work with 18%VA content and MFI = 1.83 g/ 10min was a commercial product from Taneelf Atofina, China company.

EVA pellets and Sepiolite were dried at 60°C and 110°C respectively for 24 hours. The blends were compounded by simultaneous addition of all components to counter-rotating twin-screw extruder. The adopted barrel temperature profile during compounding of all martials were 155°C at the feed section,170°C at compression section and decreasing to 160°C at the die head. The extruded materials were injection moulded using multi specimen mould into standard tensile and LOI specimens.

Tensile test was carried out with an Instron-4301 machine at room temperature, according to ASTM D 638, at a cross head speed of 50 mm/min. Five similar specimens were used in each test. Limiting oxygen index (LOI) tests were conducted according to ASTM D-2863. A specimen was

positioned vertically in a transparent test column and a mixture of oxygen and nitrogen was forced upward through the column.

Results and discussion

Figure 1 shows the effect of Sepiolite content on the tensile strength of EVA/Sepiolite nanocomposite. Generally the tensile strength was increased with the increased of Sepiolite content. The highest tensile strength was recorded at 5% Sepiolite content with 21 % increment compared with pure EVA. This can be attributed to a good dispersion and delaminated of Sepiolite in EVA matrix, high aspect ratio of surface Sepiolite with polymer and a good interface interaction between Sepiolite and EVA. However at higher than 5% of Sepiolite content, the tensile strength decreased which may be resulted from agglomeration and non-delaminate Sepiolite in nanocomposite[2, 5].

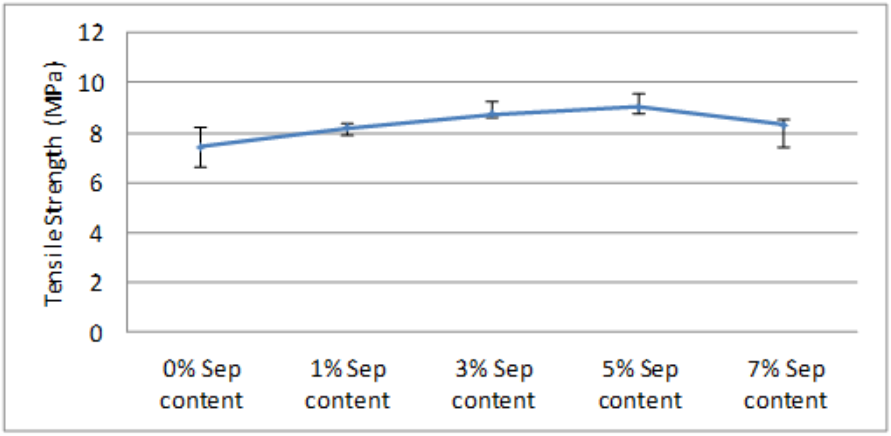

Fig. 1. The effect of Sepiolite content on the tensile strength of EVA/Sepiolite nanocomposite.

Figure 2 exhibited that the Young Modulus was obviously affected by even a small loading of Sepiolite. The Young Modulus of EVA/Sepiolite nanocomposites were significantly increased as 5% of Sepiolite with 47% higher than pure EVA, where based 5% of Sepiolite starts to be constant at higher loading. This was ascribed to a good dispersion and well interfaces interaction between Sepiolite and EVA matrix where the large surface area of Sepiolite made large interfacial area between Sepiolite and EVA [1, 6].

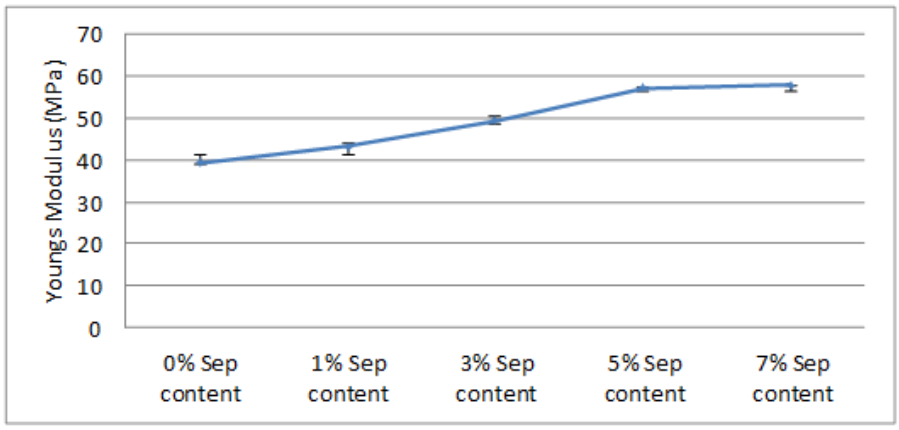

Fig. 2. The effect of Sepiolite content on the Young Modulus of EVA/Sepiolite nanocomposite.

From Figure 3, the LOI value of pure EVA was 18.2%. The LOI value of EVA/Sepiolite nanocomposite increased upon addition of Sepiolite where the highest LOI value was recorded for nanocomposite with 5% Sepiolite content at 24.3%. The increment is believed to be due to well dispersion of nanoclay and good interaction between Sepiolite and EVA matrix[7]. This can be attributed to exfoliate of nanometer sepiolite fibers in the EVA matrix and restriction on the mobility of polymer chains, as well as sepiolite acting as the mass transport barrier material which

restricted the transport of flammable vapor during burning thus increased the flammability index. The distribution and dispersion of Sepiolite in polymer matrix is greatly influence the thermal insulator and mass barrier properties thus decreased the LOI index values. This is the reason why LOI value decreased at 7% Sepiolite content in EVA matrix, since agglomeration of Sepiolite occur at this loading [1, 6].

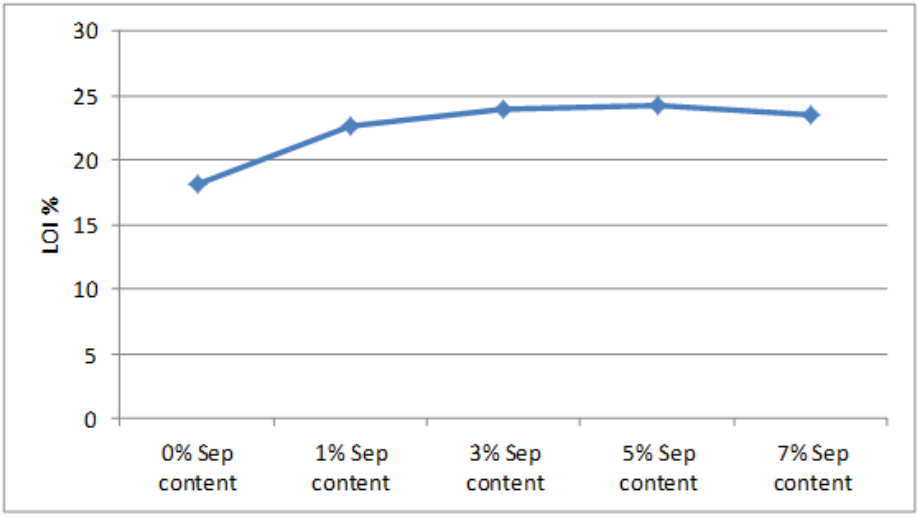

Fig. 3. The Limiting oxygen index (LOI) value of EVA/Sepiolite nanocomposites at different Sepiolite loading.

Acknowledgment
The financial support for the work of the authors by the Ministry of Higher Education (MOHE), Malaysia and the Universiti Teknologi Malaysia with a grant no 08J54 is gratefully acknowledged.

Conclusion
The Sepiolite was able to strengthen the EVA. Sepiolite was dispersed homogeneously and delaminated in EVA matrix. The mechanical properties was strongly increased by increasing Sepiolite content, and also the LOI index increased greatly with loading Sepiolite in polymer matrix . The optimal tensile properties and flame retardancy properties of the EVA/Sepiolite nanocomposites were obtained with 5% Sepiolite content in the EVA/Sepiolite nanocomposites where had good dispersion and delamination at nanocomposites.

References

[1] Chen, H., et al., Characterization and properties of sepiolite/polyurethane nanocomposites. Materials Science and Engineering: A, 2007. 445: p. 725-730.

[2] Huang, N., et al., Synergistic flame retardant effects between sepiolite and magnesium hydroxide in ethylene-vinyl acetate (EVA) matrix. Express Polymer Letters, 2010. 4: p. 227-233.

[3] Nyambo, C., E. Kandare, and C.A. Wilkie, Thermal stability and flammability characteristics of ethylene vinyl acetate (EVA) composites blended with a phenyl phosphonate-intercalated layered double hydroxide (LDH), melamine polyphosphate and/or boric acid. Polymer Degradation and Stability, 2009. 94(4): p. 513-520.

[4] Wilson, R., et al., Clay Intercalation and its Influence on the Morphology and Transport Properties of EVA/Clay Nanocomposites. The Journal of Physical Chemistry C, 2012.

[5] Huang, N., et al., Synergistic effects of sepiolite on intumescent flame retardant polypropylene. Express Polym. Lett, 2010. 4: p. 743.

[6] Zheng, Y. and Y. Zheng, Study on sepiolite-reinforced polymeric nanocomposites. Journal of applied polymer science, 2006. 99(5): p. 2163-2166.

[7] Gul, R., et al., Flame-retardant synergism of sepiolite and magnesium hydroxide in a linear low-density polyethylene composite. Journal of Applied Polymer Science, 2011. 121(5): p. 2772-2777.

Advanced Materials Research Vol. 970 (2014) pp 263-266

doi:10.4028/www.scientific.net/AMR.970.263

Effect of Vacancy and Stone-Wales Defects on The Shear Strength of Carbon Nanotube-Polymer Interfaces

Monon Mahboob[1a*], M. Zahabul Islam[1]

[1]Department of Mechanical Engineering, Bangladesh University of Engineering and Technology, Dhaka 1000, Bangladesh

[a*]mmahbub@me.buet.ac.bd

Keywords: Interfacial strength, Carbon nanotube, Molecular dynamics, Vacancy defects, Stone-Wales defects.

Abstract. In the present study interfacial characteristics of carbon nanotubes (CNTs) and their composite with different types of defects are calculated using molecular dynamics (MD) simulation. Although single-walled CNTs (SWCNTs) are found to have ultra-high stiffness and strength, an enormous scatter is also observed in available experimental results due to the presence of nanoscale defects such as vacancy and Stone-Wales defects. The current paper investigates the influences of Stone-Wales (S-W) and vacancy defects on the mechanical properties of composites containing defective CNTs.

Introduction

Polymer-based composites of carbon nanotubes (CNT) have steadily gained prominence in the materials research community over the past couple of decades. The ultra-high stiffness and low specific weight of carbon nanotubes have made it an excellent reinforcement for high performance composites [1-3]. Enhancements in elastic modulus of CNT reinforced polymer composites [2], indicate that nanotubes carry some of the applied loads. However, the actual magnitude of load transfer between the polymer and fiber is dictated by the interfacial strength. Furthermore, defects, such as Stone-Wales and atomic vacancies in the CNT structure are common [4-6] and experimental observations have revealed that topological defects play an important role in the mechanical properties of SWCNTs [7]. Vacancy defects, i.e., defects resulting from missing carbon atoms can be caused by either electron or ion-irradiation. Stone-Wales defects are composed of two pentagon–heptagon pairs, and can be formed by rotating a sp^2 bond by 90˚ (Fig. 1). Experimental results on CNT reinforced Polyvinyl Alcohol (PVA) composite [3] have shown that the presence of the nanotubes stiffens the material. This work aims for the first time, to investigate the influence of defects on the interfacial shear strength of CNT-PVA nanocomposites.

We use molecular dynamics simulations of a carbon nanotube being pulled out of a polymer matrix in order to compute the interfacial shear strength. Primary contributions of the current research are (i) Investigation of the influence of vacancy and Stone-Wales defects on the potential energy during a pull-out simulation (ii) Investigation of the effect of vacancy and Stone-Wales defects on interfacial shear strength (ISS) of defective CNT reinforced Polyvinyl Alcohol (PVA). The current research provides a useful guidance for composite systems design by predicting the elastic properties and interfacial shear strength of defective CNT based nanocomposites.

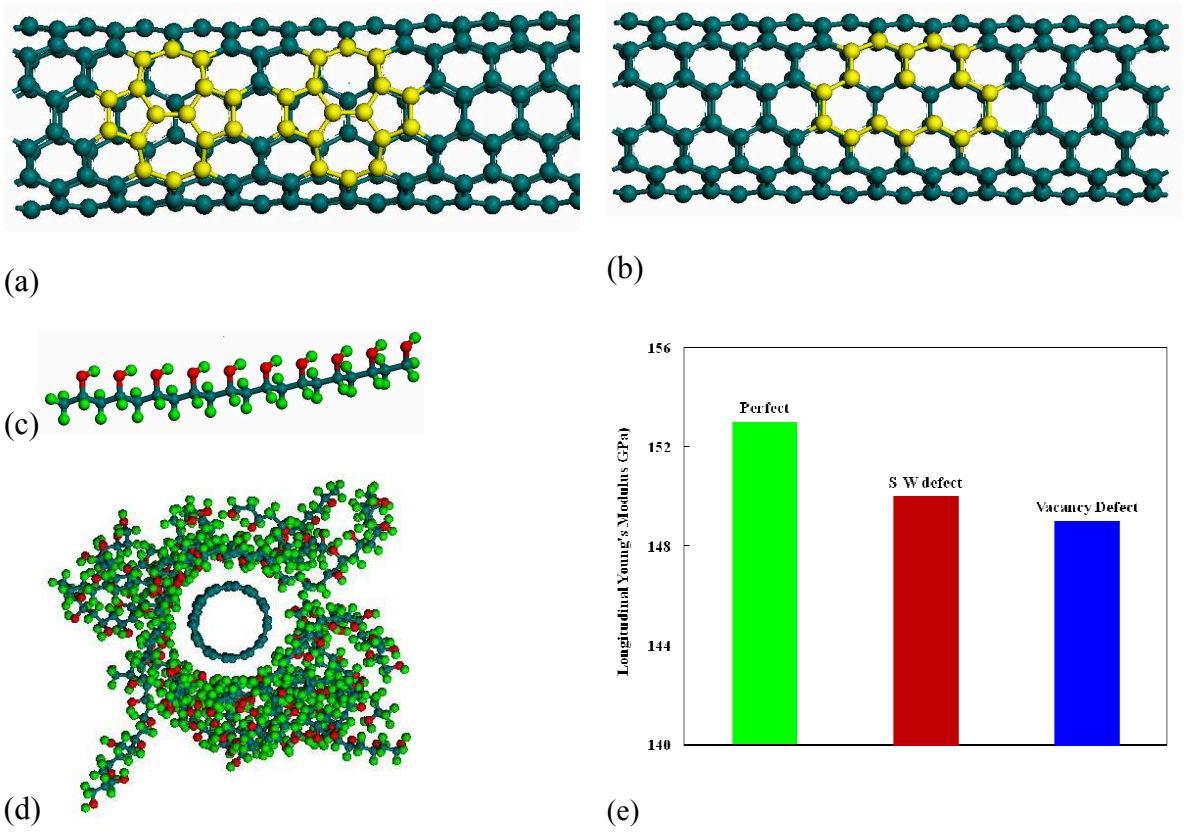

Figure 1. Carbon nanotubes with (a) Stone-Wales defect, (b) Vacancy Defects, (c) Single chain of Polyvinyl alchohol (PVA), and (d) CNT-PVA representative volume element (RVE), and (e) Longitudinal Young's Modulus of CNT-PVA nanocomposite.

Molecular Dynamics Modeling

Molecular dynamics simulation was conducted for 50 ps at a time step of 1 fs under NPT ensemble (constant no. of particles, Pressure and Temperature). During the simulation pressure and temperature were kept constant at 1 atm and 298 K respectively using velocity scaling method. However constant strain energy minimization method was applied to determine the Longitudinal young's modulus of nano composite [2]. The pullout simulations were performed to investigate the interfacial shear stress of the defect-free as well as composites with S-W and Vacancy defects. The energy difference between the fully embedded nanotube and the completely pulled-out configuration of the nanocomposite is known as the pullout energy $E_{pullout}$. The work done by the pull-out force is equal to the energy change i.e. energy increment at each pull-out step. The pullout energy can be related to the interfacial shear stress, τ_i by the following relation:

$$E_{pullout} = \int_{x=0}^{x=L} 2\pi r(L-x)\tau_i dx, \tag{1}$$

this can be evaluated as

$$\tau_i = \frac{E_{pullout}}{\pi r L^2}, \tag{2}$$

where r and L are the outer radius and length of the CNT, respectively, and x is the coordinate along the longitudinal nanotube axis [8].

Results and Discussion

Fig. 1(d) shows a CNT-PVA nanocomposite RVE. The CNT was pulled out from the RVE of the composite by applying an external force. Following each pull-out step, potential energies of the CNT-PVA nanocomposites were recalculated. Thus changes in total potential energy were traced during the entire pull-out process in order to investigate the corresponding interfacial properties of the CNT-PVA nanocomposite system.

A comparison of the longitudinal Young's modulus of composites containing pristine and defective CNTs can be seen in Fig. 1(e). The highest Young's modulus i.e. 153 GPa is observed for pristine CNT-PVA nanocomposite, and decrease of 2.0% and 2.6% are observed for composites with S-W and vacancy defective CNTs, respectively. These findings corroborate claims in earlier literature on similar nanocomposite systems containing CNTs with defects [2,5].

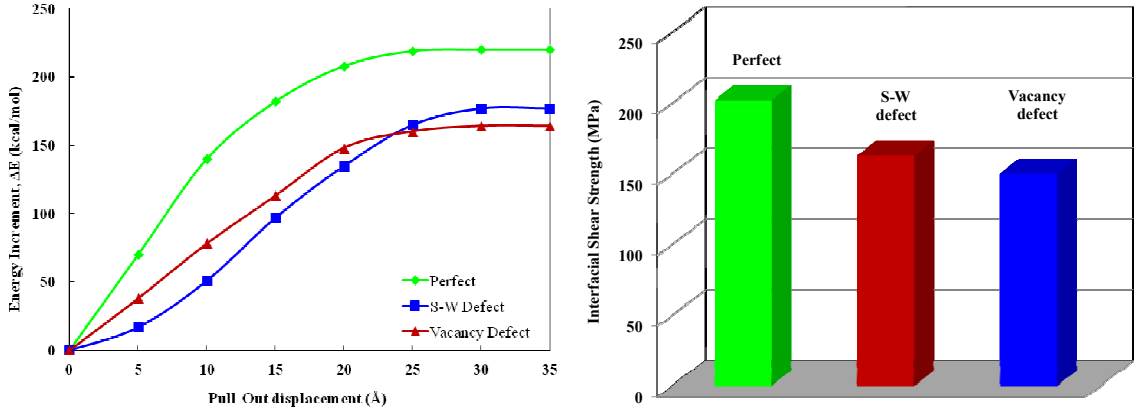

(a) (b)

Figure 2. (a) Effect of defects on energy increment of nano composite during pull out simulation for two S-W defects and two vacancy defects and (b) ISS of CNT-PVA nano composite (right)

In Fig. 2 (a) the energy increments during the pull out simulation for S-W and vacancy defective CNT-PVA composites are presented along with data for pristine CNT-PVA composites. For all three cases, the potential energy of the system increases sharply up to 20 Å of CNT displacement. However, after complete pull out of the CNT i.e. at approximately 25 Å displacement, the rate of potential energy increment is decreased. Finally, at approximately 30 Å CNT displacement, the CNT no longer interacts with the composite matrix, resulting in a plateau of potential energy beyond this point.

Using these potential energy increment data, the interfacial shear strengths are calculated applying Eq. 2 for the three types of CNT nanocomposites. A comparison of these Interfacial shear strengths (ISS) of CNT-PVA nanocomposites in Fig. 2(b) shows a trend similar to the ones reported in Fig. 1(e). ISS for pristine CNT-PVA nanocomposite (202 MPa) is higher compared to composites containing defective CNTs. ISS is decreased by 19.3% and 25.7% for S-W defective and vacancy defective nanocomposites respectively. Clearly, ISS is slightly higher for S-W defective nanocomposite than vacancy defective nanocomposite, which can be attributed to the presence of fewer number of Carbon atoms in a vacancy defect.

Conclusion

In the present study effect of Stone-Wales and vacancy defects on the mechanical properties of CNT-PVA nanocomposite has been studied via molecular dynamics simulation. Our findings reveal that defects can significantly degrade the mechanical properties of CNT-PVA nanocomposites. Furthermore, such degradation is more prominent in case of interfacial shear strength (ISS) than Young's modulus of CNT-PVA. A comparison between SW and vacancy defective CNT composites is also reported; showing greater reduction in strength for composites of CNTs with vacancy defects.

Acknowledgement

Funding for this research was provided by Bangladesh University of Engineering and Technology.

References

[1] M.M.J. Treacy, T.W. Ebbesen, and J.M. Gibson, Exceptionally high Young's modulus observed for individual carbon nanotubes, Nature 381 (1996) 678-680.

[2] M. Mahboob, M.Z. Islam, Molecular dynamics simulations of defective CNT-polyethylene composite systems, Comput. Mater. Sci. 79 (2013) 223–229.

[3] M.S.P. Shaffer, A.H. Windle, Fabrication and characterization of carbon nanotube/poly (vinyl alcohol) composites, Adv. Mater. 11 (1999) 937-941.

[4] F.H. Gojny, J. Nastalczyk, Z. Roslaniec, and K. Schulte, Surface modified multi-walled carbon nanotubes in CNT/epoxy-composites, Chem. Phys. Lett. 370 (2003) 820-824.

[5] M. Mahboob, M.Z. Islam, R.L. Lowe, and S.E. Bechtel, Molecular dynamics and atomistic finite element simulation studies of the effect of Stone-Wales defects on the mechanical properties of carbon nanotubes, Nanosci. and Nanotech. Lett. 5 (2013) 941-951.

[6] M. Sammalkorpi, A. Krasheninnikov, A. Kuronen, K. Nordlund, and K. Kaski, Mechanical properties of carbon nanotubes with vacancies and related defects, Phys. Rev. B 70 (2004) 245416.

[7] N. Chandra, S. Namilae, and C. Shet, Local elastic properties of carbon nanotubes in the presence of Stone-Wales defects, Phys. Rev. B 69 (2004) 094101.

[8] K. Liao, and S. Li, Interfacial characteristics of a carbon nanotube–polystyrene composite system, Appl. Phys. Lett. 79 (2001) 4225-4227.

Advanced Materials Research Vol. 970 (2014) pp 267-271

doi:10.4028/www.scientific.net/AMR.970.267

Effects of Heat Generation or Absorption on Free Convection Flow of a Nanofluid past an Isothermal Inclined Plate

S. Akilu[1], and M. Narahari[2,*]

[1]Department of Mechanical Engineering, Universiti Teknologi PETRONAS, 31750 Tronoh, Malaysia

[2]Department of Fundamental and Applied Sciences, Universiti Teknologi PETRONAS, 31750 Tronoh, Malaysia

[*]corresponding author : marneni@petronas.com.my

Keywords: Free convection, nanofluid, Brownian motion, thermophoresis, heat generation, heat absorption, inclined plate.

Abstract. In this paper, the effects of internal heat generation or absorption on free convection flow of a nanofluid past an isothermal inclined plate have been investigated numerically. The governing boundary-layer equations are first transformed into a system of coupled nonlinear ordinary differential equations using similarity variables. An efficient implicit finite-difference scheme known as the Keller-box method is employed to solve the resulting nonlinear equations. The effects of internal heat generation or absorption parameter on the flow fields have been presented graphically and discussed. It is found that the rate of heat transfer decreases with increasing heat generation, Brownian motion and thermophoresis parameters whereas it increases with increasing heat absorption parameter and Prandtl number.

Introduction

Before the advent of nanotechnology, conventional heat transfer fluids (water/air) were utilized as working fluids. However, low thermal conductivity of these fluids was of serious concern to the engineers. In the search for efficient heat transfer fluids, Choi [1] discovered that the heat transfer performance can be enhanced by dispersing metallic or non-metallic conductive nanoparticles into a base fluid (e.g. water) to produce a superior heat transfer mixture referred to as nanofluids. Nanofluids have shown promising characteristics that could warrant their application as coolants for many engineering processes. The attractive features common to nanofluids includes high thermal conductivity, minimal clogging in micro-channels, stability and homogeneity. Other notable properties exclusive to nanofluids have since been reported in the literature [2, 3].

The effect of heat generation or absorption on a moving fluid is an important problem in engineering mainly encountered during heat removal operations in the nuclear and geothermal industries. In light of these applications, Rana et al. [4] analyzed the effects of heat source on a mixed convection flow of a nanofluid along a vertical plate. The governing equations were solved using a robust variational finite element method. Oztop et al. [5] investigated the influence of volumetric heat sources on the free convection heat transfer in a wavy walled enclosure utilizing the finite volume method. Recently, Alsaedi et al. [6] studied the effects of internal heat generation/absorption on stagnation point flow of nanofluid over a permeable stretched surface with convective boundary condition using homotopy analysis method.

Therefore, the main objective of this paper is to extend the work of Kuznetsov and Nield [7], and Narahari et al. [8] to study the effects of internal heat generation/absorption on boundary layer flow of a nanofluid past an isothermal inclined plate. The transformed coupled nonlinear ordinary differential equations have been solved using an efficient implicit finite-difference Keller-box method. The effects of heat generation or absorption parameter on non-dimensional velocity, temperature, nanoparticle concentration and Nusselt number have been discussed through graphs.

Mathematical Formulation. Consider the two-dimensional steady state natural convection flow of a nanofluid over an isothermal flat plate inclined at an angle of γ from vertical plane in the presence of heat generation or absorption. The x- axis is taken along the plate leading edge and y-axis perpendicular to the plate. The temperature T and the nanoparticle fraction ϕ at the plate take constant values T_w and ϕ_w, respectively. The ambient values, attained as y tends to infinity, of T and ϕ are denoted by T_∞ and ϕ_∞, respectively. Applying Oberbeck-Boussinesq approximation, the governing boundary-layer equations for mass, momentum, temperature and nanoparticle volume fraction are, respectively

$$\frac{\partial u}{\partial x}+\frac{\partial v}{\partial y}=0 \tag{1}$$

$$\rho_f\left(u\frac{\partial u}{\partial x}+v\frac{\partial u}{\partial y}\right)=\mu\frac{\partial^2 u}{\partial y^2}+\left[(1-\phi_\infty)\rho_{f\infty}\beta(T-T_\infty)-(\rho_p-\rho_{f\infty})(\phi-\phi_\infty)\right]g\cos\gamma \tag{2}$$

$$(\rho c)_f\left(u\frac{\partial T}{\partial x}+v\frac{\partial T}{\partial y}\right)=k\frac{\partial^2 T}{\partial y^2}+Q_0(T-T_\infty)+(\rho c)_p\left[D_B\frac{\partial\phi}{\partial y}\frac{\partial T}{\partial y}+\left(\frac{D_T}{T_\infty}\right)\left(\frac{\partial T}{\partial y}\right)^2\right] \tag{3}$$

$$u\frac{\partial\phi}{\partial x}+v\frac{\partial\phi}{\partial y}=D_B\frac{\partial^2\phi}{\partial y^2}+\left(\frac{D_T}{T_\infty}\right)\frac{\partial^2 T}{\partial y^2} \tag{4}$$

Subject to the boundary conditions

$$\left.\begin{array}{l} u=0, v=0,\ T=T_w,\ \phi=\phi_w \quad \text{at} \quad y=0 \\ u=v=0,\ T\to T_\infty,\ \phi\to\phi_\infty \quad \text{as} \quad y\to\infty \end{array}\right\} \tag{5}$$

where, velocity components along x and y are represented by u and v, respectively, ρ_f is the density of the base fluid and ρ_p is the density of the nanoparticles, μ, k and β are the viscosity, thermal conductivity and volumetric expansion coefficient of the nanofluid, respectively, Q_0 is the volumetric rate of heat generation or absorption, γ is the angle of inclination, ϕ is the nanoparticle volume fraction, T is the local temperature, g is the acceleration due to gravity, $(\rho c)_f$ is the heat capacity of the fluid, $(\rho c)_p$ is the effective heat capacity of the nanoparticle material, D_B and D_T are the Brownian diffusion coefficient and thermophoretic diffusion coefficient, respectively. Here the subscript ∞ denotes the values far away from the plate.

Upon the introduction of the following dimensionless variables,

$$\eta=(y/x)\mathrm{Ra}_x^{1/4},\ s(\eta)=\psi/\alpha\,\mathrm{Ra}_x^{1/4},\ \theta(\eta)=(T-T_\infty)/(T_w-T_\infty),\ f(\eta)=(\phi-\phi_\infty)/(\phi_w-\phi_\infty) \tag{6}$$

with the local Rayleigh number defined as

$$\mathrm{Ra}_x=\frac{(1-\phi_\infty)\beta g(T_w-T_\infty)x^3}{\nu\alpha}=Bx^3 \tag{7}$$

where $\alpha=k/(\rho c)_f$ is the thermal diffusivity, and the stream function ψ is defined such that $u=\frac{\partial\psi}{\partial y}$ and $v=-\frac{\partial\psi}{\partial x}$ so that the continuity equation (1) is identically satisfied, the similarity transformation reduces equations (1) – (4) into a system of ordinary differential equations as given by

$$s'''+\frac{1}{4\mathrm{Pr}}\left(3ss''-2s'^2\right)+\left(\theta-\mathrm{Nr}f\right)\cos\gamma=0 \tag{8}$$

$$\theta''+\frac{3}{4}s\theta'+\mathrm{Nb}f'\theta'+\mathrm{Nt}\theta'^2+Q\theta=0 \tag{9}$$

$$f''+\frac{3}{4}\mathrm{Le}sf'+\frac{\mathrm{Nt}}{\mathrm{Nb}}\theta''=0 \tag{10}$$

In terms of new variables, the boundary conditions become

$$\left.\begin{array}{lll} s=0, s'=0, \theta=1, f=1 & \text{at} & \eta=0 \\ s'=0, \theta=0, f=0 & \text{as} & \eta\to\infty \end{array}\right\} \tag{11}$$

where primes denote differentiation with respect to η. The buoyancy-ratio parameter (Nr), Brownian motion parameter (Nb), thermophoresis parameter (Nt), heat generation or absorption parameter (Q), Prandtl numbers (Pr) and Lewis number (Le) are defined as follows:

$$\left.\begin{array}{l} \mathrm{Nr}=\dfrac{(\rho_p-\rho_{f\infty})(\phi_w-\phi_\infty)}{\rho_{f\infty}\beta(T_w-T_\infty)(1-\phi_\infty)},\ \mathrm{Nb}=\dfrac{(\rho c)_p D_B(\phi_w-\phi_\infty)}{(\rho c)_f\alpha},\ \mathrm{Nt}=\dfrac{(\rho c)_p D_T(T_w-T_\infty)}{(\rho c)_f\alpha T_\infty}, \\ Q=\dfrac{Q_0}{\alpha B^{1/2}x^{-1/2}(\rho c)_f},\ \mathrm{Pr}=\dfrac{\nu}{\alpha},\ \mathrm{Le}=\dfrac{\alpha}{D_B}. \end{array}\right\} \tag{12}$$

In this study, the physical quantity of practical interest is the dimensionless rate of heat transfer which is defined in the form of Nusselt number as

$$\mathrm{Nu}=\frac{q_w'' x}{k(T_w-T_\infty)} \tag{13}$$

where q_w'' is the wall heat flux. The reduced local Nusselt number is given by

$$\mathrm{Nur}=\mathrm{Nu}/\mathrm{Ra}_x^{1/4}=-\theta'(0) \tag{14}$$

Numerical Solution. The set of non-linear and coupled ordinary differential equations (8) - (10) subject to the boundary conditions (11) has been solved numerically by using an efficient implicit finite-difference method known as the Keller-box method (for detailed explaination on the method see Cebeci and Bradshaw [9]). To assess the accuracy of the code generated for this study, the results have been compared with previously published results available in the literature. Table 1 shows the numerical values of reduced local Nusselt number along with the results reported by Kuznetsov and Nield [7] for the case of vertical plate in the absence of heat genration or absorption, and they are found to be in very good agreement.

Table 1. Comparison of the present reduced Nusselt number (Nur) values with previously published results [7] for different Pr when Le = 10, Nr = Nb = Nt = 10^{-5}, $Q=0$ and $\gamma=0^0$.

Pr	1	10	100	1000
Nur (Kuznetsov and Nield [7])	0.401	0.463	0.481	0.484
Nur (Present)	0.401	0.459	0.473	0.474

Results and Discussion

Numerical calculations are conducted for various values of heat generation or absorption parameter Q and the results have been presented in Figs. 1 – 6 for velocity, temperature and nanoparticle concentration variables and Nusselt number. The default values of system parameters are chosen as $\mathrm{Pr}=1$, $\mathrm{Le}=10$, $\mathrm{Nr}=\mathrm{Nb}=\mathrm{Nt}=0.1$ and $\gamma=45^0$ unless otherwise specified. Fig. 1 displays the dimensionless velocity profiles for various values of heat generation or absorption parameter Q. It is found that the velocity increases with the increase of heat generation $(Q>0)$ and it decreases with the increase of heat absorption $(Q<0)$. Similar trend has been observed in the variation of temperature profiles with heat generation or absorption parameter Q as exhibited in Fig. 2. This demonstrates that the nanofluid temperature in the boundary layer can be raised/lowered by increasing the intensity of heat generation/absorption. Fig. 3 shows the concentration profiles for different values of the heat generation or absorption parameter Q. It is evident that the concentration boundary layer thickness decreases with increasing heat generation whereas it increases with increasing heat absorption parameter Q.

Fig. 4 depicts the variation of the reduced local Nusselt number with heat generation or absorption parameter Q for different values of Prandtl number. It is noticed that the reduced local

Nusselt number increases with Prandtl number for both heat generation and absorption cases. The effects of Brownian motion parameter and thermophoresis parameter on the Nusselt number at different values of heat generation or absorption parameter Q are shown in Figs. 5 and 6, respectively. It is observed that the Nusselt number decreases with increasing Brownian motion and thermophoresis parameters for fixed values of heat generation or absorption parameter Q. From Figs. 4 – 6, it is also observed that the reduced local Nusselt number decreases with increasing heat generation parameter and it increases with increasing heat absorption parameter for fixed values of Prandtl number, Brownian motion and thermophoresis parameters.

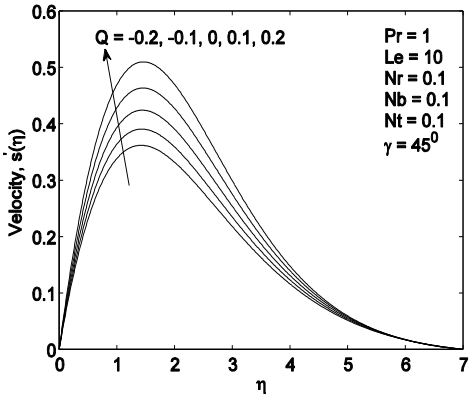

Fig. 1 Velocity profiles at different heat generation/absorption parameter

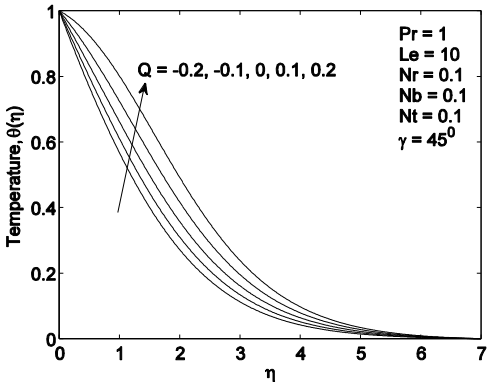

Fig. 2 Temperature profiles at different heat generation/absorption parameter

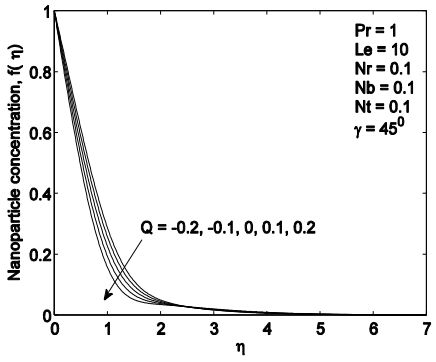

Fig. 3 Nanoparticle concentration profiles at different heat generation/ absorption parameter

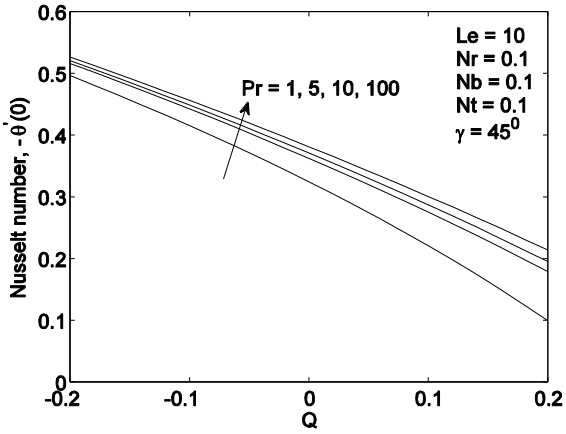

Fig. 4 Nusselt number variation with heatgeneration/absorption parameterfor different Pr

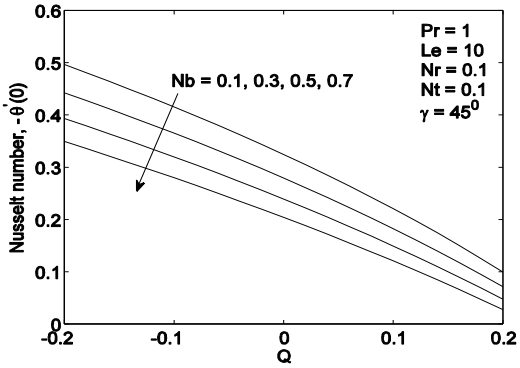

Fig. 5 Nusselt number variation with generation/absorption parameter for different Brownian motion parameter

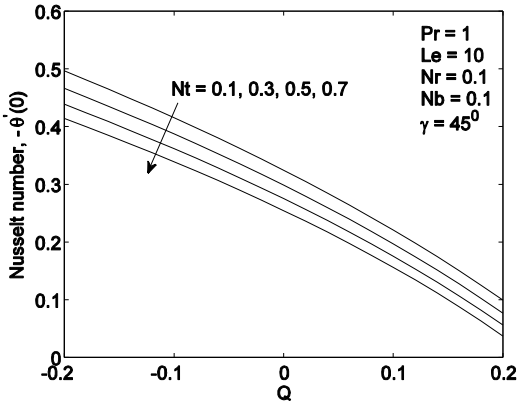

Fig. 6 Nusselt number variation with generation/absorption parameter for different thermophoresis parameter

Conclusions

The two-dimensional laminar incompressible boundary layer flow of a nanofluid past an isothermal inclined plate in the presence of heat generation/absorption is investigated numerically. The resulting coupled nonlinear ordinary differential equations using similarity variables have been solved numerically with the Keller-box method. The effects of heat generation or absorption parameter on the velocity, temperature, nanoparticle concentration and Nusselt number have been discussed. Also, the effects of Prandtl number, Brownian motion parameter and thermophoresis parameter on the Nusselt number have been examined. The results shows that the velocity and temperature increases with increasing heat generation and decreases with increasing heat absorption whereas an opposite trend is observed in the case of nanoparticle concentration. The study also revealed that the local Nusselt number increases with increasing heat absorption and Prandtl number whereas it decreases with increasing heat generation, Brownian motion and thermophoresis parameters. In the absence of heat generation/absorption and inclination angle, the numerical results for the reduced Nusselt number obtained in the present study are compared with the previously published research work and our results are found in excellent agreement.

References

[1] S. Choi, in: *Developments and Applications of Non-Newtonian Flows*, edited by D. A. Siginer and H. P. Wang, ASME, FED-Vol. 231/MD-Vol. 66 (1995), p. 99.

[2] Y. Xuan and W. Roetzel: Int. J. Heat Mass Transfer Vol. 43 (2000), p. 3701.

[3] X.-Q. Wang and A. S. Mujumdar: Int. J. Therm. Sci. Vol. 46 (2007), p. 1.

[4] P. Rana and R. Bhargava: Commun. Nonlinear Sci. Numer. Simulat. Vol. 16 (2011), p. 4318.

[5] H. F. Oztop, E. Abu-Nada, Y. Varol and A. Chamkha: Int. J. Therm. Sci. Vol. 50 (2011), p. 502.

[6] A. Alsaedi, M. Awais and T. Hayat: Commun. Nonlinear Sci. Numer. Simulat. Vol. 17 (2012), p. 4210.

[7] A. Kuznetsov and D. Nield: Int. J. Therm. Sci. Vol. 49 (2010), p. 243.

[8] M. Narahari, S. Akilu and A. Jaafar: Applied Mechanics and Materials Vol. 390 (2013), p. 129.

[9] T. Cebeci and P. Bradshaw: *Physical and Computational Aspects of Convective Heat Transfer* (Springer, New York 1988).

Advanced Materials Research Vol. 970 (2014) pp 272-278

doi:10.4028/www.scientific.net/AMR.970.272

Investigation of nanoscale structure of self-emulsifying drug delivery system containing poorly water-soluble model drug

Mont Kumpugdee-Vollrath[1,a*], Y. Weerapol[2,b], K. Schrader[3,c], and P. Sriamornsak[2,d]

[1]Beuth Hochschule für Technik Berlin - University of Applied Sciences, Faculty of Mathematics-Physics-Chemistry, Department of Pharmaceutical Engineering, Luxemburger Str. 10, 13353 Berlin, Germany;

[2]Silpakorn University, Department of Pharmaceutical Technology, and Pharmaceutical Biopolymer Group (PBiG), Faculty of Pharmacy, Nakhon Pathom 73000 Thailand;

[3]Max Rubner-Institute, Federal Research Institute of Nutrition and Food, Department of Safety and Quality of Milk and Fish Products, Hermann-Weigmann-Straße 1, 24103 Kiel, Germany

[a*]vollrath@beuth-hochschule.de, [b]wyotsanan@gmail.com, [c]katrin.schrader@mri.bund.de, [d]pornsak@su.ac.th

Keywords: resveratrol, SEDD, SAXS, PCS, TEM, self-emulsifying, nanoscale, poorly water-soluble, d-spacing

Abstract. This work has a focus on the self-emulsifying drug delivery system (SEDDS), which can be used in pharmaceutical field for increasing bioavailability of poorly water-soluble drugs. The model drug resveratrol was used because of its poor water-solubility and is of interest because of its wide range of pharmacological effects. It is beneficial to understand the mechanism of SEDDS formation in the human body, therefore, the determination of nanoscale structure was carried out. For this purpose, small angle X-ray scattering (SAXS), photon correlation spectroscopy (PCS), and transmission electron microscopy (TEM) techniques were applied. We have found that the size and size distribution of particles were in nanometers. The inner structure of SEDDS was ordered with the lamellar distances (d-spacing) of < 20 nm. It seems that the prepared SEDDS in water form large oil drops (200-400 nm) in water as well as small micelles with the droplet size of 10-20 nm.

Introduction

Resveratrol (trans-3,5,4'-trihydroxystilbene "Res") can be found in several plants like grapes, peanuts or mulberries and showed positive effects in human beings because of photoalexin behavior. Resveratrol was therefore studied by numerous research groups. Res was first isolated from leafs of the white lily (*Lilium candidum*) and is already well known in the traditional Japanese medicine for a long time. A high concentration of Res was also found in the Japanese knotgrass (*Polygonum cuspidatum*). Res has a relative molecular weight of 228.25 g/mol and a water solubility of 0.03 g/l. Because of the low water solubility Res has a low bioavailability in human body [1-4]. In order to improve bioavailability the new formulation called self-emulsifying drug delivery systems (SEDDS), was studied in this project. SEDDS are isotropic mixtures of oils, surfactants or co-surfactant, and solvents or co-solvents. The fine emulsion, microemulsion or nanoemulsion (O/W diameter of 100-300 nm) can be formed immediately (less than a minute) after the SEDD is in contact with the aqueous medium in human body. However, the mechanism of self-emulsifier was not yet reported. Therefore this project was performed to confirm our data from the former report [5]. The X-ray scattering technique represents a powerful tool for nanostructural investigations since it provides a direct sampling of the real structure of the object. The information about the repetitive structure, the shape and the bilayer or d-spacing could be recovered from the small angle X-ray scattering (SAXS) technique [6]. The photon correlation spectroscopy (PCS) can be used to determine the size and size distribution of particles in nanoscale. By applying mathematical model the size and size distribution can be calculated [7]. The transmission electron microscopy (TEM) can be applied to determine both the morphology and the size of particles in nanoscale [7]. The limitation of this technique is that the

samples have to be prepared prior to the analysis to make the structures visible and to protect the samples.

Materials and Methods

Materials. Resveratrol (trans, 98% content, Polygonum cuspidatum) was purchased from Behr GmbH (Stuttgart Germany). Diethylene glycol monoethyl ether (DGME) was purchased from Merck KGaA (Germany). Imwitor® 742 was purchased from Sasol (Germany) and Cremophor® EL is a gift from BASF (Germany).

Production of SEDDs various formulations. Different SEDDSs were prepared by mixing the components together, as demonstrated in Appendix A (in Appendix below). All components (lipid based system "LBS") without water were stored under 4°C. Prior to measure by different techniques, water at the specified amount was added into the LBS. The container was then manually shaken and vortexed to totally one minute until the emulsion (micro, nano) was formed. In case the LBS did not melt or in the fluid state before an addition of water, it can be warmed at not more than 30°C. The samples of liquid SEDDSs were stored under 4°C and protected from light if further measurements were needed. The photographs of the samples, both freshly prepared and after storage, were taken by a digital camera.

Characterization by SAXS. The experiments were performed at the small angle X-ray scattering (SAXS) instrument, beamline B1, installed at the DORIS III synchrotron source at HASYLAB/DESY in Hamburg, Germany. The SAXS patterns (0-1 $Å^{-1}$) were acquired using a large-area pixel detector (PILATUS 1M, Dectris, Switzerland) with pixel size of 172 mm x 172 mm. The samples were measured both under the detector long distance (3.583 m) as well as short distance (0.885 m) at the X-ray energy of 14 keV. Samples were filled into a glass capillary (Hilgenberg GmbH, Malsfeld, Germany) with a diameter of 1.0 mm and a wall thickness of 0.01 mm. The capillaries were sealed with epoxy resin adhesive (UHU Quickset EPOXY Resin Glue, Germany) and fixed onto a holder, which was placed into a measuring vacuum chamber. The SAXS measurements were performed at ambient temperature (297 K). The raw scattering data were background corrected, integrated and calibrated using a MATLAB-based analysis suite, which is available at the beamline.

To calculate the radius of particles (***r***) or the lamellar structure (***d***-spacing) measured by SAXS, two different mathematical equations, i.e. (i) and (ii) were used;

$$r = \frac{R_g}{\left(\frac{3}{5}\right)^{1/2}} \quad \text{(i)}$$

$$d = \frac{2\pi}{Q_{\max}} \quad \text{(ii)}$$

By drawing a graph between Q^2 and ln (I), the slope (m) of the line can be used to calculate the radius ***r*** by the equation $R_g = \sqrt{(-3 \cdot m)}$. The value R_g is the radius of gyration; Q_{max} is scattering vector at the maximum of a scattering peak.

Characterization by dynamic light scattering. The size and size distribution were determined by the dynamic light scattering (PCS, Zetasizer 1000, Malvern, England). Only some samples were measured because of technical limitation.

Characterization by transmission electron microscopy. Selected samples were examined by transmission electron microscopy. For cryoprotection, the samples were mixed with 30% glycerol before freezing. Small droplets were cryofixed by immersion into melting Freon 22 and freeze-fractured at -120 °C without etching with a BALZERS BA 400 unit. Freeze-fractured specimens were replicated by application of Pt/C and C by electron-gun evaporation. The replicas were cleaned with sodium hypochlorite, distilled water and acetone. Afterwards they were examined using a FEI Tecnai 10 transmission electron microscope operated at 80 kV.

Results and Discussions

Optical determination. Figure 1 shows different samples. The samples were clear, milky white or opaque. The macroscopic character pointed out that the milky white samples may have bigger particle sizes than the clear one. The samples were stable at least 6 months after optical monitoring.

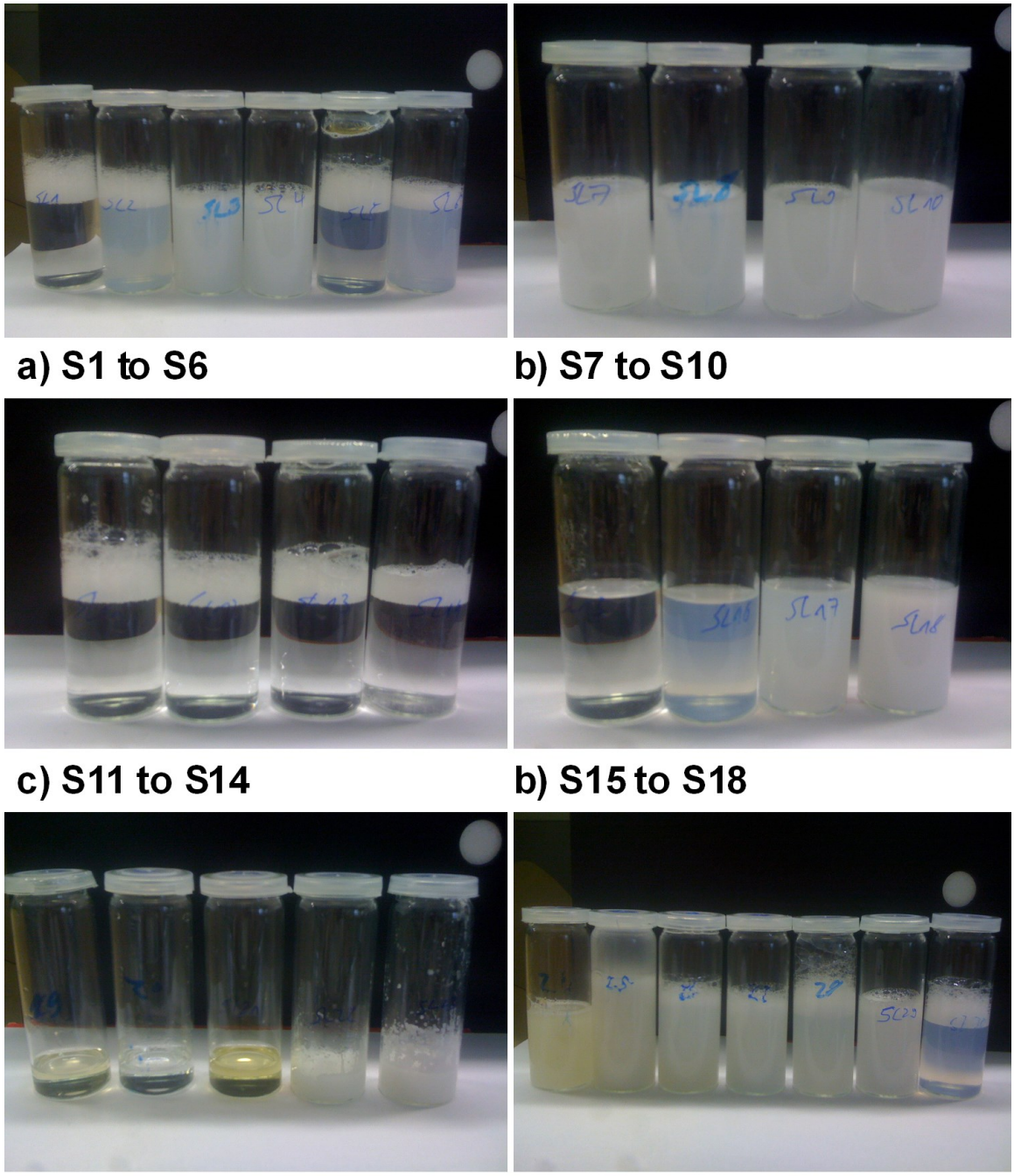

Figure 1: Optical determination of various samples (S1 to S30).

SAXS results. Table 1 shows the radius of particles and the d-spacing which were calculated by two equations (i, ii). If the correlation coefficient (R^2) is more than 0.9, the r or d-spacing values had a high confidential level. The radiuses of the particles and the d-spacing values were smaller than 16 nm. Figure 2 shows an example of the scattering X-ray pattern and the way of calculation of the slope. From Figure 2 (left), m = -2863 was obtained, while Q_{max} = 0.062 was obtained from Figure 2 (right).

Table 1: SAXS results of different samples showing R_g, r and d.

Sample	Slope, m	R_g	R^2	r in nm	d in nm
S1	-2863	92.68	0.916	11.96	10.08
S2	-3916	108.39	0.964	13.99	10.19
S3	-2298	83.03	0.821	10.72	2.70
S4	-607	42.67	0.431	5.51	2.50
S5	-2149	80.29	0.808	10.37	9.60
S6	-2556	87.57	0.882	11.30	9.38
S7	-3052	95.69	0.936	12.35	3.08
S8	-1529	67.73	0.627	8.74	2.92
S9	-2786	91.42	0.932	11.80	2.88
S10	-2336	83.71	0.862	10.81	2.88
S11	-1532	67.79	0.860	8.75	7.45
S12	-2107	79.50	0.900	10.26	7.40
S13	-1277	61.90	0.844	7.99	7.34
S14	-2121	79.77	0.937	10.30	7.34
S15	-2535	87.21	0.935	11.26	8.86
S16	-2428	85.35	0.891	11.02	9.84
S17	-3718	105.61	0.959	13.63	12.82
S18	-1795	73.38	0.838	9.47	2.82
S24	-4138	111.42	0.011	14.38	15.60
S25	-1396	64.71	0.853	8.35	9.24
S26	-2645	89.08	0.958	11.50	12.57
S27	-1828	74.05	0.727	9.56	8.38
S28	-3018	95.15	0.985	12.28	7.85
S29	-1334	63.26	0.687	8.17	14.86
S30	-2761	91.01	0.920	11.75	9.61

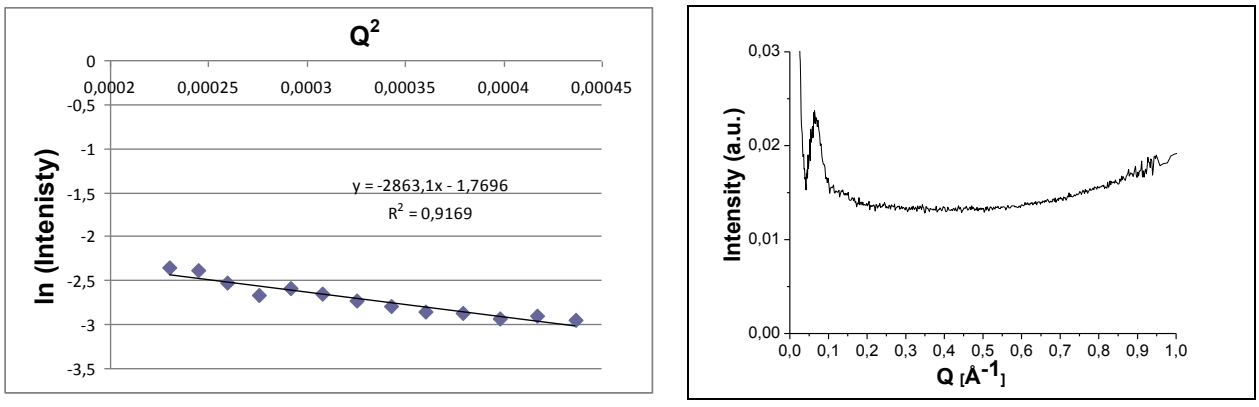

Figure 2: (left) Graph between Q^2 and ln (I) showing slope of sample S1, (right) SAXS-pattern of sample S1.

After analysis by the two equations mentioned above, the radius of gyration (R_g) of this example was found to be 92.68 Å, resulting in the radius (***r***) of 11.96 nm and ***d*** of 10.08 nm. These data showed that the SEDDS had an order system with lamellar structure. This lamellar structure formed the larger drops, which should be the oil drops. However, the sizes of oil drops were large and therefore they could not be determined by SAXS but by PCS. This hypothesis was confirmed in further experiments by PCS. We can summarize that by the SAXS technique, the particles size was small, less than 20 nm. This may result from the formation of micelles as mentioned in the literature, which indicated that the sizes of micelles are normally about 5 to 50 nm [8]. Further support of this hypothesis may be performed by focusing on the CMC values of Cremophor EL [9]. Cremophor EL can form micelles if the concentration is higher than 0.02%. In our studies, the concentration was about 0.2%, which was much higher than the CMC values. Therefore Cremophor EL can definitely form micelles, which we can detect by using SAXS.

PCS results. Figure 3 shows some results of PCS measurements. It can be seen that the particle size distribution of both samples (S2 and S30) was bimodal distribution. Most of the particles demonstrated the sizes between 50-100 nm, and 200-300 nm (mean size of 174 nm) or 30-90 nm and 100-300 nm (mean size of 128 nm), for S2 and S30, respectively. The results gave the suggestion that the emulsions showed large droplet sizes in the systems, which may represent the nanoemulsions or microemulsions.

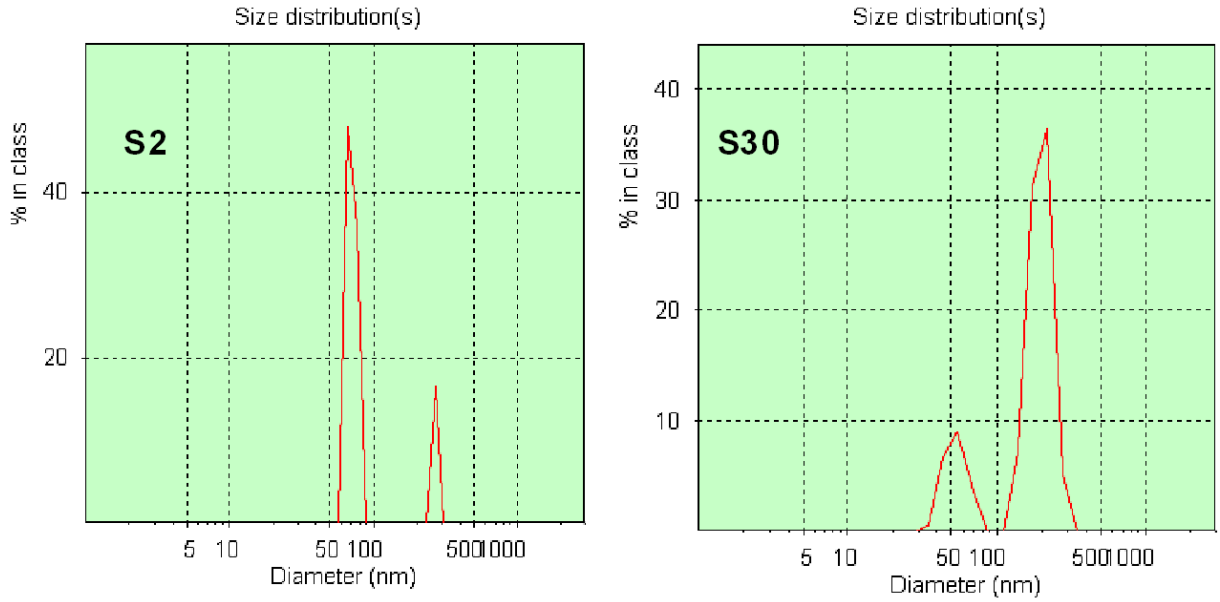

Figure 3: PCS results of some samples (S2 and S30)

TEM results. As shown in figure 4, it can be observed that the samples S1 had very small particle sizes < 100 nm, whereas the particle size of the sample S2 was larger, i.e. the size of some particles was > 200 nm.

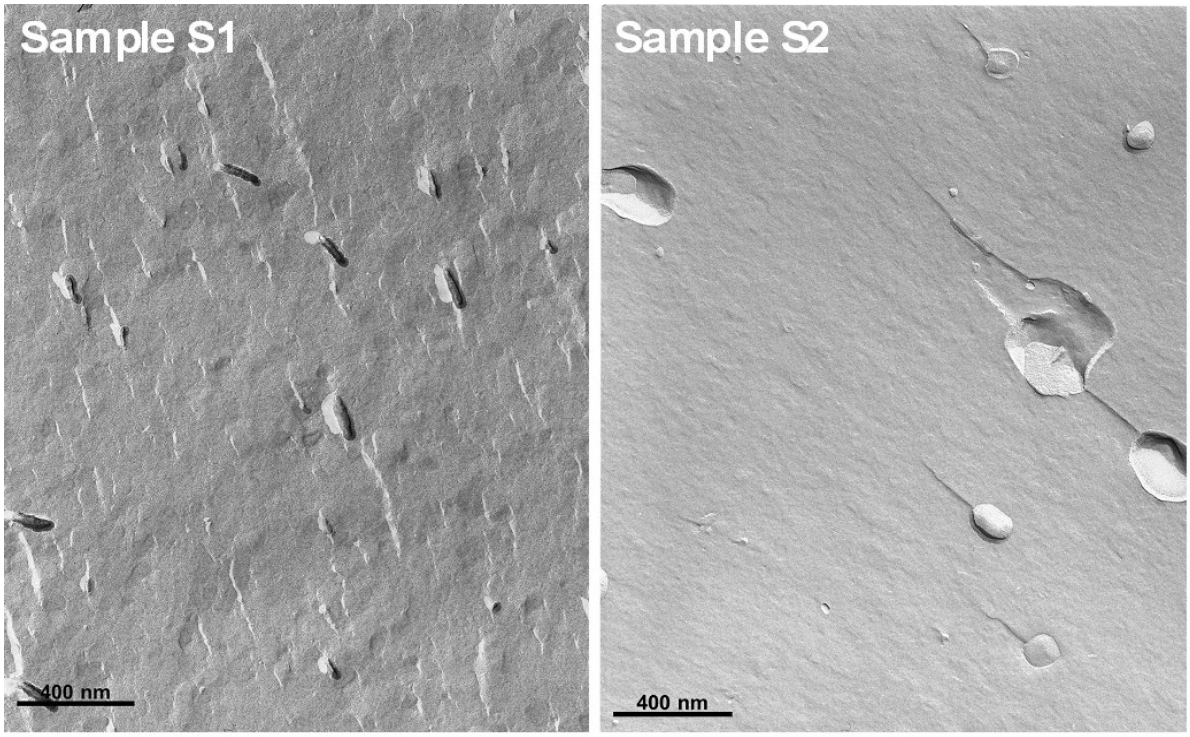

Figure 4: TEM of some SEDDS (S1 and S2) showing drops in the systems.

Conclusion

After combining the results of optical determinations, PCS and TEM, it can be seen that if the samples were clear, the particle sizes were less than 100 nm. If the samples were opaque the particle sizes were > 100 nm. However, the particle sizes of the opalescence system were bimodal with two different regions (<100 nm and >100 nm). The SEEDS should have two types of drops in the emulsion. One type was micelles with the size of < 20 nm, the other type of drops was oil drop with ordered system and the mean size of about 200 nm.

Acknowledgements

The workgroup thanks the Institut für angewandte Forschung Berlin e.V. (IFAF), the Europäischen Fonds für regionale Entwicklung (EFRE) as well as the European Regional Development Fund (ESF), Zentrales Innovationsprogramm Mittelstand (ZIM), the Federal Ministry of Economics and Technology (BMWi) of Germany for the financial support, DESY, Beamline B1, Dr. U. Vainio and S. Lemke for the SAXS-measurements and analysis.

Appendix

Appendix A. Components of various SEDDS formulations.

Sample	Resveratrol (40.114 g/L in DGME) %	Imwitor® 742 %	Cremophor® EL %	DGME %	Water (mL)
S1	20	20	60		20
S2	20	40	40		20
S3	20	60	20		20
S4	40	40	20		20
S5	40	20	40		20
S6	60	20	20		20
S7	20	80			20
S8	40	60			20
S9	60	40			20
S10	80	20			20

S11	20		80		20
S12	40		60		20
S13	60		40		20
S14	80		20		20
S15	80	20			20
S16	60	40			20
S17	40	60			20
S18	20	80			20
S19	100				
S20				100	
S21			100		
S22		100* liquid form			
S23		100* solid form			
S24	20	30	50		10
S25	20	30	50		20
S26	20	30	50		20
S27	20	30	50		20
S28	20	30	50		20
S29	20	30	50		20
S30	20	30	50		20

References

[1] S. Das, K-Y. Ng, International Journal of Pharmaceutics, 385 (2010) 20-28.
[2] C. Lucas-Abellan, Food Chemistry, 111 (2008) 262-267.
[3] Material Safety Data Sheet Resveratrol, Organic herb Inc, (2006)
[4] M. Kumpugdee-Vollrath, Y. Ibold, Advanced Materials Research, 418-420 (2012) 2231-2234.
[5] Y. Weerapol, M. Kumpugdee-Vollrath, P. Sriamornsak, Advanced Materials Research, 747 (2013) 139-142.
[6] A. Nasedkin, J. Davidsson, M. Kumpugdee-Vollrath, Journal of Synchrotron Radiation, 20 (2013) 721-728.
[7] K. Burapapadh, M. Kumpugdee-Vollrath, D. Chantasart, P. Sriamornsak, Carbohydrate Polymers, 82 (2010) 384-393.
[8] H. Schubert, Emulgiertechnik – Grundlagen Verfahren und Anwendungen-, B. Behr's Verlag, (2005) 226-229.
[9] BASF AG, Technical Information Cremophor EL, (2007)

Advanced Materials Research Vol. 970 (2014) pp 279-282

doi:10.4028/www.scientific.net/AMR.970.279

Simple and Low-cost Preparation of Carbon-Coated Titanium Dioxide via Hydrothermal Method

Mohd Hayrie Mohd Hatta[1,a], Hendrik O. Lintang[2,b], Nor Aziah Buang[1,c] and Leny Yuliati[2,d*]

[1]Department of Chemistry, Faculty of Science, Universiti Teknologi Malaysia, UTM Johor Bahru, 81310, Johor, Malaysia

[2]Ibnu Sina Institute for Fundamental Science Studies, Universiti Teknologi Malaysia, UTM Johor Bahru, 81310, Johor, Malaysia

[a]shhayrie2@live.com.my, [b]hendrik@ibnusina.utm.my, [c]noraziah@kimia.fs.utm.my, [d]leny@ibnusina.utm.my

Keywords: titanium dioxide, carbon-coated titanium dioxide, hydrothermal method, dichloromethane

Abstract. In the present study, carbon-coated titanium oxide (C-TiO_2) was synthesized by hydrothermal method using dichloromethane as the novel low-cost carbon source. XRD patterns revealed that after purification method, only diffraction peaks of anatase TiO_2 can be observed. On the other hand, the formation of carbon can be suggested from DR UV-visible spectrum and SEM image, which showed the additional of absorption band in the visible region and the successful formation of carbon that grew both on the surface with a unique noodle-like structure and surroundings of the TiO_2 with non-uniform bulk structure, respectively.

Introduction

Carbon-coated materials have been recognized as potential materials for various applications. In many cases, the functionalities of unmodified materials can be enhanced by carbon coating [1], especially those that are applied as photocatalysts. Since titanium dioxide (TiO_2) is one of the most potential photocatalysts so far, many researches have been done on the modification of TiO_2 with carbon materials by coating methods [1-8]. It has been reported that the carbon coating successfully enhanced the photocatalytic activity of TiO_2 [1-6]. The reasons for the increased photocatalytic activity have been proposed as the result of the suppression of anatase transformation to rutile at high temperature [2,3], improved adsorption ability for organic pollutants [2,3], strengthened visible light respond as carbon layer may act as sensitizer [4], significant decrease of electron-hole recombination [5], as well as increased migration efficiency of the photoinduced electron [6].

Typically, carbon-coated TiO_2 is produced by high thermal process. As example, carbon coated-TiO_2 can be prepared by mixing of poly(vinyl alcohol) (PVA) to TiO_2 before heating at temperatures of 700-1100 °C under nitrogen atmosphere [2,3], heating the TiO_2 in drip furnace with methanol as the dropping agent at 500-700 °C by gas thermal penetration method [4], or mixing the TiO_2 with the epoxidized natural rubber, followed by calcination under nitrogen atmosphere at 470-620 °C [5]. It was reported that even though carbonization of TiO_2 could be carried out at low temperature using glucose as carbon source, graphitization process occurred under nitrogen flow at high temperature of 800 °C [6]. In addition to high temperature, the process mentioned above also required specific conditions, such as the controlled nitrogen atmosphere. Therefore, hydrothermal process has been proposed as one alternative method that offers both low reaction temperature and simple method. Recently, the ease of using dextrose and poly(ethylene glycol) as the carbon source to prepare carbon-coated TiO_2 via facile hydrothermal method was reported [7]. In this study, we proposed a novel low cost dichloromethane as the carbon source to produce carbon-coated TiO_2 using a simple hydrothermal method that can be carried out at relatively low temperature.

Experimental Methods

Synthesis method. The carbon-coated TiO_2 (C-TiO_2) was synthesized using dichloromethane, CH_2Cl_2, (Fisher Chemicals, 99%) as carbon precursor while the TiO_2 used was anatase phase, TiO_2 (Sigma-Aldrich, 99.7%). The dichloromethane (20 mL) was mixed with TiO_2 (0.25 g), and then, lithium aluminium hydride, ($LiAlH_4$, 0.5 g) was added into the solution, followed by addition of sodium hydroxide aqueous (NaOH, 5 M, 15 ml) to the mixture. After ultrasonification for 30 minutes to make the mixture homogen, the mixture was placed in a stainless steel hydrothermal cell. The sample was then heated at temperature of 150 °C for 24 hours to form C-TiO_2. After the reaction completed, the solid product was collected and washed with distilled water and ethanol solution for several times in order to remove residual impurities and chloride ion before drying at 90 °C overnight. For purification process, the product (0.5 g) was stirred in solution of nitric acid (HNO_3, 3 M, 100 mL) for 30 minutes. The solution was then filtered and rinsed with distilled water for several times before drying at 90 °C for 24 hours. After drying, a brown solid product was obtained as the purified C-TiO_2.

Characterizations. The structural properties of TiO_2 and purified C-TiO_2 were characterized by X-Ray Diffraction, XRD (Bruker AXS Diffrac plus release 2000) using the Cu-Kα radiation at 40 kV and 40 mA. The optical properties of TiO_2 and prepared C-TiO_2 sample were characterized by a diffuse reflectance ultraviolet-visible spectroscopy, DR UV-Vis (Perkin Elmer Lamda 900). The surface morphology of the prepared sample was performed by scanning electron microscope, SEM (JEOL JSM-6390LV). Prior to the measurements, all samples were coated by platinum (Pt).

Results and Discussion

Structural Properties of C-TiO_2. Fig. 1 (a) shows the XRD pattern of as prepared C-TiO_2 sample. Pure anatase TiO_2 would only show diffraction peaks at 2θ of 25.3, 36.9, 37.8, 38.6, 48.1, 53.9, and 55.1° (PDF No. 86-1156). However, it is obvious that the as prepared C-TiO_2 sample has dominant diffraction peaks, which are not belong to anatase TiO_2. Some of them can be identified as the diffraction peaks of NaCl at 2θ of 26.7, 30.9, 44.4, and 55.1° (PDF No. 26-0918) and LiCl at 2θ of 22.9, 32.9, 39.1, 47.3, 53.2, 59.2° (PDF No. 02-0898), while other peaks are remained as unidentified contaminants/impurities that are originated or formed during the synthesis process. The method to remove contaminants/impurities is important since it largely depends on the reactivity of the impurities and the stability of carbon and TiO_2 towards the purification method. After purification by acid treatment, only anatase phase of TiO_2 was obtained with diffraction peaks at 27.8, 38, 48 and 55° as shown in Fig. 1 (b). This result clearly suggested that the present acid treatment was suitable and sufficient for purification of the prepared C-TiO_2.

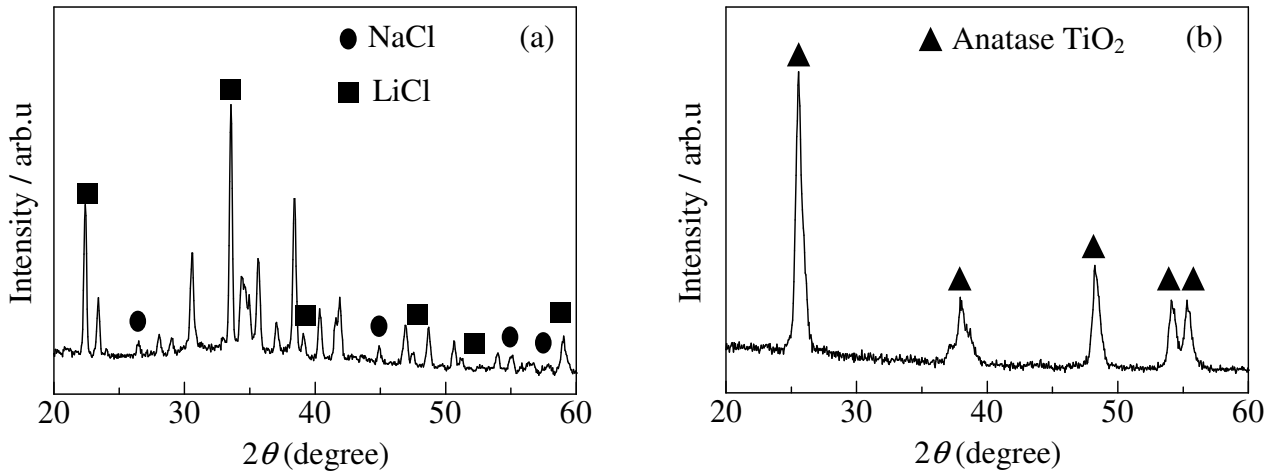

Fig. 1 XRD patterns of C-TiO_2 sample prepared by hydrothermal method, (a) as-prepared and (b) after purification process.

Optical Properties of C-TiO_2. The optical property of the purified C-TiO_2 was investigated using DR UV-visible spectroscopy by measuring the absorption peak. The recorded DR UV-visible spectra of TiO_2 and C-TiO_2 after purification are shown in Fig. 2[A] while the physical appearances of the samples are shown in Fig. 2[B]. As shown in Fig. 2[A] (a), TiO_2 showed high absorption ability at UV region with no absorption in the visible light region. On the other hand, it was obviously observed that the purified C-TiO_2 has additional absorption tails in visible region of more than 400 nm as shown in Fig. 2[A] (b), indicating the presence of carbon on the sample. The strong absorption in visible light region with the addition of carbon has been reported previously [1, 3-6, 8].

Moreover, the presence of carbon coating has been also reported to reduce the band gap of TiO_2, in which the carbon coated-TiO_2 prepared by using flame synthesis showed lowering of band gap energy of around 0.7 eV compared to the TiO_2 [8], suggesting the influence of carbon in altering the band gap energy of TiO_2. In this study, even though the presence of carbon could not be detected from XRD, it can be clearly observed from the DR UV-Vis spectra as well as its different physical appearance from white to yellowish brown colour after the addition of carbon, as shown in Fig. 2[B].

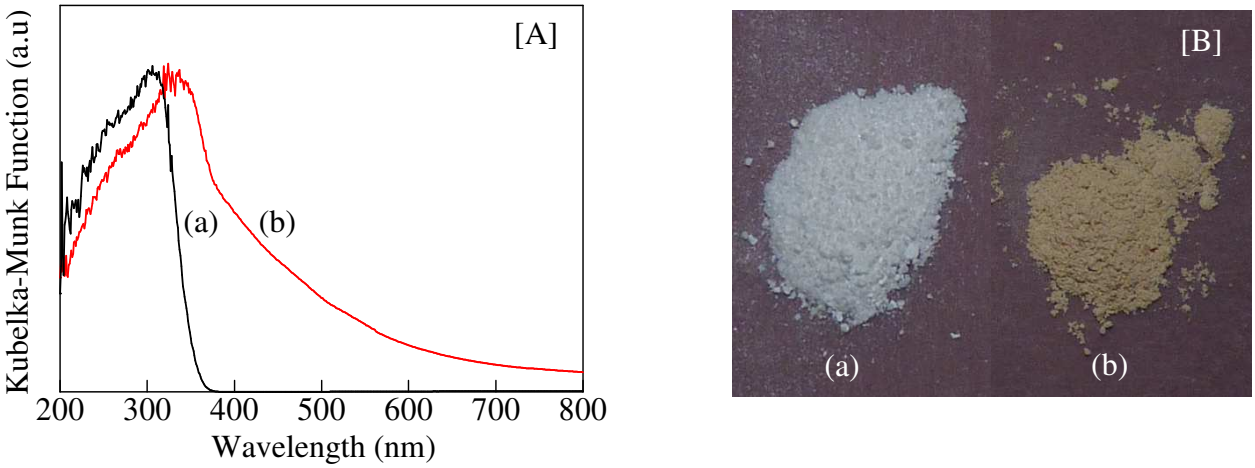

Fig. 2[A] DR UV-Vis spectra and [B] physical appearance of (a) TiO_2 and (b) purified C-TiO_2.

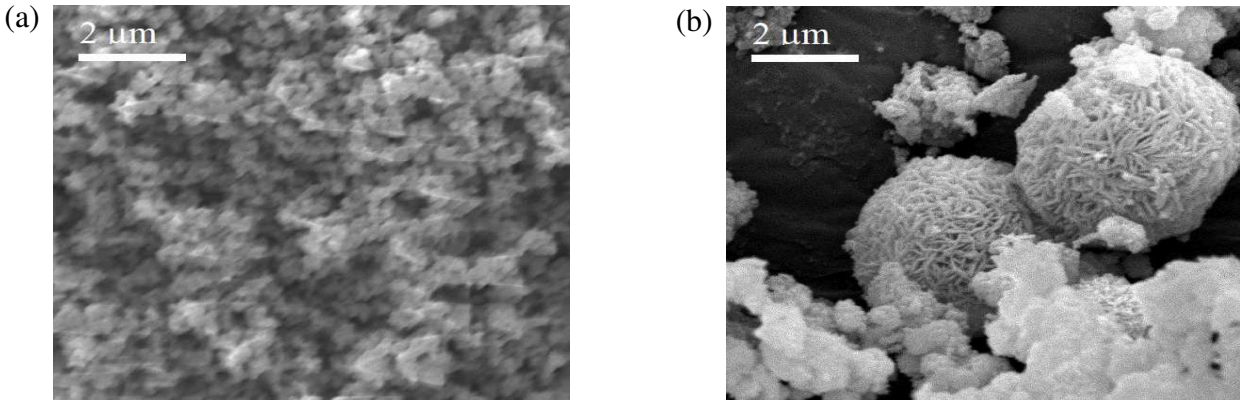

Fig. 3 SEM images of (a) TiO_2 and (b) purified C-TiO_2.

Morphology of C-TiO_2. The SEM images of the TiO_2 and purified C-TiO_2 samples are shown in Fig. 3. It can be obviously observed in Fig. 3 (a) that the TiO_2 has spherical shape with smooth surface and it has size of 300-500 nm. After introduction of carbon, the morphology was changed as shown in Fig. 3 (b). Spherical shape was still observed but agglomerated into much larger size of *ca.* 2 µm. While the spherical shape should show the TiO_2, the new small particles formed on both TiO_2 surface and its surrounding should be due to the presence of carbon. It is interesting to point out here that the TiO_2 has been coated with carbon that has a unique noodle-like structure. Those that

were not growth on the surface of TiO_2 tended to form non-uniform bulk carbon in the surrounding of the TiO_2. This might be due to the larger amount of carbon precursor compared to that of TiO_2. The carbon growth on the surface of TiO_2 nanoparticles was also reported when the mixture of dextrose and poly(ethylene glycol) was used as the carbon precursor [7]. The growth of carbon was reported to occur along spherical axis of TiO_2, thus, maintaining the spherical shape of TiO_2 after coating with the carbon. On the other hand, this study revealed the possibility to use dichloromethane as the carbon precursor to produce C-TiO_2 with unique structure, which to the best of our knowledge, has never been reported before.

Conclusions

It was demonstrated that carbon-coated TiO_2, C-TiO_2, can be prepared through simple hydrothermal method using low-cost dichloromethane as carbon precursor. XRD pattern showed that the pure anatase TiO_2 was obtained after purification process. The DR UV-Vis spectrum confirmed that the purified C-TiO_2 sample has additional absorption in the visible region, as also supported by the colour of the sample, which suggested the presence of carbon. The SEM images showed the formation of carbon on both surface with a unique noodle-like structure and surrounding of TiO_2 with no uniform bulk structure.

Acknowledgement

This work was financially supported by Ministry of Higher Education (MOHE, Malaysia) and Universiti Teknologi Malaysia (UTM, Malaysia) via Flagship Research University Grant (cost center: Q.J130000.2426.00G07).

References

[1] M. Inagaki, Carbon coating for enhancing the functionalities of materials, Carbon. 50 (2012) 3247-3266.

[2] T. Tsumura, N. Kojitani, I. Izumi, N. Iwashita, M. Toyoda, M. Inagaki, Carbon coating of anatase-type TiO_2 and photoactivity, J. Mater. Chem. 12 (2002) 1391-1396.

[3] B. Tryba, A.W. Morawski, T. Tsumura, M. Toyoda, M. Inagaki, Hybridization of adsorptivity with photocatalytic activity– carbon-coated anatase, J. Photochem. Photobiol., A. 167 (2004) 127-135.

[4] F. Jia, Z. Yao, Z. Jiang, C. Li, Preparation of carbon coated TiO_2 nanotubes film and its catalytic application for H_2 generation, Catal. Commun. 12 (2011) 497-501.

[5] M. A. Nawi, I. Nawawi, Preparation and characterization of TiO_2 coated with a thin carbon layer for photocatalytic activity under fluorescent lamp and solar light irradiations, Appl. Catal. A: Gen. 453 (2013) 80-91.

[6] L.-W. Zhang, H.-B. Fu, Y.-F Zhu, Efficient TiO_2 photocatalysts from surface hybridization of TiO_2 particles with graphite-like carbon, Adv. Funct. Mater. 18 (2008) 2180-2189.

[7] K. Olurode, G. M. Neelgund, A. Oki, Z. Luo, A facile hydrothermal approach for construction of carbon coating on TiO_2 nanoparticles, Spectrochim. Acta. Part A. 89 (2012) 333-336.

[8] D. H. Anjum, N. K. Memon, S. H. Chung, Investigating the growth mechanism and optical properties of carbon-coated titanium dioxide nanoparticles, Mater. Lett, 108 (2013) 134-138.

Advanced Materials Research Vol. 970 (2014) pp 283-287

doi:10.4028/www.scientific.net/AMR.970.283

Synthesis and Characterization of Mn^{2+} doped ZnS using Reverse Miceller Method

R. M. Ibrahim[1,a*], M.Markom[1,b], H.Abdullah[2,c]

[1]Department of Chemical Engineering and Process, Faculty of Engineering and Built Environment

Universiti Kebangsaan Malaysia, 43600 Bangi Malaysia.

[2]Department of Electrical, Electronic and System Engineering, Faculty of Engineering and Built Environment, Universiti Kebangsaan Malaysia,43600 Bangi Selangor,Malaysia

[a*]rahizana@eng.ukm.my, [b]masturah@eng.ukm.my, [c]huda@eng.ukm.my

Keywords: Nanoparticles; UV-vis absorbance spectra; quantum confinement effect; photoluminescence.

Abstract. In this work we synthesized the monodisperse of $Zn_{1-x}Mn_xS$ with x =0.00,0.02,0.04,0.06,0.08 and 0.10 nanoparticles by reverse micelle method using sodium bis(2-ethylhexyl) sulfosuccinate (AOT) as surfactant. The prepared particles were characterized using UV-Visible Spectroscopy, X-ray diffraction (XRD), Transmission Electron Microscopy (TEM) and Photoluminescence (PL) for size, morphology and optical of the samples .UV-vis absorbance spectra for all of the synthesized nanoparticles show the maximum absorption for all samples is observed at range 210 - 300 nm . The absorption edge shifted to lower wavelengths when doping with ion Mn as per UV-Vis spectroscopy. The band gap energy values were increase from 4.50eV to 4.90 eV. This blue shift is attributed to the quantum confinement effect. The size of particles is found to be 3-5nm range. The Mn^{2+} doped ZnS nanoparticles using reverse micelles method shows the enhance of PL intensity results in monodisperse nanoparticles.

Introduction

Research on nanosize semiconductors have grown rapidly over the past decade when the nanosize semiconductor showed the novel optical properties of electronic arising from quantum confinement effect[1]. When semiconductor particle size reduction to the nanometer size scale, the semiconductor band gap energy increased greatly, thereby leading to the high redox potential of the system. Among many semiconductor, zinc sulphate (ZnS), a II-VI widely used semiconductor with direct, large band gap value 3.6eV and non toxic has been research extensively due to its potential applications. More recently, the optical impurities such as transitions metal ion-doped semiconductor nanoparticles have been study [2-4]. These dopan impurities play an important role in changing the electronic structure and transition probabilities of the host material . In recent years, Manganase has been found to be a most prospective doping materials in ZnS nanoparticles. However different and even contradictory results were reported for Mn ion doped ZnS nanoparticles prepared by different methods.

In the present study, we synthesized $Zn_{1-X}Mn_xS$ nanoparticles with x=0.00,0.02,0.04,0.06,0.08 and 0.10 by reverse micelle method using n-haptane, water and AOT as a reaction medium with controlled parameter to produce the monodisperse ZnS and ZnS:Mn^{2+} nanoparticles using reverse micelles method.

Method and Materials

Synthesis of ZnS:Mn^{2+} nanoparticles were prepared in H_2O/AOT/n-haptane reverse micelle method using precipitation technique. The selected W [(H_2O)/(AOT)] in molar ratio values was 7 in all preparation solution. First, an individual reverse micelle enclosing 0.5 M Zinc acetate and 0.5 M Mangan acetate (2%) were prepared separately. The prepared two solutions were mix with continuous stirring at 80^0C. Then, another individual reverse micelles of AOT enclosing Na_2S

solution was added drop by drop into the Zn^{2+} and Mn^{2+} mixture with continuous stirring. The mixture was stirred until a homogeneous solution was obtained. The results mixture was then collected and allowed to stand for one day at room temperature for precipitation. The precipitate was repeatedly washed with ultrapure water and ethanol. Finally, the precipitate was dried in oven 4 and the product was obtained as a white powder. The same procedure was followed for remaining four doping values (4%,6%,8% and 10%). For undop ZnS, the same procedure have been done without doping. Then the free surfactant without AOT and n-haptane was also synthesized using the same precursor for sample comparison.

Results and Discussion

Optical study. The room temperature UV-vis spectra of undop ZnS and doped ZnS:Mn^{2+} are shown in Figure 1 . The absorption edge of undop ZnS is observed at the 250nm and 313nm while for all sample of ion Mn^{2+} doped ZnS show absorption edge at 240nm .The two absorption edge for undop ZnS are due to the formation of two groups size of the particles. While after doping , the graph shift to the single absorption edge value .The shifting was a results from incorporated of ion Mn^{2+} in the crystal structure of ZnS. Different percentage of ion doping in ZnS crystal structure does not shows any shifting in absorption peak but the absorption value was increased. Its indicate a wide distribution of nanoparticles at corresponding absorption wavelength area with 4 percent of doping was the best value.

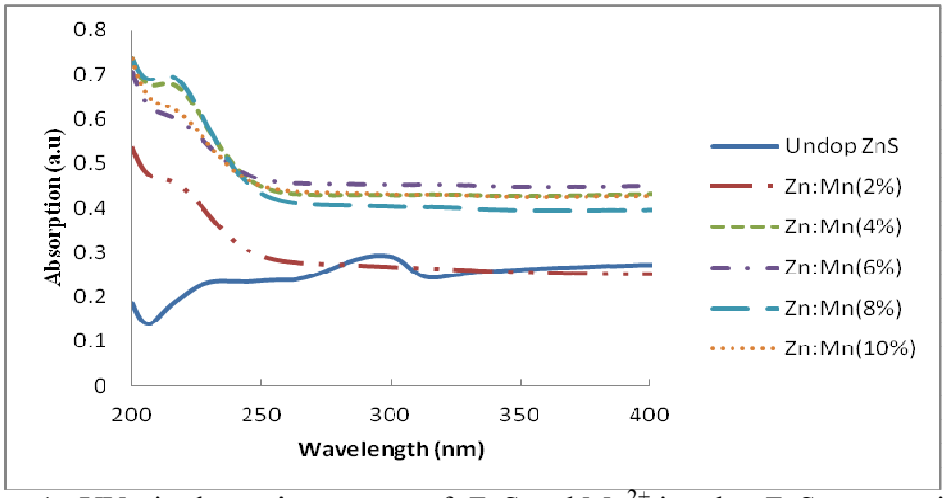

Figure 1: UV-vis absorption spectra of ZnS and Mn^{2+} ion dop ZnS nanoparticles

The optical absorption spectrum information can be used to determine the nature value of the optical bandgap . The relation between absorption coefficient (α) and incident photon energy (hv) can be written as:

$$\alpha = A(hv - E_g)^n / hv \quad (1)$$

where, A is a constant and E_g is the band gap of the material and the exponent n depends on the type of the transition. For direct and allowed transition n=1/2, indirect transition, n=2 and for direct forbidden, n = 3/2, the band gap was calculated by plotting of $(\alpha hv)^2$ versus Energy(Ev). The calculated band gap value are 3.8 eV for undop ZnS, 4.4 eV for ZnS:Mn nanoparticles. This suggests that all absorption edges are large blueshifts than the bulk ZnS (3.6 eV) crystals at room temperature [5].

X-ray diffraction. XRD pattern for prepared samples are showed in Figure 2 with broadening peaks for both samples . From the figure, the X-ray powder diffraction of nanoparticles ZnS and ZnS:Mn^{2+} revealed that both nanoparticles have zinc blende structure with plane at (1 1 1), (2 2 0)

and (3 1 1) . ZnS:Mn^{2+} nanoparticles have lesser lattice planes compare to undop ZnS nanoparticles reveal the formation of small nanoparticles than undop ZnS. From the XRD results, the average crystallize size is calculated using the Debye Scherer formula [6].

$$D = 0.89\lambda/(\beta\cos\theta) \quad (2)$$

where λ is the wavelength of incident X-ray (1.54 A) and θ is the Brangg's angle. From the calculation, the average diameter of the particles are 4.8 nm for undop ZnS and 4.2 nm for Mn^{2+} doped ZnS . According to the FWHM of the most intense peak plane, the substitution of the Zn^{2+} with Mn^{2+} ion results in a small decrease (~15%) in the lattice constant of ZnS. This decrease gives a strong evidence for the incorporation of dopant ion into the host matrix.

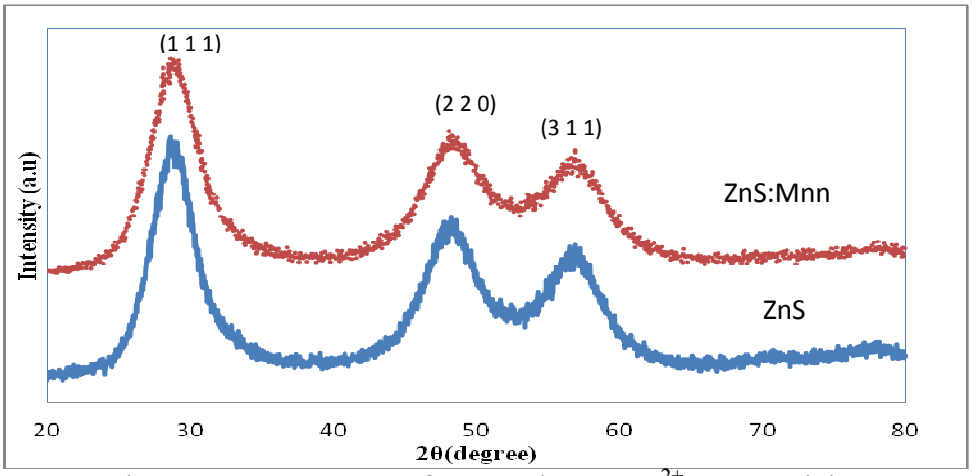

Figure 2: XRD pattern of ZnS and ZnS:Mn^{2+} nanoparticles

TEM Study. Figure 3(A) and (B) display a representative TEM images of undop ZnS and ZnS:Mn^{2+} nanoparticles. Generally, the shape of the particles in both colloids was spherical or quasi-spherical and have an average particles size of about 5 -10 nm, which is slightly increase with the value obtained from XRD analysis.

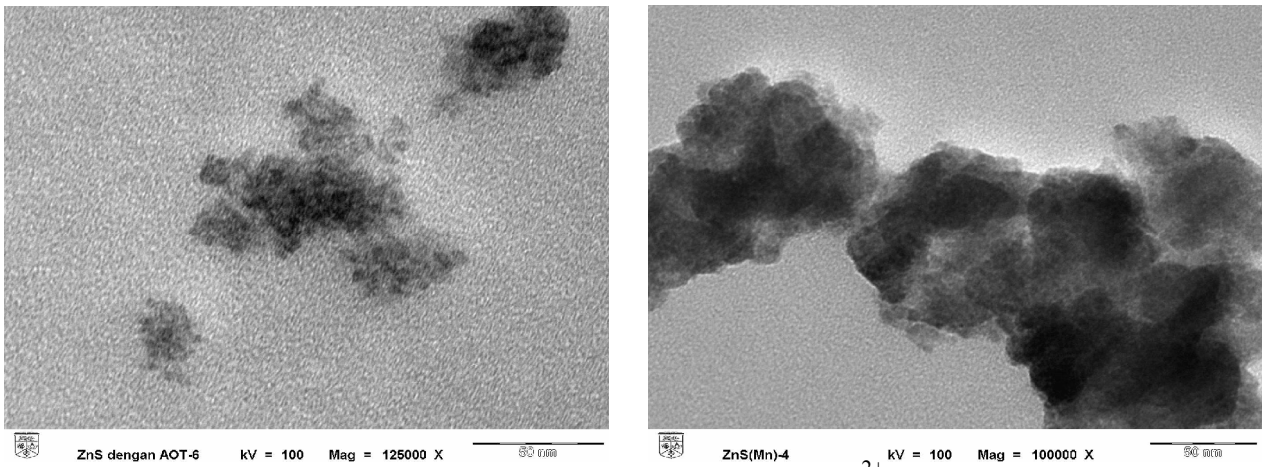

Figure 3: TEM images of (A) ZnS and (B) ZnS:Mn^{2+} nanoparticles

Photoluminescence study. Considering the graph in figure 4, the observed PL emission consists at the weak peak at 450 nm and a strong peak at 602nm. The emission intensity of the orange is ~ 33 times higher than the blues emission suggested that the quenching of blue emission happen while doping the ion Mn^{2+}. This suggested that the Mn^{2+} emission is growing at the same time there is some lost of energy in the host lattice emission [7]. From the literature most of the report show the PL emission centre for Mn^{2+} doped ZnS are between 580 – 600 nm wavelength [8]. R.M.

Krsmanović Whiffen et at [9] report that the presence of Mn^{2+} characteristic orange emission cantered at 600 nm confirmed that the samples were properly doped with Mn^{2+} ions, as the $^4T_1$-$^6A_1$ radiation transition could arise only on the basis of Mn^{2+} ions incorporated into the ZnS nanoparticles. However, not much report on the efficiency formation of homogeneous ZnS:Mn^{2+} growth. G. Murugados et at [10] in his report shows that with calculate of the ratio between intensity of orange emission to blue emission, we can get the value of efficiency of ZnS:Mn^{2+} formation. The increase efficiency indicates, increasing of homogeneous ZnS:Mn growth with decreasing the surface defect. G. Muragados et al also report that the efficiency of ZnS:Mn^{2+} was 12.62 with emission peak at 600nm. While for our observation, we find that our results have much higher efficiency value than had been reported before . This reveal that the particles growth can be controlled by the whole reverse micelles system.

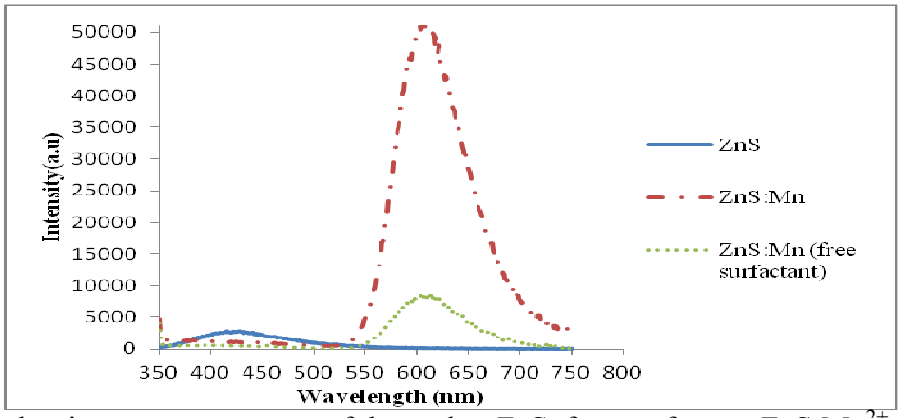

Figure 4. Photoluminescence spectrum of the undop ZnS, free-surfactant ZnS:Mn^{2+} and ZnS:Mn^{2+}

Conclusions

Mn^{2+} doped ZnS nanoparticles have been successfully synthesis by reverse micelles method using precipitation technique. This study reveal that the formation of Mn^{2+} doped ZnS are more successful using Reverse Micellles methods. All samples have zinc blande structure, as observe by X-ray diffraction he average size lies in the range of 4.0 – 5.0nm for the all samples and particles and band gap values increase greatly from the bulk value. The optical studies show that the absorption peak of the doped ZnS nanoparticles are markedly blue shifted which clearly indicate the strong quantum size effect.

Acknowledgement

This work is financially supported by Universiti Kebangsaan Malaysia which under Project UKM-GUP-2011-051.

References

[1] Karen Grieve, Paul Mulvaney, Franz Grrieser, Synthesis and electronic properties of semiconductor nanoparticles/quantum dot. Current opinion in colloid & interface science 5(2000)168-172

[2] Ping Yang, Mengkai Leuf , Dong Xu, Duorong Yuan, Chunfeng Song, Suwen Liu, Xiufeng Cheng. Luminescence characteristics of ZnS nanoparticles co-doped with Ni^{2+} and Mn^{2+}. Optical Materials 24 (2003) 497–502.

[3] G.Murugadoss, B.Rajamannan, V.Ramasamy, G.Viruthalagiri. Synthesis and Characterization of Mn^{2+} Doped ZnS Luminescent Nanocrystal. Journal of Ovonic Research Vol. 5, anao.4, August 2009, p.107 – 116.

[4] R.Saravanan ,Growth and local structure analysis of ZnS nanoparticles. Physic B 405(2010) 3700-3703.

[5] Huaming Yang, Chenghuan Huang, Xiaohui Su, Aidong Tang. Microwave-assisted synthesis and luminescent properties of pure and doped ZnS nanoparticles. Journal of Alloys and Compounds, Volume 402, Issues 1–2, 27 October 2005, Pages 274-277.

[6] He Hu, Weihua Zhan, Synthesis and properties of transition metals and rare-earth metals doped ZnS nanoparticles. Optical materials 28(2006) 536-550.

[7] Yoshihiko Kanemitsu, Atsushi Ishizumi, Luminescence properties of impurity-doped semiconductor nanoparticles. Journal of luminescence 119-120(2006)161-166.

[8] S. Ummartyotin, N.Bunnak, J. Juntaro, M. Sain, H. Manuspiya, Solid State Sciences 14 (2012) 299-304.

[9] R.M. Krsmanović Whiffen a,n, D.J.Jovanović a, Ž. Antić a, B.Bártová b, D.Milivojević a, M.D. Dramićanin a, M.G.Brik .Structural,optical and crystal field analyses of undoped and Mn^{2+}-doped ZnS nanoparticles synthesized via reverse micelle route Journal of Luminescence146(2014)133–140.

[10] G.Murugadoss. Synthesis, optical, structural and thermal characterization of Mn^{2+} doped ZnS nanoparticles using reverse micelle metod. Journal of luminescence 131(2011)2216-2223.

Advanced Materials Research Vol. 970 (2014) pp 288-292

doi:10.4028/www.scientific.net/AMR.970.288

Synthesis of Silica-coated Copper Nanoparticles and its Application to Red Color Glaze

Shohei Shiomi[1, 2, a*], Eiichiro Matsubara[1], Hajime Taguchi[2], Shozo Hashida[2] and Tadanori Yokoyama[2]

[1]Department of Materials Science and Engineering, Kyoto University, Yoshida-honmachi, Sakyo-ku, Kyoto, 606-8501 Japan

[2]Kyoto Municipal Institute of Industrial Technology and Culture, 91, Chudoji Awata-cho, Shimogyo-ku, Kyoto, 600-8815, Japan

[a*]shiomi.shouhei.86m@st.kyoto-u.ac.jp

Keywords: Nanoparticles, Copper, Silica, Core-shell, Red color glaze

Abstract. A core-shell structure of Cu@SiO_2, namely, silica-coated Cu nanoparticles, was synthesized by a simple liquid phase reaction. The reaction bath was optimized by evaluating the balance between the dissolution behavior of Cu nanoparticles and the deposition rate of SiO_2 shells for coating. The Cu nanoparticles were fabricated by an electroless deposition method. The deposition and dissolution behaviors of Cu were quantitatively evaluated by quartz crystal microbalance (QCM) measurements, combined with the reducing ability evaluated by the mixed potential measurements. SiO_2 shells were synthesized by a sol-gel process of tetraethyl orthosilicate (TEOS). The optimal responsiveness bath condition was also elucidated by the QCM measurement to evaluate the deposition rate of SiO_2 shells, which was much faster than the dissolution rate of Cu nanoparticles, indicating that the SiO_2 shells sufficiently coated the Cu nanoparticles. The stability of annealed Cu@SiO_2 nanoparticles was considerably increased and by using them, the red color glaze is achieved in easy and safe way.

Introduction

Metal nanoparticles generally have various characteristic properties which include both advantages and disadvantages. For instance, noble metal nanoparticles have attracted the attention due to their high electrical and thermal conductivity, catalytic activity, the surface plasmon resonance and so on [1-4]. However, nanoparticles are easily agglomerated and oxidized compared with the bulk materials [5,6] as they possess large active surfaces, thus it is very difficult to handle the nanoparticles. In order to overcome this problem, synthesis and characterization of "core-shell structures" have widely investigated. Especially the silica-coated metal nanoparticles (metal@SiO_2 nanoparticles) are mostly fabricated by sol-gel process of tetraethyl orthosilicate (TEOS) with NH_3 as an initiator of the reaction [7-10]. In these reports, however, core-shell structures are achieved only by the trial-and-error approaches, and the quantitative evaluation of the dissolution and deposition behaviors of target materials for optimizing the reaction bath has rarely reported. Since the dissolution of metals is induced by the decrease of the reducing ability in reaction bath, the measurements of dissolution rate accompanied with electrochemical measurements are important for the accurate evaluation of the dissolution behavior of metals. We suggest the developed *in situ* quartz crystal microbalance (QCM) measurements for determining the optimized reaction bath for the fabrication of core-shell nanoparticles. The deposition rate and the termination time of synthesis reaction of nanoparticles are quantitatively evaluated by the QCM measurements, and moreover, the electrochemical information is also available by conjunction with the mixed potential measurements [11-14].

Generally the fabrication of Cu@SiO_2 nanoparticles is difficult due to the character of Cu nanoparticles which is easily oxidized during the coating process and soluble in NH_3 solutions used as an initiator of sol-gel process. Therefore, control of the reaction bath is crucial in the fabrication of Cu@SiO_2 nanoparticles. In this study, we have successfully synthesized well silica-coated Cu

nanoparticles by a simple liquid-phase reaction by using the appropriate reaction bath condition determined by the QCM and mixed potential measurements.

Since ancient times, red glass, especially transparent and deep red glass, has been always desired, and Au or Cu has often been used as a pigment of red color glass and glaze. For example, in Kyoto, Japan, a technique of manufacturing the oxblood (deep red) glaze, called *shinsha*, using copper has been traditionally developed by proficient craftworkers. *Shinsha* glaze is generally achieved by means of heat-treating glass materials with metallic copper or copper oxide at high temperature under reducing atmosphere (CO gas). Therefore, *shinsha* glaze is one of the most dangerous and difficult glazes. We also suggest that by using the silica-coated and well-stabilized Cu nanoparticles as a pigment of glaze, red color would be achieved in more simple and safe way compared with current manufacturing method. In this work, for the evaluation of the color of glaze, we use L*a*b* color space. The L*a*b* color model is based on the human perception, and L* value visually corresponds to the lightness (L* = 0 indicates black and L* = 100 indicates white), and a* and b* value correspond to the colors (a* = negative values indicate green, a* = positive values indicate red, b* = negative values indicate blue and b* = positive values indicate yellow).

Experimental Procedures

CuO powder is purchased from Kanto Chemical, Inc. Ammonia aqueous solution (NH_3, 28 %), hydrazine monohydrate (N_2H_4 H_2O, 98 %), gelatin fine powder, ethanol (C_2H_5OH, 99.5 %), tetraethyl orthosilicate ($Si(OC_2H_5)_4$, TEOS, 95 %) and nitric acid (HNO_3, 60 %) are purchased from Nacalai Tesque, Inc. and used without further purification. Cu nanoparticles are synthesized by an electroless deposition method, and silica-shells are synthesized by a sol-gel process in one beaker with a simple procedure as shown in Figure 1.

The precursor of Cu nanoparticles was first prepared by CuO powder (3.15×10^{-3} mole, 0.25 g) dispersed into NH_3 aqueous solution (28 %, 19 ml) and gelatin (0.20 g) was added as a dispersing agent. Reducing agent solution was also prepared by hydrazine (0.08 mole, 2.0 g) mixed with NH_3 aqueous solution (28 %, 19 ml) and gelatin (0.20 g). These two solutions were agitated separately at a rate of 500 rpm with a magnetic stirrer. The temperature of the solutions was kept at 323 K throughout the reaction for synthesis of Cu nanoparticles. Additionally, the effect of dissolved oxygen was minimized by bubbling nitrogen gas for more than 30 minutes. Then the two solutions were mixed to start the reaction. In parallel to the above process, ethanol (32 ml) and TEOS (8 ml) was mixed together. The nitrogen gas was also introduced for more than 30 minutes. This solution was added to the synthesized Cu nanoparticles suspension at room temperature and stirred for more than 20 minutes to fabricate SiO_2 shells on the Cu nanoparticles. Nitrogen gas bubbling was consistently continued through this process. Finally the product was annealed in Ar gas atmosphere at 973 K for 10 hours to increase the stability of the SiO_2 shells and remove the extra gelatin.

The morphology of products was observed by a field-emission scanning electron microscope (SEM: JEOL Ltd., JSM-6500F) and a transmission electron microscope (TEM: JEOL Ltd., JEM-2010). The crystalline structure of products was investigated by X-ray diffraction (XRD: Rigaku Corporation, RINT-2500). In the XRD measurement, a soda-silicate glass capillary tube (Hilgenberg GmbH, Markröhrchen aus Glas Nr.10) or a low-background single-crystal silicon sample holder was used to hold the nanoparticles. The copper-sputtered QCM electrode (SEIKO EG&G, QA-A9M-CU) was immersed in the solution for monitoring the weight change of the QCM electrode. The thickness of QCM electrode was calculated from the density of Cu (8.9 g cm^{-3}) and the frequency of quartz substrate using the Sauerbrey equation [11,13]. At the same time as the QCM measurement, the reducing ability of a solution was evaluated by the mixed potential measured by a potentiostat/galvanostat (Hokuto Denko Co., Ltd., HA-151) using an Ag/AgCl electrode (HORIBA, 2565A-10T) as a reference electrode.

In order to check the color of glaze which contain the stabilized Cu nanoparticles, the synthesized Cu@SiO_2 particles (0.04 g) are mixed with glass frit (*raku* frit) (1.0 g) in a mortar with several drops of water, and the mixture was put on a test piece (white ceramics plate), then heat-treated in 1073 K in

ambient atmosphere. The color of fabricated glaze was quantified by L*a*b* color values measured by a colorimeter (Nippon Denshoku, NF333 spectrophotometer).

Results and Discussions

Figure 2(a) and Figure 2(b) show the SEM image and the XRD pattern of a product synthesized by mixing CuO suspension and hydrazine solution. The Cu nanoparticles are synthesized by the electroless deposition method. The diameter of Cu nanoparticles is ~30 nm. The sample was held in a soda-silicate glass capillary tube for XRD measurement. Figure 3(a) and Figure 3(c) show the dissolution behavior of Cu and mixed potential in NH_3 aqueous solution while the reducing ability was maintained, and Figure 3(b) and Figure 3(d) show the dissolution behavior of Cu and mixed potential after the decomposition of reducing agent, which means the lack of reducing ability. The stability of Cu in NH_3 aqueous solution is quantitatively evaluated by QCM and mixed potential measurements. When the mixed potential is lower than the oxidation–reduction potential of Cu/Cu(I) redox pair, Cu nanoparticles are prevented from dissolution for at least 30 minutes as shown in Figure 3(a), on the other hand, when the mixed potential is higher than the oxidation–reduction potential, Cu is continuously dissolved into the solution as shown in Figure 3(c). This result indicates that the electrochemical evaluation is effective to examine the reducing ability of solutions and dissolution behavior of nanoparticles. Figure 4 shows the time transition in the deposition amount of products on a QCM electrode during the fabrication of SiO_2. The change in the deposition amount is almost flat after 15 minutes, and thus the reaction of silica-coating is estimated to end in about 15 minutes. As the Cu nanoparticles are kept precipitated at least 30 minutes during the reducing ability is maintained as shown in Figure 3(a), the SiO_2 shells were sufficiently formed before the dissolution of Cu nanoparticles. Figure 5(a) and Figure 5(b) show the TEM image and the XRD pattern of synthesized Cu@SiO_2 nanoparticles after annealing process. The sample was held on a low-background single-crystal silicon sample holder for XRD measurement. As shown in Figure 5, Cu nanoparticles remains and the thickness of SiO_2 shell is about 30-40 nm. Figure 6(a) and Figure 6(b) show the appearance and the color value in L*a*b* color space of glaze containing synthesized Cu@SiO_2 nanoparticles. Cu nanoparticles were sufficiently stabilized by the SiO_2 shells and stably dispersed in the glaze, and thus the red color is achieved even in ambient atmosphere as shown in Figure 6.

Summary

In the present work, we have stabilized Cu nanoparticles by forming uniform SiO_2 shells on the nanoparticles via simple liquid phase reaction. Cu nanoparticles are synthesized by electroless deposition method. The electrochemical evaluation of deposition behavior of metallic nanoparticles has been attempted in some previous reports, but in this work, we also found that the measurement of QCM and mixed potential is a powerful tool for verifying the dissolving behavior of Cu. By developed QCM measurement, we have verified that Cu nanoparticles were stably precipitated in the solution bath for at least 30 minutes while the reducing ability of the solution was maintained by the reducing agent. Furthermore, in the sol-gel process of TEOS, the formation rate of SiO_2 was also verified by QCM measurement, and SiO_2 shells were fabricated much faster than the dissolution of Cu nanoparticles in this procedure, which is important for the fabrication of well coated Cu nanoparticles. The stability of annealed products was considerably increased, and by using annealed Cu@SiO_2 particles, red color glaze was achieved in easier and safer way compared with current manufacturing method.

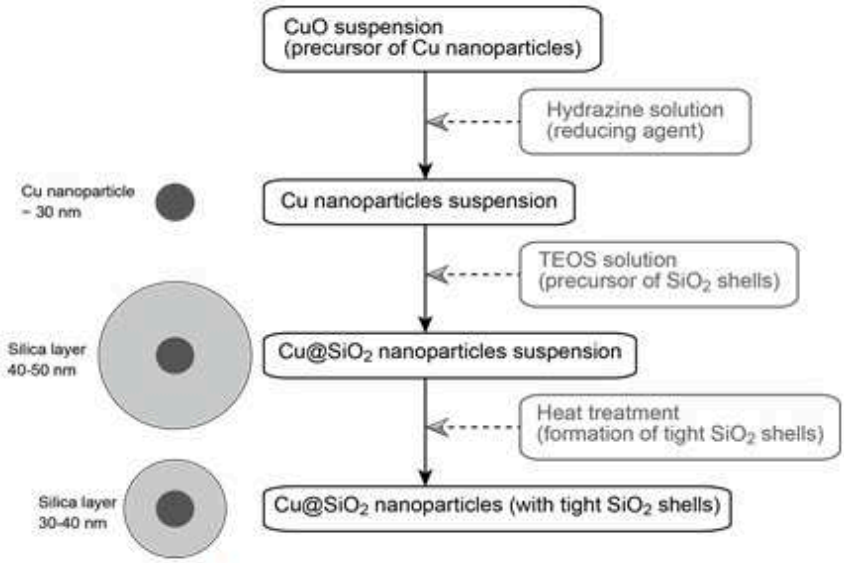

Fig. 1. Schematic diagram of the whole procedure of synthesis of $Cu@SiO_2$ nanoparticles

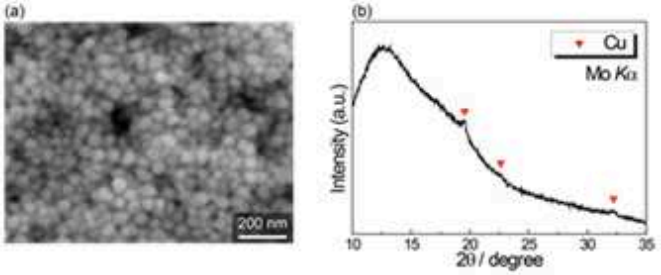

Fig. 2. (a) SEM image and (b) XRD pattern of Cu nanoparticles

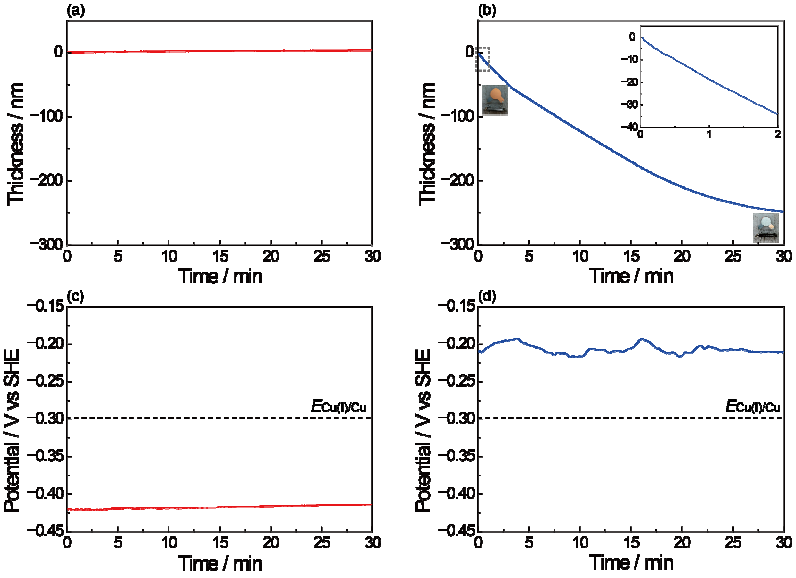

Fig. 3. Time transition in the thickness of copper-sputtered QCM electrodes immersed in Cu nanoparticles' suspension (a) during the reducing ability was maintained and (b) after the decomposition of reducing agent, and (c), (d) mixed potentials in the Cu nanoparticles' suspension measured at the same time as (a) and (b)

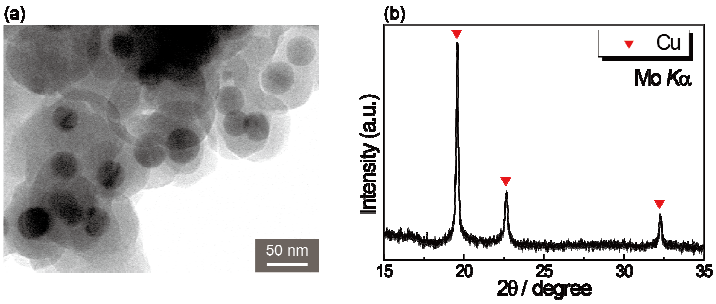

Fig. 5. (a) TEM image and (b) XRD pattern of Cu@SiO_2 core-shell particles which were annealed to form tight SiO_2 shells

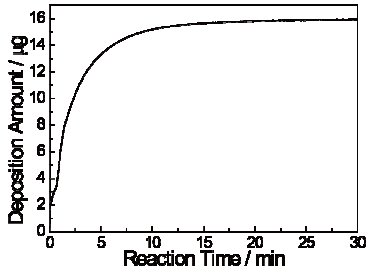

Fig. 4. Time transition in the deposition amount of SiO_2 on a QCM substrate during the fabrication of SiO_2 shells

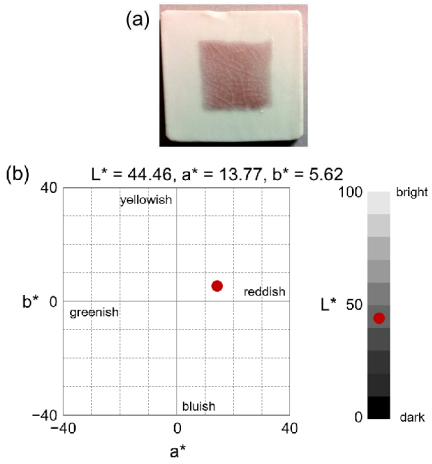

Fig. 6. (a) Photograph and (b) color values in L*a*b* color space of glaze of Cu@SiO_2 nanoparticles

References

[1] S. Link, M. A. El-Sayed, J. Phys. Chem. B. 103 (1999) 8410–8426
[2] Y. Li, Y. Wu, B. S. Ong, J. Am. Chem. Soc. 127 (2005) 3266–7
[3] X. Luo, A. Morrin, A. J. Killard, M. R. Smyth, Electroanal. 18 (2006) 319–326
[4] N. Lopez, J. Catal. 223 (2004) 232–235
[5] S. Jeong, K. Woo, D. Kim, S. Lim, J. S. Kim, H. Shin, Y. Xia, J. Moon, Adv. Funct. Mater. 18 (2008) 679–686
[6] P. Kanninen, C. Johans, J. Merta, K. Kontturi, J. Colloid Interf. Sci. 318 (2008) 88–95
[7] Y. Lu, Y. Yin, Z. Li, Y. Xia, Nano Lett. 2 (2002) 785–788
[8] E. Mine, A. Yamada, Y. Kobayashi, M. Konno, J. Colloid Interf. Sci. 264 (2003) 385–390
[9] Y. Kobayashi, H. Katakami, E. Mine, D. Nagao, M. Konno, L. M. Liz-Marzán, J. Colloid Interf. Sci. 283 (2005) 392–396
[10] J. Xu, C. C. Perry, J. Non-Cryst. Solids. 353 (2007) 1212–1215
[11] S. Yagi, H. Nakanishi, E. Matsubara, S. Matsubara, T. Ichitsubo, K. Hosoya, Y. Matsuba. J. Electrochem. Soc. 155 (2008) D474-D479
[12] S. Yagi, H. Nakanishi, T. Ichitsubo, E. Matsubara, J. Electrochem. Soc. 156 (2009) D321-D325
[13] S. Yagi, M. Kawamori, E. Matsubara, Electrochem. Solid-St. 13 (2010) E1-E3
[14] S. Yagi, M. Kawamori, E. Matsubara, J. Electrochem. Soc. 157 (2010) E92-E97

Advanced Materials Research Vol. 970 (2014) pp 293-296

doi:10.4028/www.scientific.net/AMR.970.293

Synthesis, Optical, Photocatalytic and Bactericidal Properties of Nanocrystalline ZnO Powders by Precipitation Method

Sumetha Suwanboon[1,4,a*],Pongsaton Amornpitoksuk[2,4,b],Phuwadol Bangrak[3,c]

[1]Department of Materials Science and Technology, Faculty of Science, Prince of Songkla University, Hat Yai, Songkhla 90112 Thailand

[2]Department of Chemistry, Faculty of Science, Prince of Songkla University, Hat Yai, Songkhla 90112 Thailand

[3]School of Science, Walailak University, Nakhon Si Thammarat 80160 Thailand

[4]Center of Excellence in Nanotechnology for Energy (CENE), Prince of Songkla University, Hat Yai, Songkhla 90112 Thailand

[a*]ssuwanboon@yahoo.com, [b]ampongsa@yahoo.com, [c]phuwadol1975@gmail.com

Keywords: ZnO; n-propylamine; precipitation; photocatalytic property; antibacterial activity.

Abstract. Nanocrystalline ZnO powders were synthesized by precipitation method. The n-propylamine was used as capping agent. The crystallite size of ZnO powders depended on the n-propylamine concentration. ZnO powders exhibited as agglomerated spherical shape. The optical band gap of ZnO powders were varied in a range of 3.204-3.219 eV. The photocatalytic efficiency of ZnO powders for degradation of methylene blue (MB) increased as a function of UV irradiation time and the photocatalytic efficiency was over 80% after UV irradiating for 1 h. The highest photocatalytic efficiency was 96% after UV irradiating for 1 h obtained from nanocrystalline ZnO powders modified with 0.025 mol of n-propylamine (R = 1). Nanocrystalline ZnO powders caused more damage to *Staphylococcus aureus* (*S. aureus*) than *Escherichia coli* (*E. coli*).

Intorduction

ZnO is an n-type II-VI compound semiconductor with a wide band gap of about 3.37 eV and a large exciton binding energy of 60 meV at room temperature [1]. Therefore, ZnO has attracted tremendous attention in many applications such as a catalyst [2], as an antibacterial agent [3] and for electrical and optical devices [4]. Recently, ZnO powders can be synthesized by various routes such as sol-gel [1], hydrothermal [5], thermal decomposition [6] and precipitation [7]. Among these, a precipitation method is one of popular choice due to it is unsophisticated and low cost [7]. Moreover, the morphology of ZnO was controlled easily by modifying the solution with capping agent and dopant [6]. In this study, the effect of n-propylamine concentration on structural properties was investigated because n-propylamine has a functional group that contains a basic nitrogen atom. So, the adsorption process can occur easily by sharing of the lone pair of electrons on the nitrogen atom by the oxygen atoms of ZnO [3] and only few reports were studied the influence of n-propylamine on the properties of ZnO. In this study, the dependence of optical, photocatalytic and antibacterial properties on particle size was also studied.

Experimental

First, the mixtures of 0.125 mol of lithium hydroxide (LiOH) and 0, 0.025, 0.05 and 0.075 mol of n-propylamine (C_3H_9N) were dissolved in 100 mL of distilled water by magnetic stirring. Secondly, the 0.025 mol of zinc acetate dihydrate ($Zn(CH_3COO)_2 \cdot 2H_2O$) was dissolved in 100 mL distilled water by magnetic stirring. The mole ratio of C_3H_9N to $Zn(CH_3COO)_2 \cdot 2H_2O$ (R) was 0, 1, 2 and 3, respectively. Then, the $Zn(CH_3COO)_2 \cdot 2H_2O$ solution was added dropwise into the mixtures of LiOH and C_3H_9N and the reaction products were heated at 60 ^oC for 1 h before filtering, washing with distilled water, rinsing with ethanol, drying at room temperature and calcining at 600 ^oC for 1 h.

The crystal structure and morphology of the samples were carried out by the X-ray diffraction (XRD) method (X'Pert, MPD, Philips) and scanning electron microscope (SEM, QUANTA 400, FEI), respectively. The diffuse reflectance spectra of the samples were recorded by the UV-Vis spectrophotometer (UV-Vis 2450, Shimadzu). For photocatalytic determination, samples of the ZnO powders (150 mg) were magnetically stirred in 150 mL of 1.5×10^{-5} M MB solution (pH = 6.5). A mixture was stirred for 30 min to reach the adsorption/desorption equilibrium in the dark. Then, the mixture was irradiated using three parallel blacklight fluorescent tubes (15 W). The tubes efficiently emit UVA at 315-400 nm. 3 mL of the MB solution was collected after irradiation time of 0.5, 1.0, 1.5, 2.0, 2.5 and 3 h and centrifuged to separate the powders. The concentrations of the remaining MB solutions were determined using a UV-vis spectrophotometer (Lambda 25, Perkin-Elmer) at 665 nm. The antibacterial property of ZnO powders was determined by a broth microdilution method to evaluate the minimum inhibitory concentration (MIC) value as previously described [2].

Results and discussion

The influence of n-propylamine concentrations on the crystal structure is presented in Fig. 1.

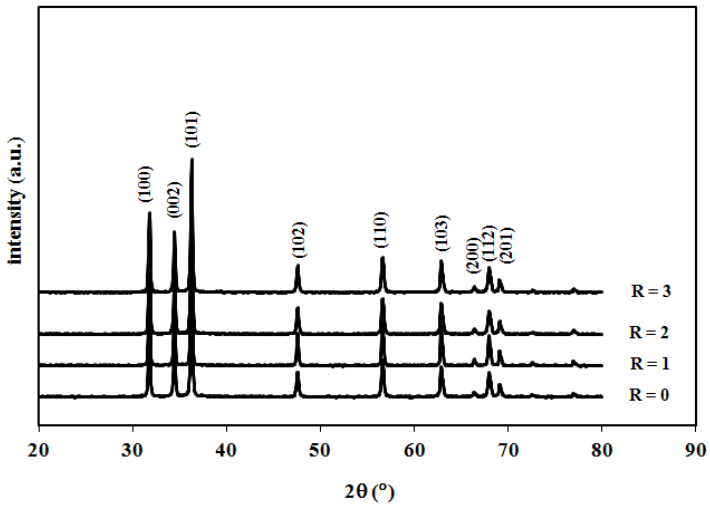

Fig. 1. XRD patterns of ZnO powders prepared with different n-propylamine concentrations.

It was evident that the diffraction peaks of all samples exhibited a hexagonal wurtzite structure (JCPDS 36-1451). The crystallite size was calculated by the Scherrer formula [1] and the results are presented in Table 1.

Table 1. Structural, optical and bactericidal properties of ZnO powders prepared with different n-propylamine concentrations.

R	D [nm]	E_g [eV]	Minimum Inhibitory Concentration (MIC) [mg/mL]	
			S. aureus	*E. coli*
0	44.47	3.219	1.5625	50
1	53.98	3.204	6.25	-
2	43.29	3.210	1.5625	50
3	42.46	3.210	1.5625	50

It was found that the crystallite size of ZnO powders increased when R was increased to 1 but decreased as R was further increased. This is because the n-propylamine induced the crystal growth when R = 1. The n-propylamine acted as a capping agent when R was higher than 1 as in the case of polyvinylpyrroridone [1]. This was in good agreement with the XRD analysis. Fig. 2 shows that n-propylamine concentration did not influence the particle shape, but it affected the particle size of ZnO powders.

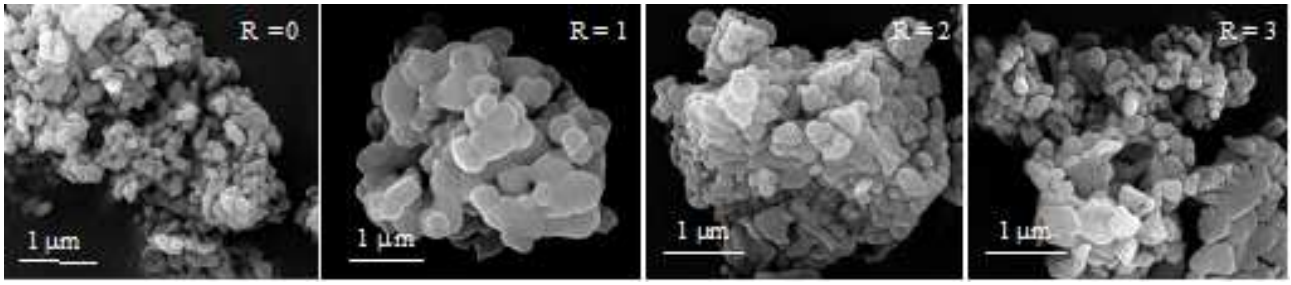

Fig. 2. SEM images of ZnO powders prepared with different n-propylamine concentrations.

Fig. 3 (a) shows the plots of $(\alpha E)^2$ versus E (where α is the absorbance coefficient and E is the photon energy) of ZnO powders prepared with different n-propylamine concentrations. The extrapolated E_g values of ZnO powders are shown in Table 1. The E_g value of the samples increased when the particle size decreased [3].

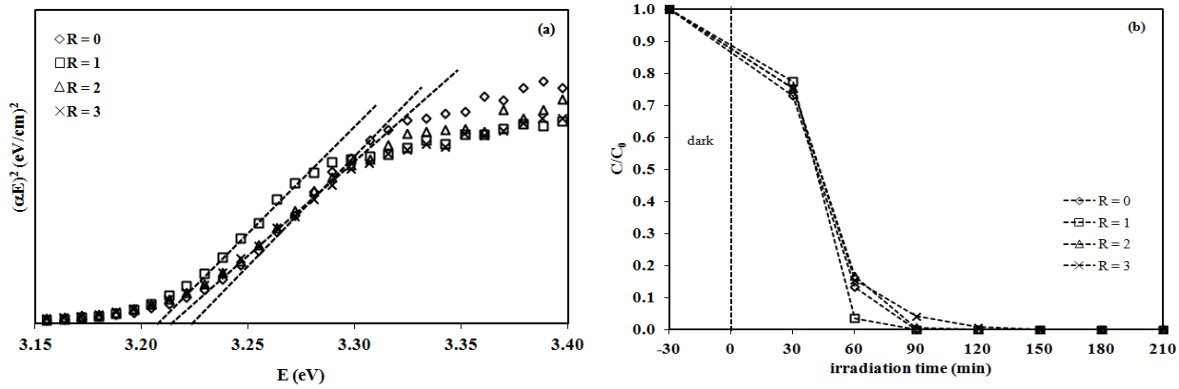

Fig. 3 (a) shows the plots of $(\alpha E)^2$ versus E for evaluating of E_g and (b) the efficiency of photocatalytic degradation of ZnO powders prepared with different n-propylamine concentrations.

Fig. 3 (b) shows the efficiency of photocatalytic degradation of ZnO powders. It was evident that the ZnO powders can more degrade the MB when the UV was irradiated for a longer time. Considering the influence of ZnO powders prepared with different n-propylamine concentrations, the highest efficiency of photocatalytic degradation when UV irradiating for 1 h was obtained from ZnO powders prepared at R = 1. This is because the sample had more specific plane for oxidizing the MB molecules due to the OH species could preferentially adsorb onto the facet to produce the hydroxyl radical ($^{\bullet}$OH) [3, 8]. Moreover, the ZnO powders prepared at R = 1 had narrowest E_g value, this might give rise to have more excited electrons in the conduction bands, so higher photocatalytic efficiency was obtained. In this study, all ZnO powders can degrade the MB completely within 150 min.

From Table 1, it was observed that the ZnO powders can more damage the *S. aureus* than *E. coli* because the bacteria had different structures [2]. In this study, the ZnO powders prepared at R = 1 had lowest efficiency, this is because the ZnO prepared at R = 1 had the largest particle size. On the other hand, ZnO powders prepared at R = 0, 2 and 3 had similar effect towards *S. aureus* and *E. coli*. This might be due to the particle sizes were in the same range [2]. The smaller particle size could have higher surface area and the Zn^{2+} ions could release increasingly from the particle and could more interact with bacteria, so the higher antibacterial activity was obtained when R = 0, 2 and 3 [9].

Conclusion

The ZnO powders with hexagonal wurtzite structure were successfully prepared by precipitation method from n-propylamine-modified lithium hydroxide solution. The n-propylamine influenced the particle growth, but it did not affect the particle shape. The E_g value of ZnO powders was in a range of 3.204-3.219 eV depending on the particle size. The smallest particle size gave

widest E_g value of 3.219 eV. The ZnO powders with largest particle size and specific plane (R = 1) exhibited the highest photocatalytic efficiency. ZnO powders can damage more *S. aureus* than *E. coli* and the smaller particle size can more damage the bacteria.

Acknowledgement

This research was supported by the Prince of Songkla University under the Contract number SCI560335s.

References

[1] S. Suwanboon, Structural and optical properties of nanocrystalline ZnO powder from sol-gel method, ScienceAsia. 34 (2008) 31-34.

[2] S. Suwanboon, P. Amornpitoksuk, P. Bangrak, N. Muensit, Optical, photocatalytic and bactericidal properties of $Zn_{1-x}La_xO$ and $Zn_{1-x}Mg_xO$ nanostructures prepared by a sol-gel method, Ceram. Int. 39 (2013) 5597-5608.

[3] M. Ramani, S. Ponnusamy, C. Muthamizhchelvan, From zinc oxide nanoparticles to microflowers: A study of growth kinetics and biocidal activity, Mater. Sci. Eng C. 32 (2012) 2381-2389.

[4] H. Kim, Y. Kwon, Y. Choe, Fabrication of nanostructured ZnO film as a hole-conducting layer of organic photovoltaic cell, Nanoscale Res. Lett. 8 (2013) 240.

[5] Y. Sun, H. Guo, F. Jiang, R. Yuan, J. Zhang, X. Zeng, T. Zhou, Y. Qiu, B. Zhang, K. Xu, H. Yang, Spatial-resolved cathode luminescence study of S-doped ZnO particles for the luminescence of UV, green and orange band emission, Appl. Surf. Sci. 283 (2013) 258-262.

[6] S. Suwanboon, P. Amornpitoksuk, A. Sukolrat, Dependence of optical properties on doping metal, crystallite size and defect concentration of M-doped ZnO nanopowders (M = Al, Mg, Ti), Ceram. Int. 37 (2011) 1359-1365.

[7] S. Suwanboon, P. Amornpitoksuk, A. Sukolrat, N. Muensit, Optical and photocatalytic properties of La-doped ZnO nanoparticles prepared via precipitation and mechanical milling method, Ceram. Int. 39 (2013) 2811-2819.

[8] K. Intarasuwan, P. Amornpitoksuk, S. Suwanboon, Effect of the mixing rate on the morphology and photocatalytic activity of ZnO powders prepared by a precipitation method, Adv. Powder Technol. 24 (2013) 999-1005.

[9] W. Zhang, G. Tu, H. Zhang, Y. Zheng, L. Yang, synthesis and antibacterial activity of mesoporous zinc oxide particle with high specific surface area, Mater. Lett. 114 (2014) 119-121.

CHAPTER 13:

Polymers

Advanced Materials Research Vol. 970 (2014) pp 299-303

doi:10.4028/www.scientific.net/AMR.970.299

Alumina reinforced epoxidized natural rubber in latex phase mixing: Effect of alumina content

C. Khaokong[1, a*], P. Phinyocheep[2, b]

[1]Department of Materials Science and Technology, Faculty of Science, Prince of Songkla University,
Hatyai, Songkhla 90112, Thailand

[2]Department of Chemistry, Faculty of Science, Mahidol University, Bangkok 10400, Thailand
[a*]chuanpit.k@psu.ac.th, [b]pranee.phi@mahidol.ac.th

Keywords: Epoxidized natural rubber, Latex phase mixing, Alumina, Epoxidation

Abstract. This work is preliminary studied of alumina-reinforced epoxidized natural rubber prepared via latex-mixing method without coupling agent. The effect of alumina content on distribution of filler and mechanical properties was investigated. Epoxidized natural rubber latex (ENR) was synthesized by *in situ* epoxidation of natural rubber using formic acid and hydrogen peroxide. The vulcanizing chemicals and alumina were then added in to ENR latex. The alumina content was varied from 10 to 75 phr. Prevulcanization at 70ºC for 24 h and post-vulcanization at 110ºC for 15 minutes was performed. The mixing time for a hour at mixing speed 600 rpm was chosen due to it shows the regular dispersion of filler in the matrix. The alumina content which can be added in epoxidized natural rubber decreased as epoxidation increased. The amount of alumina added was limited by the rigidity of high epoxidation content rubber. Modulus was increased with the increased of alumina content, whereas at alumina content 10 phr give the highest tensile strength corresponding to well dispersion of filler in matrix. Alumina addition in epoxidized natural also increases the hardness of rubber, which results to decreasing of rebound resilience property. This may caused by molecular stiffness of epoxide ring in ENR and excellent hardness of alumina particle. Furthermore, alumina addition also enhances a thermal stability of composite.

Introduction

Natural rubber is highly consumed to produce many products due to its desirable processing property and excellent elasticity; nevertheless, it has a low mechanical property. Hence, the property improvement by adding filler is one solution of their limitation. There are many kinds of filler were used to enhance its mechanical also thermal properties such as carbon black [1], silica [2,3], clay [4,5] and alumina [6-9]. Carbon black is popular filler that widely use in a rubber industry. However, the products have a color drawback which limited in many applications. Clay, silica or alumina are preferred in colored product. Considering a high thermal stability, heat-resistance and hardness, alumina is one of inorganic filler that become be interesting to incorporate in rubber. However, the compatibility of in organic filler and rubber matrix is the serious problem. Because of the different in chemical nature, the filler is difficult to disperse in a matrix. This problem can be solved by adding a compatibilizer or coupling agent to enhance the compatibility. Epoxidized natural rubber (ENR) is one choice that used as a compatibilizer in natural rubber, including synthetic rubber, composite preparation. Because ENR has a polar oxiran ring part which could interact with filler and polyisoprene part which is the same as natural rubber [4-6]. It is indicated that ENR is higher compatible with inorganic filler. With this reason, alumina loaded epoxidized natural rubber was done in this work with the hypothesis that ENR could be more compatible with alumina than natural rubber in case no coupling agent. Furthermore, ENR offer unique property such as good oil resistance, improved wet grip and rolling resistance and alumina could give an advantage in thermal property. Generally, rubber-filler mixing was done in dry state on two-roll mill or internal mixer [1,4-8]. A disadvantage of dry compounding is chemical difficult to disperse in the matrix because of very high viscosity.Solution or latex compounding [3,9-10]and *in situ* polymerization [2] are the option for easier and better dispersion. Therefore, in this work, we

areinterested in preparation of alumina incorporated epoxidized natural rubber in the latex mixing method. The dispersion alumina in ENR was examined. Moreover, the mechanical and thermal properties of the composite with different alumina content were investigated in order to study effect of alumina on the properties.

Experimental

Materials. High ammonia natural rubber latex was supplied by Chalong Latex Industry Co.,Ltd (Thailand). Hydrogen peroxide and formic acid were purchased from Fisher Chemical (UK). Chemicals for latex compounding; zinc oxide, zinc diethyl dithiocarbamate (ZDEC), Wingstay L, zinc 2-mercaptobenzothiazole (ZMBT), sulfur and dispersion agent were supplied by Kij Paiboon Chemical Limited Partnership (Thailand). Teric16A16 using as colloid stabilizer was obtained from GSP product Co.,Ltd (Thailand).Alumina A-32 with average particle sized 1.0 micron was kindly supported from Nicho Co.,Ltd (Thailand). All compounding chemicals were prepared in a 50% dispersion form before added in latex.

Alumina reinforced epoxidized natural rubber preparation. Epoxidized natural rubber latex was synthesized via *in situ* epoxidation of natural rubber latex using formic acid and hydrogen peroxide. The ratio of H_2O_2 and HCOOH to natural rubber was varied to obtain the different epoxidation level. HCOOH and H_2O_2 were slowly dropwised into latex, respectively and reaction was performed at 60°C for 8 h. After that, the compounding chemical dispersions were added in the latex, the formulation was shown in Table 1, and the latex was keep overnight at room temperature. Alumina dispersion was then added and continuously stirred at 600 rpm for 1 h. Finally the latex compound was casted in glass mould and let it dry for 2 days. The rubber film was heated at 70°C for 24 h and then post cured at 110ºC for 15 minutes.

Table 1 Recipe of ENR latex compounds

Chemicals	Amount (phr)
20% ENR latex	100
10% Teric16A	5
50% ZDEC	1
50% ZMBT	0.5
50% S	2
50% ZnO	1
50% Wingstay L	1.0
50% alumina dispersion	10, 25,50,75

Characterization. The chemical structure of epoxidized rubber was confirmed using ^{1}H-NMR spectrometer Varian Unity Inova 500MHz and epoxidation level of latex was determined. The dispersion of alumina particle in epoxidized natural rubber matrix was observed under a JEOL JSM-5800LV scanning electron microscope. Freeze-broken fracture of samples was used in a characterization. Tensile properties were tested following ASTM D412, die C using a Universal testing machine, LLOYD instrument; model LR10K, at room temperature and a cross head speed 500 mm/min. The values were average of 4-5 specimens. Hardness of the vulcanizates was also determined using a ShoreA Durometer PTC 408based on ASTM D2632. Hardness at different position on the specimen were taken and averaged. Resilience was measured using a Shore Resilionmeter SRI74000. Thermal stability of the different alumina loaded epoxidized natural rubber was investigated by Perkin Elmer TGA7 Thermogravimetric Analyzer from 50°C to 600°C with a heating rate 10°C/min under nitrogen atmosphere.

Results and Discussion

Chemical structure of epoxidized natural rubber was confirmed by appearance of the chemical shift 2.70 ppm in ^{1}H-NMR spectra corresponding to oxiran ring proton in epoxidided unit. The

epoxidation level was calculated from the ratio of oxiran ring photon to a sum of oxiran and isoprenic protons. It was found that the percentage of epoxidation increased from 17 to 41% as increased in mol ratio of H_2O_2 and HCOOH to isoprene unit from 0.5 to 1.4. In 41% epoxidized natural rubber, the amount of alumina cannot be added more than10 phr due to alumina-epoxidized natural rubber is become brittle. This caused by combination effect of the high rigidity of the high percentage of oxiran ring structure and high hardness of alumina particles. Whereas, in case of 17% epoxidized natural rubber composite, alumina content can be added up to 75 phr.

Alumina dispersion. The degree of alumina dispersion in epoxidized natural rubber was observed by SEM and the micrographs are given in Figure1. As can be seen that alumina is good dispersed in epoxidized natural rubber. Even, there are some agglomerations of alumina into largerparticle, especially, when an amount of alumina was increased. At higher alumina content, alumina particle is clearly observed and become a dominant phase. Therefore, composite with alumina content 75 phr was not study.

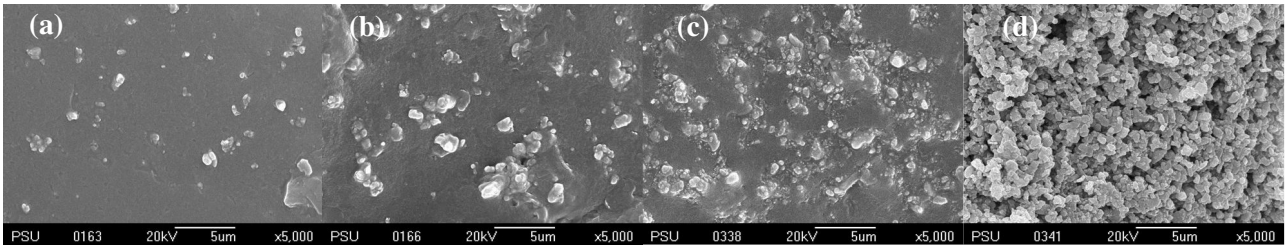

Figure 1 SEM micrographs of alumina reinforced epoxidized natural rubber with 17% epoxidation at alumina conetnt; a) 10 phr, b) 25 phr, c) 50 phr and d) 75 phr.

Mechanical properties. Figure 2 represent the tensile strength, modulus and elongation at break of composites. It can be seen that tensile strength is highest at alumina loading 10 phr and it then decrease as alumina was added at 25, 50 and 75 phr. This result corresponds with alumina dispersion, the lower tensile strength may caused from agglomeration of alumina to larger particle and the low adhesion between alumina particle and rubber matrix as well which acts as the defect part in the composite. Hence, at the alumina content was higher, the weak interface surface also increased. It results in a lower tensile strength. However, modulus of the composite is slightly increased as alumina content was increased, whereas, elongation at break was not significant change. This can be a result of low adhesion between surfaces of alumina particle and rubber; therefore, an increasing in alumina content didn't affect much to stiffness and extension of rubber composites. However, a rebound resilience slightly dropped as amount of alumina was increased, while hardness significant increase. Therefore, in this case the well dispersion and mechanical properties of alumina loading ENR without coupling agent prepared in latex phase are limited at the low content.

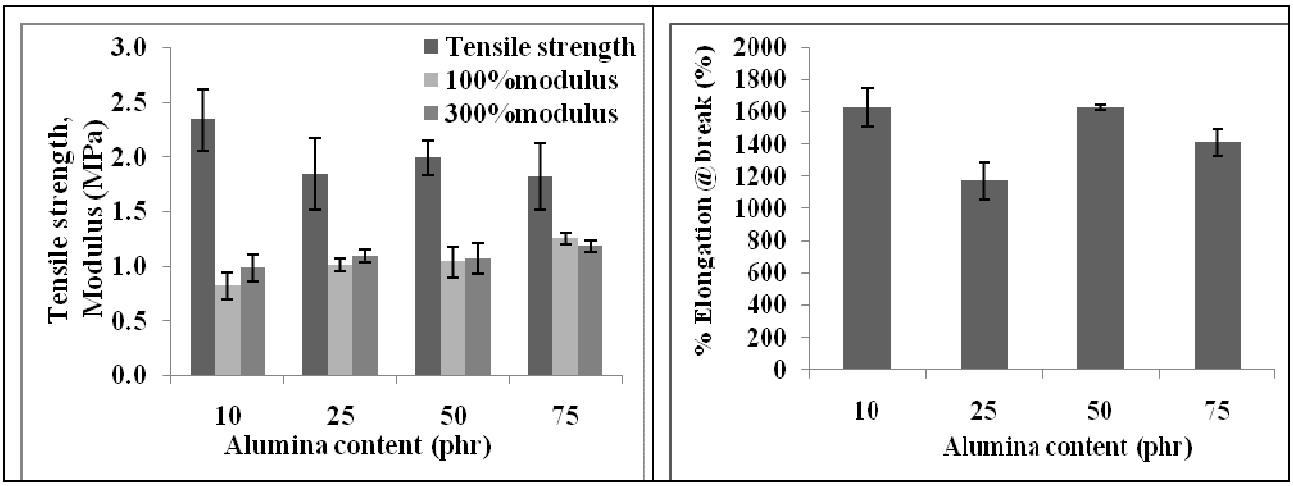

Figure 2 Mechanical properties of alumina reinforced 17% epoxidized natural rubber.

Thermal property. Thermalgravimetric analysis was used for studying the effect of alumina on the thermal stability of composite. It was found that thermal stability of composite increased as the alumina loading increased. The degradation temperature of composite increase from 369ºC to 391ºC as alumina loading increased from 10 to 50 phr. This caused by the excellent thermal stability of alumina. Alumina may attributed to low heat transfer in the composite, hence, it can prolong the degradation process of composite.

Summery

It can be conclude that alumina incorporated in epoxidized natural rubber in latex system without coupling agent can be done. The limit of alumina loading amount decreased with the increasing of epoxidation of natural rubber. Low alumina content can be incorporate without coupling agent. The alumina can disperse well in epoxidized natural rubber, even; there is low interface interaction and some agglomeration at higher alumina loading. At 10 phr of alumina loaded composite showed the highest tensile strength. Modulus of alumina reinforced epoxidized natural rubber slightly increases as the amount of alumina increase, while the resilience decreased. High alumina loading epoxidized natural rubber trends to have higher thermal stability. However, the improvement of the compatibility and properties of composite have to be further studied.

Acknowledgement

This project is financially supported by the Office of the Higher Education Commission, Thailand Research Fund and Prince of Songkla University (Grant No. MRG5480078). Authors would like to thank as well the Nicho Co.,Ltd for kindly alumina donating in this work .

References

[1] S. Salaeh, C. Nakason, Influence of modified natural rubber and structure of carbon black on properties of natural rubber compounds, Polym. Comp. 33, (2012) 489-500.

[2] A.S. Hashim, N. Kawabata, Silica reinforcement of epoxidized natural rubber by sol-gel method, J. Sol-Gel Sci. Tech. 5, (1995) 211-218.

[3] N. Rattanasom, P. Kueseng, C. Deeprasertkul, Improvement of the mechanical and thermal properties of
silica-filledpolychloropreneVulcanizates prepared from latex system, J. Appl. Polym. Sci. 124, (2012)657-2668.

[4] M.Arroyo, M.A.Lopez-Manchado, J.L.Valentin, J. Carretero, Morphology/behavior relationship of nanocomposites based on natural rubber/epoxidized blend. Comp.Sci. Tech. 67, (2007)1330-1339.

[5] P.L.Teh,Z.A. MohdIshak,A.S.Hashim, J. Karger-Kocsis,U.S.Ishiaku, Effect of epoxidized natural rubber as a compatibilizer in melt compound natural rubber-organoclay nanocompostes. Eur.Polym. J. 40, (2004) 2513-2521.

[6] N. Mohamad, A. Muchtar, M.J. Ghazali, Dahlan H.M., C.H. Azhari, The effect of filler on epoxidised natural rubber-alumina nanoparticles composites, Eur. J. Sci. Res. 24, (2008)538-547.

[7] N. Mohamad, A. Muchtar, M.J. Ghazali, H.M. Dahlan, C.H. Azhari,Epoxidizednatural rubber-alumina nanoparticle composites (ENRAN): Effect of filler loading on the tensile properties, Solid Stat. Tech. 17, (2009)133-143.

[8] B.B. Konar, S.K. Roy, T.K. Pariya, Study on the effect of naono and active particles of alumina on natural rubber-alumina composites in the presence of epoxidized natural rubber as compatibilizer, J. Macromol. Sci., Part A, 47, (2010) 416-422.

[9] S. Varghese, J. Karger-Kocsis, Natural rubber-based nanocomposites by latex compounding with layered silicates, Polymer 44, (2003)4921-4927.

[10] Z. Peng, L. X. Kong, S.-D. Li, Y. Chen, M. F. Huang, Self-assebled natural rubber/silica nanocomposites: Its preaparation and characterization, Comp. Sci. Tech., 67, (2007) 3130-3139.

Advanced Materials Research Vol. 970 (2014) pp 304-307

doi:10.4028/www.scientific.net/AMR.970.304

Changes In Characteristics and Physicochemical Through Vermicomposting of Pome Sludge by Epigeic Earthworm *E. eugeniae*

Z. Bidattul Syirat[1,a], M Hakimi Ibrahim[1,b], Astimar A. A[2,c*], and Z. Nahrul Hayawin[2,d]

[1] Division of Environmental Technology, School of Industrial Technology, Universiti Sains Malaysia, 11800 Minden, Pulau Pinang, Malaysia.

[2] Malaysian Palm Oil Board, P. O. Box 10620, 50720 Kuala Lumpur, Malaysia.

[a]bid_syirat@yahoo.com, [b]drhakimiusm@yahoo.com,

[c]astimar@mpob.gov.my (*corresponding author), [d]nahrul.hayawin@mpob.gov.my

Keywords: vermicompost, vermicomposting, physicochemical changes, POME, *E. eugeniae*

Abstract. The aims of this study was to investigate the characteristics and physicochemical changes of vermicompost during composting of palm oil mill effluent (POME) sludge processed by epigeic earthworm (*E. eugeniae*) within 60 days. The value of macronutrients, micronutrients and heavy metals and pH in vermicompost comes out to be (pH8.3), carbon (C) (45.2%), CN ratio (18.1%), phosphorus (P) (5.02%), ferum (Fe) (0.6%), copper (Cu) (16.8 ppm), zink (Zn) (119.54 ppm), mangan (Mn) (1049.86 ppm), potassium (K) (0.81%), nitrogen (N) (2.5%), calcium (Ca) (11.42%) and magnesium (Mg) (2.99%), and was compared with compost from EFB-POME sludge and compost from mesocarp fiber-POME sludge. In addition, the amino acid content in vermicompost detected was very low as compared to raw POME. Meanwhile, three types of fungus were detected in vermicompost which are from *Paecilomyces* sp., *Fusarium* sp. and *Penicillium* sp. The results suggested that POME sludge could be recycled to form compost by using vermicomposting technology, as well as act as a good organic fertilizer.

Introduction

The concept of vermicomposting started from the knowledge that certain species of earthworms consume a wide range of organic residues very rapidly, converting them into vermicompost, a humus-like, soil building substance in short time. The effective use of the earthworms in organic waste management requires a detailed understanding of the effect of the physico-chemical properties of the substrate [1].

Huge quantities of waste are produced in the palm oil mill industry. The process of oil extraction results in generation of liquid waste commonly named as palm oil mill effluent (POME). Palm oil mill effluent is generated mainly from oil extraction, washing and cleaning processes in the mill and these contain cellulosic material, fat, oil and grease etc [2]. According to Rupani (2010), palm oil mill effluent also contains substantial quantities of solids, both suspended solids and total dissolved solids [3]. These solids are commonly named palm oil mill sludges (POMS). The solid waste that are produced in the process of extraction are the leaves, trunk, decanter cake, empty fruit bunches, seed shells and fibre from the mesocarp. Meanwhile, Chooi (1984) reported that palm oil mill sludge (POMS) could be dried and used as a fertilizer as it contains high nutrient value [4]. The drying process is mostly done in open ponds, but during the rainy seasons this process becomes difficult due to slow rate of drying and over flow problem.

Therefore, in this study, the aims were to identify and study the characteristics and physicochemical changes of vermicompost from POME sludge by epigeic earthworm, *E. eugeniae* as well as its potential as a fertilizer.

Materials and Methods

Palm oil mill effluent (POME) sludge were obtained from Palm Oil Mill, Serting, Negeri Sembilan. 3 kg of POME sludge was filled into each worm bins. 50 earthworms (*Eudrillus eugeniae*) were added into the first bin and 100 earthworms of the same species were added into the next bin. For control, no earthworm was added. Experiment was done in triplicate for each worm bins. Vermicomposting process was done within two months and was done in a closed system to keep the moist of the substrates.

All samples were analyzed by using CNS analyzer (CNS Model 2000, LECO), Total Kjeldhal Method and AAS Spectroscopy (AAnalyst Model 400, Perkin Elmer) to determine the carbon, total nitrogen, nutrients and heavy metal elements respectively. Amino acid analysis was done by using Ultra Performance Liquid Chromatography (Waters, UPLC Empower 3 Software). Fungal population and species was calculated by using Total Plate Count (TPC) and identification process respectively.

Results and Discussion

Physicochemical changes of vermicompost. Table 1 shows three different composts obtained from EFB-POME sludge, mesocarp fiber-POME sludge and vermicompost, respectively.

Table 1: Chemical Characteristics of POME Vermicompost by using *E. eugeniae* compared with compost from EFB-POME sludge and compost from mesocarp fiber-POME sludge.

Properties	Compost from EFB-POME sludge[a]	Compost from mesocarp fiber-POME sludge[b]	Vermicompost[c] (*E. eugeniae* + POME sludge)
C/N	12.7	12.6	18.1
pH	8.1	7.5	8.3
Organic C (%)	28	24.8	45.2
Total N (%)	2.2	1.9	2.5
P (%)	1.3	0.3	5.02
K (%)	2.8	1.2	0.81
Ca (%)	0.7	0.9	11.42
Fe (%)	1.2	1.0	0.6
Mg (%)	1.0	0.3	2.99
Cu (ppm)	70	57	16.8
Mn (ppm)	250	151	1049.86
Zn (ppm)	91	190	119.54
Days of composting	40	50	60

[a] = Baharuddin et al. (2009); [b] = Hock et al (2009); [c] = this study.

The vermicomposted material showed comparatively more total N content than EFB-POME sludge composted and compost from mesocarp fiber-POME sludge. It is suggested that in addition to releasing N from compost material, earthworms also enhance nitrogen levels by adding their

excretory products, mucus, body fluid, enzymes etc. to the substrate [5]. Suthar (2006) suggested that decaying tissues of dead worms also add a significant amount of N to vermicomposting sub-system [6]. In general, nitrogen enrichment pattern and mineralization activities mainly depend upon the total amount of N in the initial waste material (e.g., sludge) and on the earthworm activity in the waste decomposition sub-system [7,8]. It is also suggested that the differences for N content in end product (vermicompost) could be related to the availability of metals in vermibeds, which directly affects the N mineralization rate.

The C:N ratios of substrate material reflect the organic waste mineralization and stabilization during the process of decomposition. The loss of carbon as carbon dioxide through microbial respiration and simultaneous add of nitrogen by worms in the form of mucus and nitrogenous excretory material lowered the C:N ratio of the substrate [9]. The higher the C/N ratio the lower was the process of degradation while the lower the C/N ratio the higher was the process of degradation. No change in C/N ratio indicated the completion of the composting process [10].

On the other hand, Habib et.al, (1997) reported that amino acid contents in POME sludge detected were Glysine, Histidine, Arginin, Threonine, Tyrosine and Cystine were higher than those in vermicompost, with 9.43, 1.43, 4.25, 2.58, 3.16 and 3.37 respectively [11]. Meanwhile, fungal species detected were *Fusarium* sp., *Penicillium* sp. and *Peacilomyces* sp. and their population calculated was 2.74×10^2 cfu/ml. A study of POME sludge by Chowdhury et al., (2006) reported that six out of twenty strains of *Penicillium* were isolated from four different sources of POME sludge and selected for the production of cellulase and lignin peroxidase in the POME [12]. The results revealed *Penicillium* (P1-EFB), which was isolated from empty fruit bunches, displayed the best potential strain for biodegradation in liquid state bioconversion of POME at pH 7.3.

Conclusion

Since palm oil mill effluent is non-toxic and considered as a good source of organic nutrients, land application of POME sludge can be a suitable waste management option. Use of composting as well as vermicomposting technology is also an efficient waste management option in order to form a good quality of organic compost and fertilizer.

References

[1] N.B. Singh, A.K. Khare, D.S. Bhargava, S. Bhattacharya, Effect of initial substrate pH on vermicomposting using *P. excavatus* (Perrier, 1872). Applied Ecology and Environmental Research 4(1) (2005) 85-97.

[2] P. Agamuthu. Palm oil mill effluent and utilization. In: C. A. Sastry, M. A. Hashim and P. Agamuthu, (eds). Waste treatment plant. Narosa Publishing House, New Delhi, (1995) 338-360.

[3] P. F. Rupani, R. P. Singh, M. Hakimi Ibrahim and E. Norizan. Review of Current Palm Oil Mill Effluent (POME) Treatment Methods: Vermicomposting as a Sustainable Practice, World Applied Sciences Journal 11 (1) (2010) 70-81.

[4] C.F. Chooi, Ponding System for Palm Oil Mill Effluent Treatment. (1984)

[5] S. Suthar, S. Singh. Feasibility of vermicomposting in biostabilization of sludge from a distillery industry. Science of The Total Environment 394 (2008) 237–243.

[6] S. Suthar. Potential utilization of guargum industrial waste in vermicompost production. Bioresour Technol., 97 (2006) 2474–7.

[7] R.D. Kale. Earthworms: nature's gift for utilization of organic wastes. In: Edwards CA, editor. Earthworm ecology, soil and water conservation society. New York: Ankeny, Lowa St. Lucie press, (1998) 355–73.

[8] S. Suthar. Nutrient changes and biodinemics of epigeic earthworm *Perionyx excavatus* (Perrier) during recycling of some agriculture wastes. Bioresour Technol. 98 (2007) 1608–14.

[9] S. Suthar, S. Singh. Feasibility of vermicomposting in biostabilization of sludge from a distillery industry. Science of The Total Environment 394 (2008) 237–243.

[10] N. Karmegam, E. T. Daniel, Investigating efficiency of *Lampito mauritii* (Kinberg) and *Perionyx ceylanensis* Michaelsen for vermicomposting of different types of organic substrates. Environmentalist, 29 (2009) 287–300.

[11] M.A.B. Habib, F.M. Yusoff, S.M. Phang, K.J. Ang, S. Mohamed, Nutritional values of chironomid larvae grown in palm oil mill effluent and algal culture. Aquaculture 158 (1997) 95-105.

[12] A.J.K. Chowdhury, M.Z. Alam, S.H. Shahlizah. Isolation, purification and screening of fungal strain from effective bioconversion of palm oil mill effluent. Proceedings of the 1st International Conference on Natural Resources Engineering & Technology 2006. Putrajaya, Malaysia, (2006) 167–75.

Advanced Materials Research Vol. 970 (2014) pp 308-311

doi:10.4028/www.scientific.net/AMR.970.308

Effect of the Addition of Nano-clay on the Physical Property and the Melt-Spinnability of Bacterial Polyester

Hideki Yamane[1, a *], Santa Momii[1], Shin-ichi Yagi[2], Isao Wataoka[1], and Noriyuki Suzuki[3]

[1]Kyoto Institute of Technology, Kyoto, Japan
[2]Kyoto Medical Planning, Co. Ltd, Kyoto, Japan
[3]Kaneka Corporation, Osaka, Japan

[a]hyamane@kit.ac.jp

Keywords: Bacterial polyesters, Nano-clay, Mica, Physical properties, Melt-spinnability

Abstract. Synthetic mica organically treated with alkylamines was added to poly(3-hydroxybutyrate-co-3hydroxyhexanoate) (PHBH), one of the bacterial co-polyesters. Mica dispersing in PHBH acted as a crosslinking point of PHBH chains and increased the melt viscosity of PHBH significantly. The melt spinnability of PHBH was greatly improved by the addition of mica and the crystallization of PHBH in the spinline was highly promoted. WAXD spectra showed that the as-spun fibers of PHBH/MICA contain both highly oriented α- and β-forms of PHBH crystal. Further the SAXS revealed that the mica dispersing in the PHBH fiber oriented with its surface parallel to the fiber axis. The crystalline orientation of PHBH, orientation of mica, and the formation of β-form all improve the mechanical property of PHBH fibers.

Introduction

Poly(hydroxyl alkanoate) (PHA) is a bacterial bio-based polyester whose properties are similar to those of polypropylene [1]. Although various academic and industrial researchers have made a lot of efforts to obtain the fibers of PHA with a good mechanical property, the industrial production has not been succeeded yet. This is because of the very low crystallization rate of PHA and of the glass transition temperature lower than room temperature. On slowly cooling from the melt, PHA very slowly crystallizes and forms large spherulites. Rapid cooling results in an amorphous state and subsequently followed by the secondly spherulitic crystallization even at room temperature. This spherulitic structure of PHA and its copolymers makes as-spun fiber very brittle and makes cold deformation to enhance crystalline orientation extremely difficult [2, 3].

Various efforts have been paid to process PHA and its copolymers into fibers, films, and other products [4-11]. Most of these reports emphasize the effect of the nucleating agent on the crystallization of PHA in the spinline. When the molten PHA crystallizes in the spinline under tension, the PHA chains are more or less stretched and cause c-axis orientation to the fiber direction. The fibers with this sort of oriented crystal are rather ductile and can be cold drawn easily.

In this study, the organically treated mica was added to a bacterial copolyester and the effects of the addition of mica on various physical properties such as the crystallization behavior, the melt rheology, and the melt spinnability were examined. Further the mechanical property and the higher-order structure of the melt spun fibers were evaluated.

Experimentals

Materials. Synthetic Mica ME-100 was supplied by Co-op Chemical Co., Ltd., Tokyo, Japan. Alkylamines including octyl, lauryl, and stearylamines were supplied by Nacalai Tesque and were used without further purification. The bacterial polyester used was poly(3-hydroxybutyrate-co-3-hydroxyhexanoate) (PHBH) with a weight average molecular weight 5.4 x 10^5 and a 3-hydroxyhexanoate content 7 mol%.

Organic Treatment of Mica. Mica was dispersed in the ion exchanged water and kept stirring at 80°C. Alkyl amines were dissolved in the ion exchanged water and 6N HCl was added to it. Resultant alkyl ammonium salt aqueous solutions were added to the mica dispersion. Organically treated mica was precipitated after stirring for 3 hrs at 80°C. The precipitate was then washed several times with water and dried. 5 wt% of mica treated with various alkyl amines was mixed to the PHBH at a molten state.

Melt Spinning of the PHBH/MICA. The melt-spinning of PHBH/MICA was carried out at 160°C by using a laboratory size single screw extruder equipped with a 0.5 mm mono-hole die. The extrudate was stretched at room temperature and wound on the bobbin placed at 3 m below the die.

Measurements and Observations. The degree of the organic treatment was evaluated by FTIR. Morphology of the Mica was observed by using SEM after applying a gold coating. The layer distance of the mica was determined by WAXD and SAXS. Crystallization behavior of pure PHBH and PHBH/MICAs was observed with a polarized optical microscope equipped with a hot stage. The thermal property was determined with a DSC. The dynamic viscosity of PHBH/MICA melts was measured by using a rheometer (MR-300, REOROJI) with a parallel palates mode at 160°C. The higher-order structure and the mechanical property of the PHBH/mica fibers were determined with WAXD and by tensile tests, respectively.

Results and Discussion

Organic Treatment of Mica. The extent of the organic treatment was confirmed with IR spectra. Two peaks at 2,850 cm^{-1} and 2,920 cm^{-1}, identified as C-H stretching bands, appear on the IR spectra of the organically treated mica. A large peak detected around 3,450 cm^{-1} for untreated mica is attributable to the stretching vibration of -OH in water. This peak turned to be very small after the organic treatment indicating that the intercalation of alkyl amines made the mica rather hydrophobic. SEM observations revealed that although untreated mica has more or less bulky, organically treated mica tended to have a layered morphology. WAXD spectra also revealed that the organic treatment increased the inter-layer distance of mica and the mica treated with amines with longer alkyl chain has a larger layer distance as shown in table 1.

The Effect of the Addition of Mica on the Various Physical Properties of PHBH. 5 wt% of untreated mica and those treated with various alkyl amines were mixed to the PHBH at a molten state. First of all, the ability of mica as a crystallization nucleating agent at a static state was examined. Observation of the crystal growth by using a polarizing optical microscope under crossed Nicol at 110°C after quenching from the

Table 1 Layer distances of organically treated mica before and after mixing to PHBH

Alkylamine	Layer distance [nm]	
	As organically treated	in PHBH
Untreated	0.95	-
Octylamine	1.34	2.29
Laurylamine	1.57	2.80
Stearylamine	1.90	3.46

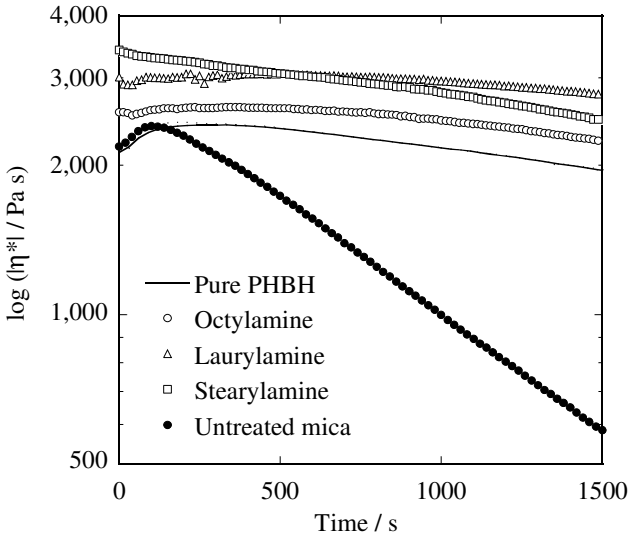

Fig. 1 Change in the melt viscosity of PHBH containing mica treated with various amines measured at 160°C.

molten state indicated that the addition of mica slightly promotes the crystallization of PHBH at a static state. This result suggests that although the mica acts as a nucleating agent, the effect is rather small at a static state.

Fig. 1 shows the change in the melt viscosity of pure PHBH and PHBH/MICAs with time measured at 160°C. The addition of mica increased the melt viscosity of PHBH comparing with that of pure PHBH. This may be due to the intercalation of PHBH chains into the mica layers acting as crosslinking points. It should be noted that the melt viscosity of PHBH containing untreated mica decreased significantly with time. This may be due to the hydrolytic degradation of PHBH by the water absorbed to the untreated mica.

Melt Spinnability and the Property and Structure of PHBH/MICA Fibers. Although the pure PHBH cannot be melt-spun at high take-up velocities, the addition of the organically treated mica significantly improved the melt-spinnability of PHBH. While pure PHBH melt spinline can be taken-up at 60 m/min at the maximum, those added with 5 wt% of organically treated mica can be taken-up at a velocity as high as 360 m/min. Besides the pure PHBH as-spun fiber was still in a molten state even on the bobbin and stuck together. On the other hand, all the PHBH/MICAs as-spun fibers were well crystallized in the spinline, irrespective of the length of the alkyl chain of the amines.

Higher-order Structure of the As-spun Fibers. It has been reported that homo poly(3-hydroxy butyrate) (PHB) is crystallized in a left-handed 2/1 helix conformation (α-form). In addition, a planar zigzag conformation (β-form) forms in some drawing and annealing conditions. The orthorhombic unit cell dimensions of α-form was a = 0.576 nm, b = 1.320 nm, and c (fiber axis) = 0.596 nm [12]. β-form shows only single, broad reflection at $2\theta = 19.7^{o}$ on the equator. Orts et al. suggested that the β-form crystallization takes place upon stretching of the amorphous tie chains between 2/1 helix α-form lamellae in the drawing process [13].

The as-spun fibers of PHBH/MICAs showed a highly oriented crystalline WAXD pattern as shown in Fig. 2. In addition to the reflections from α-form crystal with a 2/1 helix conformation, those from the β-form were also clearly observed on the equator. As Oats et al. suggested, β-form is generally observed for the highly drawn fibers. However PHBH/MICA as-spun fibers clearly showed the co-existence of α- and β-forms without applying a cold drawing process. Some of the PHBH chains were constrained between the mica layers and the crystallization under the constrained state produced the β-form.

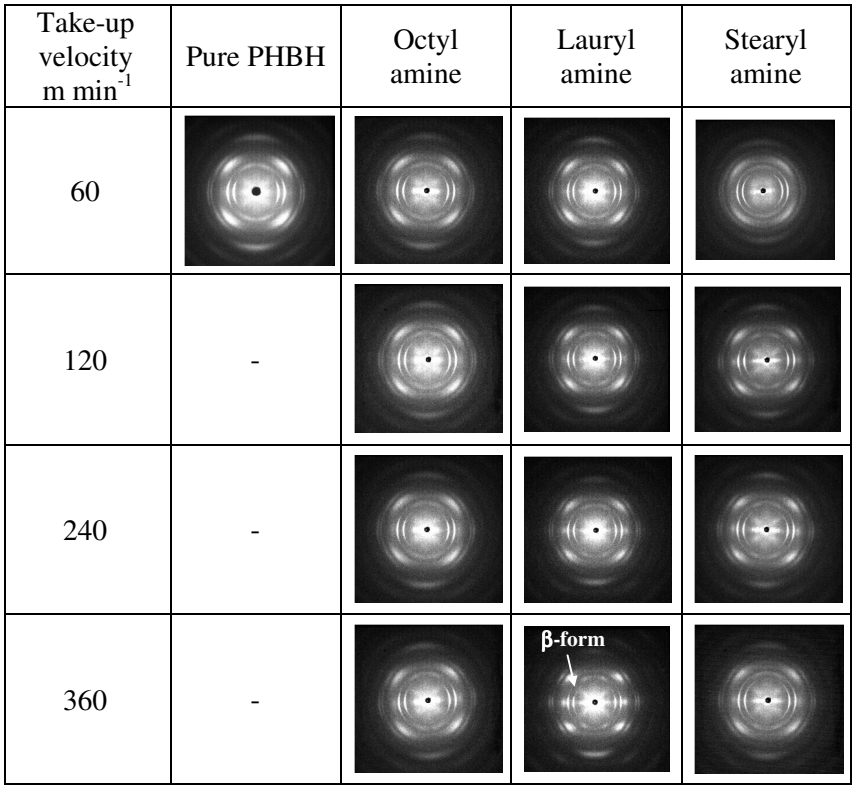

Fig. 2 WAXD pattern of the fibers of pure PHBH and PHBH/MICA fibers taken-up at various velocities.

Fig. 3 shows the SAXS patterns of the PHBH/MICAs. The strong reflections from the mica layer structure were detected on the equator of the SAXS pattern of as-spun fiber as well

as the scattering peaks from PHBH lamellar crystal around $2\theta = 1.8^{o}$ (long period). Since the reflection from mica layer concentrates on the equator of SAXS pattern, mica in the PHBH fiber is highly oriented with its surface parallel to the fiber axis. The reflections from mica layer indicate that the layer distance of mica was further increased after the mixing into PHBH as shown in table 1. Promotion of Crystalline orientation of PHBH and the orientation of mica with increasing take-up velocity improved the mechanical property of PHB/MICA fibers significantly.

Conclusion

The results obtained in this study suggest that the addition of organically treated mica does not simply increase the crystallization rate of PHBH as a nucleating agent. The crystallization of PHBH in the melt spinline is promoted by the molecular orientation given by the extensional stress in the spinline of the molten PHBH/MICAs higher than that of pure PHBH, although the mica does not promote the crystallization significantly at a static state. The spinline crystallization further improved the melt spinnability of PHBH. Some of the PHBH chains were constrained between mica particles and crystallized into β-form. The crystalline orientation of PHBH, the orientation of mica, and the formation of β-form all improved the mechanical property of PHBH fibers.

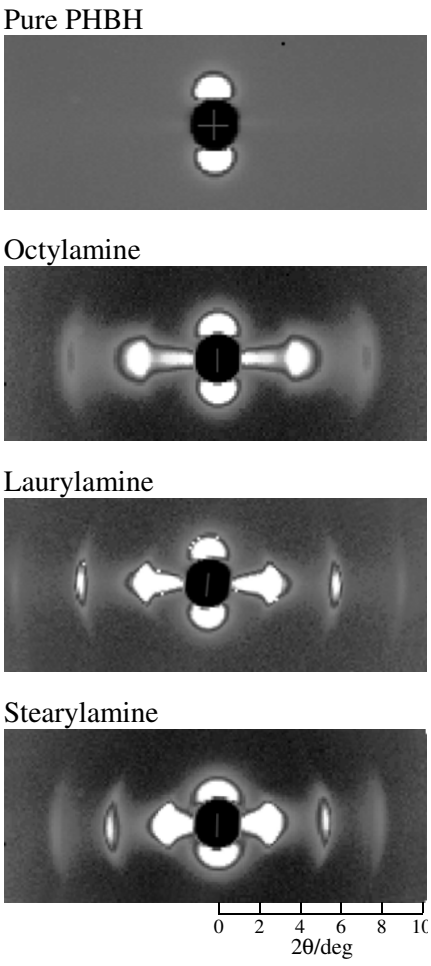

Fig. 3 SAXS pattern of the fibers of pure PHBH and PHBH/MICA.

References

[1] D. Ellar, D.G. Lundgren, K. Okamura, R.H. Marchessalt., Morphology of Poly-β-hydroxybutyrate granules, J. Mol. Biol. 35 (1968) 489-494.

[2] G.J.M. De Koning, P.J. Lemstra., Crystallization phenomena in bacterial poly[(R)-3-hydroxybutyrate]: 2. Embrittlement and rejuvenation, Polymer 34 (1993) 4089-4094.

[3] M. Scandola, G. Ceccorulli, M. Pizzoli., Macromol. Chem. Rapid Commun. 10 (1989) 47-50.

[4] T. Yamamoto, M. Kimizu, T. Kikutani, Y. Furuhashi, M. Cakmak., Intern. Polym. Process. 12 (1997) 29-37.

[5] Y. Furuhashi, H. Ito, T. Kikutani, T. Yamamoto, M. Kimizu., Sen'i Gakkaishi 53 (1997) 356-364.

[6] Y. Furuhashi, H. Ito, T. Kikutani, T. Yamamoto, M. Kimizu, M. Cakmak., J. Polym. Sci., Part B, Polym. Phys. 36 (1998) 2471-2482.

[7] S.A. Gordeyev, Y.U.P. Nekrasov., J. Mater. Sci., Lett. 18 (1999) 1691-1692.

[8] H. Yamane, K. Terao, S. Hiki, Y. Kimura., Polymer 42 (2001) 3241-3248.

[9] T. Iwata, K. Tsunoda, Y. Aoyagi, S. Kusaka, N. Yonezawa, Y. Doi., Polym. Degrad. Stab. 79 (2003) 217–224.

[10] Y. Furuhashi, Y. Imamura, Y. Jikihara, H. Yamane, Polymer 45 (2004) 5703-5712.

[11] Y. Jikihara, T. Saito, H. Yamane, Sen'i Gakkaishi 62 (2006) 115-122.

[12] M. Yokouchi, Y. Chatani, H. Tadokoro, K. Teranishi, H. Tani, Polymer 14 (1973) 267-272.

[13] W.J. Orts, R.H. Marchessault, T.L. Bluhm, G.K. Hamer, Macromolecules 23 (1990) 5368-5370.

Advanced Materials Research Vol. 970 (2014) pp 312-316

doi:10.4028/www.scientific.net/AMR.970.312

Mechanical, Thermal, and Morphological Properties of Thermoplastic Starch/Poly(lactic acid)/Poly(butylene adipate-co-terephthalate) Blends

Sujaree Tachaphiboonsap[1,a], Kasama Jarukumjorn[1,b*]

[1]School of Polymer Engineering, Institute of Engineering, Suranaree University of Technology, Nakhon Ratchasima, 30000 Thailand

[a]suj.sut@gmail.com, [b*]kasama@sut.ac.th

Keywords: Poly(lactic acid), Thermoplastic starch, Poly(butylene adipate-co-terephthalate), Poly(lactic acid) grafted with maleic anhydride, Mechanical properties, Thermal properties, Morphological properties

Abstract. Thermoplastic starch (TPS)/poly(lactic acid) (PLA) blend and thermoplastic starch (TPS)/poly(lactic acid) (PLA)/poly(butylene adipate-co-terephthalate) (PBAT) blend were prepared by melt blending method. PLA grafted with maleic anhydride (PLA-g-MA) was used as a compatibilizer to improve the compatibility of the blends. As TPS was incorporated into PLA, elongation at break was increased while tensile strength, tensile modulus, and impact strength were decreased. Tensile properties and impact properties of TPS/PLA blend were improved with adding PLA-g-MA indicating the enhancement of interfacial adhesion between PLA and TPS. With increasing PBAT content, elongation at break and impact strength of TPS/PLA blends were improved. The addition of TPS decreased glass transition temperature (T_g), crystallization temperature (T_c), and melting temperature (T_m) of PLA. T_g and T_c of TPS/PLA blend were decreased by incorporating PLA-g-MA. However, the presence of PBAT reduced T_c of TPS/PLA blend. Thermal properties of TPS/PLA/PBAT blends did not change with increasing PBAT content. SEM micrographs revealed that the compatibilized TPS/PLA blends exhibited finer morphology when compared to the uncompatibilized TPS/PLA blend.

Introduction

Poly(lactic acid) (PLA) is thermoplastic aliphatic polyester derived from renewable resources. PLA is one of the most widely used biodegradable polymers. PLA exhibits high strength, high modulus, and excellent degradability. However, its high brittleness and high cost limit its application. Blending PLA with low cost fillers and flexible polymers presents a practical and economical way to obtain economical products. Starch has been used as filler for environmental friendly polymers because its low cost and biodegradability. However, melting temperature of starch is close to degradation temperature [1,2]. Therefore, starch has been modified to obtain thermoplastic starch (TPS). The most commonly used plasticizer for TPS is glycerol due to its high boiling point and low cost [3]. The addition of TPS into PLA can decrease material cost and increase degradation rate. However, TPS/PLA blends exhibit poor mechanical properties due to poor compatibility between TPS and PLA [4]. The compatibility of TPS/PLA blends can be enhanced by adding compatibilizers [5,6]. In order to improve toughness of TPS/PLA blends, flexible polymers e.g. polycarpolactone (PCL) [7] and poly(butylene adipate-co-terephthalate) (PBAT) [8] have been incorporated into TPS/PLA blends. PBAT is considered as a good candidate for toughening PLA due to its high toughness and biodegradability. The objective of this work was to investigate the effect of PLA-g-MA on mechanical, thermal, and morphological properties of TPS/PLA blends and TPS/PLA/PBAT blends.

Experimental

Materials. Poly(lactic acid) (PLA, 4043D) was supplied from Natural Works LLC. Poly(butylene adipate-co-terephthalate) (PBAT, BASF Ecoflex FBX7011) was purchased from BASF. Cassava starch was obtained from Bankok Interfood Co., Ltd. Glycerol was supplied from Carlo Erba

Reageti Co., Ltd. 2, 5-bis (tert-butylperoxy)-2, 5 dimetthylhaxane (L101) and maleic anhydride (MA) were purchased from Sigma-Aldrich. Poly(lactic acid) grafted with maleic anhydride (PLA-g-MA) prepared in-house was used as a compatibilizer [9].

Preparation. TPS was obtained from cassava starch and glycerol at ratio of 70:30 w/w. Cassava starch was dried at 70°C for 4 h before mixing. TPS was prepared using an internal mixer (Hakke Rheomix, 3000P). The mixing temperature was kept at 120°C and the rotor speed was 60 rpm. The mixing time was 10 min.

TPS/PLA blends and TPS/PLA/PBAT blends were prepared using an internal mixer (Hakke Rheomix, 3000P). PLA, TPS, and PBAT were dried at 70°C for 4 h before mixing. The mixing temperature was kept at170°C and the rotor speed was 60 rpm. The mixing time was 10 min. The specimens were processed by a compression molding machine (Labtech, LP20-B) at temperature of 170°C and pressure of 100 MPa for 10 min. Designation and composition of TPS/PLA blends and TPS/PLA/PBAT blends are shown in Table 1.

Table 1. Designation and composition of the blends

Designation	TPS [%wt]	PLA [%wt]	PBAT [%wt]	PLA-g-MA [phr]
PLA	-	100	-	-
TPS/PLA	10	90	-	-
5c-TPS/PLA	10	90	-	5
5c-10PBAT	9	81	10	5
5c-20PBAT	8	72	20	5

Characterization.

Mechanical Properties. Tensile properties of PLA, TPS/PLA blends, and TPS/PLA/PBAT blends at various PBAT contents were tested according to ASTM D638 using a universal testing machine (Instron, 5565) with a load cell of 5 kN and a crosshead speed of 5 mm/min.

Izod impact test was performed according to ASTM D256 using an impact testing machine (Atlas, BPI).

Thermal Properties. Thermal properties of PLA, TPS/PLA blends, and TPS/PLA/PBAT blends at various PBAT contents were analyzed using a differential scanning calorimeter (NETZSCH, DSC204F1 Phoenix). All samples were heated from 25°C to 200°C with heating rate of 10°C/min (heat scan) and kept isothermal for 5 min under a nitrogen atmosphere to erase previous thermal history. Then, the sample was cooled to -50°C with cooling rate of 10°C/min and heated again to 200°C with heating rate of 10°C/min (2^{nd} heating scan).

Morphological Properties. Morphological properties of PLA, TPS/PLA blends, and TPS/PLA/PBAT blends at various PBAT contents were performed by a scanning electron microscope (JEOL, JSM-6010LV). Acceleration voltage of 10 kV was used. The fractured specimens were treated with hydrochloric acid (HCl, 6N) for 3 h. The specimens were coated with gold before analysis.

Results and Discussion

Mechanical Properties. Tensile strength and tensile modulus of PLA decreased with adding TPS while elongation at break increased as shown in Fig. 1 and Fig. 2, respectively. This result indicated that TPS led to ductile behavior [10]. With incorporating PLA-g-MA, tensile properties of TPS/PLA blend were increased due to enhanced compatibility between TPS and PLA. Tensile

strength and tensile modulus decreased whereas elongation at break increased when PBAT was added into TPS/PLA blend. This was because PBAT had lower tensile strength and tensile modulus than PLA resulting in improvement of PLA ductility. Phetwarotai et al. [11] also found that adding PBAT increased elongation at break of TPS/PLA blend but decreased tensile strength because PBAT had lower tensile strength than PLA. With increasing PBAT content, elongation at break of TPS/PLA/PBAT blend significantly increased. Impact strength of PLA reduced when TPS was added due to poor interfacial adhesion between TPS and PLA as shown in Fig. 2. When PLA-g-MA was incorporated into the blends, impact strength was increased due to enhanced interfacial adhesion between TPS and PLA. Huneault et al. [12] reported that the improvement of interfacial adhesion between TPS and PLA may enhance ductility of the materials. Impact strength of TPS/PLA blend increased with adding PBAT and further increased with increasing PBAT content.

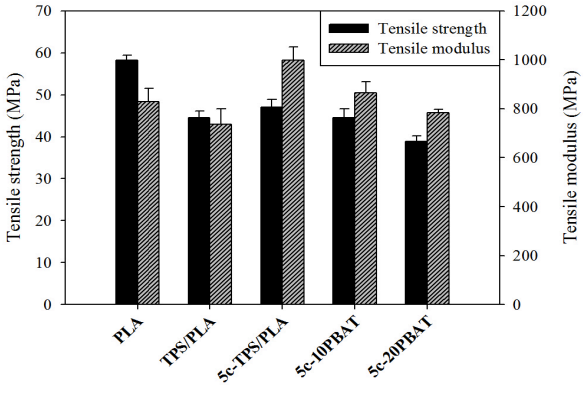

Figure 1. Tensile strength and tensile modulus of PLA, TPS/PLA blends, and TPS/PLA/PBAT blends at various PBAT contents

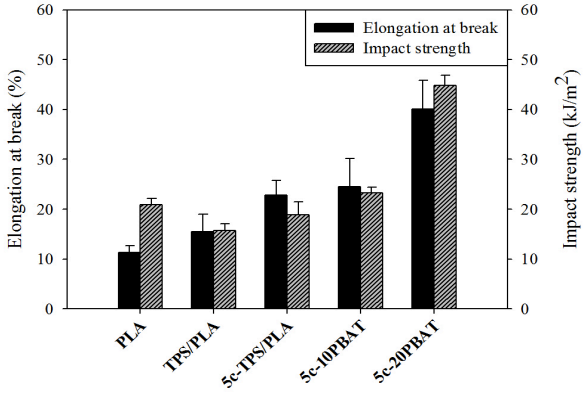

Figure 2. Elongation at break and impact strength of PLA, TPS/PLA blends, and TPS/PLA/PBAT blends at various PBAT contents

Thermal Properties. DSC thermograms of PLA, TPS/PLA blends, and TPS/PLA/PBAT blends are shown in Fig. 3 and their DSC data are listed in Table 2. There was no detectable change of the thermogram of TPS which was explained that thermal signal of TPS was weaker than conventional polymers [13]. Glass transition temperature (T_g) and crystallization temperature (T_c) of pure PLA were observed at 57.2°C and 110.3°C, respectively. PLA displayed melting temperature (T_m) at 148.6°C accompanied with shoulder-melting peak at 153.2°C. The addition of TPS decreased T_g and T_m of PLA due to the plasticizing effect of glycerol. Moreover, T_c of PLA in TPS/PLA blends was lower than pure PLA. Li et al. [14] explained that plasticizer such as water and glycerol could potentially migrate into PLA matrix leading to enhanced PLA polymer chain mobility thus increased crystallization of PLA. T_g and T_c of compatibilized TPS/PLA blend were lower than the uncompatibilized TPS/PLA blend due to improved interfacial adhesion between TPS and PLA. Karagoz et al. [15] reported that T_g and T_c of PLA in TPS/PLA blend were decreased with the addition of phenylene diisocyanate (PDI) as a compatibilizer due to the improvement of interfacial adhesion of the blend. T_g, and T_m of TPS/PLA blend did not change when PBAT was incorporated. Shi et al. [16] also reported that T_g and T_m of TPS/PLA blends insignificant changed with adding glycidyl methacrylate grafted poly(ethylene octane) (GPOE) as a toughening agent. However, the presence of PBAT reduced T_c of PLA which was consistent with the fact that PBAT enhanced crystalline ability of PLA [17]. Thermal properties of TPS/PLA/PBAT blends insignificantly changed with increasing PBAT content. Shi et al. [16] found that the increasing toughening agent content exhibited no effect on the thermal properties of TPS/PLA blend.

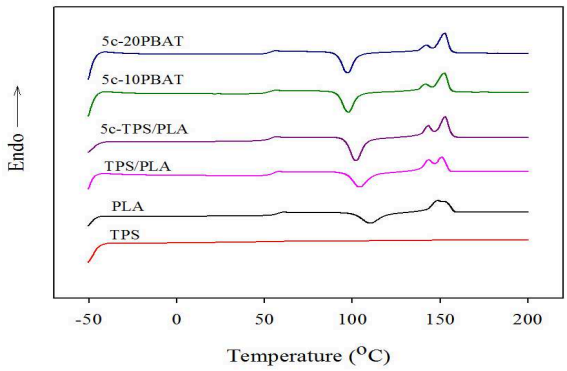

Figure 3. DSC thermograms of PLA, TPS/PLA blends, and TPS/PLA/PBAT blends (the second heating, heating rate of 10°C/min)

Table 2. Thermal properties of PLA, TPS/PLA blends, and TPS/PLA/PBAT blends

Designation	T_g [°C]	T_c [°C]	T_{m1} [°C]	T_{m2} [°C]
PLA	57.2	110.3	148.6	153.2
TPS/PLA	54.9	104.2	143.4	151.2
5c-TPS/PLA	52.1	100.5	141.3	151.0
5c-10PBAT	52.1	96.1	139.8	150.3
5c-20PBAT	52.2	95.8	140.0	150.6

Morphological Properties. SEM micrographs of the fractured surface of PLA, TPS/PLA blends, and TPS/PLA/PBAT blends are shown in Fig. 4. TPS phase in the blends was removed by 6 N HCl solution. Dispersed phase of TPS was observed in PLA matrix indicating that TPS/PLA blend was immiscible. With the addition of PLA-g-MA, the dispersed phase size of TPS in the blend was smaller than the blend without PLA-g-MA due to enhanced interfacial adhesion between TPS and PLA. Li et al. [18] also reported that PLA-g-MA compatibilized TPS/PLA blend exhibited finer morphology when compared with uncompatibilized TPS/PLA blend.

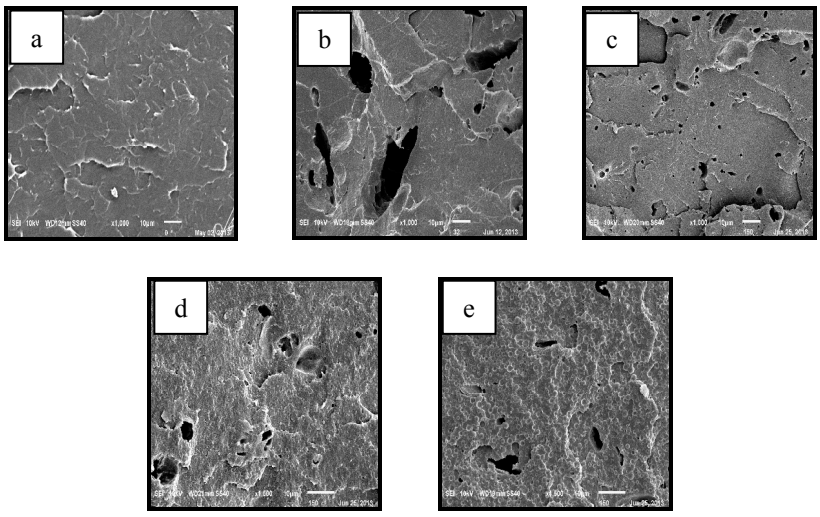

Figure 4. SEM micrographs of (a) PLA, (b) TPS/PLA, (c) 5c-TPS/PLA, (d) 5c-10PBAT, and (e) 5c-20PBAT

Summary

Tensile strength, tensile modulus, and impact strength of PLA deceased with adding TPS while elongation at break increased. The compatibilized TPS/PLA blend showed better mechanical properties than that of the uncompatibilized TPS/PLA blend. The incorporation of PBAT into the compatibilized TPS/PLA blend increased elongation at break and impact strength. The addition of TPS decreased T_g, T_c, and T_m of PLA. T_g and T_c of TPS/PLA blend were decreased by incorporating PLA-g-MA. However, the presence of PBAT reduced T_c of TPS/PLA blend. Thermal properties of TPS/PLA/PBAT blends did not change with increasing PBAT content. The compatibilized TPS/PLA blends exhibited finer morphology when compared to the uncompatibilized TPS/PLA blend.

References

[1] G. Nashed, R. P. G. Rutgers, P. A. Sopade, Starch/Stärke 55 (2003) 131-137.
[2] G. H. Yew, A. M. Mohd Yusof, Z. A. Mohd Ishak, U. S. Ishiaku, Polym. Degrad. Stab. 90 (2005) 488-500.
[3] M. Kaseem, K. Haman, F. Deri, Polym. Sci. 54 (2012 165-176.
[4] W. Ning, Y. Jiugao, M. Xiaofei, Polym. Compos. 29 (2008) 551-559.
[5] E. Schwach, J. L. Six, L. Averous, J. Polym. Environ. 16 (2008) 286-297.
[6] J. Wootthikanokkhan, P. Kasemwananimit, N. Sombatsampop, A. Kositchaiyong, S. Isarankurana Ayutthaya, N. Kaabbuathong, J. Appl. Polym. Sci. 126 (2012) E388-E395.
[7] P. Sarazin, G. Li, W. J. Orts, B. D. Favis, Polymer 49 (2008) 599-609.
[8] J. Ren, H. Fu, T. Ren, W. Yuan, Carbohydr. Polym. 77 (2009) 576-582.
[9] A. Teamsinsungvon, Physical properties of poly(lactic acid)/poly(butylene adipate-co-terephthalate) blends and their composites, Master's Thesis, Suranaree University of Technology (2011).
[10] J. Leadprathom, S. Suttiruengwong, P. Threepopnatkul, M. Seadan, J. Met. Mater. Miner. 20 (2010) 87-90.
[11] W. Phetwarotai, D. Aht-Ong, Mater. Sci. Forum 695 (2011) 178-181.
[12] M. A. Huneault, H. Li, Polymer 48 (2007) 270-280.
[13] L. Yu, E. Petinakis, K. Dean, H. Liu, Q, Yuan, J. Appl. Polym. Sci. 119 (2011) 2189-2195.
[14] H. Li, M. A. Huneault, Int. Polym. Proc. 5 (2008) 412-418.
[15] S. Karagoz, G. Ozkoc, Polym. Eng. Sci. DOI 10.1002 (2013) 1-11.
[16] Q. Shi, C. Chen, L. Geo, L. Jiao, H. Xu, W. Guo, Polym. Degrad. Stab. 96 (2011) 175-182.
[17] L. Jiang, M. P. Wolcott, J. Zhang, Biomacromolecules 7 (2006) 199-207.
[18] H. Li, M. A. Huneault, J. Appl. Polym. Sci. 122 (2011) 134-141.

Advanced Materials Research Vol. 970 (2014) pp 317-319

doi:10.4028/www.scientific.net/AMR.970.317

Quasi-Static Indentation Behaviour of Glass Fibre Reinforced Polymer

S.M.S. Azwan[a*], YAZID Yahya[b], AMRAN Ayob[c], B. Abdi[d]

Centre for Composites (C*f*C), Faculty of Mechanical Engineering,

Universiti Teknologi Malaysia, 81310 UTM Skudai, Johor, Malaysia

[a*]mr.syedmohd@yahoo.com, [b]yazid@fkm.utm.my, [c]amran@fkm.utm.my, [d]behzad.abdi@gmail.com

Keywords: Indentation, Quasi-static, Glass fibre reinforce polymer

Abstract. Fibre reinforced polymer (FRP) plates subject to quasi-static indentation loading were studied. The plates were fabricated from three layers of chopped strand mat glass fibre and polyester resin using vacuum infusion process. Indentation tests were conducted on the plates with loading rates of 1 mm/min, 10 mm/min, 100 mm/min and 500 mm/min using a hemispherical tip indenter with diameter 12.5 mm. The plates were clamped in a square fixture with an unsupported space of 100 mm × 100 mm. The loads and deflections at the indented location were measured to give energy absorption-deflection curves. The results showed that the loading rate has a large effect on the indentation behaviour and energy absorbed.

Introduction

FRP structures are normally used in the marine and aerospace industry due to excellent specific quasi-static properties [1]. The most common types are carbon fibre reinforced polymer (CFRP) and glass fibre reinforced polymer (GFRP) where the most important features are high tensile, shear and bending strength, high stiffness and fatigue resistance [1]. However, it is recognized that polymer composites do not have good resistance to dynamic loads, especially to low velocity impact. Low velocity impact is an important issue for composite structures.

Many researches have been conducted and they focused on the impact loading to identify the damage mechanisms occurring in the material [2]. According to Davies et al. [3] it is possible to use quasi-static indentation results to predict the low velocity impact resistance of some materials. The results from related studies are also consistent with Davies' findings.

Previous studies have found that the shape of the tip of the indenter has influence on the indentation response in terms of indentation at failure, energy absorption and damage area [4]. Other studies had focussed on the effect of indenter diameter, impact energy and sandwich panel configuration parameters, on the impact behaviour and resulting damage, using numerical and experimental methods [5-7].

Instead of low velocity impact loading, the quasi-static indentation loading can be used to determine the impact response of composite materials. Therefore, in this study, GFRP plates were investigated using quasi-static indentation by a rigid and hemispherical tip indenter. The loading rate was set to 1 mm/min, 10 mm/min, 100 mm/min and 500 mm/min.

Experimental Procedures

In this study, GFRP plates were fabricated with three layers of chopped strand mat glass fibres. Dry glass fibre reinforcement was laid up in a mould and then resin was driven into a dry laminate using a vacuum pressure. After vacuuming was completed, the specimen was left to cure for 1 day. Fifteen specimens were prepared for the quasi-static indentation test. The overall dimension of the specimens was 100 mm × 100 mm and total thickness of 2 mm. Quasi-static indentation tests were carried out on a 100 kN Instron universal testing machine at loading rates of 1 mm/min, 10 mm/min, 100 mm/min and 500 mm/min. The indenter had a hemispherical tip with diameter 12.5 mm. The edges of the specimens were supported in a square fixture measuring 100 mm × 100 mm. Each test was repeated three times to ensure the repeatability of the tests and to minimize experimental error due to human error.

Results and Discussions

To determine the mechanical properties of GFRP, dog bone specimens with dimensions 15 mm wide and 100 mm gauge length were prepared and tensile tested at a constant loading rate of 1 mm/min. The Young's modulus E, Poisson's ratio v, failure stress σ_F and failure strain ε_F, are extracted from the stress-strain curve as shown in Fig. 1 and the values are tabulated in Table 1.

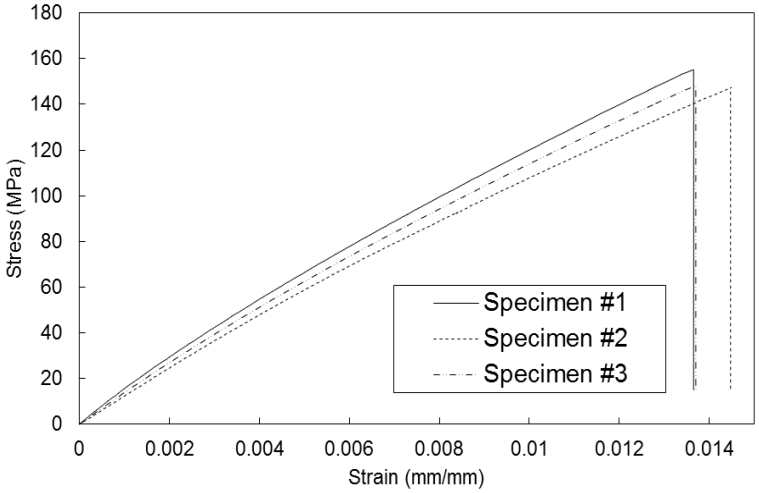

Figure 1. The stress-tensile curves of GFRP specimens

Table 1. Mechanical properties of GFRP

$E(Gpa)$	v	$\sigma_F(Mpa)$	ε_F
15.75	0.22	154.1	0.0136

From Fig. 2, increasing the loading rate from 1 to 10 mm/min, 10 to 100 mm/min and 1 to 500 mm/min, the maximum failure load increases up to 6.46%, 19% and 20.92%, respectively. However, the maximum failure load was decreased by 4.8% when the loading rate was increased from 100 to 500 mm/min.

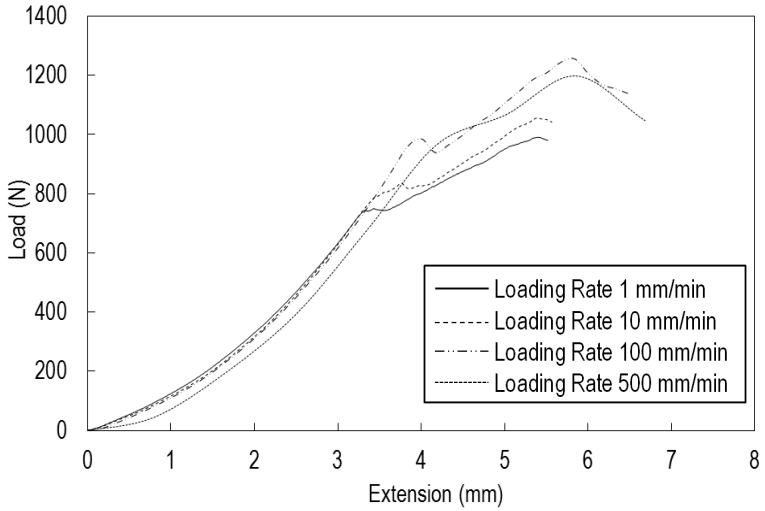

Figure 2. Load-extension curves of GFRP at different loading rate

From Fig. 3, increasing the loading rate from 10 to 100 mm/min and 1 to 500 mm/min, the energy absorption absorbed increases by 4.0%, 44.49% and 47.62%, respectively. However, the energy absorption was decreased by 1.78% when the loading rate was increased from 100 to 500 mm/min. The results from Fig. 2 and 3 confirm that the loading rate has a large influence on the indentation behaviour of GFRP.

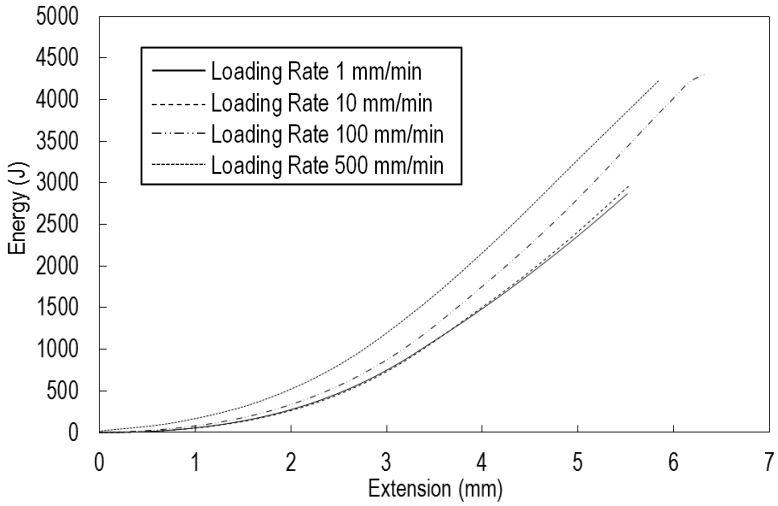

Figure 3. Energy absorption-extension curves of GFRP at different loading rate

Conclusions

GFRP plates were subjected to quasi-static indentation loading and then characterised. Load-extension curves were plotted to identify the behaviour, maximum failure load and energy absorbed by the GFRP. It has found that the loading rate has a large effect on the indentation behaviour of GFRP.

Acknowledgements

The authors are grateful for the financial support from the UTM Research University Grant (Grant No. Q.J130000.2624.07J19), the Centre for Composites (C*f*C) for their support and the awards of UTM Zamalah Scholarship (Syed Mohd Saiful Azwan Syed Hamzah).

References

[1] C. Soutis, Carbon fibre reinforced plastics in aircraft construction, Mater. Sci. Eng. A412 (2005) 171-176.

[2] G. Schoeppner, S. Abrate, Delamination threshold loads for low velocity impact on composite laminates, Compos. A: Appl. Sci. Manuf. 31 (2000) 903-915.

[3] G.A.O. Davies, X. Zhang, Impact damage prediction in carbon composites structures, Int. J. Impact Eng. 16 (1995) 149-170.

[4] E.A. Flores-Johnson, Q.M. Li, Experimental study of the indentation of sandwich panels with carbon fibre-reinforced polymer face sheets and polymeric foam core, Compos. B: Eng. 42 (2011) 1212-1219.

[5] J. Wang, A.M. Waas, H. Wang, Experimental and numerical study on the low-velocity impact behavior of foam-core sandwich panels, Compos. Struct. 96 (2013) 298-311.

[6] D. Ruan, G. Lu, Y.C. Wong, Quasi-static indentation tests on aluminium foam sandwich panels, Compos. Struct. 92 (2010) 2039-2046.

[7] S. Zhu, G.B. Chai, Damage and failure mode maps of composite sandwich panel subjected to quasi-static indentation and low velocity impact, Compos. Struct. 101 (2013) 204-214.

Advanced Materials Research Vol. 970 (2014) pp 320-323

doi:10.4028/www.scientific.net/AMR.970.320

Rheological Behavior Characterization of Natural Rubber Containing Different Gel

Saengchao Thongseenuch[1,a*], Wirach Taweepreda[1] and Krisda Suchiva[2]

[1]Department of Materials Science and Technology, Faculty of Science, Prince of Songkla University, 90112 Hat-Yai, Songkhla, Thailand

[2]Department of Chemistry, Faculty of Science, Mahidol University, 10400, Rama 6 Road, Bangkok, Thailand

[a*]saengchao.t@psu.ac.th

Keywords: Natural rubber, molecular structure, gel, first harmonic rheological properties

Abstract. This research, natural rubber containing different gel contents were prepared by deproteinization and saponification treatment from high ammonium natural rubber latex. Deproteinization natural rubber was further treated as acetone extraction and then transesterification. It was founded that gel content and molecular weights of treated natural rubber were decreased and almost absented for transesterification treatment. Rheological respond on small amplitude oscillating shear (SAOS) and large amplitude oscillating shear (LAOS) deformation of treated natural rubber were captured by using rubber process analyzer (RPA 2000). Firs harmonic rheological properties, storage modulus, G′ and loss modulus, G″ decreased as gel content and molecular weight decreased. It was believed that gels, explicitly branching points, were destroyed after the natural rubber was deproteinized, transesterification, or saponification according to the molecular structure of natural rubber presumed by Tanaka et al, which functional groups contain protein and fatty acid are participated in branching to forming gel structure. It was concluded that gel content as the same as molecular structure of natural rubber could be characterized as rheological behavior.

Introduction

Process ability and rheological properties of natural rubber (NR) are controlled by molecular structure, molecular weight (MW), molecular weight distribution (MWD), cross linked or gel fraction. The effects of MW, MWD and gel fraction on rheological and processing properties of NR have been extensively studied. However, the effects of molecular structure of NR on rheological behavior have been less well understood–since the molecular structure of NR has not been fully characterized even today. Tanaka and co-workers had made significant contribution in the elucidation of the molecular structure of NR [1–7]. They proposed that the gel phases of rubber, the so-call soft-gel, are consisted of two kinds of branching points located at the terminals of rubber chains. One is promoted of hydrogen bonds of proteins and the other is concerned with phospholipids. The former branching points can be broke after deproteinization of latex while as the later branching points are decomposed after transesterification. Saponification of NR decomposes both proteins and phospholipids. After the branching points in gel are destroyed, linear rubber chains are carried out. So that rheology of natural rubber is modified. Tanaka's study, however, was based on the uses of model compounds, chemical analysis and NMR spectroscopy.

Therefore present study interested to characterize the rheology behaviors of natural rubber containing various gel contents for verifying Tanaka's proposed molecular structure of NR by measuring rheological properties of NR using the technique of dynamic rheometry. It was believed that the study will contribute to better understanding of the molecular structure of NR and rheometry measured on small and large amplitude oscillatory shear by using rubber process analyzer was effective rheometer to characterize the natural rubber.

Materials and methods

Materials. The NR samples contain various gel contents were prepared from HA latex, chemical and enzymatic treatment of HA latex. Solid Natural Rubber (HANR) was prepared by casting HA latex in glass plate, and then allows it dried at room temperature. Deproteinized natural rubber (DPNR) was prepared from 30% drc latex by proteolytic enzyme treatment at 37 °C for 24 hours then latex was centrifuged at 13,000 rpm for 30 min. The cream was then allow to dried, or re-dispersed in distilled water for preparation saponification deproteinized natural rubber (DPSAP) by treated with NaOH as the same as HASAP was prepared from HA latex. Dried DPNR was acetone refluxed 48 hours then DPAE was subjected to dissolve in toluene for sodium methoxide treatment resulting transesterification rubber (DPAETE). NR samples then were subjected to clarify molecular weight and gel content.

Rheological Behavior Characterization. The effects of gel content to rheological properties of rubber were characterized by rubber process analyzer (RPA 2000). Frequency sweep subtests were carried out at 2 degree strain at 80, 100, 120, 140 and 160 °C SAOS. Strain sweep subtests were operated at frequency of 1 Hz at 120 °C for LAOS.

Results and discussion

After the rubbers were treated by chemical and enzymatic, it more flexibility than untreated NR since it was believed that their molecular weight and gel content were decreased as Tanaka and coworker proposed model [1]. The trend of molecular weight, molecular weight distribution MWD of sol fraction characterized by GPC and Ubbelohde viscometer, gel content were shown in Table 1. It was shown that haft gel content reduced after saponification treatment and almost absent for transesterification the same as reported [5]. Since rubber particle state in latex, deproteinization and saponification was not completely carried out. It was seen that although gel content of DPNR and HANR were same nevertheless molecular weight were differentiate. More over molecular of HASAP, DPSAP and DPAETE almost the same however contained different gel content. This believed that rubber samples except DPAETE remained branched structure but different in level.

Table 1 Molecular weight, molecular weight distribution of sol fraction, and gel content of whole and purified natural rubbers.

	Mn [10^5 g/mol]	Mw [10^5 g/mol]	Mv [10^5 g/mol]	Mw/Mn	Gel Content %
HANR	1.28	10.09	10.49	7.87	42.72
DPNR	1.24	7.98	6.33	6.43	42.76
DPAE	1.68	6.86	4.41	4.09	27.96
HASAP	1.09	4.13	2.86	3.78	21.45
DPSAP	1.32	5.14	2.72	3.88	18.63
DPAETE	1.04	4.12	2.63	3.97	0.33

Storage moduli G′ and Loss moduli G″ master curves at 120 °C constructed base on time-temperature superposition principle at of each rubber obtained from the measuring were exposed in Fig. 1. It clearly to classify them into two groups, one it seem less responded to frequency but obviously responded to temperature and another extremely took action to temperature or frequency. It was expected that former laid in the beginning of terminal zone onset and another position in terminal zone or rubbery flow region already. Hence onsets of plateau region of treated natural rubber occur at higher frequency or behaved as rubber material at lower temperature. It could explained that the rubber having higher molecular weight or more branching points better and longer stand the constrain than rubber having lower molecular weigh or branching points. It was supposed that molecular structure of natural rubber, i.e. branching points, were destroyed after treatments. Comparison to Abdel-Goad and collaborator reported rheological properties of 1, 4-

polyisoprene over a large molecular weight range it found that plateau zone of higher molecular weight molecule longer than of lower molecular weight molecule [8].

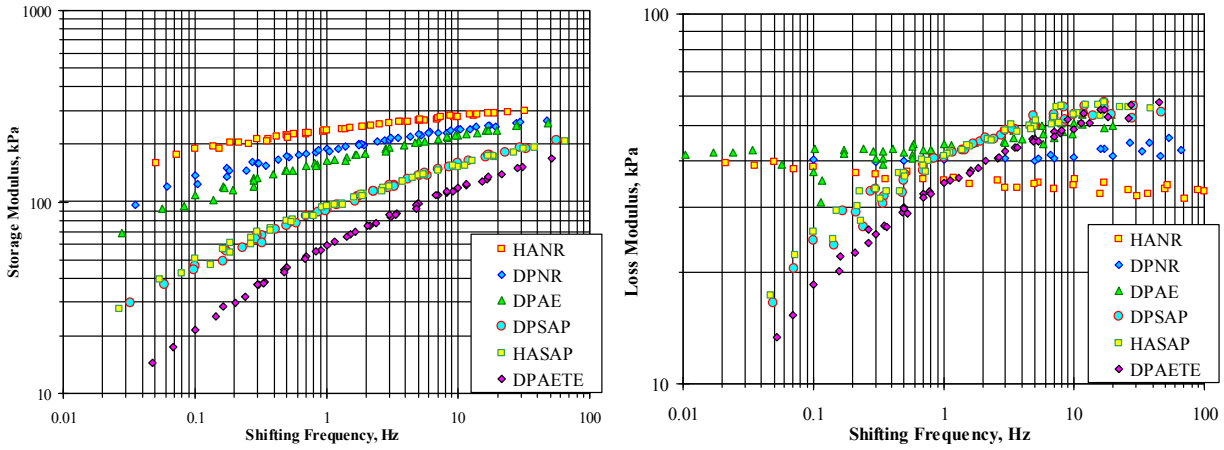

a b

Figure 1 G′ (a) and G″ (b) master curves at 120 °C of untreated and treated natural rubbers.

Fig. 2 demonstrated firs harmonic storage moduli G′ and loss moduli G″ flow curves measured at 120 °C, frequency of 1 Hz of untreated and treated natural rubbers. It was clearly seen that the firs harmonic G′ and G″ decreased as molecular weight of sol rubber, gel contents, and perhaps branching points decreased as mention in Table 1 since mobility of rubber molecules were increased. Such an experimental result showed the flow feature of rubber under large oscillatory shear strain reveal the molecular weight, gel content also branching points and perhaps include the branching points that reduced as Tanaka et al proposed after the rubber samples were treated [1, 5].

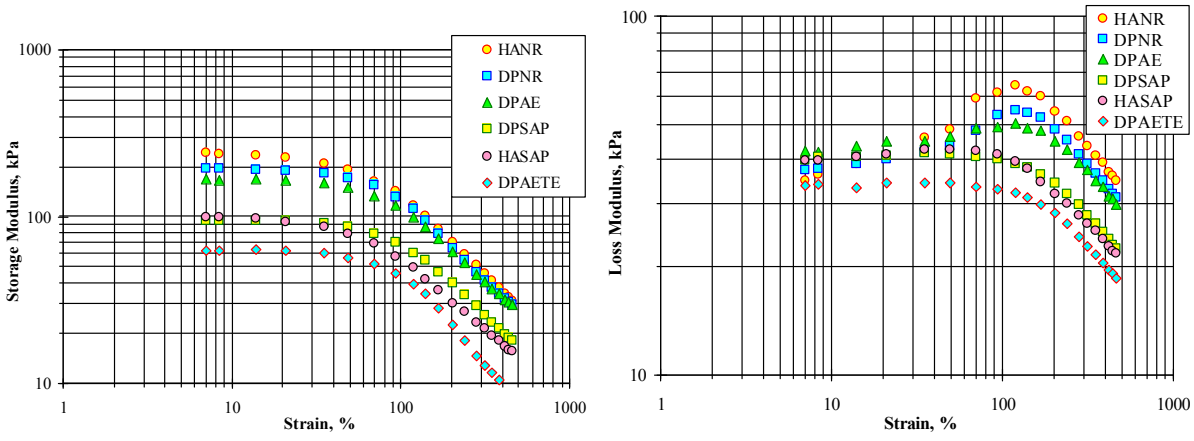

a b

Figure 2 First harmonic G′ (a) and G″ (b) flow curves measured at 120 °C, frequency 1 Hz of untreated and treated natural rubbers.

Conclusion

Gel content of solid natural rubber was successfully reduced by chemical treatment of HA latex, however the efficiency of gel decrement depended on treatment method. Rheological behavior of solid natural rubber changed after rubber samples were treated and it correlated with gel content. For all result indicated that the molecular structure which believed that gels, explicitly branching points, were destroyed after the natural rubber was deproteinized, transesterification, or saponification and maybe as Tanaka proposed and it could be characterized by using the technique of dynamic rheometry since it was effective tool that sensitive enough to detect structural difference even on the nanometer scale. Thus this result filled up the knowledge in natural rubber structure. Consequently, rheology of natural rubber could be controlled by adjusting the level of gel content. In addition dynamic rheometry was useful device for characterization the natural rubber.

Acknowledgements

The author would like to thank Prof J.L. LeBlanc, IFOCA institute, France that very kind for laboratory facility experiment especially advance rubber process analyzer and inform the author analyst rheology of the rubber. The author also thanks Asst. Prof. Toranith Navarattana, Prof J.L. Leblanc's student that they very kind to help during lived and did research in Paris, France.

References

[1] Y. Tanaka, Structural Characterization of Natural Polyisoprenes: Solve the Mystery of Natural Rubber Based on structural Study, Rubber Chem. Techno. 74 (2001) 335-375

[2] Y. Tanaka, and J.T. Sakdapipanich, Chemical Structure and Occurrence of Natural Polyisoprene, Biopolymers Online. 2005

[3] Y. Tanaka, S. Kawahara, and J. Tangpakdee, Structure Characterization of Natural Rubber, Kautsch. Gummi Kunstst. 50 (1997) 6-11

[4] J. Tangpakdee, and Y. Tanaka, Branching in Natural Rubber, J. Polym, Sci. 62 (1998) 14-21

[5] J. Tangpakdee, and Y. Tanaka, Purification of Natural Rubber, J. Nat. Rubber Res. 12 (1997) 112-119

[6] A. H. Eng, A. Kawahara, and Y. Tanaka, Tran-isoprene units in natural rubber, Rubber Chem. Technol. 67 (1994) 159-168

[7] J. Tangpakdee Sakdapipanich, Structural Characterization of Natural Rubber Based on Recent Evidence from Selective Enzymatic Treatments, J. Bioscience and bioengineering. 103 (2007) 287-292

[8] M. Abdel-Goad, W. Pyckhout-Hintzen, S. Kahle, J. Allgaier, D. Richter, L.J. Fetters, "Rheological Properties of 1,4-Polyisoprene over a Large Molecular Weight Range". Macromolecules, 37 (2004) 8135-8144

Advanced Materials Research Vol. 970 (2014) pp 324-327

doi:10.4028/www.scientific.net/AMR.970.324

Surface Modification of Poly (lactic acid) (PLA) via Alkaline Hydrolysis Degradation

C.Y. Tham, Z. A Abdul Hamid [1,a*] , Z. Ahmad[1], H. Ismail[1]

[1]School of Materials and Mineral Resources Engineering, Universiti Sains Malaysia, Seri Ampangan 14300 Nibong Tebal Seberang Perai Selatan Pulau Pinang, Malaysia

[a*]srzuratulain@eng.usm.my

Keywords: Poly (lactic acid), alkaline hydrolysis, surface modification, hydrophilicity

Abstract. Surface hydrophobicity of poly(lactic acid) have raise the concerns of surface incompatibility of PLA to function as biomaterial. Thus, various approaches have been made to improve the surface hydrophilicity of PLA. In the present paper, PLA materials were surface modified by alkaline hydrolysis. The indication of the reduction in water contact angle value, from 65˚ to 50˚ and 15˚, in 0.01M and 1M alkaline concentration respectively, proven surface hydrophilicity of PLA film was improved. Further alkaline treatment after 24 hours shows not significant reduction in contact angle. Whereas, the erosion of film surfaces treated under 1M alkaline solution have been observed under polarized optical microscopy. Intrinsic viscosity measurement was also conducted to monitor the surface treatment process. As a whole, surface treatment was successful and sufficient when no further decreased in contact angle value, thus prevent extensive surface erosion.

Introduction

Surface properties are crucial to the physical, chemical and biological interactions between materials and external environment. Materials surface modification was a simple approach to change the nature of surface properties to suit the application without depending on the development of new materials [1]. Poly (lactic acid) (PLA), a biomaterials that have combination of biocompatible, biodegradable and bioresorbable properties [2].

In this paper, the biocompatibility of PLA surfaces has been concern. The compatibility of materials in biological environment is actually been categorized to, bulk and surface. Undoubtedly, PLA was biocompatible in bulk, which is not readily produces toxic biodegradation products. However, surface properties of PLA relatively incompatible, that particularly due to the hydrophobic properties of PLA surfaces [3,4]. PLA have relative hydrophobic surfaces with approximate 80˚ of static water contact angle and surface chemically inert because lacking of reactive side-chain groups [2]. Possible drawback in application, e.g. hydrophobic surfaces would elicit inflammatory response in contact with living host in biomedical usage and chemically inert brings difficulty in surface modification [3,5].

Indeed, highly precise technologies, such as plasma and photo-induced grafting have been concomitantly revealed to improve the hydrophilicity of PLA material's surfaces [3]. However, those techniques are usually operated under certain critical conditions, with have potential to deteriorate the polymer properties, and might affect the quality of any encapsulated bioactive molecules in PLA. Current paper, alkaline-catalyzed hydrolysis was selected to modify PLA material's surfaces due to their advantages in simple and minimum chemicals usage. This method has been widely used to modify polyester textile to improve the comfort of clothes by increase the surface hydrophilic properties [6]. The basic concept was to induce alkaline as catalytic agent, to hydrolyze the ester linkages on PLA backbone chains. The cleavage of ester linkage will eventually to produce carboxylic and hydroxyl end-groups on polymer chains (Fig. 1) [7,8]. As this process occurred, the molecular weight of modified PLA was expected to be lower than original PLA [9].

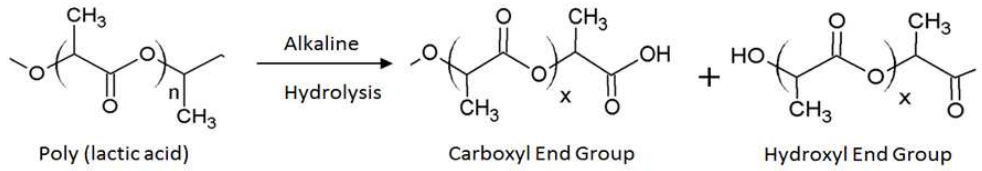

Fig 1: The hydrolysis of ester bond in PLA backbone chains created new end group, carboxyl and hydroxyl end group [10]

This research was attempted to improve the surface hydrophilicity of PLA by immersing the PLA into alkaline-catalyze aqueous solutions. Hypothesis taken in this method, the ester functional group on PLA chains can be cleavage through alkaline hydrolysis accompany by certain level of polymer degradation. From the results obtained in this research, we have also proposed that the mechanism of alkaline hydrolysis on PLA was in surface erosion mode.

Material and Methodology. Poly (lactic acid) films were prepared from PLA resin (M_w 7.40x10^6 g/mol, 3001D NatureWork) by hotpress moulding. 20 g of PLA resin was weighted and preheated on a stainless steel mold (120 x 100 x 0.7 mm) at 180 ˚C for 7 minute. The preheated resin pallet was compressed by a hydraulic compressor for 3 minutes at 180 ˚C. The mold with PLA films was then cooled to room temperature by pressing in a water jacketing compressor for 3 minutes. Subsequently, the PLA film was cut into smaller films (30 x 20 mm) by using a straight head cutter. The films were washed by ethanol prior immersed in sodium hydroxide (supplied from Merck) solution at 0.01 and 1 Molar, respectively. The duration of surface treatment was in time interval of 3, 6, 24, 48, 72, and 96 hours. Surface treated films were washed for 5 times with distilled water after sample collection and dried in desiccator for 1 week.

Surface Wettability Test. The characteristic of surface treated PLA films was measured by using Dynamic Contact Angle and Tensiometer (DCAT) (dataphysics, model-DCAT 11). The contact angle of PLA films with water medium was measured according to the Wilhelmy plate method.

Viscosity Test. The intrinsic viscosity (η) of surface treated PLA was measured by using polymer viscometer (Rheotek RPV-1 Viscometer, Ubbelohde tube) in 25 ˚C oil bath. PLA solution was prepared in dichloromethane (supplied from Merck) with concentration of 0.1, 0.2, 0.3 and 0.4 g/dL from each control and surface treated PLA films. Reduced viscosity was calculated and plotted against the concentration of PLA solution. Intrinsic viscosity was obtained from the y-intercept by extrapolation of the graphs to zero concentration. The relation between intrinsic viscosity and molecular weight was discussed according to $[\eta]= KM^a$ where K and a, was polymer-solvent pair constant [11].

Optical Microscopy. Surface treated PLA film was observed under polarizing microscopes (MEIJI Techno, MT9900 series) without further sample preparation after washed with ethanol.

Results and Discussion

The surface hydrophilic property of modified PLA was evaluated by the measurement of water contact angle. Low contact angle indicate that the interaction of material and water molecules was high, in other words the hydrophilicity of surfaces was high. From Fig. 2, the water contact angle of PLA films decreased from 65˚ to approximately 50˚ and 15˚, after 0.01M and 1M alkaline treatment respectively. It was observed that the contact angle obtained for both concentrations were reached equilibrium after 24 hours treatment without further significant reduction. The reduction of water contact angle indicated the alkaline hydrolysis was successfully improved the surface hydrophilicity of PLA films. Croll T.I. *et. al* (2004) have suggested that at equilibrium stage, the rate of removal of soluble hydrolyzed products (e.g. monomers and oligomers) equal to the rate of generation of new end groups in treatment medium.

Further evaluation of PLA molecular weight (MW) was done by measuring the intrinsic viscosity (IV) of modified PLA. Polymer with higher IV indicated higher MW. Results obtained (Fig. 2 b) was not under expectation which was expected to observe a reduction in IV as the treatment time increased. Polymer films treated from 0.01M alkaline solution tends to increase in intrinsic viscosity as treatment duration prolong. However, it shows a decreased value after 72 hours of treatment. Polymer films treated from 1M alkaline solution shows a dramatic change along the treatment duration.

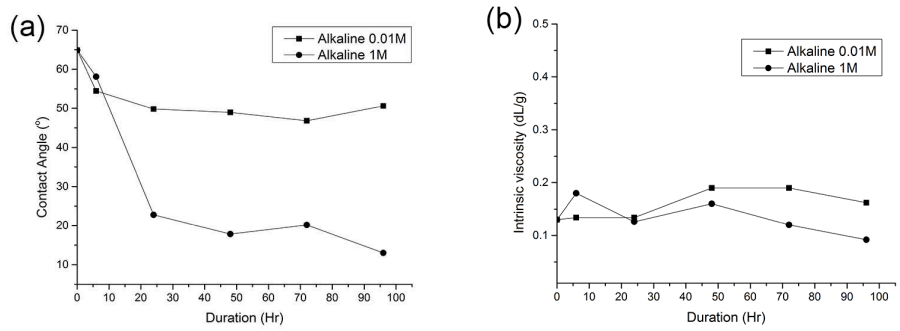

Fig 2: Measurement of (a) water contact angle and (b) intrinsic viscosity of PLA films

To give a clearer view of surface modification of PLA film, the surface morphology was observed by optical microscopic. As revealed in Fig. 3 (a & b), as compared the surfaces before and after 6 hrs of treatment, 0.01M alkaline treatment shows similar to original, while 1M alkaline treatment seems caused extensive degradation on surfaces which leads to the formation of new rough surfaces.

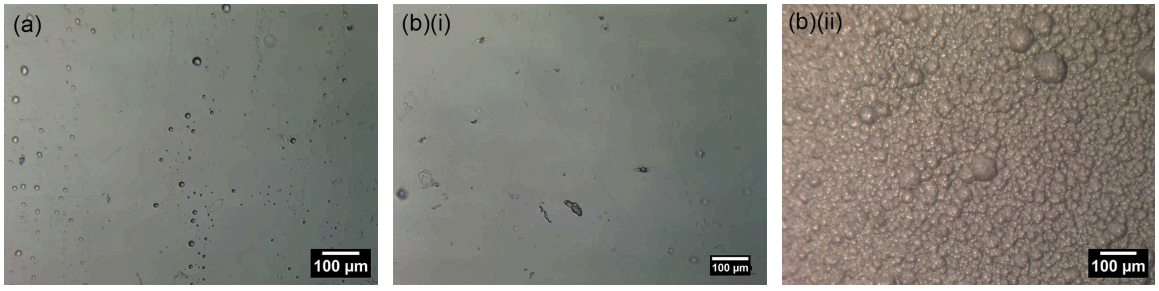

Fig. 3: Observation from optical microscope on PLA film surface (a) before and (b) after 6 hours treated in (i) 0.01M and (ii) 1M of NaOH solution.

From the results, we proposed that surface erosion of PLA occurred in the surface modification. The term, “degradation” in polymer describes the chain scission process of polymer to form oligomer and monomer. While degradation in the erosion mode, was defined as conditions of losing material owing to monomer or oligomer leaving polymer in the process of degradation [13]. In current works, the loss of materials from surfaces leads to the formation of rough surface morphology (Fig. 3b ii). In alkaline treatment, the ester bonds cleavage would produce lower molecular weight (MW) substances (e.g. lactic acid oligomer and monomer) which containing hydrophilic end group [13,14]. However, the reduction in molecular weight was not able to be observed in intrinsic viscosity measurement (Fig. 2 b). This results have proven the low MW substances was diffuse or dissolute from surfaces to the treatment medium [13,14]. The continuous dissolution of the low MW substance might causing the hydrophobicity or water contact angle not being able to further decrease along the treatment period. Hence, surface treatment of PLA should be terminated when there was not further decrease in contact angle value, and it also preventing extensive surface erosion that able to affect PLA properties.

Summary

From this works, alkaline-catalyzed hydrolysis was proven to be useful in modified the hydrophilicity of PLA surfaces. High alkaline concentration solution is more effective in reducing the water contact angle of PLA surface which indicated larger improvement in hydrophilic properties as compared to low alkaline concentration solution. However, the reduction in water contact angle will eventually reached an equilibrium stage where not further reduction observed even treatment duration prolong. In addition, surface erosion was observed on PLA modified with 1 M alkaline (high) concentration as treatment duration prolong. As a whole, alkaline-catalyzed hydrolysis can become an options surface modification PLA, and the modification process can be considered as optimum when the water contact angle of polymer shows no further reduction.

Acknowledgement. Authors would like to thank Universiti Sains Malaysia for the financial support for this works (Research University Individual Grant (RUI) 1001/PBAHAN/814201).

References:

[1] Y. Ikada, Surface modification of polymers for medical applications. Biomater. 15(1994) 725-736.
[2] R.M. Rasal, A.V. Janorkar, and D.E. Hirt, Poly(lactic acid) modifications. Prog. Polym. *Sci.* 2010. 35(2010) 338-356.
[3] Y.P. Jiao and F.Z. Cui, Surface modification of polyester biomaterials for tissue engineering. Biomed. Mater. 2(2007) R24-37.
[4] P. Roach, D. Eglin, K. Rohde, and C.C. Perry, Modern biomaterials: a review—bulk properties and implications of surface modifications. J. Mater. Sci.: Mater. Med. 18(2007) 1263-1277.
[5] S. Wang, W. Cui and J. Bei, Bulk and surface modifications of polylactide. Anal. Bioanal. Chem. 381(2005) 547-556.
[6] S. Natarajan and J.J. Moses, Surface modification of polyester fabric using polyvinyl alcohol in alkaline medium. Indian J. Fibre Text. 37(2012) 287-291.
[7] J.S. Wiggins, M.K. Hassan, K.A. Mauritz, and R.F. Storey, Hydrolytic degradation of poly(D,L-lactide) as a function of end group: carboxylic acid vs. hydroxyl. Polym. 47(2006) 1960-1969.
[8] G. Schliecker, C. Schmidt, S. Fuchs, R. Wombacher, and T. Kissel, Hydrolytic degradation of poly (lactide-co-glycolide) films: effect of oligomers on degradation rate and crystallinity. Int. J. Pharm. 266(2003) 39-49.
[9] H. Tsuji and Y. Ikada, Properties and morphology of poly(L-lactide). II. hydrolysis in alkaline solution. J. Polym. Sci. A Polym. Chem. 36(1998) 59-66.
[10] C.F.V. Nostrum, T.F.J. Veldhuis, G.W. Bos, and W.E. Hennink, Hydrolytic degradation of oligo(lactic acid): a kinetic and mechanistic study. Polym. 45(2004) 6779-6787.
[11] D.C. Hylton, Understanding Plastic Testing, first ed., Hanser, Munich, 2004
[12] T.I. Croll, A.J. O'Connor, G.W. Stevens and J.J. Cooper-White, Controllable surface modification of poly(lactic-co-glycolic acid)(PLGA) by hydrolysis or aminolysis I: physical, chemical, and theoretical aspects. Biomacromolecules. 5(2004) 463-473.
[13] A. Göpferich, Mechanisms of polymer degradation and erosion. Biomater. 17(1996)103-114.
[14] G. Schliecker, C. Schmidt, S. Fuchs, and T. Kissel, Characterization of a homologous series of D,L-lactic acid oligomers; a mechanistic study on the degradation kinetics in vitro. Biomater. 24(2003) 3835-3844.

Advanced Materials Research Vol. 970 (2014) pp 328-331

doi:10.4028/www.scientific.net/AMR.970.328

The Effect of Wollastonite Filler on Thermal Performance of Intumescent Fire Retardant Coating

M. Zia-ul-Mustafa[1,a*], Faiz Ahmad[1,b], Puteri S.M. Megat-Yusoff[1,c] and Hammad Aziz[1,d]

[1]Mechanical Engineering Department, Universiti Teknologi PETRONAS, Bandar Seri Iskandar, 31750 Tronoh, Perak, Malaysia

[a*]engr.ziamustafa@gmail.com, [b]faizahmad@petronas.com.my, [c]puteris@petronas.com.my, [d]engr.hammad.aziz03@gmail.com

Keywords: Intumescent coating, Wollastonite, Thermal performance, Char morphology, Char composition.

Abstract

Various types of intumescent fire retardant coatings (IFRC's) have been used to protect the substrates exposed to fire. In current study, high temperature filler Wollastonite (W) filler was used to improve fire performance of intumescent fire retardant coating. The basic ingredients of the coating were ammonium poly-phosphate (APP) as acid source, expandable graphite (EG) as carbon source, melamine (MEL) as blowing agent in epoxy binder, boric acid as additive and hardener as curing agent. In this study a range of coating formulations were developed by using different weight percentages of Wollastonite filler. The coated steel substrate samples were tested for fire performance using Bunsen burner and char expansion was measured using furnace fire test. Composition of the char was determined by X-ray diffraction (XRD) technique. The char morphology was studied using field emission scanning electron microscopy (FESEM). Results showed that Intumescent coating with addition of Wollastonite filler enhanced anti-oxidation of the char. Presence of phosphorus, calcium and silicon in char layer further improved the thermal stability of char.

Introduction

Structural steel is the key element for buildings, due to its excellent strength. The practice to adopt steel in construction of buildings is increasing progressively. The protection of steel structure has become necessary in all construction industries in many countries over the world [1]. The loadbearing capacity becomes half beyond the temperature of 550°C [2]. Intumescent coating is passive fire protection system, which is used to safe steel in case of fire [3].

Fire retardant coating is one the simplest and the oldest way to protect the substrate in case of fires [4]. IFRC's are formulated so that steel can maintain its integrity from one to three hours, when the temperature of surroundings increases up to 1100°C. Fire retardant system mainly consists of three components [5]. Acid source is ammonium polyphosphate which acts as catalyst so that char can be formed in the early stages of fire; it reacts with carbonizing agent to form char. The carbon source is a carbonaceous material such expandable graphite which provide carbon so that char can be formed. The gas source is usually melamine which acts as blowing agent which causes the char to swell. All three components must show suitable matching thermal behavior [6].

The purpose of this work is to develop formulations using Wollastonite filler and to investigate the effect of Wollastonite filler towards the fire retardant performance of intumescent coating which can enhance the performance of intumescent coating so that the char can protect the substrate at higher temperature.

Materials and Method

The formulations prepared are listed in Table 1.

Table 1 Weight % of IFRC formulations

No	EG	APP	Mel	Boric Acid	Epoxy	Hardener	Filler
F	5.8	11.76	5.76	11.5	43.42	21.71	0
F1	5.8	11.76	5.76	11.5	42.76	21.38	1
F2	5.8	11.76	5.76	11.5	42.1	21	2
F3	5.8	11.76	5.76	11.5	41.42	20.71	3
F4	5.8	11.76	5.76	11.5	40.76	20.38	4
F5	5.8	11.76	5.76	11.5	40.16	20.09	5

Sample Preparation

Steel surface was sand blasted to remove unwanted materials like dirt, oil and rust from the surface.

All ingredients were accurately measured as listed in table 1. Ingredients were mixed using shear mixer at 40rpm for 30mins at room temperature. Coatings were applied on steel plates using conventional brush and thickness of coating was kept 2mm. The applied coatings were allowed to cure for two days at room temperature.

Results and Discussion

Bunsen burner Fire Test

Bunsen burner was used for laboratory scale fire test according to UL-94 standards. Samples were kept 7cm apart from Bunsen burner [7]. Steel substrate backside temperature was noted from Anarittsu Data logger, Input Channel 6 Model AM-8000K for 60mins fire test and was recorded after every min. F5 gave lowest substrate temperature 153ºC, following steel substrate backside temperature of F4 which gave 174ºC. Coating without filler showed backside temperature of 261ºC after 60mins fire test. Graph between time and substrate temperature is shown in Figure 1.

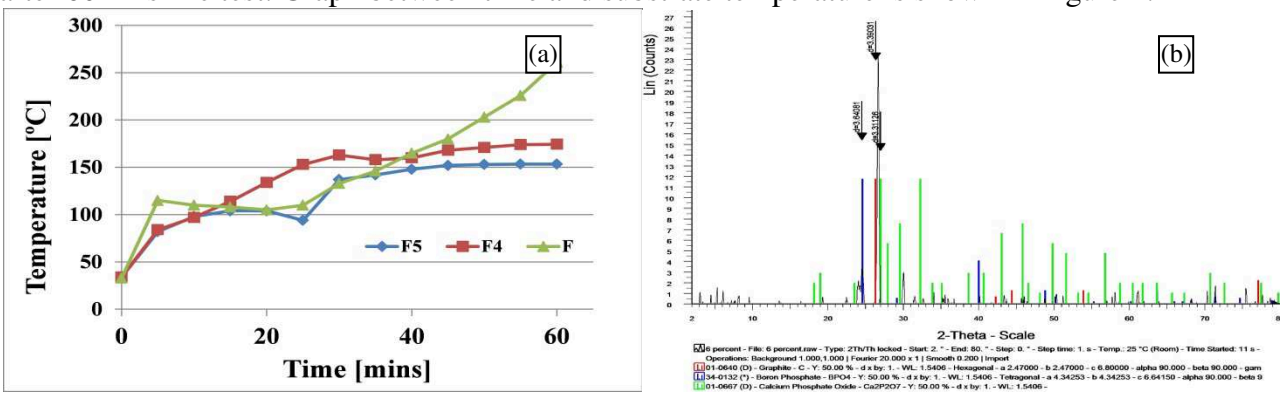

Figure 1: (a) graph showing time versus substrate temperature (b) XRD image for formulation F4

Expansion of Char

To analyze the physical properties of char such as char expansion and char structure after fire test, the IFRC's were burned in a Carbolite Furnace. Formulation F6 containing 6wt% showed highest expansion 6.95 times the original thickness. F4 and F5 gave 4.9 times and 3.2 times expansion than original thickness. So this proved addition of filler has given char expansion up to certain limits. Further samples were analyzed by FESEM to observe the micro structure.

Field Emission Scanning Electron Microscopy (FESEM)

FESEM results for 0wt. %, 4wt. % and % 5wt. % are shown in Figure 2. Figure 2(a, b) showed wormed like structure [8]. Actually EG is established in char structure in fibered fashion [9]. This structure increases resistance of char against deformation and act as function of fiber. Greater magnification in Figure 2(c, d) shows very compacted char structure. This compact char structure helps to hinder radiant heat transfer and flame transfer from source to substrate [10].

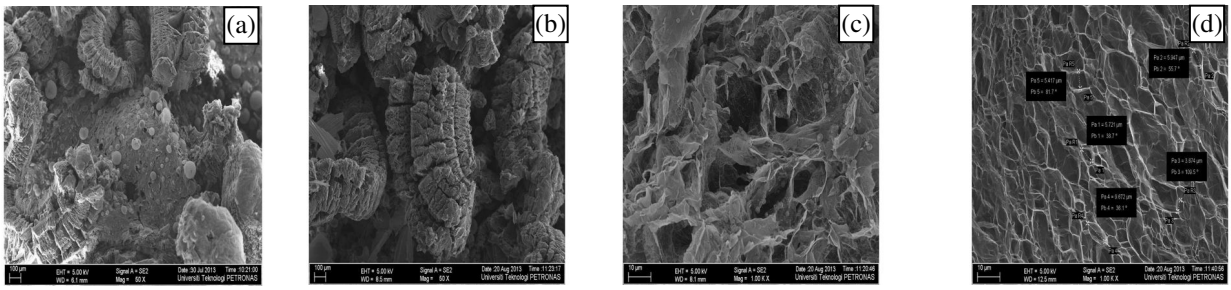

Figure 2: (a) FESEM images at lower magnification for IFRC's fibrous structure for formulation F (b) FESEM images at lower magnification for formulation F4 (d) FESEM images at higher magnification for IFRC's formulation F4 (e) FESEM images at higher magnification for formulation F5.

Average cell size distribution for F4 and F5 was 20µm and 11µm respectively. Bigger cell size distribution helps to retard heat transfer as inert gases released during combustion and entraps between these pores. But cell size should not be greater than 40 µm for effective heat, because it lead to heat transfer by convection mechanism [8].

EDX Analysis

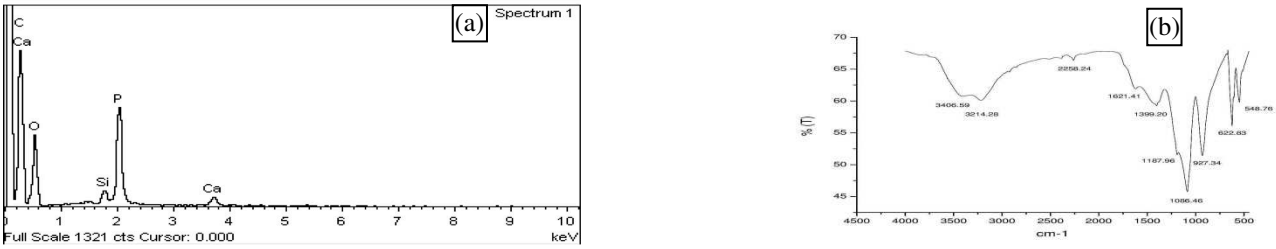

Figure 3: (a) EDX image for IFRC's for formulation F4 (b) FTIR image for IFRC's for formulation F4.

EDX images showed presence of phosphorus, calcium, carbon, oxygen and silicon elements. EDX analysis is shown in Figure 3(a).

X-Ray Diffraction (XRD)

After furnace test inorganic material and carbonaceous char left behind in the char. This residual weight increase anti-oxidation and provide shield at later stage of fire to the char. These char compositions were determined by XRD. These measurements were performed on a diffractometer Bruker AXS D8 Advance using Cu Kα radiation and a nickel filter (k = 0.150595 nm) in the range ($10° < 2\theta < 90°$). Figure 1 (b) Peak values 3.64, 3.31, 3.39 were assigned according to JCPDS card. Elements showing higher peaks in graph represent dominant elements in that sample. The peak at 3.64 showed boron phosphate. Peak at 3.64 was allocated to calcium phosphate oxide and peak at 3.39 was allotted to graphite. Graphite was dominant residue because of EG. XRD results showed boric acid, melamine APP, O2 and Wollastonite on reaction with each other enhanced anti-oxidation of the char. Boric acid in the char transformed into boron oxide and boron oxide reacted with APP and final product boron phosphate was formed. Boron phosphate is very stable compound up to 1200ºC [11].

Fourier Transform Infrared Spectroscopy (FTIR)

FTIR spectra were recorded using Shimadzu spectrometer in the range 4000-450 cm-1 with an ATR system. Samples were powdered, and 50 scans were run to obtain spectra with a fine signal-to-noise ratio. The char residues were examined with spectroscopic technique to analyze the mechanism of interaction among EG, W, APP, melamine, boric acid, epoxy, and the hardener. The FTIR spectrum for char samples which is without filler have bending peak at 3214.28 cm-1 which represents O-H group due to epoxy resin. The bending peak at 2258.24 cm-1 represents nitrile group. The bending peak at 1624.15 cm-1 represents amino group N-H. The bending peak at 1401.94 cm-1 represents C-C and some aromatic functional groups. From 1400-800 cm-1 represents P-O-P region, and phosphate is present at 932.83 cm-1. The bending peak at 625.57 cm-1

represents the B-O-P which is due to the presence of boron oxide and boron phosphate. When the coating was modified by using filler then bending peak at 548.76 cm-1 represents Si-O-Si bond which is due to Wollastonite present in coating forming silicon phosphate oxide compound. The bending peak at 927.34 cm-1 represents P-H bond due to APP. Bending peak at 622.83 cm-1 represents C-H bond. The bending peak at 1626.90 cm-1 represents N-H bond. These results showed good compatibility with those of the XRD analysis.

Conclusion

As the result, IFR coatings containing Wollastonite filler gave better results as compared to coating without filler. Among all formulation F5 was the optimized coating and gave best results than other formulations. Presence of boron phosphate, silicon phosphate oxide, graphite and calcium phosphate oxide enhance the anti-oxidation of the char and thermal stability of the char. Steel substrate backside temperature using 5% of Wollastonite was only 153ºC after 60 mins of fire test.

References

[1] M. Jimenez, S. Duquesne, S. Bourbigot, Modelling of heat transfers on a steel plate. First approach in presence of intumescent coating, in the proceedings of the COMSOL Multiphysics User's Conference, 2005.

[2] J. Rhys, Intumescent coatings and their uses, Fire Mater. 4 (1980) 154-156.

[3] R. Otáhal, D. Veselý, J. Násadová, V. Zíma, P. Nemec, P. Kalenda, Intumescent coatings based on an organic-inorganic hybrid resin and the effect of mineral fibres on fire-resistant properties of intumescent coatings, Pigm. Resin Technol. 40 (2011) 247-253.

[4] M. Wladyka-Przybylak, R. Kozlowski, The thermal characteristics of different intumescent coatings, Fire Mater. 23 (1999) 33-43.

[5] G. Wang, J. Yang, Influences of binder on fire protection and anticorrosion properties of intumescent fire resistive coating for steel structure, Surf. Coat. Technol. 204 (2010) 1186-1192.

[6] M. Jimenez, S. Duquesne, S. Bourbigot, Intumescent fire protective coating: toward a better understanding of their mechanism of action, Thermochim. Acta. 449 (2006) 16-26.

[7] D.P. Bentz, Fire Resistive Materials: Thermal Barriers between Fires and Structures, in the proceedings of Thermal Conductivity 30/Thermal Expansion 18: Joint Conferences August 29-September 2, 2009 Pittsburgh, Pennsylvania, USA, DEStech Publications, Inc. 2010, pp. 108.

[8] W.F. Mohamad, F. Ahmad, S. Ullah, Effect of Inorganic Fillers on Thermal Performance and Char Morphology of Intumescent Fire Retardant Coating, Asian J. Sci. Res. 6 (2013) 263-271.

[9] Z. Han, Y. Li, H. Zhao, An investigation on synergistic effect of EG with IFR in polyethylene, in 8th International Conference on: Properties and applications of Dielectric Materials, 2006. pp. 828-831.

[10] G. Wang, J. Yang, Influences of expandable graphite modified by polyethylene glycol on fire protection of waterborne intumescent fire resistive coating, Surf. Coat. Technol. 204 (2010) 3599-3605.

[11] S. Ullah, F. Ahmad, P. Yusoff, Effect of boric acid and melamine on the intumescent fire-retardant coating composition for the fire protection of structural steel substrates, J. Appl. Polym. Sci. (2012).

U

V

W

X

Y

Z

T

V

W

Y

Z